Thermophysics 2010

3rd to 5th November 2010
Valtice, Czech Republic
Brno University of Technology

Book cover design: Vladimír Dvonka, Michal Veselý
Printed by: Brno University of Technology, Faculty of Chemistry, 2010
ISBN 978-80-214-4166-8

Acknowledgment

Publication of this book was financially supported by the Czech Ministry of Education, Youth and Sports, under project No MSM 6840770031.

Committees

INTERNATONAL SCIENTIFIC COMMITTEE

Rachel Becker, Civil and Environmental Engineering, Technion, Haifa, Israel
Mark Bomberg, L.C. Smith College of Engineering and Computer Science, Syracuse University, Syracuse, U.S.A.
Robert Cerny, Faculty of Civil Engineering CTU, Prague, Czech Republic
Dariusz Gawin, Department of Building Physics & Building Materials, Technical University of Lodz, Lodz, Poland
John Grunewald, Faculty of Architecture, Dresden University of Technology, Dresden, Germany
Ulf Hammerschmidt, Physikalisch-Technische Bundesanstalt,Braunschweig, Germany
Hartwig M. Künzel, Fraunhofer-Institut für Bauphysik, Institutsteil Holzkirchen, Valley, Germany
Ludovit Kubicar, Institute of Physics SAC, Bratislava, Slovak Republic
Wahid Maref, National Research Council Canada, Ottawa, Canada
Peter Matiasovsky, Institute of Construction and Architecture SAC, Bratislava, Slovak Republic
Igor Medveď, Faculty of Natural Sciences, Constantine the Philosopher University, Nitra, Slovak Republic
Zbysek Pavlik, Faculty of Civil Engineering CTU, Prague, Czech Republic
Henryk Sobczuk, Faculty of Environmental Engineering, Lublin University of Technology, Lublin, Poland
Oldrich Zmeskal, Faculty of Chemistry BUT, Brno, Czech Republic

ORGANIZING COMMITTEE

Oldrich Zmeskal, FCH BUT, Brno, Czech Republic
Tomas Bzatek, FCH BUT, Brno, Czech Republic
Lenka Hrebenová, FCH BUT, Brno, Czech Republic
Zbysek Pavlik, FCE CTU, Prague, Czech Republic
Anton Trnik, FNS CPU, Nitra, Slovak Republic
Milena Pavlíková, FCE CTU, Prague, Czech Republic
Pavla Stefkova, FCH BUT, Brno, Czech Republic
Michal Vesely, FCH BUT, Brno, Czech Republic

Content

Some specific problems of thermophysics semiconducting materials

Ivan Baník, František Čulík, Jozefa Lukovičová

Department of Physics, Faculty of Civil Engineering, Slovak University of Technology,
Bratislava, Slovak Republic

***Abstract**: Semiconductors are characterized by an expressive dependence of electric conductivity on the temperature. This fact can be in principle used for measurement of thermophysical parameters by non-standard methods. Another specific factor of these groups of materials is high value of thermoelectric voltage permitting also a specific method of temperature recording in selected positions of a sample. In this article several methods are described and discussed suitable for measurement of thermophysical parameters those materials.*

***Keywords**: measuring methods, thermal parameters, semiconducting matters*

1. Introduction

We suggest some measurement methods of thermal transport parameters of semiconducting specimens in this article. These methods make use of an electric conductivity dependence on the temperature for recording a thermal pulse spreading through a sample after impulse local heating of the sample. For particular setting up the corresponding theoretical relations are introduced and used to determination of thermophysical parameters from data of particular measurement. The time of local extreme of active resistance is measured, when the thermal pulse spreading through the sample causes at a chosen position an extreme of active resistance. Onwards, we shall considerate a small change of the temperature ΔT , so it is assumed that in this case for resistivity ρ the relations

$$\rho = \rho_o (1 + \gamma \Delta T) \qquad (1)$$

is fulfilled, wherein the thermal coefficient γ is constant. Some simplifications were made in deriving theoretical relations e.g.: neglecting thermal losses by thermal radiation and heat conduction as well as by underlay. These factors in given experiment should be minimized. The other requirements are connected with finite sample dimensions as well as with an outlet of heat via instrument leads. Whenever, the conditions introduced in the work [1-3] should be respected.

2. Theoretical background of particular setting up

Set-up no 1

Set-up with Dirac heat pulse along a line segment and two nails detection. Fig. 1 shows layout chart. Steady direct current is passing through a sample so that current density in observed region is homogeneous. Probes 1 and 2 scan the voltage U_{12} between corresponding points. This voltage is compensated at beginning of measurement. Then, the sample undergoes an impulse heating along a line segment *p*. Owing to the heat spreading the compensated state of an apparatus of resistance is violated, because the resistance of the sample is changed by the change of temperature. Thermal diffusivity a of a thin plate (h – thickness, b – width) can be determined from known value of the time t_{ext} at which voltage U_{12} reaches an extreme value between probes 1 and 2 according to the relation

$$a = \frac{x_2^{\,2} - x_1^{\,2}}{4\, t_{ext} \ln\left(x_2/x_1\right)} \tag{2}$$

where x_1 and x_2 are distances of points 1 and 2 from thermal source p. For thermal conductivity λ the relation is valid Φ

$$\lambda = \frac{\rho_o Q'\gamma\, a}{2\,\Delta R_{ext} S}\left[\Phi(z_{2ext}) - \Phi(z_{1ext})\right] \tag{3}$$

where $\Phi(z)$ denotes the error function [1,4] and

$$z = \frac{x}{2\sqrt{at}},\; z_{ext} = \frac{x}{2\sqrt{at_{ext}}},\; z_{1ext} = \frac{x_1}{2\sqrt{at_{ext}}},\; z_{2ext} = \frac{x_2}{2\sqrt{at_{ext}}} \tag{3a}$$

Q' is heat added by pulse to the sample (in form of a thin plate), ΔR_{ext} is the extreme change of resistance after addition of heat, $S = bh$ plate cross section area and γ is thermal coefficient (Fig. 1).

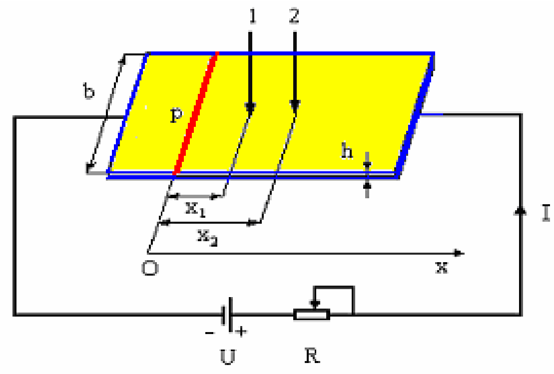

Figure 1 shows the scheme of the set-up with two nails

The relation (2) one can derive as follows. The voltage U_{12} represents potential decrease on resistance R of the piece plate between line segments $x_2 - x_1$ distant. This resistance is given as

$$R = \int_{x_1}^{x_2} \rho(x)\,\frac{dx}{bh} = R_o + \frac{\rho_o\gamma}{bh}\int_{x_1}^{x_2} \Delta T(x)\, dx \tag{4}$$

Under the assumption that the temperature distribution depends on one space coordinate x only the change of temperature at the instant of the time t in vicinity of the point x is [1,2,4]

$$\Delta T = T - T_o = \frac{Q'}{2\, cs\sqrt{\pi a t}} \exp\left(-\frac{x^2}{4at}\right) \tag{5}$$

assuming that thermal source was applied at $x = 0$ at the instant of the time $t = 0$. (c - specific heat, s - density). From (4) and (5) we have

$$\Delta R = R - R_o = \frac{\rho_o \gamma}{bhcs} \frac{Q'}{\sqrt{\pi}} \int_{z_1}^{z_2} \exp(-z^2)\, dz \tag{6}$$

where $z^2 = \dfrac{x^2}{4at}$

The condition for local extreme $\left(d\varDelta R/dt = 0\right)$ leads to the equation (7)

$$\frac{d\,\Delta R}{dt} = \frac{\rho_o \gamma\, Q'}{2\, bhcs\, \sqrt{\pi}} \frac{1}{\sqrt{4at}^{3/2}} \left[\left(x_2 \exp\left(-\frac{x_2{}^2}{4at}\right) \right) - \left(x_1 \exp\left(-\frac{x_1{}^2}{4at}\right) \right) \right] = 0 \tag{7}$$

where the fact was accounted that the limits of integral in (6) are time dependent. The voltage extreme U_{12} occurs at the time t_{ext} when the expression in square bracket of (7) is equal to zero. From (7) the relation (2) follows.

The relation (3) can be derived as follows. The difference in temperature (5) for $t = t_{ext}$ leads to the extreme change of resistance

$$\Delta R_{ext} = \int_{x_1}^{x_2} \Delta\rho \frac{dx}{S} = \rho_o \frac{\gamma}{S} \int_{x_1}^{x_2} \Delta T(t_{ext})\, dx = \frac{Q'\rho_o \gamma}{2\, csS\, \sqrt{\pi a t_{ext}}} \int_{x_1}^{x_2} \exp\left(-\frac{x^2}{4at_{ext}}\right) dx \tag{8}$$

If one applies the same substitution of integral variable (3a) as it was done in relation (3) one obtains [4]

$$\frac{1}{\sqrt{\pi}} \int_{z_1}^{z_2} \exp\left(-z^2\right) dz = \frac{1}{2} \left[\frac{2}{\sqrt{\pi}} \int_0^{z_2} \exp\left(-z^2\right) dz - \frac{2}{\sqrt{\pi}} \int_0^{z_i} \exp\left(-z^2\right) dz \right] = \frac{1}{2} \left[\Phi\left(z_2\right) - \Phi\left(z_1\right) \right]$$

Finally, one obtains

$$\Delta R_{ext} = \frac{Q'\rho_o \gamma\, a}{2\lambda S} \left[\Phi\left(z_{2ext}\right) - \Phi\left(z_{1ext}\right) \right] \tag{9a}$$

or where the relation $\lambda = acs$ was accounted. From (9) the relation (3) and the next relation follows.

$$\lambda = \frac{\rho_o Q'\gamma\, a}{2\Delta R_{ext}\, S} \left[\Phi\left(\frac{x_2}{2\sqrt{at_{ext}}}\right) - \Phi\left(\frac{x_1}{2\sqrt{at_{ext}}}\right) \right] \tag{9b}$$

Upper described method can be efficient in a case when scanned changes of voltage reach much higher values than thermoelectric ones. An advantage of resistance method of scanning is essentially higher sensibility of it (nearly two in order) than the thermoelectric method. The possible local inhomogenities at this method of scanning appear much less than at the thermoelectric one. That is the other advantage of resistance method.

Notice: The voltage scanning by probes 1 and 2 contains also thermoelectric component of voltage because the temperature at these points is different. But, this thermoelectric voltage is comparatively small and can be neglected. Thermoelectric voltage can be excluded by the use of alternating current, because thermoelectric component is direct one.

Set-up no 2

Set-up with a simple point resistance probe. A pulse heating is realized along line section *p* (Fig. 2). To detection of heat spreading a simple point resistance probe is used. A part of scanning circuit is also a nail with peak H oppressed to a sample. A direct constant current is passing through the circuit. If the electric contact between peak and the sample is sufficiently small for resistance of the circuit will be deciding only a small part of the sample in vicinity of the peak. The time of voltage extreme U_{AB} between the points A and B will correspond to the time temperature extreme at the peak location, so that for the thermal diffusivity *a* following relation can be used [1, 2]

$$a = \frac{x^2}{2t_{ext}} \tag{10}$$

Remark: The upper introduced assertion can be simple proved under the assumption that the form of the peak is a semi-sphere of a very small radius an when the contact area with the sample is also the same semi sphere. Electric field in vicinity of the peak will be radial. The simplest point resistance probe is very sensitive (nearly two in order, than at scanning of thermo voltage), but at times some current instabilities appear. For that reason it is more effective to use probes with covered contacts which will be described in the next.

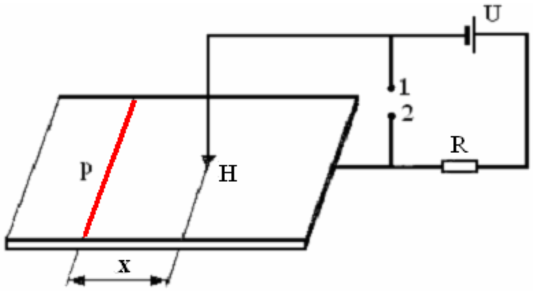

Figure 2 shows the scheme of the set-up with point resistance probe

Set-up no 3

Set-up with line resistance probe. In this case the line resistance probe is used for scanning of the temperature (Fig. 3). It consists of two very thin metallic micro-strips with feeder 1 and 2 on the surface a semiconducting sample. Electric current conduces in a region of very short gap between strips. This set-up is appropriate at semiconducting samples with relatively high resistivity. In fact, it is going on thermistor integrated into the alone sample. It guarantees perfect thermal contact of the scanner with the sample an also a minimal inertia. The result is less influenced by inhomogenities. Hence for diffusivity coefficient *a* the relation (10) is valid.

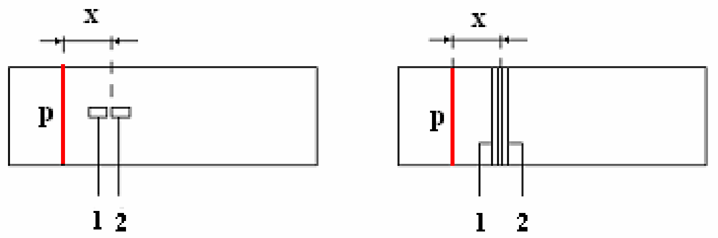

Figure 3 shows the setting with line resistance probe

Set-up no 4

Set-up with point resistance probe and surface heat source. A pulse heating of a sample is realized in this case uniformly on a rectangular area shown in Fig. 4. For scanning are used point or line resistance probes. In schema it symbolizes a special mark.

A heat supplied to the elementary area $b.dy$ at the time $t = 0$ causes near a point A an increase of the temperature [1]

$$dT = \frac{Q'dy}{2\ cs\ (y_2 - y_1)\ \sqrt{\pi a t}} \exp\left(- \frac{(x-y)^2}{4at} \right) \tag{11}$$

where Q' is the heat supplied to the whole sample. If, the heating is realized uniformly on the area $b\left(y_2 - y_1\right)$ the temperature at the point A will have the course given by the function

$$T = \frac{Q'dy}{2\ cs\ (y_2 - y_1)\ \sqrt{\pi a t}} \int_{y_1}^{y_2} \exp\left(- \frac{(x-y)^2}{4at} \right) dy \tag{12}$$

In this integral the variable x is constant. After substitution

$$z^2 = \frac{(x-y)^2}{4at} \tag{13}$$

one obtains

$$T = C \int_{z_1}^{z_2} \exp\ (-z^2)\ dz \tag{14}$$

where C is a constant. The further procedure of determination of the temperature extreme is analogous to the procedure used in set-up no 1. It leads to formula

$$a = \frac{(x-y_1)^2 - (x-y_2)^2}{4t_{ext}\ \ln \frac{x-y_2}{x-y_2}} \tag{15}$$

or if one changes $x_1 = x - y_1$, $x_2 = x - y_2$

$$a = \frac{{x_1}^2 - {x_2}^2}{4t_{ex}\ \ln \frac{x_2}{x_1}} \tag{16}$$

The sense of used symbols manifests Fig. 4.

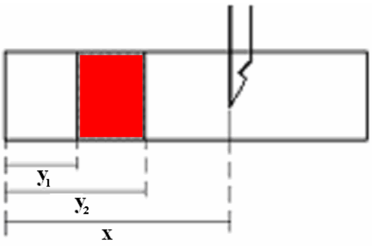

Figure 4 shows setting with point resistance probe and surface heat source

For thermal conductivity λ the relation

$$\lambda = -\frac{R_o\ \gamma\ Q'\ a}{2\ (y_2\ - y_1)\ \Delta R_{ex}}\left[\Phi(\frac{x - y_2}{2\ \sqrt{at_{ex}}} - \Phi(\frac{x - y_1}{2\ \sqrt{at_{ex}}}\right] \tag{17}$$

is valid where the relations (16) and $\Delta R_{ext} = R_0\gamma\Delta T_{ext}$, $\lambda = acs$ were used.

Set-up no 5

Set-up with Dirac circulate (ringlike) heat pulse. Experimental setting up is depicted in Fig. 5. A ring circumscribed by radii r_1 and r_2 obtains in Dirac pulse heat Q'. Point resistive scanning of temperature is realized at the center of the ring. If initial difference of temperature is zero outside the ring and is constant and equal to Δ inside the ring then distribution of temperature is given by [1]

$$\Delta T\left(r,t\right) = \Delta\int_{r_1}^{r_2}\frac{1}{4\pi at}\exp\left(-\frac{\left(r-r'\right)^2}{4at}\right)2\pi r'dr' \tag{18}$$

if we denote $\varsigma_1 = \frac{r_1 - r}{2\sqrt{at}}$, $\varsigma_2 = \frac{r_2 - r}{2\sqrt{at}}$, then

$$\Delta T\left(r,t\right) = 2\Delta at\left[\exp\left(-\frac{\left(r-r_1\right)^2}{4at}\right) - \exp\left(-\frac{\left(r-r_2\right)^2}{4at}\right)\right] + r\Delta\sqrt{at}\int_{\varsigma_1}^{\varsigma_2}\exp\left(-\varsigma^2\right)d\varsigma \tag{19}$$

At the center $r = 0$ we obtain

$$\Delta T\left(0,t\right) = 2\Delta at\left[\exp\left(-\frac{r_1^2}{4at}\right) - \exp\left(-\frac{r_2^2}{4at}\right)\right] \tag{20}$$

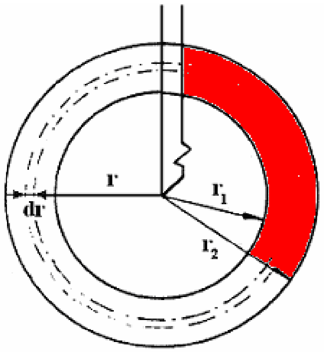

Figure 5 shows setting with point resistance probe and surface ringlike heat source

For the time t_{ext} when the temperature at the center $r = 0$ reaches extreme value we have

$$\frac{r_2^{\,2}}{r^2_{\ 1}} = \exp\left(-\frac{r_1^{\,2} - r_2^{\,2}}{4at_{ext}}\right)$$

from which follows

$$a = \frac{r_2^{\,2} - r_1^{\,2}}{8\, t_{ext} \ln r_2 / r_1} \tag{21}$$

This geometry permits also measurement of thermal conductivity λ. It holds

$$\lambda = \frac{R_o\, \gamma\, Q\, a}{d\, \varDelta R_{ext} S} \left[\exp\left(-\frac{r_1^2}{4at_{ext}}\right) - \exp\left(-\frac{r_2^2}{4at_{ext}}\right) \right] \tag{22}$$

3. Conclusion

In this paper some specific methods of measurement thermophysical parameters semiconducting materials are suggested and discussed. Because of restricted space for this article further possible versions and geometry of setting are not introduced.

References

[1] KREMPASKÝ, J.: The measurements of the thermophysical Properties, SAV, Bratislava, (1969).

[2] KUBIČÁR, Ľ.: *Pulse Method of Measuring Basic Thermophysical Parameters*, ELSEVIER Amsterdam, (1991).

[3] BARTA, Š., CESNAK, L., KREMPASKÝ, J., KUBIČÁR, Ľ. Complex analysis of disturbing factors influence upon the measurement of thermal parameters by measn of a pulse method, Czech. J. Phys. (1973) 703 B23, (1973).

[4] CARSLAW, H. S., JAEGER, J. C.:*Conduction of Heat in Solids*, 2. Ed. Clarendon Press, London, 2003, pp. 510. ISBN 0-19-853368-3, (2003).

Measurement of soils thermal properties in temperature interval from room temperature to temperature of nitrogen boiling point

Ivan Baník, Jozefa Lukovičová, Gabriela Pavlendová, Juraj Veselský

Faculty of Civil Engineering, Slovak University of Technology, Radlinského 11,

813 68 Bratislava, Slovak Republic, email: juraj.veselsky@stuba.sk

Abstract: *Freezing of soils by liquid nitrogen is applied in foundation engineering operations in environment below the ground-water level. The examples of soils freezing are presented, methods of measurements of thermal parameters of frozen soils which are the basis for determination of temperature fields and there are presented temperature and moisture dependence of some thermal properties of selected soils.*

Keywords: *Freezing, soils, thermal properties, foundation engineering*

1. Introduction

Freezing of soils in the area of planned construction represents a technological process increasing the mechanical strength of moist soils and preventing water leakage by physical means (decreasing of temperature). The technology of freezing is based on creation of a frozen layer (wall) resisting to the load of the surrounding soils during ground operations like excavation of foundation pits, furrows, a. o. The layer (wall) shall prevent earth sliding and water leakage into the building site.

The freezing technology is applied in areas where other technologies fail or turn too expensive. Assessment of economic costs of the freezing technology must be based on the liquid nitrogen consumption. It is, however, closely related with physical parameters of frozen soils, like specific heat, thermal conductivity and soil moisture (closely related with latent heat). These quantities can only be determined by physical measurements. Reliable liquid nitrogen consumption and costs determinations are based on the results of the physical measurements. This is why we present fundamental information about physical methods of thermophysical parameters measurements, and some data resulting from the measurements.

2. Frozen Constructions

Practically all ways of soils cooling can be used for soils freezing. Usually brines or liquid nitrogen are applied. The brine can only cool the soil to several grades below zero (e.g. -10 °C). Liquid nitrogen whose boiling point under normal pressure is minus 196 °C is more convenient because of a shorter freezing time and for attaining better strength properties of frozen soils. Both facts are related with the low temperature mentioned because just the low temperature enables attaining high temperature gradients during freezing and extensive heat flows in soils. This can markedly accelerate the freezing process. On the other hand, a wet soil frozen to such a low temperature exhibits a markedly raised mechanical strength. A higher mechanical strength of soils frozen to very low temperatures is also closely related with the fact that freezing of a thinner continuous soil layer is convenient for sufficient mechanical strength of the frozen construction. In other words, using liquid nitrogen will al1ow to freeze smaller volumes of wet soils, and the freezing time is shorter as well.

The frozen soil constructions are produced by means of freezing needles (up to 30m long) inserted into holes bored into earth in the place of freezing. Liquid nitrogen is supplied into needles. Cooled needles take the energy from the surrounding soil and frozen parts of soil are gradually thickening. Liquid nitrogen supplied by a distributing system from a nitrogen reservoir into freezing needles is evaporating and gradually transforming into gas. It gets the required latent heat from the surrounding soil. Liquid nitrogen is supplied by a central tube inside the needle. From the outer part of the needle (with annular section) the partly liquid and partly gaseous nitrogen returns to the exit hole of the needle.

To improve the freezing effects the outgoing nitrogen is – for the cooling purpose – conducted through another freezing needle situated on an isotherm with a higher temperature in a more distant part of the freezing construction.

Convenient location of freezing needles can provide mutual contact between the frozen parts during a sufficient freezing time and the formation of compact frozen soil constructions. They represent mechanically strong and water retaining systems enabling realization of the necessary ground- and civil engineering operations.

Frozen soils constructions for foundation engineering may have various shape and arrangement. Their mechanical properties are most important and can be classified on the basic of mechanical strength parameters values of frozen soils. They are controlled by the type of soil, its moisture, and partly by the temperature field kinetics in the soil during its freezing. Generally, the frozen soils constructions are anisotropic, determined by the course of temperature field during the formation of a new phase.

Aeration of underground spaces is a particular problem associated with the underground freezing technology. The resulting gaseous nitrogen must be removed without possible endangering of operators by a low oxygen concentration in the air. But no serious problems have so far been met in praxis.

Frozen soil constructions proposal for foundation engineering represents the process of determination of optimal geometry of a frozen construction, location of freezing needles and the complete procedure of a frozen construction. For this process the mechanical properties of the construction and economical expedience of its realization are most important. Calculations result in data on stresses, shifts, mobilization of pressure strength, tension- and shear strength of frozen and unfrozen soils in the respective area. Current calculations, methods and algorithms facilitate reliable proposals of frozen soils constructions convenient for surface and underground objects. Utilization of freezing technology will gradually increase, particularly in civil engineering and mining.

3. Measurement of thermal properties of soils

Effects of soils freezing technology is closely associated with soils thermophysical and strength parameters. The first parameters control the freezing process, the second affect the strength of the resulting frozen soil constructions. The soil strength properties actually control the dimensions of the frozen soil constructions.

Values of quoted parameters can only result from the appropriate physical measurements. As for the method of soil thermal parameters measurement, the granularity of soil, the duration of measurement, and the necessity to perform the measurement in a broad temperature interval (i.e. between the room temperature and the temperature of nitrogen boiling point -196 °C) must be considered. This concerns the measurement of thermal conductivity and heat capacity of the soil in dependence on temperature and at the appropriate moisture. Moisture controls both the liquid nitrogen consumption (with respect to latent heat) and mechanical properties of soil after freezing.

Following methods of soils thermal parameters measurement proved most reliable:

1. Impulse method with line heat source
2. Quasi-steady-state method with permanently increasing temperature
3. Differential method with one and/or two-dimensional temperature field

Description of the impulse method is in papers [1, 2]. It is convenient for measurement of thermal properties of fine-grained soils, not for the coarse-grained soils. The method enables to measure the thermal diffusivity a, the thermal conductivity λ, as well as the volumetric heat capacity $c\rho$, where ρ is the bulk density and c is specific heat. In addition, the method is possible to combine with the quasi-steady-state method in cylindrical arrangement and with the transient method, which use line step change heat source [1, 3]. The comparison of measurements by different method provided the satisfying agreement.

The apparatus used to measure thermal conductivity by this method is shown in *Figure 1*. A sample of soil is placed in cylindrical container made of duralumin. The heat source is situated in axis of the container and is fastened at either end. The heating wire running through the box is connected to current pulse source that heat it. The thermocouples that scan the response on heat impulse are inserted in distance r_1 and r_2 from the heat source. The third thermocouple scans temperature of the sample before application of heat impulse. Change of sample temperature is achieved by inserting of the sample container to Dewar vessel with liquid nitrogen.

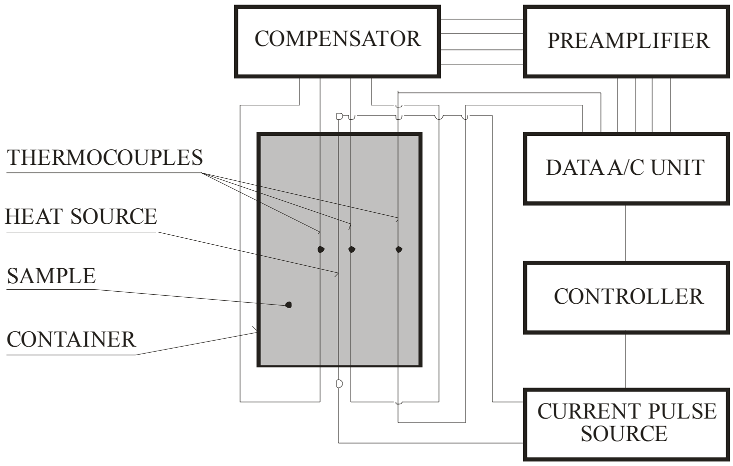

Figure 1: The scheme of the experimental apparatus used to measure by impulse method

The quasi-steady-state method works with a cylindrical sample heated by an areal heat source on the sample mantle. During the measurement the course of temperature is monitored in the axis of the sample and on its mantle.

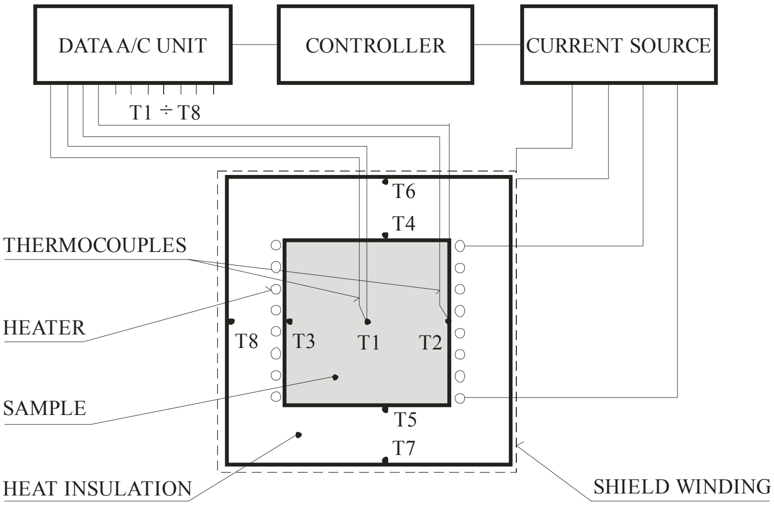

Figure 2: The scheme of measurement by the differential method

Realization of the differential method is described in [4]. It is also convenient for measurement of soil parameters with its original structure undisturbed. The measurement is done on a soil sample placed in the box of the drilling ring (in the same state as in field), *Figure 2*.

Fig. 3 illustrates another application of the differential method. It is applied to a cylindrical sample with one-dimensional vertical temperature field. The sample is heat-screened on its mantle. Progress of the temperature field along axis of the sample is monitored. The steady-state measurement and the non-steady-state measurements are both possible. The steady-state measurement enables determination of the thermal conductivity dependence on temperature. The non-steady-state measurement enables determination of temperature dependence of the soil thermal diffusivity, and indirect determination (knowing the density) of temperature dependence of the soil specific heat.

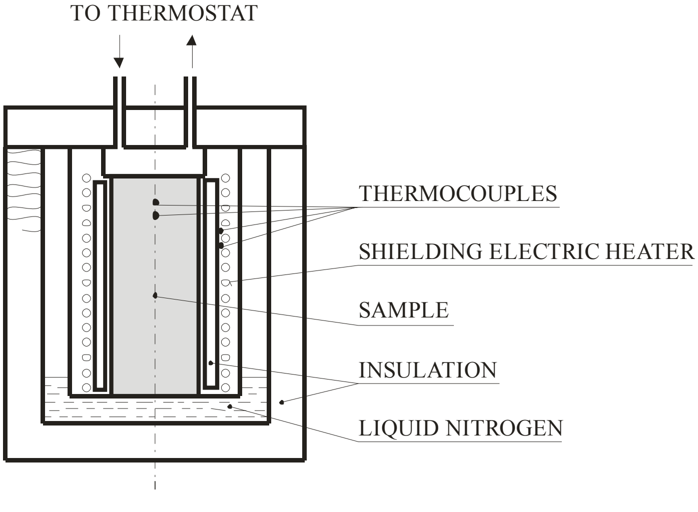

Figure 3: Scheme of measurement of thermal parameters using difference method

The experimentally obtained (by impulse method) dependence of the thermal conductivity and volumetric heat capacity of fine silica sand are presented in Fig. 4 and

Fig. 5. Fig. 6 and Fig. 7 illustrate measured temperature dependence thermal conductivity and heat capacity of silty soil achieved by difference method.

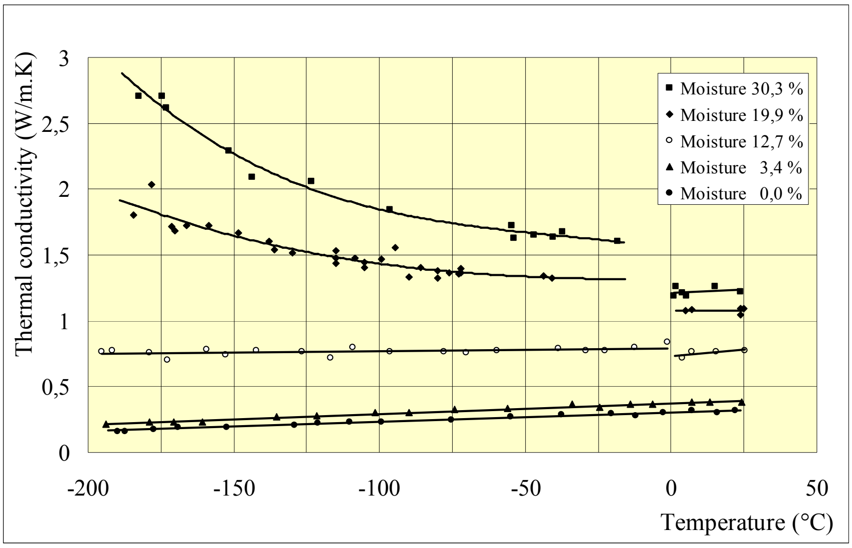

Figure 4: Dependence of thermal conductivity λ of fine silica sand on temperature

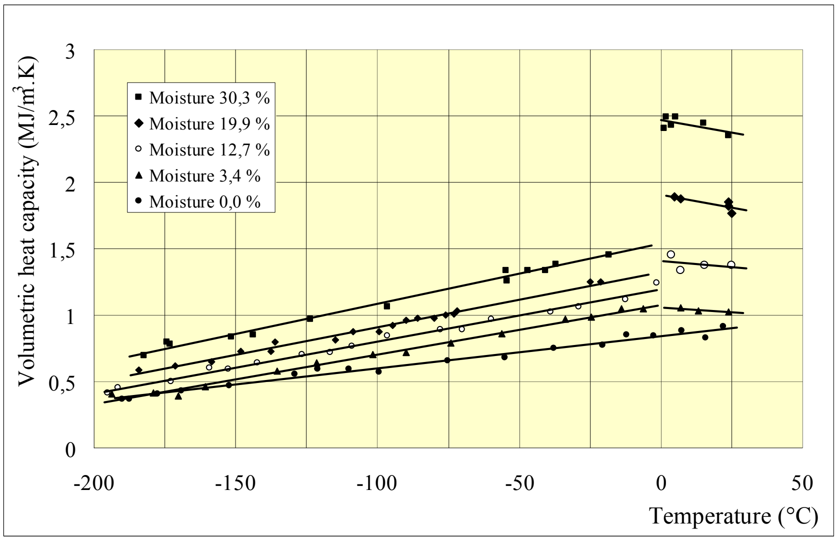

Figure 5: Dependence of volumetric heat capacity cρ of fine silica sand on temperature

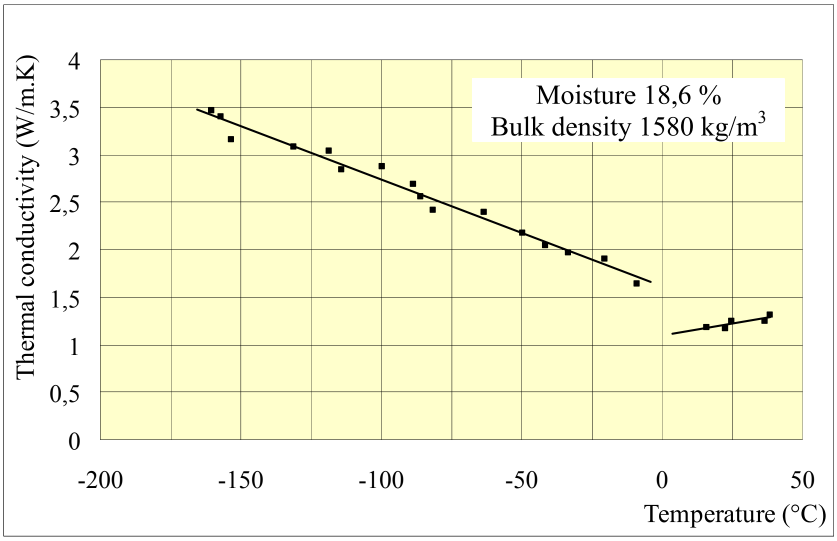

Figure 6: Dependence of thermal conductivity λ of silty soil on temperature

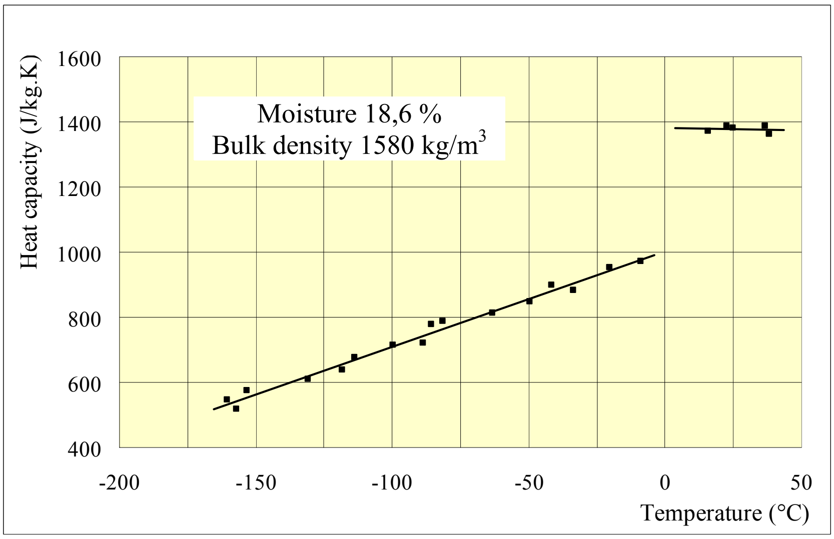

Figure 7: Dependence of heat capacity c of silty soil on temperature

Determination of strength characteristics of frozen soils samples represents a particular problem. Some results are presented in [5].

4. Conclusion

The method of soils freezing by liquid nitrogen is convenient for civil engineering (excavation of foundation pits and furrows, construction of adits, tunnels, aquifers and other underground constructions) and in mining (mining constructions penetrating tectonic disturbances in aqueous fine-grained soils).

Following are advantages of the soils freezing by liquid nitrogen in comparison with the usual methods (draining, grouting, caissons, freezing by brines): relatively simple device, high freezing effect, shorter durations, easier work, practically no lasting change in the ground-water level, no influence upon the ground-water quality, no negative effects on adjacent constructions, applicable to any depth, adaptability of the construction in size shape and dip;

easier soil exploitation (no scaffolding, no casing), applicability under conditions of flowing soils, flowing ground-water, applicability without respect to soil permeability, prevention of water infiltration to the operation site, geological setting almost undecisive.

Soils freezing technology by liquid nitrogen is convenient for all sites requiring constructions resistant to water pressure. The freezing technology can under reliable organization of building operations even reduce the building costs. The technology can be applied in both the underground and surficial constructions.

References

[1] KREMPASKÝ J. *The Measurements of the Thermophysical Properties*. Vydavateľstvo SAV, Bratislava 1969. 71-0,44-69 (in Slovak)

[2] VESELSKÝ, J. Investigation of Thermal Properties of Soil by Impulse method. In: *Thermophysics 2006.* Proceedings of the Conference. 12.-13. October 2006, Kočovce Chateau. STU, Bratislava 2006. p. 115-123. ISBN 80-227-2536-6

[3] KUBIČÁR, Ľ. *Pulse Method of Measuring Basic Thermophysical Parameters*. Vydavateľstvo VEDA SAV Bratislava 1990. 071-021-88 RMM (in Slovak)

[4] BANÍK I. *Research Report 11-8-5/02-01*. SvF SVŠT, Bratislava 1988. (in Slovak)

[5] MAĽA P. et al. *Final Report P 12-526-505-03*. Research Institute of Civil Engineering, Bratislava 1985. (in Slovak)

Measurement of thermophysical properties of heat-insulating materials by constant temperature increase

Ivan Baník, Jozefa Lukovičová, Gabriela Pavlendová, Juraj Veselský

Department of Physics, Faculty of Civil Engineering, Slovak University of Technology,

Bratislava, Slovak Republic

Abstract: *In the presented paper the method of constant temperature rise in the determination of thermal parameters of thermal insulation materials is described. The experimental results obtained by this method in measuring the properties of selected materials in a wide temperature range are also presented. In the temperature regime under the steady rise, the temperature at each point in the system increases linearly with time, while the speed increase is the same everywhere. In the case of measuring the coefficient of thermal conductivity so called accumulation core is used. This simplifies measurement because it puts less demand on the heat shield and does not demand the measurement of the performance of heating source .The regime of constant temperature increase is created only after certain start – up time after measurement start. In the start-up this method should be combined with so-called. differential method, which requires no special temperature regime. Shortening the rise time can be achieved by proper control of heating elements.*

Keywords: *thermal diffusivity, thermal conductivity, thermal-insulating material*

1. Introduction

Several hundreds measuring methods to measure thermophysical parameters have been designed so far [1-5]. The method of constant temperature increase is suitable for measuring parameters in wide temperature interval. Constant temperature increase in the system with the sample may be achieved in the way shown in the Fig. 1a, b. In the case of Fig. 1a sample from a thermal-insulating substance fills the cavity inside the metal block B, whose thermal diffusivity is very high (theoretically infinitely large). Block will therefore represent virtually isothermal body. The temperature in the whole volume of the block (and thus on the external surface of the sample) will be practically the same every time. Let us suppose that at the beginning the temperature of the system (block plus sample) is uniform everywhere. From some moment on we will evenly (linearly) increase the temperature of the metal block B with a suitable heater, computer controlled. The system will gradually establish regular mode, in which the temperature at each point of the sample will grow at the same rate [1-3]. The temperature at various points of the sample will generally be different at the same time.

A similar situation occurs in the case of the system with accumulation core AC (Fig. 1b) which is embedded in the sample. Accumulation core is also made of metal "isothermal" block with good thermal conductivity. After the establishment of the regular regime in the system would not only the temperature increase at various points in the sample, but the core temperature will increase as well. Regular accrual system can be used for measuring thermophysical parameters of thermal insulation materials. By practical implementation of measurement we prefer simple measuring arrangement with one-dimensional, respectively. two-dimensional temperature field.

2. Measurement of the coefficient of thermal diffusivity

In measuring the coefficient of thermal diffusivity a of flat, respectively multilayer samples is appropriate to use arrangement shown in Fig. 2. There are two identical circular plate samples each of thickness d within two plane metal blocks B1 and B2. If the thickness of 2d is small compared to the diameter of the sample, edge effects will practically not affect the temperature field in the axis of the sample. In this area one dimensional temperature field will be created. The situation is similar to the infinite metal blocks and infinite flat samples. If the temperature of the metal block will increase steadily using electric furnace (computer controlled), regular mode with a constant rate of temperature rise will be created in the axes area of the sample. When measuring, the temperature course will be registered in points 1, 2 and 3.

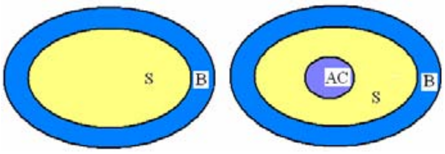

Figure 1a (left),1b (right): To the essence of the method of constant temperature rise.

The analysis of the process leads to the following equation for determining the coefficient of thermal diffusivity.

$$a = \frac{d^2}{2\Delta T_{13}} \frac{dT_1}{dt} \tag{1}$$

Where dT_1/dt is the rate of increase of temperature ($T_1 = T_2$) of metal blocks B_1, B_2 (system as well) and $\Delta T_{1,3} = T_1 - T_3$ temperature difference between the metal block temperature and the temperature T_3 in the middle point 3.

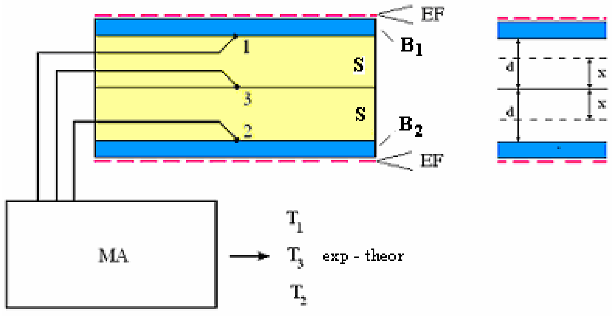

Figure 2: Plane (1D) arrangement by measuring a

This simple equation (1) we can derive by thermal balance of an appropriate selection of sample part of the section S with a thickness of 2x (Fig. 2 right). The heat in period d*t* entering the considered area of sample is entering through the two circular bases of the area *S*.

$$dQ = \lambda \left(\frac{dT}{dx} \right)_x 2S \; dt \tag{2}$$

where $(dT/dx)_x$ is the temperature gradient at the entry circular bases of the considered area. This heat is used to heat a selected sample part, so it comes to

$$dQ = cm_x dT_1 = c\rho S 2x dT_1 \tag{3}$$

where ρ is sample density, c – mass heat capacity and m_x - mass of chosen sample part.

From these two equations with regard to relation to $a = \lambda/c\rho$ we get a differential equation

$$\left(\frac{dT}{dx}\right)_X = \frac{x}{a}\frac{dT_1}{dt} \tag{4}$$

By indicating quantity dT from equation (4) and integrating within the limits from 0 to d we determine the temperature difference

$$\Delta T_{13} = \frac{d^2}{2a}\frac{dT_1}{dt} \tag{5}$$

of which we already receive equation (1) for determining the coefficient a.

Note: Using similar thermal balance in regular accrual system in two-dimensional (cylindrical) configuration according to Fig. 3 (assuming that marginal effects can be neglected in long tubes) we will come to equation

$$a = \frac{R^2}{4\Delta T_{13}}\frac{dT_1}{dt} \tag{6}$$

R being the diameter of the cylindrical sample and ΔT_1 the temperature difference between outdoor isothermal tubular-shaped metal block and the center 3 of the sample. In this case, the thermal balance is made for a cylindrical coaxial part of the sample with radius x and selected length l.

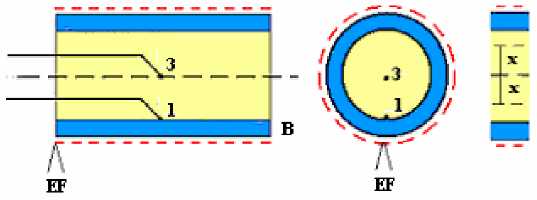

Figure 3: Cylindrical (2D) arrangement by measuring the coefficient a

3. Measurement of the coefficient of thermal conductivity

3.1 Plane layout

Measuring arrangement with accumulation core AC plane type, which is suitable to measure the coefficient of thermal conductivity λ of plane geometry samples is illustrated in Fig. 4. This is the type of one-dimensional heat transport, in which heat is transferred from outside heated metal blocks B_1, B_2 through plane sample S into isothermal metal accumulation core AC. The heating of blocks B_1, B_2 is ensured by two EF electric furnace controlled by computer. Lateral heat losses are eliminated by a heat shield ensured by regulated heating of shielding metal block with SCH with ring-shaped profile. SCH deflector plate is heated by a separate electric furnace EF' computer controlled so that for the temperature T_4 remains practically true $T_4 = T_3$. Thanks to shielding, the temperature field in the AC core accumulation could be regarded as homogeneous.

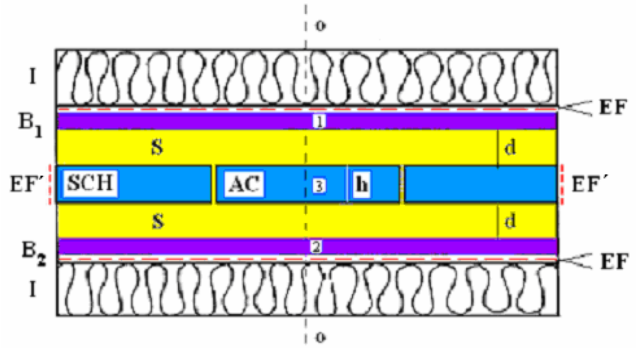

Figure 4: Measuring arrangement for measuring λ with accumulation core AC plane type.

The measurements are based on a balanced state of the system temperature. Using computer-controlled electric furnace EP temperature $T_1 = T_2$ blocks B_1 and B_2 from certain time gradually increases so as to achieve the regular mode as soon as possible. Relevant temperatures are regulated and recorded by the measuring system at regular time intervals. The theoretical description of the heat plot in the system is generally complex. In the case of uniform temperature increase we may come to the expression of the coefficient of the sample thermal conductivity in the form

$$\lambda = \frac{\frac{d}{2S} c_j m_j \frac{dT}{dt}}{\Delta T_{13} - \frac{d^2}{2a}\frac{dT}{dt}} \tag{7}$$

where S is the area of accumulation core, m_i - its mass, c_j - the mass heat capacity, d - sample thickness, a - the coefficient of thermal diffusivity of samples, where $a = \lambda / c\rho$.

Equation (7) results from the heat balance of the selected area of the system consisting of the whole accumulation core with adjacent parts of the samples of thickness x on both sides of the core (Fig. 4). It is therefore a system located inside the cylinder of height $h + 2x$, where h is the thickness of the accumulation core. The overall heat balance of the system with uniform temperature describes the following equation

$$2\lambda \left(\frac{dT}{dx}\right)_x S\, dt = c_j m_j dT_1 + 2\, c\rho\, S\, x dT_1 \tag{8}$$

A member on the left side of the equation is the heat that enters into the system through both circular bases of the cylinder (area S), that are the boundaries of our system. The expression $(dT/dx)_x$ is the temperature gradient in the sample at a distance x from the surface of accumulation core (on both sides). The first member of the right side represents heat accumulated by the accumulation core (in time dt), the second represents the heat consumed by the two halves of the sample.

If we express the differential dT from equation (8) and integrate it within the limits from 0 to d we obtain the temperature difference between heated metal blocks and accumulation core given by

$$\Delta T_{13} = \left(\frac{c_j \rho_j h d}{2\lambda} + \frac{d^2}{2a}\right)\frac{dT_1}{dt} \tag{9}$$

The relationship (9) for the coefficient λ leads to equation (7). To determine the coefficient λ we must first know the coefficient a. By measuring thermal insulation materials it often occurs that the value of the parameter a can be well estimated from the relationship $a = \lambda/c\rho$, while for λ we will take in the first approximation the value determined by equation (7) without correction to member in denominator containing a. Sometimes it is even possible to neglect the second member $d^2/2a.dT_1/dt$ in denominator of the equation (7) with respect to the first one.

3.2 Comments on cyllindrical measuring pattern

Fig. 5 shows a layout used to measure the thermal conductivity coefficient λ for cylindrical sample geometry. This corresponds to the outer tube shaped metal block B with electric furnace EF and also cylindrical shaped accumulation core AC. By constant increase of external block temperature a radial temperature field with a linear increase in temperature over time is created in the accumulation core of the sample, thanks to ends shield SCH. Thermal conductivity can be determined from the equation

$$\lambda = \frac{\frac{1}{2\pi l}\ln\frac{R}{r}\, c_j m_j \frac{dT_1}{dt}}{\Delta T_{13} - \frac{1}{2a}\left(\frac{R^2 - r^2}{2} - r^2\ln\frac{R}{r}\right)\frac{dT_1}{dt}} \tag{10}$$

where r is the internal radius of the cylindrical sample and R the outer radius. Sample length l corresponds to the length of accumulation core (without shielding end parts). The meaning of other symbols is obvious.

Equation (10) results from the heat balance of the selected cylindrical part of length l and relevant sample part bounded with cylindrical area of radius x which axis is identical to the core axis (Fig. 5). Heat entering the selected part of the sample in steady growth mode is consumed both by the core temperature increase and relevant sample part (hollow cylindrical shape), with inside radius r outside a radius of x. From equation (10) it is evident that to determine the thermal conductivity coefficient λ we should know the thermal diffusivity coefficient a of the sample as well.

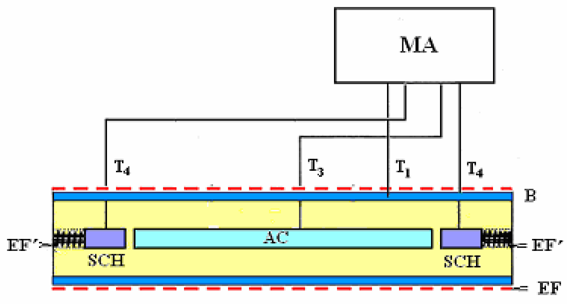

Figure 5: Measuring arrangement by measuring the thermal conductivity coefficient λ of accumulation core AC cylindrical type

3.3 Comment: Generalized equation for the accumulation core method

Next we give the equation

$$\lambda = \frac{Ac_j m_j \dfrac{dT_1}{dt}}{\Delta \mathrm{T}_{13} - \dfrac{B}{a}\dfrac{dT_1}{dt}} \tag{11}$$

which can be regarded as the generalization of equations (7) and (10). It applies to any geometric configuration type (according to Fig. 1b) to measure the coefficient of thermal conductivity by the steady growth temperature method using the accumulation core. The meaning of the symbols is evident. The constants A and B are intended only by concrete (specific) sample geometry. In the case of plate (board) geometry (as shown in Fig. 3) this equation is in agreement with equations (7, 11)

$$A = \frac{d}{2S} \quad B = \frac{d^2}{2}$$

In the case of cylindrical geometry (Fig. 5) it will be - in agreement with relations (10, 11) -

$$A = \frac{1}{2\pi l}\ln\frac{R}{r} \quad B = \frac{1}{2}\left(\frac{R^2 - r^2}{2} - r^2 \ln\frac{R}{r}\right)$$

Generalized relationship (11) was derived in [4]. In simpler geometries of the sample the constants A and B can be determined analytically. For complex geometries they can be determined by numerical methods. This can be done by modeling thermal process using differential method in the system with a given geometrical shape for arbitrarily chosen (pure model) value of the parameter λ and a. In the beginning only stationary process will be computer-modeled. Analyzing it we will determine the coefficient A. The second time we will model the accrual process. The second analysis gives constant B. Knowing the constants A and B the equation (11) can be used for determining the thermal conductivity of any thermal insulating material of given geometry at any speed of temperature increase. In other words: In evaluating the measurements we do not need any computer simulation. The equation (11) is sufficient. Let us mention that the methods of heat loss eliminations by different variants of the steady growth temperature method were solved in [5].

The steady growth temperature method is a transient method. It is suitable for measuring parameters of heat insulants within a wide temperature range.

4. The results of measurement - illustration

In the following we will illustrate the experimental results obtained in measuring the coefficient of thermal conductivity by steady growth temperature method on several samples of heat insulation materials.

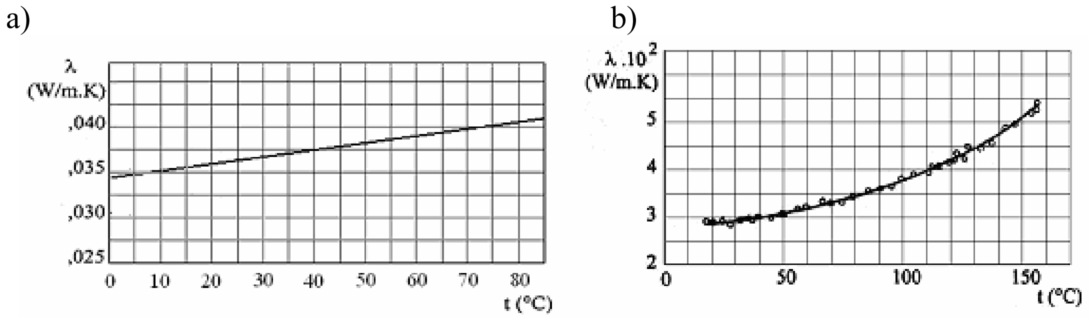

Figure 6: Temperature dependence of coefficient λ a) heat insulating material based on fiber profile with the profile of "Y" and density 102,1 kg.m⁻³ b) polyurethane sample with a density 92,4 kg.m⁻³.

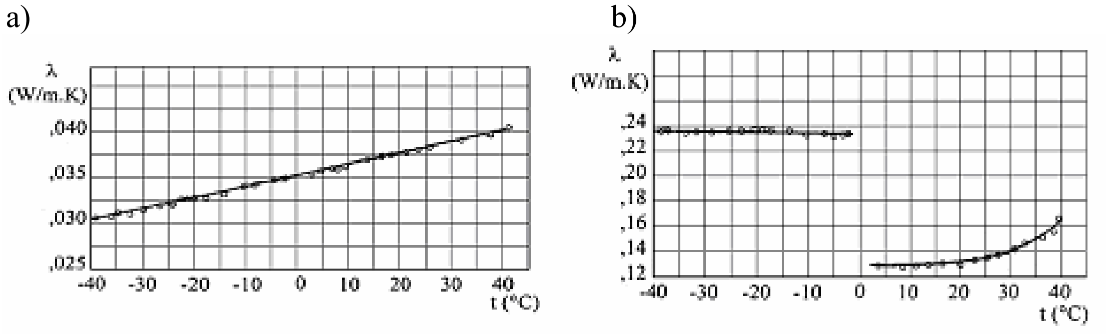

Figure 7: The temperature dependence of the coefficient of thermal conductivity λ a) dry "thermofen" with density 122 kgm⁻³, b) wet "thermofen" with mass moisture content 230 %.

References

[1] CARSLAW, H. S., JAEGER, J. C.: *Conduction of heat in solids*, 2. Ed. Clarendon Press, London, 2003 , pp. 510. ISBN 0-19-853368-3.

[2] LYKOV, A.V.: *Teorija teploprovodnosti*, Gos.izd. tech-teor. Lit., Moskva 1952

[3] KREMPASKÝ, J.: The measurements of the thermophysical properties, SAV, Bratislava, (1969).

[4] BANÍK, I.: Method of accumulation core and its use by measuring thermal parameters of porous materials, Proc.: Thermophysics 2006, Kočovce, oktober 2006, p. 103-109, (2006).

[5] BANÍK, I., LUKOVIČOVÁ, J.: Problem of elimination of undesirable thermal flows at thermophysical measurements, Proc.: Thermophysics 2007, Kočovce, oktober 2007, p. 107-119, (2007).

Effects of PCM application on thermal and energy performance of buildings in summer

Rachel Becker

Faculty of Civil and Environmental Engineering, Technion, Haifa, Israel

Abstract: *The paper presents an investigation of the effects of implementing phase change materials (PCM) at the room facing side of internal and external walls on the thermal and energy performance of residential, school and office buildings. Two construction types for residential buildings were studied: (1) a heavyweight concrete structure with concrete infill walls covered by cementitious renderings, and (2) a lightweight steel structure with lightweight external walls and gypsum wallboard partitions. For the school building the investigation addressed a heavyweight structure composed of precast concrete panels with two alternatives for the thermal insulation: (1) on the outer surface, below a stone cladding, and (2) on the interior side, behind a gypsum wallboard surface covering layer. For the office building the most typical construction type was investigated, which includes a column and beam structure with lightweight external walls and interior partitions. The main results are: (1) when the building includes a sufficient amount of internal mass, the addition of PCM improves thermal comfort during occupancy hours, but does not improve energy performance. (2) When the regular mass is very small, or not available for energy buffering at the room facing side, PCM improves both, thermal performance as well as energy performance.*

Keywords: *Phase Change Materials, Cooling Energy, Thermal Comfort, Heavyweight Construction, Lightweight Construction*

1. Introduction

The worldwide ultimate aim of building energy performance R&D is to lead to the design and construction of buildings that do not use fossil fuel energy for their operation (ZEB). Clean energy producing means that can be integrated in the building fabric and become an integral part of the architectural design are expensive and their capacity is low. Consequently, reducing energy demands remains the most important task before installing such systems.

Thermal and energy performance of buildings in heating dominated cold weather, has been studied intensively. The rules for high performance buildings are clear, and the technical solutions for wide spread implementation exist and are affordable. Adherence to the following rules can reduce heating energy demands to near zero levels even in extremely cold weather:

(1) Let solar radiation into the inner spaces, by providing large transparent areas in directions of intensive solar radiation, capture its energy in inner mass, and prevent loss to the external environment (item 4). Shading of direct radiation should be internal (drapes, Tromb wall).
(2) Exploit the heat emitted from internal heat sources, and prevent heat loss (item 4).
(3) Provide a moderate amount of inner thermal mass that will act as a daily thermal buffer.
(4) Prevent heat loss by: increased thermal insulation; elimination of thermal bridges including in window and curtain-wall frames; in windows – low U glazing with Low-E coating on external side of inner leaf; keeping open-able windows to the minimum required for summer comfort, and providing the rest of the transparent area using fixed highly insulated

glazing or transparent insulation materials (TIM); attaching external moveable insulation over windows; airtight sealing of all infiltration/exfiltration routes.

(5) Keep indoor air quality (IAQ) ventilation to that required for health and comfort needs. When heating is on avoid uncontrolled natural ventilation.
(6) Recycle exhaust heat.
(7) Keep thermal insulation dry (don't allow rainwater/moisture, interstitial condensation).
(8) Provide a warm tactile sensation using low thermal conductivity finish materials.

These means may have a less favorable effect on the performance of buildings in summer. However, studies of thermal and energy performance of buildings in the warm season, and in particular of buildings in warm climates that are cooling dominated, comprise a much smaller part of scientific studies. Moreover, as the role of internal heating sources in winter is positive, the neglect to address them causes an overestimate of heating demands and/or conservative design. Such a trend does not worry researchers, probably, and this may explain why a large part of the winter studies ignored internal heat loads. For summer conditions, however, internal heat loads should be a major concern. Surprisingly, a non-trivial part of literature still ignores them when studying building energy performance in warm climates.

The main aim of the paper was to investigate the possible thermal and energy improvements achieved in predominantly warm climates by applying Phase Change Materials (PCM) inside occupied spaces (for example at the inner surface of the walls). An additional objective was to study these effects under realistic occupancy conditions with typical internal heat loads, and to address the typical construction methods used in residential (low internal thermal loads), office (medium internal thermal loads) and school buildings (very large internal loads).

2. Investigation method, basic assumptions, and effect of conventional solutions

Promising experimental investigations of PCM were performed in the USA [1, 2, 3] and in Europe [4, 5]. However, due to the high cost of such research, these studies did not address typical situations during long term summer conditions in occupied spaces with internal heat loads. Since measures taken for improving the performance in one season may impede performance during the other seasons, annual performance has to be investigated. To gain much more insight into the actual benefits associated with implementation of PCM, the current investigation was based on dynamic thermal analysis of typical building modules using the program EnergyPlus (E+). Climatic conditions were typical to the warm Mediterranean region. Results shown were derived during several years of research. As E+ developes, its progressive versions yield somewhat different results. We thus used precisely the same version for comparative studies of a given topic, but not necessarily so for different topics.

Two residential construction types were addressed: (1) Heavyweight: concrete structure with concrete block internal partitions and autoclave aerated concrete exterior walls; (2) Lightweight: Steel structure with gypsum wallboard partitions and lightweight exterior sandwich panels. The office building was lightweight only. Two school construction types were addressed: (1) Heavyweight: concrete structure with concrete partitions and externally insulated concrete walls; (2) Semi lightweight: as the previous but with the insulation on the inner side, partitions replaced by double plate gypsum wallboard, and an acoustic ceiling added below the floor slab.

To fulfil minimal comfort and IAQ needs input data include: set-point temperatures of 20.5°C and 24.5°C during occupancy hours in winter and summer, respectively, with no active cooling or heating after hours. In winter, heating precedes occupancy by 1 hour; background IAQ ventilation according to building type and occupancy density was guaranteed during occupancy hours; during activity hours minimal luminance was 500 Lux on the working desks.

The internal heat loads in the examples discussed in this paper were: in dwellings [4 persons absent 8:00-13:00, 1 person absent 7:00-17:00 + 350W + lighting(max350W)]/100m^2; in the offices [1 person + 300W + lighting(max: 144W)]/12m^2, and in the classrooms [35people + 200W + lighting(max: 750W)]/49m^2. Values were based on a detailed Austrian data set [6].

In offices and classrooms, uncontrolled lighting is a major energy consumer and a major internal heat load. The investigation of energy improvement by PCM was preceded by a study of the effect of applying daylight dependent controls to reduce lighting loads, as shown in Figure 1. No other single means has the potential for such large energy savings. For this reason, the effects of PCM application were then studied on the improved buildings. Figure 1 also shows that when no dimming is implemented smaller windows are preferred, whereas with dimming the savings associated with lighting electricity overcome the increased cooling energy demand, and larger windows should be preferred. Further analyses yielded the following optimal combinations of window size and glazing type: for offices – 27% glazing/floor area composed of double Low-E 6mm/6mm glazing with SHGC=0.424 and Tvis=0.682; for northern classrooms – 19.3% glazing/floor area composed of double clear glazing with SHGC=0.833 and Tvis=0.838; and for southern classrooms – 15.7% glazing/floor area composed of double clear glazing with SHGC=0.833 and Tvis=0.838 (a horizontal overhang of 0.5 m deep extends above the window).

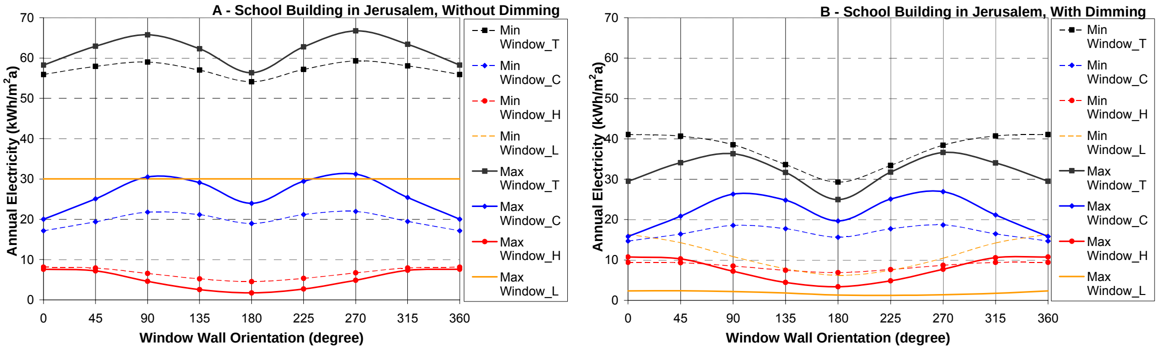

Figure 1 – Classroom energy performance without and with light dimming. Dashed lines: minimal window area (9%), full lines: maximal window (33.8%). L – lighting, H – heating, C – cooling, T – total.

To prevent heat accumulation, intensive ventilation after occupancy hours, when exterior air temperatures are lower than the set-point temperature, assists in discharging the energy stored during the preceding occupancy period. Results depicted an optimal ventilation rate of 10-15 air changes per hour (ACH), with an up to 25% net reduction of cooling+ventilation energy.

3. Effect of PCM application on annual thermal and energy performance

The amount of internal mass available for storing energy during occupancy hours depends on the construction system and building materials. Figure 2 shows the difference between heavyweight and semi-lightweight schools. Reducing the energy storage capacity caused pronounced increases in cooling energy demand and slight reductions in heating energy demand, leading to increased total consumptions in both orientations, with a larger effect on the south oriented classroom. It is apparent that construction with a large internal thermal mass performs better in the given moderately warm climate.

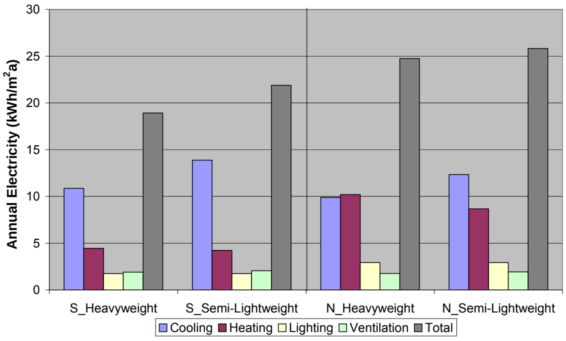

Figure 2 – Energy performance of a classroom in heavyweight and a semi-lightweight construction.

Analysis also showed that in all Israeli climatic zones, although heating demand was reduced with increasing thermal insulation, cooling demand increased. This is due to the adverse effect of insulation on heat removal from walls whenever the exterior temperature drops below the wall temperature. Consequently, in the warmer climatic zones, increasing thermal insulation thickness above a very low value proved to be ineffective from the total annual viewpoint.

The observations hereto emphasize that in warm climates it is much more important to apply other means, rather than increasing thermal insulation, which is so important in cold climates.

Despite the significance of inner mass in warm climates, construction of modern high-rise and tall buildings, as well as of low rise schools tends towards lighter components. The thermo-physical performance of the newly developed phase change materials (PCM) can replace the buffering effect of the internal mass. Such materials are expected to store energy upon melting, when the material reaches the lower melting temperature, and to hardly warm up as long as heat is flowing into them during occupancy hours. Buffering can be achieved on an everyday basis only if a period exists when the stored energy is entirely discharged from the PCM while it solidifies, leaving it ready for a next cycle of melting/solidification. The main potential for energy discharge stems from the lower exterior air temperatures at night. Intensive night ventilation is essential to materialize this potential. A melting/solidification temperature range below the set-point temperature can enhance thermal comfort and yield a secondary benefit. When the stored latent heat is not fully discharged over night, the storage capacity next day may not suffice for the new heat load and the PCM temperature will rise above the melting temperature range, storing sensible energy accompanied by material warming. The specific primary and secondary benefits of the PCM then disappear.

Table 1 delineates the material properties in the the current study. Preliminary steady state calculations for the specific weather of Jerusalem gave the values of maximal PCM thickness that can be fully discharged every night using intensive ventilation, and the accompanying area required for storing the total internal heat load as latent energy.

Summer performance of residential buildings was estimated using the degree hours summed during periods when interior temperature exceeded 26°C. Figure 3 shows the effect of PCM application in both, the heavyweight and lightweight construction types. It is evident that in general the thermal discomfort burden in heavyweight construction was much smaller than in lightweight construction, but could hardly be improved by application of PCM, whereas in the lightweight construction PCM application was very beneficial.

Table 1 – PCM and cover board properties

Material	Congealing Point °C	Melting Point °C	Latent Heat kJ/kg	Thermal Conductivity W/mK	Density Kg/m³	Specific Heat kJ/kgK
PCM	22.0	24.0	165.0	0.60	1380	2.50
Cover Board (12.5 mm)	22.5	23.0	28.7	0.58	2000	0.83

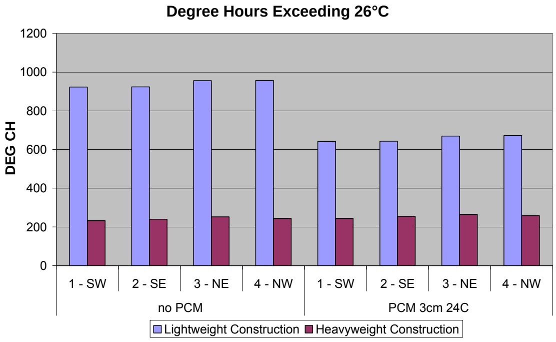

Figure 3 – Effect of PCM on thermal performance of lightweight and heavyweight residential buildings.

Figure 4 shows the effect of applying PCM in an office. The thickness range starts with the maximal thickness (5 mm) that can be discharged daily during the hottest period. The PCM was applied beneath the room facing cover boards of all the external walls and the partitions in the office. PCM with the minimal thickness was quite effective in reducing cooling energy demand in both southern and northern orientations of the office, with somewhat larger absolute savings in the southern offices, which had larger internal heat loads due to solar gains. Increasing the PCM thickness helped overcome the inability to discharge the PCM entirely every night during the hot summer periods. The energy savings increased almost linearly as the PCM thickness doubled, with a fast decreasing marginal benefit. Figures 5 and 6 show the effect of PCM thickness on internal surface temperatures in a southern and northern office, respectively, indicating the improved performance as the thickness increases.

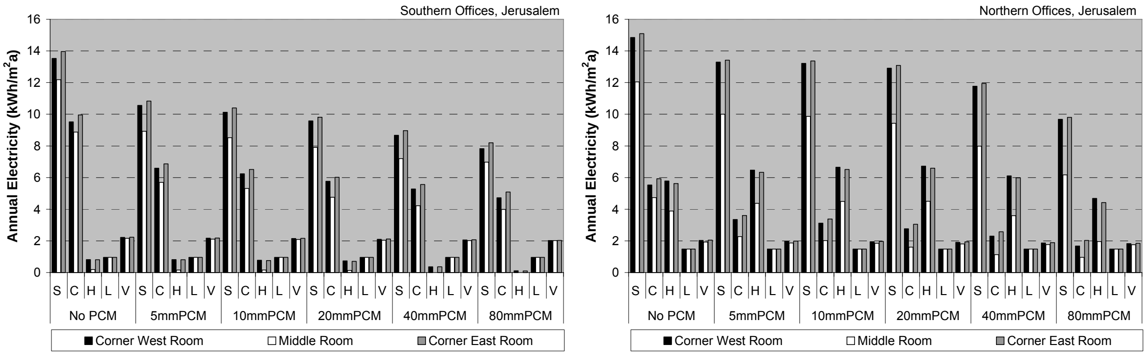

Figure 4 – Effect of PCM thickness on energy demand in an office.

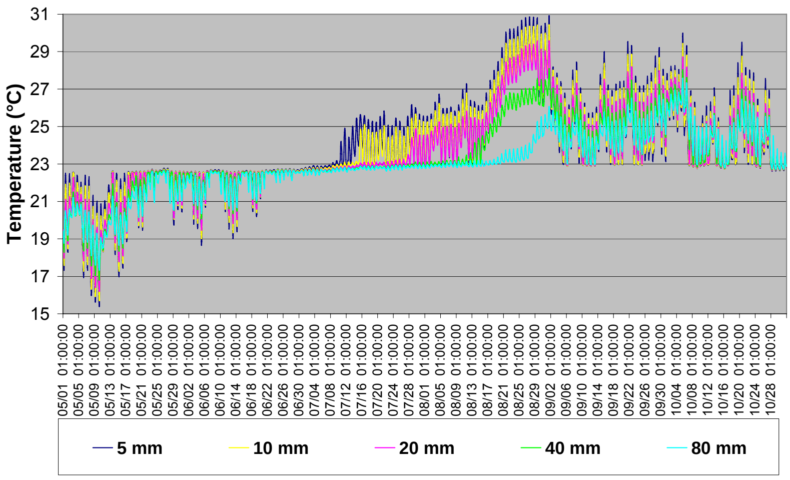

Figure 5 – Effect of PCM thickness on internal surface temperature in a southern office.

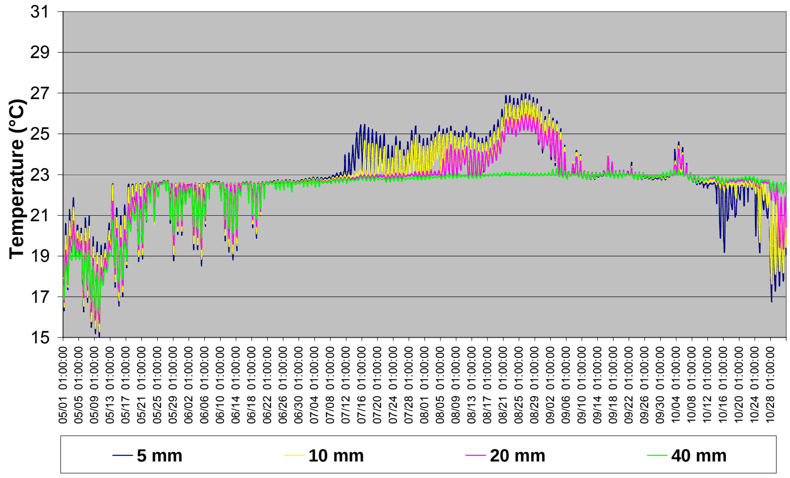

Figure 6 – Effect of PCM thickness on internal surface temperature in a northern office.

Increasing the rate of night ventilation raises the effectiveness of latent heat discharge. However, despite decreasing the cooling electricity, results showed that the increased ventilation fan electricity prevented improvement in total energy. It should be noticed, however, that the analytical simulations possible at this stage suffer from an inherent inaccuracy that stems from the embedded calculation algorithm in E+. The program does not enable to address the effect of an intensified air change rate on the dynamic values of the internal surface heat transfer coefficient. The implication of this deficiency is that actual discharge capacity may be larger than simulated, leading to better performance than estimated in the simulation. This of course must still be studied experimentally.

Addition of PCM in the heavyweight school construction proved to be energetically ineffective despite the improved thermal comfort enabled by lower surface temperatures during most of the occupancy hours. The addition of PCM in the classroom with internal insulation and false ceiling, showed, as displayed in Figure 7, that PCM can be effective in reducing the cooling energy, but even with enlarged PCM thickness, the original heavyweight classroom still displayed a superior performance.

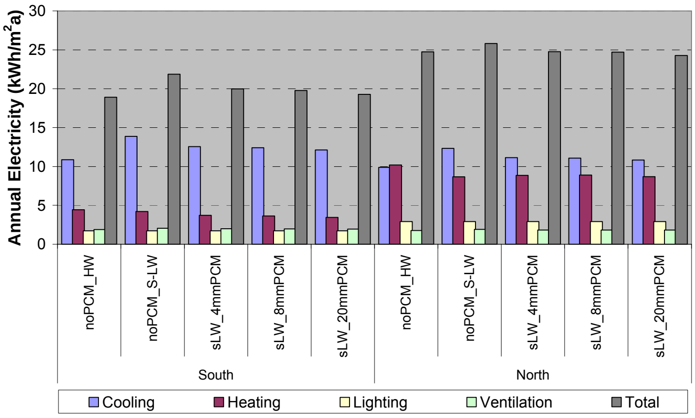

Figure 7 – Effect of PCM on energy demand in a classroom of semi-lightweight construction.

To conclude this study Figure 8 shows that improving thermal insulation of the lightweight walls from 6 cm to 10 cm (ΔR=1.0 m^{2}K/W) is less effective than implementing PCM with a minimal thickness of 5 mm.

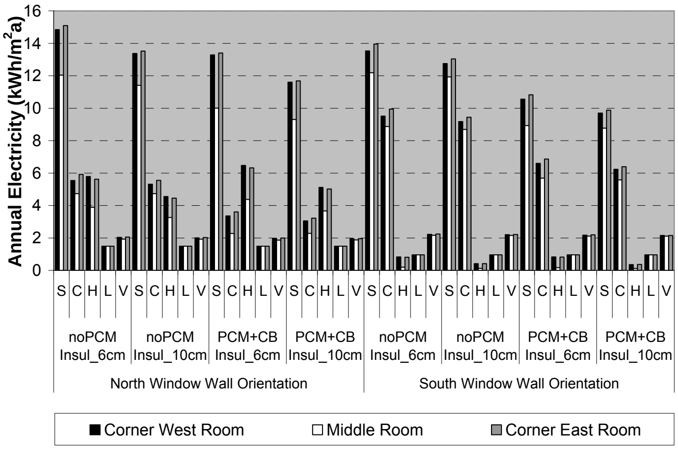

Figure 8 – Comparison of improved thermal insulation in offices with and without PCM.

The various results shown here, and many others that could not be shown due to the limited paper length, indicated that internal application of PCM can possibly improve thermal and energy performance of lightweight construction in warm climates even when large internal heat loads prevail. On the other hand, all simulation results for the heavyweight construction showed that there was hardly any energy improvement with such application, although internal surface temperatures were lower during the entire summer, providing improved thermal comfort.

4. Conclusions

The paper demonstrated that the conventional means suitable for improving energy and thermal performance of buildings in the heating season (thermal insulation, airtightness, moisture protection, minimizing IAQ ventilation to the bare necessity, recycling heat, Low-E glazing, transparent insulation, capturing heat from solar radiation and internal heat loads) are either not sufficient, or even not suitable, for improving the building thermal and energy performance in the cooling season. Additional conventional means (daylight controlled electrical lighting, combined optimization of window size and glazing properties, night ventilation, improved ventilation schemes, and increased inner thermal mass) have beneficial effects, but the remaining cooling demands are still large. To achieve the target of very low annual energy demand that can be met in the bulk of buildings by available clean energy building integrated technologies, such as photovoltaic cells and small wind turbines, there is a need for more advanced means. PCM application on the room facing side of walls was not effective in improving energy performance of heavyweight construction despite the improved thermal performance and comfort achieved during occupancy hours by the lower surface temperatures. On the other hand, such PCM application showed promising results in lightweight construction for all three types of occupancy (residential – low internal heat loads; office – medium loads; classroom – large loads). There are still gaps in knowledge regarding the overall thermal performance of actual buildings with PCM on the room facing side of walls, as well as technological and economic barriers to the application of this means in the majority of buildings. The extent of the energy improvement it provides under various circumstances needs still further research, but the results to date show that with the construction industry aiming at lighter construction ethods, this is a promising solution for modern buildings.

Acknowledgement

The author acknowledges the sponsorship provided by the Ministry of Infrastructures and of the Technion that supported the work performed by the graduate students Itamar Goldberger and Evgeniey Beagon and the MIT guest student Stella M. Schieffer. The numerical results presented in the various drawings are based on computer runs they performed during their theses work.

References

[1] Kosny, J.; Yarbrough, D.; Miller, W.; Petrie T.; Childs, P.; Syed, A.M.; Leuthold, D. Thermal performance of PCM-enhanced building envelope systems. *Proceedings of the 2007 Buildings X Conference on Thermal Performance of the Exterior Envelope of Whole Buildings*, Dec. 2-7, 2007, Clearwater Fa, USA.

[2] Pasupathy, A.; Velraj, R., Seeniraj, R.V. Phase change material-based building architecture for thermal management in residential and commercial establishments. *Renewable and Sustainable Energy Reviews*, v12, n1, (2008) p. 39-64.

[3] Medina, M., King, J. B., Zhang, M. On the heat transfer rate reduction of structural insulated panels (SIPs) outfitted with phase change materials (PCMs). *Energy*, v33, n4, (2008) p. 667-678.

[4] Cabeza, L.F.; Castellon, C.; Nogues, M.; Medrano, M.; Leppers, R.; Zubillaga, O. Use of microencapsulated PCM in concrete walls for energy savings. *Energy and Buildings*, v39, n2, (2007) p. 113-119.

[5] Schossig, P., Henning, H.M., Gschwander, S., Haussmann, T. Micro-encapsulated phase-change materials integrated into construction materials. *Solar Energy Materials and Solar Cells*, 89, (2005) p. 297-306.

[6] Varga, M. Internal heat loads. Ed. Unterpertinger, F., *Austrian Energy Agency*. Vienna, Austria.

New method to quantify liquid transport inside hydrophilic interior insulation materials

Andrea Binder[1], Daniel Zirkelbach[2], Hartwig Künzel[3]

[1]Department of Hygrothermics, Fraunhofer Institute for Building Physics IBP,
Fraunhoferstrasse 10, 83626 Valley, Germany, andrea.binder@ibp.fraunhofer.de

[2]Department of Hygrothermics, Fraunhofer Institute for Building Physics IBP,
Fraunhoferstrasse 10, 83626 Valley, Germany, daniel.zirkelbach@ibp.fraunhofer.de

[3]Department of Hygrothermics, Fraunhofer Institute for Building Physics IBP,
Fraunhoferstrasse 10, 83626 Valley, Germany, hartwig.kuenzel@ibp.fraunhofer.de

Abstract: *Interior insulation systems influence the hygrothermal behaviour of a construction. Therefore, special attention is required towards its hygrothermal design. One approach, that is recently becoming increasingly popular, is based on the concept of capillary activity. By using vapour permeable hydrophilic insulation materials, liquid moisture occurring inside the construction can be transported back towards the interior surface to a certain extent, which helps to control the moisture level inside the construction beneath critical values. To determine a building component's hygrothermal performance prior to construction, detailed material properties have to be at hand. For various reasons, the common test methods to quantify liquid transport often do not deliver adequate results for the specific purpose. Therefore, a new laboratory test has been developed, that is carried out under conditions similar to real life. Under defined boundary conditions, a temperature below the dew point is applied to a laterally sealed material sample, thus generating a gradient of partial pressure. The insetting vapour diffusion into the material leads to a rising moisture content and increased relative humidity at the cold side of the material. A liquid transport reverse to vapour diffusion sets in. By performing regular gravimetric as well as nuclear magnetic resonance measurements, both water gain and distribution across the sample are monitored, serving as a basis to fine-tune the liquid transport coefficients via hygrothermal computational simulation. On the basis of a fibrous insulation material, the results of the new measuring method are demonstrated and compared to the results of conventional test methods.*

Keywords: *Interior insulation, capillary activity, liquid transport, hydrophilic*

1. Interior insulation and moisture transport phenomena

As a result of rising energy expenses and new energy regulations, the thermal improvement of building envelopes is becoming an important issue in more and more countries. While the application of an external insulation system poses little problems, there are, especially in existing buildings, certain circumstances where another approach has to be chosen. In cases of high building density, heterogeneous ownership, or with preservation provisions applying, the only possibility to thermally retrofit a wall often is interior insulation. I.e., an insulation layer is applied to the interior side of a wall structure. Attention should be paid to the fact, however, that by adding interior insulation to an existing structure, both hygric and thermal conditions inside the original wall structure are changed, usually for the worse. Due to the rising thermal resistance at the interior side of the wall, a change of temperature conditions occurs, leading to a shift of dew point towards the interior surface. At the same time, the drying potential of the wall in summer time is reduced. These effects lead to rising moisture levels inside the construction and to rising relative humidity at the interface of insulation layer and former interior surface. This may cause damages trough mould, decay or frost inside the construction or at the exterior surface, while the conditions at the interior surface are improved. Therefore, measures have to be taken to avoid critical moisture ratios inside the walls. Next to the more common systems using vapour permeable, hydrophobic materials plus vapour control layer to the interior side of the wall, new systems are becoming more and more popular: capillary active interior insulations. These materials are applied without additional vapour control layer, keeping the moisture conditions beneath critical values by themselves. A holohedral (cavity free) adhesion of the insulation has to be ascertained, however, to ensure an optimal, damage free, mode of operation. The precise knowledge of the material characteristics is essential to determine and predict its hygrothermal behaviour.

Moisture transport phenomena in capillary active interior insulation materials

Capillary active insulation materials are rather vapour permeable. Along a gradient of partial pressure, vapour diffusion transport into the material takes place (Fig. 1, I), depending on the materials water vapour diffusion resistance. Defined primarily by the pore structure of a material, the diffusion resistance is also dependent on the materials moisture content. Inside a hydrophilic material, water molecules will adhere to the interior surface of the pores (Fig. 1, II & III), forming a moisture film reaching from mono- up to a multimolecular thickness. This effect is called sorption. As with rising film thickness, the free pore diameter available for water vapour diffusion is reduced, the diffusion through the material changes. With sufficient film thickness, surface diffusion (liquid transport inside the film) begins (Fig. 1, IV & V), following the gradient of relative humidity. With pores completely filled, yet another driving force sets in: capillary suction. This effect, called capillary activity, describes the behaviour of liquid water inside small "capillary" pores. The transport velocity here exceeds that due to surface diffusion by many times. Due to the interaction of surface tension of the liquid (cohesion) and the interfacial tension between liquid and solid face (adhesion), liquid can be transported inside the material pores in any direction, following the capillary suction power. As the suction power is dependent on the pore radius, small pores exhibit a higher suction power, but slower suction velocity as pores with larger diameter. Most building materials feature an uneven distribution of pore sizes, thus not all pores are filled at an equal amount. At lower moisture contents, smaller pores are filled already, while larger pores may still exhibit only surface diffusion (Fig. 1, III). At uneven moisture distribution inside the material, smaller pores may suck moisture out of larger pores until pressure equilibrium is reached. The transport velocity therefore depends on the amount of water offered as well as on moisture content, distribution and pore structure of a material.

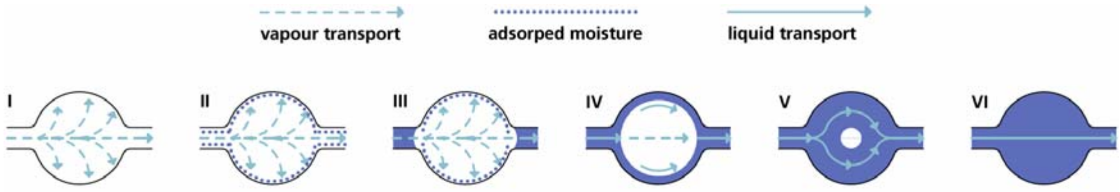

Figure 1: Moisture storage and -transport phenomena in hydrophilic, porous media.

To further identify the transport phenomena in interior insulation materials, two boundary conditions have to be distinguished: Under isothermal conditions (Figure 2, top), both the gradient of partial pressure and relative humidity have the same direction. Vapour-, as well as liquid transport therefore are coplanar. In Middle-Europe, these conditions usually occur in summer time. In winter time, the conditions dictate more complex moisture transport behaviour, however. Here, non-isothermal conditions occur, with temperature and partial pressure on the interior side of the wall exceeding that on the exterior side, generating a vapour transport towards the exterior surface. The relative humidity, however, is higher on the outside. Liquid transport therefore is directed contrary to the vapour transport; both transport mechanisms are interacting. As the vapour inside the material pores is cooled down as it migrates towards the exterior side, more and more moisture is stored at the material pores, additionally heightening the content of liquid moisture at the exterior side of the wall. As in practice, the distinction between liquid transport due to capillary pressure and surface diffusion is hardly possible due to their interactions in the complex pore structure of the material, both effects are described with the term “capillary back transport”.

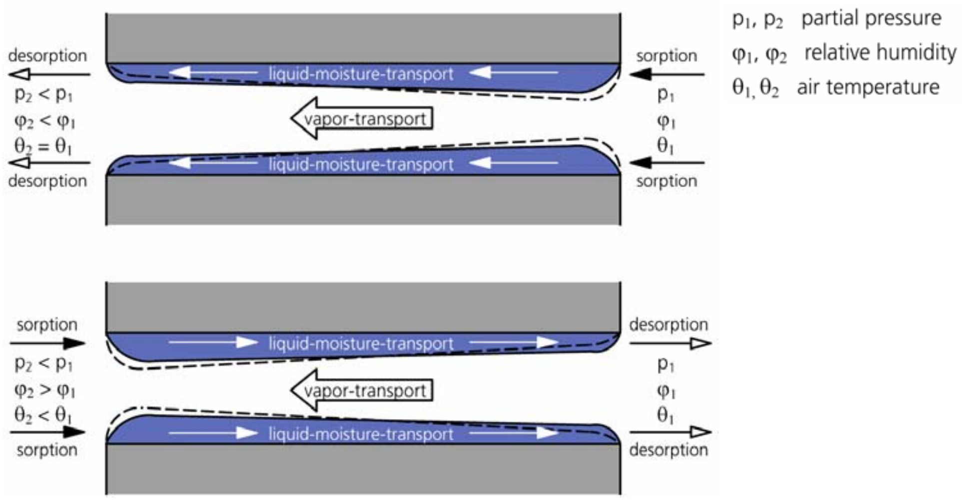

Figure 2: Influence of boundary conditions on moisture transport phenomena in hydrophilic, porous media. Top: isothermal boundary conditions; bottom: non-isothermal boundary conditions.

Constraint of conventional ways to determine liquid transport

Although there are reliable ways to determine most material characteristics through laboratory tests, there is no consensus yet on the exact determination of liquid transport characteristics in the specific conditions of interior insulations. Methods like the Drying Method [3, 5] or the Redistribution Method [2] have proved to show good accordance with many applications in practice. There is growing evidence, though, that the material characteristics based hereupon have certain restrictions concerning the specific conditions occurring in interior insulation materials. All methods have been developed and validated for materials under influence of natural weathering, thus moisture in its liquid form (precipitation). In the tests, material samples are subjected to liquid water. As described, the transport effects here are dominated by the transport in the larger pores. Interior insulation materials, however, feature moisture levels that are lower. The usually performed adaption of the coefficients to lower moisture regions may lead to a misestimation of the liquid transport. Furthermore, these methods may not be appropriate for some materials, as the high amounts of water applied may lead to structure changes of the material (agglutination or swelling). Besides, all tests are executed under isothermal conditions. The interaction of opposing moisture flows is not considered therefore. To account for the specific material structures and boundary conditions of interior insulation assemblies, test methods should reflect these as far as possible.

2. Capillary Back Transport Test

Idea and Setup

A new test method has been developed therefore to identify the liquid transport phenomena occurring in interior insulation materials. This test, called Capillary Back Transport (CBT) test, imitates the conditions that interior insulation has to face in reality. Figure 3 shows the set-up for the test schematically. In a laboratory test featuring non-isothermal conditions, a dew-point undercut is applied to a laterally sealed material sample. No water is applied during testing, liquid transport thus occurring only due to condensate arising from vapour diffusion. As at the cooled back side of the material sample the relative humidity rises, an increasing capillary back transport towards the front surface begins, that opposes the vapour diffusion. The moisture gain of the material sample in testing is slowed down more and more, until – sufficient capillary back transport being given – a dynamic equilibrium is reached. Both moisture gain (weighing with a laboratory balance) and distribution (via nuclear magnetic resonance scanning) are measured during the test period to detect the hygrothermal behaviour of the samples. By implementing the test results into hygrothermal simulations, the coefficients for the materials capillary back transport are defined.

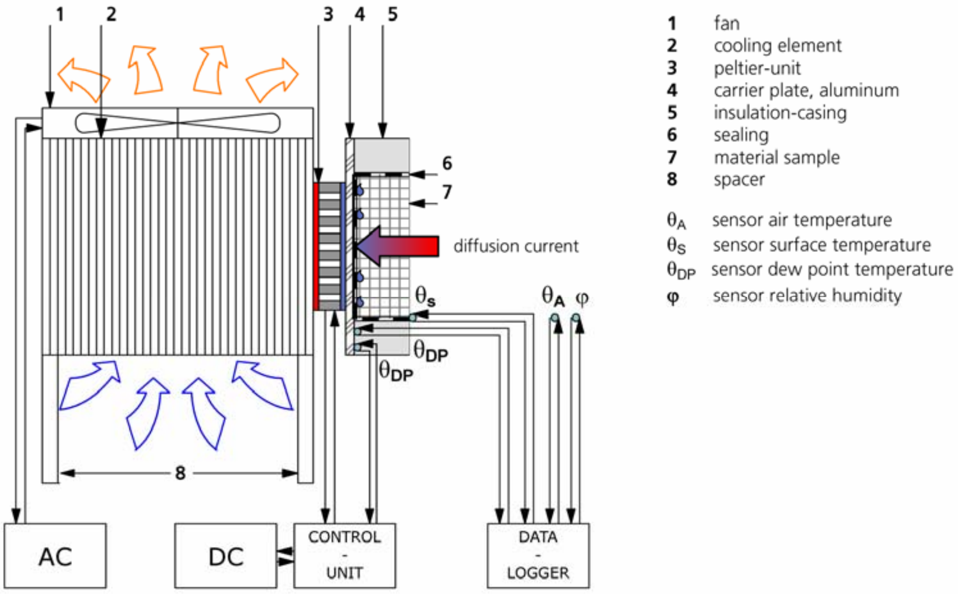

Figure 3: Schematic display of the Capillary Back Transport test setup.

Test equipment and procedures

The "dew-point" temperatures at the back side of the material sample are produced by thermoelectrical devices called Peltier-unit (PU). In the tests, single level units with a maximum temperature gradient of 73 K are used. A water proof coating provides protection from condensate occurring during testing. The temperature reduction on one side of a PU is faced by an equal temperature rise on the opposite side. To secure an effective mode of operation, a passive cooling element is applied to the warm side of the element. Enhancing the convection around the cooling element further, it is put onto spacers; a high capacity fan is installed on top. To the front side of the Peltier-unit, an aluminium plate is applied, serving as carrier for a laterally and rearward sealed material sample and the insulation casing. Sealing and insulation casing are necessary to secure one-dimensional heat and moisture transfer processes. Heat conductive paste is applied at all joints in order to maintain flawless heat transfer. To regulate the power supply and therefore the temperature of the Peltier-unit, a temperature sensor (PT 100) is installed at the front of the carrier plate. Further temperature and relative humidity sensors are used to measure and document both relative humidity and temperature of air, as well as surface and interface temperatures of the material sample.

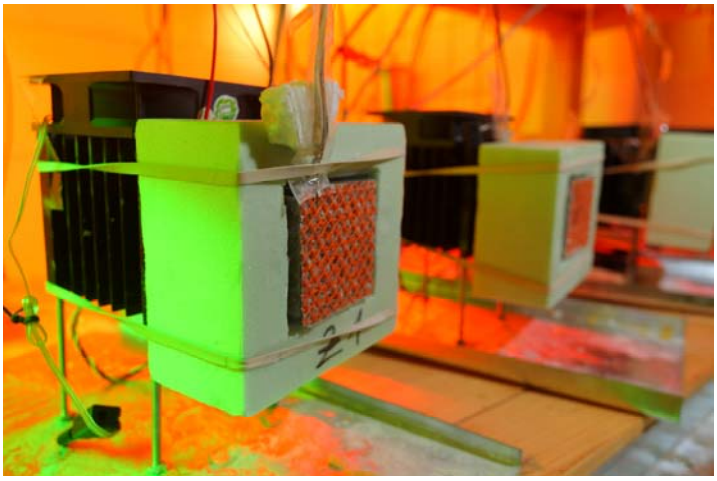

Figure 4: View of the Capillary Back Transport test setup (with cellulose fibre samples).

The samples are applied to the carrier plate for testing. Periodically, the samples are removed from the test setup in order to measure moisture content and distribution. After having cleansed the samples of remaining heat conductive paste, they are measured gravimetrically. The samples are then brought into the NMR scanner one by one. A pecking motor is moving them through the inductor with 12 millimeters per step. Along each step, 15 measure points are generated, thus, a highly detailed analysis of the moisture distribution can be performed. To account for the drying effect during the scanning process, the samples are weighed subsequently before they are put back into the test setup. This procedure continues until a dynamic equilibrium is reached.

Tested material, sample preparation and boundary conditions

This paper presents the test results for a cellulose fibre insulation material. It is made out of recycled newspaper with an addition of approximately 8 % borates serving as fire protection. The material is typically used to isolate walls, roofs or floors by either injecting or pouring it into cavities. Table 1 exhibits its standard properties. To prepare the material samples, cubic, water proof containers have been made out of conventional window pane (Ø 3 mm). The width and height are constrained by the NMR-spectrometer (50/50 mm). Although the depth can be selected freely, it has to be considered that with rising sample thickness, the time span to reach dynamic equilibrium expands. With decreasing sample thickness on the other hand, the measurement results will become more imprecise. This is especially the case for fibrous materials, as variances occurring during sample preparation will have more impact. The chosen thickness is 50 mm. In the containers, the material is inserted manually until the required density of 50 kg/m³ is reached. The front of the sample is then covered with a coarse meshed, diffusion permeable synthetic net. The samples are then dried in a drying cabinet. After having made the first NMR measurements of the dry material samples, they are stored in the test climate chamber until reaching equilibrium. Figure 5 shows the cellulose fibre samples prepared for the tests. All tests are executed under defined boundary conditions. Therefore, the test setup is placed in a climate chamber with 23 °C and 67 % RH. The dew point temperature at these conditions is 17 °C; the temperature generated at the back side of the samples is 12 °C.

Table 1: Standard properties of the cellulose fibre used in testing

Property		**Value**	**Unit**
Density	ϱ	50,0	kg/m³
Porosity	σ	95,0	%
Thermal conductivity	λ	0,037	W/mK
Water vapour diffusion resistance value	μ	1,2	-
Moisture content at 80 % RH	-	7,8	kg/m³
Moisture content at free saturation	-	430	kg/m³

Figure 5: Cellulose fibre samples prepared for Capillary Back Transport Tests.

Measurement results

Figure 6 shows the chronological developing of water gain and distribution in cellulose fibre samples (cross section) during CBT testing. As expected, the sorption moisture content (67 % RH) is evenly distributed in all samples (“start”). Once the tests are started, the interstitial temperature falls below the dew point, leading to a rise of moisture at the back side of the material sample (represented left in each picture). Compared to the high moisture content here, a steep decline of the moisture gradient can be detected across the farther section of the sample, as can be seen in the gradient for 2 days test time. In the following, a further increase of moisture across larger parts of the samples can be detected, until a dynamic equilibrium is reached (exemplified here by the gradient for 43 days test time). The liquid transport is strong enough to balance the vapour diffusion. However, the moisture level at the back side of the material reaches about 120 kg/m³. In reference to the materials moisture storage function, this means a relative humidity of 99 %. To what extent this moisture level is dangerous, however, has not been examined finally. Figure 7 shows the chronological developing of water gain of cellulose fibre samples during testing. Starting from a sorption moisture content (at 67 % RH) of about 6 kg/m³, the samples gain weight fast at the beginning of the experiment. With time advancing, the weight gain decreases. After approximately 28 days, the weight gain has almost stopped and the specimens have reached a dynamic equilibrium. The data show good correlation between the measurements of all three specimens. During the measurement procedure, a slight decrease of weight can be detected, as the moisture can dry out to a certain extent. As this weight loss is only minor (ca. 0,25 M-%), its impact on the hygric behaviour of the samples in test is negligible.

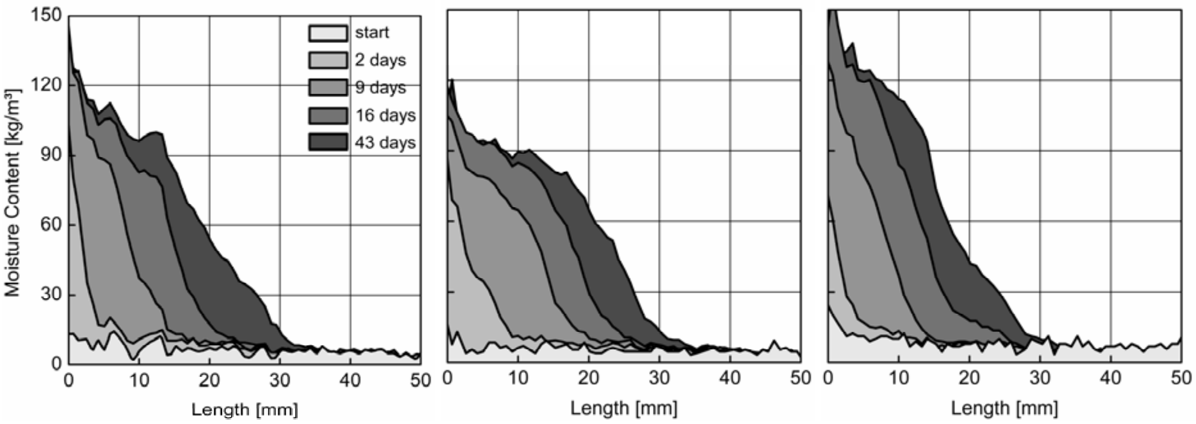

Figure 6: Water gain and distribution in cellulose fibre samples (cross section) during the Capillary Back Transport test.

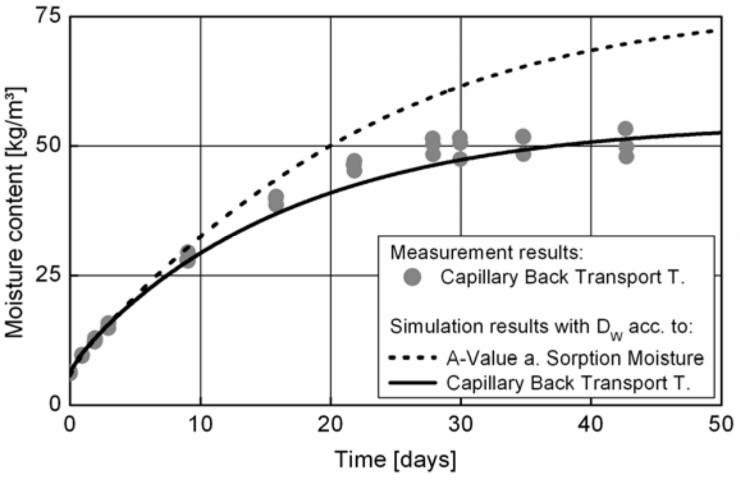

Figure 7: Water gain of cellulose fibre during the Capillary Back Transport test. Comparison of test and numerical simulation results.

Numerical hygrothermal simulation

The test results for the different material samples are reproduced by numerical simulation. This is performed by using WUFI® [4], a simulation program for the transient coupled heat- and moisture transfer in building materials. Based on the standard properties shown in Table 1, a stationary numerical simulation was performed, imitating the boundary conditions of the tests. To detect the materials capillary back transport properties, both the results for the weight gain (total test period) and distribution (day 43) were inserted in the result displays of the numerical simulation. Initially, the liquid transport properties (D_W) according to A-value and sorption moisture where taken and adapted step by step, until a good correlation between measurement and simulation both for water content and distribution in the specimens was reached. The different liquid transport coefficients are shown in table 2. Figures 7 and 8 compare the data of measurement and simulation. As can be seen in both charts, the simulation results based on the approximated liquid transport properties show a discrepancy to the measurement results. Here, an underestimation of the liquid transport exists.

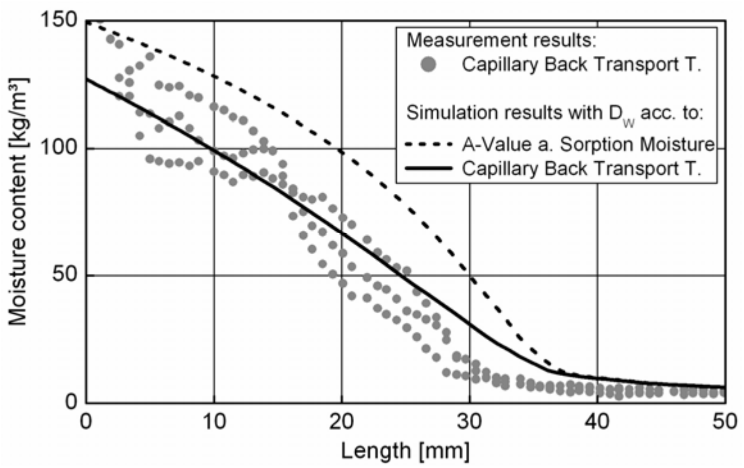

Figure 8: Moisture distribution in cellulosic fibre at dynamic equilibrium. Comparison of test results (day 43) and numerical simulation.

Table 2: Liquid transport coefficients of Cellulose fibre according to different test methods

Moisture Content [kg/m³]	**D_W acc. to A-Value a. Sorption Moisture. [m²/s]**	**D_W acc. to Capillary Back Transport Test [m²/s]**
0,0	0,0	0,0
7,8	$2{,}7 \times 10^{-10}$	$7{,}0 \times 10^{-10}$
430,0	$2{,}3 \times 10^{-8}$	$1{,}0 \times 10^{-9}$

3. Conclusion

As more and more materials with capillary active qualities come on the market, the precise determination of properties concerning this matter gains importance. The new approach to examine the behaviour of materials in laboratory tests imitating the real life boundary conditions shows good results, as the interactions of vapour and liquid transport under non-isothermal conditions can be analysed. Especially for materials whose liquid transport properties can hardly be measured because their specific structure changes in contact with bulk water (e.g. wood or cellulose fibre materials), the method promises meaningful results, as the data shown in this work proofs. While the application of conventional coefficients (developed for materials under influence of natural weathering) delivers an underestimation of the liquid transport in the lower moisture region, good correlation can be reached with the coefficients detected by the Capillary Back Transport test. As investigations with other capillary active insulation materials have shown, the capillary back transport using conventional coefficients tends to overestimate the liquid transport capacity in mineral materials [1]. This appears to be different when wood-based materials such as cellulose fibres are considered. Here, the liquid transport capacity is underestimated when conventional capillary transport coefficients are employed. Therefore, special test methods have to be tailored for interior insulation materials that produce more precise results than the conventional methods. For measuring and predicting the hygrothermal behaviour of interior insulation, the CBT method looks promising and should be used therefore as a replacement or addition to the conventional methods. As the CBT method has been developed for low capillary moisture levels, the conventional methods should still be performed for materials in contact with bulk water from natural weathering. In the future, the hygrothermal behaviour based on the new coefficients has to be examined by doing numerical simulations implying realistic climate conditions. Further laboratory as well as large scale tests and comparisons with measurements done in practice will be done to further check and validate the new test method.

References

[1] BINDER, A.; ZIRKELBACH, D.; KÜNZEL, H.; *Test method to quantify the wicking properties of porous insulation materials designed to prevent interstitial condensation,* Proceedings of the 3rd Third International Conference on Porous Media and its Applications in Science, Engineering and Industry, Montecatini, June 20-25, 2010

[2] KRUS, M.; *Moisture transport and storage coefficients of porous mineral building materials – Theoretical principals and new test methods,* Fraunhofer IRB Verlag, Stuttgart, 1996, ISBN 978-3-8167-4535-8

[3] KRUS, M.; HOLM, A.; *Simple methods to approximate the liquid transport coefficients describing the absorption and drying process,* Proceedings of the 5th Symposium 'Building Physics in the Nordic Countries', Goteborg, August 24-26, 1999, pp. 241-248

[4] KÜNZEL, H. M.; Simultaneous heat and moisture transport in building components – One and two-dimensional calculation using simple parameters, Fraunhofer IRB Verlag, Stuttgart, 1995, ISBN 978-3-8167-4103-9

[5] SCHEFFLER, G.; PLAGGE, R.; Ein Trocknungskoeffizient für Baustoffe, Bauphysik 31, Ernst & Sohn, Berlin, 2009, pp. 125-138

Hygrothermal effects in lightweight roofs shaded by PV-elements

Christian Bludau[1], Thomas Schmidt[2], Hartwig M. Künzel[3]

[1]Department of Hygrothermics, Fraunhofer Institute for Building Physics, Fraunhoferstr. 10,
83626 Valley, christian.bludau@ibp.fraunhofer.de

[2]Department of Hygrothermics, Fraunhofer Institute for Building Physics, Fraunhoferstr. 10,
83626 Valley, thomas.schmidt@ibp.fraunhofer.de

[3]Department of Hygrothermics, Fraunhofer Institute for Building Physics, Fraunhoferstr. 10,
83626 Valley, hartwig.kuenzel@ibp.fraunhofer.de

Abstract: *Sealing roof constructions against water and vapour on both sides only works well as long as the seal is perfectly tight and no water was built in, because any water trapped in the construction can not dry out. Therefore, a common way to build wooden lightweight roofs is to compensate for the vapour tightness of the roofing membrane by installing a moderately permeable membrane at the inside to provide some drying potential for safety reasons. However, drying to the indoor space will only happen if the solar heat gains of the roof are high enough to reverse the vapour flow for a sufficient time period.*

The application of PV elements on a roof leads to permanently shaded areas on the roof surface. To account for the attenuation of solar radiation below such panels a model has been developed which computes the influence of radiation on a point shaded by a quadrilateral object obscuring part of the sky. Using this data the balance of interstitial condensation in such constructions and subsequent drying is investigated using an adapted hygrothermal simulation tool for heat and moisture transport in building components. The investigations show that attaching PV elements on wooden lightweight roof constructions may cause problems by moisture accumulation in some assemblies.

Keywords: *flat roof, shaded surface, interstitial condensation, solar panels*

1. Introduction

The construction of lightweight flat roofs with vapour tight membranes on both sides has resulted in numerous damage cases in recent years. If a tight seal against any type of moisture entry is guaranteed, such roofs can perform well, as long as there is no water intruding or built in. Providing a long-term guarantee for such constructions is very difficult, therefore it often makes more sense to design constructions which can dry out to the inside. The prerequisites for the drying process include an adequate vapour drive towards the interior space. This will only occur if the roof's exterior surface temperature is high enough and a moderate vapour retarder that allows some vapour penetration is installed at the interior side. This paper investigates the hygrothermal performance of roof constructions with moderate vapour retarders with and without the influence of a surface shaded by PV elements. Based on data measured at the field test site in Holzkirchen a model is developed for considering such effects in a simulation tool for the coupled heat and moisture transfer in building components. Using the new model and some other assumptions, the influence of the shaded surface on the lightweight flat roof construction is assessed.

2. Fundamentals

Shading of the surface

Temperatures at exterior surfaces of building components are affected by heat fluxes in various ways. Beside heat fluxes due to heat conduction within the component and convective heat exchange with the surrounding air, radiation effects play a decisive role. The energy balance at the roof surface can be expressed by the following equation:

$$I_S + I_L - I_E + q_c - q_T = 0 \tag{1}$$

with:	I_S	[W/m^2] short wave solar radiation incident onto the component's surface
	I_L	[W/m^2] long wave radiation incident onto the component's surface
	I_E	[W/m^2] long wave radiation emitted by the component's surface
	q_c	[W/m^2] heat flux by ambient air convection
	q_T	[W/m^2] heat flux by thermal transmission through the component

Herein only I_S and I_L are influenced by shading.

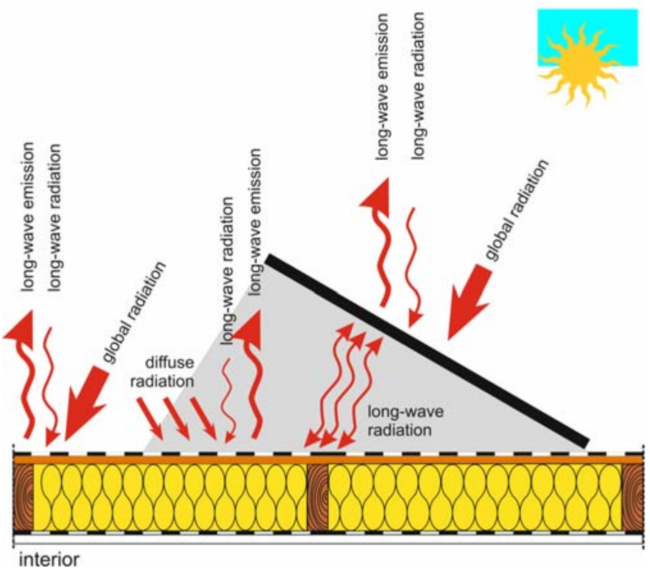

Figure 1: Radiation exchange` on a flat roof surface – unshaded and below a solar panel.

In Figure 1 the radiation processes on a roof surface and below a solar panel are displayed. On the free surface the main energy gain comes from solar radiation. The surface loses also energy by long-wave emission, which is partly compensated by the atmospheric counterradiation. In covered areas the direct solar radiation is blocked, only the diffuse part of the solar radiation can reach the surface, depending on the field of view. The long-wave emission is always the same, but the atmospheric counterradiation is reduced by the field of view. Below the covered area there is a long-wave exchange of energy between the surface and the covering's lower surface. Both surfaces have nearly the same temperature, so there is no significant energy loss below the covering. To determine the surface temperature at a certain position the calculation of the radiation balance has to be performed including detailed shading information.

Permeable membranes and humidity controlled permeability

A vapour retarder is specified by its vapour permeance or resistance. A common definition of the vapour diffusion resistance is the thickness of an air layer with equivalent resistance, the so-called sd-value given in meters. Most membranes have a constant permeance over the whole range of humidity. However, there are also some membranes available which have a variable permeance, depending on the humidity of the ambient air. These so-called smart vapour retarders were developed for increasing the drying potential towards the indoor side in roof constructions which are vapour tight to the outside. In Figure 1 permeance and sd-value of such a vapour retarder are displayed as a function of relative humidity.

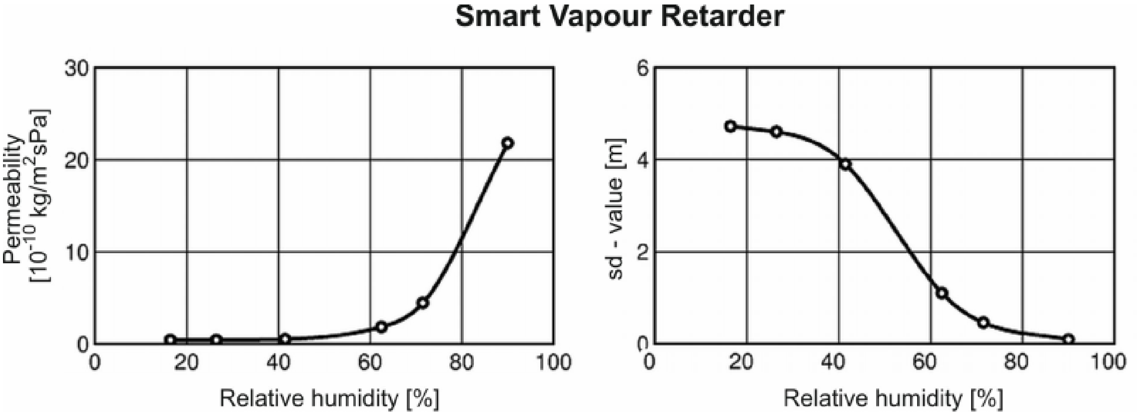

Figure 2. Permeance and s_d-value of a smart vapour retarder (PA film) as function of relative humidity.

3. Investigations

Field Tests

Considered are the measured and simulated thermal conditions on the surface of a flat roof at the field test site in Holzkirchen. The investigated roof surface consists of a membrane which is placed directly on a layer of 175 millimeters of mineral wool insulation.

Figure 3: View of the solar panel and the sensor positions, the white painted area is in the background.

One test section is shaded by a solar panel, another section is painted with a white, reflecting color. The reference section remains unaltered and undisturbed. This article only deals with the calculations concerning the shaded part. Photographs of the test roof in Holzkirchen and the solar panel as well as the white surface area are shown in Figure 3. The temperature measurements are performed using PT100 temperature sensors. Prior to the installation, all sensors are calibrated in the laboratory. The solar panel was set up on the roof in summer 2009.

Comparison of measurement and calculation

The hygrothermal simulations are performed by applying WUFI® [1], which allows the transient calculation of coupled heat and moisture transport in building components under real climate conditions. The model has already been experimentally validated by comparison with numerous field tests. The software is able to determine the hygrothermal situation in a building component using realistic boundary conditions. The program allows the use of any climatic conditions, for example given in hourly values for one year. The climatic data include temperature, humidity, wind and rain as well as radiation (global and diffuse). In order to accurately calculate the temperatures of exterior surfaces a detailed radiation model was developed at Fraunhofer IBP based on physical fundamentals [2] and implemented. For calculating the surface temperature, this model is used in combination with the new shading model. The model calculates the radiation data for a given point on a plane which is shaded by a rectangle. Direct and diffuse radiation as well as the atmospheric counterradiation are modified as demanded by the remaining fraction of unblocked sky in the field of view, and multiple reflection of the diffuse radiation is taken into account in a simplified way. Also the long-wave radiation exchange between the point and the shading layer is included. The considered radiation parts are schematically shown in Figure 4. Using this model the climatic data of the calculation input file are rewritten, replacing the original direct, diffuse and atmospheric counterradiation by their modified values. The climatic data including the shading effects are used for the hygrothermal simulations later in this paper.

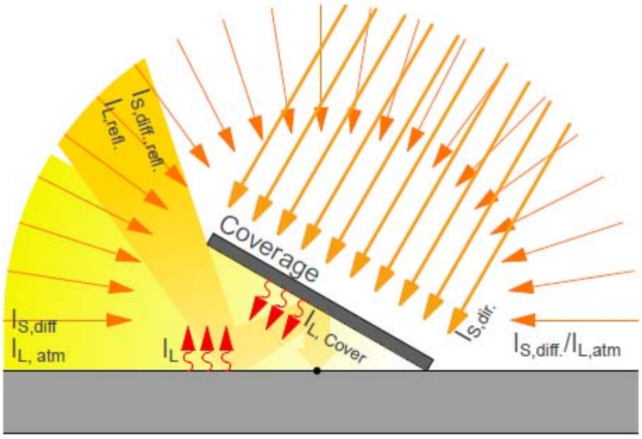

Figure 4: Radiation balance model for the investigated surface point.

The calculations comparing simulation with field testing spanned a period of six months. The outdoor conditions used for the simulation were those measured during the test period including solar radiation and long wave sky radiation from the atmosphere. The roof was modelled and simulated using the measured outdoor conditions and the shading model. The comparison of the measured and the calculated temperatures on the roof surface is displayed in Figure 5. The agreement of the temperatures is quite good. Based on the assumptions of these simulations climatic data for the shaded point were generated for the whole year 2009.

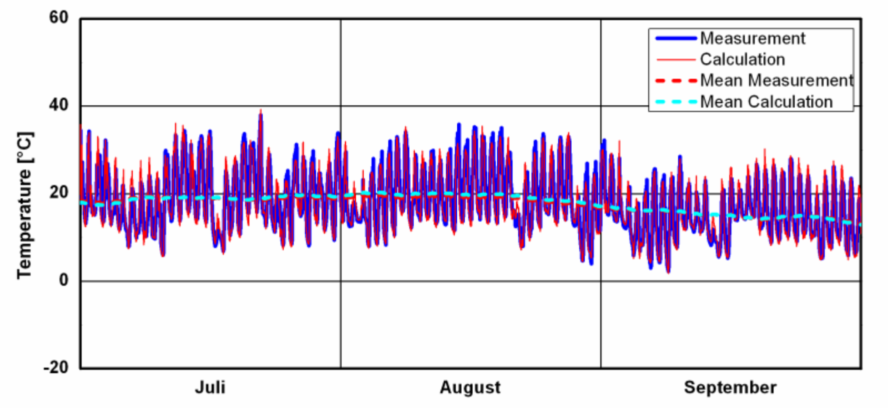

Figure 5: Comparison of the measured and calculated surface temperature.

Calculations

Based on the comparisons, simulations are performed to obtain the influence of the shading on the hygrothermal behaviour of wooden flat roof constructions. The construction assembly investigated with WUFI® is shown in Figure 6.

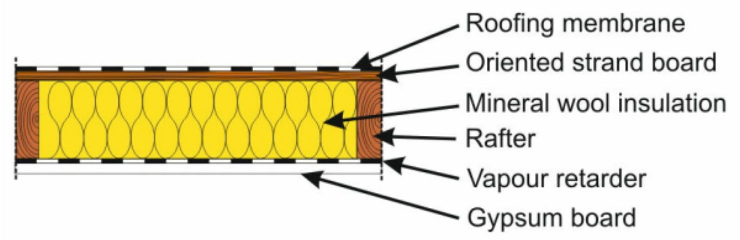

Figure 6: Wooden flat roof construction used for the simulations

For the roofing membrane a bituminous felt is adapted assuming an sd-value of 100 m. Three different situations are examined: Non-shaded dark roof; shaded dark roof and non-shaded white roof. For the non-shaded and shaded calculations a short-wave absorptivity of a=0.9 is used, the white surface has a short-wave absorptivity of a=0.3. The oriented strand board (type 3) has a thickness of 15 mm, the mineral wool insulation layer 200 mm. For the permeance of the vapour retarder three variants are considered: sd-value of 100 m, 5 m and humidity controlled (sd = 0.1 to 4.4 m). Two climatic data files for the exterior boundary conditions are used: one with measured data from the year 2009 and the same climatic data file with modified radiation data generated by the shading model. The indoor climate is generated according to EN 15026 [3] for normal occupancy. The climatic indoor data are derived from the outdoor temperature with indoor temperatures ranging between 20 and 25 °C and relative humidities between 30 and 60 percent. A moisture source is included in the roof to account for air leakages specified according to an infiltration model developed at the IBP [4]. The calculations start in October and are performed for a time period of five years.

To evaluate the construction, the water content in the OSB layer is interpreted. This layer is the critical point. During cold periods, when the temperature outside is colder than inside moisture from the interior migrates into the construction by diffusion and condenses. Additionally, if there are any air leakages, the moisture loaded indoor air penetrates the construction and may condense as well. This moisture has to be dried out during the warm periods; otherwise it can lead to mould growth or rot by wood decaying fungi. According to the standard for wood preservation DIN 68800 [5] the water content in a wooden structure may not exceed 20 percent by mass for a longer period. Thus the criterion applied to the simulation was that the water content may not rise higher than this 20 percent by mass and may not continuously increase during the years.

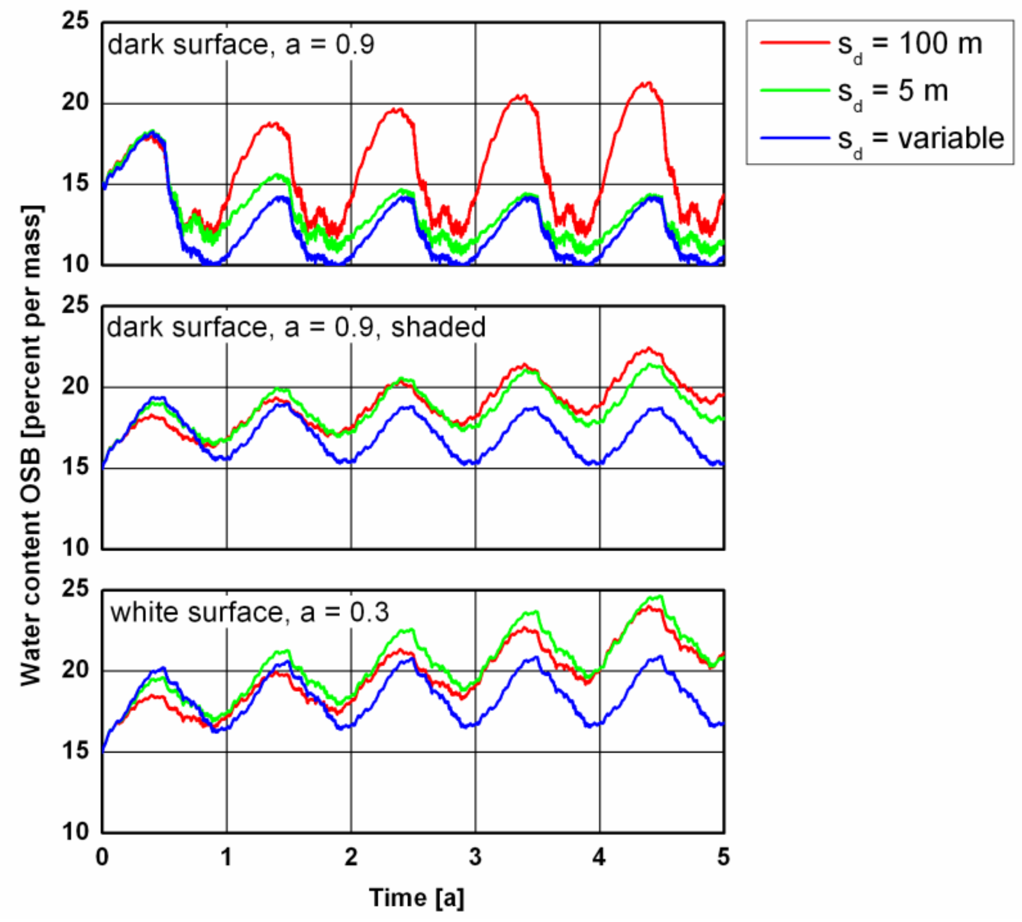

Figure 7: Calculated values of the water content in the OSB layer

The resulting water content in the OSB layer for the different variations is shown in Figure 7. In the upper diagram the results of the calculations for the dark surface are displayed. The construction with the 100 m vapour retarder shows an increasing moisture level during the calculated years. This construction would work, if one could exclude all imperfections in the assembly such as cracks, unsealed joints or perforations. However, in most building components small air-leakages do occur and therefore a vapour-tight barrier at the interior side poses a moisture damage risk. After four years the water content in the OSB layer reaches 20 percent by mass in the winter time. The version with the moderate vapour retarder (sd = 5 m) takes up some water during the cold periods, but with sufficiently high temperatures during summer time the construction dries out again. The roof with the variable (humidity-controlled) vapour retarder shows the best drying potential.

The middle diagram shows the calculation results for the dark but shaded surface. The values are generally higher than in the non-shaded version. Here the retarders with sd = 5 m and sd =

100 m both show an increasing water content over the years. A water content of 20 percent by mass is reached in the second year. This shows that these constructions are not able to shed the gained moisture during the warm period. The construction with the variable retarder still is able to dry out during summer time. Here, the values oscillate between 15 and 19 percent by mass.

The bottom diagram shows the calculated values for the white surface. In this case the surface temperature reaches nearly the same temperatures as the shaded section, but the long wave emission loss to the sky is not reduced by the solar panel. This leads to a lower surface temperature during the night and thus to a higher condensation potential in the construction. In this case even the variable vapour retarder does not provide sufficient drying potential which results in a slight moisture increase over the years which is not acceptable.

4. Conclusions

Solar roof top panels become more and more popular because the electricity they produce is sold back to the grid at a high price which is subsidized by the government. However, installing such panels on wooden lightweight flat roofs can – depending on the construction – lead to moisture problems. Common constructions, which are typical for residential buildings, need an adequate temperature on the roof surface during summer to allow the system to dry out any moisture that may have leaked in. If the roof surface is shaded or if it has a bright surface colour, the resulting temperature may not be high enough to guarantee a sufficient drying potential. While a bright surface colour represents the worst case that should be avoided, shaded sections of the roof may also be at risk. Apart from back-ventilating the roofing membrane the only solution to this problem seems to be the installation of a humidity controlled vapour retarder. However, even this solution might not be sufficient under all circumstances. Therefore, it is recommended to carry out a hygrothermal simulation for each individual design in order to make sure that the roof system will not be compromised by the shading effect of PV panels.

References

[1] Künzel, H.M.: Simultaneous Heat and Moisture Transport in Building Components. One- and two-dimensional calculation using simple parameters. IRB-Verlag Stuttgart, 1995.

[2] Kehrer, M.; Schmidt, T.: Radiation Effects On Exterior Surfaces. Nordic Symposium on Building Physics 2008. Proceedings of the 8th Symposium on Building Physics in the Nordic Countries, Copenhagen, Denmark 2008.

[3] EN 15026, Hygrothermal performance of building components and building elements – Assess¬ment of moisture transfer by numerical simulation; European Committee for standardization, Brussels 2007

[4] Zirkelbach, D., Künzel, H.M., Schafaczek, B. & Borsch-Laaks, R.: Dampfkonvektion wird berechenbar – Instationäres Modell zur Berücksichtigung von konvektivem Feuchteeintrag bei der Simulation von Leichtbaukonstruktionen. Proceedings 30. AIVC Conference, Berlin 2009

[5] DIN 68800:1996, DIN Standard 68800-2, Holzschutz – Vorbeugende Bauliche Maßnahmen im Hochbau. Deutsches Institut für Normung, Beuth Verlag, Berlin

Thermophysical properties of natural sandstone measured by Pulse transient technique. A new model for cuboid shape samples.

Vlastimil Boháč[1], Peter Dieška[2], Ľudovít Kubičár[1], Viliam Vretenár[1]

[1]Institute of Physics, SAS, Dúbravská cesta 9, 845 11 Bratislava 45, Slovak republic

[2]Department of Physics, FEI - STU, Ilkovičova 3, Bratislava, Slovak Republic

Abstract: *The microscopic defects in any kind of stone inhibit creation of macroscopic clinks or breaks that finally causes the total deterioration of blocks in nature either in constructions or monuments. Process of deterioration of stone or it's state and quality comparing it's basic or initial state should be monitored by continuous measurements (monitoring) of thermophysical properties [1, 2].*

The problems connected with deficiency in a large amount of testing material cause some problems in data evaluation as an ideal model usually assumes infinitively large specimen. The finite geometry of the specimen cause additional effects that harm the efficiency of the measurement evaluation.

In this paper a new model for square cross section of cuboid specimens that includes the effect of heat losses from the sample surface and completes the series of models introduced previously. Model was used for evaluation of thermophysical parameters of sandstone from locality "Pravčická brána" in Czech Republic.

Keywords: *pulse transient method, thermal conductivity, thermal diffusivity, specific heat, sandstone*

Introduction

Quality parameters of natural stone used as constructive or decorative building material have to be tested by suitable methods. Volume density, water absorption uniaxial compressive strength or flexural strength, coefficient of the linear thermal expansion, frost and wear resistance, in some case the resistance to ageing by some chemical agents are determined in standard way. Values of stated properties are determined from aside the rock genesis, mineral composition and structure. Recently, thermophysical properties, namely the thermal conductivity, thermal diffusivity and specific heat are highly required.

Actual review of corresponding topics is very complex. Under the area of investigation of thermophysical properties of natural stone materials the general review would take a long report. That is why our effort is to bring particular results on thermophysical data of natural stone materials and help to evaluate their durability from the testing procedures point of view. Research in basic deterioration effects is not only the matter of terrain, but also laboratory research of many analyses, concentrated on standard normative and non-traditional experimental actions based on study of microstrucrural signs on nano-scale level (Hg porosimetry, XRD, SEM...), next the thermophysical properties of stones as the thermal diffusivity, thermal conductivity, specific heat, thermal expansion, etc.[3,4].

Thermophysical properties are one of criteria for distinguishing in between different stone quality or level of their deterioration and thus quantification of material quality.

Thermophysical parameters reflect thermodynamical state of the material structure. This state changes with the consideration of the atomic structure arrangement, arrangement of crystalline components and consideration on created material defects that are responsible for further development of structure degradation. According one of the consequences of second thermodynamic law the specific heat is defined as a measure of structure arrangement [i]. The methods for measurement of thermophysical properties are very sensitive for any king of structure degradation. That is why of their use in wide range of applications during last decades.

In our case the pulse transient method was used for measurement of thermophysical parameters, e.g. the thermal diffusivity, specific heat and thermal conductivity of natural sandstone from locality "Pravčická brána" in Czech Republic. It is well known fact that this natural beauty locality created in sandstone massive is undergoing progressive state of deterioration. Such a monitoring of that state is necessary for prediction of massive rock behaviour in the future. The gained data in dry state of material will serve as background study for action sustained monitoring directly in natural locality by Hot ball method in the same way like it is done at Spiš castle [2, 3, 4].

The natural sightseeing - Pravčická brána.

Principle of Pulse transient method

The principle of the Pulse transient method is to record the temperature transient response to the heat pulse generated by a plane heat source and to calculate the thermophysical parameters from the characteristic features of the measured curve of the temperature response (Fig. 1. right). Transient temperature response measured at the distance h from the heat source is calculated according temperature function $T(x, t-t_0)$ providing that the model (Eq. 1.) is valid [2]. The ideal model assumes that the planar heat flow in infinitively large samples is not deformed as it penetrates into the depth of the specimen bulk (white-dotted area in the Fig. 1). The problem is that the temperature isotherms are not planar over the radial cross section of the specimen but they are deformed at the edges. This effect is caused by the heat losses from the sample surface in a case of large distances from the heat source, e.g. the thicknesses of material bigger than the optimal value [1, 9, 12]. In previous experiments just a correction to the ideal model considering the real pulse width was applied to ideal model [10]. The model is characterized by temperature function (Eq. 1)

$$T(h,t) = \frac{2 \cdot Q}{c\rho\sqrt{\kappa}}\left[\sqrt{t} \cdot i\Phi^*\left(\frac{h}{2\sqrt{\kappa t}}\right) - \sqrt{t-t_0} \cdot i\Phi^*\left(\frac{h}{2\sqrt{\kappa(t-t_0)}}\right)\right] \tag{1}$$

where $i\Phi^* = e^{-x^2}/\sqrt{\pi} - x \cdot erfc(x)$. Here the meanings of used symbols are the following: Q - heat flow density at source, c - specific heat, κ - thermal diffusivity, ρ - density, t - time, t_0 - heat pulse duration, *erfc* - error function, h - the specimen thickness. Equation 1 should be used for data evaluation by fitting procedure also.

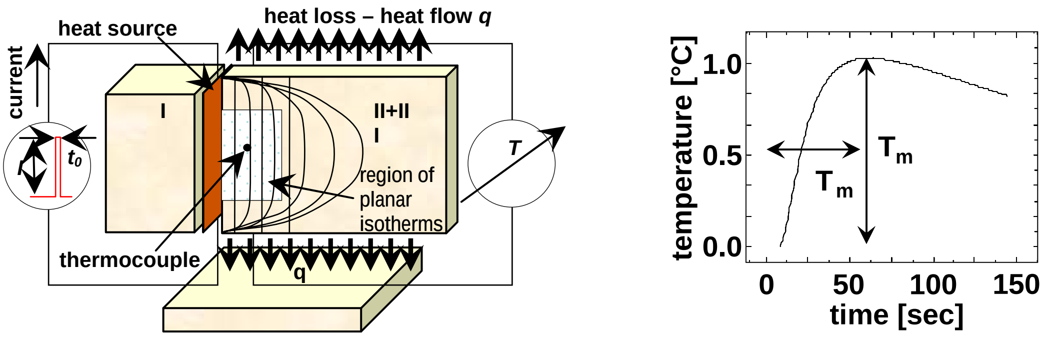

Figure 1. The principle of the pulse transient method is drawn. Sample parts II+III were drawn in sections to illustrate the planar isotherms in the middle plain of cutting. Specimen set is drawn with heat flow paths when drawn deformed isotherms are influence by heat loss effect (left). An example of the temperature response is on the right.

One point evaluation procedure

At the standard experiment due to fast calculations we use simple relations for the evaluation of thermal diffusivity, specific heat and thermal conductivity. These relations were derived for the maximum of temperature response on Fig.1. (one-point evaluation procedure). Then, the thermal diffusivity is calculated according to the equation

$$\kappa = h^2 \cdot f_\kappa / 2t_m \tag{2}$$

and the specific heat

$$c = Q \cdot f_c / \sqrt{2\pi e}\,\rho h T_m \tag{3}$$

where f_κ and f_c are correction factors [ii]. Maximum temperature of the transient response found at time t_m is T_m (Fig. 1.) Thermal conductivity is given by data consistency relation

$$\lambda = \kappa\rho\, c = h \cdot Q \cdot f_\kappa \cdot f_c / 2\sqrt{2\pi e}\;\, t_m T_m \tag{4}$$

A new model for cuboid shape samples

A previous explanation of a heat loss effect was solved in a new model developed for cuboid samples. According Fig.2 there were defined initial and boundary conditions for the basic heat transport equation. The new model assumes heat source placed in between symmetric arrangement of the specimens in the shape of semi-infinitive cuboid blocks having squared cross section.

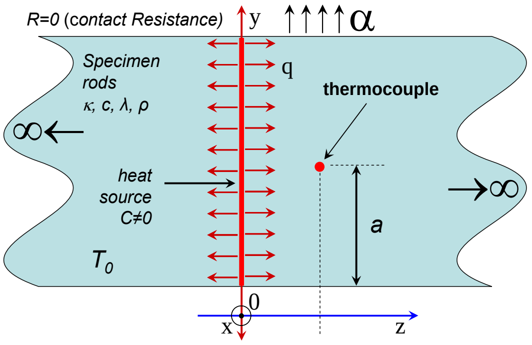

Figure 2. Model of the measurement – Sample parts II+III were drawn in section to illustrate the planar isotherms in the middle plain of cutting.

Heat source is of zero heat capacity and is in ideal heat contact with the specimen (thermal contact resistance is zero).The solution of the heat equation is a temperature function in the form

$$T(t,x,y,z) = T_0 \frac{w}{2} \sum_{n=1}^{\infty} \sum_{m=1}^{\infty} \frac{b_n b_m}{v_{nm}} F(u, v_{nm}) \varphi_n(\frac{x}{a}) \varphi_m(\frac{y}{a}) \tag{5}$$

where $\varphi_n(s) = \sqrt{\frac{2\beta}{\beta + \sin^2 \mu_n}} \cos(\mu_n s)$, $F_n(u,v) = e^{-2uv}\Phi^*(u-v) - e^{2uv}\Phi^*(u+v)$

$T_0 = \frac{qa}{\lambda}$, $\beta = \frac{a\alpha}{\lambda}$, $u = \frac{z}{2\sqrt{\kappa t}}$, $w = \frac{\sqrt{\kappa t}}{a}$, $v_{nm} = w\sqrt{\mu_n^2 + \mu_m^n}$, $b_n = \varphi_n(0)\frac{\sin(\mu_n)}{\mu_n}$

The meaning of variables:

T	temperature field in specimen body
t	time
z	axial space coordinate
x,y	transversal space coordinates
2*a*	transversal size of the sample
q	heat flow density at source
λ	thermal conductivity
κ	thermal diffusivity
α	heat transfer coefficient for sample - ambient interface

$\Phi^*(u)$ is the complementary error function

μ_n are the roots of equation $\beta \cos \mu - \mu \sin \mu = 0$

The relation (5) characterizes the step-wise measuring regime. After the duration of the heat pulse t_0, the temperature is expressed by the relation

$$T^*(t,x,y,z) = T(t,x,y,z) - T(t - t_o, x, y, z) \tag{6}$$

where $T(t,x,y,z)$ and $T(t-t_0,x,y,z)$ are given by the relation (5). The relation (6) characterizes the pulse transient regime.

Experiment

The sandstone specimen set was in a form of cuboids having finite length. The dimensions of parts I and III according Fig.1 were 50x50x30 and part II 50x50x10mm. The volume density value was 1738.7 kg m^{-3} and porosity measured by weighting dry and water saturated specimen was 27.5%. Heat source meander was etched of Ni foil and insulated by kapton foil. Its dimensions were 50x50mm. Measurements were performed in RTB 1.02 measurement chamber [3]. The heat pulse parameters were optimized to get temperature response of about 1°C. The heat pulse duration was of 2.5, 3, 4, and 6 seconds duration and current used was set from 4.3 to 5 amperes. The heat source resistance was about 2 ohms. Before the measurements the specimens of sandstone were dried in oven at 70°C till no changes in weight at three subsequent measurements in reasonable time.

The experimental details were described in [10]. Thermophysical parameters were evaluated by one point evaluation procedure (Eq. 2 and 3.) derived from ideal model. In the past the use of the ideal model and the one point evaluation procedure led to a problem with the heat loss disturbance effects shown in Fig. 1 for an illustration. This effect was described and finally avoided by optimization of specimen geometry [9, 3]. In practice this limit resulted in limits of the specimen thickness between 6 – 8mm for a class of homogeneous materials and between 18-22mm for strongly non-homogeneous materials. The new model for cuboid samples (Eq. 5) accounts heat losses from the sample surface via heat transfer coefficient in between the sample surface and surroundings.

Results

The measured data plotted in time scale give a picture on time relations at measurements. The figure 3 shows thermal history and influence of different atmosphere on the measurement results. Blue lines drawn for a group of data measured at the same temperatures serve for comparison of data before and after temperature annealing at 25, 40, and 70 °C and vacuum treatment. Running the measurements, the specimen was annealed at 40°C, then at 70°C. At 70°C the measurement chamber was evacuated and measurements continued under the vacuum. After aeration of the system at 70°C one can observe different and slightly lower values of all three thermophysical parameters than before the system evacuation. After than the sample was cooled down back to 40°C, 25°C, 5.7°C and finally frozen to -20°C at normal pressure (air). All data in Fig. 3 were calculated by one point evaluation procedure.

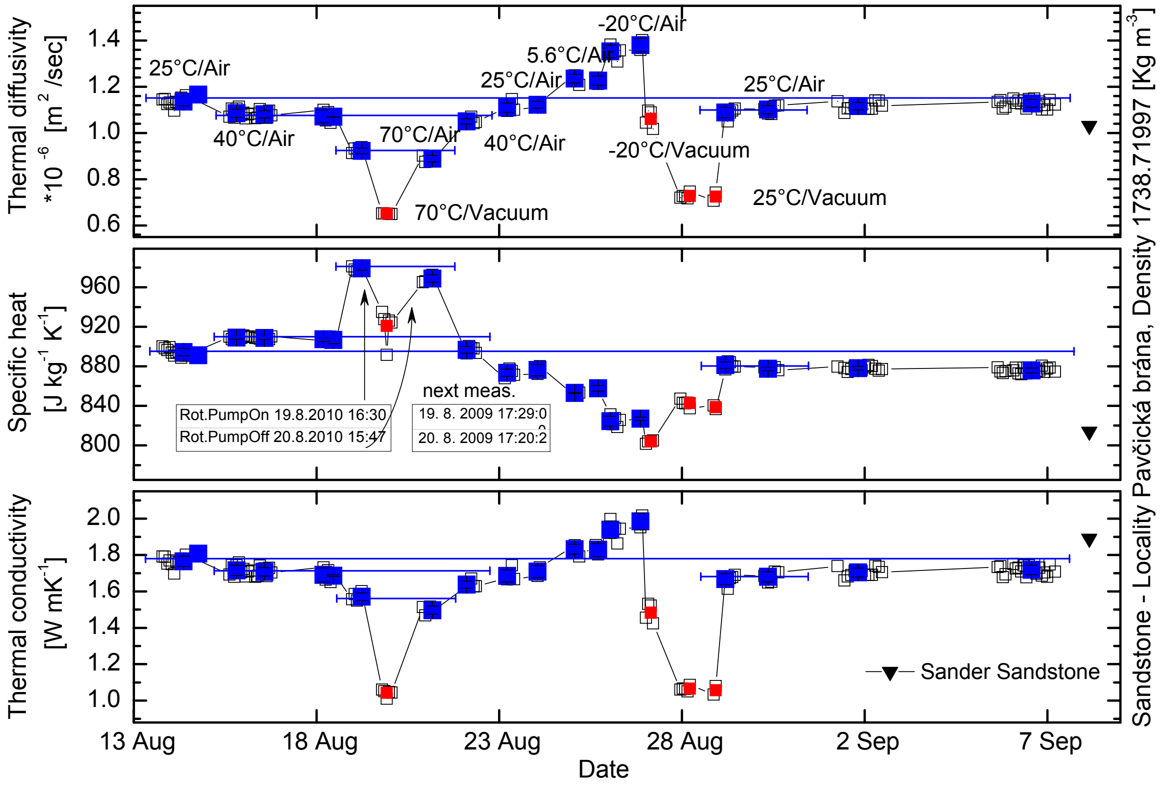

Figure 3. Measurement of thermal diffusivity, specific heat and thermal conductivity in time. The temperature and atmosphere history is marked in graph. For illustration, the time of starting rotary pump with the time of next subsequent measurement is given too. The data in blue are average values of measurements performed at the same pulse parameters. Data in red are measured under the vacuum.

The Sander sandstone data c=814 J.Kg^{-1}.K^{-1}, κ=1.04 mm^2.s^{-1}, λ=1.89 W.m^{-1}.K^{-1} were added to Fig.3 for comparison with different sandstone having higher density (2190 kg.m^{-3}) and lower porosity (14%). At -20°C the system was evacuated again and heated up to 25°C where the system was aerated. The final change due to annealing and vacuum treatment is small, but evident. One can see the clear drop of all parameters due to annealing and pumping out of resident water from the pores and structure.

The data were recalculated by new model and are plotted in figure 4 as the temperature dependence in comparison with the data from one point evaluation procedure. In a plot just data for pulse duration of 3 seconds are shown. The thermal history and vacuum treatment are denoted directly in a middle graph for the values of specific heat.

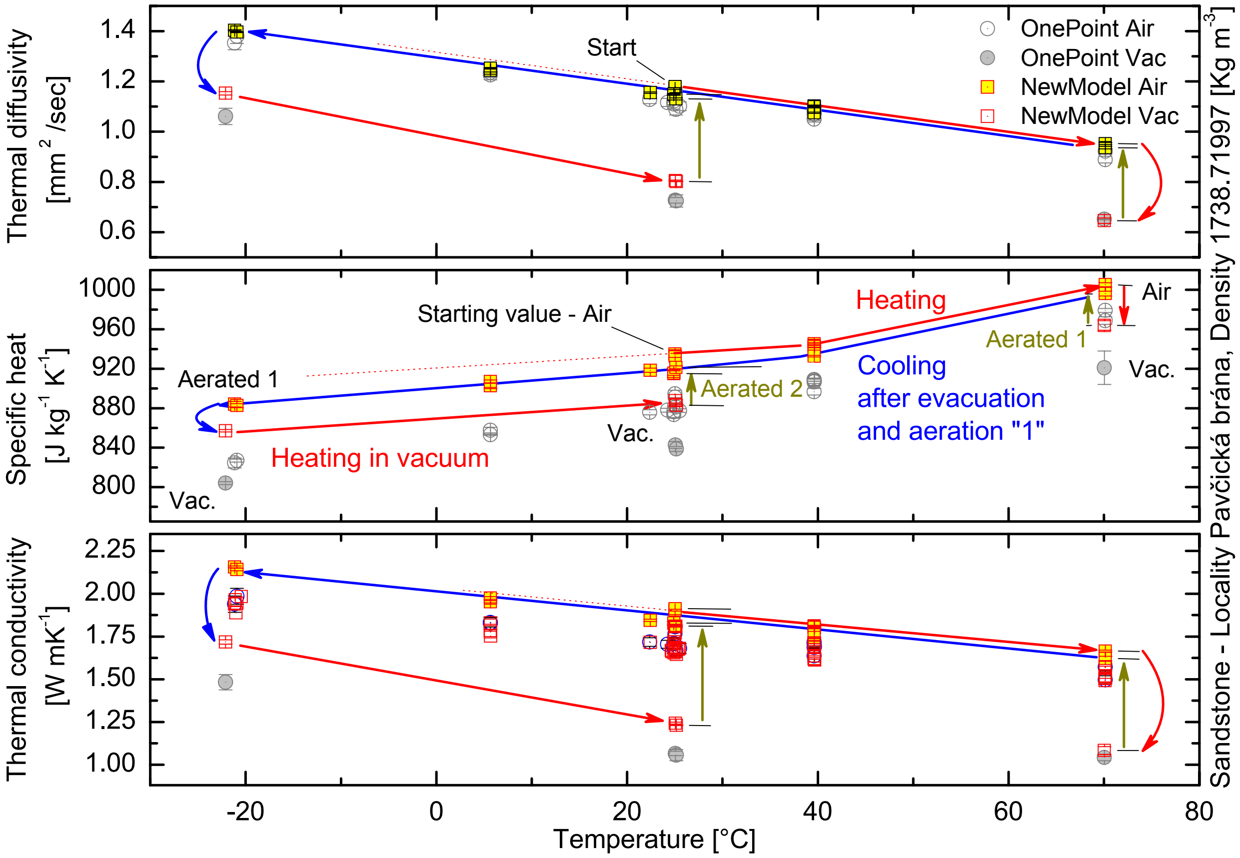

Figure 4. Temperature dependency of thermal diffusivity, specific heat and thermal conductivity with marked temperature and vacuum history. All the values after first evacuation are lower than approximated data in dot line draw down to lower temperatures. The measurement history is followed by red lined at heating and blue lines at cooling. The aeration jumps after evacuations are marked as Aerated 1 and Aerated 2.

The model (Eq.5.) fits next free parameters: thermal diffusivity, thermal conductivity and heat transfer coefficient. The figure 5 represents values for measurements at heat pulse duration of 6 seconds. The problem is, that the sensitivity coefficient for this parameter is increasing in time of measurement, so the longer pulse the longer measurement is, and better accuracy for this parameter evaluation we get. This was the reason why the data were filtered.

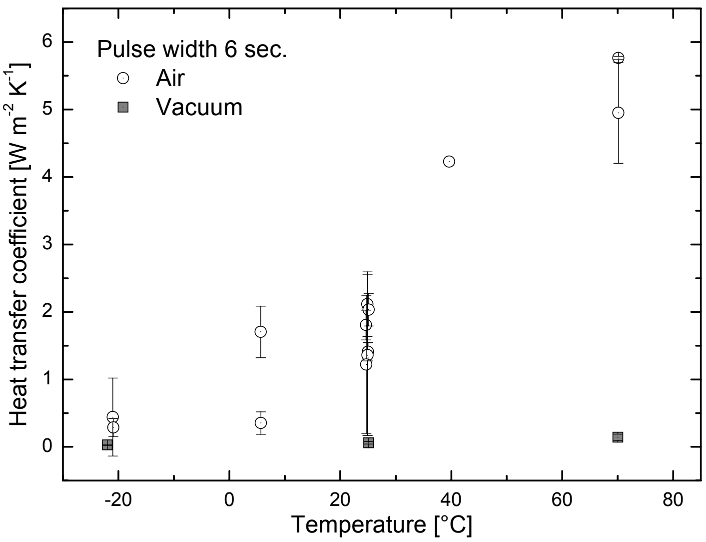

Figure 4. Temperature dependency of heat transfer coefficient (heat loss from the sample surface). The values correspond to 6 seconds pulse duration, The higher temperature, the higher value of heat loss.

Conclusions

The thermophysical properties of sandstone were investigated by pulse transient method for dry state of stone. The data were evaluated by two methods – the one pint evaluation procedure and by fitting procedure using a new model for cuboid samples that accounts heat losses from the sample surface. The new model pushed up the values of all parameters. The values of thermal diffusivity were increased just on small value, but due to data consistency condition the large increase of specific heat causes increase of thermal conductivity values remarkably.

The measurements were done in the temperature range from -20 up to 70°C. The slope of temperature dependence of transport parameters is positive, while the slope for specific heat is negative and above 40°C the rate of this slope is increasing. This effect should be the question for next discussion. The heat transfer coefficient from the sample surface to the surrounding is temperature dependent and its value is greater for higher temperatures. Te values measured in vacuum are practically the same over all temperature range.

The measurements were performed under the air as well as vacuum conditions. Annealing and the vacuum treatment causes lowering of all thermophysical parameters due to removing of remanent water from pores and structure of sandstone. Classical method of drying was not sufficient. The RTB 1.02 chamber should help to avoid problems of insufficient drying because of simultaneous evacuation of the chamber and elevation of the temperatures are more efficient in additional drying process.

Comparing all new results with the previous one measured on different and physically more compact and more strength Sander sandstone [iii]found that the mechanical strength should be next parameter that can be correlated with deterioration processes of investigates sandstone. The sandstone from Pravčická brána is very soft and thus it is able to drill it even by finger. The higher values of density 2190 kg.m^{-3} and lover value of porosity 14% as well lower value of specific heat of Sander sandstone measured at 25°C and evaluated by one point procedure (data added to Fig.3 for comparison) should point to correlation with higher values of mechanical stress properties and thus the material quality.

The data obtained are used as background data for calibration and long time monitoring of sandstone massive at locality Pravčická brána by Hot ball method.

Acknowledgements

The work was supported by Slovak grant agency VEGA under a projects No. 2/0161/08 - Study of thermal-insulation properties of low thermal conductive materials and No. 1/0499/08 Deterioration of massive rocks by influence of thermal-moisture changes. The paper was also supported by project APVV 0497-07 Thermophysical sensors.

References

[1] V. Boháč, M. Harcek, L. Kubičár, V. Vretenár, 2005, Thermophysical properties of new electrotechnical ceramics measured by pulse transient technique, Proc of the TERMANAL 2005. 12th conference on thermal analysis and calorimetry, Ed. E.Klein, Dept. of Physical Chemistry, I9SBN 80-227-2285-5

[2] V. Vretenár, Ľ. Kubičár, V. Boháč and P. Tiano, 2007, Thermophysical analysis of Gioia marble in dry and water-saturated states by pulse transient method. Int. J of Thermophysics 28, pp. 1522-1535.

[3] Vlčko J., Jezný M., Pagáčová Z., 2006, Influence of Thermal expansion on slope displacements. In: Landslides, Risk analysis and sustainable disaster management. Proc. 1. General assembly ICL, Washington, Springer, ch. 7, 71-74

[4] Kühnel R.A. 2002, Driving forces for rock degradation, Protection and Conservation of the Cultural Heritage of the Mediterranean Cities, Galán and Zezza (eds). Swets& Zeitlinger, Lisse, ISBN 90 5809 253 4, pp11-18

[5] Moore W.J., 1981, Fyzikální chemie: Physical chemistry (Orig.). Translated by Čestmír Černý - Alexandr Schütz. č. vyd. Státní nakladatelství technické literatury - SNTL Praha, ISBN 04-604-81.(Resp. 2.Vydanie ISBN 04-608-79)

[6] Boháč V., Kubičár L., Brček M., Vlčko J, Greif V., The moisture monitoring as a negative factor of deterioration of massive rocks, TEMPMEKO 2010, Book of abstracts – will be published in Int. J. of Thermophysics.

[7] Vlčko J. Jezný, M., Hvoždara, M., Durmeková, T.,Greif, V., 2007: Teplotná deformácia - faktor štruktúrneho oslabenia horninového masívu. THERMOPHYSICS 2007 October 11-12, 2007, Ed. Jozef Leja, Vydavateľstvo STU, Bratislava 2007, ISBN 978-80-227-2746-4, p. 127-147

[8] Vlčko, J., Greif, V. Gróf, V., Jezný, M. Petro, Ľ., Brček, M., 2009: Rock displacement and thermal expansion study at historic heritage sites in Slovakia. Environmental Geology, Vol. 58, No. 8, Sp. Iss. (2009), pp. 1727-1740

[9] Boháč V. et all. Methodology of parameter estimation of pulse transient method. Proc. TEMPMEKO 2004, 22 - 25 June 2004 Dubrovník, Croatia

[10] Kubičár Ľ, 1990, Pulse Method of Measuring Basic Thermophysical Parameters in Comprehensive Analytical Chemistry Vol. XII Thermal Analysis Part E Ed Svehla G, Amsterdam, Oxford, New York, Tokyo: Elsevier, pp 350.

[11] Institute of Physics, SAS, Dúbravská cesta 9, Slovakia, http://thermophys.savba.sk

[12] Boháč V, Dieška P, Kubičár Ľ. MEASUREMENT SCIENCE REVIEW, Volume 7, Section 3, No. 2, 2007

[13] Kubičár L., Vretenár V., Boháč V., Tiano, P., 2006: Thermophysical analysis of sandstone by pulse transient method, Int. J. Thermophysics 27 (1), 220-234

Numerical analysis of coupled heat and moisture transfer in porous materials at high temperatures

Kamil Ďurana, Jiří Maděra, Robert Černý

Czech Technical University in Prague, Faculty of Civil Engineering, Department of Materials
Engineering and Chemistry, Thákurova 7, 16629 Prague 6, Czech Republic

Abstract: *The effect of high temperatures on heat and moisture transport in porous materials is studied. Transport processes are simulated on a fiber reinforced cement composite using Lykov's original model. The main objective of the simulation is to determine limits of two parameters which are difficult to measure – relative thermodiffusion coefficient δ and evaporation coefficient ε. In order to specify influence of those two on temperature and moisture fields in material, a sensitivity analysis under specific conditions is performed. Further, the original model is modified by introducing dependence of ε on temperature. Then δ is examined by varying between its estimated possible limits. Finally, the influence of two studied parameters is quantified and compared with experimental data.*

Keywords: *Heat transfer, moisture transfer, high temperatures*

1. Introduction

At present, there is a big interest in investigation and testing of concrete structures subjected to high temperatures. Thermal load induces decrease of strength, spalling and other structural or chemical changes, in addition to heat conduction, vapor diffusion and liquid water flow. Characteristics of those processes are dependent on physical and chemical composition of a material, which is considered as a multi-phase (solid matrix, liquid water and the mixture of vapor with dry air). Mathematical description of such processes is important for example in nuclear engineering applications and fire safety evaluation of buildings or tunnels.

Although there have been published complex models with mechanical and chemical processes involved [1], our main goal was to verify the simple model introduced by Lykov [2], which contrary to other models includes lower number of necessary input parameters. Since even in this model not all parameters used in governing equations are well known or measurable, it is necessary to run a sensitivity analysis, which can lead to a reasonable conclusion about applicability of such model. Further, by comparing with measured data, we can decide if Lykov's approach is precise enough to predict temperature or moisture fields in a reliable way.

Mathematical model

Lykov modified his original model [3] (designed for temperatures up to 100 °C) by introducing liquid-vapor phase change coefficient ε as a rate of phase changes of water:

$$\varepsilon = \frac{d_i u}{du} = \frac{d_i u}{d_i u + d_e u} \tag{1}$$

where du is the total change of moisture, $u=u_1+u_2$ (index *1* denotes water vapor, index 2 water), $d_e u$ is the change of moisture due to its transport and $d_i u$ the change of moisture due to the phase change of water to water vapor.

Balance equations of moisture and temperature were formulated accordingly:

$$\frac{\partial u}{\partial t} = a_{m2} div\, grad\, u + a_{m2} \delta\, div\, grad\, T + \varepsilon \frac{\partial u}{\partial t} \tag{2}$$

$$\frac{\partial T}{\partial t} = a\, div\, grad\, T + \varepsilon \frac{L_{21}}{c} \frac{\partial u}{\partial t}, \tag{3}$$

where L_{21} is latent heat of evaporation, T temperature, δ relative thermodiffusion coefficient, a thermal diffusivity, ε evaporation coefficient and a_{m2} coefficient of water diffusion.

From this formulation we can deduce, that if the value of expression (1) is close to zero, there is almost no evaporation happening, no vapor and the source term of moisture is almost zero as well. If the value of expression (1) is close to one, evaporation is predominant, source term of moisture is at maximum, or there is locally gaseous moisture arising.

Lykov's idea about the coefficient ε is very simple, but turns out problematic, because it is not measurable. Its values can be found only by inverse analysis. Moreover, in original formulation it is considered as a constant, which brings complications in varying temperatures. This model is based on continuum physics and irreversible thermodynamics. It introduces Soret's effect, but not Dufour's effect. There is no pore pressure involved, nor mechanical or chemical processes. Although this model is simple, it brings insurmountable problem when determining amount of evaporated water in heat balance. It fits to situations, when there is faster water flow (for example when the material is in contact with fluid water, or transport at high temperatures). To the contrary for small amount of transferred moisture with small gradient, it will be quite inaccurate.

2. Sensitivity analysis of unknown parameters

Besides the described coefficient ε, there is another unknown parameter, relative thermodiffusion coefficient δ. Influence of those two on both temperature and moisture fields was investigated using finite element method and related computational software[2]. In order to obtain easily comparable results in a short time period, only one dimensional version was used.

To compare varying results, the dispersion of output values (difference between several values of temperature or moisture content by using different parameters) was chosen.

Preconditions of analysis

All conditions, discretization and material characteristics were set based on the real experiment as follows.

Heat loading of a constant temperature of 1000 °C took place on "exterior side" of specimen, with heat transfer coefficient $\alpha = 25\ \mathrm{W/m^2K}$. On the "interior side" the environment of common laboratory has been set, with heat transfer coefficient $\alpha = 8\ \mathrm{W/m^2K}$.

Material subjected to fire was fiber reinforced cement composite (Table 1), which characteristics are presented in Table 2 and Figure 1 [4].

---

[2] GoFEM for configuration of problem, TRFEL for FEM calculations and LTT for primary results processing

Table 1: Composition of fiber reinforced cement composite

Compound	% of mass
Cement CEM I 52.5	54.0
Siliceous sand	27.0
Mikrodorsilit 405	13.5
Microsilica 940 US	2.8
Kuralon RECS 100/12 mm	1.5
Kuralon RECS 7/ 6 mm	0.3
Glenium ACE40	1.1
Water/cement ratio	0.3

Table 2: Basic characteristics of fiber reinforced cement composite

Characteristic	symbol	units	Value
Bulk density	ϱ	[kg/m3]	2027.1
Matrix density	ϱmat	[kg/m3]	2586.7
Porosity	ψ	[%]	24.6
Moisture diffusivity	κ	[m2/s]	2.21 . 10-8
Thermal conductivity in dry state	λdry	[W/mK]	1.055
Thermal conductivity in wet state	λsat	[W/mK]	1.585

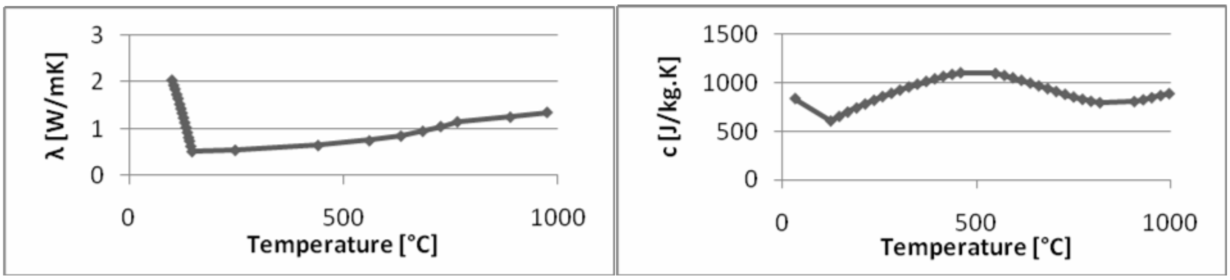

Figure 1: Thermal conductivity and specific heat capacity of fiber reinforced cement composite as a function of temperature

Initial conditions of the specimen (71 mm thick) were chosen T = 31 °C and w = 0.03 kg/kg. We used time step 1 second and the period of loading 40 minutes (based on real experiment).

Relative thermodifusion coefficient δ

The tested values were chosen between 1.10^{-15} and 0.1 K^{-1}. The effect of bigger δ value goes naturally hand in hand with the effect of bigger ε, according to (2)-(3). Admittedly, the varying δ can only cause difference of 6 °C on average and 21 °C maximally. Assuming δ in range of

1.10^{-6} and 1.10^{-11} K^{-1}, dispersion of only 0.07 °C was obtained. Deduced from those results, we consider it as an insignificant factor for temperature field.

Over against, the moisture fields are obviously more dependent on used ε and δ. At first, it was observed, that $\delta > 1.10^{-4}$ K^{-1} causes shape of evolving moisture to differ (Figure 2). Specifically, there is a decrease of moisture on heated surface at very beginning of heating.

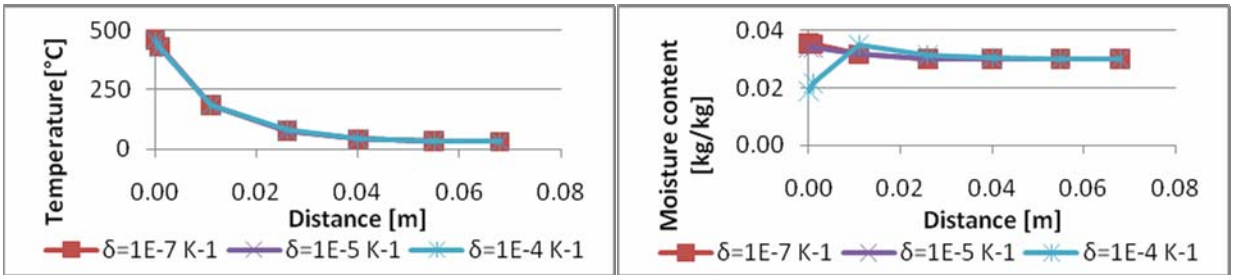

Figure 2: T and u (calculated) for various δ, distance dependence (time 4 min, ε = 0.9)

Hence, only $\delta < 1.10^{-4}$ K^{-1} was used and it was found out, that this coefficient varying between 1.10^{-6} and 1.10^{-11} K^{-1} gives the dispersion in moisture fields of $4.54.10^{-5}$ kg/kg on average and $2.1.10^{-4}$ kg/kg maximally (moreover, with $\varepsilon = 0,9$). So that we could freely use $\delta = 1.10^{-9}$ K^{-1} for such high-temperature experiment (based on [5], where δ is derived for other porous material, and the mentioned information) when the influence of ε was investigated.

Evaporation coefficient ε – constant value

Values chosen varied between 0.999 and 0.001. With both ε and δ constant, it was found out, that changes between 0.1 and 0.9 can cause only insignificant differences in temperature fields, specifically 4 °C on average and 12 °C maximally. When extreme values were chosen, it appeared that coefficient too high (i.e. $\varepsilon = 0.999$) can not only cause deviation of almost 100 °C (compared with $\varepsilon = 0.9$), but implicates temperature under 0 °C. Values less than 0.1 have no considerable influence (dispersion for $\varepsilon = 0.1$ and $\varepsilon = 0.001$ was maximally 0.35 °C). Graphic interpretations are given in Figures 3 and 4.

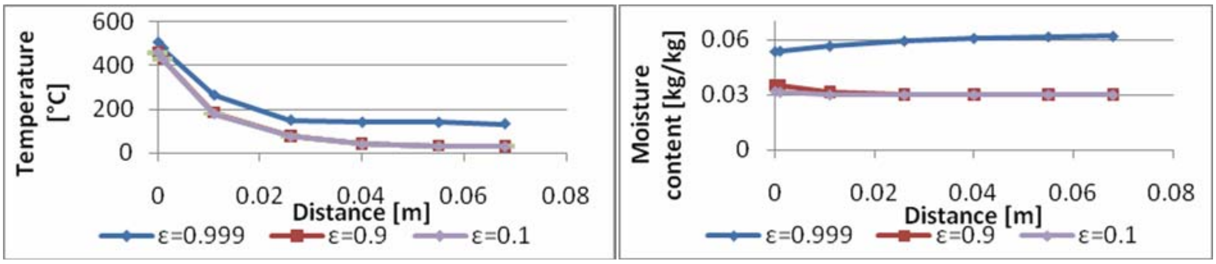

Figure 3: T and u (calculated) for varying ε, distance dependence (time 4 min, δ = 1.10-9 K-1)

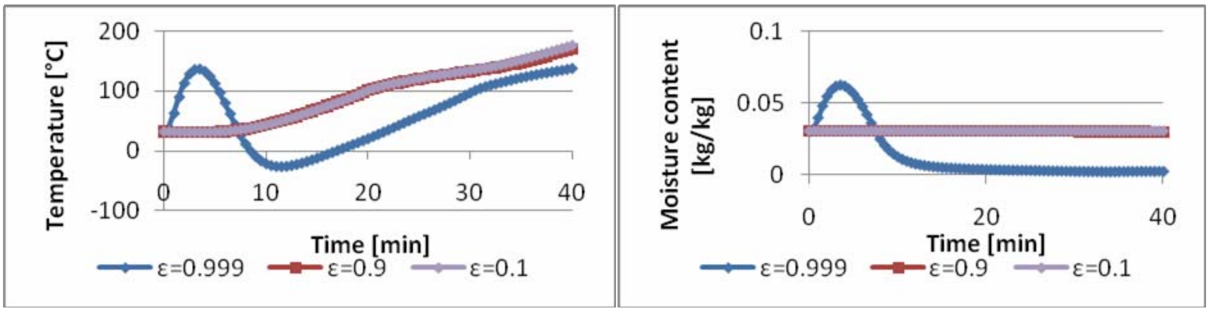

Figure 4: T and u (calculated) for varying ε, time dependence (distance 0.068 m , δ = 1.10-9 K-1)

Studies of moisture fields for ε between 0.1 and 0.9 resulted in the average dispersion 3.10^{-3} kg/kg on average and $1.4.10^{-2}$ kg/kg maximally. Compared to observed moisture range (0–0.035 kg/kg) this makes 10% dispersion on average and 41% maximally. Illustration is given in Figure 5.

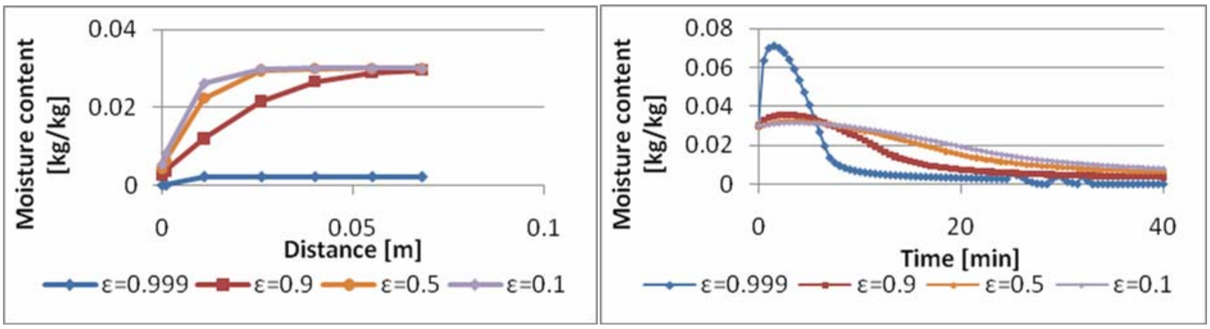

Figure 5: u (calculated) for various ε, distance and time dependence (δ = 1.10-9 K-1)

Evaporation coefficient ε – parametric version

To follow principles of real processes, the original constant value was replaced by following function:

$$\varepsilon = 0.5 + 0.5 tgh(A(0.1T - B)), \tag{4}$$

where A and B are free parameters and T is temperature. Then it is possible to set different ε for different temperatures. The values of free parameters used in our study are listed in Table 3.

Table 3: Parametric version of evaporation coefficient

Marking		Var. 1	Var. 2	Var. 3	Var. 4	Var. 5	Var. 6	Var. 7
Parameter	A	0.2	0.4	0.7	2	1	1	1
	B	15	7	6.5	5	9	10	11

With varying combinations of parameters A and B, the dispersion of 2.5 °C on average and 16.7 °C maximally was observed (which is not perceptible in a graph).

Further, it is worth mention that when $\delta = 1.10^{-4}$ K^{-1} was used, the influence of varying evaporation coefficient was strengthened, so that the dispersion was almost three times as big as with smaller *δ* (6.8 °C on average and 47.4 °C maximally), but still insignificant on the whole range. The maximal dispersion was observed only on the reverse side from heated surface, after 40 minutes of thermal load (Figure 6). The reason for such dispersion is believed to be different moisture consumption with different coefficients used.

The dispersion of moisture fields was $5.07.10^{-3}$ kg/kg on average and 3.10^{-2} kg/kg maximally. Interesting were the curves of moisture content for Var. 2 (Figure 7).

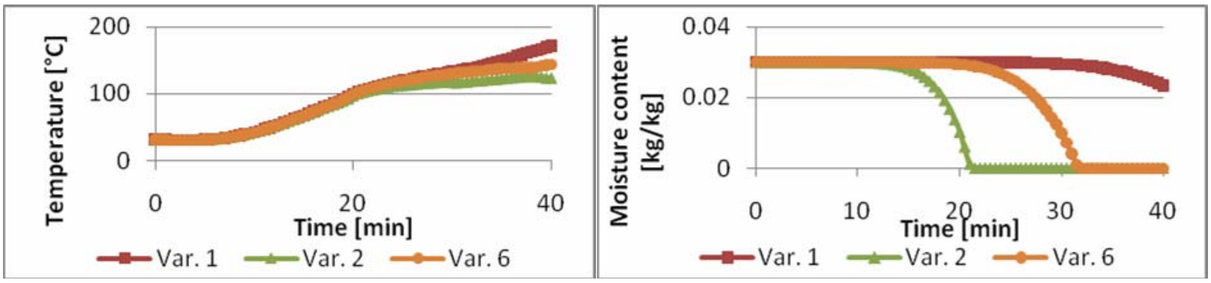

Figure 6: T and u (calculated) for varying ε, time dependence (distance 0.068 m, δ = 1.10-4 K-1)

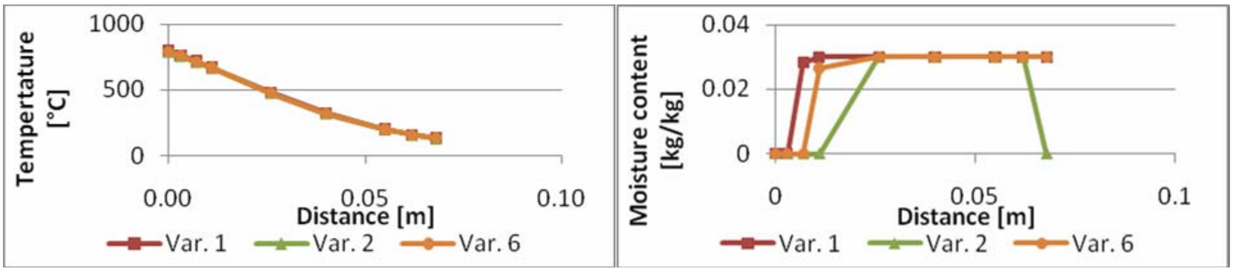

Figure 7: T and u (calculated) for various ε, distance dependence (time 40 min, δ = 1.10-9 K-1)

3. Comparison with measured data

The given data of real experiment [4] were approached by changing both *ε* and *δ*. However, it appeared that closer approach can be reached by changing transfer coefficients of interior and exterior surfaces as well.

As an indicator of an approach, the standard deviation *σ* was used, defined by:

$$\sigma = \sqrt{\frac{1}{n}\sum(x_C - x_M)^2}\,, \qquad (5)$$

where n is number of compared points (in one curve), x_C is calculated value and x_M is value measured.

Hence, within the standard heat transfer coefficients (e.g. $\alpha = 25$ W/m^{2}K for heated exterior and $\alpha = 8$ W/m^{2}K for interior), the closest approach was observed by using $\delta = 1.10^{-9}$ K^{-1} and *ε* parameterized by Var. 4. Here *σ* was up to 57.2 °C (maximum at distance 0.001 m and minimum at 0.068 m – 11.3 °C).

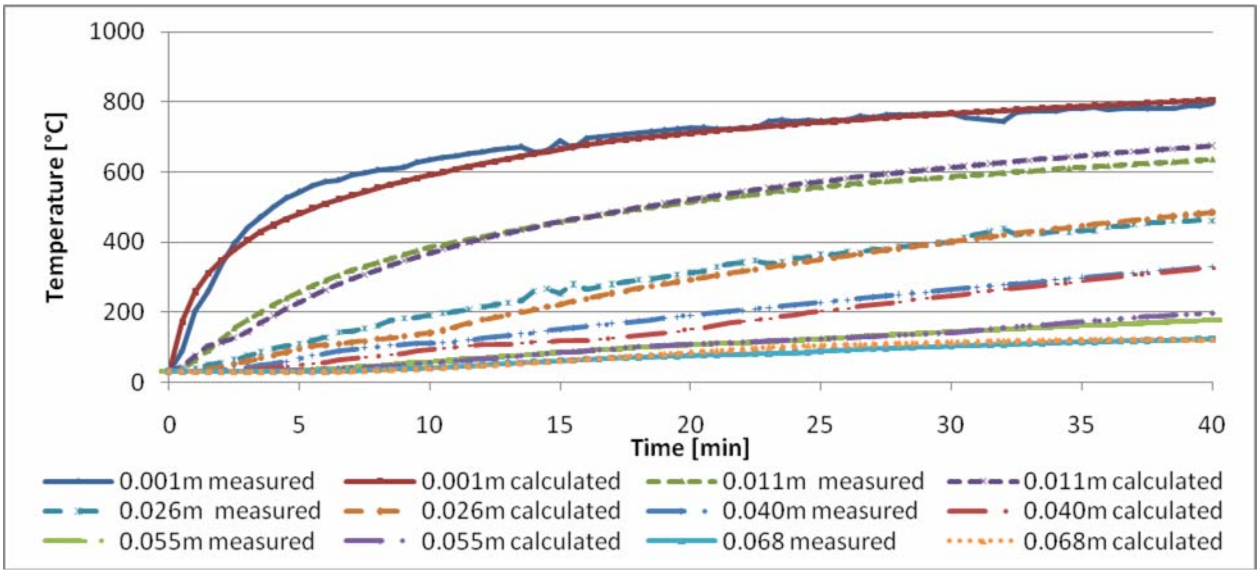

Figure 8: Comparison between measured and calculated temperature fields, time dependence

To reach specific values more closely, heat transfer coefficients were changed and the best approach was observed with values $\alpha = 27$ W/m^{2}K for heated exterior and $\alpha = 24$ W/m^{2}K for interior. Temperature field is shown in Figure 8. Coefficients used were $\delta = 1.10^{-9}\ K^{-1}$ and ε parameterized by Var. 3. Here σ was up to 29.3 °C (maximum at distance 0.001 m and minimum at 0.068m – 8.5 °C as previous). According to this approach, the moisture field was predicted and the result is given in Figure 9.

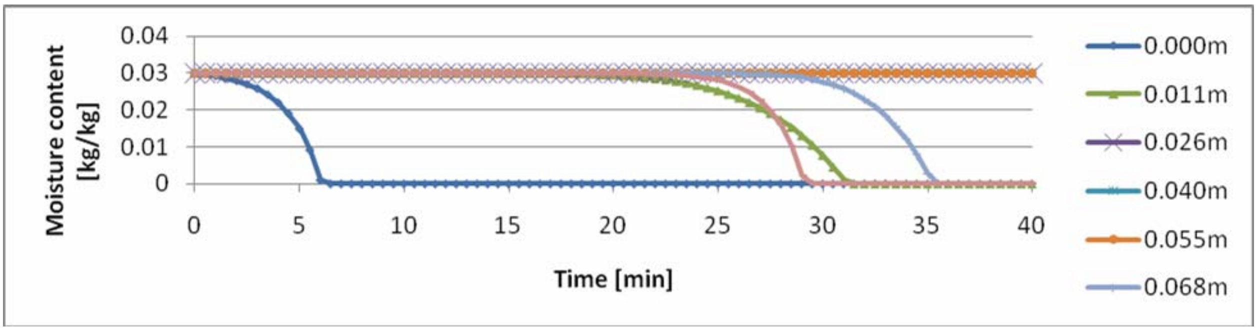

Figure 9: The prediction of moisture content

4. Conclusions

Thermal loading of fiber reinforced cement composite was simulated in specific conditions. Lykov's original model was used to obtain temperature and moisture fields, while the influence of two unknown parameters in governing equations (ε and δ) was studied.

Based on almost seven hundred computations and following data interpretation, we figured out that relative thermodiffusion coefficient δ has insignificant influence on both temperature and moisture values, when dealing with such high temperatures (up to 900 °C). The changes of δ can cause the difference of 6 °C or $4.5.10^{-5}$ kg/kg on average and 21 °C or $2.1.10^{-4}$ kg/kg maximally. The influence of constant evaporation coefficient ε on temperature was in almost all range not very significant, but the values of moisture content differed by 3.10^{-3} kg/kg on average and $1.4.10^{-2}$ kg/kg maximally, which is considered as great influence.

To approach the real processes of phase changes, the original constant evaporation coefficient was replaced by temperature dependent parameterization. With this precondition, the combination of ε, δ and boundary conditions were investigated in order to approach real measured data (temperature field). Finally, with specific values chosen, σ (take as the difference between measured and calculated data) observed was up to 29 °C, which is considered as a success in approximation of such thermophysical phenomenon. In addition, corresponding moisture field was predicted.

It is also notable, that parameters found out are strongly dependent on material, initial and boundary conditions and heat load, so that can't be considered as a characteristics of a material.

Acknowledgement

This research has been supported by the Czech Ministry of Education, Youth and Sports, under project No 6840770031.

References

[1] GAWIN D.; PESAVENTO F.; SCHREFLER B. A. A multiphase approach for the analysis of hygro-thermochemo-mechanical interactions in concrete at early ages and at high temperature. *IUTAM Proceedings on Physicochemical and Electromechanical Interactions in Porous Media*. 2005. p. 91–97.

[2] ČERNÝ R.; ROVNANÍKOVÁ P. *Transport Processes in Concrete*. 1. Ed. Spon Press , London, 2002, p. 68-70

[3] LYKOV A.V. *Teplo i massoobmen v processach sushki*. Gosenergoizdat, Moskva, 1956.

[4] VEJMELKOVÁ E.; KONVALINKA P.; PADEVĚT P.; KOPECKÝ L.; KEPPERT MARTIN; ČERNÝ R.; Mechanical, hygric and thermal properties of cement-based composite with hybrid fiber reinforcement subjected to high temperatures. *International Journal of Thermophysics* 30(2009), 1310-1322.

[5] ČERNÝ R. *Sekundární vlivy na transport vlhkosti v porézních látkách*, Habilitační práce, ČVUT, Praha 1990

Investigation of water diffusion in porous sandstone using transient hot-ball method

Danica Fidríková, Ľudovít Kubičár

Institute of Physics, Slovak Academy of Sciences, Slovak republic

Abstract: *This work is focused on water movement and moisture determination in porous structures. It is an important factor in research of building materials. Experimental sandstone has 17,8% published water porosity. Measurements were carried out using thermal conductivity sensors located in different positions along diffusion path. Principle of thermal conductivity sensor is based on Hot-ball method for measuring thermal conductivity. Local moisture content in porous stone is inspected using Hot-ball method, where the measured values of thermal conductivity are correlated to the water content. The experimental set up for investigation of water diffusion in stones is described. Results of water diffusion for different temperatures and moisture conditions are presented.*

Keywords: *thermal conductivity, moisture, water diffusion , porous materials*

1. Introduction

Many different properties of materials are used to study rock degradation under weathering cycles: thermal conductivity, permeability, saturation, sound velocity, shape and size distribution of pores, etc. Porous structures belong to a branch of materials which have a great number of applications in science, civil engineering and in industry. A broad range of physical and chemical processes take place in pores, namely condensation/evaporation, absorption/desorption, moisture transport, saturation/drying, etc. A number of experimental methods have been developed to investigate heat transport through material structures [1]. In this paper, we will focus on moisture transport and present results of a thermophysical analysis based on measurements of water diffusion in porous stones. Measurement was carried and using thermal conductivity probe based on Hot-ball method. This analysis was performed on specimens of sandstone. The working regime of thermal conductivity probe is described.

2. Experimental method

A hot-ball probe (Figure 1 left) has been constructed consisting of two elements (thermistor and resistance). Both elements are fixed using epoxy resin. The diameter of the hot-ball ranges from 1,8 to 2,5 mm. Hot-ball probe generates a constant heat flux q from the spherical source of radius r_b (Figure 1 right) into the infinitive medium for times t > 0. Simultaneously the temperature of the probe is measured, until a stabilized temperature value T_m is reached (Figure 2) [2, 3].

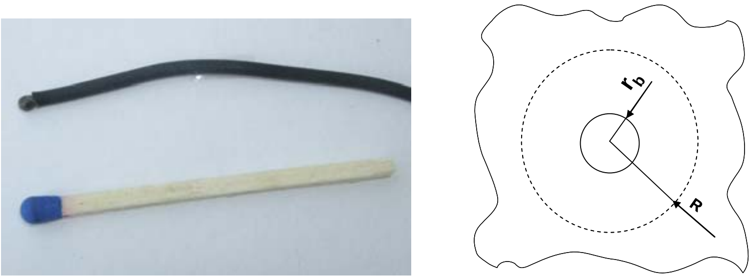

Figure 1: Real photo of Hot-ball probe compared to the match (left), model of the Hot-ball probe (right)

Then the material's thermal conductivity can be calculated using equation:

$$\lambda = \frac{q}{4\pi r_b T_m (t \to \infty)} \qquad (1)$$

where λ [W m^{-1} K^{-1}] is the thermal conductivity, q [W] is heat flux, T_m is the stabilized value of the temperature response and r_b [m] is the heat source radius. The measuring regime of such a probe is a steady state for t ◎ ∞. For data evaluation equation (1) is rewritten to the form $\lambda = A \cdot q / T_m$, where A is a calibration constant. Measurements are performed in cycles. A cycle consists of the measuring the temperature before switching on the heating (base line in Figure 2), the temperature onset after the start of the heating until its stabilization and then temperature drop back to the base line (Figure 2). Each of these cycles gives us a thermal conductivity value. A cycle repetition rate of 30 minutes is used to obtain information how thermal conductivity changes in time [2, 3].

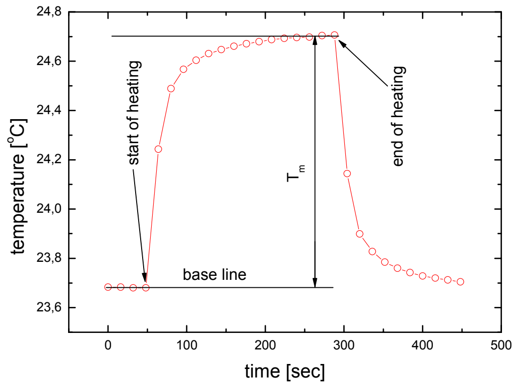

Figure 2: The temperature response (right) for constant production of heat q = const for t > 0

3. Specimens

Specimen made of sandstone (dimensions 50x50x100 mm) with 17,8% published water porosity and is used in the experiments of water diffusion. Preparation of the specimens is the following: three holes were drilled at different heights in the specimen for the insertion of the hot ball sensors (2.5 cm deep with radius of 0.2 cm). The surfaces of the holes were covered with varnish to prevent any watering of the sensors. Hot-ball probes (previously varnished as well, to make sure no water could penetrate) were placed in each hole using standard epoxy. Last step was to cover the specimen lateral surfaces with the same epoxy. The top and bottom surfaces were not covered by epoxy.

4. Experiment

In the experiment the specimen is dried and then let it moisture in water until full saturation in specimen. In the drying process the specimen was placed in the isolated chamber and subjected to higher temperatures from 70 to 90 °C in vacuum. In order to improve the contact with the heater plates the drying was performed with the specimen lying in horizontal position inside the chamber. As I already wrote, first step the sample was dried, weighted to determine mass in dry state and then the specimen was fixed in apparatus shown in Figure 3.

The specimen was put in vertical position. A special mechanism (Figure 3) under the principle of communicating vessels was used to keep a constant water level. Hot-ball probes are fixed in the stone. The specimen was placed on a bit of cotton lying on some sand powder particles (to create space for water transport). A constant water level in the dish was maintained and monitoring of diffusion water starts. Three RTM devices (Transient MS) were used to collect data moisture on local values (local moisture) (Figure 4) of thermal conductivity using Hot-ball probes. Input parameters such as start measuring, period between 2 cycles, period between 2 points in measuring and heating power (q) must be set in before measurements starts.

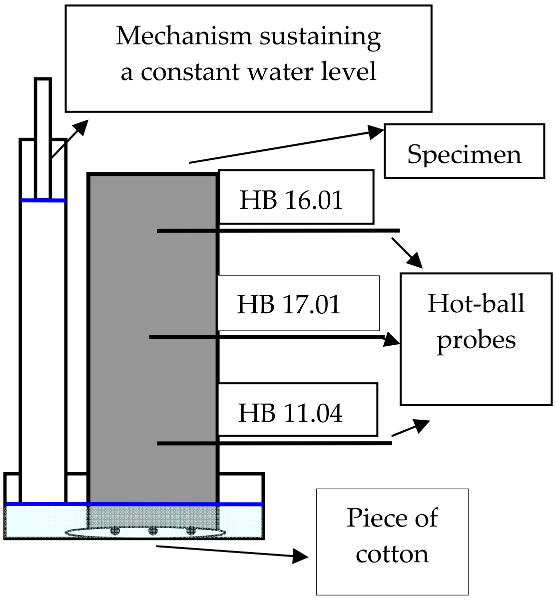

Figure 3: Placing specimens during the experiment

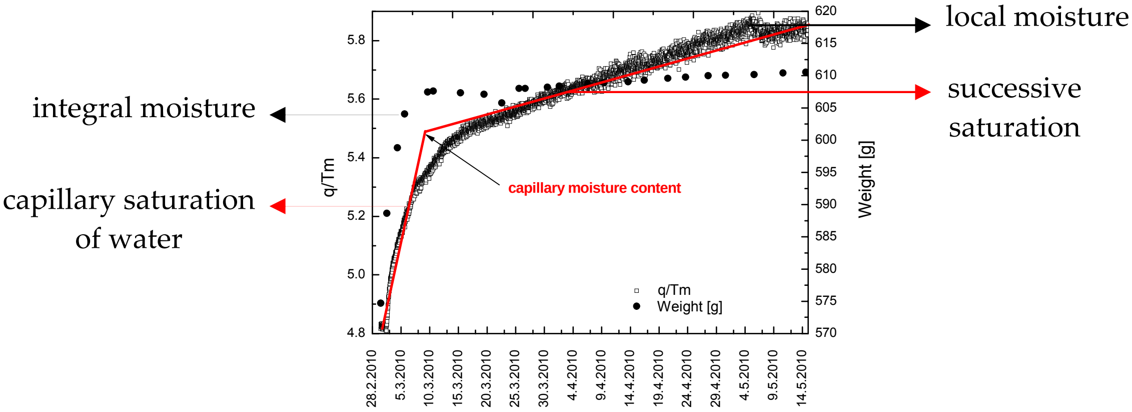

Figure 4: Resulting data after measuring and weighting

After measuring to get resulting data such as date, time and proportion heating power and temperature (q/ T_m). Devices were appropriately preset time every 30 minutes. Collected data were transferred from RTM to computer every 3 – 4 days. A reweighing of specimen was performed to find integral moisture (Figure 4). The front of water diffusion was studied through RTM´s data (q/ T_m) which are calibrated in percentage for dry and water saturated specimen. The experiment ran three months. Figure 5 shows diffusion process of water into the sandstone with 17,8% porosity by Hot-ball probes in various positions and figure 6 shows in detail advance of moisture front in sandstone.

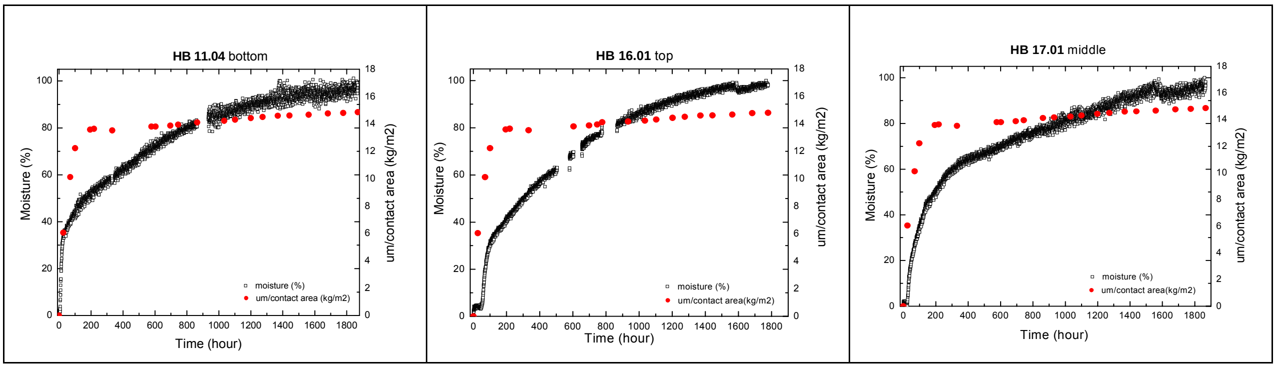

Figure 5: Graphs of moisture monitoring (integral and local moisture) in various positions in specimen by Hot-ball probes

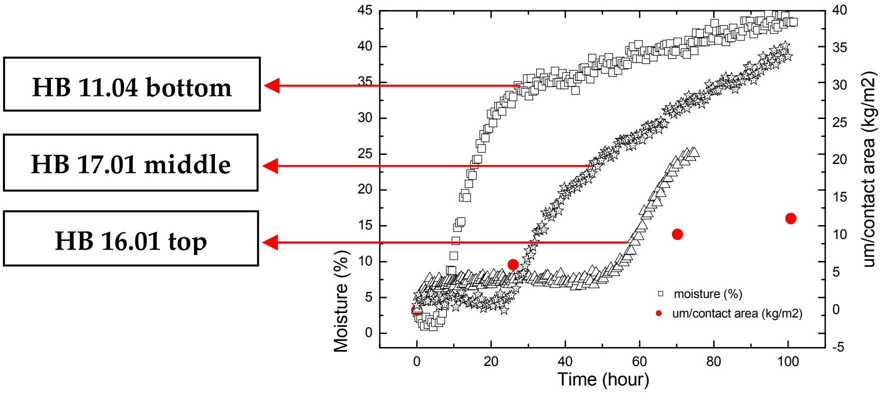

Figure 6: Advance of moisture front in sandstone in various positions

From this experiment we are able to characterize advance of moisture front in specimen. Hot-ball sensor gives thermal conductivity than after calibration provide value of moisture (in percentage).

5. Results and conclusions

Paper presents monitoring of water diffusion in sandstone with 17,8% published water porosity by Hot-ball method. This investigation shows an application the transient Hot-ball method. We believe moisture diffusion monitored by the Hot-ball method to be a highly successful way for moisture transport analysis through porous materials. Experiments show how moisture in materials influences thermal conductivity. The graphs in Figure 5 describe increase of local moisture (rising weight) and also integral moisture (increase total moisture in a material). Specimen of sandstone weighed 574,5 g in dry state and after saturated its weight has been increased to 610,68 g. An assumption was accepted that a linear correlation exists between thermal conductivity and moisture content. Then we can obtained information an advance of moisture front using monitored data (local moisture) and weighting (integral moisature) (Figure 4). Information regarding moisture transport will represent a basic assumption for achieving a better understanding and of role of water in porous structure. In the future we want to investigate a diffusion of water in materials with different porosities and under different manners temperatures and water salinities to understand the conditions of water saturation.

Acknowledgement

The paper was supported by the project LPP–0442–09

References:

[1] M. Montoto, Dept. of Geology group of Petrophysics University of Oviedo: Petrophysics at the rock matrix scale: hydraulic properties and petrografic interpretation, Enresa – Direction de Ciencia y Tecnologia, Madrid, Spain (2003)

[2] Ľ. Kubičár, V. Vretenár, V. Štofaník, V. Boháč and L. Bageľ: Thermophysical sensors: Theorhy and application of the hot ball, in Proc. of Twenty - Ninth *International Thermal Conductivity Conference, Proceedings of Seventeenth International Thermal Expansion Symposium*, June 24 - 27, 2007, edited by John R. Koenig, Heng Ban, Lancaster, Pennsylvania, DEStech Publication, Inc., (2008)

[3] Ľ. Kubičár, V. Vretenár, V. Štofaník, V. Boháč: Thermophysical sensors: Theory and application of the hot ball, Int. J. of *Thermophysics*, (2008)

Modelling chemical degradation of cement based materials with mechanics of multiphase porous media

Dariusz Gawin[1], Francesco Pesavento[2], Marcin Koniorczyk[1], Mateusz Wyrzykowski[1], Witold Grymin[1]

[1]Technical University of Lodz, Poland

[2]University of Padova, Italy

Abstract: *A general approach to modelling chemical degradation processes in cement based materials, due to combined action of hygro-thermal, chemical and mechanical loads, is presented. Mechanics of multiphase porous media and damage mechanics are applied for this purpose. The mass-, energy- and momentum balance equations, and constitutive and physical relations are briefly presented, and then numerically solved with the finite element method. Three examples of the model application for analysing ions transport and degradation processes of concrete due to chemical attack of pure water, salt crystallisation and alkali-silica reaction are presented and discussed.*

Keywords: *Cement based materials, Chemical degradation, Mechanics of multi-phase porous media.*

1. Introduction

A possibly accurate prediction of degradation of concrete structures during their whole life cycle, at normal service conditions and after exposition to chemically aggressive environment, is of great practical importance. Much research has been devoted to this subject in recent decades, and several predictive mathematical models have been developed. At the Technical University of Lodz and the University of Padova research on the modelling of building materials as a multiphase, porous medium has been carried out for many years. Concepts of effective stresses and mechanics of porous media, often used in geomechanics, have been adopted for modelling heat, mass and momentum transport in cement based materials, e.g. [1-4]. This approach has been successfully applied to the numerical analysis of such difficult problems as hygro-thermo-chemical behaviour of concrete at early ages or degradation at high temperature, giving results in good agreement with experimental data, [1-3]. Here, a general approach to modelling degradation processes in a cement based material, due to combined action of hygro-thermal, chemical and mechanical loads, is presented. Mechanics of multiphase porous media is applied for this purpose [1, 3]. The mass-, energy- and momentum balance equations, and constitutive and physical relations are briefly presented, and then numerically solved with the finite element method. Three examples of the model application for analysing ions transport and degradation processes of concrete due to chemical attack of pure water (calcium leaching), salt crystallisation and expansive alkali-silica reaction, are presented and discussed.

2. Mathematical model

The balance equations are written by considering cement based materials as a multi-phase porous medium, which is assumed to be in hygro-thermal equilibrium state locally. More specifically, in the present case the solid skeleton voids are filled partly by liquid water (the wetting phase) and partly by a gas phase (the non-wetting phase). The liquid phase consists of physically bound water and capillary water, which appears when the degree of water saturation exceeds the upper limit of the hygroscopic region, S_{ssp}. The gas phase is a mixture of dry air and water vapour, which is a condensable gas constituent.

In the following, subscripts mean physical quantities related to the whole volume of medium, and upper indices their intrinsic values related to the single phase or constituent only. By constituent we indicate a matter which is uniform throughout in chemical composition, while phase means here different physical state of a matter (solid, liquid or gaseous). Symbols *s*, *w*, *l*, *g*, *gw* and *ga* denote solid skeleton, pure liquid water, the whole liquid phase (i.e. water + ions), gas phase in general, vapour and dry air, respectively. The solid phase is assumed to be in contact with all fluids in the pores. When calcium leaching is modelled, *Ca* indicates the calcium ions in the liquid solution, and *Ca-p* indicates the calcium precipitated from the liquid solution. When any other chemical degradation processes is analysed, the latter subscript should be substituted by the one indicating the ions involved in the process. The full development of the model equations, starting from the local, microscopic balance equations with successive volume averaging, and further transformations are presented in [1, 4].

The final form of the *governing equations*, written at microscopic level in terms of the *primary variables*, i.e. gas pressure, capillary pressure, temperature, calcium concentration in water and displacement vector (p^g, p^c, T, C_{Ca}, $\mathbf{u}$), taking into account the small deformation theory, is:

- *Dry air mass balance equation* (including the solid skeleton mass balance) takes into account both diffusive and advective air flow, as well as variations of porosity caused by leaching processes and deformations of the skeleton. It has the following form:

$$-n\frac{D^sS_w}{Dt}-\beta_s\left(1-n\right)S_g\frac{D^sT}{Dt}+S_g div\,\mathbf{v}^s+\frac{S_g n}{\rho^{ga}}\frac{D^s\rho^{ga}}{Dt}+\frac{1}{\rho^{ga}}div\,\mathbf{J}_g^{ga}+\frac{1}{\rho^{ga}}div\left(nS_g\rho^{ga}\mathbf{v}^{gs}\right)=-\frac{\dot{m}_{dis}}{\rho^s}S_g \qquad (1)$$

where S_w and S_g are the water and gas saturation level respectively, β_s is the thermal expansion coefficient of the solid phase, ρ^{ga} is the dry air density, $\mathbf{J}_g^{ga}$ is the dry air diffusive flux and n is the porosity. The term at the right hand side represents the source terms related to the leaching process ($\dot{m}_{dis}$).

- *Water species (liquid+vapour) mass balance equation* (including the solid skeleton mass balance) considers diffusive and advective flow of water vapour, mass sources related to phase changes of vapour (evaporation/condensation and physical adsorption/desorption), and variations of porosity caused by leaching process and deformations of the skeleton, resulting in the following equation:

$$\begin{gathered}n\left(\rho^w-\rho^{gw}\right)\frac{D^sS_w}{Dt}+\left(\rho^wS_w+\rho^{gw}S_g\right)\alpha\, div\,\mathbf{v}^s-\beta_{swg}^*\frac{D^sT}{Dt}+S_g n\frac{D^s\rho^{gw}}{Dt}+div\,\mathbf{J}_g^{gw}+div\left(nS_w\rho^w\mathbf{v}^{ls}\right)\\ +div\left(nS_g\rho^{gw}\mathbf{v}^{gs}\right)-\left(\rho^wS_w+\rho^{gw}S_g\right)\frac{\left(1-n\right)}{\rho^s}\left[\frac{D^s\rho^s}{D\Gamma_{leach}}\frac{D^s\Gamma_{leach}}{Dt}\right]=-\frac{\dot{m}_{diss}}{\rho^s}\left(\rho^{gw}S_g+\rho^wS_w\right)\end{gathered} \qquad (2)$$

where $\beta_{swg}^*=\beta_s\left(1-n\right)\left(S_g\rho^{gw}+\rho^wS_w\right)+n\beta_w\rho^wS_w$ is the thermal expansion coefficient of the multiphase system, ρ^{gw} is the water vapour density, Γ_{leach} the leaching degree and $\mathbf{J}_g^{gw}$ the water vapour diffusive flux.

- *Energy balance equation* (for the whole system) accounting for the conductive and convective heat flow, heat effects of phase changes, dissolution and precipitation processes, can be written as:

$$\begin{aligned}&\left(\rho C_p\right)_{eff}\frac{\partial T}{\partial t}+\left(\rho_w C_p^w \mathbf{v}^w+\rho_g C_p^g \mathbf{v}^g\right)\cdot grad\,T-div\left(\chi_{eff}\,grad\,T\right)=\\&=-\dot{m}_{vap}\Delta H_{vap}+\dot{m}_{dis}\Delta H_{dis}+\dot{m}_{prec}\Delta H_{prec}\end{aligned}\qquad(3)$$

where χ_{eff} is effective conductivity from experiments, while $\left(\rho C_p\right)_{eff}=\rho_s C_p^s+\rho_w C_p^w+\rho_g C_p^g$ the thermal capacity of the multiphase system, and the enthalpy of vaporization, dissolution and precipitation are respectively:

$$\Delta H_{vap}=H^{gw}-H^{w},\qquad \Delta H_{dis}=H^{s}-H^{Ca},\qquad \Delta H_{prec}=H^{Ca}-H^{Ca-p}.\qquad(4)$$

- *Calcium mass balance equation* (leaching case) including the diffusion of ionic species, the advection and the chemical reaction related to the dissolution of the calcium contained in the solid skeleton [3] and precipitation of calcium salt, [4]:

$$\begin{aligned}&\left(1-n\right)C_{Ca}S_w\frac{1}{\rho^s}\frac{\partial\rho^s}{\partial\Gamma_{leach}}\frac{\partial\Gamma_{leach}}{\partial t}+nC_{Ca}\frac{\partial S_w}{\partial t}+nS_w\frac{\partial C_{Ca}}{\partial t}+\alpha C_{Ca}S_w\,div\,\mathbf{v}^s\\&+\frac{1}{\rho^w}div\,\mathbf{J}_d^{Ca}+\frac{1}{\rho^w}div\left(C_{Ca}nS_w\rho^w\mathbf{v}^{ls}\right)=\frac{\dot{m}_{dis}}{\rho^w}-\frac{\dot{m}_{prec}}{\rho^w}-\frac{\dot{m}_{dis}}{\rho^s}C_{Ca}S_w\end{aligned}\qquad(5)$$

where C_{Ca} is the calcium concentration in the liquid solution, $\mathbf{v}^{ls}$ is the velocity of the solution with respect to the solid skeleton, and finally $\mathbf{J}_d^{Ca}$ is the diffusion mass flux of the Ca^{2+} ions in the water solution.

- *Linear momentum balance equation* (for the multiphase system) in the rate form:

$$div\left(\dot{\mathbf{t}}^{total}\right)+\dot{\rho}\mathbf{g}=0,\qquad(6)$$

where $\mathbf{t}^{total}$ is the total stress tensor, ρ is the apparent density of the multiphase material, $\mathbf{g}$ is the vector of gravity acceleration.

Evolution equations

The progress of chemical degradation processes (calcium leaching, precipitation or ASR reaction) is described by the *evolution equations* written in terms of the *evolution variables*: calcium degree of leaching, saturation degree with precipitated salt, and ASR reaction extent (Γ_{leach}, S_p, Γ_{ASR}).

- *Evolution equation for non-isothermal calcium leaching* has the following form, [3]

$$\frac{\partial\Gamma_{leach}}{\partial t}=-\frac{A_s}{s_{Ca}^0RT_{ref}\,\tau_{leach}},\qquad(7)$$

where chemical affinity of the leaching process is defined as follows

$$A_s=\int_{s_{Ca}^0}^{s_{Ca}^*}\kappa\left(\bar{s},T_{ref}\right)d\bar{s}-\int_{s_{Ca}^0}^{s_{Ca}}\kappa\left(\bar{s},T_{ref}\right)d\bar{s}\qquad(8)$$

$\tau_{leach} = f\left(s_{Ca}, T\right)$ is the characteristic time of the process, T_{ref} is the reference temperature, κ is the equilibrium function, s_{Ca}^0 and s_{Ca} are the initial and actual values of solid calcium content (i.e. the calcium phase being leached from the skeleton),. The characteristic time τ_{leach} for different phases of solid calcium can be expressed by the following approximate relationship [3]:

$$\tau_{leach}^{\pi}\left(T\right) \cong \tau_{leach}^{\pi}\left(T_{ref}\right) \times \exp\left[A_{\tau}\left(T - T_{ref}\right)\right] \tag{9}$$

where T_{ref}= 298.15 K, A_{τ}= -0.0239 K^{-1}, and superscript π= *por, etr, CSH* means the portlandite, ettringite or CSH phases, respectively. One should underline that non-isothermal calcium leaching is an irreversible process and it is described here by a non-equilibrium model. More details concerning modelling this process can be found in [3].

- *Evolution equation for salt precipitation,* depending on the super-saturation ratio of the salt concentration, $S = C_{Ca} / C_{Ca}^{\max}$, has the following form, [5]:

$$\frac{dS_p}{dt} = \begin{cases} S_w K(C_{Ca} - A' C_{Ca}^{\max})^p, & C_{Ca} \geq A' C_{Ca}^{\max} \\ -S_w K | C_{Ca} - A' C_{Ca}^{\max} |^p, & C_{Ca} < A' C_{Ca}^{\max} \wedge 0 < S_p < 1 \end{cases} \tag{10}$$

where the saturation degree with precipitated salt $S_p = 1 - S_w - S_g$, p is the process order, depending on the properties of porous material and kind of the salt, $C_{Ca}^{\max}\left(T\right)$ is the maximum calcium concentration at temperature T, K is the rate constant. For primary crystallization the super-saturation parameter $A' \geq 1$, and when first salt crystals appear in the pores further crystallization proceeds at $A' = 1$. Equation (10) is also valid for the dissolution of salt crystals.

- *Evolution equation for non-isothermal ASR reaction* has the following form, [6, 7],

$$\frac{\partial \Gamma_{ASR}}{\partial t} = \frac{1 - \Gamma_{ASR}}{\tau_r\left(T, S_w\right) \cdot \lambda\left(T, S_w, \Gamma_{ASR}\right)} \tag{11}$$

where $\tau_r\left(T, S_w\right)$ is the characteristic time of ASR reaction at temperature T and moisture content S_w, while $\lambda\left(T, S_w, \Gamma_{ASR}\right)$ is experimentally determined material function, given by, [6],

$$\lambda\left(T, S_w, \Gamma_{ASR}\right) = \frac{1 + \exp\left(-\tau_L / \tau_r\right)}{\Gamma_{ASR} + \exp\left(-\tau_L / \tau_r\right)} \tag{12}$$

with τ_L being the latency time of reaction. The presented formulation combines the three existing models [6, 7] to take into account effect of the temperature, constant and variable moisture content and aging upon the progress of ASR reation.

Effective stress principle

Cement based materials are multi-phase porous media, hence analysing the stress state and the deformation of the material it is necessary to consider not only the action of an external load, but also the pressure exerted on the skeleton by fluids present in its voids. The total stress tensor acting in a point of the porous medium may be split into the effective stress tef, which accounts for stress effects due to changes in porosity, spatial variation of porosity and the deformations of the solid matrix, and a part accounting for the solid phase pressure exerted by the pore fluids, Ps, [1],

$$\mathbf{t}^{tot} = \mathbf{t}^{ef} - \alpha P^s \mathbf{I} = \mathbf{t}^{ef} - \left(p^g - \chi_s^{ws} p^c \right) \mathbf{I}, \tag{13}$$

where **I** is the second order unit tensor, α is the Biot coefficient, and χ_s^{ws} the fraction of skeleton area in contact with water. In equation (13) capillary pressure is defined in such a way that it has physical meaning also in the hygroscopic range of moisture content, [1],

$$p^c \equiv p^g - p^w = \Pi^f - \gamma^{wg} J_{wg}^w . \tag{14}$$

In this region it takes also into account the effect of disjoining pressure, Π^f, besides the curvature and surface tension of the water/gas interface, J_{wg}^w and γ^{wg}. At higher relative humidity, in the capillary moisture range, the effect of disjoining pressure is neglected ($\Pi^f = 0$).

3. Numerical examples

The model equations are discretized in space by means of the finite element method. The unknown variables are expressed in terms of their nodal values and shape functions $\mathbf{N}_\pi$ as,

$$\begin{aligned} &p^g(t) \cong \mathbf{N}_p \bar{\mathbf{p}}^g(t), \quad p^c(t) \cong \mathbf{N}_p \bar{\mathbf{p}}^c(t), \quad T(t) \cong \mathbf{N}_t \bar{\mathbf{T}}(t), \\ &C_{Ca}(t) \cong \mathbf{N}_{Ca} \bar{\mathbf{C}}_{Ca}(t), \quad \mathbf{u}(t) \cong \mathbf{N}_u \bar{\mathbf{u}}(t). \end{aligned} \tag{15}$$

The discretized form of the model equations was obtained in [3] by means of Galerkin's method and can be written in the following concise matrix form:

$$\mathbf{C}_{ij}(\mathbf{x}) \frac{\partial \mathbf{x}}{\partial t} + \mathbf{K}_{ij}(\mathbf{x}) \mathbf{x} = \mathbf{f}_i(\mathbf{x}), \qquad \mathbf{x} = \left\{ \bar{\mathbf{p}}^g, \bar{\mathbf{p}}^c, \bar{\mathbf{T}}, \bar{\mathbf{C}}_{Ca}, \bar{\mathbf{u}} \right\}^T, \tag{16}$$

where the non-linear matrix coefficients $\mathbf{C}_{ij}(\mathbf{x})$, $\mathbf{K}_{ij}(\mathbf{x})$ and $\mathbf{f}_i(\mathbf{x})$ are defined in detail in [3]. The time discretization is accomplished through a fully implicit finite difference scheme,

$$\mathbf{\Psi}^i\left(\mathbf{x}_{n+1}\right) = \mathbf{C}_{ij}\left(\mathbf{x}_{n+1}\right) \frac{\mathbf{x}_{n+1} - \mathbf{x}_n}{\Delta t} + \mathbf{K}_{ij}\left(\mathbf{x}_{n+1}\right) \mathbf{x}_{n+1} - \mathbf{f}_i\left(\mathbf{x}_{n+1}\right) = \mathbf{0}, \tag{17}$$

where superscript i ($i = g, c, t, Ca, u$) denotes the state variable, n is the time step number and Δt is the time step length. The equation set (17) is solved by means of a monolithic Newton-Raphson type iterative procedure using a frontal solver [1, 3].

Non-isothermal calcium leaching

The first example deals with a 1-D calcium leaching problem where chemical action of deionized water on the surface of a 16-cm cement paste wall is modelled with convective BCs. Similar diffusion – reaction problem, but for the isothermal case with T=25°C, was previously solved in [3]. The calcium concentration in the liquid solution in contact with the wall surface is decreasing progressively in a time span of 1000 days from the initial value of 17.885 mol/m^3, corresponding to thermodynamic equilibrium at T=60°C, down to 1 mol/m^3. The problem is solved for two different conditions for the thermal field: uniform temperature equal to 60°C (case 1) and with a thermal gradient 25°C/60°C between the surfaces of the wall (case 2). The latter one is obtained by the cooling process on the same side of the wall starting from T_0=60°C in the same time interval. For the both cases the calcium mass exchange coefficient equal to 10^{-5} kg/(m^{2}s) is assumed. The material properties assumed in the simulations are the same as in [3]. The simulations are performed with time step length Δt= 0.1 day, for the time span of $1 \cdot 10^5$ days.

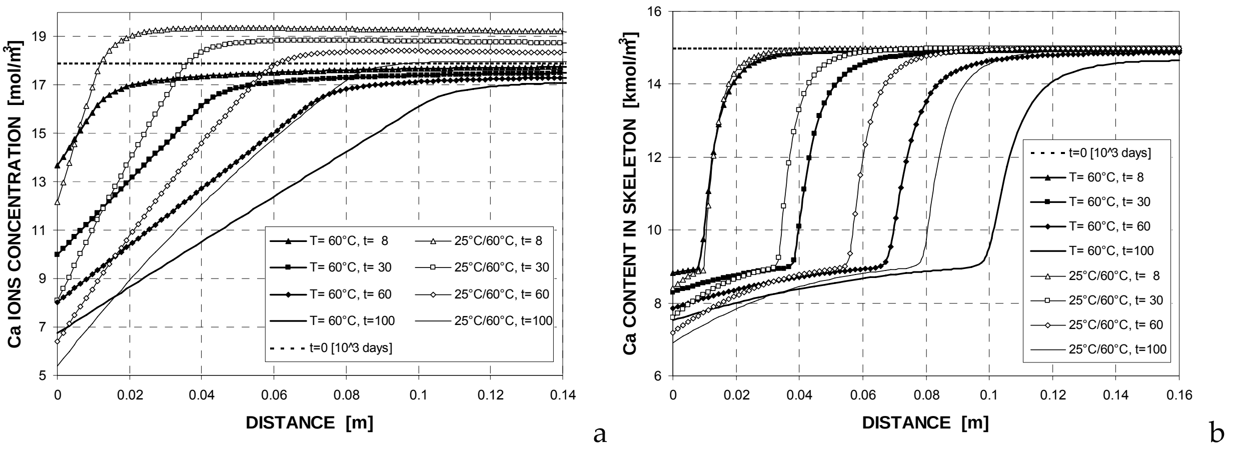

Figure 1: Comparison of the space distributions of calcium concentration (a) and solid calcium content (b) during leaching of a concrete wall at T= 60oC and with temperature gradient 25oC/60oC.

Figure 1 shows a comparison between the results concerning calcium ions concentration in the pore solution (Fig. 2a) and solid calcium content in the skeleton (Fig. 2b) for the two cases considered, highlighting the role played by the temperature gradient. In the case with uniform temperature the liquid solution contains less calcium ions (Fig. 2a), what results in a faster dissolution of calcium from the material skeleton (Fig. 2b) and faster progress of the material chemical degradation process. As can be observed, temperature has an important effect of the calcium leaching in cement based materials.

Salt precipitation during drying

The second problem deals with drying of a wall containing NaCl in water solution. The 20 cm thick wall is made of cement mortar. The material has intrinsic permeability of 3.0 10^{-21} m^2 and porosity of 12%. Other material parameters are given in [5]. The initial conditions are as follows: $p^g = 101325$ Pa, $S_w = 0.69$, $T = 20$ C, $C_{Ca} = 15\%$M. In the evolution equation (10), the rate constant $K = 0.05$ and the process order are equal to 1, 2 or 4. The drying of the material is triggered by the rapid fall of the ambient air humidity to 3.5 g/m^3, while its temperature remains unchanged. On the wall surfaces the convective boundary condition with the heat exchange coefficient of 23 W/m^2K and the mass exchange coefficient of 0.023 m/s are assumed. Figure 2 shows the results of simulation obtained for the second order evolution law (i.e. p=2) for salt precipitation (10). One can notice a rapid decrease of the liquid saturation degree in the vicinity of the surface, Fig. 2a. The change of the dissolved salt concentration profiles for the same case is shown in Fig. 2b. For all the analysed cases one can observe the U-like profiles. The lowest value of the dissolved salt concentration on the surface can be noticed for the case with p=1 (C_{Ca}=0.26), while the highest one for the case with p=4 (C_{Ca}=0.31). The saturation concentration of the salt solution is equal to 0,26 kg/kg. For the comparison, the same experiment is simulated assuming thermodynamic equilibrium between dissolved and precipitated salt. Two types of binding isotherms are assumed, Freundlich's and Langmuir's ones. The obtained results are compared in Fig. 3a. The profiles of saturation degree with the crystallized salt for the case with p=2 are presented in Fig. 3b indicating that the salt precipitates only close to the wall surface.

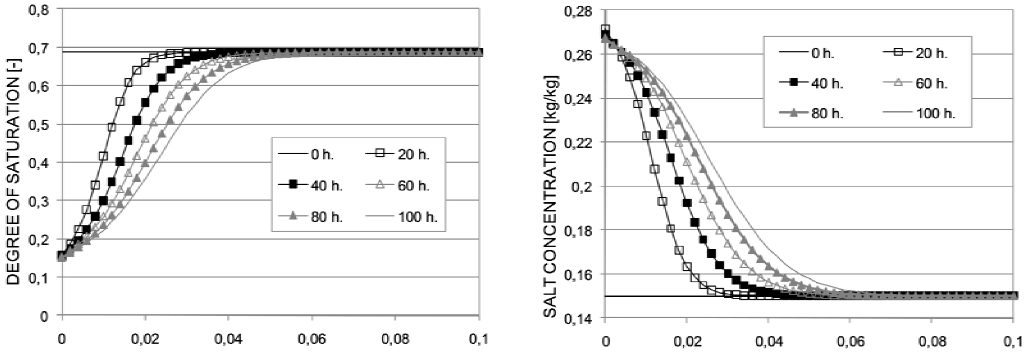

a b

Figure 2: Profiles of the degree of saturation with liquid phase (a) and the dissolved salt concentration (b) at the beginning and after 20, 40, 60, 80 and 100 hours, for the 2nd order rate law for precipitation (p=2).

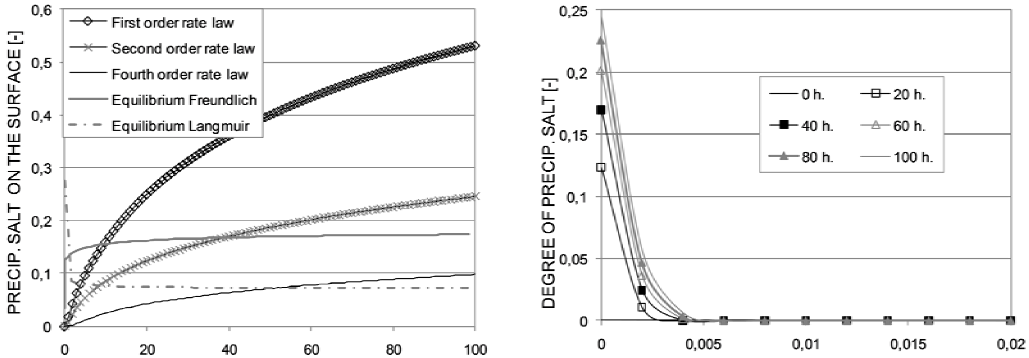

a b

Figure 3. Comparison of the change of the saturation degree with the precipitated salt on the surface between the kinetic and equilibrium approaches (a), the profiles of the saturation degree with the precipitated salt for the second order rate law (p=2).

Expansion due to ASR reaction

The third problem is based on the experimental tests [6] and it deals with a cement mortar specimen exposed to various hygral and thermal conditions. The material contained reactive aggregates hence considerable swelling strains due to the ASR reaction were observed. The simulations are performed for three different values of ambient temperature, 23°C, 38°C and 60°C, at the same relative humidity of 92%, and then for four different values of ambient relative humidity, 100% (in water), 98%RH, 92% and 86% at the same temperature of 38°C. The same materials parameters are used for all the analysed cases. The comparison of the simulation results with the experimental ones [6] is presented in Fig. 4, showing their good agreement.

4. Conclusions

A general model for chemo-thermo-hygro-mechanical behaviour of cement based materials, considering their multiphase nature, has been presented. It can be adapted to very different types of chemical degradation, e.g. leaching, salt precipitation or expansive chemical reaction. The model is thermodynamically consistent and it has been developed within framework of mechanics of multi-phase porous media. Three applications to concrete leaching, salt transport and precipitation, and expansive ASR reaction show the potentialities of the model.

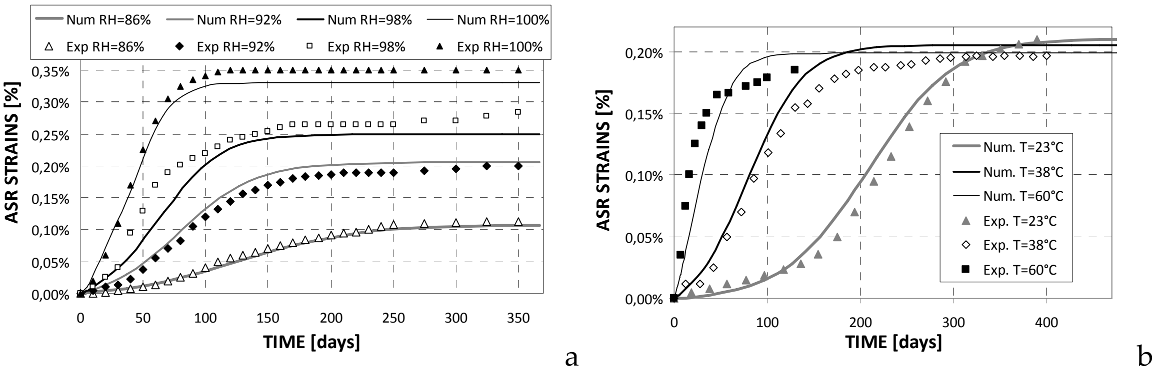

Figure 4. Comparison of the ASR strains obtained from simulations with the experimental data [6]: a) for 4 different values RH at T=38°C; b) for 3 different values temperature at RH=92%.

5. Aknowledgement

The work reported here has been partially funded by the project POIG.01.01.02-10-106/09-00 "Innovative means and effective methods to improve the safety and durability of building structures and transportation infrastructures in the strategy of sustainable development".

References

[1] PESAVENTO, F., GAWIN, D., SCHREFLER, B.A. Modeling cementitious materials as multiphase porous media: theoretical framework and applications. In Acta Mechanica, 2008. 201(1-4). p. 313-339. ISSN 0001-5970

[2] GAWIN, D., WYRZYKOWSKI, M., PESAVENTO, F. Modeling hygro-thermal performance and strains of cementitious building materials maturing in variable conditions. In Journal of Building Physics. 2008. 31(4). p. 301-318. ISSN 1744-2591

[3] GAWIN, D., PESAVENTO, F., SCHREFLER, B.A. Modeling deterioration of cementitious materials exposed to calcium leaching in non-isothermal conditions. In Computer Methods in Applied Mechanics and Engineering. 2009. 198(37-40). p. 3051-3083. ISSN 0045-7825

[4] KONIORCZYK, M., GAWIN, D. Heat and moisture transport in porous building materials containing salt. In Journal of Building Physics. 2008. 31(4). p. 279–300. ISSN 1744-2591

[5] KONIORCZYK, M. Modelling the phase change of salt dissolved in pore water – Equilibrium and non-equilibrium approach. In Construction and Building Materials. 2010. 24(7). p. 1119-1128. ISSN 0950-0618

[6] ULM, F.-J., COUSSY, O., LI, K., LARIVE, C. Thermo-chemo-mechanics of ASR expansion in concrete structures. In Journal of Engineering Mechanics. ASCE. 2000. 126(3). p. 233-242. ISSN 0733-9399

[7] STEFFENS, A., LI, K., COUSSY, O. Aging Approach to Water Effect on Alkali–Silica Reaction Degradation of Structures. In Journal of Engineering Mechanics. ASCE. 2003. 129(1). p. 50-59. ISSN 0733-9399

Comparison of field measurements and calculations of relative humidity and temperature in wood framed walls

S. Olof Hägerstedt[1], Jesper Arfvidsson[2]

[1,2] Department of Building Physics, Faculty of Engineering, Lund University, P.O. Box 118, 221 00 LUND, SWEDEN, email: olof.hagerstedt@byggtek.lth.se.

Abstract: *Energy efficient wood frame buildings give besides a number of positive effects also risks for moisture damages. To avoid moisture damage in wood houses some parts of the Swedish construction industry use WUFI 1D calculation tool in the design phase. The purpose of this study is to demonstrate the coupling between measured and WUFI 1D calculated values of relative humidity and temperature. The first step presents a comparison between measurements and blind calculations of relative humidity and temperature at different positions in a wooden wall with an air gap. In the second step has boundary conditions for calculated values been adjusted in order to achieve better agreement. The result of the comparisons between calculated and measured values are analyzed. The general conclusion of this study is that it is of great importance to apply a correct airflow in air gap. Results also show that it is possible to obtain reliable calculated values with a proper flow in the air gap.*

Keywords: *Moisture, Wood framed hoses, WUFI, Relative humidity.*

1. Introduction

Background

New laws and demands from consumers have increased the interest in well insulated wood frame houses. Besides a number of positive effects of reduced energy need there are also risks with well insulated wood frame houses. Critical parts of the building envelope become more often exposed to higher relative humidity than before. That provides increased probability for the occurrence of mould growth. To minimize the risk of moisture damages the Swedish wood house industry need a user friendly and reliable moisture calculation tool. This paper show the possibilities to use WUFI 1D to calculate the moisture performance for Swedish conditions.

Aim

The purpose of this study is to demonstrate the coupling between measured values of relative humidity and temperature compared with the same parameters calculated in WUFI 1D. The intension is to show if WUFI 1D is a tool that is suitable for the Swedish house industry during the design of wooden framed houses.

Limitations

The limitations for the measurements in this study are governed by the project schedule and building location. Measuring period, instrumentation and production schedule allows only data for one design and one building section, exposed to central Swedish climate, to be presented. This study does not deal with detailed information about functions and parameters used in the calculation program.

2. Method

In this chapter is a briefly method description given. A complete detailed method description with defined sources of error is given in a separated report (Hägerstedt, O. 2010, in press)

Relative humidity and temperature has been measured at different positions in a wall. Calculations of relative humidity and temperature have been carried out for the same positions with WUFI 1D 4.2 (WUFI 2009). Measured and calculated values for the relative humidity and temperature are then compared hour by hour in two steps. The first step is a blind comparison. In the second step the boundary conditions for calculated values have been adjusted in order to get better agreement. The comparisons between calculated and measured values are analyzed.

Measurements are carried out in the northwest facade for different depths in positions A to D as shown in figure 1. Northwest facade has been chosen because it often becomes the most moisture critical. This facade is also exposed to least amount of short wave radiation, which is a missing boundary condition. Measurements of temperature and relative humidity have been carried out every hour using a wireless Protimeter Hygro Trac system (Fjellström, P. et al. 2009; GE Sensing 2006; Hoogenboom, C. 2009). Measurements in position A to D, started 2008-11-08.

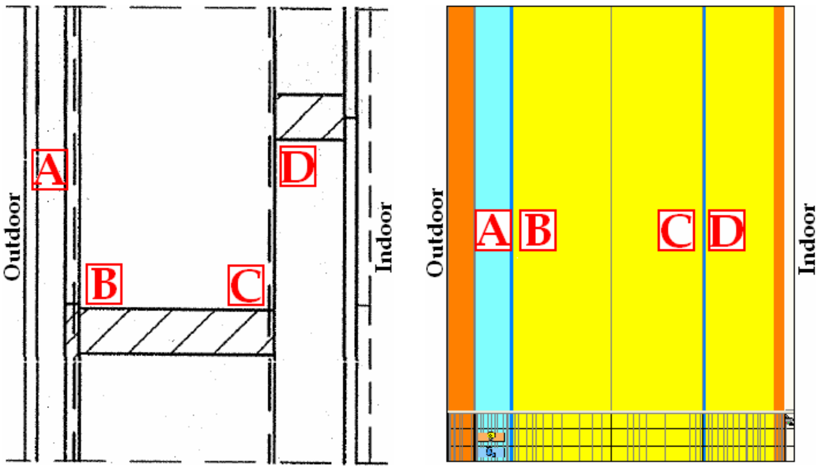

21 mm Spruce radial1, including paint Sd = 1m2

30 mm Air layer1, step 1 = 0,5 air/h, step 2 = 20 air/h

1 mm Weather resistive barrier1, Sd = 0,2m

195 mm Mineral wool3

1 mm Vapour retarder1, Sd = 100m

70 mm Mineral wool3

13 mm Chipboard1

13 mm Gypsum board4

Figure 1: Wall construction, measuring positions (A to D) and calculation model showing calculated positions (A to D). (1. IBP, 2.Nevander, L. et al. 1994, 3. IEA Annex 24 1996 4. Krus, M. 1996)

Boundary conditions in the calculation model are set to match measurement conditions. Applied outdoor climate for calculations are taken from SMHI, Swedish meteorological and hydrological institute, at a climate station nearby. Lack of data for longer periods has been replaced with the previous year's values for the period. Measured indoor climate have been possible to use for indoor boundary conditions from 2009-04-07. Previous period has constant values of 22°C and 40% relative humidity in calculations. Monitor position has also been changed 2009-09-23. Periods of significant lacks of climate data are shown in result charts.

Sources of error

Losses of climate data are the biggest sources of error. The constant conditions in the air gap are also of importance. Those losses in boundary conditions are bigger in a normal design phase and not reasonable to solve in context of this project. Deficiencies in WUFI physical model and bad coincides between calculated material and real material is seen as a part of the limitations. The loss of wooden beams in the 1D model, as show in figure 1, is also difficult to affect.

3. Result Blind Test

In order to limit the report only characteristic comparisons between blind calculated and measured values are presented. A short written result explanation is presented for all positions. Complete results are presented on the website www.framtidenstrahus.se.

Comparison between blind calculated and measured values for relative humidity and temperature for position C are shown in chart 1 and for position D in chart 2.

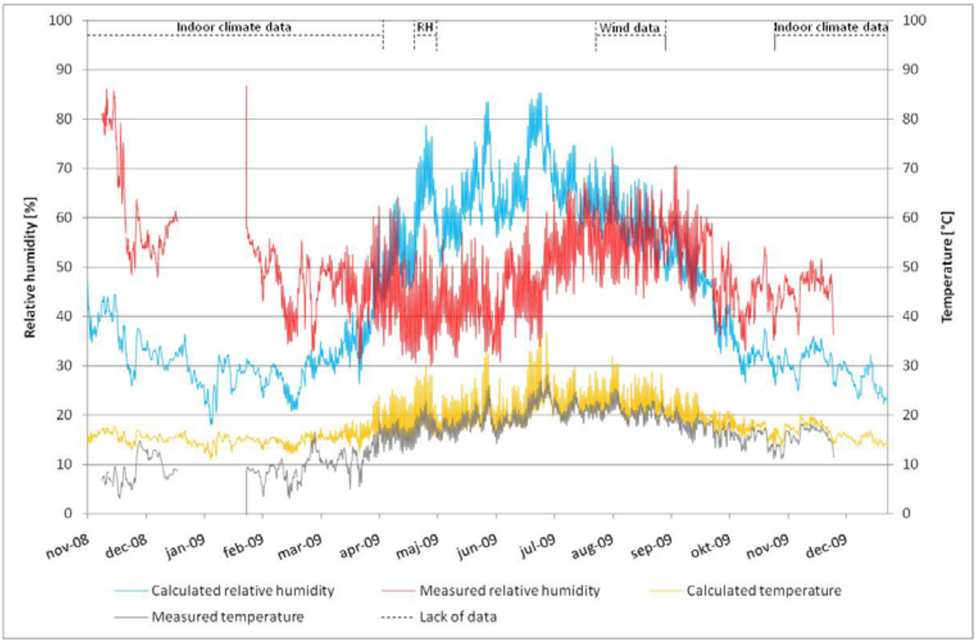

Chart 1: Position C. Relative humidity: Blind calculated (blue), measured (red). Temperature: Blind calculated (yellow), measured (grey). Periods without measured boundary conditions are shown in top.

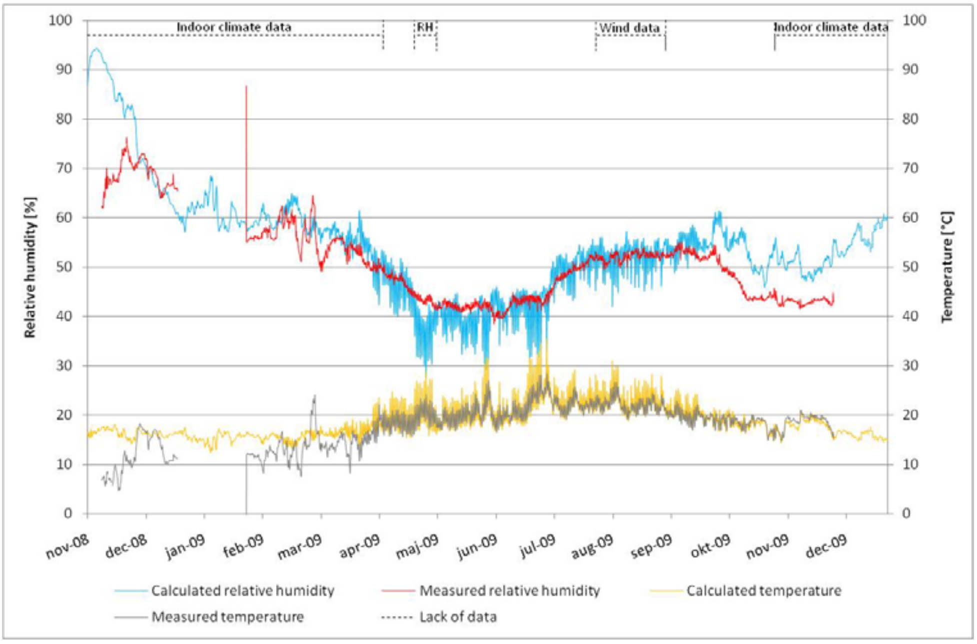

Chart 2: Position D. Relative humidity: Blind calculated (blue), measured (red). Temperature: Blind calculated (yellow), measured (grey). Periods without measured boundary conditions are shown in top.

Results for position C, as shown in chart 1, are characteristic for positions A, B and C outside the vapour barrier. Estimated and measured values follow each other for temperature but do not comply for relative humidity. Comparison of blind calculated and measured values in position D, as shown in chart 2, complies in both temperature and relative humidity.

4. Analysis Blind Test

Estimated and measured relative humidity does not match for positions at the cold side of the vapour barrier. At the same time there is a good correlation between calculated and measured temperature for all positions and relative humidity on the warm side of the vapour barrier.

This means that outdoor temperature and complete indoor climate seem to be correct applied. The relative humidity generally follows the temperature. That means that the reason for the mismatch of the relative humidity in position A, B and C has to do with additional or removed moisture outside the vapour barrier. The two possibilities for this in the calculation model are the amount of construction moisture or the airflow rate in the air gap behind the panel. Construction moisture should be dried out early in the calculation and is affected by the airflow in the air gap. The conclusion is therefore that the bad compliance in relative humidity in positions A, B and C depends on incorrect estimated airflow.

Adjustment of airflow

The airflow of 0,5 air changes/h, used in blind calculations, is taken from previous studies (Wadsö, L. 1986) and are assumed because of the horizontal wood strips in the air gap. Used airflow can be improperly adopted because the measuring points are located near a corner and a window which create leaks. The air in the air gap could also move more horizontally than expected.

Calculations with varied airflows are therefore made and compared with measurements from the air gap. Comparison shows that 20 air changes/h is a more reasonable value in terms of the whole year. During colder periods of the year, a lower flow of about 10 air changes/h give a better agreement. By changing the airflow in the air gap during the year gives the possibility to obtain very good correlations in all points over the whole year. A higher number of air changes than 20 air changes/h does not affect the calculated results significant.

Note that the airflow in both initial blind and adjusted calculations is constant during the calculation period, which itself gives rise to a source of error. It is not possible to further measure or study changes of airflow in context of this project.

5. Result with Adjusted Airflow

In the following comparisons the airflow in the air gap behind the wood panel are adjusted to 20 air changes/h in all calculations. In order to limit the report a characteristic period is chosen for each position to show the comparison between calculated and measured values. This is a short period for some positions and the entire period for other positions. Complete results are presented on the website www.framtidenstrahus.se. Results from this study are summarized and discussed in the analysis section.

In order to show the influence of the amplitude in calculated values carts have been extended with 12 hourly averages.

Position A – Air gap

Calculated and measured relative humidity and temperature in position A are shown in chart 3.

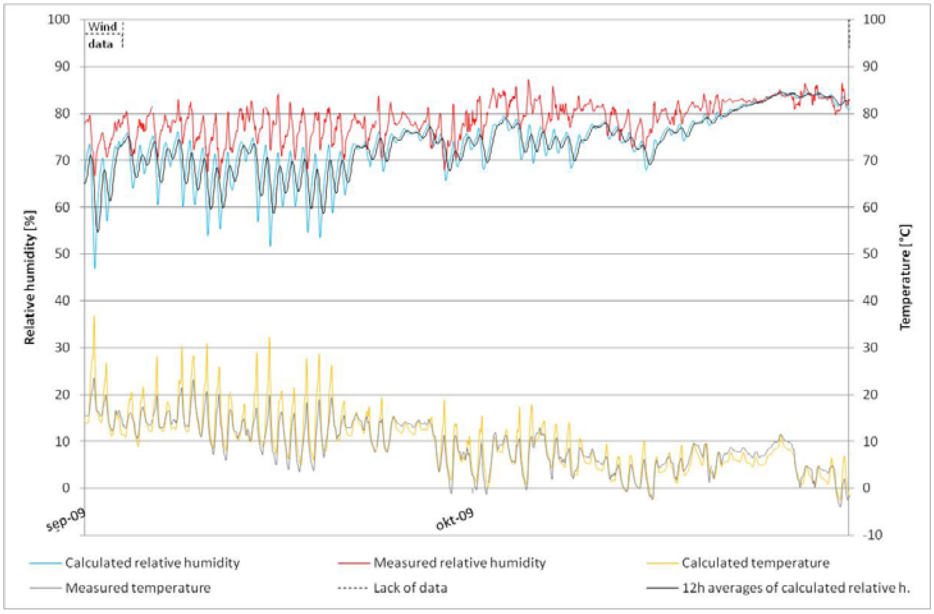

Chart 3: Position A – Air gap. Period: September - October. Relative humidity: Calculated (blue), measured (red). Temperature: Calculated (yellow), measured (grey). Periods without measured boundary conditions are shown in top. 12 hourly averages for calculated relative humidity (black).

Position B – Outside frame

Calculated and measured relative humidity and temperature in position B are shown in chart 4.

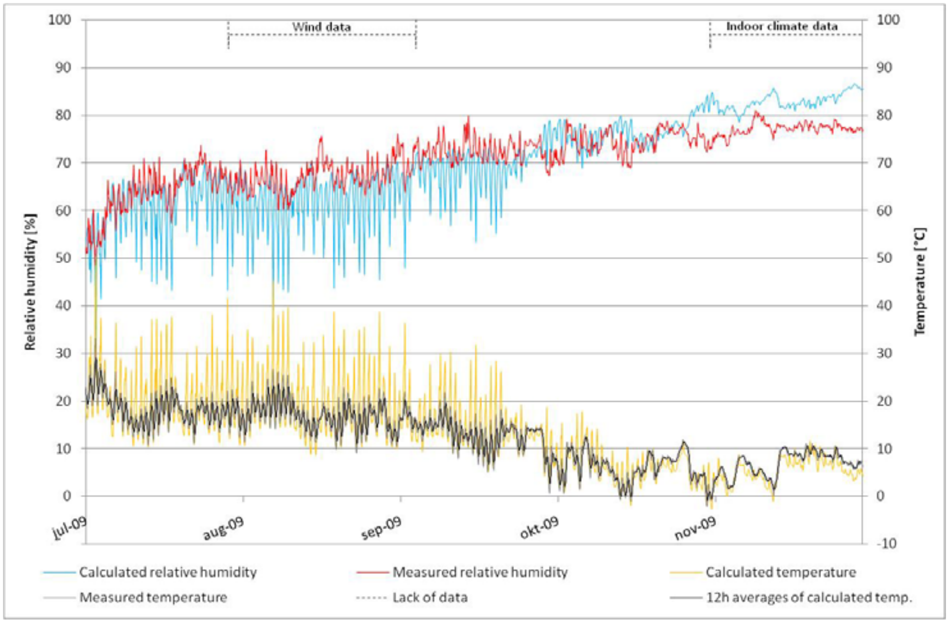

Chart 4: Position B – outside frame. Period: July - November. Relative humidity: Calculated (blue), measured (red). Temperature: Calculated (yellow), measured (grey). Periods without measured boundary conditions are shown in top. 12 hourly averages for calculated temperature (black).

Position C – Cold side of vapour retarder

Calculated and measured relative humidity and temperature in position C are shown in chart 5.

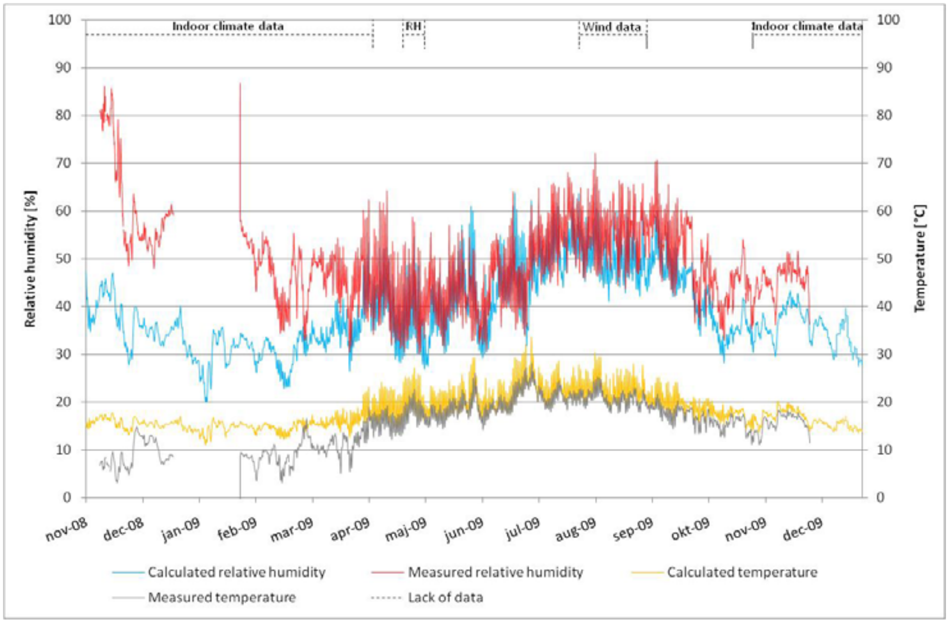

Chart 5: Position C – Cold side of vapour retarder. Period: November 2008 – December 2009. Relative humidity: Calculated (blue), measured (red). Temperature: Calculated (yellow), measured (grey). Periods without measured boundary conditions are shown in top.

Position D – Warm side of vapour retarder

Calculated and measured relative humidity and temperature in position D are shown in chart 6.

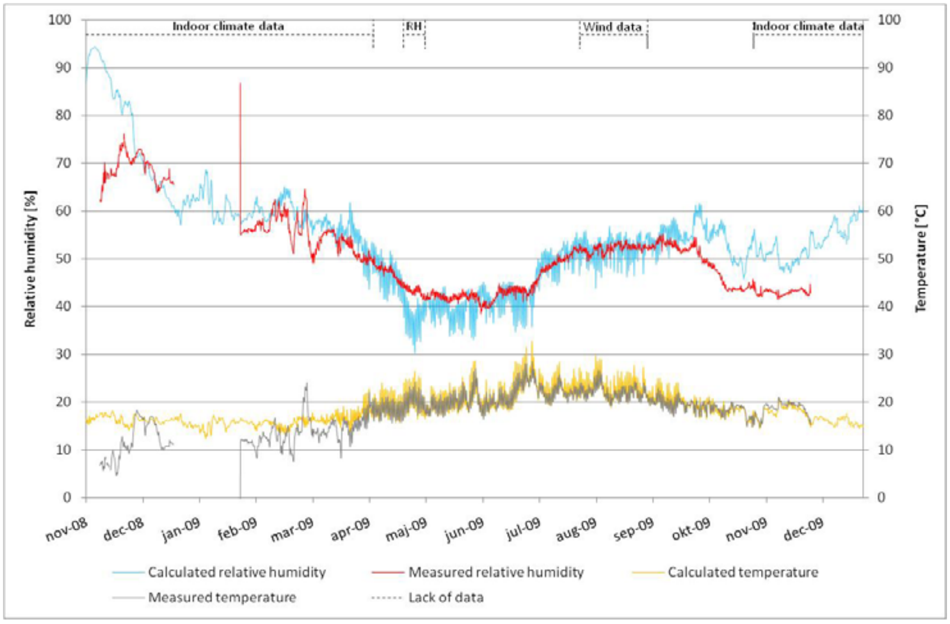

Chart 6: Position D – warm side of vapour retarder. Period: November 2008 – December 2009. Relative humidity: Calculated (blue), measured (red). Temperature: Calculated (yellow), measured (grey). Periods without measured boundary conditions are shown in top.

6. Analysis – with adjusted airflow

Besides some individual periods, and the size of amplitude for daily values, there is at good correlation between calculated and measured temperature in all studied positions. By adding the mean value for every 12 hours on calculated temperature, as shown in chart 4, the daily amplitude size is reduced and gives a perfect agreement with measured values.

Apart from some individual periods, and the size of amplitude for daily values, calculated and measured relative humidity follows each other. Calculated values of relative humidity are constantly five to ten percent lower compared to measured values for positions A, B and C, outside the vapour barrier. The mean value for every 12 hours in calculated relative humidity, as shown in chart 3, reduce the size of the daily amplitude to corresponds to the measured amplitude.

Deviations between calculated and measured values outside the vapour barrier during the cold period could, as mentioned earlier, be remedied by reducing the airflow in the air gap. The effort to indentify the impact of outdoor climate on the conditions in the air gap was not possible to do within the context of this project.

The lack of boundary conditions for relative humidity in the end of April could be noticed in position C and D, as show in chart 5 and 6.

Especially position C and D shows a bad correlation between calculated and measured values for both relative humidity and temperature until indoor climate is applied 2009-04-01 in the calculations. Position C and D are closer to the inside and therefore more affected of the lack of boundary conditions compared to positions further out in the construction. Besides the loss of boundary conditions for indoor climate during this period, the house is not inhabited, and construction moisture may retain and effect measurements.

The comparison between calculations and measurements in position D, as shown in chart 6, clearly shows that the monitor for indoor boundary conditions has been moved 2009-09-23.

The amplitude of the daily calculated values for both relative humidity and temperature are bigger than measured in all positions during the warm period. During the cold period the amplitude of calculated and measured values is equal. Lower daily amplitude obtains for positions deeper into the construction. This probably depends on a more even temperature distribution from the indoor climate. The amplitude for calculated and measured values also has a better correlation deeper into the construction. The reason for constant higher amplitude for calculated values is unknown. Installations of monitors in the wood frame with higher heat and moisture capacity may cause the amplitude of the measurements to be lower. The monitors may also have a weak ability to register rapid temperature shifts, or calculation could be more sensitive to temperature fluctuations compared to measurement. In positions A, B and D there is also higher amplitude on calculated relative humidity compare to measured. It is easy to assume that the high amplitude of the calculated temperature gives corresponding errors to calculated relative humidity. It is therefore surprising that the amplitude of the calculated relative humidity is the same as the measured relative humidity in position C, while there is a difference in amplitude of the calculated and measured temperature. By adding the floating mean value for every 12 hours on calculated values, as shown in chart 3 and 4, the amplitude is reduced which give a better correspondence to measured values.

7. Conclusion

The general conclusion of this study is that conditions of the airflow in the air gap behind the panel must be known to give a good correlation between calculated and measured values.

The difference in results for the relative humidity between blind calculations with airflow of 0.5 air changes/h and the calculated values with an adjusted airflow for 20 air changes/h shows the great importance using a correct air flow in the model. The use of a relevant airflow in the air space is essential for evaluation of the risk for moisture damages and mould growth. Applied airflow in the air space has a big influence in all points of the frame that are located on the outside of the vapour retarder.

Deviations and differences between calculated and measured values can be attributed to relevant sources. It is entirely possible that the airflow in the air gap behind the panel varies in a manner which gives a good correlation between calculated and measured values. Since the condition in the air gap is not measured it is not possible to confirm that this is the case. In respond to known and unknown sources of error the correlation between calculated and measured values are considered as good.

Future work on development of WUFI 1D should focus on designing a model for airflow in air gaps behind facade layer. Another solution could be to look for context in settled airflow in other studies where comparisons between calculated and measured values in facades with underlying air space made. It would have been helpful if a general model of varying airflow in air gaps could be created and applied in calculations.

References

[1] FJELLSTRÖM, P-A.; POUSETTE, A.; SANDBERG, K. *Verification measurements in Woodbuild project. Verifieringsmätningar inom Woodbuild*, in Swedish. SP Trätek, Skellefteå, 2010.

[2] GE SENSING, *Protime*ter HygroTrac, Wireless environmental monitoring. 2006.

[3] HOOGENBOOM, C. *GE Sensing Report on Calibration issues affecting HygroTrac model.* 2009.

[4] HÄGERSTEDT. O. *Calculation and field measurement method for wood framed house.*
Department of Building Physics, Lund University, Report TVBH-XXXX, 2010, In press.
IBP. Fraunhofer Institute for Building Physics.
http://www.ibp.fraunhofer.de/index_e.html.

[6] IEA Annex 24. *Heat, air and moisture transfer through new and retrofitted insulated envelope parts.* 1996.

[7] KRUS, M. *Moisture Transport and Storage Coefficients of Porous Mineral Building Materials.* Fraunhofer IRB Verlag. 1996.

[8] NEVANDER, L-E.; ELMARSSON, B. Moisture guide book, *Fukt handbok.* In Swedish. AB Svensk Byggtjänst 1994. Elanders Svenskt Tryck AB, Stockholm 2001.

[9] SMHI, Swedish meteorological and hydrological institute, *Climat data. Klimatdata.* http://www.smhi.se/klimatdata.

[10] WADSÖ, L. *Air movement in brick wall facades. Luftrörelser i skalmursspalter,* In Swedish. Department of Building Materials, Lund University, Report TBBM-5009, 1996.

[11] WUFI 4.2. http://www.hoki.ibp.fhg.de/wufi/wufi_frame_e.html. 2009.

Thermal and hygric properties of autoclaved aerated concrete

Miloš Jerman, Václav Kočí, Jaroslav Výborný, Robert Černý

Czech Technical University in Prague, Faculty of Civil Engineering

***Abstract**: Thermal and hygric transport and storage properties of two different autoclaved aerated concretes (AAC) are studied and compared with the data published by the particular producers. Apparent moisture diffusivity is determined using the results of water sorptivity measurements, water vapor diffusion permeability is measured by the cup method. Sorption isotherms are determined by the desiccator method in the range of relative humidity of 11% – 96%. Thermal conductivity and specific heat capacity are measured by impulse technique. The obtained data will serve as input parameters for service life prediction models of AAC-based structures. Using this kind of precise data already in the design process can help in reduction of failures of AAC building envelopes.*

***Keywords**: Aerated autoclaved concrete, thermal properties, hygric properties*

1. Introduction

The design of building structures based on autoclaved aerated concrete (AAC) has mostly been done by empirical rules for construction until now. As a result, approaches to design have differed case by case and failures appeared as a result of incorrect specifications and errors in construction. Typical failure examples are cracking of both external and internal finishes, detachment of renders from the AAC blocks, sometimes with the AAC itself, cracks around windows or doors, frost failure of external render.

The current standards cannot help to the designers in preventing failure. Moisture analysis in both Czech and European codes is restricted to water vapor transport in steady-state conditions. This presents a risk for a designer as for instance liquid water transport and the cross effects between heat and moisture transport are not considered. As a consequence, the amount of liquid water in the envelope can be underestimated or the condensation zone can appear in another place than predicted by the standard calculation. Hygric and thermal movements are also not considered in standards and the designer is not required to evaluate the thermo- and hygro-mechanical response of the envelope.

2. Studied Materials

Both studied materials were delivered by Xella. The first studied AAC was low-density material P 1.8 – 300, and second one was AAC P 4 – 500. Tab. 1 summarizes the material properties, which are published by the producer in his technical data sheets [1]. Water vapor diffusion resistance factor is shown for both states, wet and dry, according to Czech and European standards. Thermal conductivity and specific heat capacity are measured only in dry state.

Table 1: Parameters of AAC according to the producer's data sheet

Material	Thermal conductivity [W $m^{-1}K^{-1}$]	Specific heat capacity [kJ kg^{-1} K^{-1}]	Water vapor diffusion resistance factor [-]
P1.8 300	0.08 (dry state)	1	5/10
P4 500	0.12 (dry state)	1	5/10

3. Experimental Methods

3.1. Basic material characteristics

As basic physical material characteristics, bulk density [kg m^{-3}], open porosity [Vol.-%] and matrix density [kg m^{-3}] were determined. The matrix density ρ was measured by helium pycnometry, bulk density ρ_b by measuring the mass and dimensions of specimens. The total porosity P was calculated as:

$$P = 1 - \frac{\rho_b}{\rho} \tag{1}$$

3.2. Thermal properties

The thermal conductivity and specific heat capacity were measured in dependence on moisture content and temperature. For measuring the commercial device ISOMET 2104 (Applied Precision, Ltd.) was used. ISOMET 2104 is a multifunctional instrument for measuring thermal conductivity, thermal diffusivity, and volumetric heat capacity. It is equipped with various types of optional probes, needle probes are for porous, fibrous or soft materials, and surface probes are suitable for hard materials. The measurement is based on the analysis of the temperature response of the analyzed material to heat flow impulses. The heat flow is induced by electrical heating using a resistor heater having a direct thermal contact with the surface of the sample. The measurements in this paper were done using the surface probe. Thermal properties in dependence on moisture content were measured in laboratory conditions at the average temperature of 25°C. The measurement of thermal conductivity in dependence on temperature was done in a thermal box on dried samples. The lowest temperature was 2 °C, the highest 40 °C.

3.3. Water vapour transport properties

The wet cup method and dry cup method were employed in the measurements of the water vapour diffusion parameters [2]. The specimens were water and vapour proof insulated by epoxy resin on all lateral sides, put into the cup and sealed by technical plasticine. In the wet cup method the sealed cup containing water (the equilibrium relative humidity above the solution was 97.8%) was placed into an air-conditioned box with 50% relative humidity and weighed periodically. The measurements were done at 25°C in a period of two weeks. The steady state values of mass loss determined by linear regression for the last five readings were used for the determination of water vapour diffusion coefficient. In the dry cup method the sealed cup containing dried $CaCl_2$ (the equilibrium relative humidity above the desiccant was 5%) was placed in an air-conditioned box with 50% relative humidity. Otherwise the measurement was done in the same way as in the wet cup method.

The water vapour diffusion coefficient D was calculated from the measured data according to the equation:

$$D = \frac{\Delta m \cdot d \cdot R \cdot T}{S \cdot \tau \cdot M \cdot \Delta p_p} \tag{2}$$

where Δm [kg] is the amount of water vapour diffused through the sample, d [m] the sample thickness, S [m2] the specimen surface, τ [s] the period of time corresponding to the transport of mass of water vapour Δm, pressure in the air under and above specific specimen surface, R the universal gas constant, M the molar mass of water, T [K] the absolute temperature.

On the basis of the diffusion coefficient D, the water vapour diffusion resistance factor μ was determined:

$$\mu = \frac{D_a}{D} \tag{3}$$

where D_a is the diffusion coefficient of water vapor in the air [$m^2\ s^{-1}$].

The samples for determination of water vapor transport properties had a shape of cylinder with diameter of 100 mm and height of 20 mm.

3.4. Water transport properties

The water sorptivity was measured using a standard experimental setup [3]. The specimen was water and vapor-proof insulated on four lateral sides and the face side was immersed 1-2 mm in the water. The automatic balance allowed recording the increase of mass. The water absorption coefficient A [$kgm^{-2}s^{-1/2}$] was then calculated using the formula:

$$i = A \cdot \sqrt{t} \tag{4}$$

where i is the cumulative water absorption [kgm^{-2}], t is the time from the beginning of the suction experiment. The water absorption coefficient was then employed for the calculation of the apparent moisture diffusivity in the form:

$$\kappa_{app} \approx \left(\frac{A}{w_c - w_0} \right)^2 \tag{5}$$

where w_c is the saturated moisture content [kgm^{-3}] and w_0 the initial moisture content [kgm^{-3}] [2]. The samples for determination of water transport properties had a size of 50 x 50 x 20 mm.

3.5. Sorption isotherms

The water vapor sorption isotherms were measured using the desiccator method in the desorption phase [2]. The samples had a size of 40 x 40 x 10 mm. In the first step, the samples were put into a desiccator with K_2SO_4, which represent 97% relative humidity, and left here until steady state value of mass was achieved. Then they were placed into the desiccators with different salt solutions to simulate different values of relative humidity. The mass of samples was measured in specified periods of time until steady state value of mass was achieved. Then, the moisture content by mass was calculated according to the equation:

$$u = \frac{m_w - m_0}{m_0} \tag{6}$$

where m_w is the mass of wet sample and m_0 is the mass of dry sample [kg].

4. Experimental results

4.1. Basic material characteristics

The results of basic properties measurement are shown in Table 2. The bulk density of P1.8-300 was slightly higher than the data declared by the producers. The open porosity of P1.8-300 was almost 10% higher as compared with P4-500 as a consequence of its lower bulk density.

Table 2: Basic physical parameters of AAC

Material	Matrix density [kgm^{-3}]	Total open porosity [Vol.-%]	Bulk density [kgm^{-3}]
P 1.8-300	2451	87.4	304
P 4-500	2527	80.2	500

4.2. Thermal properties

Table 3 shows that the thermal conductivity of both AAC increased with increasing temperature in a very significant way. The about 50% difference between the values measured at 2 °C and 40 °C is very substantial for thermal calculations in the practice. On the other hand, the agreement of the data measured at 25 °C with the producer's data sheets was excellent.

Table 3: Thermal conductivity of AAC in dependence on temperature

Material/temperature	2 °C	10 °C	15 °C	25 °C	30 °C	40 °C
P 1.8-300	0.0625	0.0700	0.0737	0.0802	0.0815	0.0938
P 4-500	0.0941	0.1060	0.1088	0.1218	0.1288	0.1438

The dependence of the thermal properties of the studied AAC on moisture content is shown in Figs. 1, 2. AAC P 1.8-300 exhibited significantly lower thermal conductivity than P 4-500 over the whole moisture range but for both materials the increase of thermal conductivity with increasing moisture content was enormous. In the water saturated state, the thermal conductivity was about eight times higher than in the dry state. This underlines the importance of using the thermal conductivity as a function of moisture content in all hygrothermal calculations involving AAC. On the other hand, the results of specific heat capacity measurements were very similar.

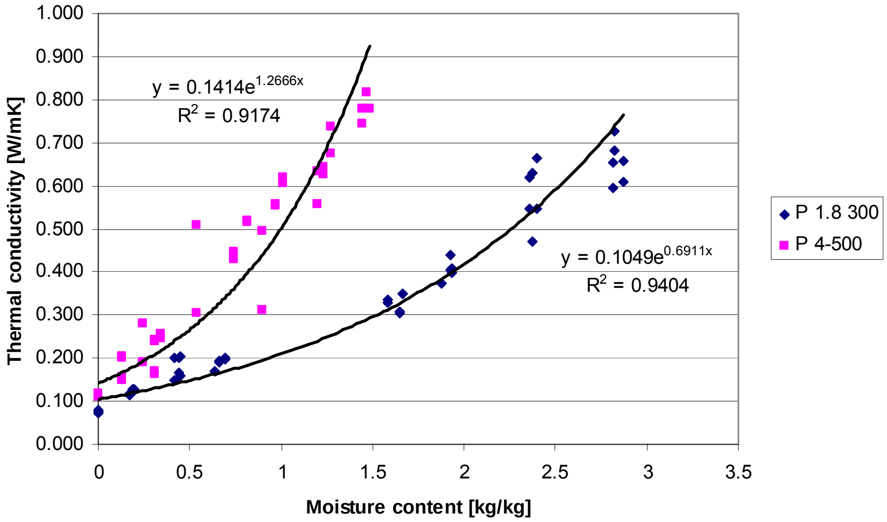

Figure 1: Dependence of moisture content on thermal conductivity of AAC

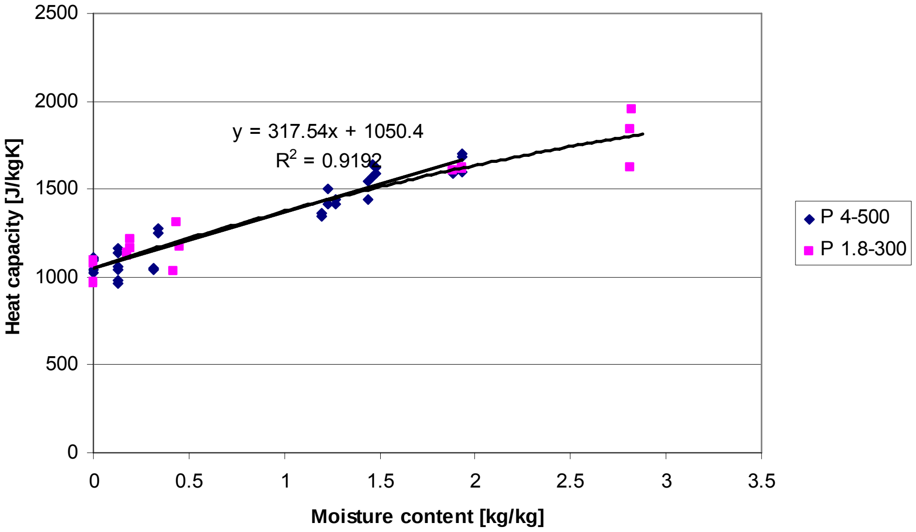

Figure 2: Dependence of moisture content on specific heat capacity of AAC

4.3. Water vapour transport properties

Water vapour transport properties are shown in Table 4. AAC P 1.8 – 300 exhibited slightly lower water vapour diffusion resistance factor than AAC P 4 500, which is in accordance with its lower bulk density. However, the μ values were up to 50% lower than the data given in the producer's data sheets (except for the P 4-500 dry-cup measurement). So, the producer's declaration on the same water vapor diffusion parameters of both materials was not confirmed.

Table 4. Water vapor transport properties

Material	D [10^{-6} m^2s^{-1}]		μ [-]	
	5/50 RH %	97/50 RH %	5/50 RH%	97/50 RH%
P 1.8 300	3.4	10.5	7.1	2.2
P 4-500	2.6	7.5	9.7	3.0

4.4. Water transport properties

Water transport properties are shown in Table 5. P 4-500 achieved about 50% higher water absorption coefficient than P 1.8 – 300 which reflected its higher bulk density.

Table 5. Water transport properties

	A [kg m^{-2} s$^{-1/2}$]	κ[m^2 s^{-1}]
P1.8 - 300	0.028	1.0*10-9
P4 - 500	0.044	7.6*10^{-9}

4.5. Sorption isotherms

Figure 3 shows the measured desorption isotherms of tested materials. The material P1.8 - 300 exhibited systematically higher values of adsorbed moisture than P 4 - 500 in the whole range of relative humidity. This might be due to its finer pore structure.

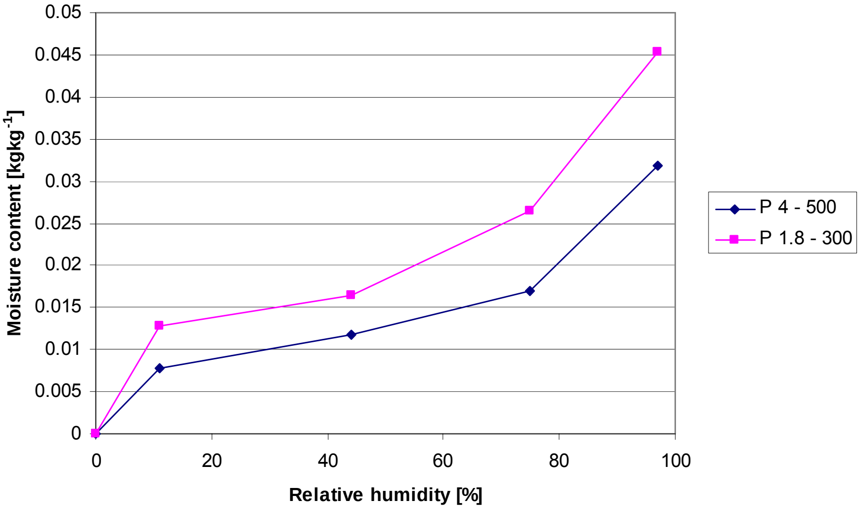

Figure 3: Desorption isotherms

5. Conclusions

Experimental results presented in this paper showed that the thermal conductivity values of both studied AAC in dry state declared by the producer were in an excellent agreement with the measurements done by the impulse technique at 25 °C. However, thermal conductivity was found to depend on both temperature and moisture content in a very significant way. Therefore, using just the values of thermal conductivity in dry state in hygrothermal calculations may lead to departure from the physical reality. The values of water vapor diffusion resistance factor measured in this paper were systematically lower than the data declared in producer’s data sheets. However, this does not seem to be a substantial problem in hygrothermal analyses as the μ factors were very low in both cases.

The water transport parameters and desorption isotherms could not be compared with the producer’s data as they were not included there. This might present a serious deficiency for hygrothermal calculations if they were performed with the data from producer’s data sheets only. Liquid water transport parameters and water storage parameters are very important for any sound assessment of the hygrothermal performance of building envelopes as it has been shown in many previous experimental and computational analyses of various multi-layered material systems [4]-[8].

Acknowledgement

This research has been supported by the Czech Science Foundation, under grant No 103/09/0016.

References

[1] Xella – technical parameters of products. URL: < http://www.xella.cz/downloads/czk/product/ytong-lambda.pdf> [cit. 2010-01-26]

[2] Roels, S., Carmeliet, J., Hens, H., Adan, O., Brocken, H., Černý, R., Pavlík, Z., Hall, C., Kumaran, K., Pel, L. & Plagge, R. 2004. Interlaboratory Comparison of Hygric Properties of Porous Building Materials. Journal of Ther-mal Envelope and Building Science 27, 307-325. ISSN 1097-1963

[3] Vejmelková, E., Pavlíková, M., Jerman, M. & Černý, R. 2009. Free Water Intake as Means of Material Characterization. Journal of Building Physics 33, 29-44. ISSN 1744-2591

[4] Z. Pavlík, R. Černý, Experimental Assessment of Hygrothermal Performance of an Interior Thermal Insulation System Using a Laboratory Technique Simulating On-Site Conditions. Energy and Buildings 40(2008), 673-678. ISSN 0378-7788

[5] Z. Pavlík, R. Černý, Hygrothermal Performance Study of an Innovative Interior Thermal Insulation System. Applied Thermal Engineering 29(2009), 1941-1946. ISSN 1359-4311

[6] J. Toman, A. Vimmrová, R. Černý, Long-Term On-Site Assessment of Hygrothermal Performance of Interior Thermal Insulation System without Water Vapour Barier. Energy and Buildings 41(2009), 51-55. ISSN 0378-7788

[7] V. Kočí, J. Maděra, R. Černý, P. Rovnaníková, Application of a combined computational-experimental approach for service life estimate of exterior plasters of historical buildings. Structural Studies, Repairs and Maintenance of Heritage Architecture XI, C. Brebbia, (ed.), WIT Press, Southampton, 2009, 303-314. ISBN 84564-196-2

[8] J. Maděra, J. Kočí, E. Vejmelková, R. Černý, P. Rovnaníková, M. Ondráček, M. Sedlmajer, Influence of material characteristics of concrete and thermal insulation on the service life of exterior renders. Computational Methods and Experimental Measurements XIV, C. Brebbia, G. M. Carlomagno (eds.), WIT Press, Southampton, 2009, 13-23. ISBN 978-1-84564-187-0

How good is the insulation quality of IR reflective insulation products?

Matthias Kersken[1], Almuth Schade[2]

[1]Fraunhofer-Institut für Bauphysik, Institutsteil Holzkirchen, Valley, Germany

[2]Fraunhofer-Institut für Bauphysik, Institutsteil Holzkirchen, Valley, Germany

Abstract: *Some manufacturers of IR reflective insulation products claim, that their products feature a high insulation quality that can not be described by traditional methods of building physics. Field experiences indicate a different behaviour. How good are IR reflective insulations really?*

On the outdoor testing facilities of the Fraunhofer Institute for Building Physics in Holzkirchen near Munich are two identical buildings in family house size. In one attic a mineral wool roof system is installed, in the other an IR reflective insulation roof system. Both houses possess extensive measurement equipment in the attics for monitoring all important temperatures and heat flows. The comparative measurements of the attics are done parallel during several winter and summer measurement periods. Traditional laboratory measurements are done in the Fraunhofer Institute for building physics at Stuttgart. The results of the in-Situ and the laboratory measurement are compared. Further the examinations are completed by dynamic calculations. Therefore the simulation model is validated by the measurement data itself.

In all measurements and simulations the examined roof system with IR reflective insulation shows typical characteristics of insulations with lower thermal resistance. The values of the traditional measurements match with the results of the in situ measurements.

Conclusion of the measurements and simulations carried out are that the IR reflective products can be described by the means of the traditional building physics.

1. Introduction

For the thermal insulation of pitched roofs infrared reflecting insulation materials (RI) (Figure 1) are offered in France in particular, but recently also in Germany. The thermal insulation effect of these systems primarily results from the infrared reflecting surfaces. Some manufacturers suggest that these relatively thin products achieve almost equivalent thermal insulation properties compared to highly insulated roof constructions. To verify this and to compare the thermal insulation quality of these insulation systems with conventional products, e.g. mineral wool, experiments are carried out and analyzed at the roof constructions of two identical houses.

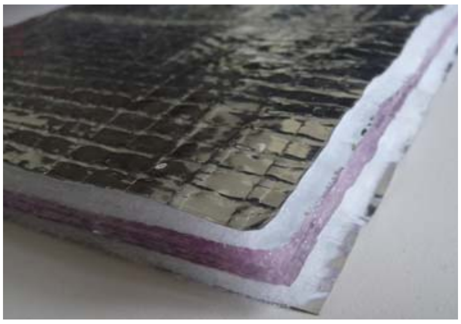

Figure 1: Infrared reflective insulation (RI)

2. Experimental Concept

On the Holzkirchen (Germany) outdoor testing facility run by the Fraunhofer Institute for Building Physics (IBP), two single family houses of identical construction and equal orientation are raised (Figure 2). These houses allow comparative measurements of two different thermal insulation systems under identical boundary conditions. The pitched roof of one house is equipped with a conventional thermal insulation system of mineral wool, the roof of the other house with infrared reflecting thermal insulation. For this investigation only the attics are examined. To eliminate or minimize other influences but the roof systems under examination, heat losses through all envelopes besides the roof are kept as low as possible: no windows, attic walls and ground floor are highly insulated. The attics are not ventilated during the investigations. The same air tightness of both attics yield to the same infiltration losses for both attics. The roof systems are installed according the instructions of the manufacturer considering the national standards. Evaluation of the roof systems is done by comparing the energy consumption of both attics, in winter periods to maintain a constant temperature of 21 °C, in summer to cool the attics.

Figure 2: Experimental buildings, view from south west

3. Measurement Set-up

Identical measuring systems are installed in the two houses. For precise analysis of the thermal behaviour of the two insulation systems 6 measurement axes (Figure 3) are set up for each roof construction: 3 on the southern side and 3 on the northern side of the roof, respectively. Temperature sensors are installed in each layer of the roof systems and additional heat flow sensors on the plasterboard cover each measurement axis. To collect all heat losses the heat flows and surface temperatures of all envelope areas are measured. Moreover, air temperatures as well as heating and cooling output are measured. Meteorological boundary conditions are recorded by the Institute´s weather station. Air tightness in both attics is checked by blower door tests before starting the measurement to secure equal air tightness. Infiltration losses are checked by tracer gas measurement at regular intervals during the investigations. Infrared thermography is used to verify that there are no significant thermal weak spots in the envelope.

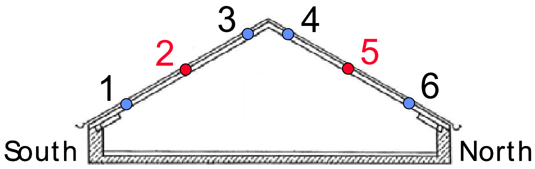

Figure 3: Measurement axes

4. Investigated Roof Systems

During two winter seasons and one summer season different roof systems are investigated (Table 1): two RI systems (insulation installed on the inside and on the outside of the rafters), three different mineral wool roof systems with insulation thicknesses of 180 mm to 200 mm. Furthermore different rates of air tightness are investigated: very airtight ($n_{50} < 1/h$), EnEV [1] design limit for natural ventilated buildings ($n_{50} \simeq 3/h$), not airtight ($n_{50} \simeq 10/h$).

Table 1: Investigated roof systems

Roof system	**Insulation thickness**	**Position**
Infrared reflecting insulation RI 1	-	inside rafters
Infrared reflecting insulation RI 2	-	outside rafters
Mineral wool MW 1	200 mm	between rafters
Mineral wool MW 2	200 mm	inside rafters
Mineral wool MW 3	180 mm	between rafters

5. Heating energy consumption: different roof systems

During Winter 2007/2008 three measurement periods are carried out comparing a RI material on the inside of the rafters (RI 1) with all 3 mineral wool systems (MW 1, MW 2, MW 3). In every period the energy consumption to maintain an air temperature of 21 °C is supplied by electric convector heaters. In Table 2 the energy balances of for both attics are compared for all three measurement periods: transmission heat flows for all envelope areas besides the roof, heat losses due to infiltration and heating energy. The transmission heat losses through the roof areas result from the compilation of the energy balance. Table 2 shows that the attic with the RI roof system has an energy consumption about twice as much as the attic with the MW roof system. Regarding only the transmission heat losses through the roof areas calculated by the energy balance, the RI roof system loses 2 to 2.5 times more heat than the MW roof system.

Table 2: Energy balance winter 2007/2008

Winter 2007/2008 **Energy balance of the 3 measurement periods**	**11.12.2007–21.1.2008** **(41 days – 984 h)**		**19.2.2008–6.3.2008** **(17 days – 408 h)**		**22.3.2008–30.4.2008** **(17 days – 408 h)**	
Climatic boundary conditions (mean values): External temperature Global radiation Wind speed	-2.0 °C 46 W/m² 2.1 m/s		-4.9 °C 108 W/m² 3.9 m/s		-5.4 °C 162 W/m² 3.0 m/s	
	MW 1	**RI 1**	**MW 2**	**RI 1**	**MW 3**	**RI 1**
Heat losses envelope areas besides the roof (calculated by measured heat flows)	172 kWh	184 kWh	47 kWh	57 kWh	108 kWh	121 kWh
Infiltration heat losses (acc. EN 832 [2] determined by tracer gas measurement)	33 kWh	45 kWh	33 kWh	17 kWh	50 kWh	23 kWh
Energy consumption (measured)	617 kWh **100 %**	1264 kWh **205 %**	195 kWh **100 %**	369 kWh **189 %**	439 kWh **100 %**	806 kWh **184 %**
Heat losses through the roof (determined by energy balance)	412 kWh	1035 kWh	115 kWh	295 kWh	281 kWh	662 kWh
	100 %	**251 %**	**100 %**	**257 %**	**100 %**	**236 %**

The analysis of days with extreme weather conditions (low and high radiation, low and high wind) shows variations of the ratio between the energy consumption of both attics. Wind impact in the mineral wool reduces its thermal resistance. Therefore on days with high wind impact the ratio of the energy consumption between the RI attic and the MW attic is less than the mean value shown in Table 2. The influence of high radiation is shown on an exemplary day (8 January 2008). In Figure 4 the prevailing weather conditions of 8 January 2008 and the heat losses of the south and north side of the roofs (mean values of the 3 measurement axes) are shown. At night in both attics the heat losses of the south and the north side of the roof are almost the same. The reduction of the heat losses due to radiation during the day is higher at the RI roof than at the MW roof due to the lower thermal resistance of the RI roof.

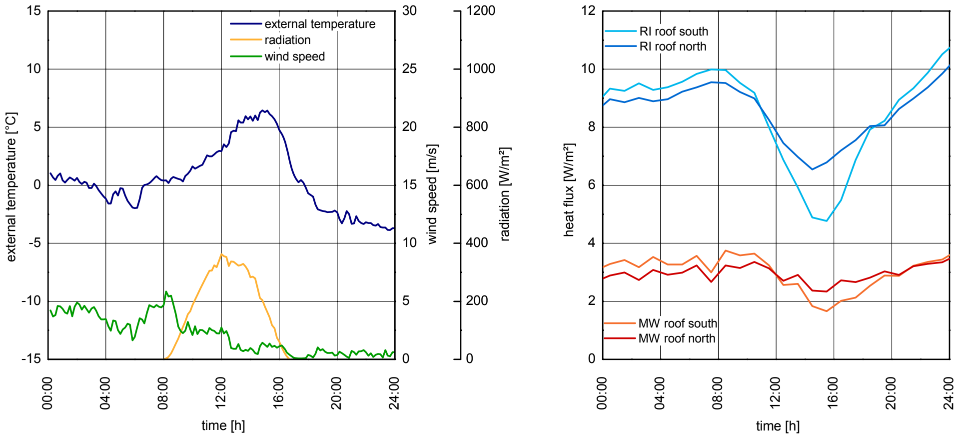

Figure 4: Weather conditions and heat flows on a day with high solar radiation (8 January 2008)

6. Heating energy consumption: different air tightness

During Winter 2008/2009 three measurement periods are carried out to work out the influence of the air tightness. Roof system RI 2 and roof system MW 3 are compared during 3 measurement periods:

1. very airtight ($n_{50} < 1/h$)
2. EnEV [1] design limit for natural ventilated buildings ($n_{50} \simeq 3/h$)
3. not airtight ($n_{50} \simeq 10/h$)

Like before the energy consumption to maintain 21 °C is determined. The energy balance of all 3 measurement periods is shown in Table 3. The ratio between the energy consumption of the attic with the RI roof and the attic with the MW roof is around two for all three measurement periods. Considering the heat losses through the roof areas the ratio increases to more than three. The investigations show, that the air tightness does not have an essential influence on the ratio between the energy consumption of both attics.

Table 3: Energy balance of all 3 measurement periods

Winter 2008/2009 **Energy balance of the 3 measurement periods**		**n_{50} 0.7 h^{-1}** 48 days – 1152 h		**n_{50} 3 h^{-1}** 36 days – 864 h		**n_{50} 10 h^{-1}** 44 days – 1056 h	
Climatic boundary conditions (mean values)	External temperature Global radiation Wind speed	-2.2 °C 44 W/m² 2.1 m/s		-1.0 °C 84 W/m² 3.6 m/s		-8.6 °C 199 W/m² 2.8 m/s	
		MW 3	**RI 2**	**MW 3**	**RI 2**	**MW 3**	**RI 2**
Heat losses envelope areas besides the roof (calculated by measured heat flows)		200 kWh	205 kWh	160 kWh	138 kWh	82 kWh	70 kWh
Infiltration heat losses (acc. EN 832 [2] determined by tracer gas measurement)		116 kWh	128 kWh	174 kWh	146 kWh	large fluctuations due to very low air tightness	
Energy consumption (measured)		790 kWh **100 %**	1787 kWh **226 %**	642 kWh **100 %**	1336 kWh **208 %**	426 kWh **100 %**	852 kWh **200 %**
Heat losses through the roof (determined by energy balance respectively for n_{50} □ 10 h^{-1} determined by measured heat flow)		474 kWh **100 %**	1454 kWh **307 %**	308 kWh **100 %**	1052 kWh **342 %**	205 kWh **100 %**	687 kWh **335 %**

7. Thermal Resistance (R-Values): laboratory – in-situ

For the first measurement period in Winter 2007/2008 (roof systems: MW 1 and RI 1) the accredited laboratory of the Fraunhofer Institute for Building Physics in Stuttgart determined the thermal resistance with an established method. These values are shown in Table 4. For the RI material two values are determined by two different methods. According the installation of the insulation the value of the hot plate method with a squeezed horizontal installation may be used for the rafter areas, where the insulation is squeezed due to mounting. The value of the hot box method with a vertical installation should be used for the area between the rafters, where the insulation is not squeezed. In such way the R-values are used for the simulation.

The thermal resistance for the roof systems (Table 5) consists of the thermal resistance of all layers from plasterboard to under tile liner. Thereby the R-values of the air gaps are determined to 0.16 m²K/W for adjacent surfaces with high emissivity and to 0.51 m²K/W for adjacent surfaces with low emissivity according to DIN EN ISO 6946 [3]. The resulting thermal resistance for both roof systems is shown in Table 5 . It shows that the R-value of the RI roof system consists around 50 % of the adjacent air gaps. The reason for less thermal resistance of the second RI roof system (RI 2) is the missing second air gap.

Constant climatic boundary conditions allow to determine the thermal resistance of building components during in-situ tests. The international standard ISO 9869 “Thermal insulation – building elements – in-situ measurement of thermal resistance and thermal transmittance” [4] describes the heat flow meter method for the measurement of the thermal transmission properties of plane building components This standard is not intended as a high precision method replacing laboratory instruments, but it allows a prediction under real boundary conditions. In accordance with this international standard, investigations of the in-situ R-values are performed at both attics. A 2-day period from 11 December 2007 to 12 December 2007 was characterized by an almost constant temperature, low radiation and low wind. Hence it is suited for determining the in-situ R-value. The mean R-value of all measurement axes, shown in Table 5, is determined according ISO 9869 [4].

Table 4: measured values of the insulation materials

Material	Mineral Wool MW	Infrared Reflecting Insulation RI	
Thermal Resistance R [m²K/W]	5.69	1.00	0.5
Method	Hot plate method according DIN EN 12 667 (2001) installation: horizontal	Hotbox according DIN 52 611 – 1 installation: vertical	Hot plate method according DIN EN 12 667 (2001) installation: horizontal
Emissivity [-]	not determined	0.05	

Table 5: determined R-values

	Mineral Wool MW	Infrared Reflecting Insulation RI
Roof system	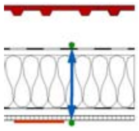	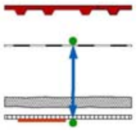
Thermal resistance (incl. laboratory measurement values) R [m²K/W]	6,0	2,1
In-situ thermal resistance Rinsitu [m²K/W] (mean values of all 6 measurement axes)	6,4	2,0

8. Summer results

Also in summer 2008 the attics are under investigation. Unfortunately many different, partial contrary effects occur. Higher day time temperatures interact with faster cooling-down at night, different wind velocities and directions interfere with the effects of the different roof systems. That makes it hard to extract reliable results on the differences between the two roof systems. To get results on the summer behaviour dynamic building simulation is used. On the one hand an accurate numerical model allows the evaluation of the behaviour over one complete year, so the occurring differences are more significant, on the other hand it is possible to check which boundary conditions have an influence on the observed behaviour of the insulation systems. To ensure that the numerical models of the two roof systems are accurate, the models are validated against the temperatures measured in the summer periods. As Figure 5 shows exemplary the calculated room temperatures are always within the ranges of the air temperatures measured at all five sensor positions in the attics. This good compliance of the measured and the calculated values shows that it is possible to model infrared reflective insulations by the means of traditional building physics. The only difficulty is to select the appropriate value for the specific part of the construction. In a compressed situation, like at rafters, the values from the hot plate test have to be used. When hanging free, like in compartment areas, the results of the hot box method have to be used and have to be elevated by the influence of the infrared reflective properties on the thermal resistance on the adjacent air layers.

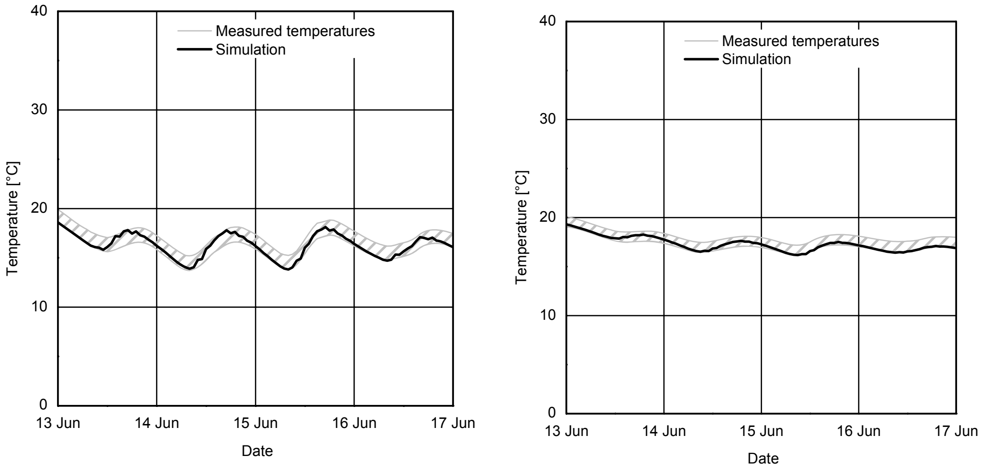

Figure 5: Calculated and measured air temperatures in the RI attic (left) and the mineral wool attic (right) 13.6.2008 – 17.6.2008

In this numerical investigation the net cooling demand for attic temperatures below 26 °C is used as indicator for the summer behaviour. The cooling demand is chosen because the use of temperatures for evaluation would require additional assumptions such as comfort models. Five different locations have been investigated to ensure the behaviour does not depend on the climatic region. In every region the net cooling demand of the RI attic is higher than the demand of the MW attic as Table 6 shows.

Table 6: Difference of the net cooling demand of the RI-roof referring to the mineral wool roof

Madrid (ES)	**Carpentras (F)**	**Porto (P)**	**Mannheim (D) (hot)**	**Essen (D) (average)**
+ 14.4 %	+ 11.8 %	+ 8.2 %	+ 14.2 %	+ 29.1 %

To evaluate the influence of the infiltration the basis infiltration of 0,3 h^{-1} is varied between 0 and 1,0 h^{-1}. Here the net cooling demand of the RI attic is 14.3 - 14.7 kWh/m²a and of the reference attic it is 11.5 - 13.5 kWh/m²a; so the demand of the RI attic is always higher.

To ensure the energetic behaviour is the same also with different maxiumum temperatures, the allowed maximum of 26 °C is varied between 20 and 28 °C. Here the net cooling demand of the RI-attic is 33.6 – 9.9 kWh/m²a and of the reference attic it is 27.7 – 8.5 kWh/m²a. Also here the energy demand of the classic mineral wool attic is always lower.

In the numerical models as in the field test there are no windows in the attics. To proof that the influence of windows will not reverse the observed behaviour, two skylights of 1 m² each are inserted in the two roofages. Also the building and its windows are turned by 90 °. Again the net cooling demand of IR-attic is higher than the reference. In the basic case the difference is 14.4 % (Table 6), with windows this difference is reduced to 7.8 % and if the building is turned additionaly, the difference is 13.1 %.

In the basic case the internal heat sources are constant at 5 W/m² over 24 h (120 Wh/m²d). To observe the influence of a daily profile, a profile maintaining the 120 Wh/m²d is developed and investigated with different boundary conditions. The changes in the net cooling demand stay lower than 5 %. If the rate of the internal heat sources is elevated starting at 0 W/m², at first the net cooling demand of the reference roof is lower. That changes at a level of the internal heat gains of 10.1 W/m². Using internal heat sources higher than 10.1 W/m² the demand of the RI attic is lower. When the two skylights are inserted these intersection point is at 8.6 W/m². It should be mentioned that usual internal heat sources in residential buildungs are 2.1 – 5 W/m² [5; 6], so the intersection is at a level of the heat sources that is not to be expected in real buildings. Offices building could reach such levels of internal heat sources but the numerical model used for this investigation is not fit for transfering on the results on non-residential buildings!

9. Conclusion

In extensive investigations different RI roof systems are compared with different mineral wool roof systems. The results of the field tests show that infrared reflective insulation systems may be described by building physic standards. The in-situ thermal resistances confirm the resistances determined by traditional laboratory methods. Simulation and related model-validations confirm this conclusion. The heating energy consumption of the RI attic is always more than twice as high as the consumption of the MW attic. That means the RI roof system has a thermal resistance which is less than half of every investigated mineral wool roof system.

Reducing the air tightness of both attics to the same, lower level does not change this ratio considerably; so there is no advantage for the RI roof system due to less air tightness. Days with high wind velocities show, that airflow through the insulation may reduce the thermal resistance of mineral wool. Therefore on days with strong wind the ratio of the energy consumption between the two attics is lower than the mean ratio in favour of the RI attic.

High solar radiation reduces the heat consumption of the RI attic more than at the MW attic because of higher heat gains through the roof, which is typical for roof systems with lower thermal resistances. In case of extreme high internal heat sources there is not need for a high thermal resistance of the envelope, so the lower thermal resistance of the RI roof may be an advantage due to higher night-cool-down in summer. Such high internal heat sources are not to be expected in residential buildings.

References

[1] Energieeinsparverordnung EnEV 2007

[2] EN 832, 2000-02-25 Thermal performance of buildings - calculation of energy use for heating - residential buildings

[3] DIN EN ISO 6946, 2008-04, Building components and building elements - Thermal resistance and thermal transmittance - Calculation method (ISO 6946: 2007)

[4] ISO 9869, 1994-08, Thermal insulation – building elements – in-situ measurement of thermal resistance and thermal transmittance

[5] DIN V 18599-10, 2007-02, Energy efficiency of buildings – Calculation of net, final and primary energy demand for heating, cooling, ventilation, domestic hot water and lightning. Part 10: Boundary conditions of use, climatic data

[6] DIN 4108-2, 2003-07, Wärmeschutz und Energie-Einsparung in Gebäuden. Teil 2: Mindestanforderungen an den Wärmeschutz

Physical and mathematical models of coupled heat and moisture transport: A comparative analysis

Jan Kočí, Václav Kočí, Jiří Maděra, Robert Černý

Department of Materials Engineering and Chemistry, Faculty of Civil Engineering, Czech Technical University in Prague, Thákurova 7, 166 29 Prague 6, Czech Republic

***Abstract**: Several physical and mathematical models of coupled heat and moisture transport in porous building materials are analyzed from the points of view of physical exactness and availability of input parameters. Among them, Künzel's and Grunewald's models are chosen as representatives of diffusion models, convective models are represented by Milly's model. A typical example of computational simulation of temperature and moisture fields using the mentioned models is performed for a chosen multi-layered building envelope, and the strong and weak points of the applied models are assessed. Both the theoretical issues and results of practical application are discussed.*

***Keywords**: mathematical models, comparative analysis, Milly, Künzel, Grunwald*

1. Introduction

Mathematical models of coupled heat and moisture transport in porous building materials are very often formulated by people solving moisture transport at first. According to moisture transport the models are then categorized into diffusion, convective and hybrid models. Basic diffusion theory of moisture transport in porous materials is based on assumption that moisture in gaseous or liquid phase is transported in porous system by mechanism similar to transport of two gases. Convective theory of moisture transport in porous environment is based on assumption, that water contained in porous systems flows through particular channels like in pipes.

Basic diffusion theory of moisture transport was solved independently by Krischer (1942) [1] and Lykov (1954) [2]. These theories were developed in time into other diffusion models (e.g. Kiessl). Nowadays the Künzel's model [3] formulated in 1995 is most frequently used.

Convective theory of moisture transport in porous environment is based on assumption, that water contained in porous systems flows through particular channels like in pipes. The convective models are most frequently applied for water flux in soils. The first empirical equation was formulated by Darcy, which investigated water flux in vertically oriented column of sand (see e.g. [7]). The most representative from convective models of coupled heat and moisture transport is model of Philip and de Vries (1957) [4] and its later modification in de Vries (1987) [5]. The model of Philip and de Vries was later developed into Milly's model [6], which can be assumed as purely convective model.

2. Mathematical models

Künzel's model

Künzel continued in Kiessl's idea of definition of moisture potential, but the difference was that for description of coupled water and water vapor transport in overhygroscopic and capillary water range the relative humidity of air φ was chosen. Thanks to that, description of moisture transport in multi-layered constructions guaranteed a continuous quantity on material interface. Final balance equations were formulated as

$$\frac{d\rho_v}{d\varphi}\frac{\partial\varphi}{\partial t} = div\left[D_\varphi grad\varphi + \delta_p grad(\varphi p_s)\right] \tag{1}$$

$$\frac{dH}{dT}\frac{\partial T}{\partial t} = div(\lambda gradT) + L_v div\left[\delta_p grad(\varphi p_s)\right], \tag{2}$$

where ρ_v is the partial moisture density, φ the relative humidity, δ_p the water vapor permeability, p_s the partial pressure of saturated water vapor in the air, H the enthalpy density, L_v the latent heat of evaporation of water, λ the thermal conductivity and T is the temperature. The liquid water transport coefficient is defined as

$$D_\varphi = D_w \frac{d\rho_v}{d\varphi} \tag{3}$$

where D_w is the moisture diffusivity.

Grunewald's model

Grunewald's model includes in its general form heat, moisture, air and salt transport. In this paper we use its simplified version where heat and moisture transport are taken into account only. The moisture and heat balance equations are formulated as

$$\begin{aligned}&\left[\rho_w - \rho_v + \frac{a}{R_v T} p_{vs} \frac{d\varphi}{dw}\right]\frac{\partial w}{\partial t} + \left[w\frac{d\rho_v}{dT} + \frac{a}{R_v T}\left(p_{vs}\frac{d\varphi}{dT} + \varphi\frac{dp_{vs}}{dT} - \frac{p_v}{T}\right)\right]\frac{\partial T}{\partial t} = \\ &= div\left[\left(\rho_w D_w + p_s \delta_p \frac{d\varphi}{dw}\right) gradw\right] + div\left[\left(\delta_p \frac{dp_s}{dT}\varphi + p_{vs}\delta_p\frac{d\varphi}{dT}\right) gradT\right]\end{aligned} \tag{4}$$

$$\begin{aligned}&\left[\rho_w u_w + u_v\left(\frac{a}{R_v T} p_{vs}\frac{d\varphi}{dw} - \rho_v\right)\right]\frac{\partial w}{\partial t} + \left[\begin{matrix}\rho_m \frac{du_m}{dT} + \rho_w w \frac{du_w}{dT} + \rho_v \frac{du_v}{dT} a + u_w w \frac{d\rho_w}{dT} + \\ + u_v \frac{a}{R_v T}\left(p_{vs}\frac{d\varphi}{dT} + \varphi\frac{dp_{vs}}{dT} - \frac{p_v}{T}\right)\end{matrix}\right]\frac{\partial T}{\partial t} = \\ &= div\left[\left(\rho_w D_w u_w + h_v p_{vs}\delta_p \frac{d\varphi}{dw}\right) gradw\right] + div\left[\left(\lambda + \delta_p \varphi h_v \frac{dp_{vs}}{dT} + \delta_p p_{vs} h_v \frac{d\varphi}{dT}\right) gradT\right]\end{aligned} \tag{5}$$

where ρ_v is the partial moisture density, ρ_w the water density, ρ_m the material density, φ the relative humidity, δ_p the water vapor permeability, p_{vs} the partial pressure of saturated water vapor in the air, p_v the partial pressure of water vapor in the air, R_v the gas constant of water vapor, u_m the specific internal energy of the solid material, u_w the specific internal energy of the liquid water, u_v the specific internal energy of water vapor, λ the thermal conductivity, T the temperature and a the relative volume ratio of the air in partially saturated material.

This model does not use relative humidity but moisture content as primary variable which is not continuous across the material interfaces. That means it is necessary during the calculations to solve the discontinuities on material interfaces [8].

Milly's model

Milly's model is based on the original Philip and de Vries (1957) model. While previous two models are classified as diffusion models, Milly's model can be accepted as convective one. The final balance equations used in calculations are

$$\begin{aligned}
&\left\{\left(1-\frac{1}{\rho_l}\varphi p_{vs}\frac{M}{RT}\right)\frac{\partial u_l}{\partial \psi}+\frac{a}{\rho_s}\varphi p_{vs} g\left(\frac{M}{RT}\right)^2\right\}\frac{\partial \psi}{\partial t}+ \\
&+\left\{\left(1-\frac{1}{\rho_l}\varphi p_{vs}\frac{M}{RT}\right)\frac{\partial u_l}{\partial T}+\frac{a}{\rho_s}\varphi p_{vs}\frac{M}{RT}\left(-\frac{\psi g M}{RT^2}+\frac{1}{p_{vs}}\frac{dp_{vs}}{dT}-\frac{1}{T}\right)\right\}\frac{\partial T}{\partial t}= \\
&=\frac{\rho_l}{\rho_s}\left\{div\left[\left(k_l+k_v\right)grad\,\psi+D_{Tv}\,gradT\right]\right\}
\end{aligned} \tag{6}$$

$$\begin{aligned}
&\left\{\begin{bmatrix}\left(h_l-\dfrac{1}{\rho_l}\varphi p_{vs}\dfrac{M}{RT}h_v\right)\dfrac{\partial u_l}{\partial \psi}+ \\ \dfrac{a}{\rho_s}\varphi p_{vs} g\left(\dfrac{M}{RT}\right)^2 h_v\end{bmatrix}\right\}\frac{\partial \psi}{\partial t}+\left\{\begin{bmatrix}\left(h_l-\dfrac{1}{\rho_l}\varphi p_{vs}\dfrac{M}{RT}h_v\right)\dfrac{\partial u_l}{\partial T}+ \\ \begin{bmatrix} c_s+c_l u_l+c_v u_v+ \\ h_v\dfrac{a}{\rho_s}\varphi p_{vs}\dfrac{M}{RT}\begin{pmatrix}-\dfrac{\psi g M}{RT^2}+ \\ \dfrac{1}{p_{vs}}\dfrac{dp_{vs}}{dT}-\dfrac{1}{T}\end{pmatrix}\end{bmatrix}\end{bmatrix}\right\}\frac{\partial T}{\partial t}= \\
&=\frac{1}{\rho_s}\left\{div\begin{bmatrix}\left(h_l\rho_l k_l+h_v\rho_l k_v\right)grad\,\psi+ \\ \left(\lambda+h_v\rho_l D_{Tv}\right)gradT\end{bmatrix}\right\}
\end{aligned} \tag{7}$$

u_l is the liquid moisture content, u_v the gaseous moisture content, ρ_l the density of water, ρ_v the partial density of water vapor in the porous body, ρ_s the partial density of the porous matrix, k_l the hydraulic conductivity, ψ the pressure head, α the tortuosity ($\alpha \ll 1$), a geometrical factor which expresses the extension of the path length of a molecule in the system of curved pores in a comparison to its path in the air, a the relative volume ratio of the air in partially saturated material, D the diffusion coefficient of water vapor in the air, p the total pressure, p_v the partial pressure of water vapor in the air, c_l, c_v the specific heat capacities of the liquid and gaseous phases of water, respectively, h_s the specific enthalpy of the porous matrix, h_l the specific enthalpy of the liquid phase of water, h_v the specific enthalpy of the gaseous phase of water.

3. Computational simulation

All computations presented in this paper were performed by HEMOT computational code, developed at the Department of Materials Engineering and Chemistry, Faculty of Civil Engineering, Czech Technical University in Prague on the basis of the general finite element method package SIFEL [9].

There is a simple reason why HEMOT and SIFEL were chosen as a simulation tool for comparing different mathematical model. Because HEMOT and SIFEL are property of Department of Materials Engineering and Chemistry and Department of Mechanics, we have direct access to its source codes. Therefore contrary to Delphin [10] or WUFI [11] software, the source code of HEMOT could be modified and new mathematical models could be easily implemented.

Scheme of analyzed construction

In order to analyze all above mentioned mathematical models a building envelope with load bearing structure made of AAC provided with external thermal insulation made of mineral wool. The thickness of AAC was 300 mm, thickness of mineral wool was 100 mm. The envelope is plastered both on exterior and interior side.

Load bearing material was assumed as autoclaved aerated concrete P2-400 produced by H+H Czech Republic, Ltd. Thermal insulation was assumed as hydrophobic mineral wool produced by Rockwool. As external and internal finish Baumit MVR Uni plaster was used, which is plaster developed for AAC building envelopes especially. Figure 1 shows the scheme of analyzed building envelope.

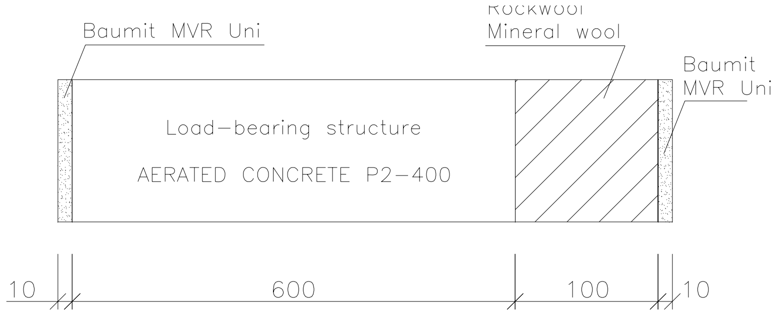

Figure 1: Scheme of analyzed building envelope

Material characteristics

The material parameters of all involved materials were obtained in laboratories of Department of Materials Engineering and Chemistry (see [12], [13] and [14]). These parameters were used in calculation with diffusion model types. The overview of material parameters is given in Table 1. The following symbols are used: ρ - bulk density, p - porosity, c – specific heat capacity, μ - water vapor diffusion resistance factor, λ_{dry} – thermal conductivity in dry state, λ_{sat} thermal conductivity in water saturated state, κ_{av} - average value of moisture diffusivity, w_{hyg} - hygroscopic moisture content.

Table 1. Material characteristics of used materials

	AAC H+H P2-400	Rockwool hydrophobic mineral wool	Baumit MVR Uni plaster
ρ [kg m^{-3}]	412	270	1402
p ◎[%]	80.3	88.0	44.4
c [J kg^{-1} K^{-1}]	1250 – 1385	630	1020 – 1780
μ [-]	3.7 – 14.4	2.1 – 3.7	4.5 – 12.4
λ_{dry} [W m^{-1} K^{-1}]	0.094	0.045	0.443
λ_{sat} [W m^{-1} K^{-1}]	0.434	0.246	1.380
κ_{av} [m^2 s^{-1}]	1.12e-9	2.51e-10	1.59e-9
w_{hyg} [m^3 m^{-3}]	0.019	0.007	0.042

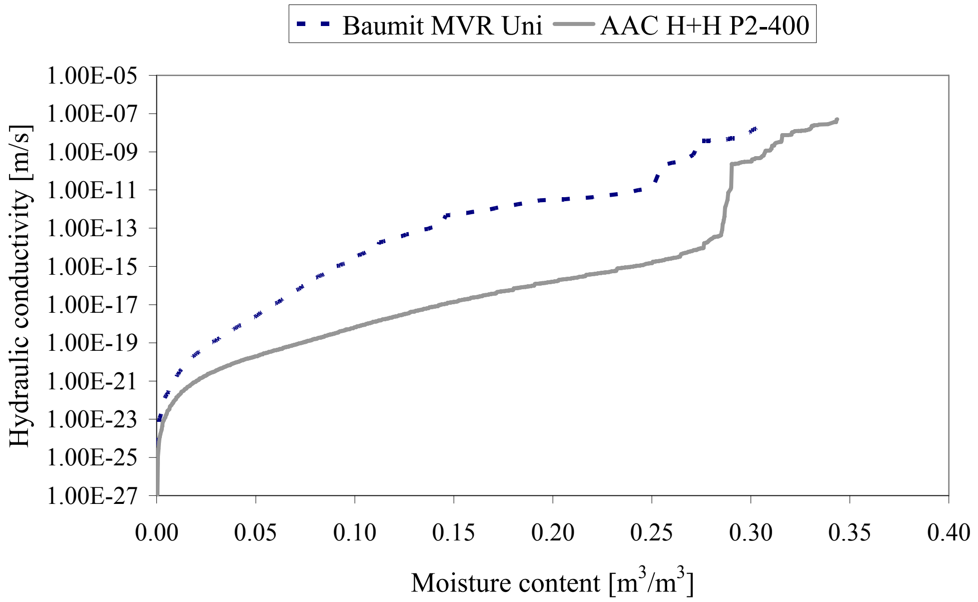

Figure 2: Hydraulic conductivity of AAC and plaster

Hydraulic conductivity (see Fig. 2) was determined in an analogous way according to (8) and (9)

$$k_r(w) = \left(\frac{w}{w_{sat}}\right)^n \frac{\int_{R_{\min}}^{R} r^2 f(r) dr}{\int_{R_{\min}}^{R_{\max}} r^2 f(r) dr} \tag{8}$$

$$k_r = \frac{k}{k_{sat}} \tag{9}$$

where k_{sat} is the saturated value of hydraulic conductivity.

The hydraulic conductivity was measured by high pressure permeameter PR-101A made by company CNE (Cyprus). The experiment is based on Darcy's law [16]. Hydraulic conductivity was then calculated according to formula

$$k_{sat} = \frac{Q}{\Delta p} \frac{4\rho g l}{\pi d^2} \tag{10}$$

where ρ is the density of water, g the gravity acceleration, l the length of the sample, d its diameter, Q volumetric flow rate and Δp pressure gradient over the sample.

Simulation results

The temperature comparison shown in Figure 3 doesn't reveal any differences, whereas the relative humidity outputs of each mathematical model differed more substantial way (see Figure 4) Especially the Milly's model as representative of convective models shows the biggest differences in computational results.

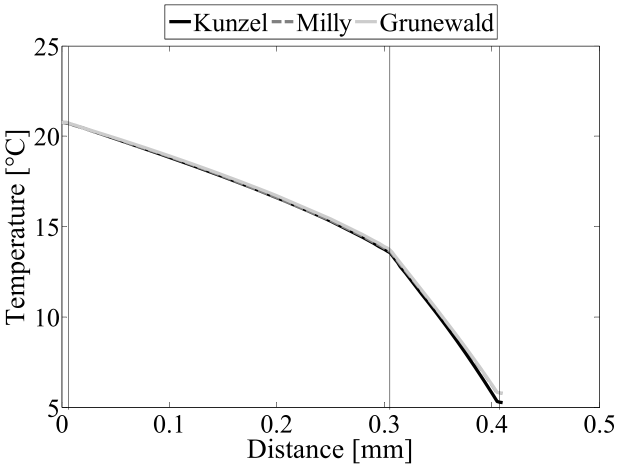

Figure 3: Distribution of temperature across the building envelope

The apparent reason was that Milly's model calculated the liquid moisture transport in a more accurate way than both diffusion models. However, having the large uncertainty in liquid moisture transport parameter of diffusion models in mind, the differences in calculated relative humidity were relatively low, within the range of 3-5%. Also, it can be anticipated that if the moisture diffusivity was determined as a function of moisture content using an inverse analysis of moisture profiles (these data were not available for the studied materials) which is the most often used method [15], the accuracy of the data obtained by diffusion models would increase. Therefore, definite conclusions on the suitability of the different models for simulation of moisture and temperature fields are difficult to draw

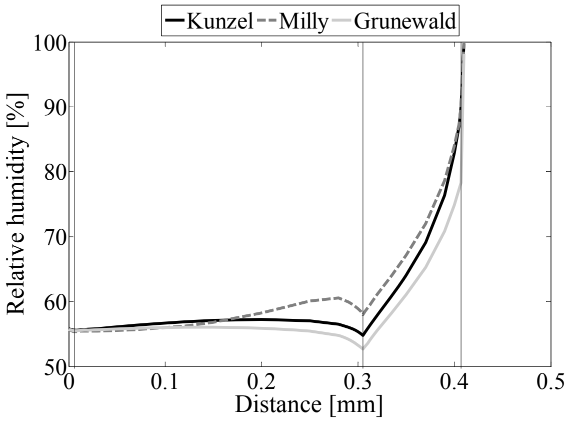

Figure 4: Distribution of relative humidity across the building envelope

4. Conclusion

Based on analysis of models of coupled heat and moisture transport in porous building materials it can be concluded that in the current state of knowledge the most advantageous are diffusion models of moisture transport. The main argument is the relatively simple way of acquiring the parameters of liquid water transport. Based on simplicity and number of input parameters, Künzel's model can be evaluated as the most convenient among the diffusion models. In addition, this model includes a suitable solution of moisture transport over material interfaces. However, from the long-term point of view the convective models should not be completely disregarded. As it follows from the analysis of measurement methods of water transport, there are some perspective ways how the input parameters of convective models could be acquired for compact building materials. Therefore, the complex system of methods should include both types of models and Künzel's diffusion model and Milly's convective model are recommended for inclusion into the complex system of methods.

Acknowledgement

This research has been supported by Czech Ministry of Education, Youth and Sports, under project No ME10112 and SGS10/128/OHK1/2T/11.

References

[1] KRISCHER, O. Der Wärme- und Stoffaustausch im Trocknungsgut. VDI - Forschungsheft, 415, 1942, p. 1-22.

[2] LYKOV, A. V. Javlenija perenosa v kapilljarnoporistych telach. Gosenergoizdat, Moskva (in Russian), 1954.

[3] KÜNZEL, H. M. Simultaneous Heat and Moisture Transport in Building Components, Ph.D. Thesis, IRB Verlag: Stuttgart, 1995, p. 1–135.

[4] PHILIP, J. R.; De Vries, D. A. Moisture movement in porous materials under temperature gradients. Transactions of the American Geophysical Union, 38, 1957, p. 222 – 232.

[5] DE VRIES, D.A. The theory of heat and moisture transfer in porous media revisited. International Journal of Heat and Mass Transfer, 30, 1987, p. 1343 – 1350.

[6] MILLY, P. C. D. Moisture and heat transport in hysteretic, inhomogeneous porous media: a matrix head-based formulation and a numerical model. Water Resources Research, 18, 1982, p. 489-498.

[7] ČERNÝ, R.; ROVNANÍKOVÁ P., Transport Processes in Concrete. Spon Press, London, 2002.

[8] KRUIS, J.; MADĚRA, J. Numerical Analysis of Coupled Heat and Moisture Transfer with Discontinuities on Material Interfaces *In: Computational Methods for Coupled Problems in Science and Engineering III [CD-ROM].* Barcelona: International Center for Numerical Methods in Engineering (CIMNE), 2009.

[9] KRUIS, J.; KOUDELKA, T.; KREJČÍ, T. Efficient computer implementation of coupled hydro-thermo-mechanical analysis. *Mathematics and Computers in Simulation*, doi:10.1016/j.matcom.2008.11.010

[10] GRUNEWALD, J. DELPHIN 4.1 - Documentation, Theoretical Fundamentals. TU Dresden, Dresden, 2000.

[11] HOLM, A.; WORCH, A. Einsatzmöglichkeiten des Computersimulationsprogramms WUFI bei Putzen. FAS-Schriftenreihe, Heft 9, Putzinstandsetzung: Vorträge anläßlich der 9. Hanseatischen Sanierungstage im November 1998. Ostseebad Kühlungsborn, 1998.

[12] VÝBORNÝ, J. Stanovení tepelných parametrů a smrštění při vysychání vybraných pórobetonových tvárnic firmy H+H Česká republika s.r.o. a Xella CZ. *In: Proceedings of the International Conference 15th Construmat 2009*. Praha: České vysoké učení technické v Praze, 2009, p. 449-461.

[13] JIŘIČKOVÁ, M.; ČERNÝ, R. Effect of Hydrophilic Admixtures on Moisture and Heat Transport and Storage Parameters of Mineral Wool. *Construction and Building Materials* 20, 2006, p. 425-434.

[14] FUČÍKOVÁ, L. Moisture Properties of AAC Blocks in dependence on the Environment Focused on Problems with Durability. Diploma thesis. Praha: Czech Technical University in Prague, 2009.

[15] ČERNÝ, R.; ROVNANÍKOVÁ, P. Transport Processes in Concrete, 1. ed. London: Spon Press, 2002, p. 26 – 29.

[16] KEPPERT, M.; VYTLAČILOVÁ, V.; REITERMAN, P.; DVORSKÝ, T.; ČERNÝ, R. Vodotěsnost a permeabilita vysokohodnotného betonu. *Stavební obzor*, Vol. 5, 2010, p. 145 - 148 .

Determination of moisture diffusivity of building materials by using genetic algorithm

Jan Kočí, Jiří Maděra, Robert Černý

Faculty of Civil Engineering, Czech Technical University in Prague, Thákurova 7, CZ-166 29
Prague, Czech Republic

Abstract: *Contemporary experimental techniques for assessment of moisture diffusivity of building materials are based on simplified laboratory experiments. Due to this simplification, laboratory experiments are restricted only for setting of adsorption curve which neglects effects of hysteresis. In case we want to involve the hysteretic effects of moisture diffusivity into the computations, it is necessary to find new and more universal method for setting desorption curve of moisture diffusivity. In this article we present genetic algorithms as a possible solution of determining moisture diffusivity of building materials during desorption phase. The genetic algorithm is applied on simple laboratory experiment aimed at sorption phase only in order to verify its functionality. The verification is completed by comparing results obtained by genetic algorithm with results obtained by traditional methods for setting sorption curve of moisture diffusivity.*

Keywords: *inverse analysis, moisture transport, genetic algorithm, moisture diffusivity*

1. Introduction

For proper description of moisture transport within building materials it is necessary to obtain material parameters very precisely. As far as liquid moisture transport is concerned, the biggest part is played by moisture diffusivity. In general, there are two methods of determination of moisture diffusivity under laboratory conditions – stationary and non-stationary method. Stationary methods are unsuitable for most building materials due to their time consumption as well as impossibility of setting adsorption curve of the material, because moisture balance state is equal to homogenous saturation. On the other hand there are several non-stationary methods of determination of moisture diffusivity that are suitable for building materials. These methods are based on principles of inverse analysis. This means that for determination of moisture diffusivity it is necessary to obtain at least one moisture profile (distribution of moisture across the material).

The moisture diffusivity is markedly dependent on moisture content within the material. It can differ up to few orders of magnitude between dry and wet state of the same material. This fact complicates the solution of inverse problem of moisture transport and from mathematical point of view it is so-called "ill-posed" problem. The particular solution is usually done by simplification of initial and boundary conditions, which guarantees monotonous moisture profiles functioning as input parameters for the solution. Usually this is reached by choosing Dirichlet's boundary condition and constant initial condition. Unfortunately such experimental setup is possible only for setting of adsorption curve of moisture diffusivity, where the front face of the specimen is in direct contact with water (Dirichlet's boundary condtition) and on the beginning of the experiment is the specimen dried out (constant initial condition). The desorption experiment is different. Although the constant initial condition could be achieved by full saturation of the specimen, the effect of Dirichlet's boundary condition is unrealistic because the material is faced to air. This implies the use of Newton's boundary condition instead; the water transfer from solid to gaseous environment is realized in the form of convective transfer of water evaporated from the surface. Therefore, for desorption phase it is impossible to use common methods as for absorption phase. As it was proved in different papers, e.g. [1], moisture diffusivity exhibits considerable effect of hysteresis, which can rise up to about one order of magnitude. Thus, it is very important to find new method for setting desorption curve of moisture diffusivity.

Among all possible solutions, the genetic algorithms have big potential for solving inverse problems of moisture transport, fortunately not only for absorption phase, but for desorption phase either.

2. Contemporary methods for determination of moisture diffusivity

Moisture diffusivity is a material parameter characterizing the transport of liquid moisture in porous matter. One-dimensional diffusion equation describing the transport of liquid moisture can be written as

$$\frac{\partial u}{\partial t} = \frac{\partial}{\partial x}\left(\kappa(u)\frac{\partial u}{\partial x}\right), \tag{1}$$

$$u = \frac{m_w - m_d}{m_d}, \tag{2}$$

where m_w [kg] is the mass of wet sample and m_d [kg] the mass of dry sample.

Moisture diffusivity is determined by solving the inverse problem applied to a simple laboratory experiment. The experiment is usually conducted on elongated prism, where one dimension is markedly bigger than the other dimensions. The front face of the specimen is in direct contact with water, the other face is in contact with air having the same relative humidity as the air in the pore system of the specimen in the beginning of the experiment.

The principle of the experiment consists in obtaining moisture profiles (moisture as a function of time and position) for example by using capacitance method [2]. On such profiles the inverse analysis is applied. At these days there exist few inverse methods that can be used for determination of moisture diffusivity (e.g. Matano's method [3], double integration method [4] etc.). But as it was described above, these methods are restricted to use only for water absorption phase.

3. Genetic algorithm GRADE

Genetic algorithms belong to a group of evolution algorithms, which includes also evolution strategies and genetic programming. At present, genetic algorithms belong to the most modern optimization methods available. They follow an analogy of processes that occur in living nature within the evolution of live organisms during period of many millions of years. The principles of genetic algorithms were first proposed by Holland [5]; the books of Goldberg [6] and Michalewicz [7] are the most popular publications dealing with this topic.

The GRADE algorithm [8], used for optimization of material parameters, was developed at Department of Mechanics, Faculty of Civil Engineering, Czech Technical University in Prague from its previous version called SADE [9]. Comparing to the SADE algorithm, the GRADE operates with a few new features and modifications. These modifications reduce the number of external parameters of the algorithm and thus increase the convergence rate of the algorithm for smooth objective functions with just one optimum. This algorithm uses the simplified differential operator, but contrary to the differential evolution, the GRADE method uses the algorithmic scheme very similar to the standard genetic algorithm:

1) As the first step, the initial population is generated randomly and the objective function value is assigned to all chromosomes in the population. The size of the population is defined as the number of variables of objective function multiplied by parameter *pop_rate*.
2) Several new chromosomes are created using the mutation operator. Total number of mutations depends on the value of parameter called *radioactivity*.
3) Other new chromosomes are created using the simplified differential operator crossing-over. The total amount of chromosomes is now two times higher than in the beginning.
4) Each newly created chromosome is evaluated by objective function.
5) The amount of chromosomes in the population is reduced by operator called selection. Hence, the amount of individuals is decreased to its original value.

Steps 2-5 are repeated until stopping criterion is reached.

Next follows description of introduced operators in more detail. Let $x_i(g)$ be the *i*-th chromosome in a generation *g*,

$$x_i(g) = (x_{i1}(g), x_{i2}(g), \dots, x_{in}(g)), \tag{3}$$

where *n* is a number of variables of objective function. With such definition the genetic algorithms can be described as follows:

mutation - If a certain chromosome $x_i(g)$ was chosen to be muted, a random chromosome x_{RP} is generated and subsequently chromosome $x_k(g+1)$ is computed using relation:

$$x_k(g+1) = (x_i(g) + MR(x_{RP} - x_i(g)), \tag{4}$$

where *MR* is a parameter called *mutation_rate.* Contrary to the SADE, the *MR* parameter in GRADE algorithm is no more constant, but for each new chromosome chosen for mutation is randomly generated from <0, 1>

crossing-over – GRADE algorithm uses a simplified differential operator borrowed from differential evolution. The operator can be written as

$$x_k(g+1) = \max(x_q(g); x_r(g)) + CR(x_q(g) - x_r(g)) \tag{5}$$

Only two chromosomes $x_q(g)$ and $x_r(q)$ are randomly chosen from the current population. Their difference vector is reduced by parameter *CR* and (contrarily to the SADE algorithm) is added to "better one" of the two chromosomes. Geometrical meaning of simplified differential operator in GRADE algorithm is shown on Fig. 1

selection – this method serves as a reducing tool of the amount of chromosomes in the population, which is now twice as high as in the beginning (due to crossing-over). It is similar to play-off method: two randomly chosen chromosomes are compared to each other and the one with lower value of fitness function is eliminated. Thus is the population size decreased by one and therefore is this cycle repeated until the number of chromosomes in the population is reduced to its initial value.

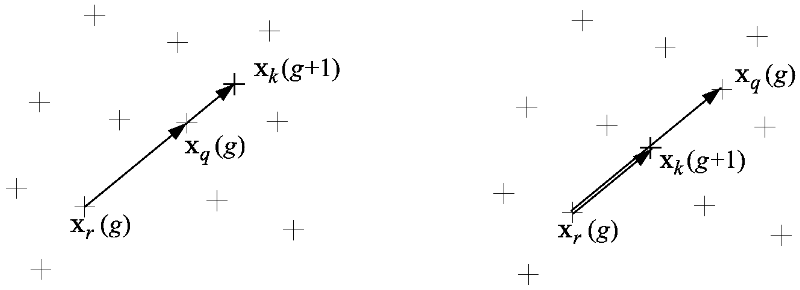

Fig. 1: Geometrical meaning of simplified differential operator in GRADE algorithm

4. Determination of moisture diffusivity using GRADE algorithm

The application of genetic algorithms can be demonstrated on a simple laboratory experiment aimed at determination of moisture diffusivity of autoclaved aerated concrete (AAC). The experiment was conducted on sample having dimensions of 20/40/300 mm, which was insulated on four longitudinal sides in order to prevent the sample from water evaporation. Basic material parameters of AAC were measured within the project HAMSTAD [10] and are shown in Table 1 (ϱ is the bulk density, c the specific heat capacity, μ the water vapour diffusion resistance factor, θ_{sat} the saturation moisture content, θ_{hyg} the maximum hygroscopic moisture content) , measured moisture profiles are shown in Fig. 2.

Tab. 1: Basic material parameters of AAC

ρ [kg/m³]	c [kJ/kgK]	μ [-]	θ_{sat} [m³/m³]	θ_{hyg} [m³/m³]
475	800	9.6	0.78	0.05

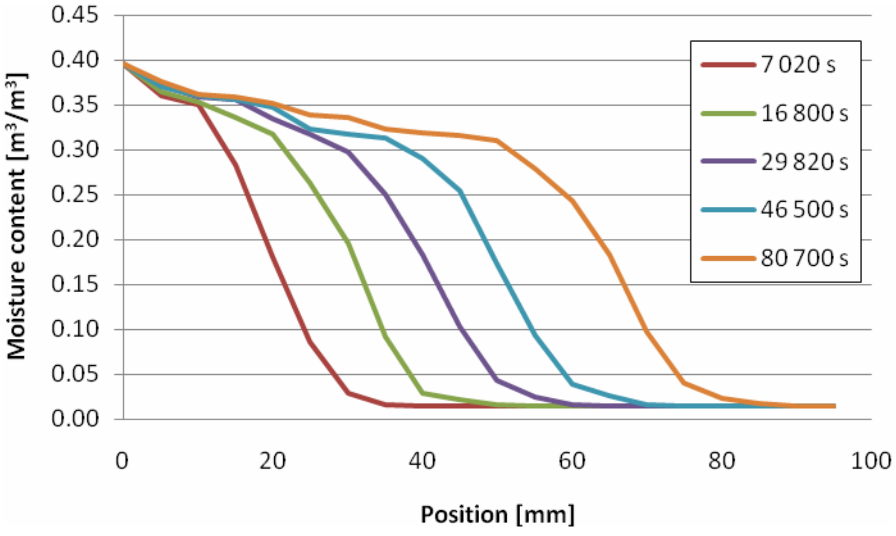

Fig. 2: Measured moisture profiles of AAC

The main aim of application of genetic algorithm was to find moisture diffusivity as a function of moisture content. At first, the moisture diffusivity was approximated by exponential function with two unknown parameters and then, in the second phase, by nine isolated points with predefined x-coordinates (moisture content). It is obvious that the optimization using exponential function is much faster, because the genetic algorithm has to optimize only two parameters, but on the other hand, the accuracy of such found solution is usually not sufficient. The found moisture profiles for optimization with two unknown parameters are shown in Fig. 3. The average time of optimization was about 21 minutes.

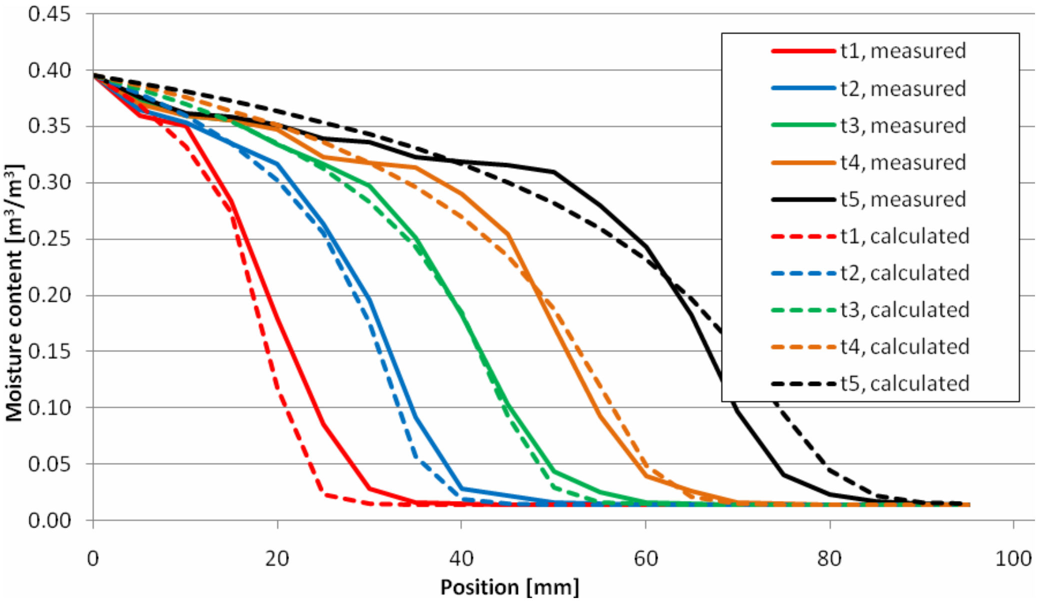

Fig. 3: Comparison of measured and calculated moisture profiles – exponential function

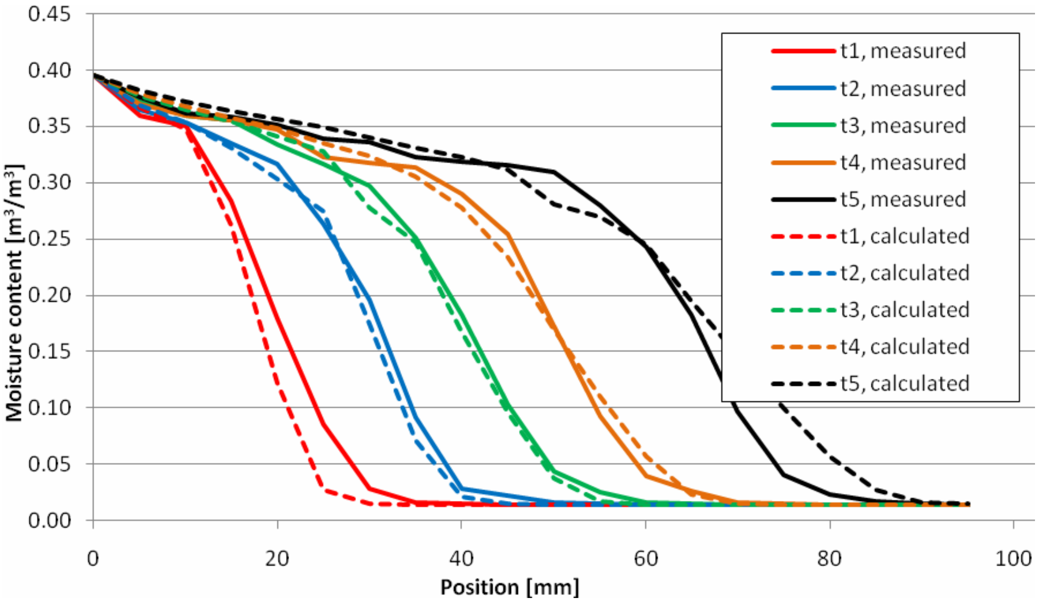

Fig. 4: Comparison of measured and calculated moisture profiles - nine isolated points

The result of the second optimization with nine unknown parameters is shown in Fig. 4. The average time of optimization was about 6 hours.

Moisture diffusivities identified in both simulations are shown in Fig. 5 and compared with moisture diffusivity determined by standard double integration method. It is important to say that the moisture diffusivity defined by 9-point curve is more accurate than the other one from double integration method.

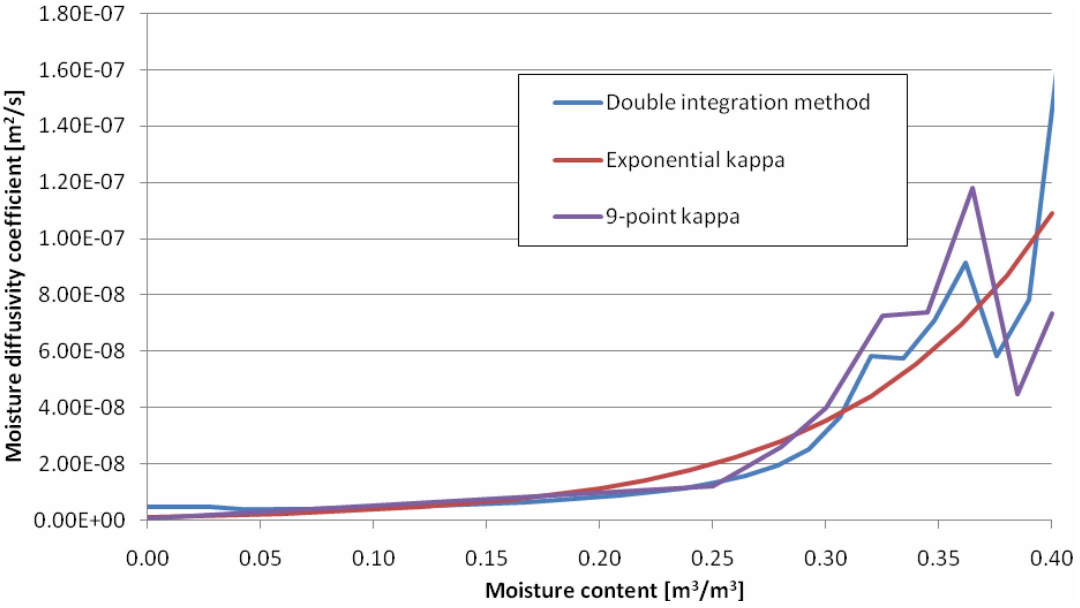

Fig. 5: Comparison of moisture diffusivities determined using different methods

The comparison of calculated results by method of least squares is shown in Table 2. For each optimization it was compared five moisture profiles consisted from twenty isolated points.

Tab. 2: Comparison of the results by method of least squares

	Value of least squares
Exponential kappa	0.02396 $(m^3/m^3)^2$
9-point kappa	0.02063 $(m^3/m^3)^2$
Double integration method	0.04400 $(m^3/m^3)^2$

The method of least squares showed that simulation outputs obtained with moisture diffusivities from GRADE algorithm (exponential curve of moisture diffusivity, 9-point curve of moisture diffusivity) are more accurate than the results with moisture diffusivity measured in laboratory (moisture diffusivity determined using double integration method).

5. Conclusion

In this paper we presented the use of genetic algorithm on a simple water-absorption laboratory experiment for determination of moisture diffusivity as a function of moisture content. The results were compared to results obtained by the common double integration method. The comparison presented in this paper proved that application of genetic algorithms leads to results of sufficient accuracy and so the genetic algorithms are suitable for solving inverse problems of moisture transport. Therefore, the next stage of research should be aimed especially at problems of drying-out of the material, where moisture profiles measured at desorption will be taken into account, so that the desorption curve of moisture diffusivity will be expressed. With the knowledge of absorption and desorption curve of moisture diffusivity, the effect of hysteresis can be studied which may significantly improve the accuracy of mathematical simulations of moisture and heat transport within the building materials.

Acknowledgement

This research has been supported by Czech Ministry of Education, Youth and Sports, under project No SGS10/127/OHK1/2T/11.

References

[1] ČERNÝ, R.; MADĚRA, J.; KOČÍ, J.; VEJMELKOVÁ, E. Heat and moisture transport in porous materials involving cyclic wetting and drying. *Fourteenth International Conference on Computational Methods and Experimental Measurements*, Algarve, Portugal. Southampton: WIT PRESS, 2009. p. 3-12.

[2] SEMERÁK, P.; ČERNÝ, R. *Kapacitní metoda měření vlhkosti stavebních materiálů*. Stavební obzor, roč. 6, č. 4, 1997. p. 102-103.

[3] MATANO, C. *On the Relation between the Diffusion Coefficient and Concentration of Solid Metals*. Jap. J. Phys., Vol. 8, 1933. p. 109-113.

[4] DRCHALOVÁ, J.; ČERNÝ, R. Non-Steady-State Methods for Determining the Moisture Diffusivity of Porous Materials. In *Int. Comm. in Heat and Mass Transfer,* Vol. 25, 1998. p. 109-116.

[5] HOLLAND, J. H. Adaptation in natural and artificial systems. Internal report. Ann Arbor, University of Michigan, 1975.

[6] GOLDBERG, E. D. Genetic algorithms in search, optimization and machine learning. Reading, Addison-Wesley, 1989.

[7] MICHALEWICZ, Z. Genetic algorithms + data structures = evolution programs, 3rd ed. Berlin, Springer, 1996.

[8] KUČEROVÁ, A. Identification of nonlinear mechanical model parameters based on softcomputing methods. PhD thesis, Ecole Normale Supérieure de Cachan, 2007.

[9] HRSTKA,O. (WWW), Homepage of SADE. http://klobouk.fsv.cvut.cz/~ondra/sade/sade.htm

[14] JIŘIČKOVÁ M. Application of TDR Microprobes, Minitensiometry and Minihygrometry to the Determination of Moisture Transport and Moisture Storage Parameters of Building Materials, CTU Reports, No. 2, Vol. 8, 2004.

Computer code HEMOT for hygrothermal assessment of thermal insulation systems

Václav Kočí, Jan Kočí, Jiří Maděra, Robert Černý

Department of Materials Engineering and Chemistry, Faculty of Civil Engineering, Czech Technical University in Prague, Thákurova 7, 166 29 Prague 6, Czech republic

Abstract: *Coupled heat and moisture transport in building materials and their multi-layered systems is modeled using many different models and computer codes. Almost every university active in building-physics related calculations has its own model and computer code. In this paper, we introduce a computer simulation tool HEMOT for modeling coupled heat and moisture transport which was developed at the Faculty of Civil Engineering, Czech Technical University in Prague. The simulation of transport phenomena in constructive building details is possible for 1D and 2D problems. The modeling of transient transport processes leads into a system of non-linear partial differential equations. The basic variables characterizing the hygro-thermal state of building constructions (temperature, moisture content, relative humidity) can be obtained as functions of space and time. A particular advantage of the numerical simulation program is the possibility of investigation of variants concerning different constructions, different materials and different climatic loads. Constructive details of buildings and building materials can be optimized using the numerical simulation, and the reliability of constructions for different given indoor and outdoor climates can be judged. In an example of application of HEMOT computer code, hygrothermal assessment of selected thermal insulation systems is presented.*

Keywords: *hygrothermal performance, computer code, thermal insulation system, computational simulation*

1. Introduction

These days there are lots of numerical simulation tools that are dealing with coupled heat and moisture transport in porous building materials. In addition to these tools, there are also programs dealing with heat and moisture transport separately, but they are not very convenient in civil engineering. For example this group of programs is represented by simple calculation tools served to designers as assessing vehicle according to national standards (AREA [1], TEPLO [2], COND [3] etc.).

Most programs dealing with coupled heat and moisture transport are developed within the research projects or as a part of postgraduate thesis, which means their development has been already finished (UMIDUS [4], MATCH BOX [5], MOIST [6], HAM [7] etc.). As these projects were closed more than 5 years ago, it is necessary to face incompatibility issues with current operation systems. Moreover, the new program mistakes that have occurred cannot be easily fixed. Some of these tools are dealing with one-dimensional transport only (HAM, MOIST, UMIDUS), some of them have never been verified by real experiments (UMIDUS). Other programs have different drawbacks, for example neglecting liquid water transport (HAM) or constant calculation step (MATCH BOX).

Most popular and used programs in this time are DELPHIN [8] and WUFI [9]. They include material databases and meteorological data for different locations and are able to solve one- or two- dimensional problems. On the other hand, DELPHIN is handicapped by its complicated mathematical model that needs plenty of input parameters. Some of these parameters are difficult to obtain and they have strong impact on calculation results. WUFI is easily available and its mathematical model is relatively simple but it is a black box for regular users. In addition, it does not offer any choice between different mathematical models and any changes of the applied model which greatly limits its application for scientific purposes.

Therefore, a new computer simulation tool HEMOT (HEat and MOisture Transport) was devised. One of the main reasons why to use HEMOT is its open structure. That means, computer code can be modified based on any recently developed experimental method. HEMOT is qualitatively equal to both DELPHIN and WUFI and its biggest advantage is free license, which is another reason to use this software.

2. Basic characteristics of computer code HEMOT

The computer code HEMOT has been developed at the Department of Materials Engineering and Chemistry, Faculty of Civil Engineering, Czech Technical University in Prague in order to support coupled heat and water transport in porous building materials. The simulation of transport phenomena in constructive building details is possible for 1D and 2D problems. The modeling of transient transport processes leads into a system of non-linear partial differential equations. The basic variables characterizing the hygro-thermal state of building constructions (temperature, moisture content, relative humidity) can be obtained as functions of space and time. A particular advantage of the numerical simulation program is the possibility of investigation of variants concerning different constructions, different materials and different climatic loads. Constructive details of buildings and building materials can be optimized using the numerical simulation, and the reliability of constructions for different given indoor and outdoor climates can be judged.

HEMOT is using the material database as a data source, which simplifies computations and allows obtaining more complex results. The material database was developed at the Department of Materials Engineering and Chemistry and serves as the data centralization tool. Input data originate from experiments, which are performed at the Faculty of Civil Engineering, Czech Technical University in Prague as well as from other resources.

Modelling of project in computer code HEMOT is split up into several steps (Fig. 1). First of all, the basic parameters of calculation (mathematical model [10], time specification, computational step e.g.) are set. In the next step, the grid of solved construction detail has to be meshed (Fig. 2). After that, it is necessary to assign the materials with their complete material characteristics that mean bulk density, open porosity, water vapor diffusion resistance factor, specific heat capacity, thermal conductivity, moisture diffusivity and sorption isotherm. All these parameters can be taken as constant values or as a function of moisture content.

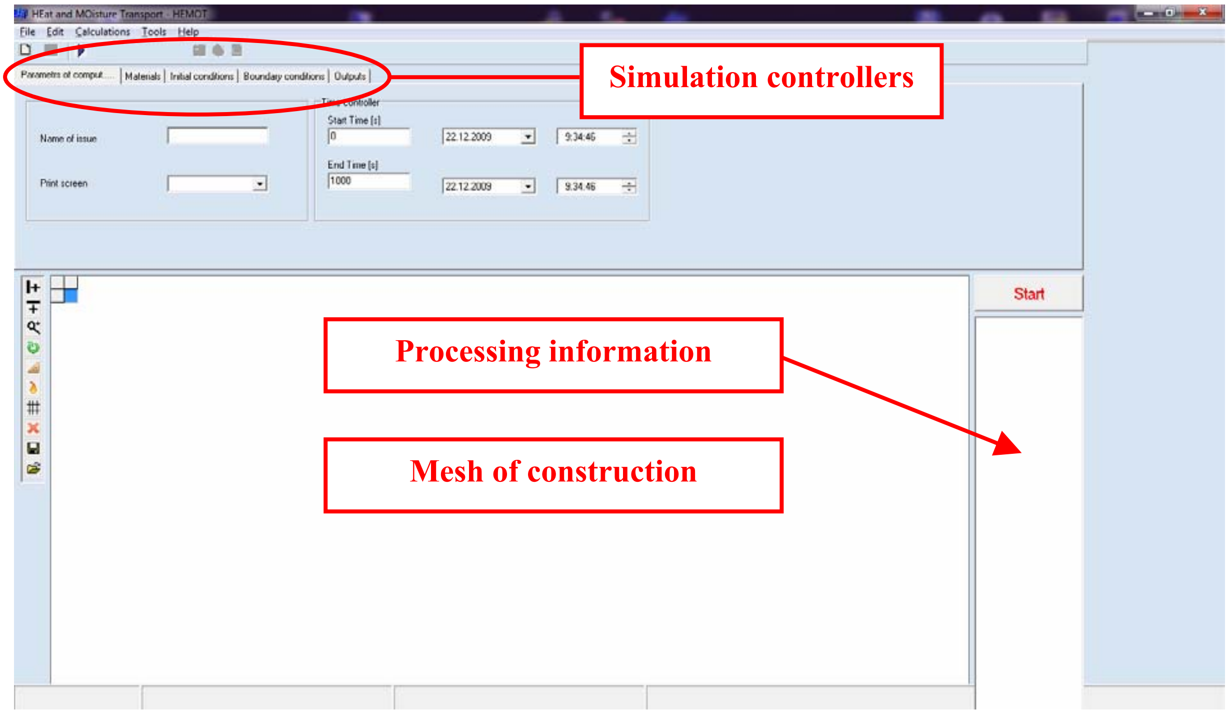

Name of issue
Print screen
Start Time [s] 0 22.12.2009 9:34:46
End Time [s] 1000 22.12.2009 9:34:46

Figure 1: User interface of computer code HEMOT

Another important part of input data are the initial and boundary conditions. The boundary conditions can be set as constant values which are usually used for interior or they can be set as climatic boundary conditions which are usual for exterior (Fig. 3). The climatic data are based on hourly values of long term average of temperature, relative humidity, rainfall, wind velocity and direction and sun radiation.

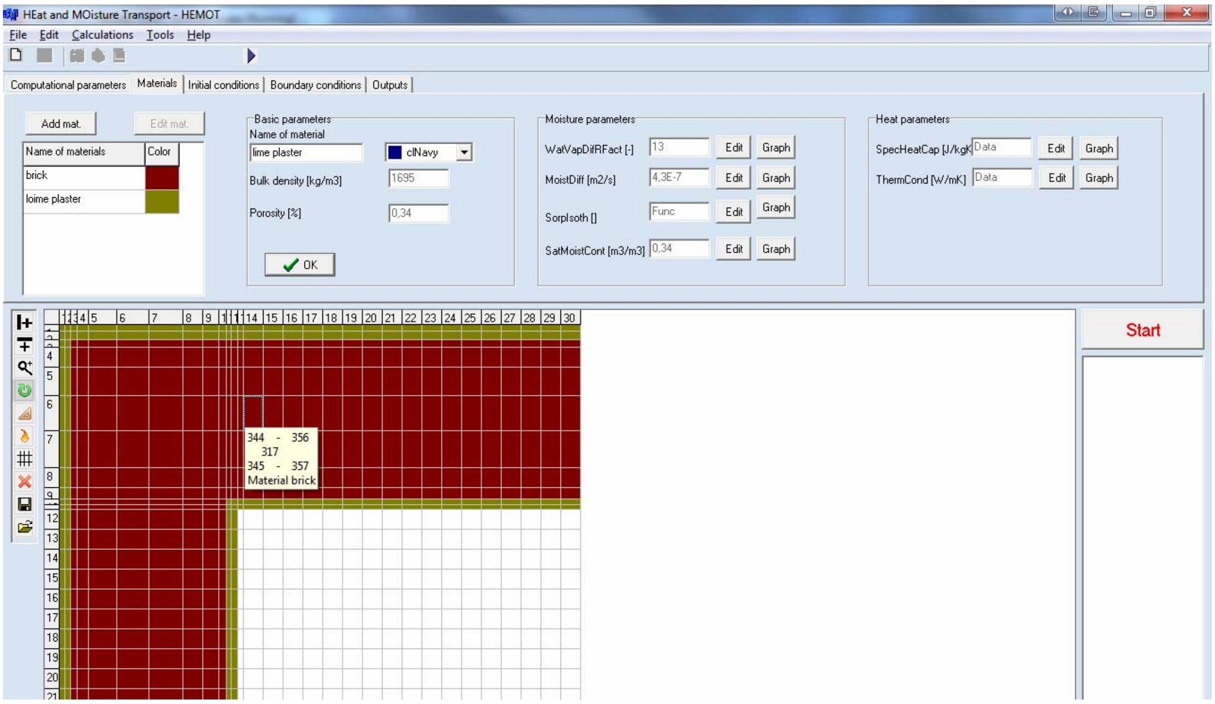

Name of materials	Color
brick	🟥
loime plaster	🟩

Name of material: lime plaster, clNavy
Bulk density [kg/m3] 1695
Porosity [%] 0,34
WatVapDifRFact [-] 13
MoistDiff [m2/s] 4,3E-7
SorpIsoth [] Func
SatMoistCont [m3/m3] 0,34
SpecHeatCap [J/kgK] Data
ThermCond [W/mK] Data

344 - 356
317
345 - 357
Material brick

Figure 2: Modelling of construction grid

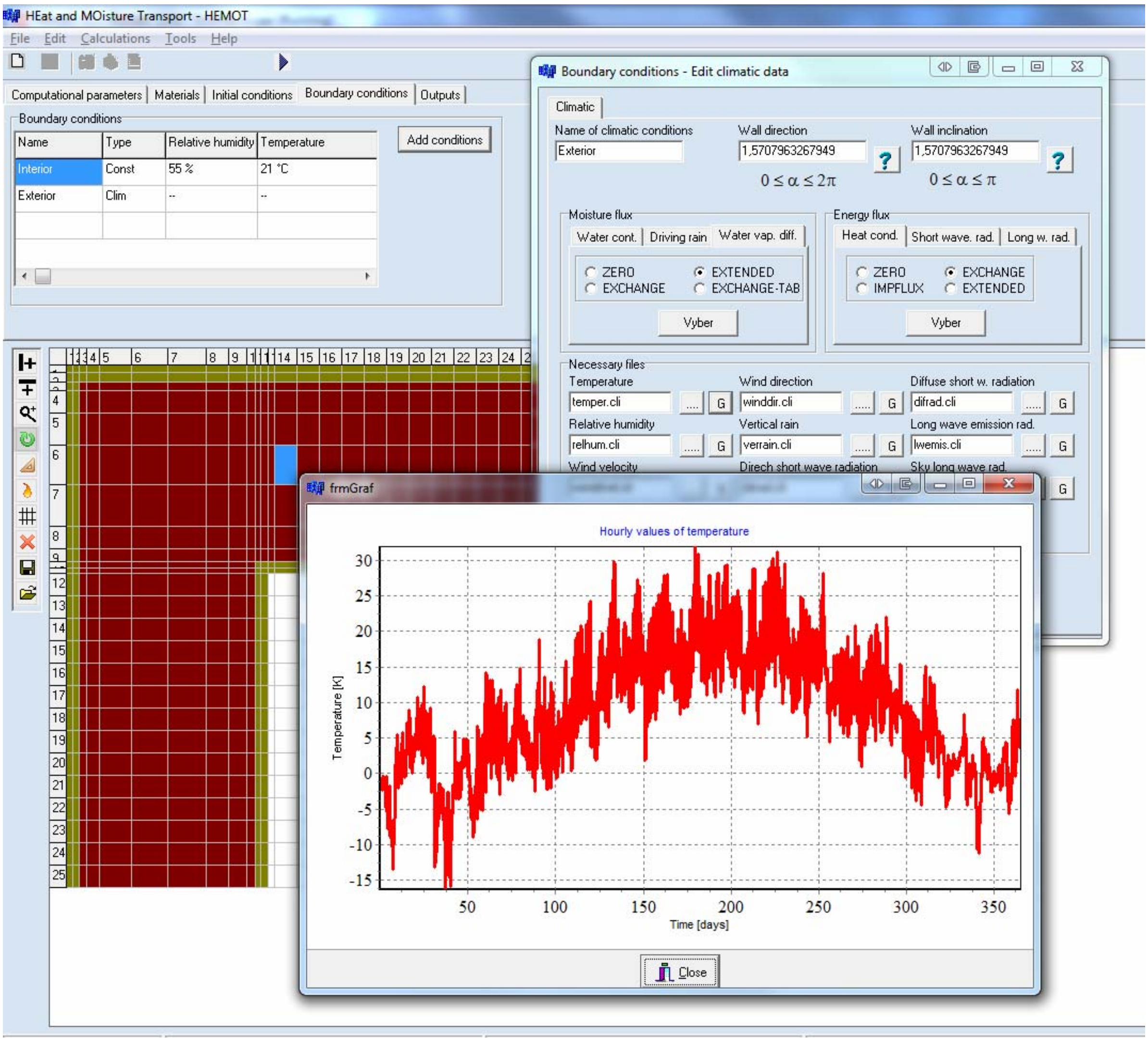

Boundary conditions

Name	Type	Relative humidity	Temperature
Interior	Const	55 %	21 °C
Exterior	Clim	--	--

Name of climatic conditions: Exterior

Wall direction: 1,5707963267949 $0 \le \alpha \le 2\pi$

Wall inclination: 1,5707963267949 $0 \le \alpha \le \pi$

Moisture flux: Water cont. | Driving rain | Water vap. diff.

○ ZERO ● EXTENDED
○ EXCHANGE ○ EXCHANGE-TAB

Energy flux: Heat cond. | Short wave. rad. | Long w. rad.

○ ZERO ● EXCHANGE
○ IMPFLUX ○ EXTENDED

Necessary files

Temperature: temper.cli
Wind direction: winddir.cli
Diffuse short w. radiation: difrad.cli
Relative humidity: relhum.cli
Vertical rain: verrain.cli
Long wave emission rad.: lwemis.cli
Wind velocity
Direch short wave radiation
Sky long wave rad.

Figure 3: Climatic boundary conditions

3. Example of computational modelling

3.1 Description of construction

AAC-based building envelope was chosen for simulation in order to analyze the hygrothermal performance. The AAC brick was provided with external thermal insulation system (mineral wool) and exterior plaster. On the material interface between mineral wool and AAC an adhesive mortar layer was placed. Description of used materials in more detail is given in next subsection. Scheme of constructive detail including the dimensions of each layer is shown in Fig. 4.

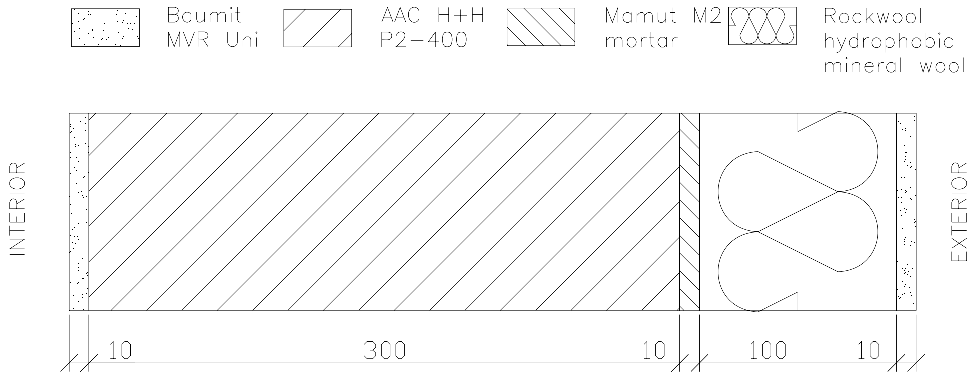

Figure 4: Scheme of constructive detail

3.2 Description of material characteristics

All the material characteristics were measured in laboratories of transport processes at the Department of Materials Engineering and Chemistry, Faculty of Civil Engineering, Czech Technical University in Prague [11-13]. The characteristics are summarized in Table 1. We used following symbols: ρ – bulk density [kg/m^3], ψ – porosity [%], c – specific heat capacity [J/kgK], μ – water vapour diffusion resistance factor [-], w – moisture content by volume [m^3/m^3], λ – thermal conductivity [W/mK], κ - moisture diffusivity [m^2/s].

Table 1: Material characteristics

	AAC H+H P2-400	Mamut M2 mortar	Rockwool hydrophobic mineral wool	Baumit MVR Uni plaster
ρ [kg m^{-3}]	412	1430	270	1402
ψ [%]	80.3	42.6	88.0	44.4
c [J kg^{-1} K^{-1}]	1250 - 1385	1020	630	1020 - 1780
μ [-]	3.7 – 14.4	12.4	2.1 – 3.7	4.5 – 12.4
λ_{dry} [W m^{-1} K^{-1}]	0.094	0.481	0.045	0.443
λ_{sat} [W m^{-1} K^{-1}]	0.434	2.022	0.246	1.380
κ [m^2 s^{-1}]	1.12e-9	1.07e-9	2.51e-10	1.59e-9
w_{hyg} [m^3 m^{-3}]	0.019	0.201	0.007	0.042

3.3 Initial and boundary conditions and time interval of simulation

Initial and boundary conditions should be as realistic as possible. This was the reason why we used climatic data in the exterior in the form of Test Reference Year for Prague which contained average data for 30 years. On the interior side we used constant value of relative humidity 55% and temperature 21°C (Fig. 5). The simulation started on 1st July and took 5 years. The final results show data during the last year.

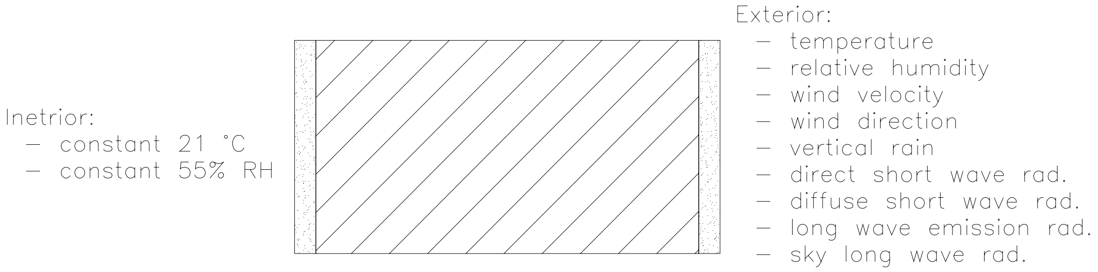

Figure 5: Boundary conditions

3.4 Computational results

As the results of computer code HEMOT we obtain computational data representing values of space and time function of hygrothermal performance of the investigated building envelope. According to our needs, we can transform the data into clearly presented simple or space graphs (Figs. 6 and 7).

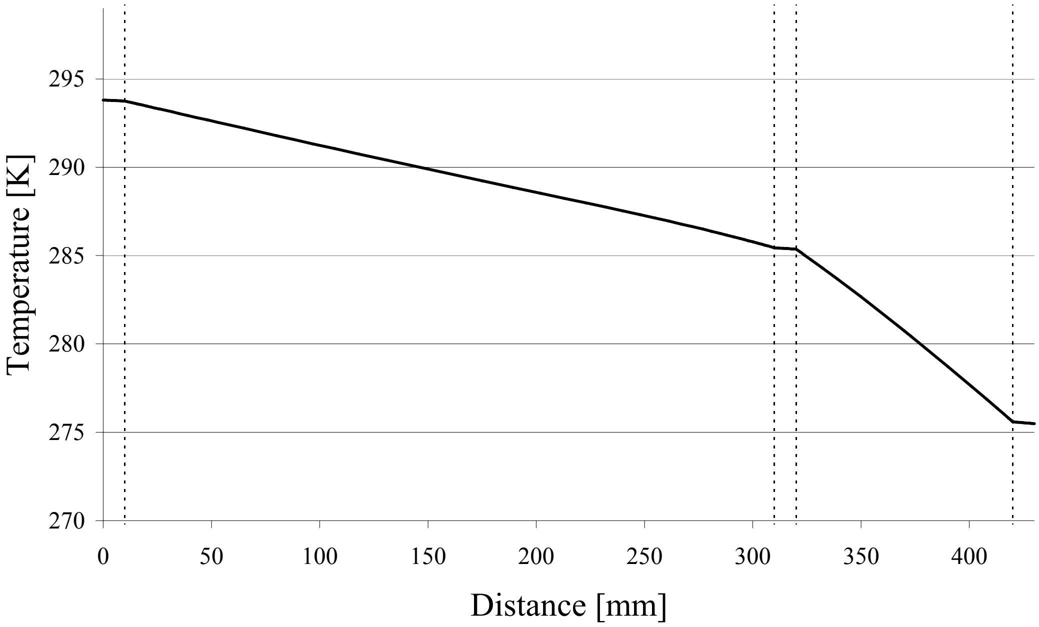

Figure 6: Distribution of temperature across the building envelope

In Figure 6, distribution of temperature is shown. The vertical lines show the material interfaces. Dimensions of construction are related to the horizontal axis, temperature is related to vertical axis.

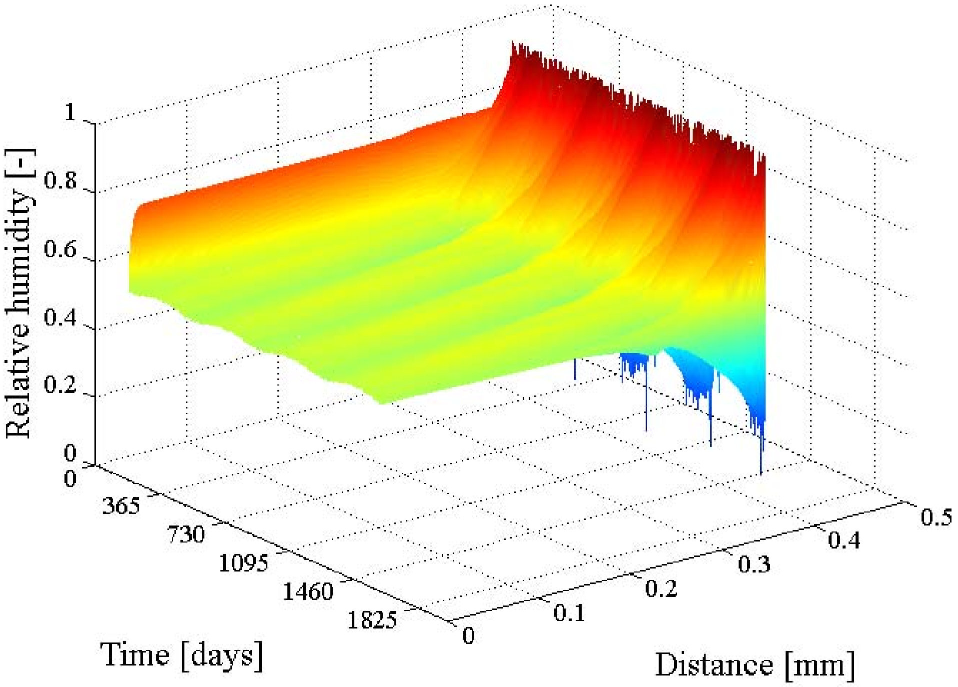

Figure 7: Time dependence of distribution of relative humidity across the building envelope

Space and time distribution of relative humidity is presented in Figure 7. Values of relative humidity are related to the vertical axis, time and dimension of construction are related to the horizontal axis.

4. Discussion

There are many ways how to use the results given by computer code HEMOT. We can predict distribution of temperature and moisture fields in the building envelope which effectively helps us to avoid the defects in design before the construction is built.

On the other hand, we can judge the hygrothermal performance of material or building envelope in order to estimate their service life. Combination of temperature and moisture fields allows us to get real image about the behaviour of contained water and then we can find out, whether the water can get frozen or not. If we complete our knowledge with freeze-thaw resistance results given by experimental analysis, we can reliably estimate the service life of the building envelope or the durability of each material.

Based on these facts, we are able to choose proper material for reconstruction or to design new material composition. If we come out from assumption of directed design, we can assign the most optimal parameters of building materials and based on that the new building material can be developed.

5. Conclusions

As it was shown in this paper, computer code HEMOT presents one of relatively new tools suitable for determination of hygrothermal performance of building materials or building envelopes. This computational approach opens a lot of possibilities of further improvement of materials, like identification of suitable material combination leading to extension of durability, elimination of failures during material's service life or prediction of future problems.

Acknowledgement

This research has been supported by Czech Ministry of Education, Youth and Sports, under project No ME10112.

References

[1] AREA, 2010, http://www.kcad.cz/

[2] TEPLO, 2010, http://www.kcad.cz/

[3] COND, 2010, http://www.bauklimatik-dresden.de/cond/index.php

[4] MENDES, N.; RIDLEY, I.; LAMBERTS, R.; PHILPPI, C.; BUDAG, K. UMIDUS: a PC program for the prediction of heat and moisture transfer in porous building elements. *Proceedings of the Sixth International IBPSA Conference, Building Simulation*. Kyoto, Japan, 1999, pp. 277–283.

[5] MATCH BOX, 2003, Moisture and temperature calculations for constructions of hygroscopic materials. http://www.match-box.dk.

[6] BURCH, D.M.; CHI, J. *MOIST: a PC program for predicting heat and moisture transfer in building envelopes*. Release 3.0, 1997.

[7] HAGENTOFT, C.E. *PC-program: 1D-HAM. Notes on heat transfer.* 5-93. Department of Building Physics, Lund University. Report TVBH-7147. 1993.

[8] GRUNEWALD, J.; *DELPHIN 4.1 - Documentation, Theoretical Fundamentals*. TU Dresden, Dresden. 2000.

[9] HOLM, A.; WORCH, A. Einsatzmöglichkeiten des Computersimulationsprogramms WUFI bei Putzen. FAS-Schriftenreihe, Heft 9. *Putzinstandsetzung: Vorträge anläßlich der 9. Hanseatischen Sanierungstage im November 1998*. Ostseebad Kühlungsborn.

[10] KÜNZEL, H. M.; *Simultaneous Heat and Moisture Transport in Building Components.* PhD Thesis, Fraunhofer IRB Verlag, Stuttgart. 1995.

[11] VÝBORNÝ, J. Stanovení tepelných parametrů a smrštění při vysychání vybraných pórobetonových tvárnic firmy H+H Česká republika s.r.o. a Xella CZ. *In: Proceedings of the International Conference 15th Construmat 2009*. Praha: České vysoké učení technické v Praze, 2009, pp. 449-461.

[12] JIŘIČKOVÁ, M.; ČERNÝ, R. Effect of Hydrophilic Admixtures on Moisture and Heat Transport and Storage Parameters of Mineral Wool. *Construction and Building Materials*, 2006, **20**, pp. 425-434.

[13] FUČÍKOVÁ, L. *Moisture Properties of AAC Blocks in dependence on the Environment Focused on Problems with Durability*. Diploma thesis. Praha: Czech Technical University in Prague, 2009.

Behaviour of gypsum wall during fire test

Tomas Korecky[1], Pavel Tesarek[2], Jan Toman[1], Robert Cerny[1]

[1]Czech Technical University in Prague, Faculty of Civil Engineering, Department of Materials Engineering and Chemistry, Thákurova 7, CZ-166 29 Prague 6, CZECH REPUBLIC.

[2]Czech Technical University in Prague, Faculty of Civil Engineering, Department of Mechanic, Thákurova 7, CZ-166 29 Prague 6, CZECH REPUBLIC.

***Abstract**: The problem of monitoring gypsum wall properties during a fire test in Mokrsko is presented in this paper. The test was performed under the management of CVUT on the 18th of September 2008 in Příbram district. According to a pre-calculated temperature curve, we expected a top temperature of 1057°C; after 63 minutes the building collapsed after attaining a maximum temperature of only 935°C. Monitored wall was made of gypsum blocks made by company GYPSTREND with proportions of 170 x 300 x 600 mm. For measurement of the thermal field six sensors placed at different heights of the wall were used. These were put in place during the construction of the wall. Each sensor composed of six thermo-couples. Thus it was possible to measure the temperatures at different depths of the wall (1 cm in front of; on the surface of the wall; 1, 2, 4 and 6 cm inside the wall). The method was based on measuring the temperature as dependent on time and position inside the wall, because in the middle part of the wall it was possible to expect only one dimensional heat propagation. Each temperature on all thermo-couples was recorded on the control panel for further interpretation.*

***Keywords**: gypsum wall, thermal field, fire test*

1. Introduction

Gypsum blocks used for building must fulfill many other demands in addition to those of fire protection. According to literature, solidified gypsum; calcium sulphate dihydrate, stable from the aspect of temperature influence only up to the temperature rang 40 to 60°C. At higher temperatures resistance levels fall [1]; despite this products based on gypsum are used as part of fire protection. Most often it is used in form of gypsum fibrillate or gypsum plasterboards and blocks.

Gypsum, because of good thermal qualities, is considered to be fireproof from the view of fire protection. For some time, it can protect against high temperatures and direct flames [1]. This time depends on wall thickness and its parameters.

It is possible to explain this effect in the way that action on the surface of gypsum becomes dehydrated and results in an inner layer caused by vapour, as a result of the effects of high temperatures. The temperature in these places doesn´t to rise more than approx. 100°C until all the water is vapourised. After dehydration gypsum is more porous and its temperature properties improve [1]. Mechanical properties, for example pressure resistance, became worse due to rising temperatures [2]. Heating gypsum to over 100°C results in a decrease of circa 46%; at over 200°C the resistance decreases by 60%. At 400°C the resistance of solidified gypsum falls to 39% of original (initial) value. At 700°C the resistance falls nearly to zero [2].

By using fibres or applying gypsum plaster on to steal fencing it is possible to increase the resistance power of gypsum. In this way it is possible to prevent the breakdown of gypsum after reaching 900°C, at which calcium sulphate disintegrates.

2. Description of the fire test

The fire test in Mokrsko realized on the 18th September 2008 under the management of CVUT and other partners should verified behaviour of the structure stressed by fire. The fire test implicitly join to the before made tests in English Cardington. By the test were tested more kinds of materials used as building solution of ceiling and cladding constructions. The structure represented one floor of the administrative building of size 18 x 12 meters.

The fire load created wooden cribs 50 x 50 mm of length 1 m of soft wood. The cribs were placed into 50 piles consisted of 12 rows with 10 cribs. It simulated the fire load 620 MJ/m^2. This amount is more 50% than characteristic fire load of administrative building [4].

According to a pre-calculated temperature curve, it was expected a top temperature of 1057°C. But after 63 minutes the building collapsed after attaining a maximum temperature of only 935°C. By this the test was finished and fire lost intensity extremely [4].

3. Description of the gypsum wall used in the experiment

The tested gypsum wall was built from rabbet gypsum blocks of 170 x 300 x 600 mm. The wall was wide 1800 mm and 3600 mm high.

The gypsum was made by the corporation GYPSTREND Pty. Ltd., in two material alternatives which were marked MS 84 and MS 86. These alternatives were chosen as the most suitable for the production of gypsum blocks for the external cladding of buildings after a few years of collective research between GYPSTREND, Institute of Chemistry at the Faculty of Civil Engineering in VUT Brno and the Department of Material Engineering and Chemistry at Faculty of Civil Engineering at CVUT in Prague.

The base material, used for the production of cast gypsum blocks was grey gypsum matrix produced by company GYPSTREND, which is classified by CSN 72 2301 as G2 BII. Into this matrix, in order to improve its useful properties, the agent Polyfor, water-repelent additive MH 1107 and Perlit EP 150 or EP 180 were added to both aforementioned alternatives. 45 pieces were produced for the purpose of fire testing.

The experimental gypsum wall was built on a concrete base in front of 250 mm wide iron-concrete wall made of concrete C 30/37. The upper part of the gypsum wall ended 100 mm below the ceiling and the remaining space was filled with the mineral wool Rockwoll. Gypsum blocks were lined up on the gypsum universal matter SPECIAL which is designated for bonding, pointing and graveling blocks. After that, the wall was covered with a 5 mm thick layer of gypsum matter PRO GYPSUM. The gap between the concrete and the gypsum wall was 5 mm and was used for the distribution of the cables, beginning from the thermocouples which were positioned at different heights of the gypsum wall. From the side this gap was filled with gypsum plaster in order to stop the flames and heat breaking through from the side of construction. Thereby it is possible to consider one-dimensional heat spreading in the middle of the wall. In Figure 1 adjustment of both alternative gypsum blocks, MS 84 and MS 86, is shown in the experimental wall.

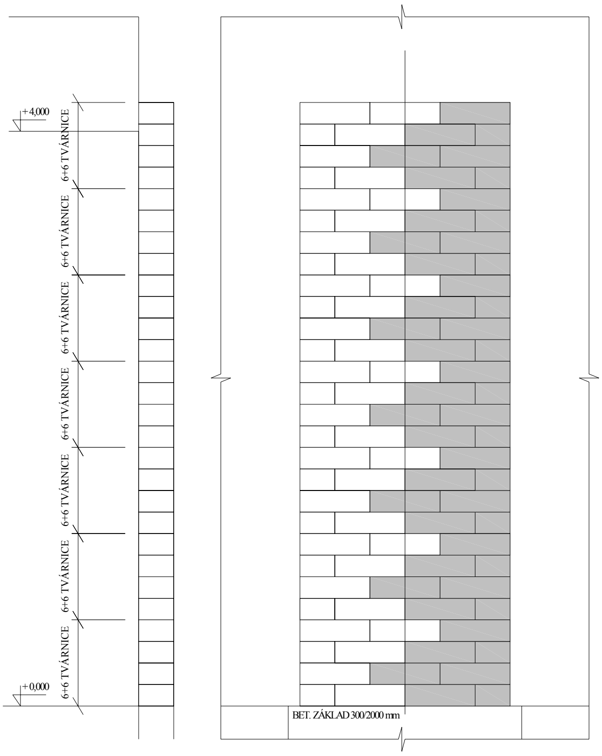

Figure 1: The scheme of the gypsum wall

Six temperature probes used for monitoring the temperature field in dependence on height and depth were positioned in the wall. Temperature probes 2 and 3 were positioned 3.5 m above the floor, temperature probe 5 was position 1.5 m above the floor and temperature probe 6 was 0.6 m above the floor.

4. Method of measuring

The method of temperature field measurement at different depths of material is based on measurements which are used in the high temperatures laboratory at the Department of Material Engineering and Chemistry at Faculty of Civil Engineering at CVUT in Prague. This method deals with the measurement of the thermal field inside a one-dimensional temperature stressed material. It is based on the measurement of temperature dependence over time. Measurement is carried out with built-in thermal probes in the measured samples.

In order to record the distribution of the thermal field in the measured material at one-dimensional heat, the thermal probes must be inserted in a precisely-defined configuration. In Figure 2, the used probe is shown, which consists of 6 thermocouples chromel-alumel. Individual thermocouples were at least 1 cm from each other and enabled temperature measurement along to longitudinal axis in distances of 0, 1, 2, 3, 5, 7 cm. These thermal probes were inserted into the gypsum wall so that there were measured temperatures 1 cm in front of the wall inside the building, on the surface on the wall, 1, 2, 4 and 6 cm inside the wall. All the temperature probes were connected to recording units, which during the measurement recorded individual temperatures at particular time intervals.

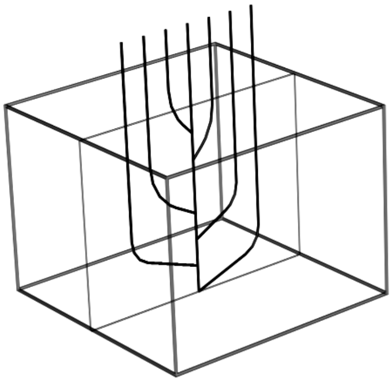

Figure 2: The used thermal probe

5. Results of measuring

The experimental gypsum wall wasn´t heavily damaged by the fire. It was only disturbed in its upper part due to the collapse of the building after about one hour of the duration of the fire test. Ceiling construction (Spiroll panels) fell on the upper part of the wall. In Figures 3 and 4 is the wall is documented in the course of the construction and after the fire test.

From this it is evident that the wall built from gypsum blocks resisted the fire test. The wall was damaged as a consequence of the fallen ceiling. As a result there was deflection of the wall, cracking of ledge gaps in the upper third of the wall and parting of a gypsum block.

The damage to the wall was visible with the naked eye. In the parts which were affected by the fire several layers were formed. In a small part of the wall a layer of the plaster of thickness 5 to 6 mm separated from the wall. The plaster and 5 mm thick layer of block were clearly yellow in colour. There is a gray layer, reaching the depths of 25 to 35 mm. This layer also separated at some parts. On the edge of this layer some cracks appeared and due to mechanical stress this layer separated. The subsequent part of the blocks seemed to be compact.

Another interesting fact is that the plaster wasn't totally destroyed, even by temperatures of over 800°C. The plaster had only peeled at some particular places. But it is necessary to claim that the resistance of the plaster and from part of the wall dropped very much.

The application of the gypsum wall as fire protection was successful because the part of the surface of the concrete wall protected by the gypsum wall wasn't destroyed as a consequence of the fire. On the other parts of the concrete wall the top layers were broken off to the level of the amour because of water vapour pressure, it means to a depth of 70 mm.

Figure 3: The gypsum wall before the fire test

Figure 4: The gypsum wall after the fire test

6. Analysis of results and discussion

All measured temperatures describing thermal field during the fire test were plotted into graphs. In Figure 5 the temperatures at each depth in dependence on time are shown. Position -1 cm means that thermocouple was located 10 mm from surface of the gypsum wall inside building. Position 0 means allocating of thermocouple on the inner surface of the wall and other positions (1, 2, 4 and 6 cm) mean the depth of allocation of thermocouples inside the wall from surface.

The maximum temperature of 800° C was measured just before the collapse of the building it was 10 mm in front of surface of the gypsum wall on the thermo-probe 5 which was located 1.5 m above the ground. The temperatures of all thermocouples of the thermo- probe 5 are plotted in the figure 5. On the thermocouple of thermo-probe number 6, which was located 0.25 m above the ground, the maximum temperature measured here was 725° C. On the thermo-probes 2 and 3 located 3.5 m above the ground the maximum temperature reached were 680° C (thermo probe 2) and 740° C (thermo probe 3). On thermo-probe 6 at the depth of 6 cm in the wall the temperature of 100° C slightly increased after the collapse of building and finally reached 130°C. On the other probes the measured temperatures at the depth of 6 cm weren´t higher than 100° C.

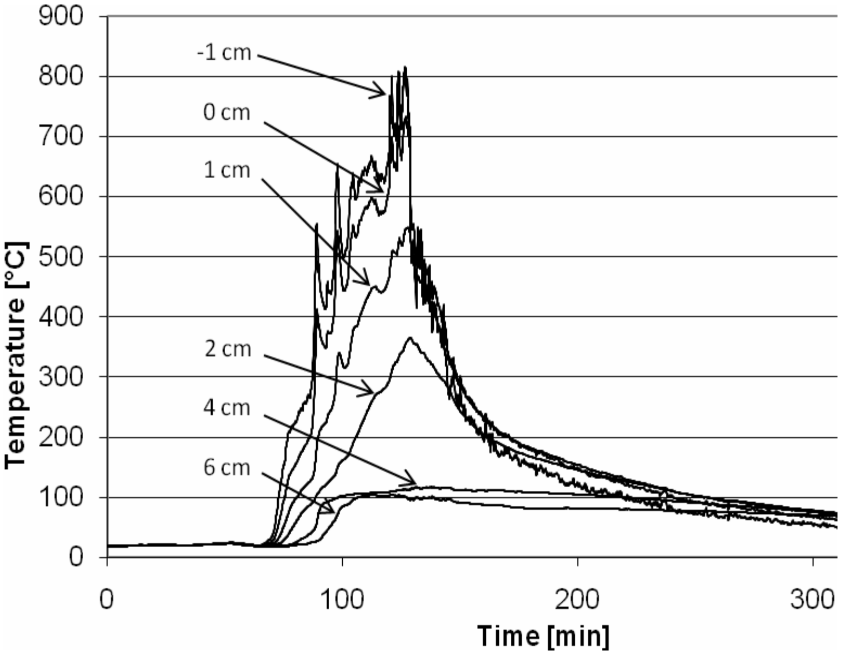

Figure 5: Graph of the temperature field measured by probe 5

In this Figure number 6 and 7 thermo profile of the gypsum wall measured with probe 5 at 15 minutes intervals is shown. In Figure 6 the growth of the temperature from the beginning of the fire test to the moment just before the collapse of the building is shown. In Figure 7 the cooling of the structure just after the collapse is shown.

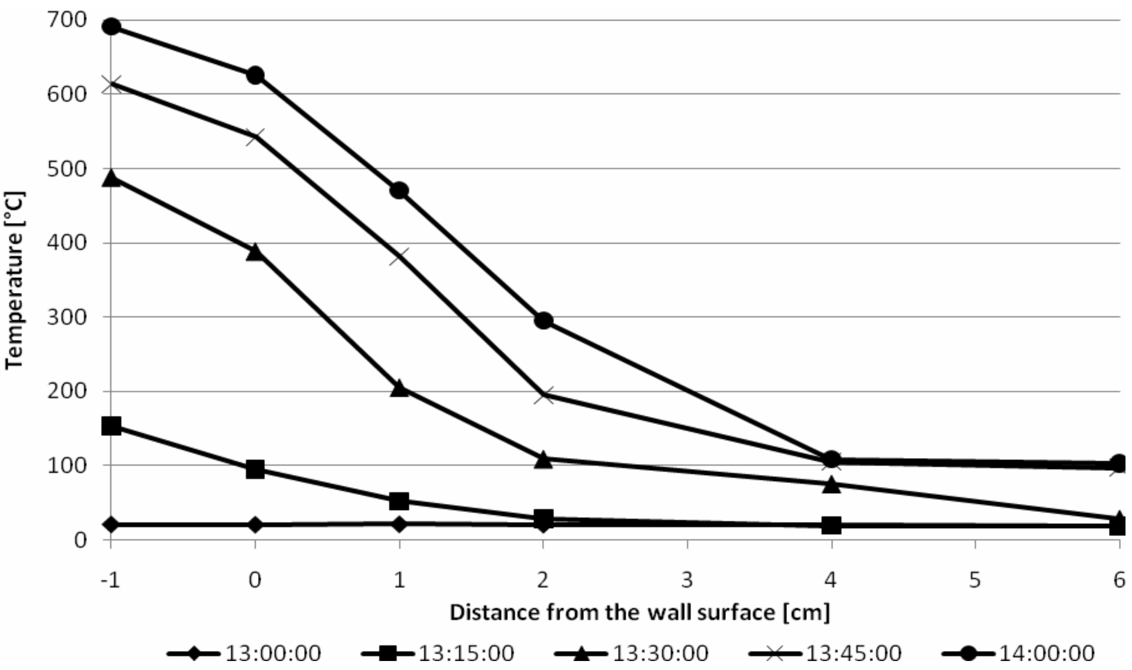

Figure 6: The thermo profile of gypsum wall measured by probe 5 before the collapse

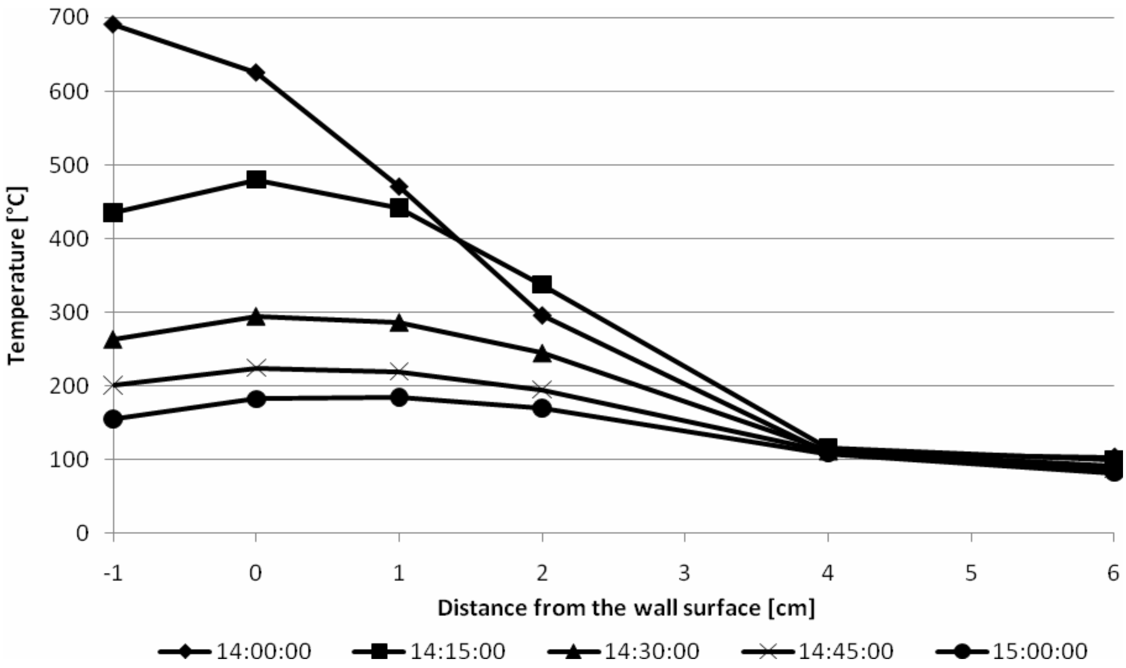

Figure 7: The thermo profile of gypsum wall measured by probe 5 after the collapse

7. Conclusion

The fire test in Mokrsko verified the possibility of the application of the gypsum blocks as a new material which can be used in the cladding of buildings. Apart from many other useful properties it will also meet the demand of fire protection necessitated by this kind of construction.

Because there wasn´t complete destruction of the gypsum wall which was built from gypsum blocks and plaster, these layers fulfilled also secondary function of the isolation against fire, even though the values of its resistance are nearly reaching zero.

The loss of resistance caused by higher temperature develops only in a thin top layer, which within the frame of the total construction only has a minor effect.

The fire resistance of the gypsum wall was verified by spectral analysis of 1 cm layers cut from the gypsum block, starting from the beginning of the heated surface. The analysis provide change of dihydrate to anhydrate on surface. Hemihydrate was detected to the depth maximal of 2 cm.

Acknowledgement

This work has been financially supported by the Ministry of Education, Youth and Sports of Czech Republic, under projects No MSM: 6840770031 and SGS10/007/OHK1/1T/11.

References

[1] LEJSEK, L. Využití sádry ve stavebnictví. In *Sádra ve stavebnictví*, Brno: Československá vědecko technická společnost, 1967, s. 28-48

[2] KUPILÍK, V. Chování sádry v různých provozních podmínkách. In *Sádra v památkové péči*, Seminář společnosti STOP, Praha: STOP, 2002, s. 14-22.

[3] WIRSCHING, F. Drying and Agglomeration of Flue Gas Gypsum. In The *Chemistry and Technology of Gypsum*, Philadelphia: American Society for Testing and Materials, 1984, p. 161-174.

[4] Draft Summary of Results from Fire Test in Mokrsko 2008. WALD, F., KALLERO-VÁ, P. (eds.), [online],[cit. 20. 6. 2010].

Microstructure and water vapour adsorption of capillary-porous building materials

Olga Koronthalyova

Institute of Construction and Architecture, Slovak Academy of Sciences, Dubravska c. 9

SK-845 03 Bratislava, Slovak Republic, email: usarkoro@savba.sk

Abstract: *The actual adsorption/desorption curves are dependent on the material microstructure. In order to study the actual microstructure – water vapour sorption isotherm relation the nitrogen and water vapour isotherms of the chosen building materials - ceramic bricks, calcium silicate boards and autoclaved aerated concrete (AAC) - were compared and the obtained results were analysed. Water vapour adsorption isotherms were measured in the range 0 – 98% RH by the desiccator method. The nitrogen adsorption measurements were performed with the volumetric ASAP2400 instrument enabling to obtain isotherms in the 0.01 – 0.98 relative pressure range.*

The water vapour adsorption isotherms of different materials were in good coincidence with the pore size distribution results, determined by nitrogen sorption. The absolute amounts of adsorbate obtained by nitrogen and water vapour were comparable in case of bricks and differed significantly for AAC and calcium silicates. On the other hand, the storage capacities obtained by nitrogen and water vapour adsorption were in satisfactorily agreement for all tested materials except for the range of very low relative pressures.

Based on the analysis of the experimental results a possibility of using nitrogen data for the verification or the prediction of the water vapour adsorption curve was discussed.

Keywords: *Water vapour adsorption, nitrogen adsorption, storage capacity, porous building material*

1. Introduction

Porous building materials in structures always contain a certain amount of moisture, physically bound in the pore structure. The moisture bound in a material directly affects its properties, such as strength, shrinkage, and thermal conductivity. Therefore the ability to accumulate moisture is one of the key material parameters, necessary for an evaluation of the building structures performance.

In a hygroscopic range the equilibrium moisture content of a porous building material is characterised in terms of water vapour adsorption/desorption isotherms. The next important parameter of a hygrothermal performance evaluation is the moisture storage capacity, which is defined as the slope of the sorption isotherm.

The classical method of obtaining sorption isotherm consists of conditioning the samples in desiccators or a climatic chamber under constant relative humidity and temperature until static equilibrium is achieved [2]. In spite of the fact that the methods of water vapour sorption isotherm determination are well defined, there is a relatively large variation in the water vapour sorption results reported by different laboratories [5, 6]. Therefore searching of an alternative way of verification or prediction of the sorption isotherm is meaningful.

In previous work [3], it has been found that the prediction of water vapour adsorption isotherms was possible using the measured equilibrium moisture content at low relative pressure and the storage capacity determined from nitrogen adsorption curve for two types of autoclaved aerated concrete and burnt clay brick. In this work the relation between the nitrogen and water vapour adsorption capacities and a possibility of using nitrogen adsorption data for the prediction/evaluation of water vapour adsorption isotherm was tested for the another building materials.

The measurements were done for three different types of building materials – burnt clay bricks, calcium silicate boards (CS) and autoclaved aerated concrete (AAC). Into the comparison of the water vapour and the nitrogen adsorption results also the data for 28 day old hardened cement paste (HCP) taken from [4] have been involved.

2. Experimental part

The tested materials were characterised by the following basic parameters: bulk density, total open porosity and capillary moisture content. The bulk density was calculated from volume and mass of the dried out samples (oven drying at 105°C). The total open porosity was obtained from a water saturation test. The capillary moisture content was obtained from a one-dimensional free imbibition experiment, in which an oven-dry sample is allowed to absorb liquid water from a free water plane [6].

Water vapour sorption isotherms were determined by the standard gravimetric desiccator method, which consists of conditioning the samples in desiccators under constant relative humidity (RH) and temperature until the static equilibrium is achieved [2]. The desiccators were placed in an air conditioned test-room with the temperature controlled at 22.5 ± 0.5°C. The measurements were done for seven RH values: 11.3%, 33%, 53%, 75%, 85%, 94% and 98%. The dimensions of the samples were ca 40 x 40 x 25 mm. The samples were oven dried beforehand at 105 °C. The mass of the samples was weighed by means of electronic scales with the accuracy 0.001g.

The nitrogen adsorption measurements were performed with the volumetric ASAP2400 instrument, enabling to obtain isotherms in the 0.01 – 0.98 relative pressure range. Prior to the measurement the samples were degassed overnight at 150 °C and 2 Pa.

The specific surface area of pores was determined by the BET method, using the relation (1) [1]:

$$SSA = n_m \cdot N_A \cdot \sigma = V_m \cdot N_A \cdot \sigma / V_M = m_m \cdot N_A \cdot \sigma / M \quad (1)$$

where SSA is the specific surface area [m^2/g], n_m is the amount of mono-layer adsorbate [mol/g], N_A is the Avogadro number, $N_A = 6.023 \cdot 10^{23}$ mol^{-1}, σ is the area occupied by each adsorbed molecule of adsorbate ($1.62 \cdot 10^{-19}$ m^2 and $1.05 \cdot 10^{-19}$ m^2 for N_2 and H_2O respectively), V_m is the volume of mono-layer adsorbate [m^3/g], V_M is molar volume [m^3/mol], m_m is the mass of mono-layer adsorbate [g/g], M is the molar mass [g/mol].

The storage capacity was calculated from adsorption isotherm according to the relation (2):

$$\xi(p/p_0) = \frac{dv_{ads}}{d(p/p_0)} \quad (2)$$

where ξ is the storage capacity [cm^3 liquid/g], v_{ads} is the adsorbed amount [cm^3 liquid /g], p/p_0 is the relative pressure [-]. For water, the adsorbed amount expressed in cm^3 liquid/g is equal to the mass by mass moisture content.

3. Results and discussion

The basic material parameters and the comparison of specific surface areas (SSA) determined from the nitrogen and the water vapour sorption (both by the BET method) are presented in Table 1. The agreement between water vapour and nitrogen SSA values is good for brick S and acceptable for brick P. In case of CS materials and AAC, the water SSA values are higher than the nitrogen ones, the highest difference between the water and nitrogen value has been obtained for AAC. It can be most likely explained by the presence of micropores with radius or entrance being smaller than 2 nm, inaccessible to nitrogen but accessible by water vapour.

Table 1: Basic material properties and BET SSA values of tested materials

Material	Bulk density [kg/m^3]	Open porosity [%]	Capillary moisture content [m^3/m^3]	SSA BET water [m^2/g]	SSA BET nitrogen [m^2/g]
CS 250	314	90	0.89	36.6	22.5
CS B	263	93	0.82	60.0	41.0
Brick P	1377	42	0.37	8.1	14.2
Brick S	1426	44	0.39	3.6	4. 7
AAC	500	80	0.29	37.0	14.6

Figure 1 shows the nitrogen pore size distributions of the tested materials and Figure 2 presents the obtained water vapour and nitrogen adsorption isotherms. When the pore size distribution results and the amounts of water adsorbate are compared it is necessary to take into account the effect of the different bulk density of the tested materials. Then it can be concluded that the amounts of water adsorbate correspond very well to the nitrogen pore size distribution. The correspondency between the nitrogen and water isotherms is quite good for the bricks, whereas for the AAC and the CS materials the amount of the water vapour adsorbate is consistently and considerably higher than the nitrogen one (Fig. 2). On the other hand, excluding the range of very low pressures, the shapes of the nitrogen and the water vapour adsorption curves are very similar for all tested materials. The noticed differences in the range of very low pressures are in accordance with the different accessibility of nitrogen and water into the very small micropores.

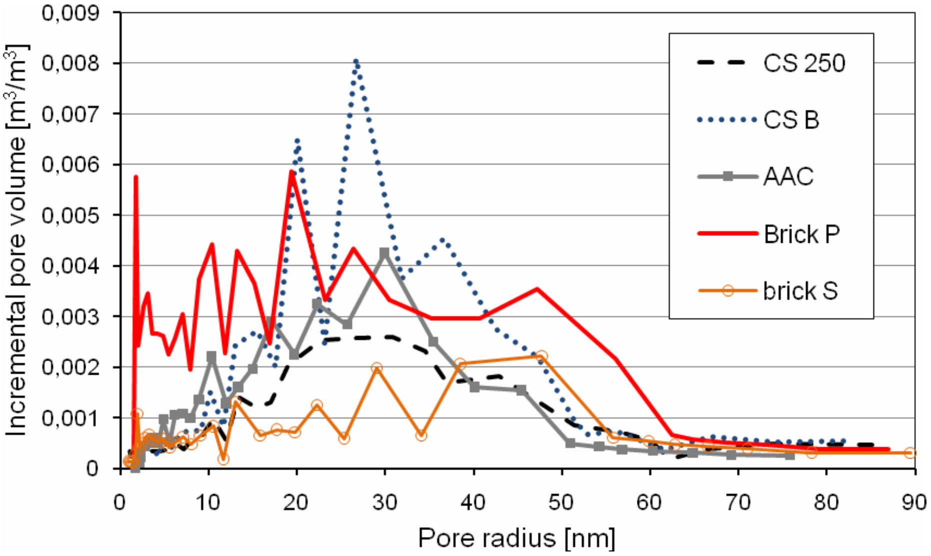

Figure 1: Comparison of the CS 250, CS B, AAC, brick P and brick S pore size distributions by nitrogen desorption

In order to analyze the nitrogen and water vapour adsorption similarity in more detail, the adsorption storage capacities were compared (Fig. 3). The storage capacities by nitrogen and water vapour differ slightly for bricks and CS materials and significantly for AAC up to the relative pressure value of about 0.2. After this point, they are practically identical for all tested materials up to the relative pressure value of about 0.96. In the range of relative pressures higher than 0.96, the slightly higher values of water storage capacity were noticed in case of both CS materials. Differences in the range of very small relative pressures can be explained by the presence of very small micropores, inaccesible to nitrogen. As to the range of relative pressures higher than 0.96, one of the possible reasons of the noticed difference could be caused by generally accepted lower preciseness of the nitrogen as well as the water sorption results in this range of relative pressures.

As to the HCP results, it has to be taken into account that the results shown in Fig. 2 and Fig. 3 are only estimative ones, taken from the figures presented in [4]. Another fact that could probably influence the HCP results is that a different method (measurement by the automated sorption analyzer [4]) was used for the determination of the water vapour isotherm. Nevertheless also for the HCP it can be concluded that the agreement between the nitrogen and the water storage capacity is acceptable.

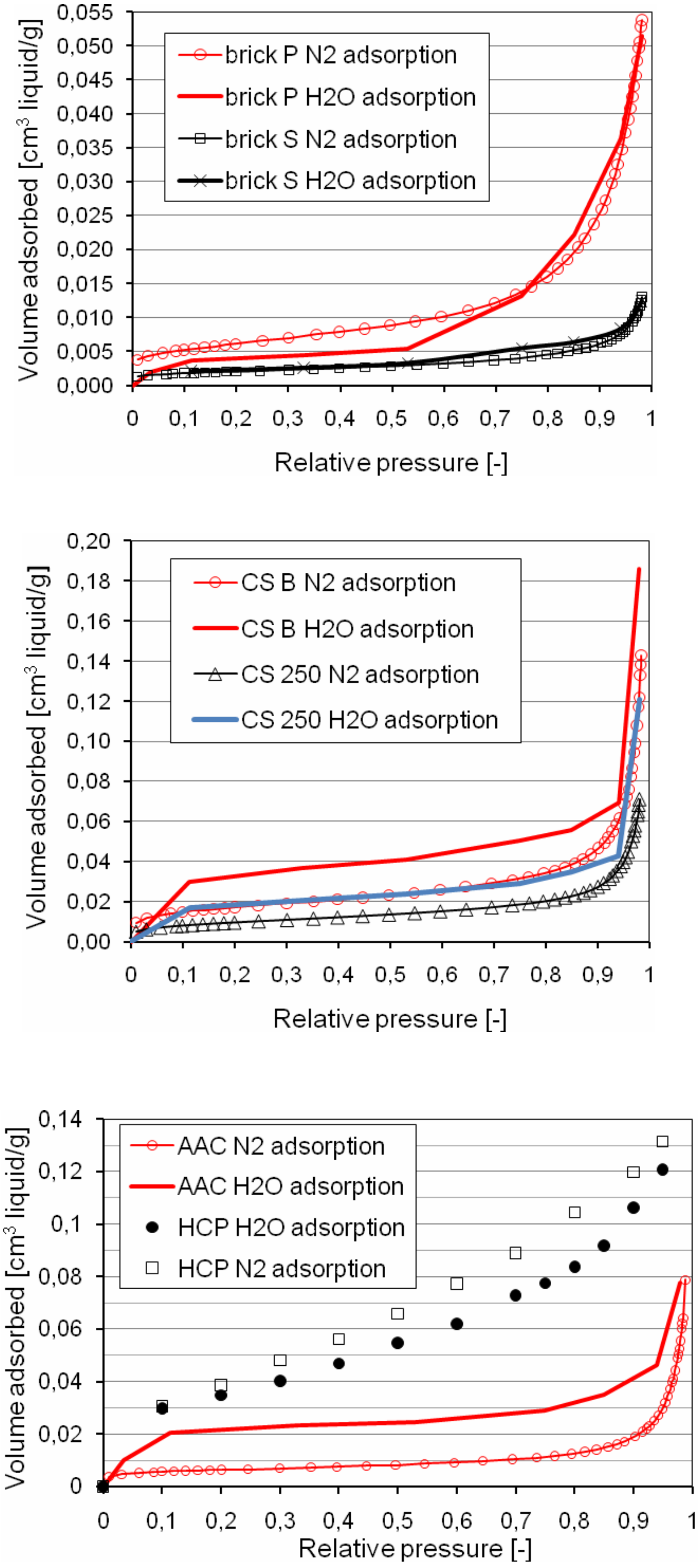

Figure 2: Comparison of water vapour and nitrogen adsorption for bricks, calcium silicates, autoclaved aerated concrete and hardened cement paste

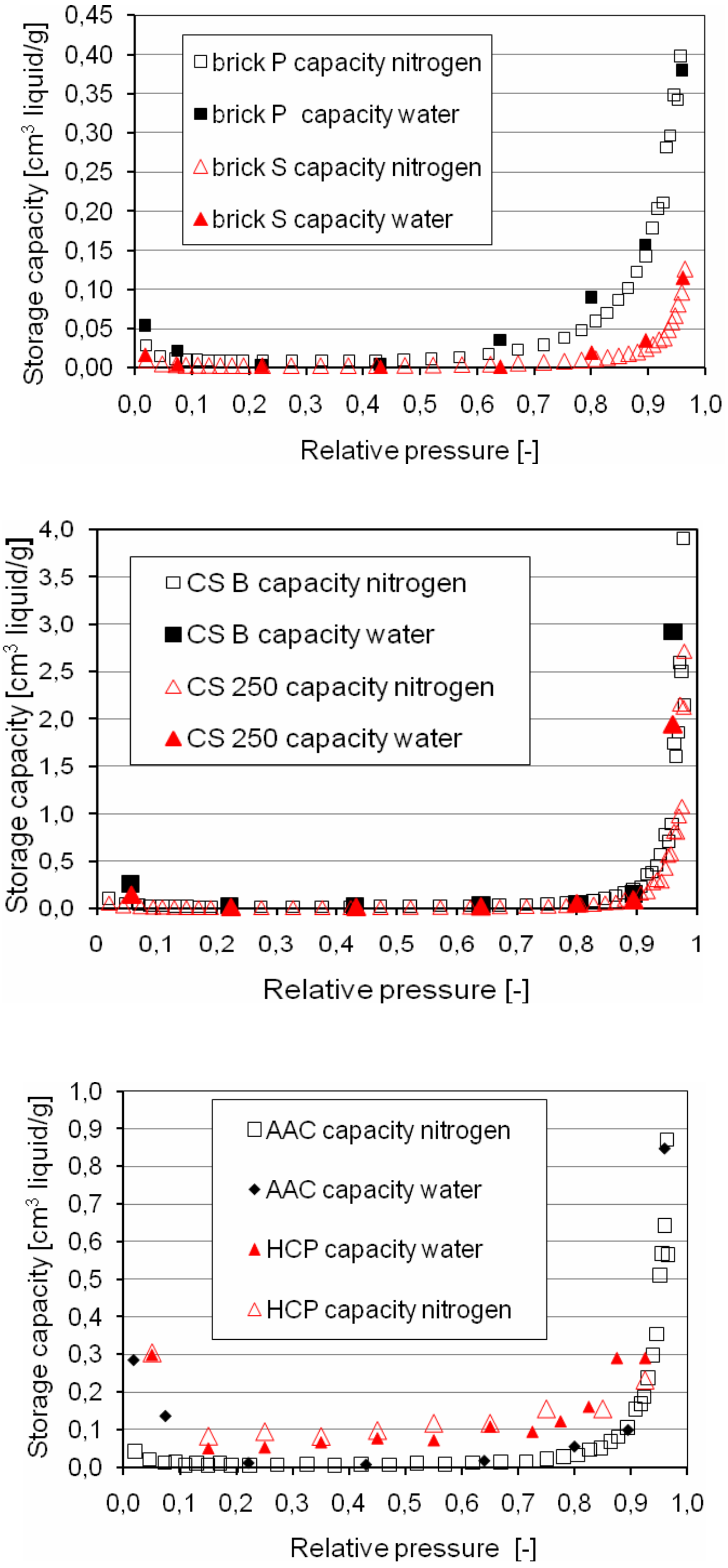

Figure 3: Comparison of the storage capacity values obtained from water and nitrogen adsorption for bricks, calcium silicates, autoclaved aerated concrete and hardened cement paste

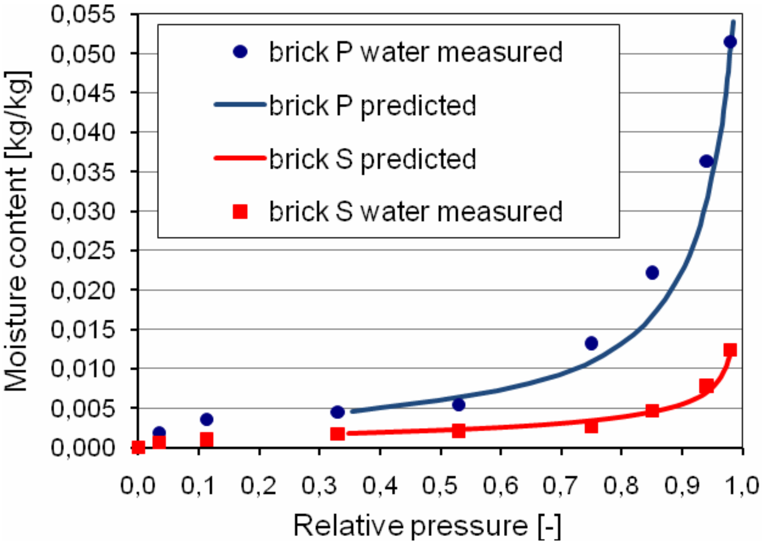

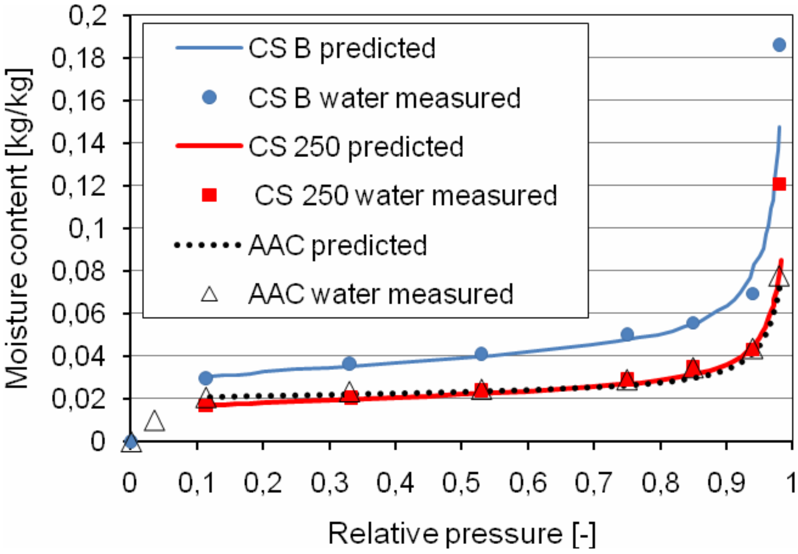

Figure 4: Comparison of the measured and predicted (relation 3) water vapour adsorption isotherms

Taking into account the identified adsorption capacity agreement, the prediction of the adsorption moisture content was done using the measured moisture content at the lower part of water vapour adsorption curve and storage capacity ξ (p/p_0), determined from nitrogen adsorption. The resultant relation for the calculation of the moisture content at mean relative pressure between p_n/p_0 and p_{n-1}/p_0 is as follows:

$$u_m\left((p_n + p_{n-1})/2 \cdot p_0\right) = u_m(p_1/p_0) + \sum_{2}^{n} \xi\left((p_n + p_{n-1})/2 \cdot p_0\right) \cdot (p_n - p_{n-1})/p_0 \qquad (3)$$

where u_m is the moisture content [kg/kg], the starting value u_m (p_1/p_0) is equal to the measured moisture content at some of the lower relative pressures.

Figure 4 shows the comparison between the measured and predicted data. As can be seen from the comparison, the agreement is very good for all tested materials.

4. Conclusions

The relation between the nitrogen and the water vapour adsorption isotherms and storage capacities was analysed for ceramic bricks, calcium silicate boards, AAC and HCP.

The absolute amount of adsorbate obtained by nitrogen and water vapour practically coincided for bricks and differed for calcium silicates and AAC. On the other hand, the storage capacities by nitrogen and water vapour adsorption were in very good agreement for all analysed materials, except for the range of very low and very high relative pressures.

For all measured materials, the prediction of water vapour adsorption isotherms was possible by using the measured equilibrium moisture content at low relative pressure and the storage capacity determined from nitrogen adsorption curve.

Acknowledgement

This research was supported by the Slovak Grant Agency VEGA (Grant No 2/0159/10)

References

[1] Aligizaki, K.K. *Pore Structure of Cement-Based Materials.* Taylor& Francis, London and New York, 2006. ISBN 0-419-22800-4.

[2] EN ISO 12571:2000 *Hygrothermal performance of building materials and products - Determination of hygroscopic sorption properties*

[3] Koronthályová, O. Moisture storage capacity and microstructure of ceramic brick and autoclaved aerated concrete. In *Construction and Building Materials (2010), doi:10.1016/j.conbuildmat.2010.06.098*

[4] Pane, I. – HANSEN, W. Surface Characterization of Blended Cements by H_2O and N_2 sorption. In J.Weiss, K. Kovler, J.Marchand, S.Mindess (Eds.). *Proceedings of the 1st International Symposium on Advances in Concrete through Science and Engineering*, Chicago, USA, RILEM PRO048, 2004.

[5] Peuhkuri, R.; RODE,C.; HANSEN, K. K. Effect of method, step size and drying temperature on sorption isotherms. In *Nordic Journal of Building Physics*, Articles from the 7th symposium on Building Physics in the Nordic Countries, Reykjavik, 2005.

[6] Roels, S. et al. Interlaboratory Comparison of Hygric Properties of Porous Building Materials. In *Journal of Building Physics.* 2004. 27. p. 307–325. ISSN 17442591.

Measurement of the thermal conductivity and diffusivity in a kaolin-based ceramics by the hot-wire method: A comparison study

Jozef Kováč[1], Igor Medveď[1,2]

[1]Department of Physics, Constantine the Philosopher University, Tr. A. Hlinku 1, SK-94974 Nitra, Slovakia, email: imedved@ukf.sk

[2]Department of Materials Engineering and Chemistry, Thákurova 7, Czech Technical University, CZ-16629 Prague, Czech Republic

Abstract: *We measure the thermal conductivity, λ, and thermal diffusivity, a, of kaolin-based ceramic cylindrical samples in dependence on the temperature by the hot-wire method. Using the experimental data, λ and a are first calculated in the standard way – from the slope of the linear part of the dependence of ΔT(ln t) of the temperature rise, ΔT, inside a sample on the logarithm of time. We then apply an alternative method, using the full version of the well-known theoretical formula for the dependence ΔT(t) of the temperature rise on time to find its best least-square fit to the experimental data and subsequently re-calculate λ and a. The alternative values of λ and a are often rather different from those calculated in the standard way. However, if one restricts oneself to times less than the time up to which the ΔT vs. ln t plot is linear, then we argue that the alternative values of λ and a should be more accurate and provide more reliable results than the ones obtained by the standard method.*

Keywords: *thermal conductivity, thermal diffusivity, hot-wire method, kaolin-based ceramics*

1. Introduction

The hot wire method is a dynamic method based on the measurement of a temperature rise in a defined distance from a linear heat source embedded in a sample. This method is well known by now [1] and has been widely used to measure thermal conductivity of solids, fluids, and gases [2-13].

The mathematical model of the method is based on an infinite line heat source which is embedded in an infinite medium. Assuming that the temperature of a sample varies only with the radial position r and time t, the temperature rise, ΔT, may be described, in the cylindrical coordinate system, by the equation

$$\frac{\rho c}{\lambda}\frac{\partial T}{\partial t}=\frac{1}{r}\frac{\partial}{\partial r}\left(r\frac{\partial \Delta T}{\partial r}\right), \tag{1}$$

where ρ is the density, c is the heat capacity, and λ is the thermal conductivity. Considering the following initial and boundary conditions

$$\Delta T(r,0)=0,\quad \Delta T(\infty,t)=0,\quad \left[r\frac{\partial \Delta T}{\partial r}\right]_{r=0}=-\frac{q}{2\pi\lambda}, \tag{2}$$

where q is the constant quantity of heat production per unit time and per unit length of the heating wire, the solution of Eq. (1) may be written as [1]

$$\Delta T(r,t) = -\frac{q}{4\pi\lambda} E_i\left(-\frac{r^2}{4at}\right). \tag{3}$$

Here $a = \rho c/\lambda$ is the thermal diffusivity, and E_i is the exponential integral,

$$E_i(x) = -\int_{-x}^{\infty} \frac{e^{-u}}{u} du . \tag{4}$$

Expanding E_i into the Taylor series, one obtains

$$T(r,t) = \frac{q}{4\pi\lambda}\left[-\gamma + \ln\left(\frac{4at}{r^2}\right) + \frac{r^2}{4at} - \frac{1}{4}\left(\frac{r^2}{4at}\right)^2 + \frac{1}{9}\left(\frac{r^2}{4at}\right)^3 + \ldots\right], \tag{5}$$

where γ is the Euler's constant. If the condition $r^2/4at \ll 1$ is fulfilled (the time t is sufficiently long and the radial distance r is sufficiently small), then one may approximate Eq. (5) by taking only the first and second terms, i.e.,

$$T(r,t) \approx \frac{q}{4\pi\lambda}\left(\ln t + \ln\frac{4a}{r^2 e^{\gamma}}\right), \qquad \frac{r^2}{4at} << 1 . \tag{6}$$

Thus, the thermal conductivity can be simply calculated from the slope, A, of the dependence of the temperature rise on the natural logarithm of time, while the thermal diffusivity can be simply obtained from the slope and the intercept, B, of this dependence. Namely,

$$\lambda = \frac{q}{4\pi A}, \quad a = \frac{r^2}{4} e^{\gamma + B/A} . \tag{7}$$

Therefore, recording the dependence ΔT on $\ln t$ from an experiment, one may readily evaluate both λ and a from the linear segment of this dependence, using a linear least-square fit.

However, this standard way of measuring the thermal conductivity and diffusivity may have disadvantages. Perhaps most importantly, the precise identification of the linear segment (of its two end-points) may be ambiguous, leading to possible errors in the obtained values of λ and a. In fact, modifications and corrections to this standard measuring method have been proposed in which, for example, the effects of a finite axial length, finite wire thickness, or wire coating were included [13,14].

In this paper we discuss that the measurement of λ and a by the standard method based on Eq. (6) can be improved when Eq. (3) is used instead because instead of two end-points only one end-point is needed when Eq. (3) is fitted to experimental data. We shall present the results for kaolin-based ceramic cylindrical samples.

2. Experimental results

We measured the thermal conductivity of kaolin-based ceramics whose composition was 27 % of kaolin and clays, 50 % of Al_2O_3, and 23 % of feldspars. Each sample was cast in the shape of a cylinder of radius 8 cm. A thin kanthal wire of radius 4 mm was placed at the axis of the cylindrical samples and was used as the hot wire. In addition, a thermocouple was embedded parallelly with the wire at the distance 2 mm. After casting, the samples were let dry at the room temperature and then placed in a furnace [15-17]. The measure ments were performed at 18 different temperatures ranging from 20 °C to 650 °C that were reached by a linear heating with the rate 1 °C/min, guaranteeing that samples were not destroyed by intensive water evaporation.

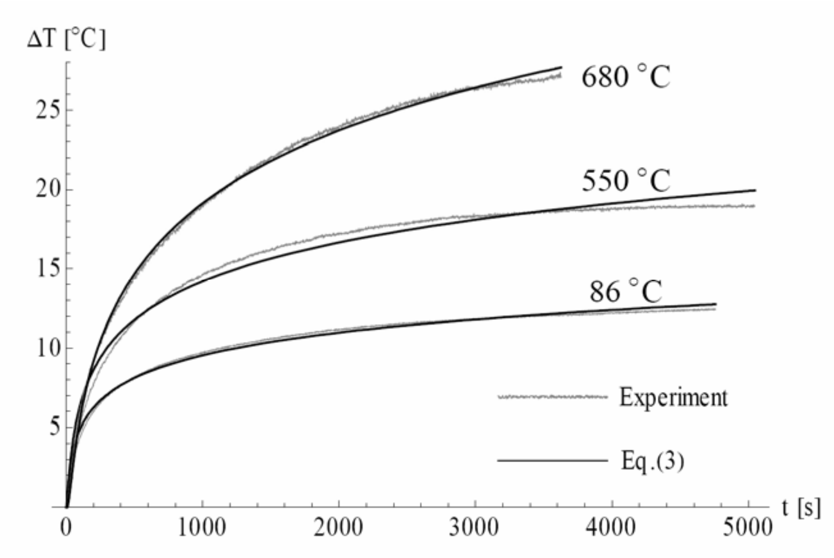

Figure 1: The temperature rise as a function of time for the temperatures 86 °C, 550 °C, and 680 °C (from bottom to top). The gray curves represent the experimental data, the black curves the fits obtained from Eq. (3).

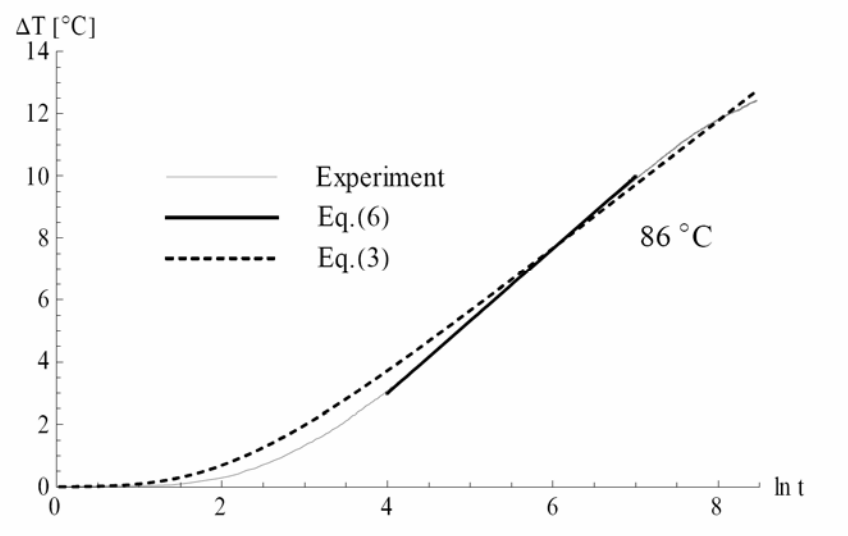

Figure 2: The temperature rise as a function of the logarithm of time for the temperature 86°C. The gray curve represents the experimental data, the black curve the fit obtained from Eq. (3), and the thick line segment the linear fit obtained from Eq. (6).

Upon reaching the required temperature, we first let the samples reach the temperature of the furnace within all of their volumes. The temperature inside the samples was determined by the thermocouple. After the temperature in the samples became steady, we applied a voltage from a stabilized source at the ends of the kanthal wire. The values of the wire voltage and current were measured by a multimeter. Besides applying the voltage at the wire ends, the voltage on the thermocouple was recorded at the same time, thus determining the temperature in the samples and its time evolution. The plots of the temperature rise vs. time are shown in Fig. 1 for the furnace temperatures 86 °C, 550 °C, and 680 °C. From these experimental data the plots of the temperature rise vs. the logarithm of time can be readily obtained (see Fig. 2).

3. Theoretical results and discussion

Using the experimental data from the hot wire method as described in the previous section, the thermal conductivity, λ, and thermal diffusivity, a, was calculated in two ways. First, we used the standard technique based on Eq. (6). Hence, we obtained the slope, A, and intercept, B, of the linear part of the dependence of the temperature rise, ΔT, on the logarithm of time. Namely, the values of A and B were calculated from the linear least square fits of the linear parts of the dependencies $\Delta T(\ln t)$. The end-points of the linear parts of these dependencies were identified to be ~4.0 and ~7.0, respectively (see Fig. 2). Having the values of A and B, we then applied Eq. (7) to evaluate λ and a. The results are shown in Figs. 3 and 4 (circles and dashed lines).

The second method (conveniently referred to as the alternative method in the following) of the measurement of λ and a is based on finding the best (non-linear) least square fit of the formula $\Delta T = C \times E_i(D/t)$ from Eq. (3) to the experimental plots of the temperature rise, ΔT, vs. time. From the values of the fitting parameters, C and D, one may obtain λ and a by applying the formulas

$$\lambda = -\frac{q}{4\pi C}, \quad a = -\frac{r^2}{4D} \tag{8}$$

following from Eq. (3). The results are also shown in Figs. 3 and 4 (squares and full lines).

As the plots in Figs. 3 and 4 show, the temperature dependencies of λ and a obtained by both the methods are basically monotonously decreasing. Nevertheless, they have two major descents. One takes place at ~100 °C and is related to the evaporation of physically bonded water (green ceramic samples contain about 1 % of physically bonded water). The other descent occurs at ~500 °C and is related to the dehydroxylation of kaolinite. Indeed, the basic crystallographic structure of kaolinite is composed of tetraedric layers of $[Si_2O_5]^{2-}$ alternating with octaedric layers of $[Al_2(OH)_4]^{2+}$ [18]. During dehydroxylation, kaolinite is changed into metakaolinite according to the chemical equation $Al_2O_3.2SiO_2.2H_2O$ ◎ $Al_2O_3.2SiO_2 + 2H_2O$. First signs of dehydroxylation occur at ~420 °C. The presence of defects in the structure of kaolinite affects the dehydroxylation temperature: the more defects there are, the more stable kaolinite is, leading to higher dehydroxylation temperatures [18].

Although the temperature dependencies of λ and a are basically similar for both above-mentioned methods of measurement, one clearly observes from Figs. 3 and 4 that the specific values of λ and a are for many temperatures rather different. One might argue that the alternative method should yield more accurate results for the single reason that it uses the whole time interval for fitting the experimental data, while the standard method uses only the time interval where the dependence of ΔT on $\ln t$ is linear, which in our case ranges between $\ln t$ ~ 4.0 and $\ln t$ ~ 7.0 (see Fig. 2). In other words, the standard technique uses only the data for times between ~55 s and ~1100 s. However, the performed measurements ended at between ~3600 s and ~7800 s. Therefore, in applying the standard method, one uses only 14 % to 30 % of all experimental data, which should cause inaccuracies in the corresponding results as compared to the alternative method Eq. (3).

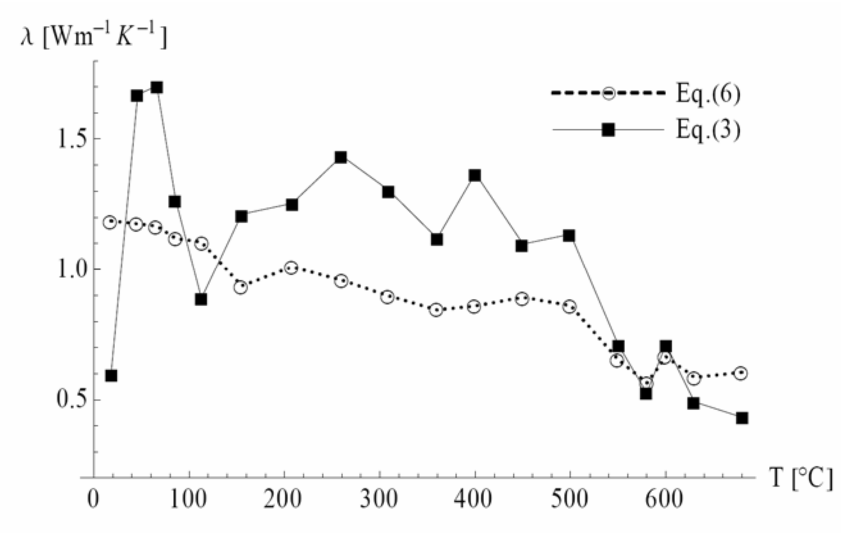

Figure 3: The temperature dependence of the thermal conductivity obtained from Eqs. (3) and (6).

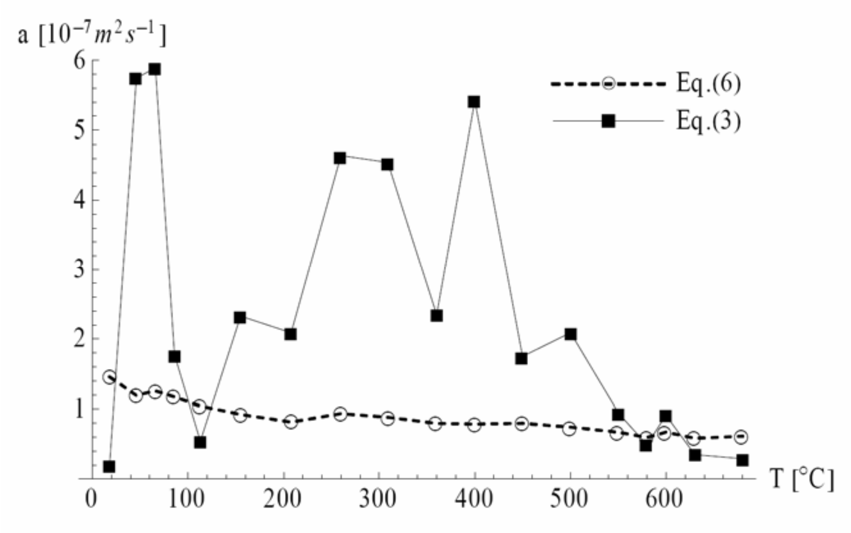

Figure 4: The temperature dependence of the thermal diffusivity obtained from Eqs. (3) and (6).

Nevertheless, it would be erroneous to conclude from this argument that the standard method is imprecise or improper for the measurement of thermal conductivity and diffusivity. Indeed, the standard method yields rather smooth dependencies of λ and a on the temperature, which is physically plausible, whereas the temperature dependencies of λ and a obtained by the alternative method are quite irregular and have several unexpected and inexplicable drops and rises that cannot be reasonably attributed to real physical or chemical processes that might take place in the samples as the temperature grows. In addition, the formula from Eq. (3) on which the alternative method is based predicts that the temperature rise, ΔT, increases to infinity as t ◎ ∞, and this is inconsistent with the experimental data. As a matter of fact, in deriving Eq. (3), various simplifications were adopted, and the most serious of these must be released in order that theory could well correspond to experiments. For example, finite dimensions of samples and wire or wire coating should be taken into account. However, then the corresponding set of equations can be usually solved only numerically [13,14] and the fitting to experimental data is a much more complicated procedure.

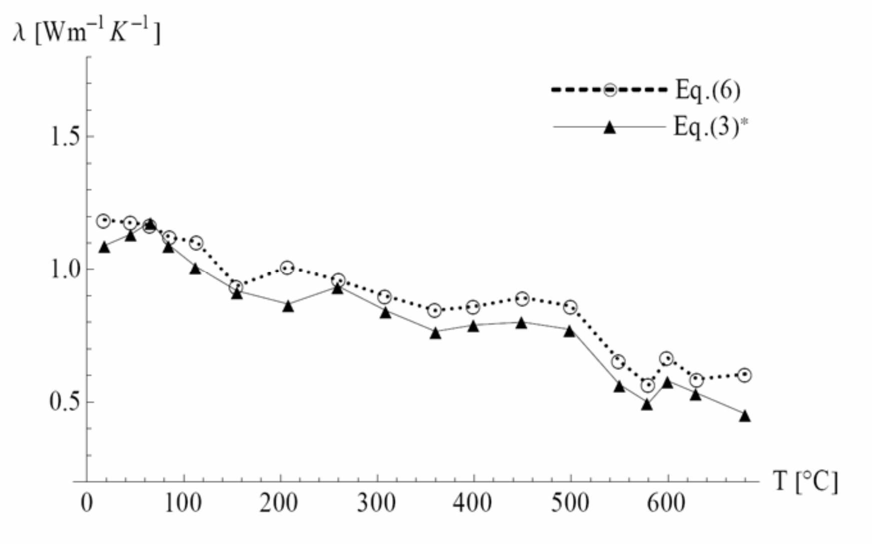

Figure 5: The temperature dependence of the thermal conductivity obtained from Eqs. (3) and (6) using only the experimental data for times less than exp(7.0) (indicated by a star).

Still, let us argue that the measurement of λ and a by the alternative method is not meaningless and may produce more reliable results than the standard method. However, to this end, it is necessary to modify the alternative method by considering only the times less than some upper limit, say, less than the upper end-point, t_u, of linear parts in ΔT vs. ln t plots; recall that t_u ~ exp(7.0) s ~ 1100 s (in fact, the use of the upper limit eliminates the effect of the finite sample dimension in both the standard and alternative methods). The corresponding results are given in Figs. 5 and 6 (triangles and full lines). Obviously, the modified alternative method produces values of λ and a that are much more smoother and in better correspondence with the results obtained by the standard method. More importantly, since only one end-point, t_u, needs to be identified (the other end-point being unambiguous – the initial time of measurement), the modified alternative technique should be more appropriate than the standard method in which two end-points must be identified. Therefore, it seems that the values of λ and a obtained from the modified alternative method and shown in Figs. 5 and 6 are more accurate than the values obtained by the standard method.

4. Conclusion

We measured thermal conductivity, λ, and diffusivity, a, by the hot-wire method, using Eq. (6) (the standard method) and Eq. (3) (the alternative method) to fit experimental data

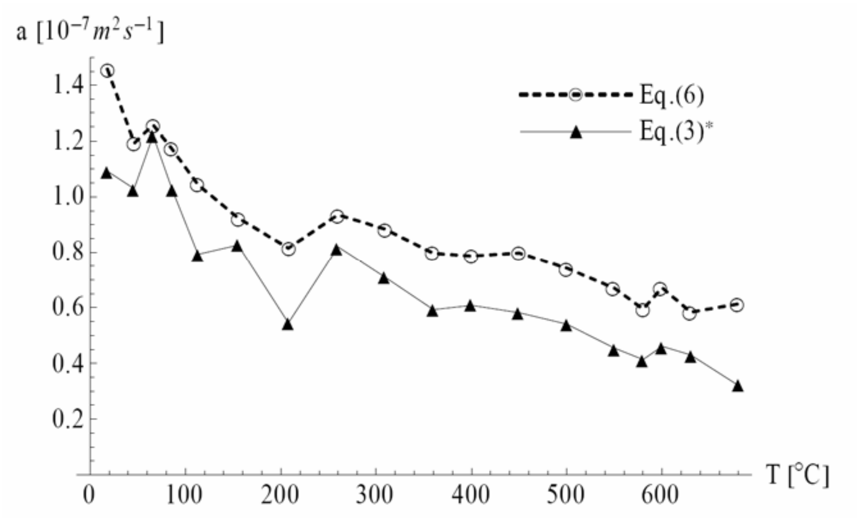

Figure 6: The temperature dependence of the thermal diffusivity obtained from Eqs. (3) and (6) using only the experimental data for times less than exp(7.0) (indicated by a star).

on the time dependence of the temperature rise, Δ*T*, inside kaoline-based ceramic samples of cylindrical shapes. We argued that the alternative method is more suitable and reliable than the standard method, provided one restricts himself to times less than the time, t_u, up to which the Δ*T* vs. ln *t* plot shows linear dependence (t_u ~ exp(7.0) s ~1100 s in our case). The reason for such a conclusion was that while the alternative method requires the identification of just a single time instant (t_u), the standard method requires the identification of one more time instant besides t_u, thus leading to more inaccurate results. Moreover, the alternative method (with the upper time limit restriction) is much more easier to apply than the more involved numerical methods that include correction with respect to finite dimensions of samples and wire or with respect to the hot-wire coating.

Acknowledgement

This work was supported by the project VEGA 1/0302/09, APVV SK-CZ-0004-09, UGA VI/7/2010, the FCVV grant I-06-399-01, and by the Ministry of Education, Youth and Sports of the Czech Republic, under the project No. MSM: 6840770031.

References

[1] HEALY, J. J.; de GROOT, J. J.; KESTIN, J. The theory of the transient hot-wire method for measuring thermal conductivity. In *Physica B+C*. 1976. 82(2). p. 392-408.

[2] WAKEHAM, W. A.; NAGASHIMA, A.; SENGERS, J. V. eds. *Experimental thermodynamics. Vol. III Measurements of the transport properties of fluids.* Blackwell Scientific Publications, London, 1991. ISBN 0-632-02997-8

[3] YU, F.; ZHANG, X.; GAO, G. Thermal Conductivity Measurement of Semitransparent Solids by Hot-Wire Technique. In *International Journal of Thermophysics*. 2000. 21(2). p. 465-478. ISSN 0195-928X

[4] ZHANG, X.; FUJII, M. Simultaneous Measurements of the Thermal Conductivity and Thermal Diffusivity of Molten Salts with a Transient Short-Hot-Wire Method. In *International Journal of Thermophysics*. 2000. 21(1). p. 71 – 84. ISSN 0195-928X

[5] ASSAEL, M. J.; DIX, M.; GIALOU, K.; VOZAR, L.; WAKEHAM, W. A. Application of the transient hot-wire technique to the measurement of the thermal conductivity of solids. In *International Journal of Thermophysics*. 2002. 23(3). p. 615-633. ISSN 0195-928X

[6] WATANABE, H. Further examination of the transient hot-wire method for the simultaneous measurement of thermal conductivity and thermal diffusivity. In *Metrologia*. 2002. 39(1). p. 65-81. ISSN 0026-1394.

[7] ZHANG, X.; HENDRO, W.; FUJII, M.; TOMIMURA, T.; IMAISHI, N. Measurements of the Thermal Conductivity and Thermal Diffusivity of Polymer Melts with the Short-Hot-Wire Method. In *International Journal of Thermophysics*. 2002. 23(4). p. 1077 – 1090. ISSN 0195-928X

[8] ASSAEL, M.J.; GIALOU, K. A Transient Hot-Wire Instrument for the Measurement of the Thermal Conductivity of Solids up to 590 K. In *International Journal of Thermophysics*. 2003. 24(3). p. 667-674. ISSN 0195-928X

[9] BILEK, J.; ATKINSON, J.K.; WAKEHAM, W.A. Repeatability and Refinement of a Transient Hot-Wire Instrument for Measuring the Thermal Conductivity of High-Temperature Melts. In *International Journal of Thermophysics*. 2006. 27(6). p. 1626 – 1637. ISSN 0195-928X

[10] XIE, H.; GU, H.; FUJII, M.; ZHANG, X. Short hot wire technique for measuring thermal conductivity and thermal diffusivity of various material. In *Measurement Science and Technology*. 2006. 17(1). p. 208–214. ISSN 0957-0233

[11] RUSCONI, R; et al. Numerical Analysis of Convective Instabilities in a Transient Short-Hot-Wire Setup for Measurement of Liquid Thermal Conductivity. In *International Journal of*Thermophysics. 2007. 28(4). p. 1131-1146. ISSN 0195-928X

[12] ASSAEL, M.J.; ANTONIADIS, K. D.; KAKOSIMOS, K. E.; Metaxa, I. N. An Improved Application of the Transient Hot-Wire Technique for the Absolute Accurate Measurement of the Thermal Conductivity of Pyroceram 9606 up to 420K. In *International Journal of Thermophysics*. 2008. 29(2). p. 445–456. ISSN 0195-928X

[13] WOODFIELD, P. L.; FUKAI, J.; FUJI, M.; TAKATA, Y. An accelerated two-dimensional unsteady heat conduction calculation procedure for thermal-conductivity measurement by the transient short-hot-wire method. In *International Journal of Thermophysics*. 2009. 30(3). p. 796-809. ISSN 0195-928X.

[14] LIANG, X.-G. The boundary induced error on the measurement of thermal conductivity by transient hot wire method. In *Measurement Science and Technology*. 1995. 6(5). p. 467-471. ISSN 0957-0233.

[15] VOZÁR, L. A computer-controlled apparatus for thermal conductivity measurement by the transient hot wire method. In *Journal of Thermal Analysis. Vol. 46*. 1996. p. 495-505. ISSN 1388-6150.

[16] ŠTUBŇA, I.; TRNÍK, A.; VOZÁR, L. Thermomechanical analysis of quartz porcelain in temperature cycles. In *Ceramics International*. 2007. 33(10). p. 1287-1291. ISSN 0272-8842.

[17] ŠTUBŇA, I.; TRNÍK, A.; VOZÁR, L. Thermomechanical and thermodilatometric analysis of green alumina porcelain. In: *Ceramics International*. 2009. 35(3). p. 1181-1185. ISSN 0272-8842.

[18] ŠTUBŇA, I.; TRNÍK, A.; VARGA, G. Dehydroxylation of kalolinite – a brief overview. In *Silika*. 2006. 16(3-4). p. 67-69. ISSN 1213-3930. (In Slovak)

Measuring regime and accuracy of the transient hot-ball method

Ľudovít Kubičár[1], Ulf Hammerschmidt[2] , Danica Fidriková[1], Peter Dieška[3], and Viliam Vretenár[1]

[1]Institute of Physics SAS, Dubravska cesta 9, 845 11 Bratislava, Slovakia, kubicar@savba.s,

[2]Physikalisch-Technische Bundesanstalt, Bundesallee 100, 38116 Braunschweig, Germany

[3]Faculty of Electrical Engieneering and Information Technology STU, Ilkovičová 3, 81219 Bratislava, Slovakia

Abstract: *The report discusses the principle of the hot ball sensor for measuring the thermophysical properties of solids and liquids. The operation is based on a ball-shaped sensor that delivers heat in a stepwise regime to the surrounding material. The ball surface temperature is a measure of the thermophysical properties of the surrounding material under test. Depending on the specific evaluation technique, either the thermal conductivity or specific heat or thermal diffusivity and thermal conductivity can be determined. Both evaluation techniques here dealt with are based on an ideal model of heat conduction.They strongly depend on a proper choice of the corresponding time interval of the temperature response. Fitting and approximation procedures were used for final data evaluation. Measuring regime and evaluation procedures are tested on distilled water and glycerol. Both, the sensor radius and the known thermal diffusivity are parameters that indicate the reliability of the measuring method.*

Keywords: *transient method, hot-ball method, thermophysical parameters, thermophysical sensor*

1. Introduction

During the last years, a lot of different types of thermophysical sensors operating in transient mode have spread into research laboratories as well as in industry. Among them, the most frequently used thermophysical sensors can be grouped into the hot disc [1], hot bridge [2] and hot-ball [3] techniques. Depending on sensor geometry and measuring regime, the thermal conductivity, thermal diffusivity and specific heat can be determined simultaneously. In contrast to steady-state instruments, thermophysical sensors can work with "infinite" specimens: this is important for in-situ monitoring of objects where the sensor can be embedded inside an entire construction unit, e.g., a block of concrete. The measuring process runs as follows: after having ensured that the monitored object is in thermodynamic equilibrium, the sensor generates a small amount of heat. Simultaneously, the temperature response of the material under test is measured, typically by the same sensor. From the stimulus and the response, the thermophysical properties can be determined according to an appropriate mathematical model. The stimulus is kept small enough not to significantly perturb the actual thermodynamic equilibrium.

This report deals with the analysis of the measuring regime of the hot-ball sensor and its accuracy. Hot ball sensors are very versatile because of their small size and thus, especially suited for measurements inside „infinite" specimens.

2. Principle of the hot-ball method

A simple model of the hot-ball sensor is shown in figure 1 (left). The sketch depicts an infinite medium in which an empty sphere of radius r_0 is placed arbitrarily. At $t = t_0 = 0$, a constant rate of heat flow q is generated inside the sphere. For times $t > t_0$, the heat penetrates through the sphere's surface into the surrounding medium. The temperature of the hot-ball thus rises in time according to the curve given in figure 1 (center). During this measuring period, the heat further penetrates through the material up to a volume of radius R (see figure.1). As can be seen from the diagram, the temperature signal consists of a transient and a steady-state interval of temperature $T = T_m$. Both different regions can be used for data evaluation. From the initial transient period, thermal conductivity, specific heat and thermal diffusivity can be determined. From the transient period, just thermal conductivity can be deduced.

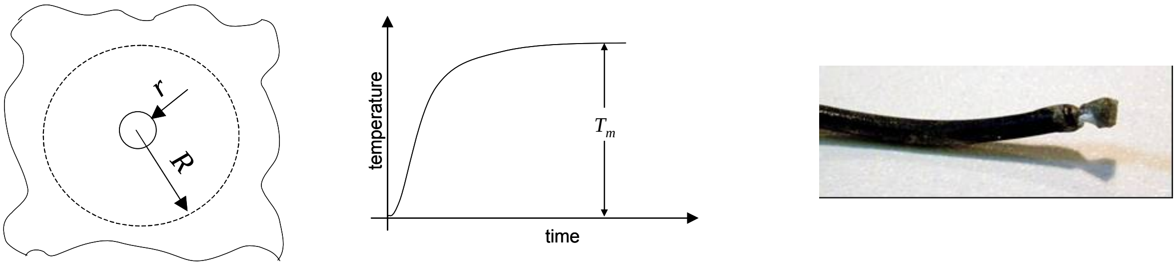

Figure 1.: Principle of the hot ball sensor (left), signal of the sensor (center) and photo of the sensor (right).

The structure of a hot-ball sensor consists of a heater and a thermometer. These two devices are glued together to give the sensor a shape most similar to a ball (figure 1 right). Drawbacks of a hot-ball sensor are (1) unavoidable deviations from a perfect ball shape can influence the transient period of the sensor signal [1] and (2) to reach the steady-state period can take a long time, especially, when used with poor conducting specimens.

3. Theory of the hot-ball sensor

There are several slightly different theoretical models to mathematically represent a real hot ball sensor [3]. Here, we begin with an analysis of the most simple ideal model to find deviations of the ideal and the real measurement signal. In the ideal model, the function characterising the temporal temperature $T = T(t, r_0)$ of the surface of an empty ball (figure 1 left) reads

$$T(t, r_0) = T_0\left[1 - \exp(u^2)\Theta^*(u)\right] \tag{1}$$

where

$$T_0 = \frac{q}{4\pi r_0 \lambda}, \quad u = \frac{\sqrt{at}}{r_0}$$

and λ and a are thermal conductivity and thermal diffusivity, respectively. $\Theta^*(u)$ is the complementary error function. Equation can be derived from the partial differential equation governing heat conduction and by further considering the initial condition $T(0, r) = 0$

and the boundary condition

$$-\lambda \frac{\partial T}{\partial r}_{r=r_0} = ql(t) .$$

When time tends to infinity, $t \to \infty$, equation (1) reduces to its steady-state value

$$T_m = \frac{q}{4\pi r_0 \lambda} . \tag{2}$$

Rearranging the latter equation yields the working equation of the hot-ball sensor

$$\lambda = \frac{q}{4\pi r_0 T_m} . \tag{3}$$

This result is often called the working equation of the thermal-conductivity sensor.

There are two different evaluation strategies for a hot-ball signal (see Figure 1 (middle)), namely, a fitting procedure based on function (1) to be applied over the entire monitored temperature response or the direct use of working equation (3) for the steady-state regime only. The fitting procedure is based on the determination of a time window to be taken out of the temperature response where, on the one hand, enough high sensitivity coefficients of thermophysical properties should exist and, on the other hand, where the construction parameters of the sensor (e.g., deviations from perfect ball-shape) do not significantly influence its temperature response. As is mostly the case, the latter perturbations occur during the initial period of a run. Both strategies require the further knowledge of the radius of the sensor, r_0. This parameter suffers from a relatively large uncertainty due to the details of construction (see figure 1 right). That is why, a thorough calibration procedure based on equation (1) or (3) has to be used to obtain r_0 by the help of a fitting scheme. This calibration is performed with the sensor immersed in a wetting standard liquid like distilled water or glycerol to avoid any contact thermal resistance between the sensor and the ambient medium. As an alternative to equation (1), one can apply an approximation based on a series expansion of the equation mentioned. This procedure avoids the use of the complementary error function

$$T(t, r_0) = \frac{q}{4\pi r_0 \lambda} - \frac{q}{4\pi^{3/2} \lambda} . \frac{1}{\sqrt{at}} + \ldots \tag{4}$$

A plot of $T(t, r_0)$ vs. $(1/\sqrt{t})$ and the subsequent extrapolation of $1/\sqrt{at} \to \infty$ furnishes the unknown sensor radius r_0.

4. Experiment

Two different liquids, water and glycerol, were used for the analysis of the size of the measuring and evaluation regimes. The material properties of these liquids are given in Table 1. A hot-ball of type RTM 1.01 (Transient MS) was taken for the measurements. All runs were realized in measuring cycles, each at room temperature and normal atmospheric condition. Every cycle comprises (1) measurement of the initial temperature, (2) applying a constant rate of heat flow and (3) scanning the temperature response of the sensor. A series of runs was obtained for each liquid. In between times, a 30 minutes repetition rate was complied with. Measuring parameters for every fluid are given in Table 2.

Table 1: Thermophysical data of certified fluids at 25 °C

Fluid	**Density** **[kg m^{-3}]**	**Thermal conductivity** **[W m^{-1} K^{-1}]**	**Thermal diffusivity** **[mm^2 s^{-1}]**	**Specific heat** **[J kg^{-1} K^{-1}]**
Distilled water [4]	1000	0.58	0.14	4184
Glycerol [4]	1257.7	0.29	0.0952	2381

Table 2: Parameters of measurement

Parameter	**Distilled water**	**Glycerol**
Heat output [mW]	1.645	2.82
Measuring period [s]	96	496
Number of scanned points	24	31

5. Results and Discussion

All evaluated data are given in Table 3. Radius and thermal diffusivity were found from fit procedures. The time window for the fits was chosen to start at the third data point and end with each heating period. The difference in the position of the time window is demonstrated in second and third row of Table 4.

Table 3: Measuring Results

Parameter	**Distilled water**	**Glycerol**
Sensor radius from fitting [mm]	0.893	1.36
Thermal diffusivity from fitting [mm^2 s^{-1}]	0.201	0.176
Average fitting error [%]	0.23	0.16
Sensor radius from approximate procedure [mm]	0.851	1.27

Here, the second row shows fit results that correspond to the entire run time. In the third row, results are presented where several points from the beginning of the temperature response were omitted. These points are strongly influenced by imperfect sensor properties. Clearly, the results are significantly better for the latter case. Data of the first row are shifted for the case when the time window for a fit is localized between the first data point and the end of heating. Any cycle number corresponds to data shown in the first row of the 'stable data region'. Results found by fitting and by approximation according to equation (4) are given in Table 3 (distilled water: cycle number 99, glycerol: cycle number 38 (see Table 4)).

Though, due to construction imperfections, the sensor radius is not constant (see figure 1 right) we estimate this value to be approximately 1.1 mm. Both the approximation and the fitting give values that are near to the real radius. Discrepancies in sensor radius and individual values of thermal diffusivity of the liquids have to be ascribed to deviations between the ideal model and the real construction of the sensor. Clearly, a more realistic model has to be considered.

Table 4: Fitted parameters for different time windows

Distilled water	Glycerol
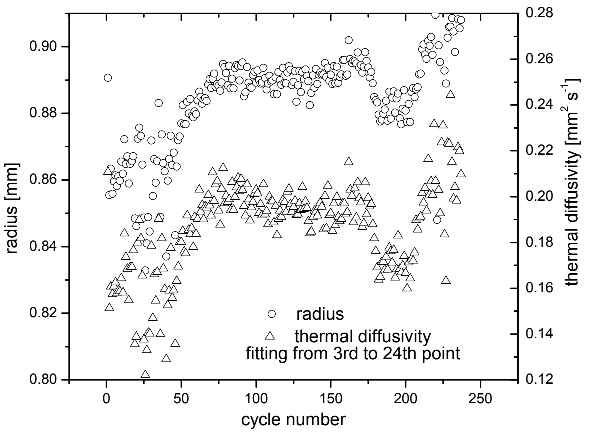	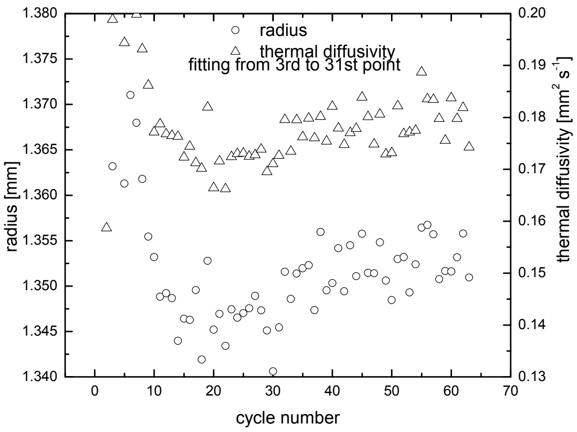
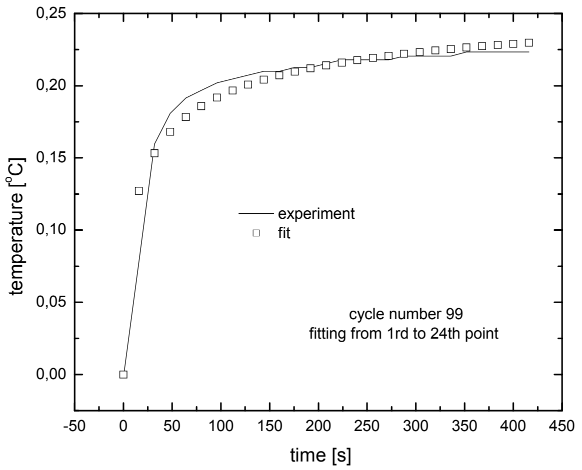	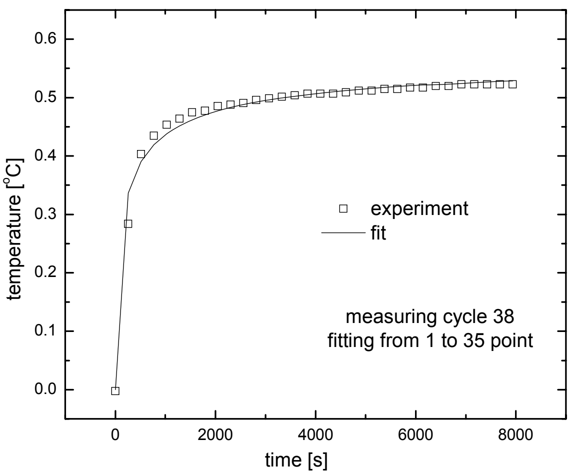
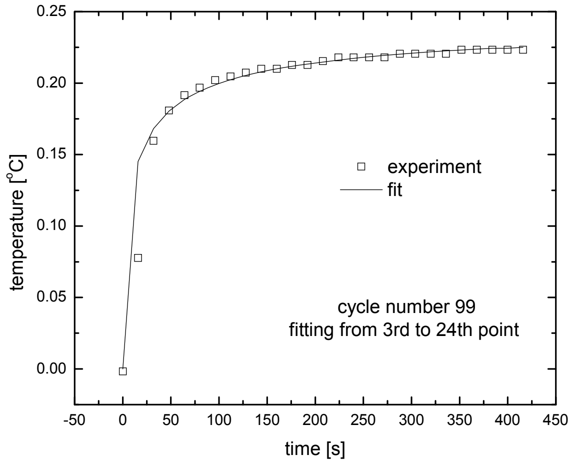	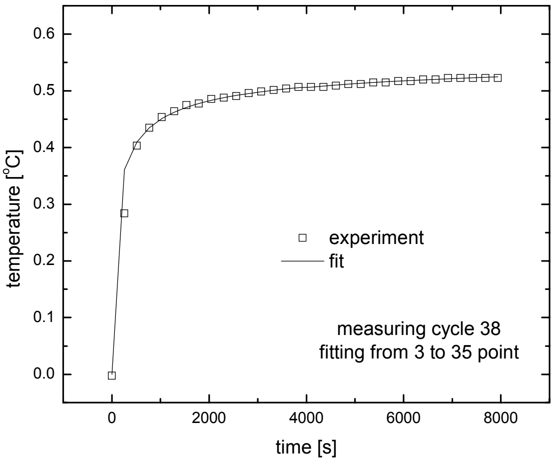

Acknowledgement

This work has been supported by APVV projects LPP-0442-09 and APVV-0497-07.

References

[1] Gustafsson S E, 1991, Rev. Sci. Instrum. 62, 767 - 804

[2] Hammerschmidt U and Sabuga W, 1995 Int. J on Thermophysics 21 1255 - 1278

[3] Ľ. Kubičár, V. Vretenár, V. Štofanik, V. Boháč: Hot-ball method for measuring thermal conductivity, Int. J. Thermophysics, DOI 10.1007/s 10765-008-0544-4

[4] http://scholar.lib.vt.edu/theses/available/etd-12698-1093/unrestricted/dissall.pdf

Resistance of concrete with added metakaolin to salt scaling

Petr Máca, Dagmar Jandeková, Petr Konvalinka

Faculty of Civil Engineering, Czech Technical University in Prague, Thákurova 7,

166 29 Praha, Czech Republic, email: petr.maca@fst.cvut.cz

***Abstract**: The resistance of high performance concrete to salt scaling was studied in this experimental work. In the concrete mixtures 10% by weight of cement was replaced by metakaolin. The salt-scaling resistance of high performance concrete with metakaolin was compared both to normal concrete and air-entrained concrete. It was found, that the resistance of concrete that contained metakaolin was better compared to normal concrete but worse compared to air-entrained concrete. In addition, during the experimental work, it was found that the state of the surface layer has critical influence on the results of the scaling test. The samples where the surface of fresh concrete was brushed to simulate field conditions performed an order of magnitude worse than samples with soft surface.*

***Keywords**: salt-scaling, metakaolin, HPC, surface treatment*

1. Introduction

Concrete is one of the most extensively used construction materials in the world, with two billion tons placed worldwide each year [1]. One of the great advantages of concrete is that it is extremely versatile and can be casted into variety of structural configurations and shapes. It is also resistant to water and chemically inert in comparison with other structural materials such as metals or polymers. Unfortunately there are several disadvantages of conventional concrete such as low resistance to frost and de-icing chemicals. These durability properties are very important especially in highway and bridge construction. For instance in the United States the National Research Council estimates that repair of the infrastructure costs nearly $50 billion annually [2].

This paper is focused on the studying of the effect of metakaolin (MK) on the durability of concrete. Metakaolin is a reactive aluminosilicate *pozzolan* formed by calcining purified kaolinite at a temperature range between 600 and 800 °C in a controlled manufacture process. Therefore, it does not contain impurities like other artificial pozzolans. Many researchers [3, 4, 5] believe that high reactive metakaolin has similar positive effects on concrete as micro silica fume (SF) and can be used in formulation of new generation of high performance concretes (HPC) [6]. The properties of such HPC, especially its resistance to salt scaling due to the application of de-icing chemicals were studied in this experimental work.

The salt scaling is defined as superficial damage caused by freezing a saline solution on the surface of a concrete body. This damage is progressive and nearly linearly dependent on the number of F-T cycles. It consists of the removal of small chips or flakes of material [7]. In contrary to conventional freezing and thawing salt scaling does not jeopardize the mechanical integrity of a concrete microstructure. However, this type of damage diminishes cover of steel reinforcement, leads to the formation of surface microcracks and can accelerate corrosion of concrete by aggressive species that threaten overall durability of concrete. Moreover it is not aesthetically pleasing because it often results in exposure of coarse aggregate.

2. Materials

This paper describes the investigation of the resistance of HPC with added metakaolin to salt scaling due to de-icing chemicals. In the concrete mix design (Tab. 1) ten percent by weight of cement (CEM I 42,5R Mokrá) was replaced by commercially available metakaolin from two producers Keramost (KM40) and ČELUZ (Mefisto K05), respectively. The ten percent cement replacement level was chosen based on the literature research [4] and [3] and previous experience.

Table 1: Concrete mixture

	Air-entrained concrete	Concrete with metakaolin	Concrete with metakaolin
Notation:	**Control**	**KM 40**	**M 05**
Components	Quantity in [kg/m^3]		
CEM I 42,5 R Mokrá	440	400	400
Metakaolin	N/A	40	40
Fine agg. 0-4	795	795	795
Coarse agg. 4-8	315	315	315
Coarse agg. 8-16	670	670	670
Superplasticizer (Stachement 2090)	4.18	5.5	4.4
Air-entrainer	2,42	N/A	N/A
Water	177	177	177
w/b[3] ratio	0.4	0.4	0.4
Air content[4]	5.8	1.7	1.6

The concrete was designed to satisfy C 50/60 concrete class requirements. The consistency of the fresh concrete was given by flowability around 60 cm as defined in ČSN EN 12350-5 [8]. To comply with these requirements, it was necessary to increase the superplasticizer dosage by 0.3% for concerte containing metakaolin.

---

[3] w/b (water/binder ratio) is a ratio between water and binder (cement+pozzolan).

[4] Determined by following ČSN EN 12350-7 – pressure method.

Experimental Procedure

The scaling resistance of concrete was measured according to ČSN 73 1326/Z1 – Method C: Automated Cycling [9] with several modifications undertaken from ASTM C 672M [10]. However, these changes in experimental procedure and especially in the preparation of the specimens proved to have major influence on the results and are discussed in more detail in the next chapter.

The specimens were casted in plastic round moulds with the diameter of 150 mm and height of 50 mm. All fabrication procedures of the specimens were carried out in accordance with ČSN EN 12350-1, ČSN EN 12390-1 and ČSN EN 12390-2. The top surface of the fresh concrete in the mould was levelled with sawing-motion of a steel strike-off board. Afterwards the surface was brushed with medium-stiff brush as a final finishing operation. This type of finishing is not included in the ČSN 73 1326/Z1 [9] and was used only for the first series of specimens. The second series was levelled just by short vibration and the surface was left intact. At the age of 28 days, rubber band was glued onto its circumference and fastened with a steel sleeve to ensure impermeable connection. The schematic of specimen prepared for scaling test is shown in Figure 1. After the specimens were prepared a 3 mm layer of water at 20 ± 2°C was poured on the test surface. It was found that 58 ml of water gives approximately 3 mm thick layer. This pre-wetting condition lasted for 24 hours.

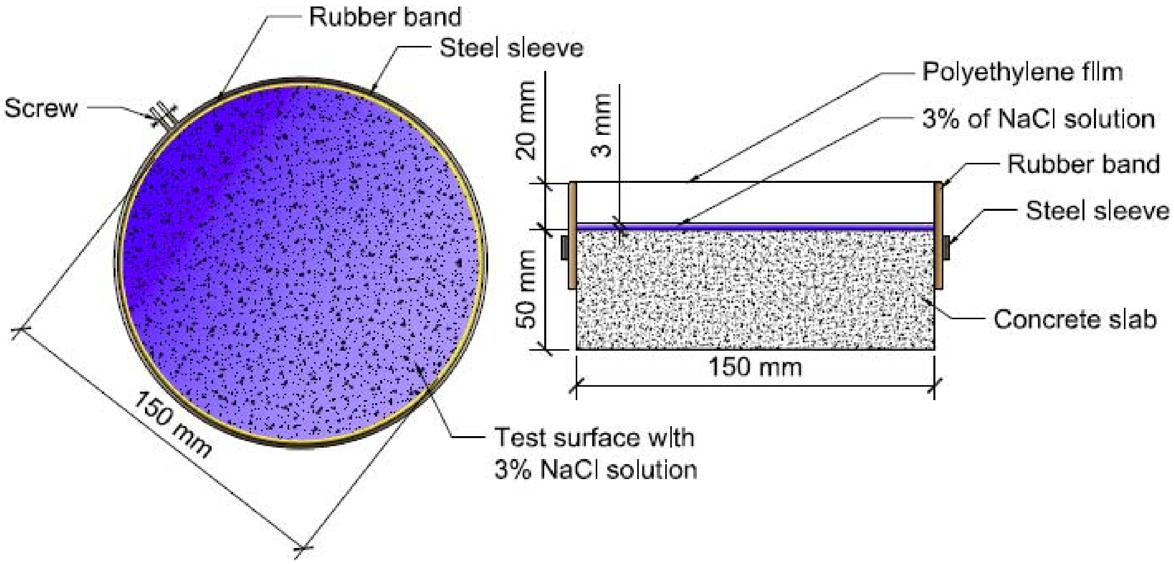

Figure 1: Setup of the scaling test.

After the pre-wetting the water was removed and a 58 ml of 3% by mass solution of NaCl was poured on the test surface. To prevent evaporation of the solution the specimen was covered by polyethylene film (cling film) as shown in Figure 1. The specimens were placed randomly into climatic chamber Weiss WT3 600/40 and were subjected to repeated freezing and thawing. Temperature was continuously monitored throughout the experimental procedure in the middle of the chamber. The freezing period lasted 3 hours at -18°C and the thawing phase lasted 3 hours at the temperature of 5°C. A good air-circulation was provided by massive fan in the chamber and lots of space between specimens. After every 24 cycles, that is 6 days, the specimens were taken out from the chamber and the amount of scaled concrete was measured.

This was repeated until 120 cycles were reached. The resistance of concrete against de-icing chemicals after n cycles was expressed as the mass of scaled-off material on the unit area following equation:

$$\rho_n = \frac{\sum_0^n m_n}{A} \tag{1}$$

where ρ_n is the mass of scaled material [g/m²], $\sum_0^n m_n$ is the summation of all masses of scaled material until n-th cycle [g], A is the area of the test surface exposed to de-icing medium.

3. Results

The results of the experimental work are shown in Figure 2 as a cumulative curve of scaled material recalculated on 1 m² (Eq. 1) against number of cycles. According to ČSN 73 1326/Z1 [9] the concrete is resistant to scaling when the mass of cumulative scaled material is lower than 1000 g/m² (shown as a dashed line in Fig. 4). The number of cycles when the cumulative curve intercepts this threshold is called the D1 criterion and is shown as a red number in Figure 2.

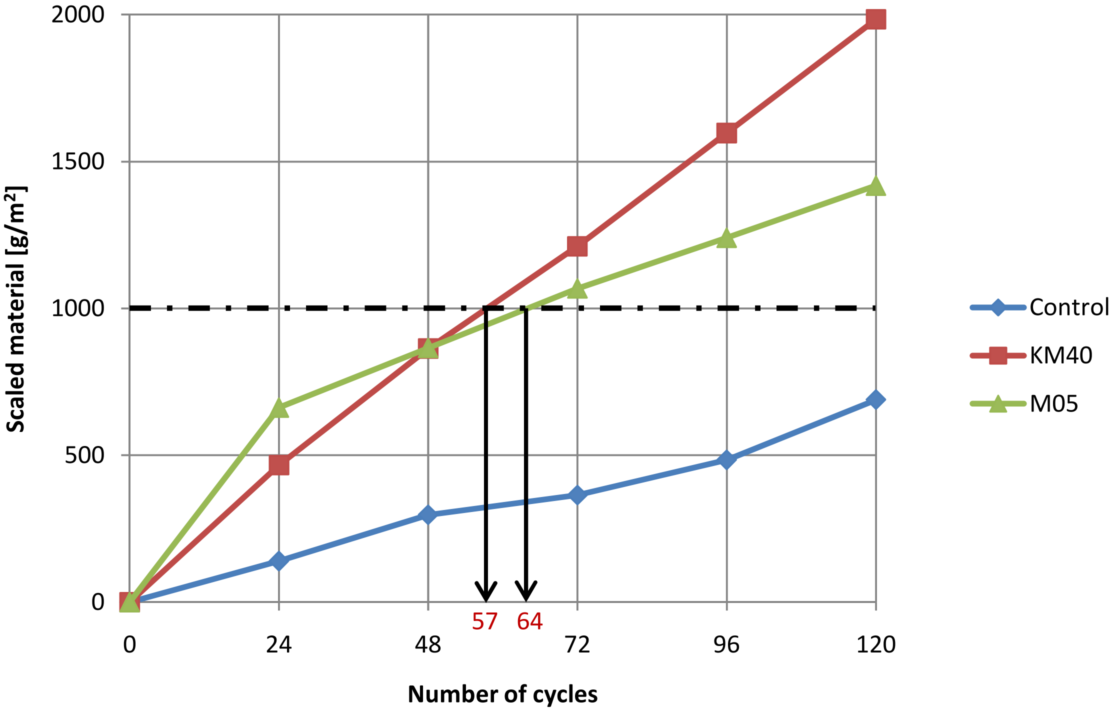

Figure 2: Mass of scaled material against number of F-T cycles. The results are average from four measurements.

The scaling residues for air-entrained concrete were relatively low and the cumulative mass of scaled material did not reach the D1 criterion. Therefore, based on this set of results only air-entrained concrete can be considered as resistant against salt scaling. However, this is nothing surprising and was intended from the beginning of the experiment. What was highly surprising was the extremely bad performance of concrete with added metakaolin. This experiment was designed based on previous experimental work done at Czech Technical University [11] using similar metakaolins where the authors reported scaling residues an order of magnitude lower to those measured in this experimental work. For this reason, air-entrained concrete was chosen as reference and it was still expected that concretes with metakaolin would perform better.

It is also important to mention that the results presented in Figure 2 are an average from four measurements. However, the variance for specimens with metakaolin KM40 was nearly 50% which indicates that the quality of surface was for every specimen different and was highly influenced by the surface treatment of the fresh concrete. According to Dohnálek *et al.* [12] the usual variance for this type of test is from 20 to 30%. Figure 3 shows the state of the surface layer of the specimens with metakaolin after 0; 24 and 120 cycles.

Figure 3: State of the surface layer after 0; 24 and 120 cycles for concrete with added metakaolin.

Before discussing the results in detail, there are several important facts that need to be mentioned. The standard ČSN 73 1326 [9] does not clearly specify surface treatment of the specimens. In this experimental research the surface was after casting into moulds brushed with moist medium-hard brush to simulate field conditions. During the highway construction the surfaces of carriageways are roughened by the finisher to improve adherence of the vehicles. This surface treatment is normally used in American version of the test [10].

4. Discussion

To be able to identify the large difference between the results reported in this paper compared to those presented by other researchers at CTU [11] four changes in boundary conditions that could influence the results were identified:

1. Specimens used in this research had w/b ratio of 0.4 compared to w/b ratio of 0.36 that was used in the previous work [11].
2. Different climatic chamber and testing equipment was used that allowed faster temperature changes resulting in greater temperature gradients.
3. The surface of fresh specimen was modified with a moist brush.
4. The laboratory and the operator were different.

After performing additional tests, it was found that the influence of the surface treatment of the specimens proved to be absolutely critical with respect to the results. For this purpose, a second series of specimens with same mixture composition as KM40 was prepared. The surface of the specimens in this second series was left intact, whereas surfaces of the fresh concretes from the first series were brushed with moist medium-hard brush to simulate in-situ conditions.

The influence of the surface treatment on the results of salt-scaling is shown in

Figure 4. In addition, 30% error bars are shown in Figure 4 to highlight that the differences in the results are statistically significant. At first glance it is apparent that the cumulative mass of scaled material after *N* cycles is an order of magnitude larger for specimens from the first series with brushed surface compared to specimens with intact surface. The results of the specimens with intact surface were close to results reported by other authors [11, 13] who used similar concrete mixture designs with 10% of added metakaolin. Because the standard ČSN 73 1326 [9] is not specific about the surface treatment it can be expected that the surface was left intact as was done in the second series in this experimental work.

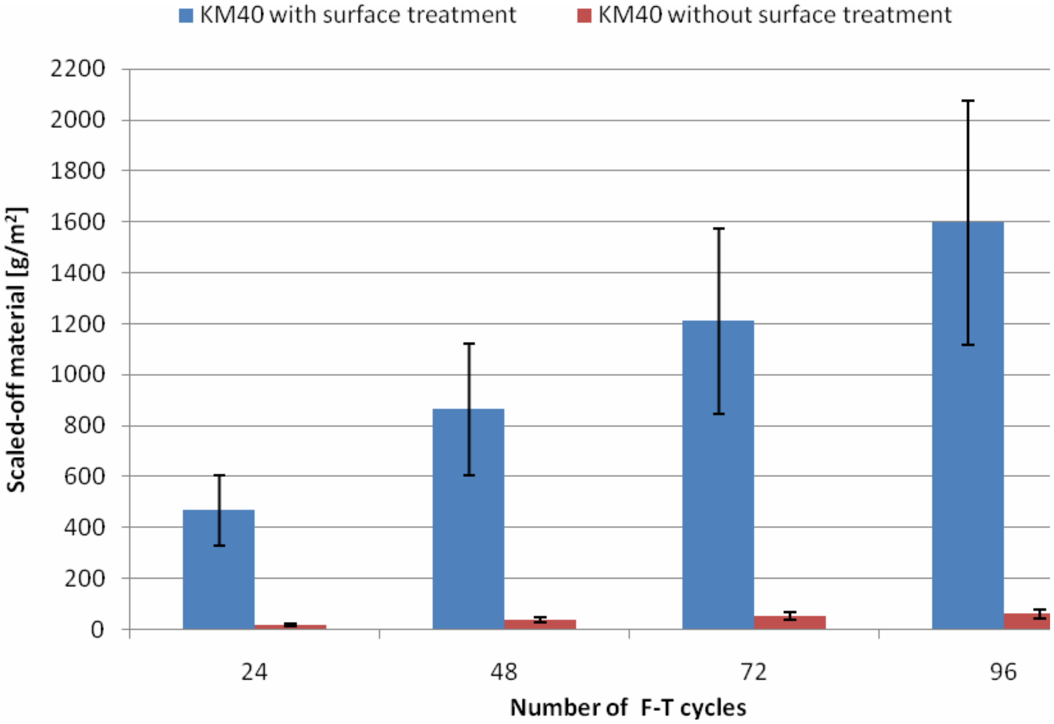

Figure 4: The influence of surface treatment on salt-scaling results. Both mixtures have exactly the same design and testing procedure – only the surface changed.

5. Conclusion

The scaling test results proved that air-entrainment definitely improves the resistance of concrete against scaling due to de-icing chemicals. The effect of metakaolin is contradictory and needs to be investigated in more detail. When the top surface of the fresh concrete was treated by brushing the results of hardened MK-blended concretes were unsatisfactory. However, when the surface was left intact, the performance of concretes with added metakaolin was exceptionally good, which was also supported by other researchers studying similar concrete mixtures. This leads to the conclusion, that the strength of the surface layer is absolutely critical to the scaling test results.

To explain why the strength of the surface layer changes during brushing four possible reasons were suggested, all of them connected with decrease of the strength of the surface layer.

1. Brushing significantly increases specific surface of the specimen.
2. When brushing, more water is introduced to the surface, which leads to local increase in w/b ratio.
3. Fines from the surface are brushed away.
4. Exposure of coarse aggregate that is possibly not frost resistant.

The reasons stated above are probably not exhaustive and possibly other reasons can be argued. With high degree of probability, the influence of the surface treatment is caused by the combination of the above factors. It has been suggested that more extensive research needs to be employed in this area. It is also not clear if this phenomenon is applicable for normal concretes or only for concretes with added metakaolin. Other important factors influencing this experiment are: specimen preparation and handling, curing procedures and bleeding. These and many more factors need to be investigated in further work.

Acknowledgement

This research was supported by the Ministry of Industry and Trade of the Czech Republic under the project №: 6840770031 and Student Grant Competition on CTU in Prague under the project №: 802320. Author would like deeply appreciate his supervisor prof. Ing. Petr Konvalinka, CSc. for his exceptional guiding skills and outstanding support.

References

[1] MINDESS, S.; YOUNG, J. F. and DARWIN, D.; Concrete, 2. Ed. Upper Saddle River, NJ: Prentice Hall, 2003. ISBN 0130646326.

[2] Infrastructure,Committee on Nonconventional Concrete Technologies for Renewal of the Highway; Nonconventional Concrete Technologies: Renewal of the Highway Infrastructure (Compass Series) National Academies Press, 03-25, 1997. ISBN 030905687X.

[3]. ZHANG, M. H.; and MALHOTRA, V. M. Characteristics of a Thermally Activated Alumino-Silicate Pozzolanic Material and its use in Concrete. Cement and Concrete Research, 12, 1995, vol. 25, no. 8. pp. 1713-1725. ISSN 0008-8846.

[4] CALDARONE, M.; GRUBER, K.and BURG, R. High-Reactivity Metakaolin a New Generation Mineral Admixture. , 01/01, 1994.

[5] GLEIZE, J. P.; CYR, Martinand ESCADEILLAS, Gilles. Effects of Metakaolin on Autogenous Shrinkage of Cement Pastes. Cement and Concrete Composites, 2, 2007, vol. 29, no. 2. pp. 80-87. ISSN 0958-9465.

[6] TAFRAOUI, Ahmed, et al. Metakaolin in the Formulation of UHPC. Construction and Building Materials, 2, 2009, vol. 23, no. 2. pp. 669-674. ISSN 0950-0618.

[7] VALENZA II, John J.; and SCHERER, George W. A Review of Salt Scaling: I. Phenomenology. Cement and Concrete Research, 7, 2007, vol. 37, no. 7. pp. 1007-1021. ISSN 0008-8846.

[8] ČSN EN 12350-5 (731301) Zkoušení čerstvého betonu - Část 5: Zkouška rozlitím. Praha: Český normalizační institut, 2000.

[9] ČSN 73 1326 (731326) Stanovení odolnosti povrchu cementového betonu proti působení vody a chemických rozmrazovacích látek. Praha: Český normalizační institut, 2003.

[10] ASTM C672 / C672M -03 Standard Test Method for Scaling Resistance of Concrete Surfaces Exposed.. West Conshohocken. PA.: ASTM International. , 2009.

[11] KOLÁŘ, K., et al. Vliv cyklů zmrazování - rozmrazování na trvanlivost betonu s přídavkem metakaolinu. . ROVNANÍKOVÁ, P.; a KERŠNER, Z. eds., 1 vyd ed. V Brně: Vysoké učení technické v Brně, 2008. ISBN 978-80-214-3582-7.

[12] HELA, Rudolf; DOHNÁLEK, Jiří and KOLÍSKO, Jiří. Zkoušení mrazuvzdornosti betonů dle různých normových předpisů a jejich vzájemný vztah. Praha ed. Praha: 2008. ISBN 978-80-87158-09-8.

[13] ROVNANÍKOVÁ, P.; ROVNANÍK, P.and SCHMID, P. Korozní odolnost betonů s metakaolínem. ROVNANÍKOVÁ, P.; and KERŠNER, Z. eds., 1 vyd ed. V Brně: Vysoké učení technické v Brně, 2008. ISBN 978-80-214-3339-7.

Computational analysis of hygrothermal performance of building envelope under different climatic conditions

Jiří Maděra[1], Václav Kočí[1], Jan Kočí[1], Tomáš Korecký[1], Robert Černý[1], Xinying Lu[2]

[1]Faculty of Civil Engineering, Czech Technical University in Prague, Thákurova 7, CZ- 166 29
Prague 6, Czech Republic, email: madera@fsv.cvut.cz

[2]Department of Civil Engineering, Tsinghua University, Beijing 100084, China

Abstract: *Effect of two different climates on hygrothermal performance of AAC-based building envelope is investigated. Inland climate of temperate zone and oceanic climate of subtropical zone are chosen for comparison. The computational analysis is accomplished using computer code HEMOT which is designed for modeling coupled heat and moisture transport in porous building materials. The code can provide basic state variables (moisture content, relative humidity, temperature) as functions of space and time for a given part of building structure.*

Keywords: *heat transport, moisture transport, autoclaved aerated concrete, computational analysis, climatic zones*

1. Introduction

One of main trends of these days in building industry is to bring in computational analysis on solving more sophisticated problems. The same is applied to solution of hygrothermal performance of building materials and structures. Quick development breeds usage problems of new materials in load bearing structures or in thermal insulation systems. One of most common building material across Europe is autoclaved aerated concrete (AAC) thanks to its mechanical and thermal properties. These days, when attention is paid to energy saving, grows up the importance of proper design of thermal insulation system. For correct design of thermal insulation system, it is necessary to use appropriate climatic conditions with regard to location of analyzed object. Research of thermal behavior of building envelope under different climatic conditions was accomplished for instance by Yilmaz [1].

2. Details of computational analysis

The computational analysis was accomplished by computer code HEMOT 2.1 [2], which was developed at the Department of Material Engineering and Chemistry, Faculty of Civil Engineering, Czech Technical University in Prague on the basis of the general finite element package SIFEL [3]. As basic input parameters of the mathematical model, material parameters of used materials, construction detail, initial and boundary conditions and time specification of simulation were required. Description of all input parameters in more detail is presented later.

Computational analysis was aimed at comparison of effects of different climate conditions on hygrothermal performance of AAC-based building envelope provided with thermal insulation. In the simulation, inland climate of temperate zone and oceanic climate of subtropical zone were chosen for comparison.

2.1 Mathematical model

Künzel's model [4] was used for the description of coupled heat and moisture transport in the studied building envelope. The moisture and heat balance equations were formulated as

$$\frac{d\rho_v}{d\varphi}\frac{\partial\varphi}{\partial t} = div\left[D_\varphi grad\varphi + \delta_p grad(\varphi p_s)\right] \tag{1}$$

$$\frac{dH}{dT}\frac{\partial T}{\partial t} = div(\lambda gradT) + L_v div\left[\delta_p grad(\varphi p_s)\right] \tag{2}$$

where ρ_v is the partial density of moisture, φ relative humidity, δ_p diffusion permeability of water vapour, p_s partial pressure of saturated water vapour, H enthalpy density, L_v heat of evaporation, λ thermal conductivity, T temperature,

$$D_\varphi = D_w \frac{d\rho_v}{d\varphi} \tag{3}$$

is liquid moisture diffusivity coefficient, D_w capillary transport coefficient.

2.2 *Construction scheme*

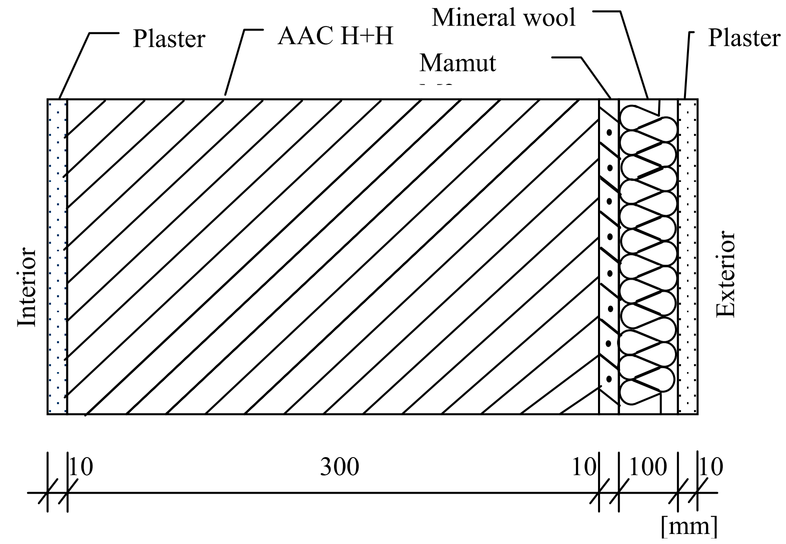

Figure 1: Scheme of analyzed construction

Figure 1 shows the scheme of construction used in the simulation. Autoclaved aerated concrete P2-400 produced by H+H Czech Republic, Ltd. was the material of load bearing structure. As material for exterior and interior renders we used Baumit MVR Uni Plaster, which is single-layer plaster for exterior and interior surfaces especially recommended for AAC. As the thermal insulation we assumed Rockwool hydrophobic and hydrophilic mineral wools. For adhesive layer between AAC and mineral wool we used Mamut M2 mortar.

2.3 *Input parameters*

Basic material parameters of used materials are shown in Table 1 where ρ is the bulk density [kg/m^3], ψ the porosity [%], μ the water vapour diffusion resistance factor [-], w_{hyg} the hygroscopic moisture content by volume [m^3/m^3], κ the moisture diffusivity [m^2/s],

c the specific heat capacity [J/kgK], λ_{dry} the thermal conductivity in dry conditions [W/mK],

λ_{sat} the thermal conductivity in water saturated conditions [W/mK]. All these parameters were measured in Laboratory of Transport Processes of the Department of Materials Engineering and Chemistry, Faculty of Civil Engineering, Czech Technical University in Prague [5][6][7][8][9]. Data for Mamut M2 mortar were measured by M. Jerman from the same laboratory and have not been published yet.

Table 1: Material characteristics

	AAC H+H P2-400	Mamut M2 mortar	Rockwool hydrophobic mineral wool	Rockwool hydrophilic mineral wool	Baumit MVR Uni plaster
ρ [kg m^{-3}]	412	1430	270	71	1402
ψ [%]	80.3	42.6	88.0	96.0	44.4
c [J kg^{-1} K^{-1}]	1250 - 1385	1020	630	810	1020 - 1780
μ [-]	3.7 – 14.4	12.4	2.1 – 3.7	4.3	4.5 – 12.4
λ_{dry} [W m^{-1} K^{-1}]	0.094	0.481	0.045	0.043	0.443
λ_{sat} [W m^{-1} K^{-1}]	0.434	2.022	0.246	0.246	1.380
κ [m^2 s^{-1}]	1.12e-9	1.07e-9	2.51e-10	8.4e-6	1.59e-9
w_{hyg} [m^3 m^{-3}]	0.019	0.201	0.007	0.000046	0.042

As the first boundary conditions in the exterior were used climatic data for Prague (inland climate of temperate zone) in the form of Test Reference Year (TRY), which contains hourly values of average climatic data for 30 years. Distributions of temperature and relative humidity during the year are shown in Figures 2a and 3a, respectively. The second boundary conditions in the exterior were for oceanic climate of subtropical zone in Hong Kong (Figures 2b, 3b). These data were measured in 2009 in Hong Kong's observatory. On the interior side were used constant values of relative humidity and temperature, 55 % and 21 °C, respectively. The simulation was started in 14th July and was done for 5 years.

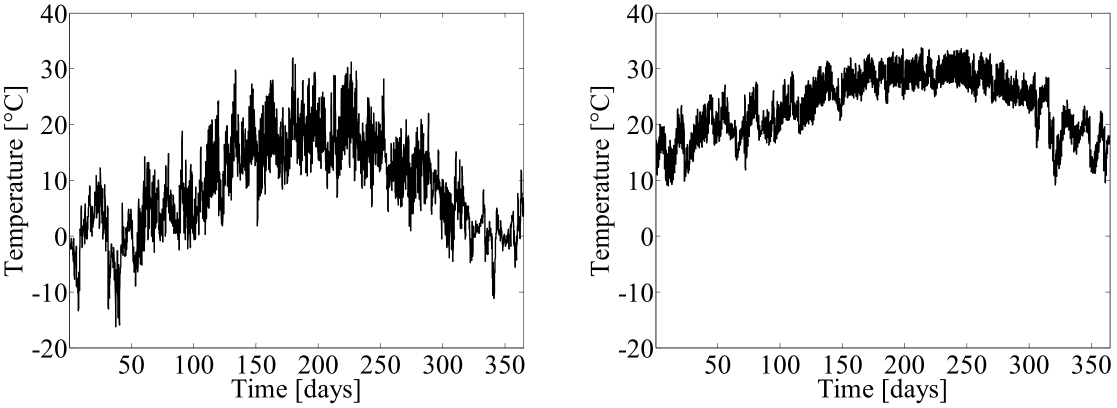

Figure 2: Temperature a) for Prague b) for Hong Kong

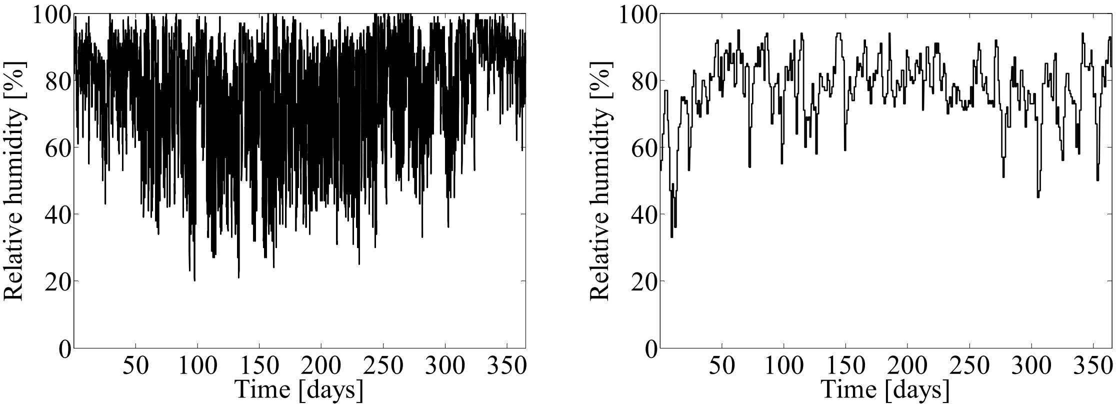

Figure 3: Relative humidity a) for Prague, b) for Hong Kong

3. Computational results

The results of computational simulation are summarized in a set of figures which describe hygric and thermal performance of studied building envelope.

Prague

Figure 4 presents the hygric behavior of studied construction. Exterior hydrophobic mineral wool reliably protects the construction against moisture increase. That limits the amount of relative humidity which reaches at most 60 %. Distribution of temperature shown in Figure 5 confirms that the thermal insulation system works well.

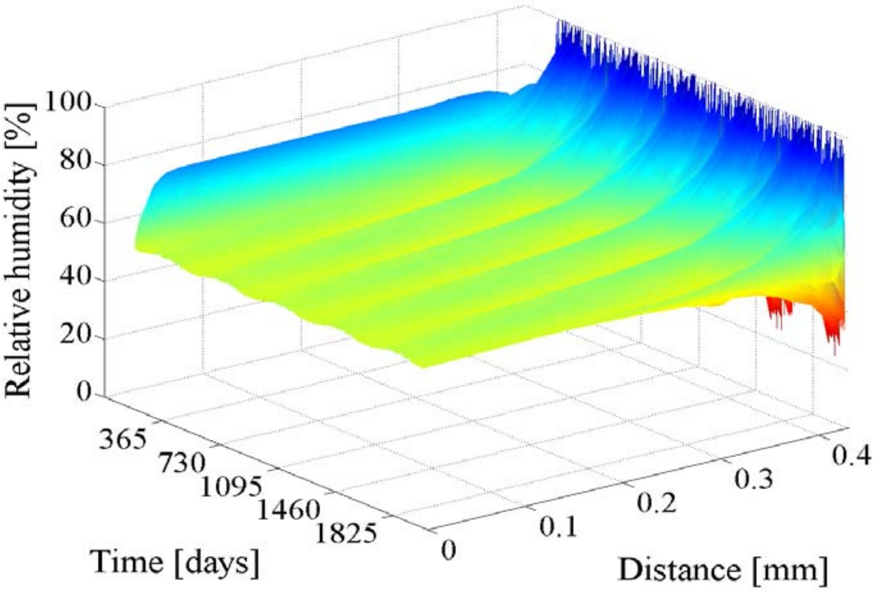

Figure 4: Time dependence of relative humidity for Prague TRY, hydrophobic mineral wool

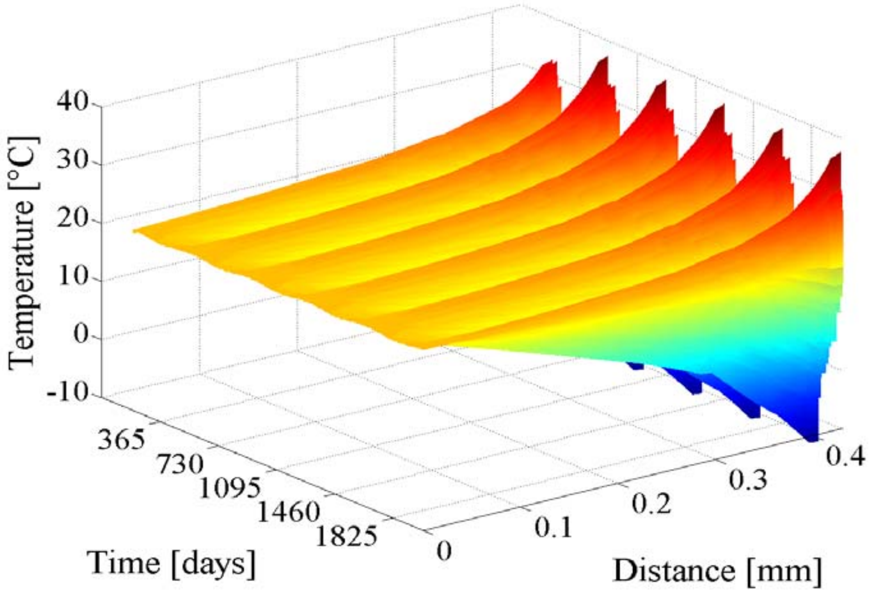

Figure 5: Time dependence of temperature for Prague TRY, hydrophobic mineral wool

Hong Kong

In Figures 6 and 7, results of hygrothermal performance of the studied envelope for Hong Kong's climatic data are presented. Values of relative humidity in thermal insulation reach 97%. High values of relative humidity are observed in the load bearing wall as well.

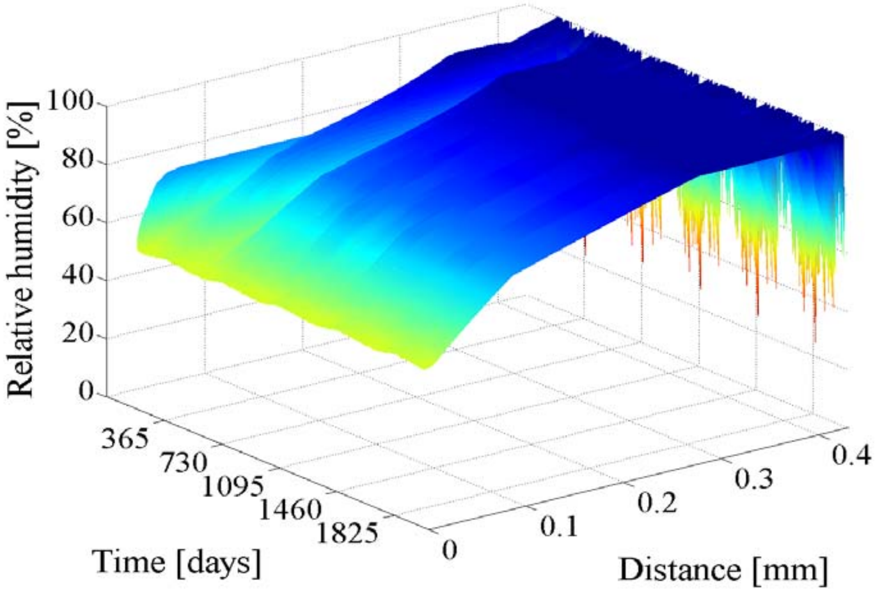

Figure 6: Time dependence of relative humidity for Hong Kong, hydrophobic mineral wool

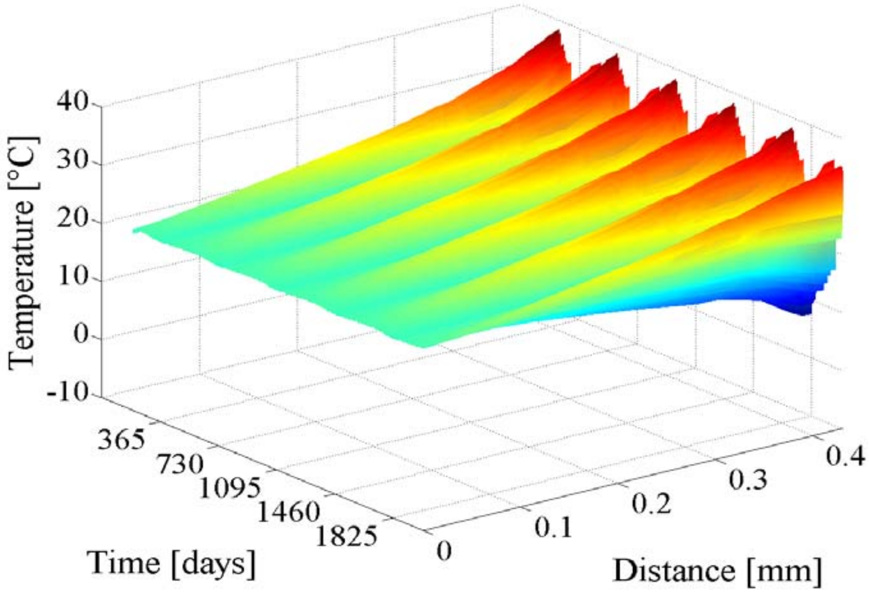

Figure 7: Time dependence of temperature for Hong Kong, hydrophobic mineral wool

Figure 8 shows distribution of relative humidity in building envelope provided with hydrophilic mineral wool. As it is obvious, values of relative humidity decrease to 70 % that means moisture-induced strain of construction is reduced. Thermal behavior does not differ significantly compared to building envelope provided with hydrophobic mineral wool.

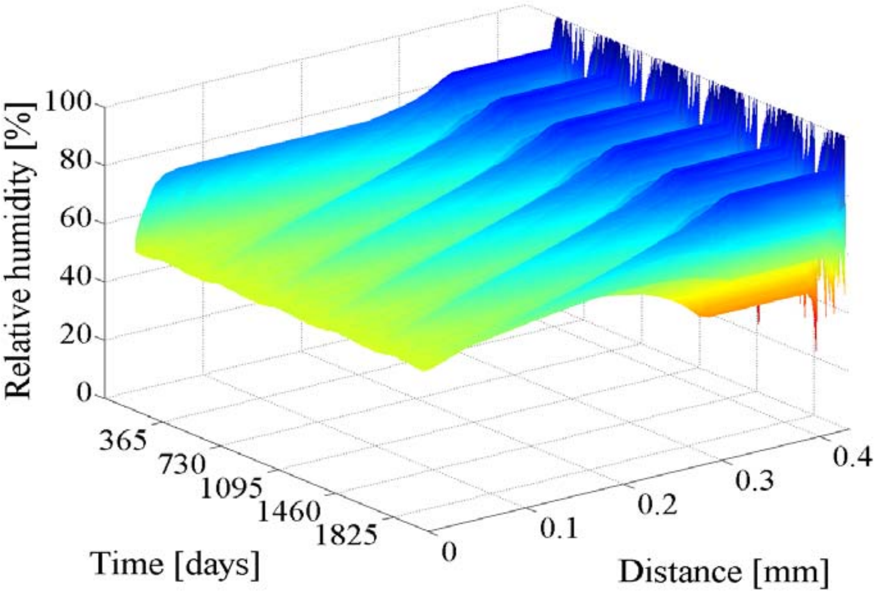

Figure 8: Time dependence of relative humidity for Hong Kong, hydrophilic mineral wool

4. Discussion

External insulation system based on hydrophobic mineral wool was for the studied AAC envelope apparently a good choice under conditions of inland climate of temperate zone. This system reliably protected the construction against increase of moisture content and against high temperature changes during the year. This prevents degradation of both load bearing construction and thermal insulation system because two conditions have to be fulfilled at the same time. Namely, the temperature has to drop below zero and moisture content has to reach over hygroscopic range. These conditions can be achieved only in the surface layers of exterior plaster, but this does not lead to damage of whole insulation system.

In the second case, when Hong Kong's climatic data were under assumption, external insulation system based on hydrophobic mineral wool seemed to be improper. It was caused by moisture increase, as the values of relative humidity during first year reached almost 97 %. This limit was particularly important from point of view of liquid moisture transport. In the next years the moisture content slowly increased also in load bearing construction which could make worse the conditions in interior. Increase of moisture content may be consequence of intensive rainfalls, which are characteristic for this climate zone, so that relative humidity of air does not drop under 80 % during whole year. On the other hand, high temperatures did not allow the contained water to get frozen over the whole year, so this type of material degradation could be omitted.

When capillary active hydrophilic mineral wool was used under Hong Kong's climatic conditions, it led to significant improvement of hygrothermal performance of whole building envelope. Although relative humidity in the thermal insulation layer was relatively high, due to its high moisture diffusivity this water could transported to the other parts of the structure.

5. Conclusions

The results of computational simulation accomplished in this paper showed that it was necessary to assume corresponding climatic conditions when design of thermal insulation system was made. It was proved that usual design assuming external insulation system based on hydrophobic mineral wool which used to work well under inland climate of temperate zone was completely improper under oceanic climate conditions of subtropical climate of Hong Kong. Therefore, it was required to design the thermal insulation system with regard to respective climatic zone and choose hydrophilic mineral wool instead.

Acknowledgement

This research has been supported by the Czech Ministry of Education, Youth and Sports, under project No 6840770031 and SGS10/128/OHK1/2T/11.

References

[1] YILMAZ Z. Evaluation of energy efficient design strategies for different climatic zones: Comparison of thermal performance of buildings in temperate-humid and hot-dry climate, In *Energy and Buildings 39* ,2007, p. 306–316.

[2] ČERNÝ R., Complex System of Methods for Directed Design and Assessment of Functional Properties of Building Materials: Assessment and Synthesis of Analytical Data and Construction of the System, CTN ČVUT v Praze, 2010, pp. 192 – 201.

[3] KRUIS J.; KOUDELKA T.; KREJČÍ T. Efficient computer implementation of coupled hydro-thermo-mechanical analysis. In *Mathematics and Computers in Simulation*, doi:10.1016/j.matcom.2008.11.010

[4] KÜNZEL, H.M., *Simultaneous Heat and Moisture Transport in Building Components*, Ph.D. Thesis, IRB Verlag: Stuttgart, 1995, p. 1–135.

[5] PERNICOVÁ, R., PAVLÍKOVÁ, M, PAVLÍK, Z., ČERNÝ, R. Vliv metakaolinu na mechanické, tepelné a vlhkostní vlastnosti vápenných omítek. *In: Metakaolin 2007*. Brno: VUT FAST, 2007, pp. 70-77.

[6] VÝBORNÝ, J. Stanovení tepelných parametrů a smrštění při vysychání vybraných pórobetonových tvárnic firmy H+H Česká republika s.r.o. a Xella CZ. *In: Proceedings of the International Conference 15th Construmat 2009*. Praha: České vysoké učení technické v Praze, 2009, pp. 449-461.example of book chapter

[7] JIŘIČKOVÁ, M., ČERNÝ, R., Effect of Hydrophilic Admixtures on Moisture and Heat Transport and Storage Parameters of Mineral Wool. *Construction and Building Materials*, 2006, 20, pp. 425-434.

[8] FUČÍKOVÁ, L., Moisture Properties of AAC Blocks in dependence on the Environment Focused on Problems with Durability. Diploma thesis. Praha: Czech Technical University in Prague, 2009.

[9] Jerman, M.; Maděra, J.; Černý, R., Computational Modeling of Heat and Moisture Transport in a Building Envelope with Hydrophilic Mineral Wool Insulation

In: Proceedings of the 8th Symposium on Building Physics in the Nordic Countries. Lyngby: Technical University of Denmark, BYG.DTU, 2008, p. 449-456. ISBN 978-87-7877-265-7.

Measurement of thermophysical properties of polypropylene-talc composite

Svetozár Malinarič

Department of Physics, Constantine the Philosopher University, Trieda Andreja Hlinku 1, 94974 Nitra, Slovak Republic

Abstract: *The Extended Dynamic Plane Source (EDPS) method is one among many transient techniques for measuring thermophysical properties. The principle of this method is based on the step-wise heating of the resistive element sandwiched between two pieces of the investigated material. From the temperature response it is possible to compute the thermal conductivity and diffusivity. The theory and the experimental technique of the EDPS method is outlined. The method is used for measuring thermophysical properties of polypropylene-talc composites with the talc fraction of 0 to 50%. The following quantities were studied as a function of talc fraction: density, thermal conductivity, thermal diffusivity, mass heat capacity and volumetric heat capacity.*

Keywords: *Transient method, thermal conductivity, thermal diffusivity, composite*

1. Introduction

Dynamic methods [1] for measurement of thermophysical properties can be divided into contact (transient) and non-contact (flash) methods. The former are based on generation of a dynamic temperature field inside the specimen. This experimental arrangement suppresses the sample surface influence on the measuring process. Transient methods use both a two-probe system (heat source and thermometer are separated) and one-probe system (heat source serves as the thermometer).

A theoretical model of the experiment is described by the heat equation. The temperature function is a solution of this equation with boundary and initial conditions corresponding to the experimental arrangement. The principle of the method consists of fitting the temperature function to the experimental points (temperature response).

2. Extended Dynamic Plane Source method

The EDPS method [2-4] is arranged for one-dimensional heat flow into a finite solid with low thermal conductivity. The heat source, which simultaneously serves as the thermometer, is placed between two identical specimens. The heat sink, made of a very good thermal conducting material, provides isothermal boundary condition of the experiment. Heat is produced by the passage of an electrical current in the form of a stepwise function through the planar electrical resistance - heat source. The thermal conductivity λ and thermal diffusivity a of the specimen can be calculated from the temperature response.

The model of the EDPS experiment consists of the following conditions:

(i) The heat flow is one-dimensional, and the heat source and specimens are infinite, parallel slabs.

(ii) The heat source is homogenous with negligible thickness and heat capacity.

(iii) There is a constant contact thermal resistance between the heat source and specimen.

(iv) The heat sink is semi-infinite with known thermal properties.

(v) There is ideal thermal contact between the specimen and heat sink.

(vi) The input heat power is constant.

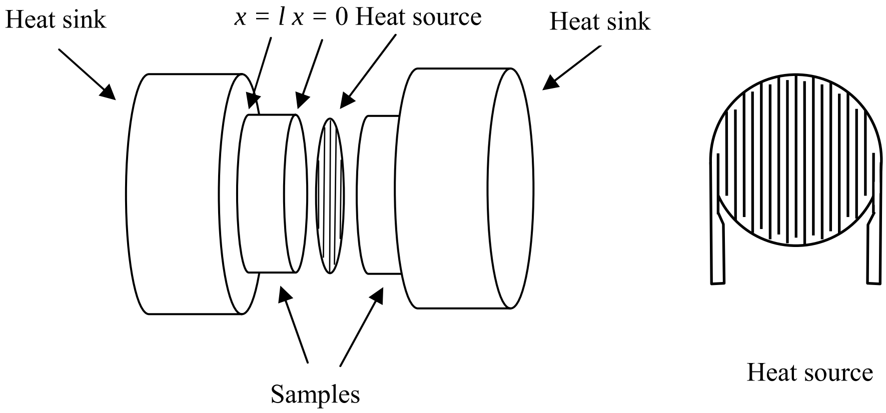

Figure 1: Setup of the EDPS experiment

The experimental arrangement of the EDPS method is shown in Fig. 1. Before the start of the experiment, the temperature of the specimen, heat source, and heat sink is stabilized and is equal to T_0. A short time Θ_k after the start, a steady state at the boundary between the heat source and specimen is reached and Newton's cooling law can be written as

$$q = h(T_\mathrm{h} - T|_{x=0}) \tag{1}$$

where q is the heat current density, h is the heat transfer coefficient, and T_h is the temperature increase of the heat source. The temperature difference is caused not only by the thermal contact between the specimen and heat source but also by its meander-like shape.

Then the temperature of the heat source can be expressed as

$$T_\mathrm{H}(t) = T_0 + T_\mathrm{h}(t) = T_0 + \frac{q}{h} + T|_{x=0} \tag{2}$$

and the temperature increase of the specimen in the plane for x=0 (temperature function) is given by [2]

$$T|_{x=0} = \frac{F(t,a)}{\lambda} \tag{3}$$

where

$$F(t,a) = q\sqrt{\frac{at}{\pi}}\left(1 + 2\sqrt{\pi}\sum_{\mathrm{n}=1}^{\infty}\beta^{\mathrm{n}}\,\mathrm{ierfc}\left(\frac{\mathrm{n}l}{\sqrt{at}}\right)\right) \tag{4}$$

l is the thickness of the specimen and ierfc is the error function integral [5]. Parameter β describes the heat sink imperfection and is given by

$$\beta=\left(\lambda/\sqrt{a}-\lambda_{\mathrm{s}}/\sqrt{a_{\mathrm{s}}}\right)/\left(\lambda/\sqrt{a}+\lambda_{\mathrm{s}}/\sqrt{a_{\mathrm{s}}}\right) \tag{5}$$

where λ_s is the thermal conductivity and a_s is the thermal diffusivity of the heat sink. The heat source temperature can be converted to resistance by the following formula:

$$R=R_0\left(1+\alpha T\right) \tag{6}$$

where R_0 is the resistance at temperature T=0 and α is the temperature coefficient of the heat source resistivity. Then the predicted values of the heat source resistance can be determined using Eqs. 3 and 6 as

$$r\left(t\right)=R_0\left(1+\frac{\alpha}{\lambda}F\left(t,a\right)\right) \tag{7}$$

Two thermophysical parameters, λ and a and one nuisance parameter R_0 should be iterated until the sum of $\left(r(t_i)-r_i\right)^2$ reaches its minimum, where $\left[t_i,r_i\right]$ are measured points.

3. Least squares fitting

The principle of the method is based on fitting the function (7) to the experimental points. As the function is nonlinear only in one parameter we can expand it using Taylor series as follows

$$r(t,\lambda,a,R_0)=r(t,\lambda,a_0,R_0)+\left(\frac{\partial r(t,\lambda,a,R_0)}{\partial a}\right)_{a=a_0}\cdot(a-a_0) \tag{8}$$

where a_0 represents a good guess for parameter a. Then it can be written as the linear combination of 3 functions

$$r(t,\lambda,a,\tau)=R_0\frac{\alpha}{\lambda}\cdot F(t,a_0)+R_0\frac{\alpha}{\lambda}(a-a_0)\cdot\left(\frac{\partial F(t,a)}{\partial a}\right)_{a=a_0}+R_0\cdot 1=b_1 f_1+b_2 f_2+b_3 f_3 \tag{9}$$

The linear least squares procedure in matrix notation is given by the form

$$\vec{r}=\mathbf{X}\cdot\vec{b}+\vec{\varepsilon} \tag{10}$$

where $\vec{r}$ is the observation vector of heat source resistance, $\vec{b}$ is the vector of unknown parameters, $\vec{\varepsilon}$ is the vector of errors and $\mathbf{X}$ is sensitivity matrix defined by

$$\{\mathbf{X}\}_{ij}=f_j(t_i) \tag{11}$$

The least squares estimate of the parameter vector is given

$$\vec{b}_{\mathrm{LS}}=\left(\mathbf{X}^T\cdot\mathbf{X}\right)^{-1}\cdot\mathbf{X}^T\cdot\vec{y} \tag{12}$$

and thermophysical parameters can be computed using the following relations

$$\lambda=\frac{b_{\mathrm{LS}\,3}\cdot\alpha}{b_{\mathrm{LS}\,1}},\qquad a=a_0+\frac{b_{\mathrm{LS2}}}{b_{\mathrm{LS1}}},\qquad R_0=b_{\mathrm{LS3}} \tag{13}$$

So that only one parameter a should be iterated.

4. Measurement results

The composites were made in VÚSAPL a. s. Nitra from Polypropylene TATREN HG 10 07 and Talc EK II F delivered by GE.NE.S. a.s. Hnúšťa. The mass fraction of the talc filling was 0 to 50%. The specimens with diameter of 30 mm and thickness about 3 mm were prepared by injection moulding technology. The results of thermal conductivity and diffusivity measurements are plotted in Fig.2 and 3., respectively. The figures shows the results of two repeated measurements on the same specimens.

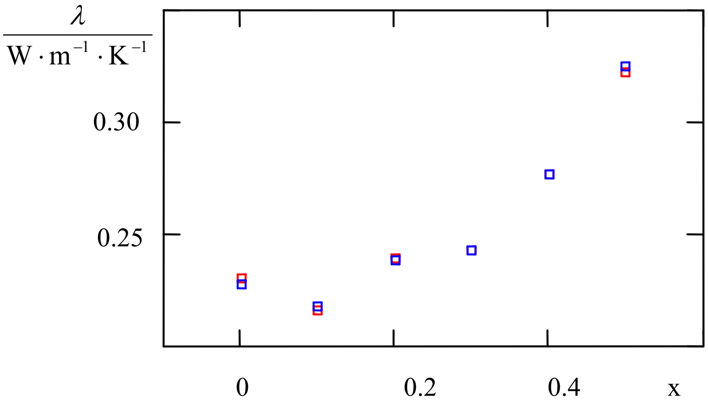

Figure 2: Thermal conductivity as a function of the mass fraction of talc x.

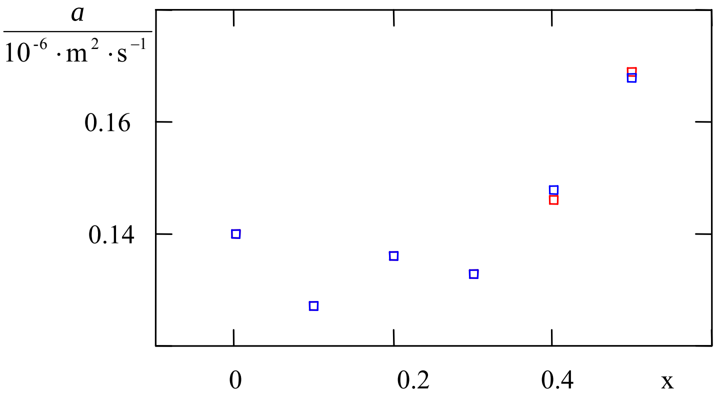

Figure 3: Thermal diffusivity as a function of the mass fraction of talc x.

The volumetric heat capacity c_V and mass heat capacity c_M were calculated using the following formulas

$$c_V = \frac{\lambda}{a} \qquad\qquad c_M = \frac{c_V}{\rho}, \tag{14}$$

where ρ is the density of the composites determined by measuring the mass and dimensions of the specimens. The results of volumetric heat capacity and density measurements are plotted in Fig.4 and 5., respectively.

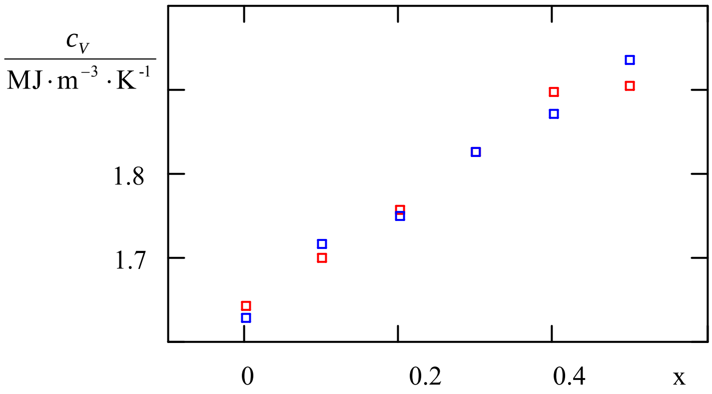

Figure 4: Volumetric heat capacity as a function of the mass fraction of talc x.

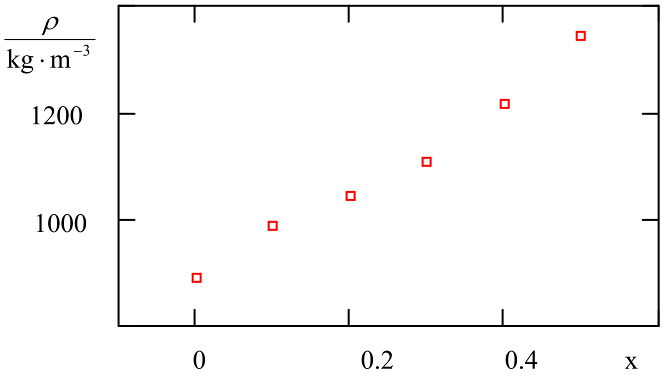

Figure 5: Density as a function of the mass fraction of talc x.

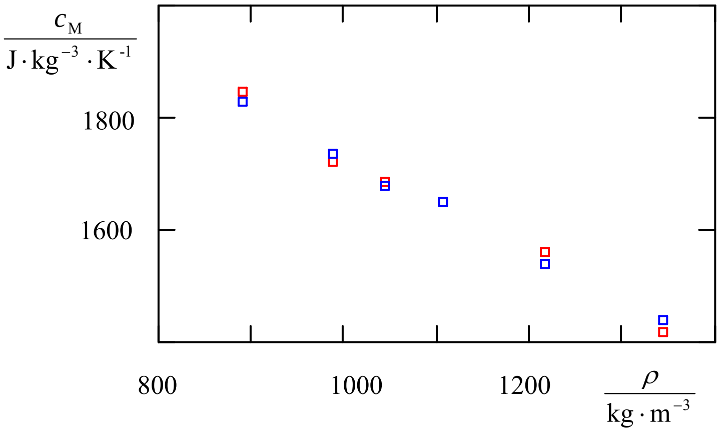

Figure 6: Mass heat capacity as a function of the specimen density.

5. Conclusions

The EDPS method was used for simultaneous measurements of the thermal conductivity and diffusivity of polypropylene-talc composites. Figures 2 and 3 show the increase of both thermophysical properties with talc filling content. The scattering of measured points can be the result of measurement error or composite preparation error. On the other side it is surprising that there is no scattering in Figures 4 and 6 showing the volumetric and mass heat capacity. In order to verify the composite preparation the specimen density was determined and plotted against the mass fraction of talc filling. The linear growth in Fig. 4 proved that the volumetric heat capacity of the filling is higher than that of the polypropylene matrix. Similarly, the growth in Fig. 5 showed that the density of the talc filling was higher than that of the matrix. But the fall in Fig. 6 shows that the mass heat capacity of the filling is lower than that of the matrix.

Acknowledgement

Author wishes to thank the Slovak Science Grant Agency for financial support under Contract 1/0302/09.

References

[1] KUBIČÁR, Ľ.; BOHÁČ V. Review of several dynamic methods of measuring thermophysical parameters. In *Proc. of 24th Int. Conf. on Thermal Conductivity/12th Int. Thermal Expansion Symp.*, ed. by P.S. Gaal, D.E. Apostolescu (Technomic Pub., Lancaster, Pennsylvania, 1999), p. 135-149. ISSN 1-56676-711

[2] KARAWACKI, E.; SULEIMAN, B.M.; UL-HAQ, I.; NHI, B. An extension to the dynamic plane source technique for measuring thermal conductivity, thermal diffusivity, and specific heat of dielectric solids. In *Rev. Sci. Instrum.* 1992. 63. p. 4390-4397 ISSN 0034-6748

[3] MALINARIČ, S. Parameter estimation in dynamic plane source method. In *Meas. Sci. Technol.* 2004. 15. p. 807-813 ISSN 0957-0233

[4] MALINARIČ, S. Contribution to the Sensitivity Coefficients Analysis in the Extended Dynamic Plane Source (EDPS) Method. In *Int. J. Thermophys.* 2004. 25. p. 1913-1919 ISSN 0021-9568

[5] CARSLAW, H. S.; JAEGER, J. C. *Conduction of Heat in Solids*, 2. Ed. Clarendon Press, London, 2003. ISBN 0-19-853368-3

Critical moisture content of silicate-based building materials

Peter Matiasovsky, Lubomir Bagel

Institute of Construction and Architecture, Slovak Academy of Sciences, Dubravska cesta 9, 845 03 Bratislava, Slovakia, e-mail: usarmat@savba.sk

Abstract: *The critical moisture content is defined as a minimum water amount necessary for the capillary transport. It is determined by the pore structure parameters of a given material and represents one of the material characteristics important for modelling the moisture transport parameters. A difference between the actual and critical moisture contents represents the pore volume relevant for a capillary water flow at a given degree of saturation. In the paper the critical moisture content for various silicate-based building materials was determined from drying tests. The obtained results were analysed by modelling the water absorption coefficient by a power law and correlated with the mercury intrusion porosimetry data.*

Keywords: *Water permeability, critical moisture content, hydraulic radius, mercury intrusion porosimetry, pore structure*

1. Introduction

In [1] the values of critical moisture content and saturation moisture content were analysed by means of the expression of water absorption coefficient based on the modified sharp water penetration profile model [2]. The movement of the water front within the real capillary system is expressed in this model by the movement of water in an equivalent (cylindrical) capillary, representing the capillary system. The equivalent capillary is defined by the permeability, dependent on the equivalent (usually hydraulic) radius and the relevant porosity. The modification was based on the expression of a tortuosity by the power function of relevant porosity, with a critical exponent. The relevant porosity is the total porosity reduced by the critical moisture content and the volume of air entrapped during the water absorption process. Its value is determined by the difference between capillary moisture content and critical moisture content during the suction experiment. The equivalent capillary radius was interpreted as the radius of largest pore fraction of the critical moisture content governing the movement of the water penetration front, so it was coupled with the critical moisture content. In order to stress the coupling no a priori assumption concerning the equivalent radius, including the hydraulic radius was made. The model enabled fitting the water absorption coefficients, selecting the optimum critical moisture content - equivalent radius couples for various silicate-based building materials in order to cover a wide range of porosities, water absorption coefficients and capillary moisture contents. The analysed materials included burned clay bricks, autoclaved aerated concretes, mortars, lightweight plasters, calcium silicates and lightweight carbonates. The necessary data were obtained from the water suction and mercury intrusion porosimetry (MIP) tests.

The determined optimum critical moisture contents were confronted with critical moisture content data obtained from the tests of drying of the analysed materials. During the drying tests the critical moisture contents were determined as the moisture contents of the material samples corresponding to the moments of a sudden decrease of the drying rate when the continuous liquid water paths were depercolated. For example the critical moisture content of the burned clay brick sample was reached after ca 5 hours of its drying (Fig. 1).

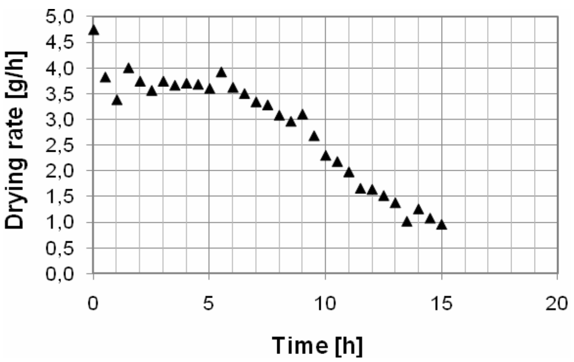

Figure 1: Drying test – burned clay brick

The values of critical moisture content estimated by the absorption coefficients fitting were compared with the values obtained from drying tests. The comparison confirmed the correspondence of mean and extreme values, but a weak correlation. The fitting of two unknowns showed to be very uncertain in spite of their coupling. A solution is in identification of the equivalent capillary radius as a pore structure parameter, especially as the hydraulic radius of the cylindrical pores for the analysed building materials.

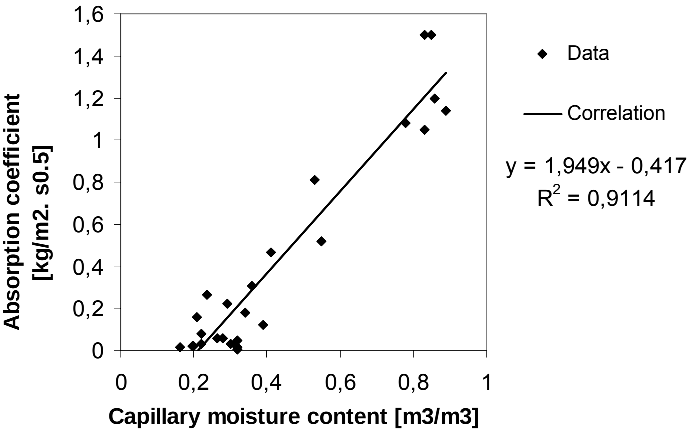

Figure 2: Relationship between capillary moisture content and water absorption coefficient

2. Water absorption coefficient models

There is a significant correlation between the capillary moisture content and the water absorption coefficient (Fig. 2). The relationship between the capillary moisture content and the water absorption coefficient can be expressed by the sharp water penetration profile model of the water absorption coefficient (Fig 3):

$$A = \rho_w \cdot u_{cap} \cdot \sqrt{\frac{4 \cdot K \cdot \sigma_{lg}}{\eta \cdot u_{cap} \cdot r_{eq}}} \tag{1}$$

where ρ_w = the water density [kg/m^3]; u_{cap} = the capillary moisture content [-]; K = the permeability [m^2]; σ_{lg} = the surface tension for water [N/m], η = the dynamic viscosity [Pa.s]; r_{eq} = the equivalent radius [m].

Applying the Carman-Kozeny equation and expressing the tortuosity effects by a power function of the relevant porosity, the permeability has a general form:

$$K = \frac{r_{eq}^2 \cdot \left(u_{cap} - u_{crit}\right)^n}{8} \tag{2}$$

where u_{crit} = critical moisture content [-].

Inserting Equation (2) into Equation (1) the water absorption coefficient has the following form:

$$A = \rho_w \cdot u_{cap} \cdot \sqrt{\frac{\left(u_{cap} - u_{crit}\right)^n}{u_{cap}} \cdot \frac{r_{eq} \cdot \sigma_{lg}}{2 \cdot \eta}} \tag{3}$$

According to relationship (3) the simplified water penetration profile will have a trapezoidal shape (Fig. 3) determined by the critical and capillary moisture contents.

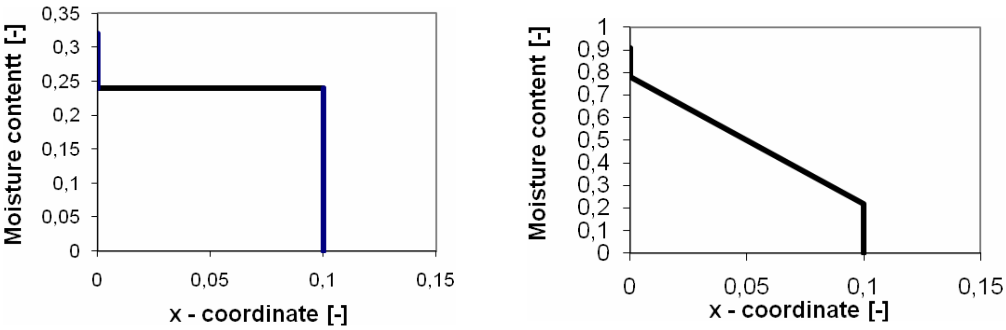

Figure 3: Sharp (left) and trapezoidal (right) water penetration profile models

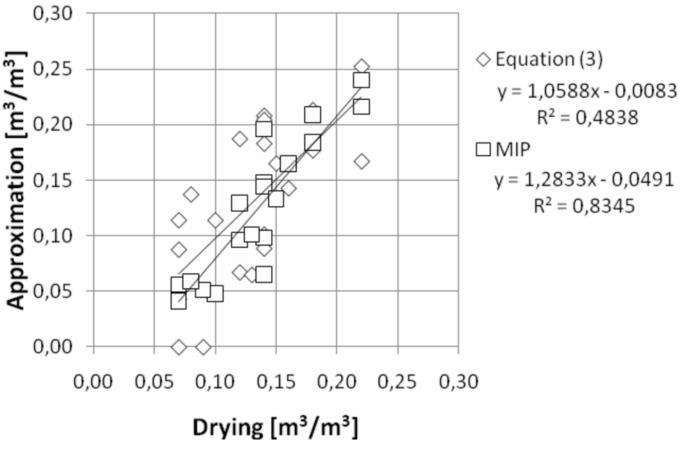

Figure 4: Comparison of critical moisture content approximations with critical moisture content data determined at drying tests

In Equations (2) and (3), besides the bulk density and capillary moisture content, the values of critical exponent n, the equivalent capillary radius r_{eq} and the relevant porosity $u_{cap} - u_{crit}$ must be known.

The value of the critical exponent depends on the fractal dimension (FD) of pores, which expresses the regularity of a pore structure, namely on the fractal dimension of the largest relevant pore volume fractions, according to the relationship $n = 1 + FD$. From the fractal analysis of the pore size distributions made for considered materials the average value of fractal dimension close to 2 was determined, with the consequent critical exponent value equal to 3.

3. Pore structure equivalent of critical moisture content

Let us consider that the equivalent capillary radius is identical with the hydraulic radius r_H. The hydraulic radius is calculated from the porosity and the pore surface area. In order to verify the assumption the critical pore volumes were calculated with use of Equation (3) for $r_{eq} = r_H$. The critical volumes calculated for the analysed materials this way were compared with the critical moisture contents determined from drying tests (Fig. 4). Simultaneously in Figure 4 the volumes of the pores smaller than the calculated hydraulic radii were compared with the critical moisture contents. The compared values show a mutual similarity, which indicates that the hydraulic radius is equivalent to the capillary radius defined as the radius of largest pores filled with the water at the critical moisture content. Nevertheless a difference occurred at some materials, especially at burned clay bricks, where the values determined from drying are significantly higher, which can be partly interpreted by the moisture absorption hysteresis of these materials. The critical moisture contents at drying and water absorption are not identical for all analysed materials and the differences are given by their pore structure. The critical volumes limited by hydraulic radii represent approximately 25 % of the porosity determined by MIP. This value is identical to the theoretical random bond percolation threshold for the three-dimensional cubic lattice, connectivity of which equals 6 [3]. A better correlation gives a comparison with the microporosity - the volume of pores smaller than 7500 nm (Fig. 5).

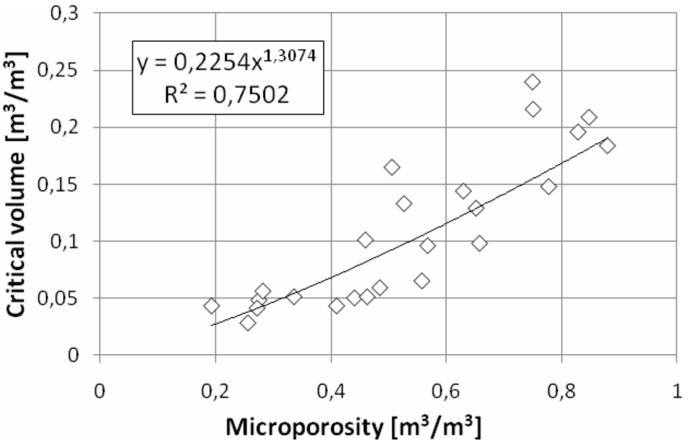

Figure 5: Relationship between critical volume limited by hydraulic radius and microporosity

The values of the measured critical moisture content as well as their equivalents identified from the pore structure parameters were also analysed in respect of mean fractal dimension of micropores. A significant correlation was found (Fig. 6).

An application of the critical moisture content approximations approximation based on the critical volume limited by hydraulic radius and the 22 % of microporosity in the calculations of the water absorption coefficient according to Equation (3) is illustrated in Figure 7. In the figure discrepancies for the small values corresponding to some materials like burned clay bricks are apparent.

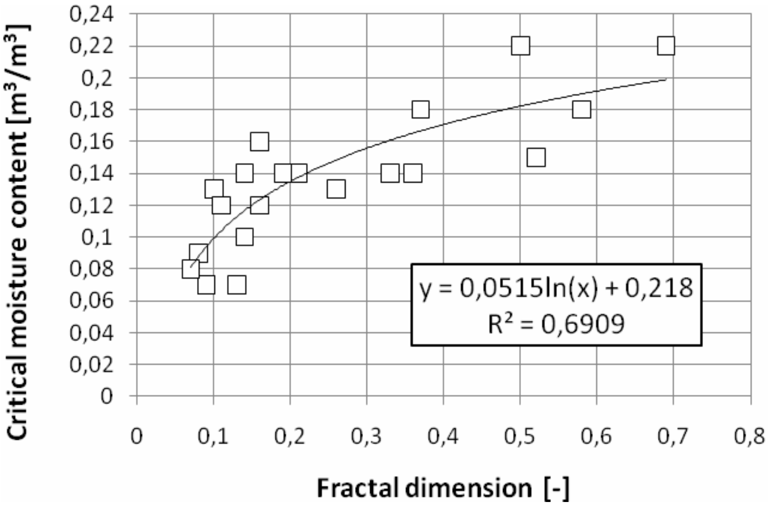

Figure 6: Relationship between critical moisture content and mean fractal dimension of micropores

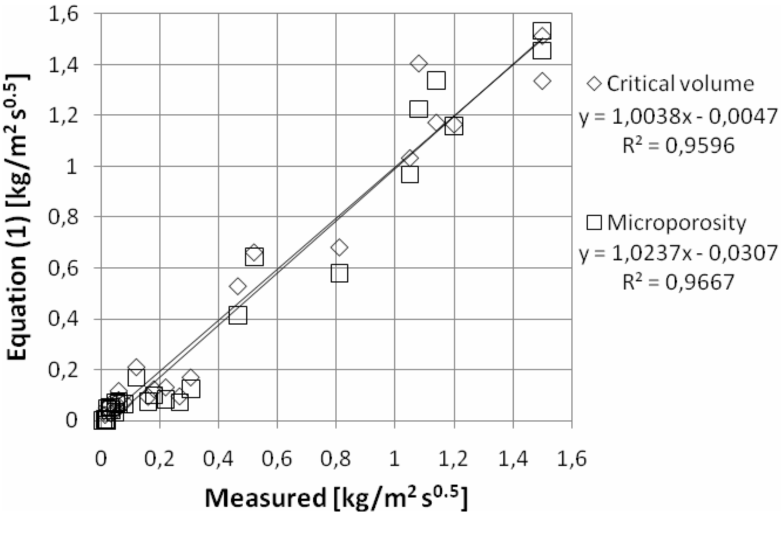

Figure 7: Comparison of water absorption coefficients approximations based on critical volume limited by hydraulic radius and on 22 % of microporosity with measured data

4. Conclusions

In comparison with the sharp moisture penetration profile model of the water absorption coefficient, based on a simplified assumption of the equivalent capillary defined by the effective porosity and capillary radius, the trapezoidal moisture penetration profile model requires information on the capillary moisture content, the critical exponent and the critical moisture content with the corresponding equivalent capillary radius. The tortuosity is expressed by a power law in this water absorption coefficient model. The validity of the trapezoidal water absorption coefficient model was analysed. In the analysis the pore structure parameters and the results of water absorption and drying tests for various silicate-based building materials were used. The trapezoidal moisture penetration profile water absorption model is valid if the pore structure equivalent capillary radius is represented by the hydraulic radius and the critical volume is expressed by the volume of pores smaller than hydraulic radius. The critical moisture content can be estimated as a function of the mean fractal dimension of microporosity. The critical exponent is a function of the fractal dimension of the largest pore volume fraction.

Acknowledgement

This article has been produced with the financial assistance of the European Regional Development Fund (ERDF) under the Operational Programme Research and Development/Measure 4.1 Support of centres of excellence/Project Creating the centre of excellence for research and development of structural composite materials for mechanical and civil engineering and medical applications.

The authors also wish to thank the APVT-51-030704, APVV-0744-07 projects for the financial support of this work.

References

[1] MATIASOVSKY P.; KORONTHALYOVA O. Critical moisture contents for water and air transport in case of imbibition tests. *Research in Building Physics and Building Engineering.* Taylor & Francis, *London,* 2006, p. 43 - 48. ISBN 0-415-41675-2

[2] HALL CH.; HOFF W. *Water transport in brick, stone and concrete.* Taylor & Francis, New York, 2002, pp. 318. ISBN 0-4198-22890-X

[3] DESCAMPS, F. *Continuum and discrete modelling of isothermal water and air transfer in porous media.* PhD-dissertation, K. U. Leuven, Leuven, 1997, pp. 182. ISBN 90-5682-064-8

[4] KHEIPHETZ, L. I.; NEUMARK, A. V. *Multiphase processes in porous media.* Chimia, Moscow, 1982. (in Russian)

[5] KUMARAN, M. K. *Heat, Air, and Moisture Transfer in In-sulated Enveloped Parts. Final report. Task 3: Material Properties*. K.U. Leuven, Leuven, 1996, pp. 135. ISBN 90-75741-01-4

[6] MOLDRUP, P. ET AL Tortuosity, diffusisvity, and permeability in the soil liquid and gaseous phases. In *Soil Sci. Am. J.* 2001. 65: p. 613 - 623. ISSN: 0361-5995

[71] GARBOCZI, E. J.; BENTZ, D. P. Modelling of the micro-structure and transport properties of concrete. In *Construction Building Materials.* 1996, 10, p. 293 - 300. ISSN 0950-0618

Determination of liquid water diffusivity of lime-cement perlite plaster at cyclic wetting and drying regimes

Peter Mihalka[1], Peter Matiasovsky[1], Matus Holubek[2]

[1]Institution of Construction and Architecture, Slovak Academy of Sciences, Dubravska cesta 9, 845 03 Bratislava, email: usarmipe@savba.sk

[2]Slovak Technical University, Faculty of Civil Engineering, Slovakia, Radlinskeho 11, 813 68 Bratislava, Slovakia, e-mail: holubek@svf.stuba.sk

***Abstract**: The TDR method was used to study the cyclic process of water uptake and drying of the perlite lime-cement plaster. Evaluating the water uptake experiment, the λ-w profiles were created for every water uptake cycle. The change of pore structure caused by the additional hydration of the plaster is presented.*

***Keywords**: TDR, capillary active plaster, moisture transport*

1. Introduction

Current requirements on existing buildings renovations demand the increase of thermal performance of envelope structures and the elimination of water vapour condensation and mould growth. In the cases where it is not possible to use standard external thermal insulation systems, the insulation from the interior side can be used. An application of the internal thermal insulation of building envelope structures in the temperate climatic zones is connected with specific problems. The water vapour diffuses through internal thermal insulation, where it hits the cold vapour-tight surface and condensates. Furthermore, the overcooling of the insulated structure can occur. The frozen water causes also the acceleration of degradation of the building materials. For elimination of the condensation, the capillary active plaster made of the light carbonate is being developed at the Institute of Construction and Architecture, SAS. The properties of this new material are compared with the commercial insulation lime-cement perlite plaster. This contribution deals with determination of the liquid water diffusivity of lime cement perlite plaster at the multiple cyclic process of water uptake in order to investigate the relationship between the stability and moisture transport properties of this reference material. Due to the presence of the cement particles in the material its additional hydration is assumed during the experiments. The impact of the hydration on the change of pore structure and liquid water diffusivity was analysed. The water uptake process was monitored using the time domain reflectometry (TDR) [1-3] method.

2. TDR calibration

Concerning the dielectric moisture measurements of porous materials, an important feature of water is the polar structure of its molecules. The water molecule has a permanent dipole momentum. The polarity of the water molecules is the reason of a much higher relative permittivity of water (ε_w = 81) in comparison with the relative permittivity of solid phase (porous building material ε_z = 2 - 5). The relative permittivity of a moist porous material depends strongly on its moisture content. Therefore the dielectric measurements of moist porous building materials can be based on the relative permittivity measurement.

If a considered porous material represents the moist dielectric, the measurement of its moisture content is easy. It is sufficient to measure the electric capacity of the capacitor filled with considered material. We can recalculate the measured value of capacity to the appropriate moisture content by means of the calibration curve.

A specially manufactured specimen of the plaster with a cylindrical shape had the radius r = 0.023 m and the height h = 0.12 m. The probe was fixed through the plastic cover and glued in the specimen axis. A sophisticated system of the specimens closing the airtight plastic containers provided a stable moisture conditions during conditioning the specimens. After the fixation of probes the specimens were kept three days in moulds then they were de-moulded and matured a week under laboratory conditions. After obtaining the appropriate moisture content they were placed into the CO_2 incubator to mature. Afterwards all specimens were placed into the drier at 40°C temperature and they were prepared for experiments. The moisture content interval from w = 0 g/g to w_{cap} = 0.627g/g was divided to the 10 measurements, 5 specimens were conditioned to the stable moisture contents during 4 days. After a gradual determination of the relative permittivity and consequent equilibrium moisture content (determined by the gravimetric method) we moisturized all specimens to higher equilibrium constants and let them to stabilize during the same period. The checking of the moisture content stability was provided by continuous monitoring of the relative permittivity at 5 minutes intervals. The calibration function is approximated by the polynomial function of the 4th order, figure 2.

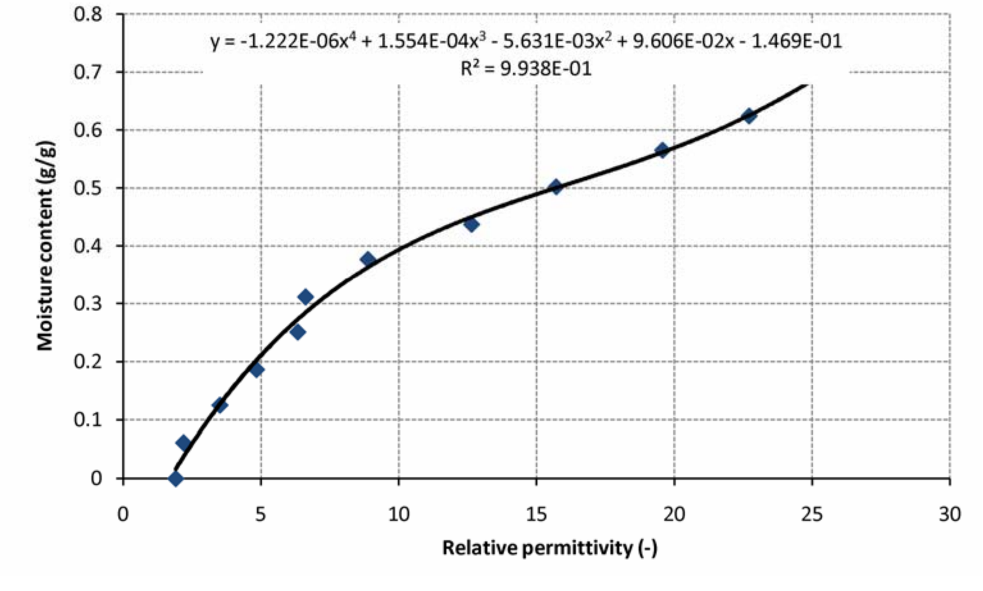

Figure 1: Relationship between moisture content and relative permittivity of lime cement perlite plaster

3. Water uptake experiment

A prism of the plaster with dimensions of 120x50x360 mm was made in a procedure similar with the procedure described in the previous paragraph. During the sample casting, 10 TDR probes were fixed in the sample. The 1st probe was at 30 mm distance from the bottom, the distance between the probes was 30 mm, see Figure 2. The method of probes installation eliminates the effect of probe contact with the material.

Figure 2: Photograph of water uptake and drying experiment

Before the 1st water uptake cycle, the sample was dried at 40°C. In order to provide an approximately isothermal suction, the sample was kept at room temperature and protected against the water vapour adsorption from the ambient air. The water uptake experiment was carried out at a laboratory temperature.

A direct comparison of the measured moisture profiles is difficult, therefore Boltzmann transformation in the form (1) [4] was used:

$$\lambda = x \cdot t^{-1/2} \tag{1}$$

If the Boltzmann-conditions are fulfilled (a constant boundary condition applied to the semi-infinite homogeneous medium that is initially at an uniform moisture content), all the measured moisture profiles should fall on a single *λ-w* profile [4].

The liquid water diffusivity can be determined from transient moisture content profiles using one-dimensional isothermal differential liquid water transfer equation (2):

$$\frac{\partial w}{\partial t} = \frac{\partial}{\partial x} \cdot \left(D(w) \cdot \frac{\partial w}{\partial x} \right) \tag{2}$$

For initial conditions ($w = w_0$ at $x > 0$ at $t = 0$) and boundary conditions ($w = w_B$ at $x=0$ and $t > 0$), the non-linear partial differential equation can be reduced to an ordinary differential equation.

$$-\frac{\lambda}{2} \frac{dw}{\partial \lambda} = \frac{d}{d\lambda} \cdot \left(D(w) \cdot \frac{\partial w}{\partial \lambda} \right) \tag{3}$$

Integrating equation (3), the liquid water diffusivity is given by equation (4) [4]:

$$D(w) = -\frac{1}{2} \cdot \frac{\int_{w_0}^{w} \lambda du}{\partial w / \partial \lambda} \tag{4}$$

Based on the Boltzmann approximation, the λ-w profile for 1st water uptake experiment was constructed, see Fig.3. The positions of the probes are measured from the bottom of the sample.

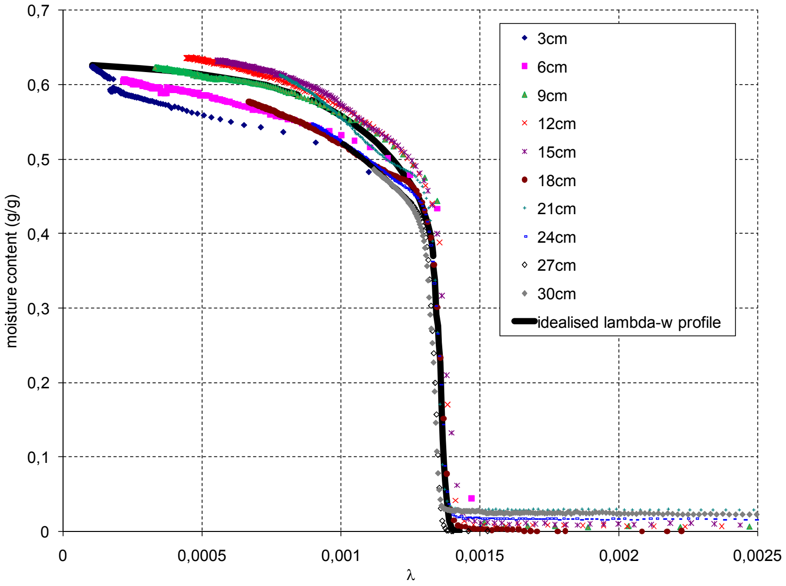

Figure 3: λ-w profile constructed after 1st sorption cycle.

After the capillary saturation, the sample dried for about one and half months at the laboratory temperature, the drying took place only in one direction. In the next step, the sample was dried at 40°C and the water uptake experiment was repeated. In the second cycle the λ-w profile was significantly changed which is shown in Fig. 4.

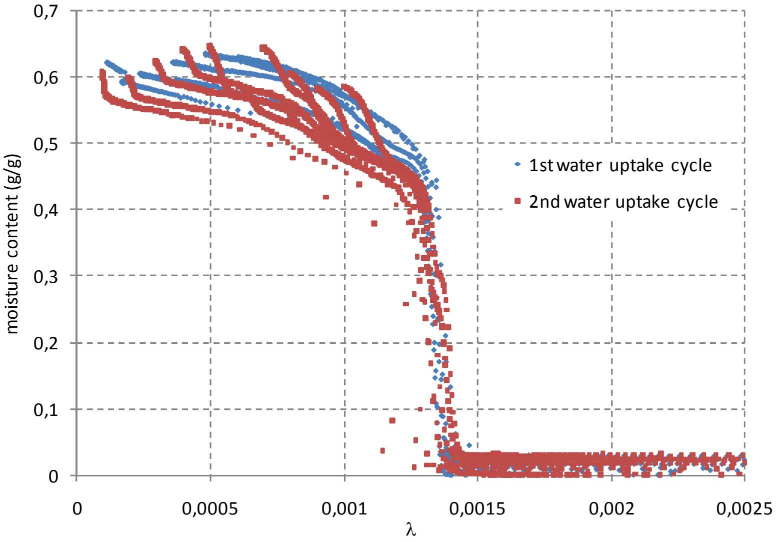

Figure 4: Comparison of λ-w profile after 1st and 2nd water uptake cycle

The deviation of the λ-w profile was significant in the range of $\lambda = 0.008$ to 0.012. The deviation confirmed the assumed additional hydration the plaster.

The change of the *λ-w* profile was reflected in the course of the liquid water diffusivity coefficient of. In fig. 5 the calculated liquid water diffusivity functions determined from particular *λ-w* profiles are shown.

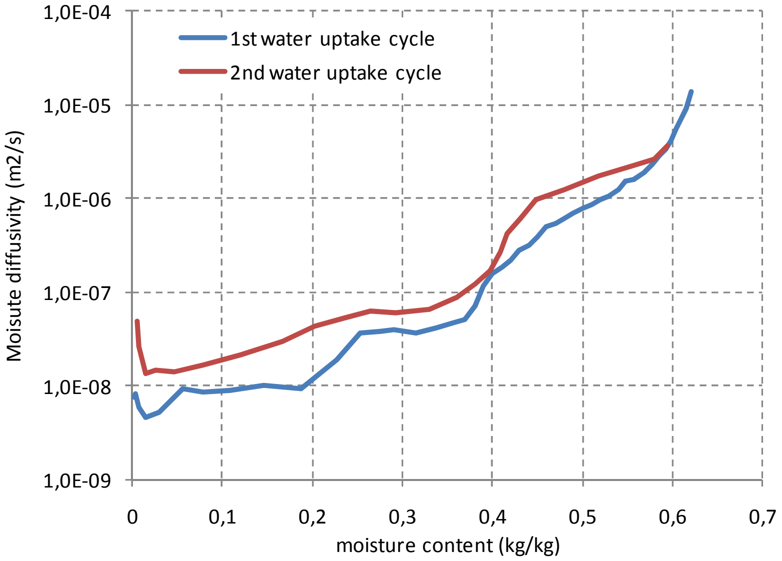

Figure 5: Liquid water diffusivity after 1st and 2nd water uptake cycle

A change of the plaster pore structure was analyzed by the mercury intrusion porosimetry method. The results are shown in Figures 5 and 6.

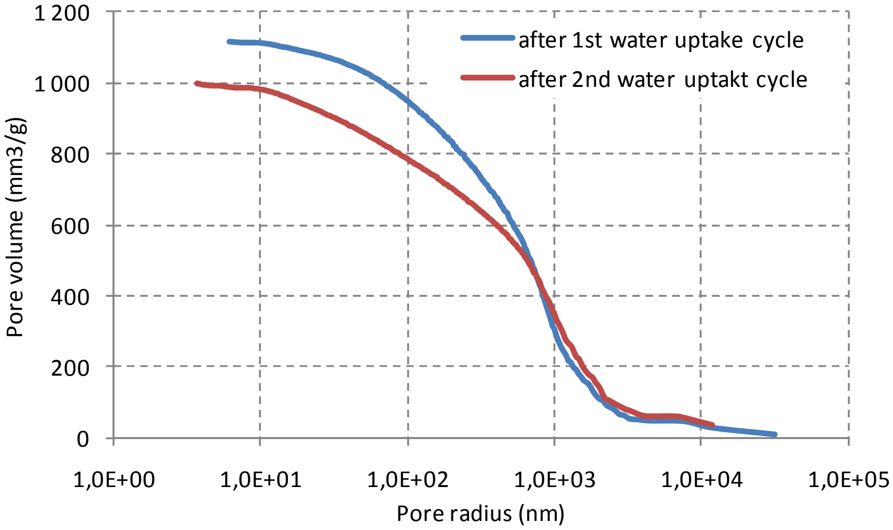

Figure 6: Cumulative pore size distribution after 1st and 2nd water uptake experiment

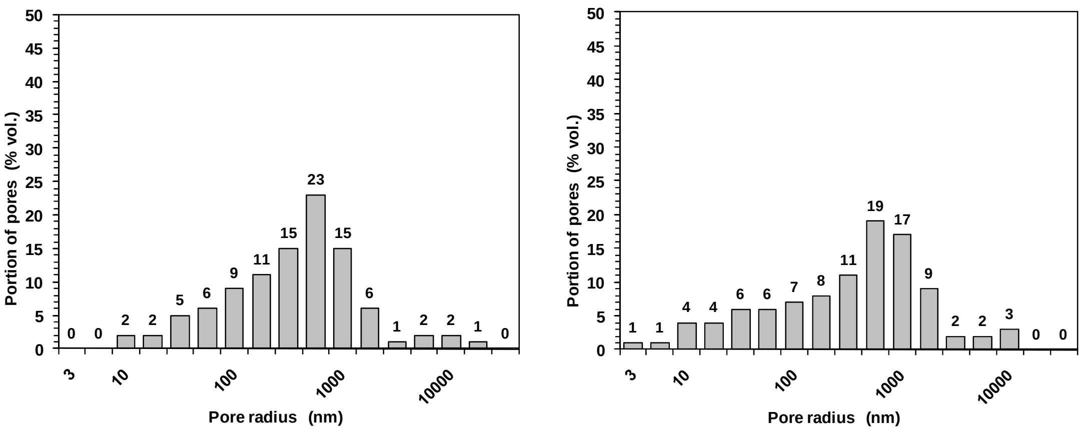

a b

Figure 7: Differential pore size distribution. a – after 1st water uptake, b – after 2nd water uptake

Comparing figures 5, 6a and 6b shows that the change in pore size parameters is significant. The pore radius median increased, whilst the porosity decreased. This resulted in increase the liquid water diffusivity after 2nd water uptake cycle.

4. Conclusions

This paper deals with determination of the liquid water diffusivity of the lime-cement perlite plaster at a multiple cyclic process of the water uptake. The water uptake process was monitored using the time domain reflectometry method. The impact of the additional hydration of the tested material to its liquid water diffusivity and change of pore structure was analysed. The additional hydration of the plaster, caused the changes in the pore structure and liquid water diffusivity of the analysed material. The lime-cement perlite plaster is not the chemically stable material in a contact with water.

Acknowledgement

Autors wish to thank the APVT-51-030704, APVV-0744-07 and VMSP-P-0153-09 projects for the financial support of this work.

References

[1] TOPP, G.C., DAVIS, J.L., ANNAN, A. P. Electromagnetic determination of soil water content: measurements in coaxial transmission lines, In: *Water Resources Research 16*, 1980, p. 574–582, ISSN 0043-1397

[2] MALICKI, M.A., PLAGGE, R., ROTH, C.H. Improving the calibration of dielectric TDR soil moisture determination taking into account the solid soil, in: *European Journal of Soil Science 47*, 1996, p. 357–366, ISSN 1351-0754

[3] DALTON, F.N. Development of time-domain reflectrometry for measuring soil water content and bulk soil electrical conductivity. In: *Advances in Measurement of Soil Physical Properties: Bringing Theory into Practice*, 1992, p.143–167, ISBN 0891188010

[4] ROELS, S.; CARMELIET, J.; HENS. H. HAMSTAD, WP1: Final report, Moisture transport properties and materials characterisation, 2003

Investigation of moisture transport in aluminium cooling panel plaster at cyclic water sorption regimes

Peter Mihalka, Peter Matiasovsky

Institution of Construction and Architecture, Slovak Academy of Sciences, Dubravska cesta 9,
845 03 Bratislava, email: usarmipe@savba.sk

***Abstract**: The cooling ceiling panels made of the aluminium foam, with integrated circulation water distribution system, were developed. The properties of the aluminium foam (the relatively high thermal conductivity, the low bulk density) can predetermine these panels as the efficiently and rapidly reacting heat exchange elements. At the design of these cooling systems, it is necessary to prevent potential hygiene problems during their operation. The surface temperature of the panels must be higher than the dew point temperature and also higher than the temperature critical for growth of fungi. Therefore the temperature of cooling medium is limited and cannot fall below this critical value. To use the lower temperatures, the indoor air humidity, as well as the humidity of panel surface have to be maintained below the water vapour saturation values. This can be attained by the dehumidification devices in a room in a combination with the effectively designed hygroscopic panel surfaces. Therefore, the hygroscopic surface finishing plasters of the aluminium panels were developed. The simulation model of coupled 1D heat and moisture transport taking into account the sorption hysteresis in hygroscopic region was used to analyse the moisture response of the surface finishing plaster.*

***Keywords**: cooling panel, hygroscopic plaster, moisture transport, hysteresis*

1. Introduction

A hygroscopic plaster as the surface finishing of aluminium-foam cooling panel was designed in order to avoid the water vapour condensation and a growth of the fungi.

The moisture buffering materials in a room decrease directly the interior dew point temperature and allow for a longer operation of the cooling system [5]. An example of an analysis of the influence of the moisture buffering of gypsum cooling ceilings taking into account the simplified EMPD approach in comparison with the complex HAM was analysed in [4]. In the analysis the water vapour sorption hysteresis of the material was not considered.

The purpose of this work is to investigate the influence of vapour sorption hysteresis of hygroscopic plaster to its moisture response. In most of the simulation tools, the process of water vapour adsorption and desorption in building constructions is controlled by one function only, usually by the middle between the adsorption and desorption isotherms. In a case of hysteretic materials, the process of adsorption and desorption is not the same. The equilibrium moisture content during the desorption process is higher than the moisture content during the adsorption at the same relative humidity. The influence of this effect to the cooling panel - surface finishing contact hygrothermal performance was analysed numerically.

The analysis was carried out in the hygroscopic region. Three simplifications of the moisture storage function: adsorption isotherm, desorption isotherm and the middle curve were compared with the moisture hysteresis model in the simulations.

2. Mathematical model

The simulation model of coupled 1D heat and moisture transport taking into account the sorption hysteresis in hygroscopic region was used to analyse the moisture response of the surface finishing plaster.

The heat and moisture balance in the plate shape structure is formulated by the system of two partial differential equations:

$$\rho \cdot c \cdot \frac{\partial \theta}{\partial t} = \frac{\partial}{\partial x}\left(\lambda \cdot \frac{\partial \theta}{\partial x}\right) \tag{1}$$

$$\frac{\partial w_c}{\partial \varphi} \cdot \frac{\partial \varphi}{\partial t} = \frac{\partial}{\partial x}\left(\delta_p \cdot \frac{\partial (p_{sat} \cdot \varphi)}{\partial x}\right) \tag{2}$$

where: ρ = bulk density, c = specific heat capacity, λ = thermal conductivity, t = time, θ = temperature, x = dimension, φ = the relative humidity, w_c = the moisture content, $\partial wc/\partial\varphi$ = the moisture capacity, p_{sat} = the partial pressure of saturated water vapour, δ_p = the permeability of water vapour.

The boundary conditions are given by indoor the air temperature and relative humidity, the surface transfer coefficients and by the cooling water temperature.

In the hysteretic material, the moisture capacity is given the by slope of the scanning sorption curves. The scanning curves always lie between the main adsorption and desorption isotherms. A simple empirical model describing the scanning curves was proposed by [3]. In this model the moisture capacity in the hysteresis region is represented by the slope of the scanning curves:

$$\xi_{hys} = \frac{\gamma_a \cdot (u - u_{adsorption})^A \cdot \xi_{desorption} + (u - u_{desorption})^A \cdot \xi_{adsorption}}{(u_{desorption} - u_{adsorption})^A} \tag{3}$$

$$\xi_{hys} = \frac{(u - u_{adsorption})^D \cdot \xi_{desorption} + \gamma_d \cdot (u - u_{desorption})^D \cdot \xi_{adsorption}}{(u_{desorption} - u_{adsorption})^D} \tag{4}$$

where: ξ_{hys} = the moisture capacity, u = the water content, $u_{adsorption}$ = the water content calculated from main adsorption isotherm, $u_{desorption}$ = the water content calculated from main desorption isotherm, $\xi_{adsorption}$ = the moisture capacity calculated from main adsorption isotherm, $\xi_{desorption}$ = the moisture capacity calculated from main desorption isotherm, $\xi_{desorption}$ = the moisture capacity calculated from main desorption isotherm, A, γ_a = the parameters of hysteresis during adsorption, D, γ_d = the parameters of hysteresis during desorption. The parameters A, γ_a, D, γ_d were determined for various building materials in [1].

The main adsorption and desorption curves and the middle curve were described by combination of BET [7] and Hansen [6] functions in the form [8]:

$$u(\varphi) = (1 - \varphi^k) \cdot u_m \cdot C \cdot \frac{\varphi}{(1-\varphi) \cdot [1 - (C-1) \cdot \varphi]} + \varphi^k \cdot u_h \cdot \left(1 - \frac{\ln(\varphi)}{A}\right)^{-\frac{1}{n}} \tag{5}$$

where: u = the moisture content (g/g), φ = the relative humidity (-), u_h = the hygroscopic moisture content (g/g), u_m = the monomolecular moisture content, A = parameter, n,k = exponents. The parameters are listed in Table 2.

The moisture capacity of main adsorption and desorption curves are in the form:

$$\frac{\partial u}{\partial \varphi}(\varphi) = \frac{-\varphi^k \cdot k \cdot u_m \cdot C}{(1-\varphi)\cdot[1+(C-1)\cdot\varphi]} + \frac{(1-\varphi^k)\cdot u_m \cdot C}{(1-\varphi)\cdot[1+(C-1)\cdot\varphi]} + \frac{(1-\varphi^k)\cdot u_m\cdot C\cdot\varphi}{(1-\varphi)^2\cdot[1+(C-1)\cdot\varphi]}$$
$$- \frac{(1-\varphi^k)\cdot u_m\cdot C\cdot\varphi}{(1-\varphi)\cdot[1+(C-1)\cdot\varphi]^2} + \frac{k}{\varphi}\cdot\varphi^k\cdot u_h\cdot\left(1-\frac{\ln(\varphi)}{A}\right)^{-\frac{1}{n}} + \varphi^k\cdot u_h\cdot\frac{\left(1-\frac{\ln(\varphi)}{A}\right)^{-\frac{1}{n}}}{n\cdot\varphi\cdot A\cdot\left(1-\frac{\ln(\varphi)}{A}\right)} \tag{6}$$

The main desorption isotherm was approximated by the relationship between adsorption and desorption isotherms [9]:

$$\varphi_{desorption} = \varphi^2_{sorption} \tag{7}$$

3. Simulations

A simplified fragment of the aluminium cooling panel with surface finishing plaster was analysed. The parameters of the fragment are in Table 1. For the analysed plaster the main adsorption isotherm and the trends of the primary desorption scanning curves were determined in dessicators using the standard gravimetric technique (Fig. 1).

Table 1. Parameters of cooling panel

Layer	Thickness (m)	Porosity -	Thermal conductivity (W/m.K)	Vapour permeability (kg/m.s.Pa)
aluminium foam	0.010	85 %	15	-
plaster	0.005	67 %	0.07	Eq.8 [10]

$$\delta(\varphi) = 1.96\cdot 10^{-10}\cdot(0.1675\cdot 10^{-4} + 42.55\cdot 10^{-4}\cdot e^{(4.491\cdot\varphi)} \tag{8}$$

The best fitting parameters of the adsorption isotherm with the parameters of desorption and middle curves are listed in Table 1.

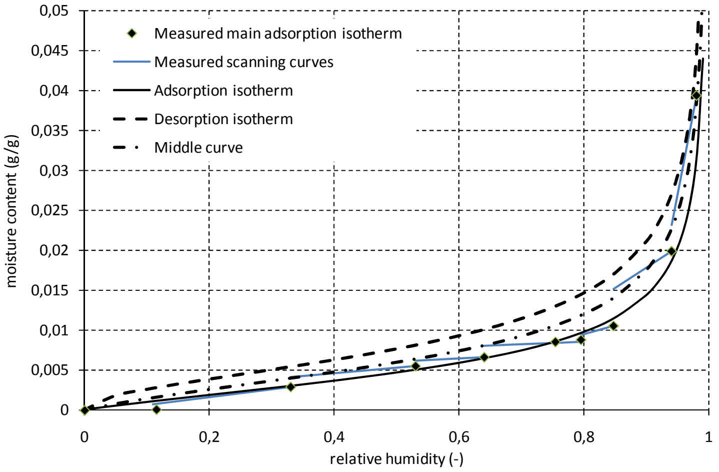

Figure 1: Main adsorption and desorption isotherm, scanning curves and middle curve.

Table 2. Parameters of sorption isotherm model

Sorption isotherm	u_m	C	u_h	A	n	k
adsorption	0.003	1	0.23	0.00038	2	0.8
desorption	0.003	2	0.28	0.00035	2.3	0.8
middle curve	0.003	1.5	0.25	0.00037	2.15	0.9

A possible range of the parameters used in the presented hysteresis model was analysed in [1]. For most of the inorganic materials, the optimal values of the exponent $A = D = 2.0$. The parameters of γ_a and γ_d are optimal within range 0.7 – 0.95. For a correct determination of hysteresis model parameters, the main desorption isotherm with more scanning curves have to be known. New parameters should be determined using the procedure in [1]. In this contribution, the following parameters were used: $A = D = 2.0$, $\gamma_a = \gamma_d = 0.90$.

As a result of the thermal and vapour balance in a room the boundary conditions for Equations (1) and (2) are expressed in the form of daily periodical courses of the indoor air temperature and the cooling panel surface (determined by the cooling water) temperature (Fig. 2). The indoor air relative humidity was assumed to be kept constant equal to 50 %. No water vapour condensation resulted from the simulations.

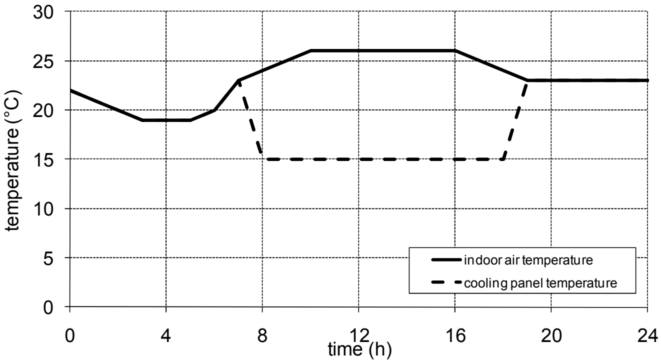

Figure 2: Indoor air temperature and cooling panel surface temperature.

The calculations were repeated until the quasi-steady state was reached.

4. Results

The courses of the scanning curves until the quasi-steady state at the surface, in the middle of the plaster and at its contact with the aluminium foam panel are in Figure 3.

The calculated moisture content and relative humidity with a consideration of the main curves, the middle curve and the sorption hysteresis are shown in Figures 4 and 5 respectively.

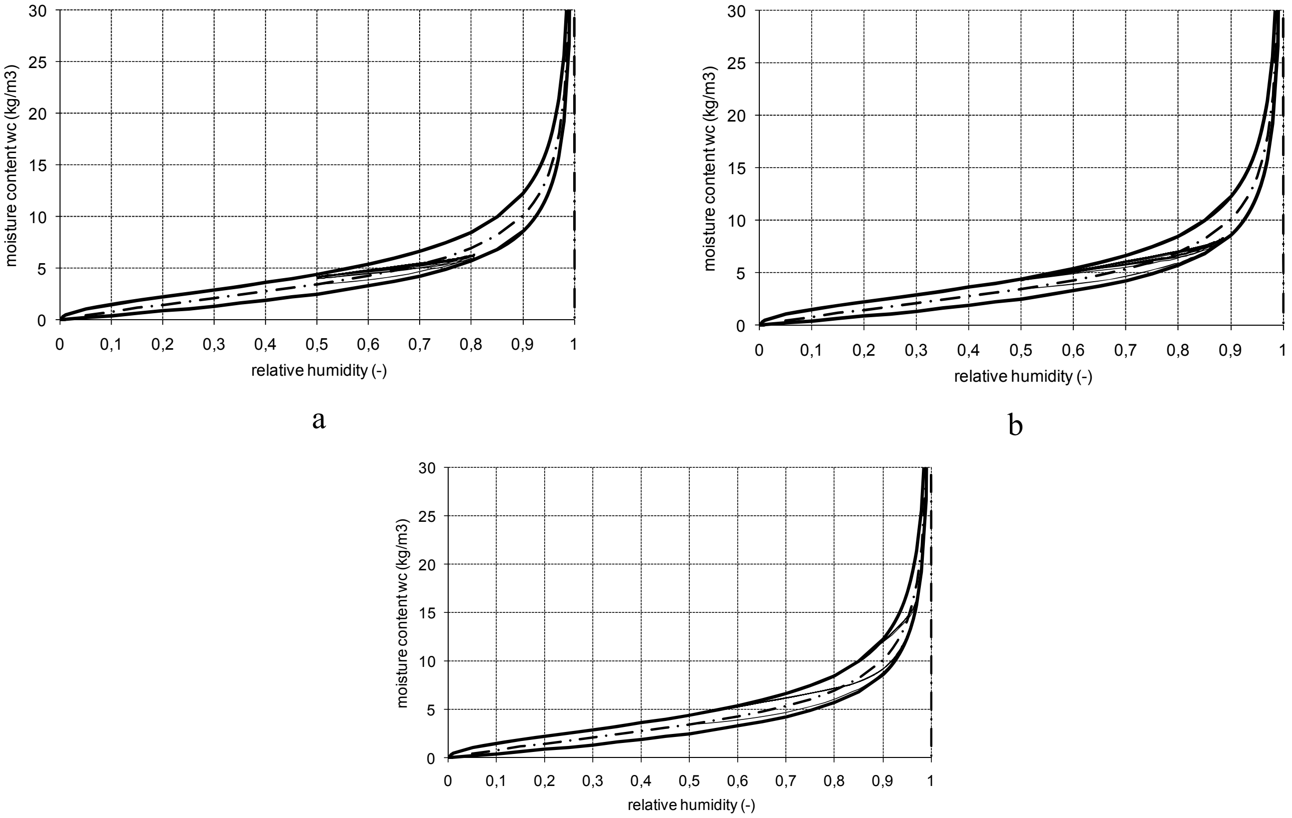

a

b

c

Figure 3: Scanning curves, a –surface, b – middle of the plaster, c – contact with the aluminium cooling panel.

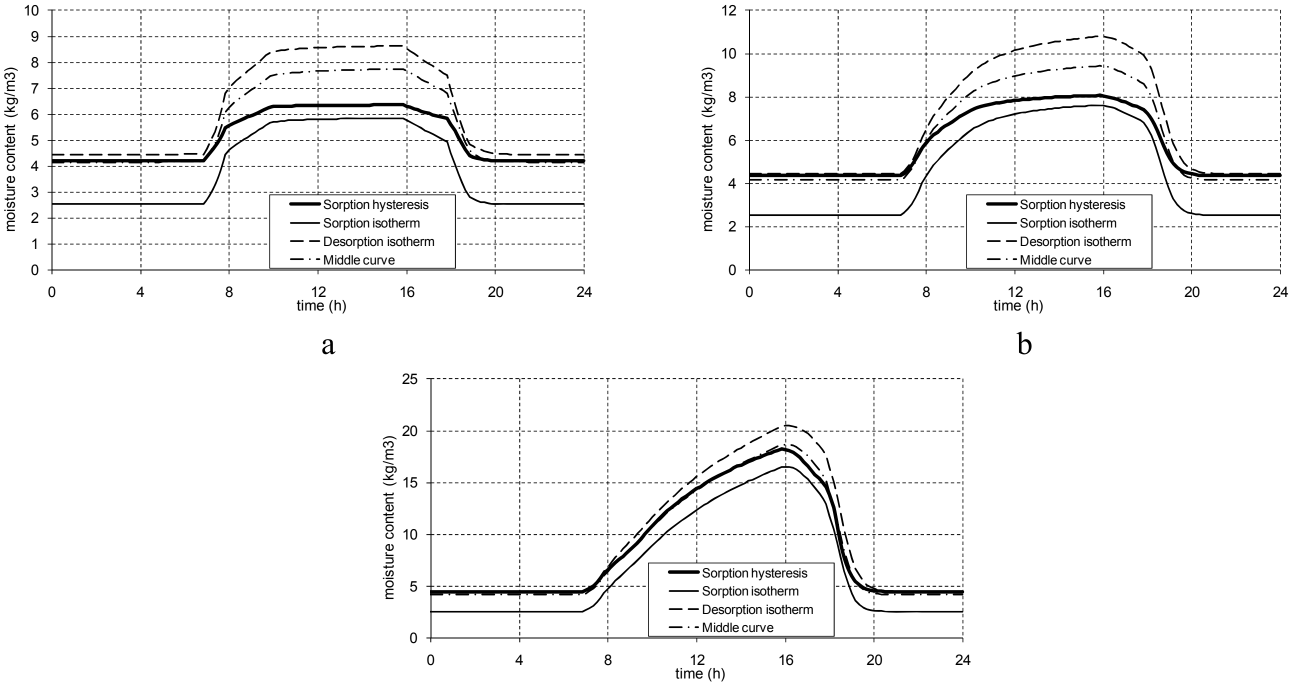

a

b

c

Figure 4. Calculated moisture content course after reaching quasi-steady state, a –surface, b – middle of the plaster, c – contact with the aluminium foam cooling panel.

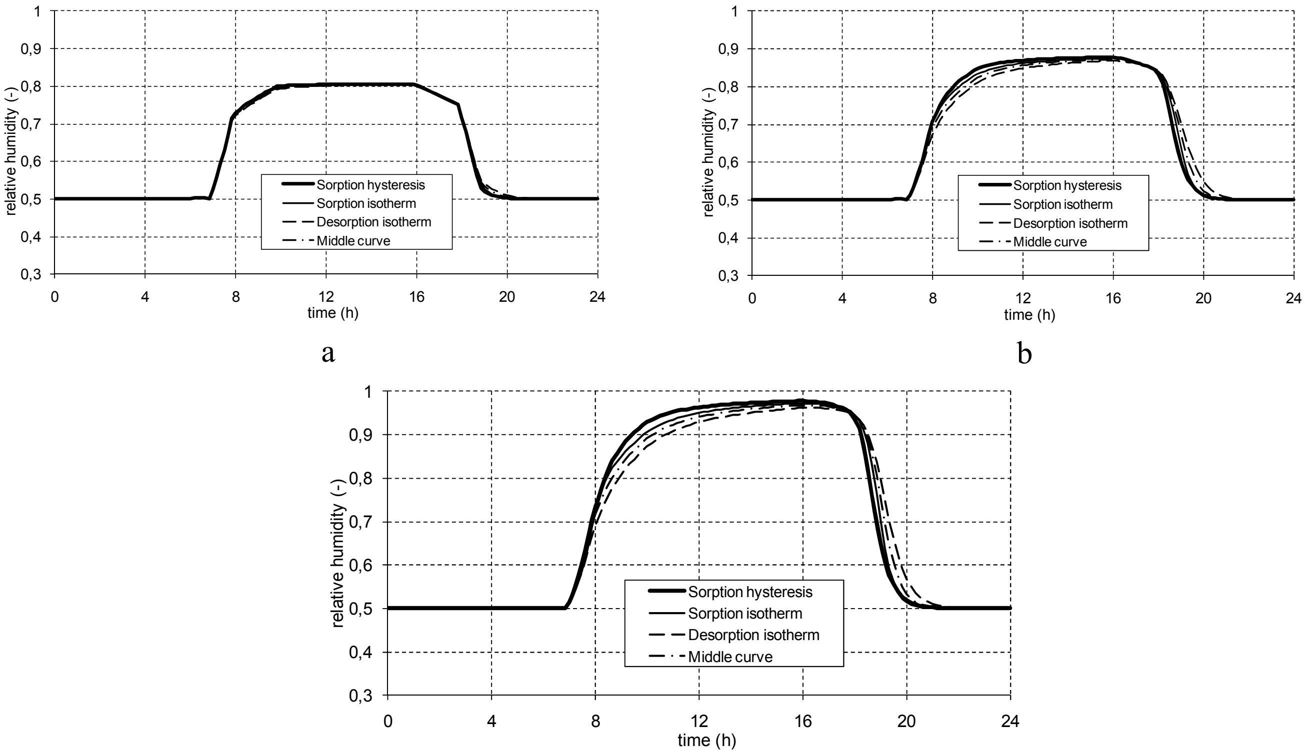

a

b

c

Figure 5. Calculated relative humidity course after reaching quasi-steady state, a –surface, b – middle of the plaster, c – contact with the aluminium foam cooling panel.

The calculated scanning curves at surface and in the middle of the plaster always lie near the middle between main curves, but they have lower slopes than the middle curve (Fig. 3a, b). A different situation is on the contact of the plaster with the aluminium foam cooling panel. The diffused water vapour near the cold vapour-tight panel increases the moisture content and the drying process below 80 % relative humidity is significantly controlled by the desorption isotherm.

On the plaster surface the different approach to the moisture accumulation modelling was noticeable only in the case when the hygric state of the plaster was expressed by the moisture content (Fig. 4a). The highest value of the moisture content was reached with the desorption isotherm. The calculation with middle curve gives higher values of the moisture content than in the case of sorption hysteresis. The difference in relative humidity is neglible (Fig. 5a).

In the middle of the plaster, the influence of the moisture accumulation rises (Fig. 4b). The highest moisture content was reached with desorption isotherm model again, but the relative humidity was lower. This was affected by a higher moisture capacity (Fig. 3b). A calculation with the middle curve again overestimated the moisture content in comparison with the sorption hysteresis model.

At the contact of the plaster with the aluminium cooling panel, the highest relative humidity was reached with the sorption hysteresis (Fig. 5c). The highest moisture content was achieved with the desorption isotherm (Fig. 4c). The calculation with the sorption hysteresis gives lower values than with the middle curve.

5. Conclusions

The application of the hygroscopic plaster eliminates the risk of the cooling panel surface condensation. A hysteretic behaviour of the water vapour sorption in the hygroscopic plaster on the aluminium foam cooling panel was numerically investigated. Three simplifications of the moisture accumulation curve were compared with the hysteresis model. At the relative humidities below 90 %, the simulation with sorption hysteresis gives lower moisture contents than the simulation with the middle curve, but above 90 % relative humidity the calculated moisture content is significantly higher than in the case of middle curve. On the surface, the influence of hysteretic behaviour to the relative humidity is negligible. The results confirm that the application of the sorption hysteresis in the hygrothermal performance simulation enables a more correct analysis of the condensation risk, than the simplified approaches.

Acknowledgement

Authors wish to thank the APVT-51-030704, APVV-0744-07, VMSP-P-0153-09 and VEGA Grant No 2/0159/10 projects for the financial support of this work.

References

[1] MIHALKA, P., MATIASOVSKY, P. Analysis of moisture hysteresis of building materials in hygroscopic range. In: *Thermophysics 2009 conference proceedings*, 2009, p.101-106, ISBN 978-80-214-3986-3

[2] MIHALKA, P. ET AL. Simulation of hysteretic behaviour at dynamic moisture response, In: *Proceedings of Thermophysics 2008*, 2008, p.101-105, ISBN 978-80-227-2968-0

[3] PEDERSEN, C.R. Combined heat and moisture transfer in Building Constructions, PhD Thesis, 1990, Technical University of Denmark.

[4] STEEMAN, M. ET AL. On coupling 1D non-isothermal heat and mass transfer in porous materials with a multizone building energy simulation model, In: *Building and Environment*, 2010, p.865-877, ISBN 0360-1323

[5] CATALINA, T. ET AL. Impact of moisture buffering on energy performance of cooling ceilings, Annex 41, 2006

[6] HANSEN, K.K. Sorption isotherms, a catalogue. Department of Civil Engineering, Technical University Denmark, 1986.

[7] BRUNAUER, S.; EMMET, P.H. ;TELLER, E.: Adsorption of Gases in Multimolecular Layers, In: *Journal of the American Chemical Society, vol.60*, 1938, p.309-311, ISSN 0002-7863

[8] MATIASOVSKY, P., TAKACSOVA, Z. Analysis of water vapour sorption process in static dessicator method, Thermophysics 2009 conference proceedings, 2009, 88-93, ISBN 978-80-214-3986-3

[9] GREGG, S.J., SING, K.S.W. Adsorption, surface area and Porosity, Academic Press, 1982, ISBN 0123009561

[10] ROELS, S., DEPRAETRE, W., CARMELIET, J., HENS, H. Simulating Non-Isothermal Water Vapour Transfer: An Experimental Validation on Multi-Layered Building Components, In: Journal of Building Physics, SAGE, 1999, 17-40, ISSN 1744-2583

Thermal diffusivity in electroceramics during linear heating

Ján Ondruška[1], Igor Medveď[1,2], Anton Trník[1,2]

1Department of Physics, Constantine the Philosopher University, 94974 Nitra, Slovakia

2Department of Materials Engineering and Chemistry, Czech Technical University, 16629 Prague, Czech Republic, e-mail: jan.ondruska@ukf.sk

Abstract: *Ceramic mixtures used as electric insulators usually contain kaolinite. In the temperature range 450 – 650 °C the process of dehydroxylation occurs, and kaolinite changes into metakaolinite. During this reaction, physical properties of ceramic materials, including the thermal diffusivity, may rather strongly vary. Using experimental measurements of thermal fields in cylindrical electroceramic samples during linear heating, we determine the dependence of the thermal diffusivity on the temperature.*

Keywords: *thermal diffusivity, inverse method, ceramics*

1. Introduction

Green ceramic mixtures during heating change their physical and mechanical properties [1, 2, 3]. The first process which can be observed is the liberation of physically bonded water in the temperature region ~100 - 250 °C [2]. Another process which results in a weight loss in kaolinite crystals is called dehydroxylation. This process starts at the temperature ~400 °C and finishes at the temperature ~650 °C and is connected with the phase transformation of kaolinite into metakaolinite [1, 4]. At the end of a firing process, ~850 - 900 °C, one can observe the reaction connected with the metakaolinite-to-spinel phase transformation [5, 6]. All these reactions are endothermic processes. In large samples the endothermic reaction causes that the thermal field in the sample is not uniformly distributed. As a result, the thermal diffusivity is dependent on the temperature.

In this paper we study the thermal diffusivity in traditional electroceramics. We focus on the thermal fields which describe the distribution of processes occurring in the samples. From these thermal fields we calculate the thermal diffusivity, using standard numerical methods.

2. Sample and methods

The samples were prepared from the wet plastic ceramic mass provided by the electro-porcelain plant PPC Čab, Slovakia. The initial composition of the ceramic material was 48 wt. % of kaolin and clay, 30 wt. % of alumina, and 22 wt. % of feldspar. The samples have a cylindrical shape of diameter 80 mm and length 120 mm. Four holes (of diameter 2 mm) were bored in the samples as shown in Fig.1, and thermocouples Pt-PtRh10 were placed in these holes.

First, the samples were dried in the furnace at the isothermal regime at 150 °C for 400 minutes. The temperature 150 °C was reached by a linear heating with the heating rate 0.5 °C/min. Then the samples were cooled down to the room temperature. We prepared some samples pre-heated at the temperatures 150 °C, 500 °C, 700 °C, and 1000 °C.

The main measurement was performed by a linear heating up to 1000 °C with the heating rate 1 °C/min. During the heating temperatures were measured with the Pt-PtRh10 thermocouples at four different radial positions of the sample: 0 cm, 1 cm, 2 cm, and 3 cm (see Fig.1).

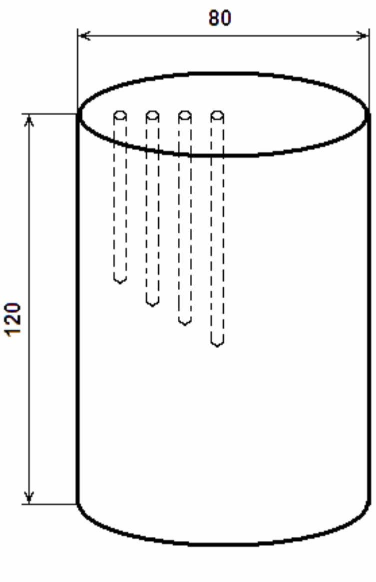

Figure 1: A cylindrical sample with four holes for thermocouples.

The dimensions are in mm.

The thermal diffusivity, *a*, was numerically calculated from the heat conduction equation with no internal heat source that is given in the cylindrical coordinates as [7]

$$\frac{\partial T}{\partial t} = a\frac{1}{r}\left(\frac{\partial T}{\partial r} + r\frac{\partial^2 T}{\partial r^2}\right) \tag{1}$$

where, in the numerical calculation, we used the finite-different formulas

$$\frac{\partial T_{i,j}}{\partial t} = \frac{-T_{i+2,j} + 8T_{i+1,j} - 8T_{i-1,j} + T_{i-2,j}}{12\Delta t}, \tag{2}$$

$$\frac{\partial T_{i,j}}{\partial r} = \frac{T_{i,j-2} - 6T_{i,j-1} + 3T_{i,j} + 2T_{i,j+1}}{6\Delta r}, \tag{3}$$

$$\frac{\partial T_{i,j}}{\partial r} = \frac{T_{i,j+1} - 2T_{i,j} + T_{i,j-1}}{\Delta r^2}. \tag{4}$$

Here $T_{i,j}$ is the temperature at time t_i and radial position r_j.

3. Results and discussion

Figures 2 - 5 describe the dependence of the thermal diffusivity on the temperature for samples pre-heated into different temperatures (150 °C, 500 °C, 700 °C, and 1000 °C).

In Figure 2 we can see several important peaks. The first peak is in the temperature region ~100 - 150 °C and it represents the elimination of physically bonded water. The second peak with a maximum at ~600 °C represents the dehydroxylation of kaolinite. The last peak with a maximum at ~950 °C represents the metakaolinite-to-spinel phase transformation. All these reactions have an effect on a value of the thermal diffusivity.

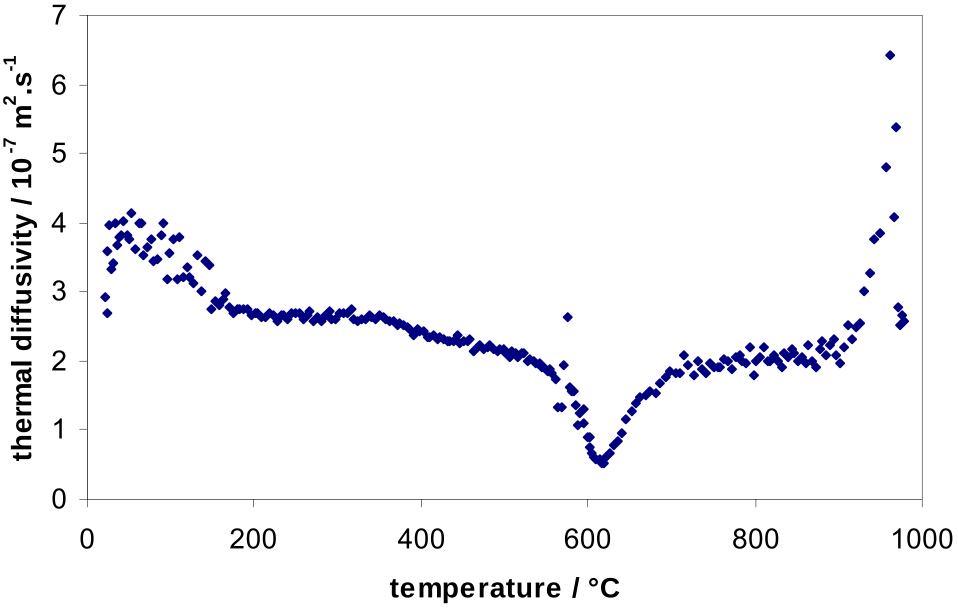

Figure 2: The dependence of the thermal diffusivity on the temperature

for a cylindrical sample pre-heated to 150 °C.

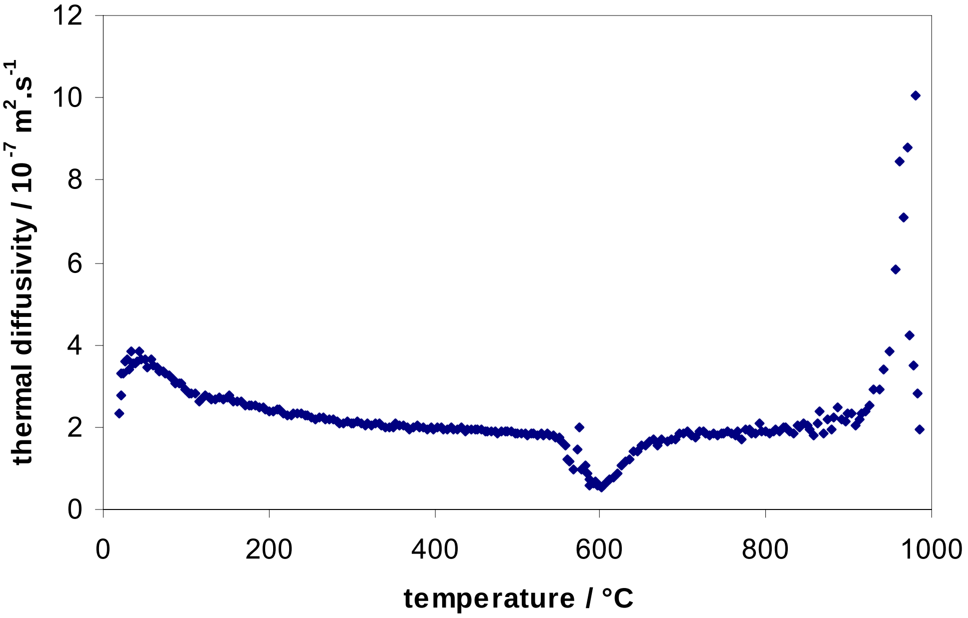

Figure 3: The dependence of the thermal diffusivity on the temperature

for a cylindrical sample pre-heated to 500 °C.

In Figure 3 we can observe similar peaks as in Figure 2. At the temperature ~500 °C the dehydroxylation is still running, but is not yet finished. This is the reason why the peak in the dehydroxylation region is shown again.

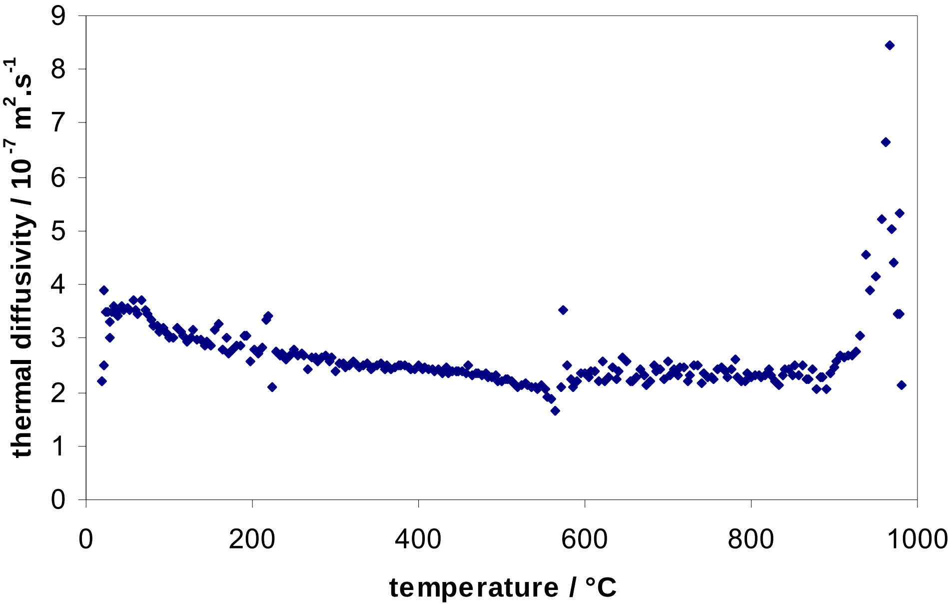

Figure 4: The dependence of the thermal diffusivity on the temperature

for a cylindrical sample pre-heated to 700 °C.

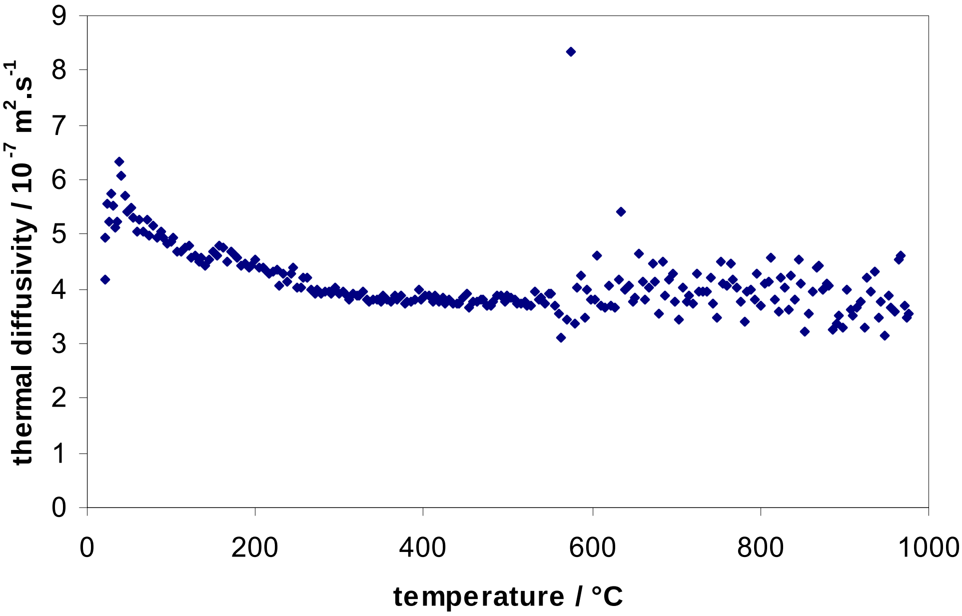

Figure 5: The dependence of the thermal diffusivity on the temperature

for a cylindrical sample pre-heated to 1000 °C.

In Figure 4 there is no peak in the temperature region ~450 °C – 650 °C which means that the dehydroxylation is already finished. At ~950 °C the phase transformation of metakaolinite into spinel still occurrs.

The Figure 5 depicts somewhat different results. There are no peaks in the whole temperature region because this sample was already pre-heated to 1000 °C for 400 minutes and both phase transitions (kaolinite into metakaolinite and matakaolinite into spinel), which are non-reversible processes, had already taken place and do not occur again. The data dispersion is caused by using numerical derivations during calculating the thermal diffusivity.

4. Conclusion

We performed measurements of the temperature in dependence on time and radial distance for cylindrical electroceramic samples pre-heated to four different temperatures. The results of our experiments show that the thermal diffusivity may strongly depend on the temperature during firing process. The dependence is most varying during the liberation of physicaly bonded water (~100 - 250 °C), dehydroxylation (~400 - 650 °C), and metakaolinite-to-spinel phase transformation (~850 - 900 °C). After finishing the firing process, the dependence of the thermal diffusivity on the temperature is almost constant.

Acknowledgement

This work was supported by grants VEGA 1/0302/09, APVV SK-CZ-0004-09, and UGA I-09-304-01 as well as by the cooperation of electro-porcelain plant PPC Čab, Slovakia, a member of the international PPC Insulators Group.

References

[1] BRINDLEY, G. W.; SHARP, J. H.; PATTERSON, J. H.; NARAHARI, B. N. Kinetics and mechanism of dehydroxylation process, I. temperature and vapor pressure dependence on dehydroxylation of kaolinite. In *The American Mineralogist*. 1967.52(N1-2). p.201-211

[2] KOZÍK, T. et al. The temperature dependence of the electric conductivity of unfired porcelain mixture. In *Ceramics – Silikáty*. 1992.36. p. 69-72

[3] KOZÍK, T.; ŠTUBŇA, I. Mechanical strength of the ceramic material in the dehydroxylation temperature region. In *Silikáty*. 1981.25. p. 237-241

[4] ČÍČEL, B.; NOVÁK, I.; HORVÁTH, I. *Mineralogy and crystalochemistry of clays*. SAV Bratislava, 1981

[5] ŽIVANOVIČ, B.; JANOVIČ, O. Dehydroxylation of kaolinite. In *Hem. Ind.* 1978.32(N8). p.512-516

[6] POPPE, L.; GABOR, M.; WAJAND, J.; SZABÓ, Z. Two-step dehydroxylation of the kaolinite. In *Proc. 1st Symp. Thermal Anal*. Salford 1976, p.332-335

[7] ÖZIȘIK, M., N. *Heat conduction*. John Willey & Sons, Inc., New York, 1993, pp.692, ISBN 0-471-53256-8

Comparative-complementary investigations of thermophysical properties – high thermal resolution procedures in practice

Andrzej J. Panas

Military University of Technology, Kaliskiego 2 Street, 00-908 Warsaw, Poland / Air Force Institute of Technology, Księcia Bolesława 6 Street, 01-494 Warsaw, Poland, email: Andrzej.Panas@wat.edu.pl

Abstract: *The paper deals with multiproperty complementary investigation of thermophysical properties. The attention is focussed on high thermal (temperature) resolution investigations, which suggests investigations of materials exhibiting temperature dependence of properties including phase transitions. Because of a common micro-physical background for different phenomenological features the comparative analysis create a unique opportunity for better understanding of experimental results and contributes to further development of the theory. Very close relations link thermal expansion with specific heat and thermal conductivity with electrical conductivity. In this case selected problems of such complementary multiproperty investigation are recalled having in mind mainly dilatometric and microcalorimetric studies. Issues of theoretical relations between the two measured properties, temperature gradient and temperature heating/cooling rate effects, as well as handling high thermal resolution experimental handling using B-spline approximation are discussed in brief. The analysis is illustrated with the results of experiments performed on materials exhibiting phase transitions. The measurements were performed applying laser interferometry apparatus and differential scanning calorimeter.*

Keywords: *thermophysical properties, thermal expansion, specific heat, thermal diffusivity, laser inetrferometry, differential scanning calorimetry, temperature oscillation method*

Notation

a	$m^2\cdot s^{-1}$	- thermal diffusivity (TD)
C_p	$J\cdot kmol^{-1}\cdot K^{-1}$	- molar heat capacity at constant pressure
C_V	$J\cdot kmol^{-1}\cdot K^{-1}$	- molar heat capacity at constant volume
c_p	$J\cdot kg^{-1}\cdot K^{-1}$	- heat capacity at constant pressure / specific heat
e	C	- elementary charge
G	J	- free enthalpy (Gibbs free energy)
H	J	- enthalpy
k_B	$J\cdot K^{-1}$	- Boltzmann constant
l	m	- length
m	kg	- mass
p	Pa	- pressure
q_V	$W\cdot m^{-3}$	- heat source volumetric density

S	$\mathrm{J \cdot K^{-1}}$	- entropy
r	m	- radial coordinate
T	K	- absolute temperature
t	°C	- temperature
p	Pa	- pressure
$w(T)$	n.d.	- weight function
x,y,z / z	m	- space coordinates / axial coordinate
α	$\mathrm{K^{-1}}$	- coefficient of linear thermal expansion
α^*	$\mathrm{K^{-1}}$	- "experimental" coefficient of linear thermal expansion (CLTE)
β	$\mathrm{K^{-1}}$	- cubic (volumetric) expansion coefficient (thermal expansivity)
ε	$\mathrm{mm \cdot m^{-1}}$	- linear expansion
γ_G	n.d.	- Grüneisen parameter
κ_T	$\mathrm{Pa^{-1}}$	- isothermal compressibility
λ	$\mathrm{W \cdot m^{-1} \cdot K^{-1}}$	- thermal conductivity (TC)
θ_D	K	- Debye temperature
ρ	$\mathrm{kg \cdot m^{-3}}$	- density
σ	$\mathrm{S \cdot m^{-1}}$	- electrical conductivity
τ	s	- time
ψ	n.a.	- a certain thermophysical parameter
DSC		- differential scanning calorimetry
MTDSC		- modulated temperature DSC
LF		- laser flash
PTFE		- polytetrafluoroethylene

1. Introduction

It is a well-known fact that all thermophysical properties are closely related to each other [7]. These relations have roots in a molecular level interaction [7, 11, 18, 36]. They manifest themselves in linking formulae developed on the basis of statistical molecular physics or on the basis of phenomenological thermodynamics. They are complemented by many experimental formulae or by relations stemming from mathematical transformations. The closest relations could be recognised within two characteristic groups of properties. The first group brings together properties related to energy accumulation phenomena which translate into the system (medium) structure. The relations between the heat capacity and thermal expansivity or between the density and the melting temperature [7] can serve as a typical example. The second group of properties is related to the energy (thermal energy) transfer It includes thermal conductivity and electrical conductivity [7, 9]. The relations facilitate complex investigations of thermal properties when procedures of individual property complementary studies are applied [24, 26, 27]. Even in the case of complex experiments, like those described in [12], they enable a widened range of post- experimental analyses.

The mutual relations or interdependence between thermophysical properties is most beneficial when temperature dependent thermal characteristics are measured or analysed. The term thermal or temperature characteristic refers to the temperature dependence of a certain thermal property. Strong temperature dependence usually characterises low temperature (cryogenic) behaviour of the matter and is also typical for the regions of phase transitions of different types (comp. e.g. [7], [9], [10] and [11]). Experimental investigation of thermophysical properties which are strongly temperature dependent produces several problems. One of the major preconditions for representativeness and compatibility of the experimental data is preservation of high thermal resolution of measurements.

The high thermal, or in other words, high temperature resolution means that a certain thermophysical property is obtained within a very small temperature interval so that the error of averaging can be neglected and the experimental data can be referred directly to a certain thermal characteristic. In turn, the need for increasing the temperature resolution results in other phenomena affecting the measurement accuracy. However, comparing the multiproperty investigation data and applying special data processing techniques one can obtain satisfactory results even when dealing with strongly irregular temperature dependence. Moreover, such complementary studies can reveal some hidden effects or features of the investigated substance or structure. A few typical examples of such studies performed on solids will be presented in this paper.

2. Representativeness and compatibility of thermophysical data

2.1. Examples of typical interrelations of individual thermophysical parameters

There are many thermodynamic coefficients defined on the basis of equilibrium and non-equilibrium thermodynamics (comp. e.g. [5], [10], [20]). In fact, every physical property showing temperature dependence can be recognised as thermophysical one [7]. However, the experimental thermophysics textbooks usually refer to the heat capacity, thermal conductivity, thermal diffusivity, thermal expansivity and density regarded as the major ones and to electric conductivity in addition [15, 16, 36]. As was mentioned before the two groups of properties can be recognised amongst them: thermal accumulation and thermal transport properties. The model relation linking properties from the first group is as follows [10, 11]:

$$\alpha = \frac{1}{\beta} = \frac{1}{3V}\left(\frac{\partial^2 G}{\partial p \partial T}\right) = \frac{\kappa_T}{3}\left[\frac{\partial S}{\partial V}\right]_T = -\left[\frac{\partial \ln T}{\partial \ln V}\right]_S \frac{\overline{C}_V \kappa_T}{3V} = \gamma_{\mathrm{G}} \frac{\overline{C}_V \kappa_T}{3V} \tag{1}$$

that is valid for isotropic media (comp. [7, 22]). In practice, this relation is mainly applied for comparative analyses of the heat capacity and thermal expansivity (thermal linear expansivity; see e.g. [27]). The Wiedemann-Franz law is a typical relation of the second group [7, 11]:

$$\frac{\lambda}{\sigma T} = L\,, \qquad L = \frac{\pi^2}{3}\left(\frac{k_B}{e}\right)^2 \frac{\tau_{\text{th}}}{\tau_{\text{el}}} \tag{2}$$

where τ_{th} and τ_{el} are thermal and electrical phenomena lifetimes respectively. The relation is limited to thermal and electrical conductors and links thermal conductivity with electric conductivity.

Despite differences, these and other formulae of a similar type are justified on the basis of statistical physics, phenomenological thermodynamics or both of them (comp. [6, 7]; see also Fig.1). Usually it is also possible to differentiate between types of interactions contributing to the global property: phonon, electron, magnetic, etc. For example, the relation (2), refers to electronic contribution. This fact makes comparative analyses of any type easier enabling predicting value of one parameter from another (comp. [32]).

Relations originating from thermodynamics of solids are complimented with one more that is recognised as the definition of thermal diffusivity[5]:

$$a = \frac{\lambda}{\rho\, c_p} \tag{3}$$

This relation can be obtained after transformation of the Fourier-Kirchhoff equation to simplified form [20]:

$$\rho\, c_p \frac{\partial T}{\partial \tau} = \nabla(\lambda\, \nabla T) + q_V \quad \wedge \;\; \lambda = \text{const} \qquad \Rightarrow \qquad \frac{\partial T}{\partial \tau} = \frac{\lambda}{\rho\, c_p} \nabla^2 T + q_V \tag{4}$$

and is valid only for space and temperature independent thermal conductivity. The physical significance of thermal diffusivity is wrongly associated with the speed of propagation of heat (comp. e.g. [20]). In fact there is no such notion as the speed of heat and the thermal diffusivity can be only interpreted in association with the time needed to achieve a certain temperature change at transient heat exchange. The formula (4) links together all main "engineering" thermophysical parameters characterising system behaviour at transient heat exchange, i.e. thermal conductivity, heat capacity and density. Despite the limitation introduced by assumption of constant thermal conductivity it is common practice to apply an extended relation

$$a(T) = \frac{\lambda(T)}{\rho(T)\, c_p(T)} \tag{5}$$

for recalculation of the results of multiproperty complementary measurement, mostly in prediction of the thermal conductivity from thermal diffusivity results [15].

---

[5] For isotropic media – problems of non-isotropic media will not be discussed here.

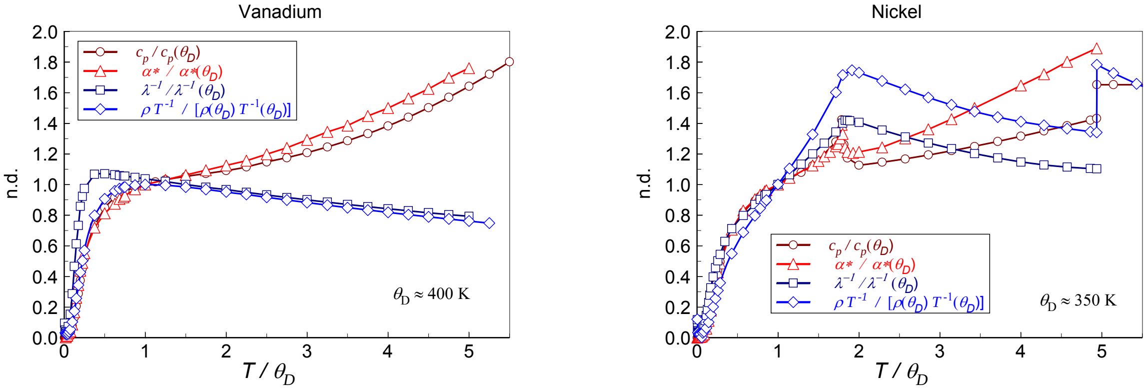

a *b*

Fig. 1. Comparison between normalised temperature characteristics illustrating relations specific heat with thermal expansion and thermal conductivity with electric conductivity for metallic elements [35]: a – vanadium, b – nickel (with ferromagnetic 2nd order phase transition at 625 K)

2.2. Finite thermal (temperature) resolution effect

The problem of thermal resolution is associated with temperature dependence of thermophysical properties. The term thermal or temperature resolution refers directly to the experimental investigation procedure. In most experimental techniques a certain temperature change or a certain temperature gradient is needed to obtain the appropriate property or a set of properties in multiproperty investigation. Moreover, in qusistatic and transient experiments the system temperature is being changed [12, 21] so possible changes of the measured property have to be accounted for. It concerns almost all the most common methods of thermophysical properties measurement: differential scanning calorimetry [17, 19, 26, 37], modulated temperature DSC [34], laser flash [15, 24], dilatometry [15, 30], pulse heating [12], regular heating regime [15, 29], inverse methods [21] etc. Because of that, every system under investigation can be characterised by a certain temperature ΔT associated with the time and spatial temperature differences

$$\Delta T_i = \max_{k,l}\left\{T(x_k, y_k, z_k, \tau_k) - T(x_l, y_l, z_l, \tau_l) : (x, y, z)_{k,l} \in \Omega \wedge \tau_{k,l} \in [\tau_i, \tau_{i+1}]\right\} \qquad (6)$$

where Ω is the region of the system under investigation and $[\tau_i, \tau_{i+1}]$ is the time interval of the experimental data collection[6]. The experimentally obtained value of a certain temperature dependent parameter $\psi(T)$ is a certain mean value

$$\overline{\psi}_{\Delta T_i} = F\left\{T(x, y, z, \tau), [\tau_i, \tau_{i+1}]\right\} \qquad (7)$$

represented by functional accounting for the temperature distribution within the investigated system. In the case of quasi-static and quasi-dynamic measurements, when the spatial

---

[6] More precisely – the time interval for collection of the experimental data that are applied for a certain property calculation or evaluation.

temperature changes can be neglected in comparison with the temperature changes with time (comp. [22]), the experimental value can be described as a weighted average

$$\overline{\psi}_{\Delta T_i} = \overline{\psi}_i = \frac{1}{T_{i+1} - T_i} \int_{T_i}^{T_{i+1}} w(\xi)\psi(\xi)d\xi \tag{8}$$

which, for evenly distributed and evenly weighted experimental data, simplifies to

$$\overline{\psi}_i = \psi\Big|_{T_i}^{T_{i+1}} = \frac{1}{T_{i+1} - T_i} \int_{T_i}^{T_{i+1}} \psi(\xi)d\xi \tag{9}$$

In that case quite simple estimations of the "metrological" averaging error are possible. Thus, for the coefficient of thermal linear expansion [8]

$$\alpha(T) = \frac{1}{l(T)}\left[\frac{dl(T)}{dT}\right]_p = \left[\frac{d\ln l(T)}{dT}\right]_p, \tag{10}$$

applying symmetric finite difference approximation for $dl(T)$ within $\left[T - \Delta T/2, T + \Delta T/2\right]$, we get ([22]; comp. also [14])

$$|\Delta\alpha| = \left|\alpha(T) - \alpha\Big|_{T-\frac{\Delta T}{2}}^{T+\frac{\Delta T}{2}}\right| < \frac{(\Delta T)^2}{24}\left|\frac{d^2\alpha(T)}{dT^2} + \alpha(T)\frac{d\alpha(T)}{dT} - [\alpha(T)]^3\right| \tag{11}$$

where the appropriate subscripts have been omitted for simplification reasons. The estimation is even simpler in the instance of the experimental CLTE and the specific heat [8, 9, 35]:

$$\alpha^*(T) = \frac{1}{l(T_0)}\left[\frac{dl(T)}{dT}\right]_p = \frac{1}{l_0}\left[\frac{dl(T)}{dT}\right]_p \quad ; \qquad c_p = \frac{1}{m}\left(\frac{\partial H}{\partial T}\right)_p \tag{12.a,b}$$

where "0" subscript denotes the reference length (usually room temperature value). The appropriate formulae are as follows [22]:

$$|\Delta\alpha^*| = \left|\alpha^* - \alpha^*\Big|_{T-\frac{\Delta T}{2}}^{T+\frac{\Delta T}{2}}\right| < \frac{(\Delta T)^2}{24}\left|\frac{d^2\alpha(T)}{dT^2}\right| \quad ; \qquad |\Delta c_p| = \left|c_p - c_p\Big|_{T-\frac{\Delta T}{2}}^{T+\frac{\Delta T}{2}}\right| < \frac{(\Delta T)^2}{24}\left|\frac{d^2 c_p(T)}{dT^2}\right| \tag{13.a,b}$$

Similar relations can be also derived for other properties. However, in all the instances the error attributed to the finite temperature resolution occurs when the temperature dependence of a certain parameter is nonlinear. The uncertainty of the estimation of a certain parameter instantaneous value is proportional to squared value of the temperature span – temperature resolution ΔT and to the value of the parameter second derivative[7].

---

[7] In the case of differentially defined thermodynamic coefficients – thermal properties – comp. [9].

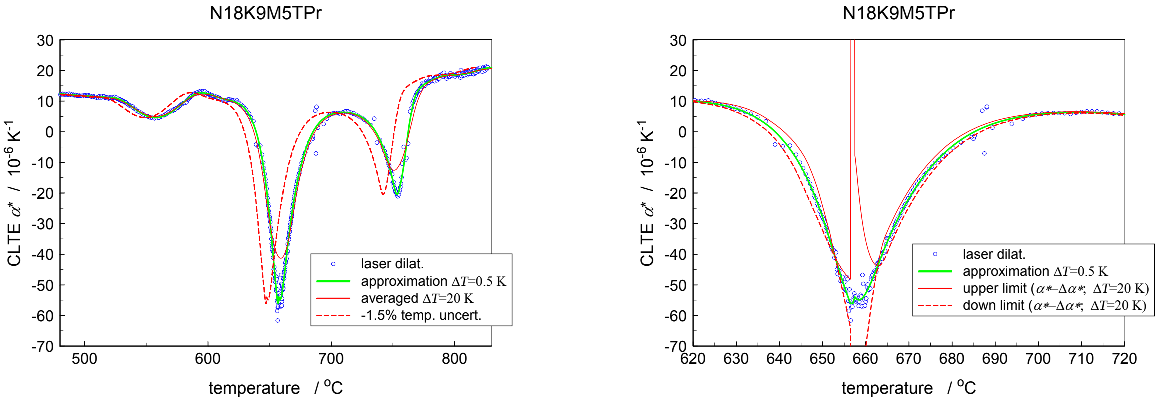

a *b*

Fig. 2. Finite temperature resolution and the reference temperature measurement uncertainty effects: a – decreasing the transition peak (solid red) and shifting the characteristic (dashed red); b - visualisation of the thermal resolution related uncertainty limits (Eq. 13.a). The depicted data came from laser interferometer dilometry measurements of N18K9M5TPr alloy over a region of the 1st order phase transition. The experimental data (blue circles) were approximated using B-splines [4, 25] – the temperature resolution of the resultant characteristic was equal to 0.5 K (red solid line)

In real experiments the "metrological" averaging results in attenuation of rapid changes of the investigated characteristic, mainly in rounding or "blurring" the peaks. Such effect is illustrated in Fig. 2. The experimental results from dilatometric investigation of the N18K9M5TPr stainless steel were applied for the visualisation. The averaging was simulated by moving average filtration of the $\Delta T = 0.5$ K data (green curve) with the filter span $\Delta T = 20$ K (red solid curve).

2.3. *Effects related to the temperature resolution*

There are two other issues related to the temperature resolution: the problem of temperature referencing and the general question of representativeness of non-isothermal experimental data.

The first problem is directly associated with a complicated structure of the functional (7) in the case of transient heat exchange. Because of that it is difficult to perform appropriate calculations in practice. The difficulty in evaluating mean value concerns both the investigated parameter ψ and the investigated system temperature T. This leads to the problem attributing of a certain $\overline{\psi}$ value to an adequate reference temperature and finally results in a horizontal shift of the outcome characteristic. The terminating effect is similar to that caused by the uncertainty in the reference temperature measurement (Fig. 2.a – dashed red curve). Of course the smaller ΔT is the smaller the closing error is. The overestimation for the reference temperature changes is as follows:

$$T_{\min,i} \le \overline{T}_i \le T_{\max,i} \quad , \qquad \Delta T_i = T_{\max,i} - T_{\min,i} \tag{14}$$

where subscripts "min" and "max" are attributed to the minimum and maximum value of a local system temperature within the time limits from τ_i to τ_{i+1} (time interval for collecting the experimental data).

The second issue will be only outlined. The core of the problem is the representativity of a certain property measurement result obtained at non-isothermal conditions. From theoretical point of view every thermodynamic parameter is attributed to a certain reference temperature. At non-isothermal conditions the system of temperature dependent parameters behaves "effectively". For example, when the phase transition occurs the complex response of the non-homogeneous system depends on the properties of all its phase constituents. The discussion over this problem arose some time ago regarding representativeness of DSC specific heat results (comp. e.g. [15] and [37]). Later on, the MTDSC technique has been introduced and the problem became even more complicated [34]. Nowadays, as far as DSC data are concerned, the differentiation between static and dynamic[8] system behaviour has been commonly accepted by the thermal science community. Nevertheless, in all the instances the temperature resolution – the maximum temperature difference – plays a crucial role in characterisation of the experimentally obtained data.

2.4. Multiproperty investigation – experimental data processing and comparison

When optimising procedures of themophysical property measurement, one faces the following problem of contradicting requirements: when decreasing the ΔT span, the uncertainty in the temperature difference evaluation is increased. Regardless of the measured property and the applied method the increased thermal resolution typically results in the increased scatter of the obtained data. Such an effect is illustrated in Fig. 3. The diagram shows the experimental data from dilatometric investigations of ARMCO iron [22].

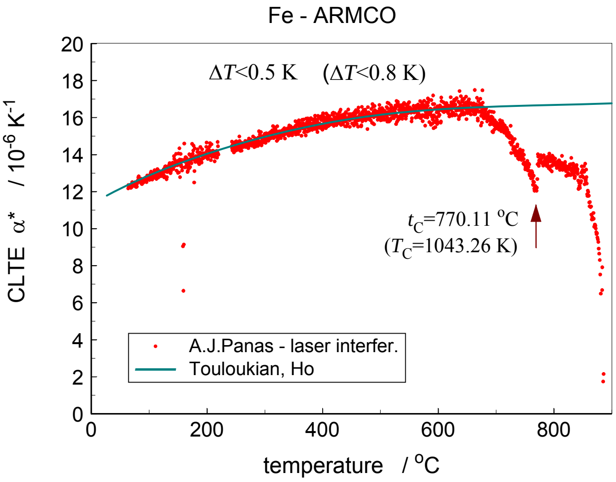

Fig. 3. Direct results from laser interferometry dilatometer [22] compared with literature data of ARMCO iron [35]

To manage this problem a special technique of experimental data processing needs to be implemented. The applied procedure should affect the original temperature resolution of measurements as little as possible. As was proved before more than satisfactory results can be obtained utilising B-spline approximation techniques [23, 25, 27, 28, 30]. The details concerning

---

[8] Differentiation between real and imaginary part of the MTDSC heat capacity [34].

the technique itself one can find in the appropriate monographs by Björck, Å., Dahlquist [2], De Boor [4] and Ciesielski [6]. However, reliability and precision of the spline reconstruction of the investigated characteristic depends on the procedure inputs. Major difficulties usually occur at regions of irregular changes of the investigated parameter, in which case, comparative analysis of the multiproperty experimental data can provide additional substantial information. Moreover, in the case when the appropriate thermophysical properties are measured separately, higher temperature resolution data supplement the other ones. Considering all the standard thermophysical property investigation methods (comp. [15], [16], [37]) the microcalorimetric – DSC experiments provide the best thermal resolution. It is due to small size and mass of the utilised specimens. Exhibiting the best temperature resolution the DSC measurements provide the most valuable information for reference.

2.5. Numerical evaluation of temperature resolution effects – DSC case

Even in microcalorimetric measurement, effects related to the non-uniform temperature distribution within the investigated specimen can be noticeable or even significant. This is a major problem concerning not only the DSC method but also all thermal analyses [37]. To illustrate typical phenomena, results of numerical simulation will be utilised. For numerical investigation two examples of DSC experiments performed on Perkin Elemer Pyris 1 apparatus were selected. The "measured" substances were polytetrafluoroethylene and water. In both cases the attention was focused on the 1st order phase transition: solid to solid for the model PTFE specimen and solid to liquid for the model water specimen. The water, exhibiting extreme value of the phase change enthalpy, was selected to create the reference data for possible comparisons. The real object parameters (comp. Fig. 4.a,b with [17], [26] and [27]) were recreated utilising in 2-D axially symmetric geometry. A standard procedure of a constant heating rate operation at scanning mode was analysed. When building the model, convection and radiation heat loses from outer system surfaces to the ambient of 293.15 K were taken into account. The effect of the increased heat transfer inside the measuring chamber due to internal

Table 1: The assumed model parameters for numerical simulation of Perkin-Elmer Pyris 1 DSC measurement on PTFE [24, 26] and water specimen [31]

Parameter	**Unit**	**PTFE**	**H_2O**
Heating rate	$K \cdot min^{-1}$	10	5
Density	$kg \cdot m^{-3}$	2200	1000
Phase transition ONSET temperature	°C	11.15	-0,15
Phase transition END temperature	°C	21.6	0.15
Phase transition specific enthalpy	$J \cdot g^{-1}$	4.520	333.0
Thermal conductivity below phase transition	$W \cdot m^{-1} \cdot K^{-1}$	0.4	2.0
Thermal conductivity above phase transition	$W \cdot m^{-1} \cdot K^{-1}$	0.4	0.5
Heat capacity c_p below phase transition	$J \cdot g^{-1} \cdot K^{-1}$	$0.92+8 \cdot t/°C$	2.2
Heat capacity c_p above phase transition	$J \cdot g^{-1} \cdot K^{-1}$	$0.92+8 \cdot t/°C$	4.2

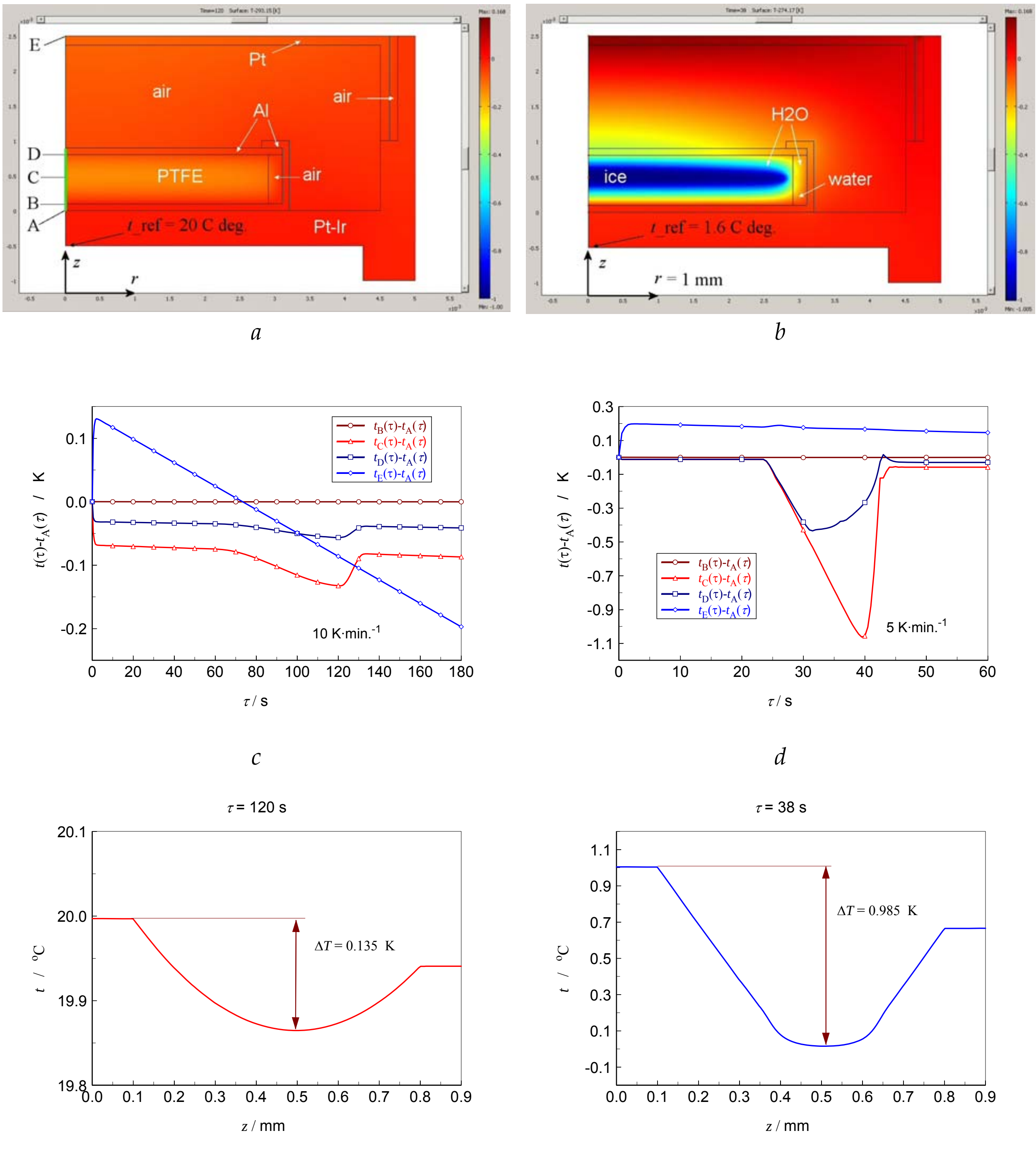

a *b*

c *d*

e *f*

Fig. 4. The numerical model geometry and selected results of numerical simulation: a, b – distribution of the temperature referred to a certain r_ref value at the state of about maximum temperature differences within the investigated specimens PTFE (τ=120 s) and H2O (τ=120 s) respectively (scale from –1.000 K to 0.165 K); c, d – changes of the temperature at points B, C, D E referred to the actual temperature at point A; e, f – axial temperature distribution across the specimen (a – green line starting at A) enclosed in aluminium sample pan for PTFE (τ=120 s) and H_2O respectively (τ=120 s)

gas convection was considered but phenomena of contact heat resistance were temporarily ignored. Numerical calculations were carried out applying Comsol software. Selected representative results of these calculations are visualised in Fig. 4. The highest temperature differences within the investigated specimen at regular heating regime (comp. [13, 16]) range from 0.07 K to 0.09 K for PTFE heated at 10 K/min and from 0.014 K below melting up to 0.06 K above melting for water heated at 10 K/min. These values can be assumed as negligibly small. However, it should be reminded that effects of contact heat resistance were neglected in the analysed model. In real experiments the contact temperature gap is accounted for during instrument calibration [17] but it limits the range of analyses only to studies performed on heating. When experiments are performed on both heating and cooling, as was described in [27], this problem requires additional attention.

Quite the contrary, when irregular dynamic changes occur, the temperature differences become more significant (comp. Fig. 4.e and 4.f). This results in effects discussed before: "metrological" averaging and the referencing temperature shift. It should be reminded that in the case of microcalorimetric measurements these effects are usually the least influential. For more bulky specimens the problem becomes more serious. However, by decreasing the specimen mass and slowing the temperature changes one gives rise to substantial increse of the temperature measurement accuracy and to increased scatter of the experimental data.

3. Selected examples of experimental results

For the main presentation there have been selected experimental results of:

- heat capacity and linear thermal expansion of cobalt (Figs 5 and 6; [27]),
- linear thermal expansion, specific heat and thermal diffusivity of PTFE (Figs 7, 8 and 9; [24, 26]),
- linear thermal expansion of ARMCO iron (Fig. 3; [22]),
- linear thermal expansion of Inconel 600 (Fig. 10).

Except the iron case all the analysed data were collected on both heating and cooling. In all instances the attention was focused on preserving the best possible temperature resolution. The relevant information concerning this parameter has been provided with the pictures. Concerning the methodology the microcalorimetric measurements were performed using Perkin-Elmer Pyris 1 apparatus [17]. In this case special procedures were applied to obtain specific heat data on heating and cooling [24, 26, 27]. Dilatometric investigations were carried out on a laser interferometry stand [22, 26, 27]. The thermal diffusivity data were acquired applying temperature oscillation method [31, 33]. Supplementary gravimetric measurements were done using a specially equipped Mettler-Toledo AT 261DR microbalance (for the details see e.g. [24]). The selected experimental data contain examples of:

- 1st order phase transitions typical for pure elements (Co: α-β; Fe: α–γ; see also [35]),
- a weaker 1st order phase transition of PTFE,
- 2nd order magnetic phase transition (Fe: Curie transition; see [35])
- and a relatively weak and "mushy" phase transition in the case of Inconel 600.

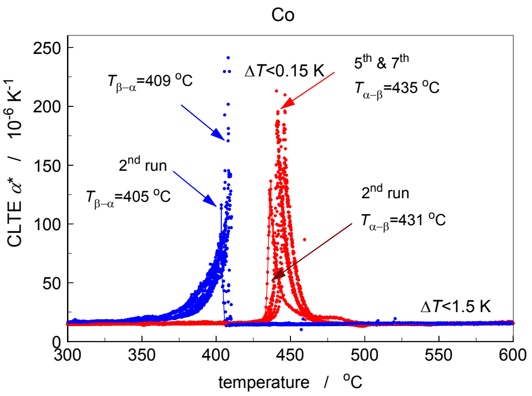

Fig. 5. Results of seven consecutive runs of dilatometric investigations of cobalt specimen from the region of α-β transition [27]

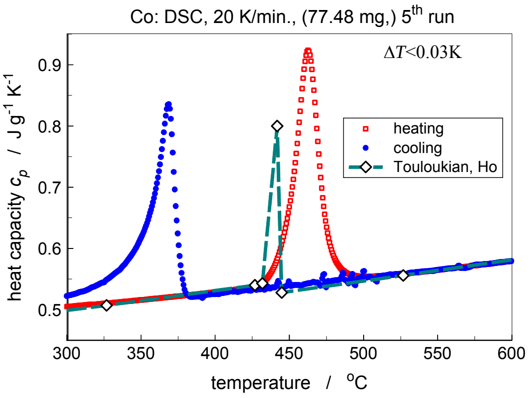

Fig. 6. Comparison between the processed results of DSC investigations of cobalt specimen [25] at α-β transition and the literature data [35]

In general, the presented data prove consistency between dilatometric and DSC measurement results. Regarding the theory such a conclusion was expected. The same concerns results of the thermal diffusivity derived from examination of amplitude attenuation [1, 31, 33]. However, this is not the case regarding the "phase" thermal diffusivity data. There are also other phenomena that need additional attention.

Analysis of the results obtained for cobalt (Figs 5 and 6) should be complemented with information that the investigated samples were of polycrystalline structure. Other details of the performed experiments are given in [27]. Explanation of the extended procedure applied for DSC data processing (Fig. 6) is provided also in [25]. The information is relevant because of revealed discrepancies in the width and the onset temperature of α–β phase changes in Co identified from dilatometric and calorimetric studies. The discrepancy exceeds limits of the ΔT related uncertainty. The phenomenon is most probably related to difference in the specimen masses and difference in heat transfer phenomena. Analysis of the increased thermal lag in DSC experiments can contribute to the global evaluation of the obtained data.

Comparing dilatomeric (Fig. 5) and DSC (Fig. 6) data one can notice a difference in proportions between maximal changes of the investigated parameter with respect to its baseline value in the temperature range of phase transition. The CLTE local change reaches value of 13:1 while for the heat capacity it does not exceed 2:1. The CTLE proves to be a more sensitive parameter to the changes of the specimen structure than the specific heat. This does not concern only the range of the phase transition. Within the whole interval the specific heat experimental curves are smooth while irregularities have been observed on the linear thermal expansion characteristics (comp. [27]). Distortions of the CLTE experimental characteristics from the local average value provide additional information about the phenomena that occur.

The revealed quantitative discrepancy between cobalt heat capacity and thermal expansion characteristics recalls general question of these two parameters inconsistency when solids are considered. Heat capacity is a scalar while the coefficient of linear thermal expansion is a tensor [9, 22]. However, the discussion is outside the scope of this study so we can only conclude that comparative analysis of high temperature resolution results can contribute to better understanding of this question.

The c_p and α^* results for PTFE are in good agreement regarding both qualitative and quantitative analyses of two transitions that occur at room temperature (Figs 7 and 8). The same concerns the thermal diffusivity results from amplitude data processing of oscillating temperature experiment (Fig. 8). The measurements were performed on a 4.4 mm thick flat disc specimen with the oscillation frequency 1/60 Hz and oscillation amplitude not exceeding 0.45 K at scanning mode of 0.5 K/min (comp. [31]). Unlike amplitude, the phase processing results exhibit different behaviour regarding the low temperature stage of phase transitions. The effect can be attributed to reversing and non-reversing heat flow components or to real (storage) and imaginary (loss) components of the total heat capacity [34]. Similarly to the previous case, we will not discuss the subject in details but will only point out the advantages of comparative analyses.

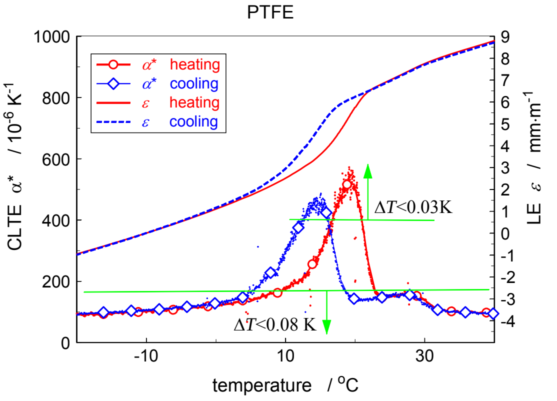

Fig. 7. Results of dilatometric measurements of polytetrafluoroethylene (PTFE/teflon) [24, 26]

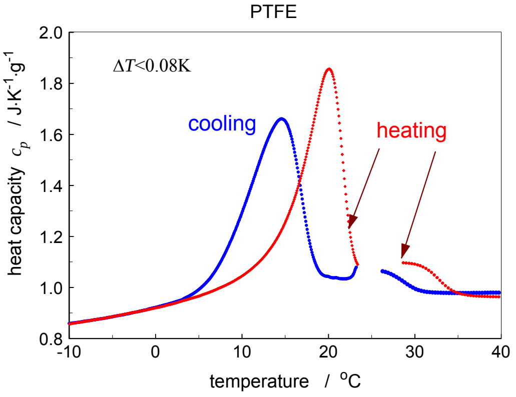

Fig. 8. Results of DSC investigations of PTFE – heat capacity [25]

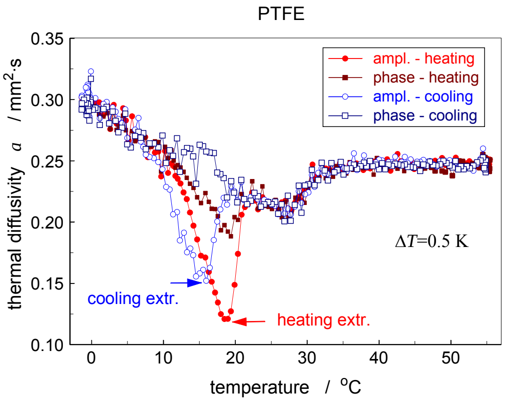

Fig. 9. Thermal diffusivity of PTFE from temperature oscillation measurements at scanning mode (comp. e.g. [31])

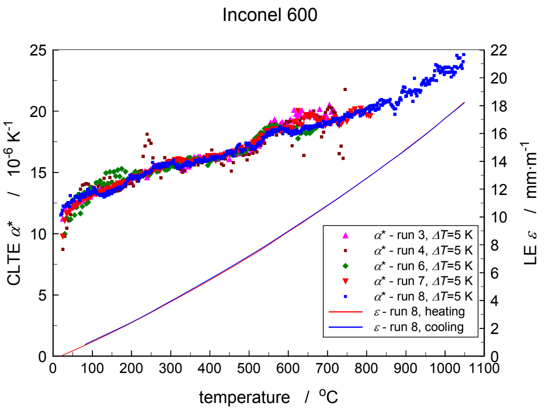

Fig. 10. Results from five selscted runs of dilatometric investigations of Inconel 600 alloy: CLTE data averaged to ΔT = 5 K

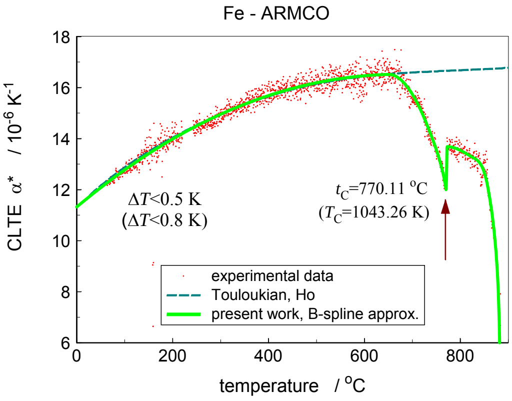

Fig. 11. *Results of B-spline treatment of ARMCO iron dilatometric data*

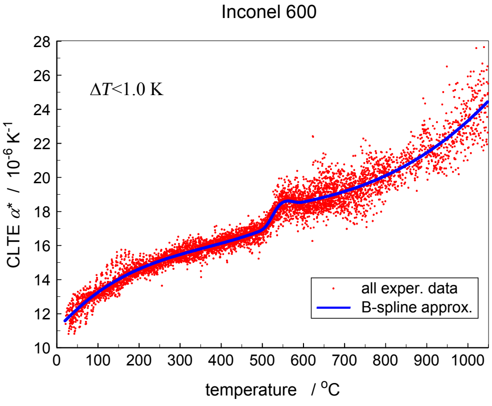

Fig. 12. *Results of B-spline treatment of Inconel 600 dilatometric data from five consecutive runs*

The high temperature resolution CLTE data have been proved to be more sensitive to any structural changes in comparison with DSC results. That effect can be also observed in the case of dilatometric investigation of Inconel 600. As it is shown in Fig. 10 every CLTE characteristic from every one individual experiment exhibits distinct irregularity with reference to the temperature changes. The instantaneous changes of α^* exceed the uncertainty limits of the experiment (comp. [2]). The differences are not recognisable when linear expansion $\varepsilon(T)$ is taken into account. The comparison of CLTE results with DSC data [3] suggests differentiation between temporal and permanent behaviour of this material under the temperature changes.

In order to set apart these effects the technique of B-spline approximation has been applied. The B-spline procedure proved to be very effective for reconstruction of any rapidly changing thermal characteristics [2, 25, 27, 28, 30]. It is a very useful technique regarding high thermal resolution information processing. Performance of the B-spline treatment of the experimental data is illustrated by the ARMCO iron data recalculation (see Fig. 3). As it is shown in Fig. 11 the eventual characteristic (green line) displays all the expected features: it smoothes the scattered data outside the 2nd order phase transition peak preserving the needed discontinuity at the Curie point (T_C = 770.11 °C). Regarding Inconel 600 the major task was to reveal or enhance regular, i.e. typical for every single experiment run, changes of the CLTE. The final effect of the experimental data processing is shown in Fig. 11. The processed high temperature resolution data were taken from five consecutive experiments. Despite the substantial scatter of the experimental points the revealed phase transition that occurs between 500 °C and 600 °C is perfectly recognisable. The results are in agreement with the specific heat data published in [3]. However, the thermal diffusivity results from [3] show slightly different location of the transition peak that appears within the interval from 550 °C to 750 °C.

The review of high temperature resolution investigations will be concluded with an example of overall analysis of complex multiproperty results. The Fig. 13 illustrates performance of the applied measurement methods, B-spline data processing and the applied prediction techniques in estimation of all the main thermopysical parameters. The investigated material was a tungsten heavy alloy 90W-7Ni-3Fe [32]. The heat capacity was obtained applying the DSC technique, the CLTE by laser dilatometry stand and thermal diffusivity using a laser flash apparatus. The density changes according to the temperature change were evaluated on the basis of B-spline processed dilatometry results. Next, the thermal conductivity was calculated from Eq. 5 and finally the electrical conductivity was predicted from relation (2). The depicted data are referred to their room temperature values that are shown in Table 2. The literature originated estimation of the room temperature electrical conductivity of the investigated alloy is marked with dashed grey line. The predicted results fall within the shown interval.

Table 2: Thermophysical properties of 90W-7Ni-3Fe tungsten heavy alloy at 20 ℃ [32]

Measured				Calculated	Predicted
c_p	$\alpha^{*}10^6$ - heating	$a \cdot 10^6$	ρ	λ	$\sigma \cdot 10^6$
$J \cdot g^{-1} \cdot K^{-1}$	K^{-1}	$m^2 \cdot s^{-1}$	$kg \cdot m^{-3}$	$W \cdot m^{-1} \cdot K^{-1}$	$S \cdot m^{-1}$
0.17040	4.750	18.72	15850	50.56	8.103

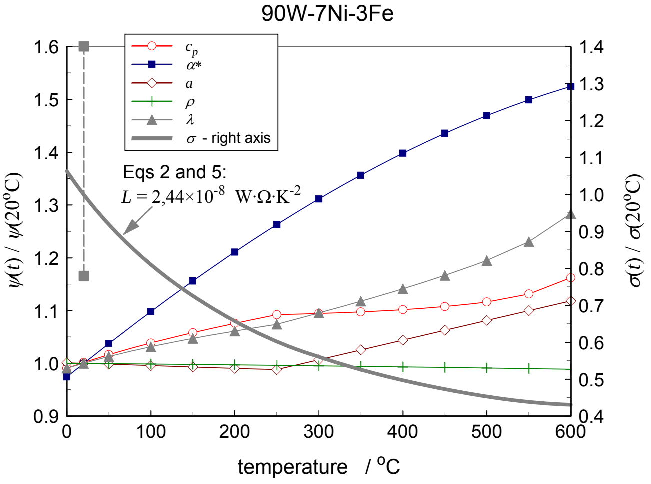

Fig. 13. The relative changes of thermophysical properties of 90W-7Ni-3Fe alloy due to temperature chnage [35]. The depicted data come from multiproperty measurements (DSC, laser dilatometry, LF and gravimetry) and from recalculation of the results to the thermal conductivity (Eq. 5). The electrical conductivity has been predicted using Wiedemann-Franz relation (Eq. 2)

4. Conclusion

The present work has focused on reviewing some selected problems of high temperature resolution measurements of thermophysical parameters. The thermal resolution problem concerns mostly studies carried out on materials with properties strongly dependent on temperature. It needs special attention when multiproperty comparative studies or complex measurements are performed. In such cases preliminary analysis of the finite temperature resolution effects are necessary to get reliable results for further analyses.

The multiproperty studies benefit from theoretical relations that link certain properties. Among other relations, the closest ones relate specific heat with thermal expansion and thermal conductivity with electrical conductivity. The appropriate examples of such a correlation in the case of experimental data have been provided in the paper. However, the content also includes examples of phenomena not explainable with the acquired experimental data. This concerns the revealed discrepancy in the temperature gap between heating and cooling phase transition in Co observed when comparing the DSC and laser dilatometry data.

As has been shown, the increasing temperature resolution usually results in the increased uncertainty of the temperature measurement. This leads to the increased scatter of the raw experimental data. For that reason a special treatment of the measurement results is needed. The recommended technique for the data processing is its approximation applying spline functions. The most important advantage of this technique is its performance in reconstruction of singularity of any order for the identified characteristic. Singularities are related to phase transition critical points. The comparative analysis of multiproperty measurements facilitates data processing and increases reliability of final results.

Acknowledgement

The author appreciates the Netzsch GmBH company for providing the Inconel 600 specimen.

References

[1] Belling, J.M., Unsworth, J., *Modified Ångström's method for measurement of thermal diffusivity of materials with low conductivity*. Rev. Sci. Instrum. 1987. 58 (6), p. 997-1002

[2] Björck, Å., Dahlquist, G., *Numerical Methods*, Prentice-Hall, London, 1974

[3] Blumm, J., Lindemann, A., Niedrig., B., *Measurement of the thermophysical properties of an NPL thermal conductivity standard Inconel 600*, 17th European Conference on Thermophysical properties, 5th – 7th September 2005, Bratislava

[4] De Boor, C., *A Practical Guide to Splines*, Appl. Math. Sciences v. 27, Springer Verlag, Berlin, 1976

[5] Carslaw, H. S.; Jaeger, J. C. *Conduction of Heat in Solids*, 2nd Edition, Oxford - Clarendon Press, London, 2003

[6] Ciesielski, Z., *Theory of Spline Functions*, University of Gdańsk, Gdańsk, 1976/1977 (in Polish)

[7] Grimvall, G., *Thermophysical Properties of Materials*, Elsevier Sc. Publ. B.V., Amsterdam, 1986

[8] Ho, C.Y, Taylor, R.E., *Thermal Expansion of Solids (Cindas Data Series on Material Properties, V. I-4)*, ASM International, Materials Park, OH, 1998

[9] Kaviany, M., *Heat Transfer Physics*, Oxford University Press, Cambridge, 2008

[10] Kondepudi, D., Prigogine I., *Modern Thermodynamics. From Heat Engines to Dissipative Structures*, John Willey & Sons, New York 1999

[11] Kittel, C., *Introduction to Solid State Physic.* John Willey & Sons, Inc., Berkeley, 2004

[12] Kubičar, L. *Pulse Method of measuring Basic Thermophysical Parameters*, 1990, Elsevier Sc. Publ. Co., Inc. and Veda Publ. House of the Slovak Academy of Sciences (*Thermal Analysis*, V. XII, Part E, A Sub-Series of Monographs Ed. by W.W. Wendlandt)

[13] Lykov A.V., *Tieoria tirploprovodnosti*. Vyshaia Schola, Moskva 1967

[14] Nowikowa, S. I., *Teplovoije rozshirenije tviordych tiel*. Nauka, Moskva, 1974

[15] Maglić, K. D., Cezairliyan, A. and Peletsky, V. E., eds. *Compendium of Thermophysical Property Measurement Methods*. Plenum Press, New York 1984

[16] Maglić, K. D., Cezairliyan, A. and Peletsky, V. E., eds. *Compendium of Thermophysical Property Measurement Methods. Volume 2: Recommended measurement Techniques and Practices,* Plenum Press, New York 1992

[17] McNaughton, J. L. , Mortimer, C. T. , *Differential Scanning Calorimetry, IRS Physical Chemistry Series 2, Volume 10*, Butterworths, London 1975

[18] Miller, A. P., *Theory of Specific Heat of Solids* in *Specific Heat of Solid*, Ho C. Y., Cezairliyan A. eds., Hemisphere, New York, NY, 1988, pp. 1-89

[19] Mraw, S. C., *Differential Scanning Calorimetry* in *Specific Heat of Solid,* Ho C. Y., Cezairliyan A. eds., Hemisphere, New York, NY, 1988, pp. 395-435

[20] Özişik, M.N., *Heat Conduction*, 2-nd Ed., John Willey & Sons, Inc. , 1993

[21] Özişik, M.N., Orlande, H.R.B., *Inverse Heat Transfer. Fundamentals and Applications,* Taylor & Francis, New York, 2000

[22] Panas, A. J., *Investigation of Thermal Characteristics of the Linear Expansivity – Dilatometric Thermal Analysis*. WAT, Warszawa,1998, (in Polish)

[23] Panas, A. J. and Terpiłowski, J. , in *Proc. of the 7th International Symposium on Temperature and Thermal Measurements in Industry and Science TEMPMEKO'99,* May 30 – June 3, Delft 1999, pp. 493-498

[24] Panas, A.J., Cudziło, S., Terpiłowski, J., *High Temperatures - High Pressures*, v. 34, 2003, pp. 691-698

[25] Panas, A. J., *Achives of Thermodynamics*, 24 (4), 2003, pp. 47-65

[26] Panas, A.J., Cudziło, S., *Journal of Thermal Analysis and Calorimetry,* vol. 77 (2004) pp. 329÷340

[27] Panas, A. J., *Comparative dilatometric and calorimetric studies of α–β phase transitions in Co* in *Thermal Conductivity 26 / Thermal Expansion 14,* Dinwiddie R. B., Mannello R. Eds., DEStech Publications, Inc., Lancaster PA, 2005, pp. 530-539

[28] Panas, A. J., *Dilatometric Investigations of Phase Transitions Using B-Spline Data Processing*, in *Thermal Conductivity 27 / Thermal Expansion 15,* Wang H., Porter W. Eds., DEStech Publications, Inc., Lancaster PA, 2005, pp. 584-594

[29] Panas, A. J., Jerzy Sypek, J., *International Journal of Thermophysics*, Vol. 27, 2006, 1844÷1858

[30] Panas, A.J., *B-spline Processing of 90W-7Ni-3Fe WHA Dilatometric Data,* Thermophysics 2008 Proceedings, Kočovce, October 16th - 17th, 2008, Vydavatel'stvo STU, Bratislava 2008, ISBN 978-80-227-2968-0, pp. 119-130

[31] Panas, A.J., Nowakowski M., *Numerical validation of the scanning mode procedure of thermal diffusivity investigation applying temperature oscillation,* Thermophysics 2009 Proceedings, Brno University of Technology, Faculty of Chemistry, 2009, pp.252-259

[32] Panas, A.J., Terpiłowski, J., Majewski, T., *Investigation and analysis of thermophysical properties of a 90W-7Ni-3Fe heavy alloy, MUT Bulletin (Biuletyn WAT),* Vol. LIX (in print)

[33] Phylippov, L.P. *Temperature Wave Techniques* in *Compendium of Thermophysical Property Measurement Methods,* Maglić K. D., Cezairliyan A. and Peletsky V. E., eds., Plenum Press, New York 1984, pp. 337-365

[34] Schawe, J.E.K., Thermochimica Acta, 260, 1995, pp. 1-16

[35] Touloukian, Y.S., Ho., C. Y., *Properties of Selected Ferrous Alloing Elements. McGraw-Hill/CINDAS Data Series on Material Properties, Volume III-1,* McGRAW-HILL, New York, NY, 1976, pp. 53-93

[36] Tye, R. P., ed., *Thermal Conductivity*, Academic Press Inc. Ltd., London 1969

[37] Wendlandt, W. Wm., *Thermal Analysis*, John Willey & Sons, New York, 1986

Secondary effects on reliability of moisture measurement methods at in-situ conditions as necessary information for hygrothermal analysis of materials performance

Zbyšek Pavlík, Jan Mihulka, Milena Pavlíková

Czech Technical University in Prague, Faculty of Civil Engineering, Department of Materials Engineering and Chemistry, Thákurova 7, 166 29 Prague 6, Czech Republic,
email:pavlikz@fsv.cvut.cz

Abstract: *In this paper, short overview of currently applied moisture measurement methods is done regarding to their strong and weak points. Here, especially temperature effects and electrical conductivity changes and their influence on the applicability and reliability of listed moisture measurement methods are introduced and discussed. The specific attention is paid to the Time Domain Reflectometry (TDR) method that is introduced as highly advanced tool for moisture measurement in laboratory as well as in-situ conditions. In the final part of the paper, practical example of calibration and application of TDR method for moisture monitoring in calcium silicate material is given in respect to electrical conductivity changes of absorbing media.*

Keywords: *moisture measurement, temperature and electrical conductivity effects, TDR*

1. Introduction

Present building industry and its modern trends are characteristic by enhanced requirements on quality and comfort of buildings interior climate and prolonged durability and service life of structures. These requirements are induced not only by the building users and occupiers, but also by investors of newly built or reconstructed buildings that pay attention on quality as well as on price of construction works and materials. The continuous rising of above given requirements can be meet only with the use of newly developed advanced building materials that should maintain their hygric, thermophysical, and mechanical properties even in the case of unfavourable conditions.

The properties of porous materials are strictly dependent on their environment, especially on the temperature, relative humidity, air pressure, and moisture changes. The most significant factors that affect the hygrothermal performance of building materials are probably temperature and moisture changes. Therefore, the properties of porous building materials should be accessed as functions of both temperature and moisture content to ensure their optimized performance in real climatic conditions [1], [2], [3].

For assumption of current state of material, what is decisive information for estimation of its functionality, there is necessary to assess its moisture and temperature. Several advanced temperature measurement methods were developed and tested until know. Among them, thermoelectric and resistance thermometers are most frequently applied methods for continuous temperature measurement. On the other hand, there is a need of building research as well as of practice to develop sophisticated and reliable moisture measurement method that will respect also temperature and other secondary effects.

Since the presence of water affects many material properties, several methods of moisture measurement were designed and constructed until now [4], [5]. The moisture measurement methods can be basically divided into two main groups; absolute (direct) methods, which determine the real water content in the material after its removal from the investigated specimen, and relative (indirect) methods, which determine the amount of water in the specimen on the basis of measuring another physical quantity, as relative permittivity, electrical conductivity, thermal conductivity, absorption of radiation energy, etc. Probably the most frequently used method of moisture measurement in building practise represents gravimetric method that is used especially for its simplicity and low requirements on experimental apparatuses. Although this method is considered by many authors as universal and is often applied for calibration of relative moisture meters, its reliability and accuracy is from the scientific point of view debatable. Within the gravimetric moisture measurement, water is removed from the specimen by drying in exactly defined conditions, and its amount is determined from the loss of weight after drying. This experimental procedure looks very simple. However, it requires basic knowledge on the bond energy of water to porous matrix. The knowledge of the bond energy enables determination of total amount of residual water content in material within the gravimetric experiment. In practice, no correction for residual water in porous material after drying is done. Instead of this, such drying conditions are chosen that the amount of residual water in the studied material sample is negligible compared to the measured water loss within the drying process. On that account, the optimal drying temperature is decisive parameter of the accuracy of gravimetric moisture measurement method.

Looking at accuracy of indirect moisture measurement methods, they have several weak points that must be considered within their practical application. The accuracy of moisture content measurement using the electrical methods (dielectric methods, resistance methods) is highly dependent on the temperature. In case of dielectric methods, the changes of permittivity due to the change of moisture are of the same order as the changes due to the change of temperature. In practical application, either the temperature must be maintained constant or temperature compensation has to be included. For example, the detailed research on effect of ambient temperature on accuracy of TDR method for moisture measurement was done by Skierucha [6] that derived temperature-correction formula adjusting the soil moisture determined by TDR at various temperature values to the corresponding value at 25°C. Within his research, he has performed simultaneous measurement of electrical conductivity, and he has observed no influence of temperature changes on examined electrical conductivity values.

The accuracy and reproducibility of several moisture methods is strictly dependent also on the amount of dissolved salts in water and present in porous system of materials. This feature is remarkable especially for relative methods, where the measured physical quantity is highly dependent on salt concentration. Typical examples are resistance moisture meters although they are often used in building practice even in materials containing salts. For materials with a high amount of salts, the resistance moisture meters are practically inapplicable, because the errors rapidly increase with the increasing moisture content.

The salt dissolved in water is present in form of dissociated ions. On the conduction of electrical current take part free salt ions in solution. In dependence on ion concentration, the electrical conductivity of material is increasing. For lower concentrations of salt water solutions there is valid direct proportionality between salt concentration and electrical conductivity. This dependence is given in Figure 1 [7].

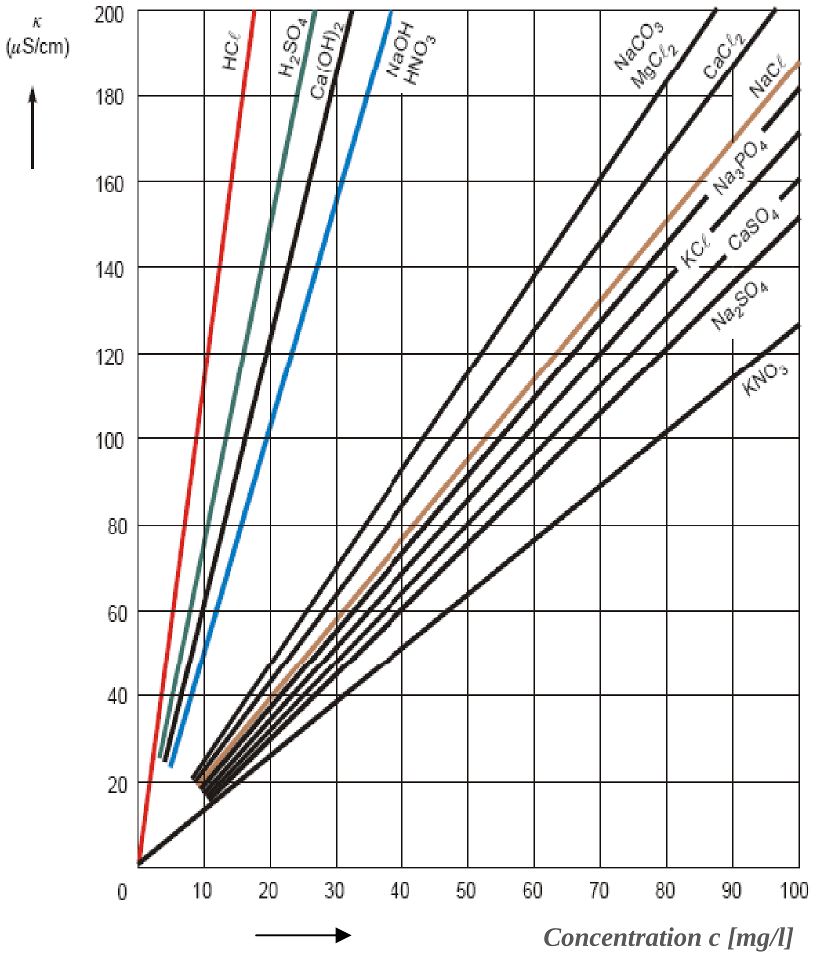

Figure 1: Dependence of electrical conductivity of electrolyte on chemical substances concentration.

On the other hand, electrical conductivity is limited by the free migration of ions. It means that in certain value of ion concentration the migration of ions is reduced, and electrical conductivity of such solutions decreases. This feature is demonstrated in Figure 2, where is presented dependence of electrical conductivity on solution concentrations in higher range [7].

Since the presence of dissolved salts affects the conductivity of water in a significant way (see above), the low frequency operating dielectric methods are not applicable for moisture measurement in salt laden materials. On the other hand, with increasing frequency of microwaves, the importance of salt content for the measured values decreases. The imaginary part of water permittivity increases with frequency (it has a maximum at so called critical frequency, f_{cr} = 23.4 GHz), and therefore the relative importance of conductivity decreases. On this account, the application of high frequency microwave method looks very promising for moisture measurement in materials containing salts. From other indirect methods of moisture measurement, also γ-ray attenuation method exhibits minimal effect of salts on the measured values of moisture.

In this paper we have focused on the testing of applicability of TDR moisture measurement method for measurement in materials containing salts. It is one of the high frequency methods of moisture measurement working on the frequency close to 2.0 GHz that proved its capability for monitoring of moisture changes in porous building materials (see e.g. [8] – [12]).

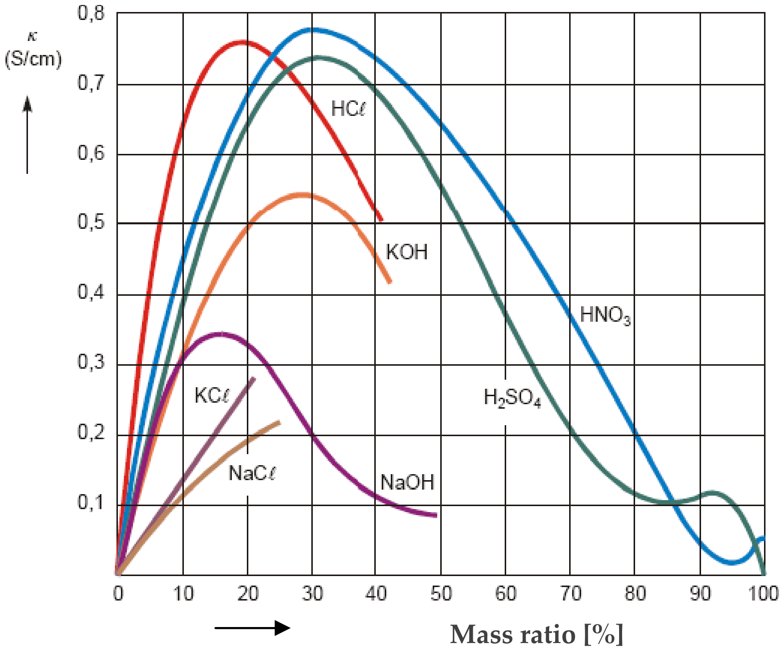

Figure 2: Dependence of electrical conductivity on solution concentrations.

2. Experimental

The experiments presented in this paper were proposed in order to evaluate the effect of salinity on the accuracy of TDR method for moisture measurement. The temperature within the performed experiments was maintained constant, so the temperature compensation was not necessary. For the measurement, sophisticated cable tester TDR/MUX/mts produced by Polish company Easy Test was used. This device is based on TDR technology with sin^2-like needle pulse having rise-time of about 250 ps and allows monitoring of complex relative permittivity, temperature and electrical conductivity of porous media. Using this device, monitoring of moisture, temperature, and salt concentration fields can be done. Accuracy and measuring range of used TDR device is given in the following table.

Table 1: Accuracy and measuring range of used TDR apparatus

Measured quantity	**Measuring range**	**Accuracy**
Relative permittivity ε	2 ÷ 90	Absolute error: ± 1 for 2 ≤ ε ≤6 ± 2 for ε ≥ 6
Electrical conductivity σ	(0 ÷ 1) S/m	Relative error: ± 5%
Temperature T	(-30 ÷ +80)°C	Absolute error: max. ± 2

For monitoring of complex relative permittivity, two-rod laboratory miniprobes LP/ms (Easy Test) were used [13], [14]. Applied TDR sensor represent section of a transmission line made of two, 53 mm long parallel stainless steel rods having diameter 0.8 mm and separated by 5 mm (see Figure 3). Cable length from the sensor to the terminating connector is 2 m. The sphere of influence of the sensor creates the cylinder having diameter about 7 mm and height about 60 mm, circumference around the rods of sensor.

The measurements of moisture content were done on calcium silicate samples having dimensions of 40/40/100 mm. Calcium silicate is material that has found use as thermal insulation in interior thermal insulation systems without water vapor barrier. It has high thermal insulation properties (thermal conductivity is 0.063 W/m K), low bulk density (230 kg/m^3), high total open porosity (87%), low resistivity against water vapor transport (water vapor resistance factor is 2.6), and from the chemical point of view is formed by Ca_2SiO_4. For details of this material see [14].

Figure 3: Applied laboratory miniprobe LP/ms designed for monitoring of changes in moisture and salt distribution.

Within the experiments, the TDR sensors were placed into the particular samples and sealed by silica gel. Since the material is rather soft, the sensors were placed into the samples by simple impress. The samples were partially saturated by water and insulated to prevent water evaporation from the studied samples. The relative permittivity of wet samples was then continuously monitored until the measured values reached the constant value. Then, the experiment was interrupted, sensors removed from the samples and moisture content in the samples was determined using gravimetric method. In this way, the empirical calibration curve of calcium silicate material was obtained. Simultaneously with calibration for pure distilled water, the experiments were done also for penetration for 0.1 M and 0.01 M NaCl water solution. These experiments were done in order to access the influence of salt concentration on the accuracy and reliability of obtained calibration curve.

3. Results

The measured values of complex relative permittivity and corresponding moisture contents are plotted in Figure 3.

From the obtained results there is evident high dependence of calcium silicate relative permittivity on moisture content rising. The value of measured relative permittivity of dry material is 1.5, whereas in moisture content close to the maximum water saturation the relative permittivity reached value of 44. From the point of view of the effect of salt concentration on the accuracy and reproducibility of the obtained TDR data, the measured results validated the applicability of high frequency microwave methods for moisture content measurement even in the case of salt ions presence.

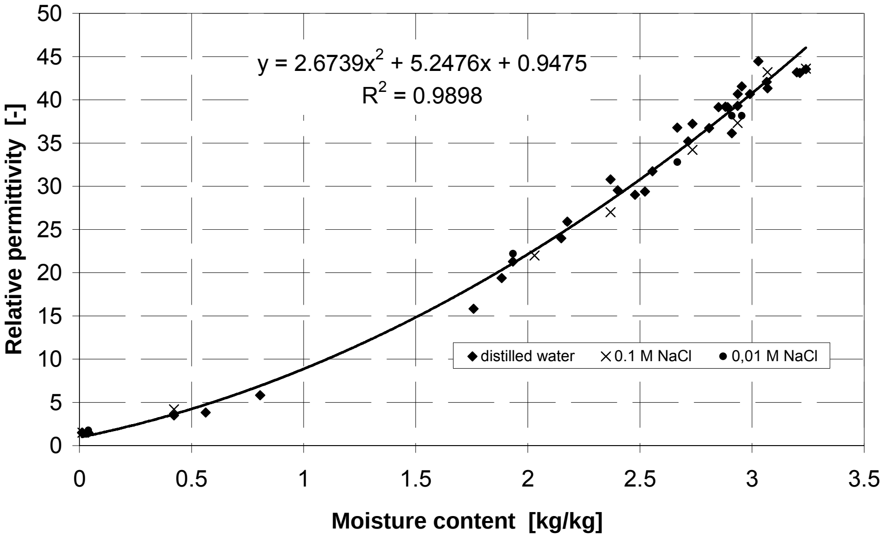

Figure 4: Calibration curve of TDR moisture measurement method for calcium silicate.

4. Conclusions

The experiments presented in this paper proved the capability of TDR method for measurement of moisture content in materials containing salts. This finding represents valuable information for building practice and research, where the reliable and precise method for moisture measurement is needed. The TDR method can find use also in in-situ investigation of current state of buildings with regard to moisture related durability problems, since its temperature compensation is possible using experimental procedure and correction formulas.

Acknowledgment

This research has been supported by the Czech Ministry of Education, Youth and Sports, under project No MSM 6840770031.

References

[1] ŠTUBŇA, I.; LINTNEROVÁ, A; TRNÍK, A. Mechanical properties and thermal expansit of clay ceramics measured on laboratoř samples, Industrial Ceramics, vol. 29(1), pp. 39-42, 2009. ISSN 1121-7588.

[1] PAVLÍK, Z.; MICHÁLEK, P.; PAVLÍKOVÁ, M.; KOPECKÁ, I.;, MAXOVÁ, I.; ČERNÝ, R. Water and Salt Transport and Storage Properties of Mšené Sandstone, *Construction and Building Materials*, vol. 22(8), pp. 1736-1748, 2008. ISSN 0950-0618

[2] ŠTUBŇA, I.; TRNÍK, A.; VOZÁR, L. Thermomechanical analysis of quartz porcelán in temperature cycles, *Ceramics International*, vol. 33(7), pp. 1287-1291, 2007. ISSN 0272-8842

[3] ČERNÝ R.; ROVNANÍKOVÁ P. *Transport Processes in Concrete*, 1st ed., London: Spon Press, 2002. ISBN 0-415-24264-9

[4] PAVLÍK, Z. *Methods for Determination of Moisture Content of Porous Building Materials*, Czech Technical University in Prague, 2010. ISBN 978-80-01-04508-4

[5] SKIERUCHA, W. Temperature dependence of time domain reflectometry-measured soil dielectric permittivity, *J. Plant Nutr. Soil Sci.*, vol. 172, pp. 186-193, 2009.

[6] MACHAČ, J. Měření koncentrace roztoků pomocí elektrolytické vodivosti, http://www.vscht.cz/ufmt/cs/pomucky/machacj/lab_mt.html, (in Czech)

[7] PAVLÍK, Z.; MIHULKA, J.; PAVLÍKOVÁ, M.; ČERNÝ, R., Monitoring Coupled Moisture and Salt Transport Using Single Vertical Suction experiment, in Proc. of *14th International Conference on Computational Methods and Experimental Measurements*, Algarve, Portugal, 2009, Wessex, WIT PRESS, pp. 157-167. ISBN 978-1-84564-187-0

[8] PAVLÍK, Z.; FIALA, L.; ČERNÝ, R.; SOBCZUK, H. Effect of particle shape on the accuracy of dielectric mixing models applied for determination of moisture content of building materials, Energy Efficiency and New Approaches, *Fourth International Building Physics Conference*, Topkapi, Istanbul, Beysan Matbaacilik ve Reklamcilik, 2009, 33-39. ISBN 978-975-561-350-5.

[9] PLAGGE R.; GRUNEWALD J., Measurement of Continuous Drying out of Subterranean Concrete Walls, in *Proc. of 6th International Conference on Electromagnetic Wave Interaction with Water and Moist Substances*, ISEMA, 2005, pp. 294 – 301, 2005.

[10] PLAGEE R.; GRUNEWALD J.; HÄUPL P., Application of Time Domain Reflectometry to determine water content and electrical conductivity of capillary porous media, in *Proc. of the International Symposium of Building Physics in Nordic Countries*, Chalmers University of Technology, Sweden, pp. 337-344, 1999.

[11] KUPFER K.; TRINKS E.; SCHÄFER TH.; WAGNER N.; HÖBNER CH., Measurement Method for Detection of Moisture Profiles in a Saline Environment, in *Proc. of 6th International Conference on Electromagnetic Wave Interaction with Water and Moist Substances*, ISEMA, 2005, pp. 429 – 438, 2005.

[12] MALICKI M. A.; PLAGGE R.; RENGER M.; WALCZAK R. T., Application of time-domain reflectometry (TDR) soil moisture miniprobe for the determination of unsaturated soil water characteristics from undisturbed soil cores, *Irrigation Science*, vol. 13, pp. 65-72, 1992.

[13] JIŘIČKOVÁ M., Application of TDR Microprobes, Minitensiometry and Minihygrometry to the Determination of Moisture Transport and Moisture Storage Parameters of Building Materials, *CTU Reports*, No. 2, Vol. 8, 2004. , ISBN 80-01-02954-9

Accurate determination of moisture content: a necessary condition for thermal assessment of multi-layered systems of porous materials

Zbyšek Pavlík[1], Milena Pavlíková[1], Lukáš Fiala[1], Zbigniew Suchorab[2], Henryk Sobczuk[2], and Robert Černý[1]

[1]Department of Materials Engineering and Chemistry, Faculty of Civil Engineering, Czech Technical University in Prague, Thákurova 7, 166 29 Prague 6, Czech Republic

[2]Faculty of Environmental Engineering, Lublin University of Technology, Nadbystrzycka 40b, 20-618 Lublin, Poland

Abstract: *Thermophysical measurements of porous materials are affected by their moisture content. The values of thermal conductivity, specific heat capacity and thermal diffusivity of wet materials can be several times higher as compared with the dry state. This may have serious effect on any thermal assessment of multi-layered systems of porous materials. Therefore, exact determination of moisture content in porous materials is very important also in thermophysics. The time domain reflectometry (TDR) is still a relatively new method for building materials. In contrast to most other methods commonly used for that purpose, it does not require calibration for every material, in general. The TDR probe calibration can be done in advance all once for every single probe. Another advantage of the TDR method is that it is well applicable for the materials with higher salt content, where an application of methods such as the resistance method or the capacitance method is impaired by a significant loss of accuracy. However, problems with TDR sensor installation can occur in some cases, in particular for compact materials with high strength. In this paper, three different experimental approaches of TDR sensors placement into compact materials are analyzed and their applicability for laboratory and on site measurements are discussed.*

Keywords: *determination of moisture content, porous materials, TDR*

1. Introduction

Thermal conductivity, specific heat capacity and thermal diffusivity belong to the most frequently measured parameters of porous building materials, mainly because they are essential for any analysis of energy efficiency of buildings in terms of their energy consumption. Thermal assessment of any building envelope which generally presents a multi-layered system of porous materials cannot be done without a reliable knowledge of these parameters. Despite this well known fact the lists of material producers and many national standards still include just one value of thermal conductivity, often in dry state, sometimes in so called "equilibrium state" which is (as for the thermal conductivity value) very close to the dry state. Even the advanced state-of-the-art studies work often with those values [1]. So, in the energy audits which the building practice requires with an increasing rate the engineers have no choice but to work with these limited (and mostly the only available) data. However, the thermal parameters are affected by temperature and moisture content in an extent which may not even be conceivable for many designers in the practice. While the values of thermal conductivity in the temperature range corresponding to common operation conditions of buildings were found typically within a 10-20% interval [2, 3], the effect of moisture on thermal conductivity was for most materials more significant. The thermal conductivity of high performance concrete was reported to increase by 20-50%, comparing the values measured in dry and water saturated state, for cracked high performance concrete it was 80-140% [4]. For fiber reinforced cement composites [5, 6] the thermal conductivity of wet specimens increased in the reference state up to 150-200%, for damaged specimens up to three times. Lime composites were affected by increased moisture content in a more significant way than cement based composites; their thermal conductivity in water saturated state increased more than three times [7, 8]. Thermal conductivity of insulation materials such as polystyrene or calcium silicate was shown to increase up to four times due to moisture increase [3]. The highest effect of moisture on thermal conductivity resulting in an up to 20 times increase was reported for mineral wool [9].

As follows from the above survey, in the case liquid moisture appears in a structure, particularly the thermal conductivity of insulation materials can be so high that the energy balance of a building envelope is affected in a serious way. Simple calculation methods used in most energy audits are not able to include these effects. They work with steady state models and do not count with moisture transport in liquid form. In such a case more sophisticated models of heat and moisture transport are to be used [10-14].

However, also sophisticated models need reliable input data. So, at least the dependence of thermal conductivity and specific heat capacity on moisture content should be available. While the specific heat capacity of a wet material can be easily estimated using the superposition principle, the thermal conductivity must be measured in whole required moisture range. This can take a month or two of laboratory measurements, contrary to the couple of minutes or hours for a dry-material value. Nevertheless, the data for databases of thermal and hygric parameters are collected by many universities [10, 11, 15] so that in future this may not be considered a problem for common materials.

In many practical case studies, the reconstruction and restoration works in particular, a hygrothermal assessment of the designed solution is necessary. For the long-term prediction of hygrothermal behavior of reconstructed building not only the material parameters are to be included into the model but also the initial conditions have to be known. The initial moisture content in a reconstructed wall is one of the principal parameters. It affects not only the rate of drying of the envelope but also the thermal conditions in the wall. If the moisture is in liquid state it can be transported also into the thermal insulation layer which delays the expected effect of additional thermal insulation on energy efficiency of the building. This underlines the necessity to perform moisture measurements before and after the reconstruction with a sufficient accuracy. The hygrothermal predictions can be done with a much higher accuracy if the hygric conditions in the wall are well known.

The moisture measurements on building site should preferably be done in a nondestructive way and with the highest possible precision which are contradictory requirements. Therefore, compromises are to be adopted. The most frequently used techniques for determining moisture content in building materials are methods based on electrical conductivity measurement, and electrical capacitance measurement methods at lower frequencies. These methods can be employed both in the laboratory and on building site, but their accuracy is limited, particularly in long-term monitoring conditions. More advanced although not so frequently used for building materials are methods based on neutron imaging, nuclear magnetic resonance, microwave transmission, X-ray absorption or γ-ray attenuation techniques. These methods can be employed mainly in the laboratory and are not suitable for in situ measurements. The standard gravimetric method is accurate and reliable enough but destructive which disqualifies it for measurements in wider scale on a building.

The time domain reflectometry (TDR) is still a relatively new method for building materials. In contrast to most other methods commonly used for that purpose, it does not require calibration for every material, in general. The TDR probe calibration can be done in advance all once for every single probe. Another advantage of the TDR method is that it is well applicable for the materials with higher salt content, where an application of methods such as the resistance method or the capacitance method is impaired by a significant loss of accuracy. The TDR method can be used for long-term measurements with a number of probes inbuilt into a wall during the reconstruction process which can remain there for years without a necessity to be replaced. However, problems with TDR sensor installation can occur in some cases, in particular for compact materials with high strength. In this paper, three different experimental approaches of TDR sensors placement into compact materials are analyzed and their applicability for laboratory and on site measurements are discussed.

2. Experimental setup

For the TDR measurements, the cable tester LOM/4/mpts produced by Easy Test was used in combination with second-level multiplexers for sensors connection (see Fig. 1 for example of structure of LOM/4/mpts for recording instantaneous profiles of moisture, temperature, salinity and capillary pressure). LOM/4/mps is TDR-technology based, computer-aided instrument originally designed for measurement of soil moisture and other soil properties. This apparatus works with $\sin^2$-like needle pulse having rise-time of about 250 ps. Within the moisture measurement, the built-in computer serves for controlling TDR needle-pulse circuitry action, recording TDR voltage-versus-time traces, and calculating the pulse propagation time along particular TDR probe rods and the relative permittivity of measured material. The measuring range, accuracy and resolution of complex relative permittivity readings of LOM/4/mpts are given in Table 1.

Table 1: Basic characteristics of applied TDR device

Measured quantity	**Measuring range**	**Accuracy**	**Resolution**
Relative permittivity ◎	2 ÷ 90	Absolute error ± 2	0.1

A two-rod miniprobe LP/ms (Easy Test) designed by Malicki et al. [16] was used for the determination of moisture content. The sensor is made of two 53 mm long parallel stainless steel rods, having 0.8 mm in diameter and separated by 5 mm. The sphere of sensor influence was determined with the help of a simple experiment. The probe was fixed in the beaker and during the measurement, there was added water step by step. From the measured data (relative permittivity in dependence on water level) there was found out that the sphere of influence creates the cylinder having diameter about 7 mm and height about 60 mm, circumference around the rods of sensor.

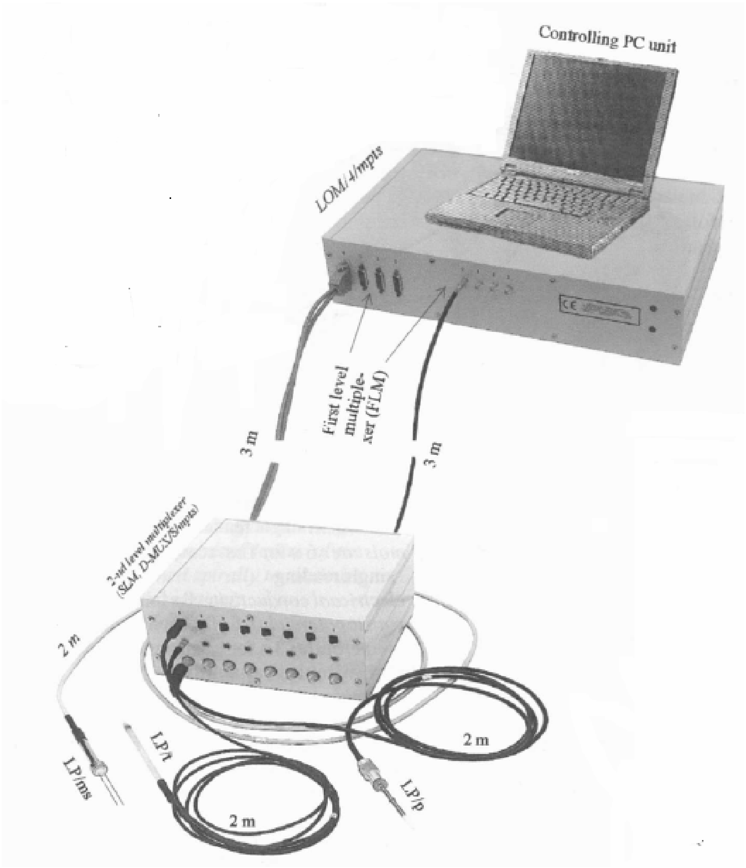

Fig. 1: Experimental set-up of LOM/4/mpts for monitoring of field variables in porous media.

The first studied method of sensor installation consists in boring of two parallel holes having the same dimensions as the sensor rod. For good contact of sensor with material, the bored powder of the studied material was partially placed back into the bored holes. The second method is based on application of electrical conducting gel that is placed into the bored holes and ensures the ideal contact of rods and wet material. In the third method, the samples of studied materials are cut into two parts and the slots having similar thickness as sensor rods are recessed on one of the sample parts.

The samples having cylindrical shape, with the height of 100 mm and diameter of 50 mm were used for the calibration experiments. After placing the sensors, all the measured samples were partially saturated by water and insulated to prevent water evaporation. The relative permittivity of wet samples was then continuously monitored until the measured values reached the constant value. Then, the experiment was interrupted, sensors removed from the samples and moisture content determined using gravimetric method. Finally, the measured values of permittivity were assigned to the gravimetric moisture content.

3. Calibration procedure

The calibration was done in three different ways. The first approach was based on the application of reference gravimetric method for moisture measurement. This approach we have already described above. The second method of calibration used empirical conversion functions that were originally proposed for application in soil science. In this work, the conversion functions proposed by Topp et al. [17] and Malicki et al. [18] were used.

The Topp's third-order polynomial relation [17] is expressed by equation

$$\theta = -5.3*10^{-2} + 2.92*10^{-2} * \varepsilon_{eff} - 5.5*10^{-4} * \varepsilon_{eff}^2 + 4.3*10^{-6} * \varepsilon_{eff}^3, \tag{1}$$

where ε_{eff} is the relative permittivity and θ the moisture content in the porous body [m³/m³]. It had for the originally studied materials standard error of estimate 0.0468 and was proposed for materials having the bulk density close to 1500 kg/m³.

The normalized conversion function proposed by Malicki et al. [18] is considered presently by many authors as universal for different types of materials. The Malicki's function can be expressed as

$$\theta = \frac{\sqrt{\varepsilon_{eff}} - 0.819 + 0.168 * \rho - 0.159 * \rho^2}{7.17 + 1.18 * \rho}, \tag{2}$$

where ρ is the bulk density of dry material. It had for the originally studied materials standard error of estimate 0.0269. Since the application of Malicki's function assumes knowledge of bulk density of studied material, measurement of basic material parameters of investigated ceramic brick were done as well. For the measurement, automatic helium pycnometer Pycnomatic ATC was used. The basic material parameters of studied ceramic brick are given in Table 2.

Table 2: *Basic material parameters of studied ceramic brick*

Bulk density [kg/m³]	**Matrix density [kg/m³]**	**Total open porosity [Vol. %]**
1882	2684	29.9

The third method that was used for calibration of TDR method for studied ceramic brick represent dielectric mixing models based on the effective media theory. In terms of homogenization, a porous material can be considered as a mixture of three phases, namely solid, liquid and gaseous phase. Here, in case of ceramic brick, the solid phase is formed by burnt clay minerals, liquid phase by water and gaseous phase by air. In the case of dry material, only the solid and gaseous phases are considered. The volumetric fraction of air in porous body is given by the measured total open porosity. In case of penetration of water, part of the porous space is filled by water. For the evaluation of relative permittivity of the whole material, the permittivities of the particular constituents forming the porous body have to be known. In our case, the relative permittivity of matrix of ceramic brick ε_{mat} was determined on the basis of the measurement of relative permittivity of dry samples ε_d. From the known ε_{eff}, the ε_{mat} value was calculated using the Rayleigh formula

$$\frac{\varepsilon_{mat} - 1}{\varepsilon_{mat} + 2} = f_d \left(\frac{\varepsilon_d - 1}{\varepsilon_d + 2} \right) + f_a \left(\frac{\varepsilon_a - 1}{\varepsilon_a + 2} \right), \tag{3}$$

where f_d and f_a are volumetric fractions of solid and air in the material; ε_a the relative permittivity of air (1.0).

The effective relative permittivity of a multi-phase composite cannot exceed the bounds given by the relative permittivities and volumetric fractions of its constituents. The upper bound is reached in a system consisting of plane-parallel layers disposed along the electric field vector. The lower bound is reached in a similar system but with the layers perpendicular to the electric field. These bounds are usually called Wiener's bounds, and can be expressed by the relations

$$\varepsilon_{eff} = \frac{1}{\frac{f_1}{\varepsilon_1} + \frac{f_2}{\varepsilon_2} + \frac{f_3}{\varepsilon_3}}, \tag{4}$$

$$\varepsilon_{eff} = f_1\varepsilon_1 + f_2\varepsilon_2 + f_3\varepsilon_3, \tag{5}$$

where Eq. (4) represents the lower limit and Eq. (5) the upper limit of effective relative permittivity (f_j is the volumetric fraction of the particular phase; ε_j its relative permittivity).

The mixing of phases resulting in moisture de-pendent relative permittivity function falling between the Wiener's bounds can be done using many different techniques. In this work, we have tested the fittingness of Lichtenecker's equation [19]

$$\varepsilon_{eff}^{\ k} = f_1\varepsilon_1^{\ k} + f_2\,\varepsilon_2^{\ k} + f_3\,\varepsilon_3^{\ k}, \tag{6}$$

where the parameter *k* varies within the [-1,1] range. Thus, the extreme values of *k* correspond to the Wiener's boundary values. The parameter *k* may be considered as describing a transition from anisotropy at *k* = -1.0 to anisotropy at *k* = 1.0. However, the Lichtenecker's equation may be also applied for isotropic materials. In this work, we have used *k* as the fitting parameter and tried to find the acceptable agreement between measured and calculated results.

4. Experimental results and discussion

The moisture dependent relative permittivities obtained by the different methods of sensor installation are given in Fig. 2.

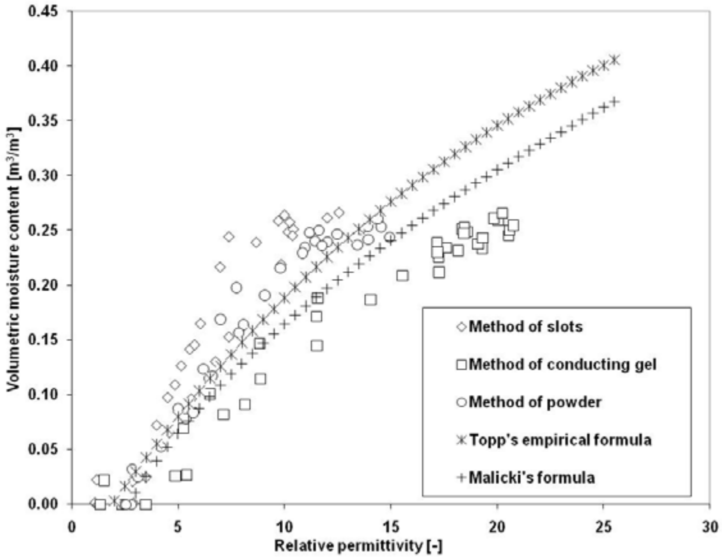

Fig. 2: Moisture dependent relative permittivity of ceramic brick.

As for the data obtained by the empirical conversion functions, the Topp's method achieved a reasonable agreement with the results of powder method in the whole range of moisture content. For the Malicki's method satisfactory agreement was observed only for lower relative permittivity.

Data obtained by application of Lichtenecker's equation are summarized in Figs. 3 – 5. Apparently, a relatively good agreement between measured and calculated data was obtained for two methods of sensor's installation, namely the refilled powder and slots method. In the case of gel application, the homogenization procedure completely failed. This can be explained by the high permittivity of gel covering the sensor's rods that was not considered within the calculations.

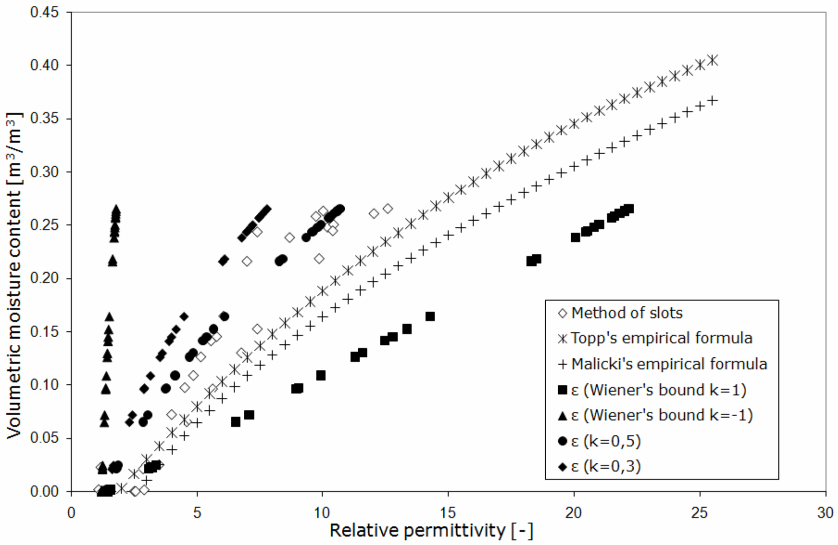

Fig. 3: Moisture dependent relative permittivity of ceramic brick – method of slots.

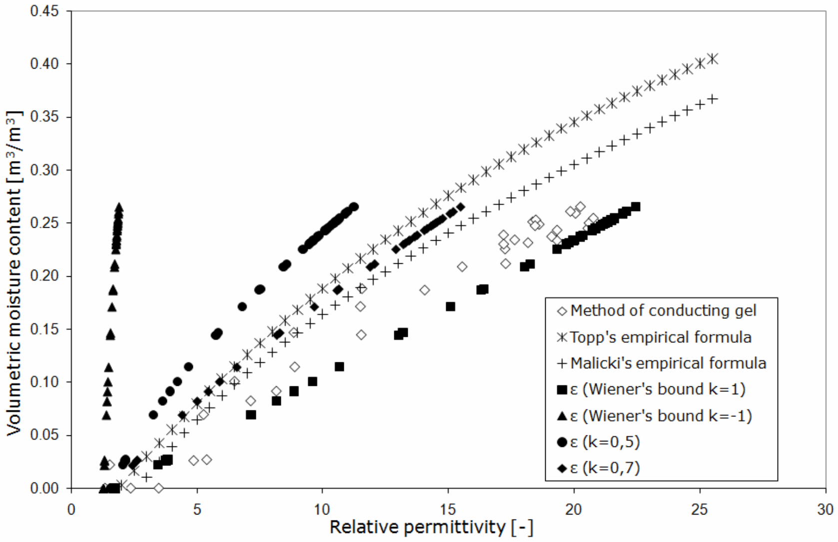

Fig. 4: Moisture dependent relative permittivity of ceramic brick – method of gel.

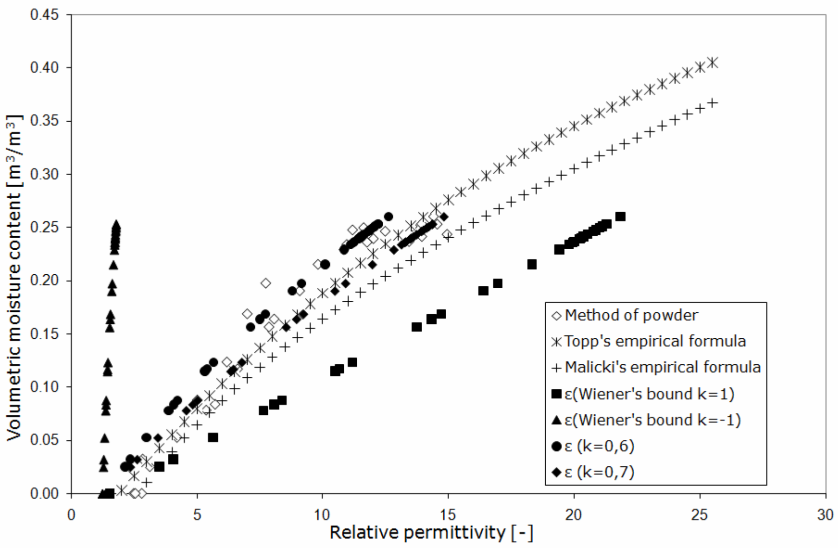

Fig. 4: Moisture dependent relative permittivity of ceramic brick – method of powder.

5. Conclusions

The experimental results presented in this paper have shown that the powder method of sensor installation was probably the most accurate from the theoretical point of view. The method of slots was negatively affected by a possibly imperfect contact of sensor rods with the material of the sample. The conducting gel method was influenced by the high relative permittivity of the gel layer.

However, from the point of view of practical measurements of moisture content in porous materials it seems that all three studied methods of sensor installation are possible to be applied without any serious risk of the loss of accuracy. The calibration curves are reasonably smooth and if the same method is applied in the process of calibration and in the subsequent measurements for instance on building site, the obtained data for moisture content should be reliable enough.

Acknowledgment

This research has been supported by the Czech Ministry of Education, Youth and Sports, under project No MSM 6840770031.

References

[1] PAPADOPOULOS, A. M. State of the art in thermal insulation materials and aims for future developments. Energy and Buildings, Vol. 37, 2005, p. 77–86

[2] AL-AJLAN, S. A. Measurements of thermal properties of insulation materials by using transient plane source technique. Applied Thermal Engineering, Vol. 26, 2006, p. 2184–2191

[3] MAR, J. D. – LITOVSKY, E. – KLEIMAN, J. Modeling and Database Development of Conductive and Apparent Thermal Conductivity of Moist Insulation Materials. Journal of Building Physics, Vol. 32, 2008, p. 9-31

[4] VEJMELKOVÁ, E.; PADEVĚT, P.; ČERNÝ, R. Effect of Cracks on Hygric and Thermal Characteristics of Concrete. Bauphysik, Vol. 30, 2008, p. 438-444.

[5] MŇAHONČÁKOVÁ, E.; JIŘIČKOVÁ, M.; PAVLÍK, P.; FIALA, L.; ROVNANÍKOVÁ, P.; BAYER, P.; ČERNÝ, R. Effect of Moisture on Thermal Conductivity of a Cementitious Composite. International Journal of Thermophysics, Vol. 27, 2006, p. 1228-1240.

[6] VEJMELKOVÁ, E.; KONVALINKA, P.; PADEVĚT, P.; KOPECKÝ, L.; KEPPERT, M.; ČERNÝ, R. Mechanical, hygric and thermal properties of cement-based composite with hybrid fiber reinforcement subjected to high temperatures. International Journal of Thermophysics, Vol. 30, 2009, p. 1310-1322.

[7] ČERNÝ, R.; KUNCA, A.; TYDLITÁT, V.; DRCHALOVÁ, J.; ROVNANÍKOVÁ, P. Effect of Pozzolanic Admixtures on Mechanical, Thermal and Hygric Properties of Lime Plasters. Construction and Building Materials, Vol. 20, 2006, p. 849-857.

[8] PAVLÍK, Z.; VEJMELKOVÁ, E.; FIALA, L.; ČERNÝ, R. Effect of Moisture on Thermal Conductivity of Lime-Based Composites. International Journal of Thermophysics, Vol. 30, 2009, p. 1999-2014.

[9] JIŘIČKOVÁ, M. – ČERNÝ, R. Effect of Hydrophilic Admixtures on Moisture and Heat Transport and Storage Parameters of Mineral Wool. Construction and Building Materials, Vol. 20, 2006, p. 425-434.

[10] GRUNEWALD, J. DELPHIN 4.1 - Documentation, Theoretical Fundamentals. TU Dresden, Dresden, 2000.

[11] HOLM, A.; WORCH, A., Einsatzmöglichkeiten des Computersimulationsprogramms WUFI bei Putzen. FAS-Schriftenreihe, Heft 9, Putzinstandsetzung: Vorträge anläßlich der 9. Hanseatischen Sanierungstage im November 1998. Ostseebad Kühlungsborn, 1998.

[12] ČERNÝ, R.; MADĚRA, J.; KOČÍ, J.; VEJMELKOVÁ, E. Heat and moisture transport in porous materials involving cyclic wetting and drying. Computational Methods and Experimental Measurements XIV, C. Brebbia, G. M. Carlomagno (eds.), WIT Press, Southampton, 2009, p. 3-12.

[13] KOČÍ, V.; MADĚRA, J.; ČERNÝ, R.; ROVNANÍKOVÁ, P. Application of a combined computational-experimental approach for service life estimate of exterior plasters of historical buildings. Structural Studies, Repairs and Maintenance of Heritage Architecture XI, C. Brebbia, (ed.), WIT Press, Southampton, 2009, p. 303-314.

[14] MADĚRA, J.; KOČÍ, J.; VEJMELKOVÁ, E.; ČERNÝ, R.; ROVNANÍKOVÁ, P.; ONDRÁČEK, M.; SEDLMAJER, M. Influence of material characteristics of concrete and thermal insulation on the service life of exterior renders. Computational Methods and Experimental Measurements XIV, C. Brebbia, G. M. Carlomagno (eds.), WIT Press, Southampton, 2009, p. 13-23.

[15] KOČÍ, V.; KOČÍ, J.; MADĚRA, J.; ČERNÝ, R. Computer code HEMOT for hygrothermal assessment of thermal insulation systems. This Proceedings book.

[16] MALICKI, M. A.; PLAGGE, R.; RENGER, M.; WALCZAK, R. T. Application of time-domain reflectometry (TDR) soil moisture miniprobe for the determination of unsaturated

soil water characteristics from undisturbed soil cores, Irrigation Science, vol. 13, 1992, p. 65-72.

[17] TOPP, G. C.; DAVIS, J. L.; ANNAN, A. P. Electromagnetic determination of soil water content: Measurements in coaxial transmission lines, Water Resources Research, vol. 16, 1980, p. 574-582.

[18] MALICKI, M. A.; PLAGGE, R.; ROTH, C. H. Improving the calibration of dielectric TDR soil moisture determination taking into account the solid soil, European Journal of Soil Science, vol. 47, 1996, p. 357-366.

[19] LICHTENECKER, K. Die dielektrizitatskonstante naturlicher und kunstlicher mischkorper", Physikalische Zeitschrift, Vol. 27, 1926, p. 115–158.

Estimation of thermophysical parameters of stainless steel 1H18N9T by an inverse method

Janusz Zmywaczyk , Marcin Gapski

Faculty of Mechatronics, Military University of Technology (MUT), Kaliskiego 2, 00-908 Warsaw, Poland, e-mail: janusz.zmywaczyk@wat.edu.pl

Abstract: *The temperature-dependent thermal conductivity* λ*, the volumetric heat capacity (*ρcp*) and the heat transfer coefficient h of stainless steel 1H18N9T were estimated simultaneously using an inverse method. The experimental setup consisted of a thin-layer Kapton heater put symmetrically into the sample which was divided into four parts. Temperature histories were recorded using the K-type thermocouples on the rear and on the side surface of the sample adjacent to the heater. The finite volume method was used to solve the direct problem of 2-D unsteady heat conduction in an axial-symmetric geometry. The thin-layer heater was treated as a volumetric heat source so as to take into account its thermal inertia. The Levenberg-Marquardt optimization method was applied when solving the inverse problem. Temperatue range of investigation was 20-60 0C.*

Keywords: *thermophysical parameters, inverse method, stainless steel 1H18N9T*

1. Introduction

The austenic stainless steel 1H18N9T with density ρ=7900 kg/m^3 known as X6CrNiTi18-10 (ISO EN) or 321 (AISI) or A240 (ASTM) is widely used material especially in airplane exhaust pipes, heat exchangers and tanks used for storage acids or parts of pumps in chemical, varnish, pharmaceutical and food industry. It is difficult to find information about temperature-dependent thermal conductivity λ and specific heat c_p for this type of steel in an available literature. The EN-10088 part 1 standard describes only the values of thermophysical properties at room temperature T=20 ^{0}C: ρ=7900 kg/m^3, λ=15 W/m/K, c_p = 500 J/kg/K. The commercial thermophysical properties database MPDB v7.08 includes λ(T) and $c_p(T)$ thermal characteristics of the A321 steel, nevertheless density at room temperature is about ρ=9000 kg/m^3, which is too large difference in relation to the 1H18N9T steel.

In this paper identification of thermophysical parameters (λ, ρc_p) of the 1H18N9T stainless steel with density ρ=7890 kg/m^3 at room temperature T=23 ^{0}C using coefficient inverse technique has been described. The presented method is based on adjustment of real (experimental) and modeled temperature response for a given form of heating pulses mathematically described as rectangular or sinusoidal pulse functions of a certain duration. The heating pulses influence on the estimated parameters has been examined. Thus work is a continuation of the earlier studies concernig solid's thermophysical parameters identification by an inverse method. Results for Black Foamglas obtained before were published in THERMOPHYSICS 2009 proceedings [1] .

2. Problem formulation

The boundary-value problem of heat conduction was given in [1] and there is no need to be repeted it here as a whole. But this time the thin-layer Kapton-metallic foil heater of thickness H_g=0.15mm and of effective diameter $2R_g$=29.09mm is regarded as a volumetric heat source of efective density q$_v$ acting on the thin layer of the sample. In contrast to the heat transfer model (Eqs. 1-2 [1]), the thin-layer heater(1) – sample(2) – sample(3) – insulating sample made of PMMA(4) are taken as separate solids (subscript *i*). Thus, the governing equation has the form

$$r\rho c_{p,i}\frac{\partial \vartheta_i}{\partial t}=\frac{\partial}{\partial r}\left(r\cdot\lambda_{r,i}\frac{\partial \vartheta_i}{\partial r}\right)+\frac{\partial}{\partial z}\left(r\cdot\lambda_{z,i}\frac{\partial \vartheta_i}{\partial z}\right)+q_v(r,z,t)$$

$$(r,z,t)\in(0,R)\times(0,H_i)\times(0,t_f],\ \ i=\overline{1,4} \tag{1}$$

where $\vartheta_i = \vartheta_i\,(r, z; t)$ is the temperature excess over the initial homogeneous temperature T_0

$$\vartheta_i(r,z;t)=T_i(r,z;t)-T_0 \tag{2}$$

and the volumetric heat source q$_v$ is given by

$$q_v(r,z;\,t)=\begin{cases}\dfrac{1}{2}\dfrac{U_g(t)I_g(t)}{A_gH_g} & \text{for } (r,z;\,t)\in[0,R_g]\times[0,H_g]\times(0,t_g]\\ 0 & \text{otherwise}\end{cases} \tag{3}$$

where t_g is the time of heating, U_g , I_g are the voltage and current of heater and $A_g = \pi\,(R_g)^2$

It is assumed that there are thermal contact resistances at the border of sample faces which can be expressed as

$$\lambda_{i+1}\frac{\partial\vartheta_{i+1}}{\partial z}\Big|_{z=H_i}-\lambda_i\frac{\partial\vartheta_i}{\partial z}\Big|_{z=H_i}=h_i(\vartheta_i-\vartheta_{i+1}),\ \ i=\overline{1,3} \tag{4}$$

where h_i stand for thermal conductances.

In the inverse problem formulation the unknown parameters to be estimated are: the thermal conductivity in radial λ_r and axial λ_z directions, the heat transfer coefficient h_r at the sample border $r=R$ and the specific heat c_p which can be treated as components of the vector

$$\boldsymbol{u}^{\mathrm{T}}=[\lambda_r,\lambda_z,h_r,c_p] \tag{5}$$

minimizing the mean square functional $J(\mathbf{u}^{\mathrm{T}})$

$$J(\boldsymbol{u}^{\mathrm{T}})=\sum_{j=1}^{\mathrm{NMP}}\sum_{n=1}^{Nt}\left[T(P^j,t_n;\boldsymbol{u}^{\mathrm{T}})-Y_j(t_n)\right]^2=\boldsymbol{e}^{\mathrm{T}}\boldsymbol{e}\rightarrow\min \tag{6}$$

where
$T(P^j , t_n ; \mathbf{u}^{\mathrm{T}})$ is the model temperature being a solution of the direct problem at the same locations P^j and moments t_n as the measured temperatures $Y_j(t_n)$ for the currently estimated components of the vector **u**, and vector **e** stands for the residual vector with components $\mathbf{e}_j = T(P^j, t_n; \mathbf{u}^{\mathrm{T}}) - Y_j(t_n)$

2.1 Solution of the direct problem

The finite volume method was used to solve the direct problem formulated in [1] with changes given in chapter 2. A brief description of the method is as follows.

The energy balance within the finite volume V_C depicted in Fig. 1 has the form

$$\rho c_p (T_C - \overline{T}_C)\Delta V_C = [K_e(T_E - T_C) - K_w(T_C - T_W)]\Delta t + [K_n(T_N - T_C) - K_s(T_C - T_S)]\Delta t + q_v \Delta V_C \Delta t \tag{7}$$

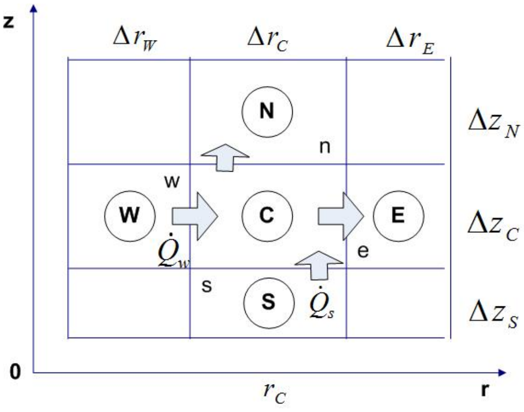

Figure 1: Sketch of finite volume VC

where *K* stand for the element conductances defined by

$$K_e = \frac{2\pi \Delta z_C}{\frac{1}{\lambda_E}\ln\left(\frac{r_E}{r_e}\right) + \frac{1}{\lambda_C}\ln\left(\frac{r_e}{r_C}\right)(+)\frac{1}{r_e h_e}}, \quad K_w = \frac{2\pi \Delta z_C}{\frac{1}{\lambda_C}\ln\left(\frac{r_C}{r_w}\right) + \frac{1}{\lambda_W}\ln\left(\frac{r_w}{r_W}\right)(+)\frac{1}{r_w h_w}}$$

$$K_n = \frac{2\pi r_C \Delta r_C}{\frac{1}{2}\frac{\Delta z_N}{\lambda_N} + \frac{1}{2}\frac{\Delta z_C}{\lambda_C}(+)\frac{1}{h_n}}, \qquad K_s = \frac{2\pi r_C \Delta r_C}{\frac{1}{2}\frac{\Delta z_C}{\lambda_C} + \frac{1}{2}\frac{\Delta z_S}{\lambda_S}(+)\frac{1}{h_s}}$$

and $\overline{T}_C = T_C^{old}$, $\Delta V_C = 2\pi r_C \Delta r_C \Delta z_C$, $\dot{Q}_w = -K_w(T_C - T_W)$, $r_C = r_W + 0.5\Delta r_W + 0.5\Delta r_C$ (8)

The term after (+) in Eq. 8 denotes the thermal contact resistance (1/*h*) between the finite elements when they are taking into acount.

To calulate a non-stationary 2D temperature field of the system under consideration an ADI (alternating direction implicite) with Peaceman-Rachford algorithm was used in the form

$$\begin{cases} \rho c_p \dfrac{T_C - \overline{T}_C}{\Delta t/2} = [K_e(T_E - T_C) - K_w(T_C - T_w) + \overline{K}_n(\overline{T}_N - \overline{T}_C) - \overline{K}_s(\overline{T}_C - \overline{T}_S)]\dfrac{1}{\Delta V_c} + q_v \\ \rho \hat{c}_p \dfrac{\hat{T}_C - T_C}{\Delta t/2} = [K_e(T_E - T_C) - K_w(T_C - T_w) + \hat{K}_n(\hat{T}_N - \hat{T}_C) - \hat{K}_s(\hat{T}_C - \hat{T}_S)]\dfrac{1}{\Delta V_c} + q_v \end{cases} \tag{9}$$

where $\overline{T}_C = T_C(t_n)$; $T_C = T_C(t_{n+1/2})$; $\hat{T}_C = T_C(t_{n+1})$

3. An experiment

The sketch of experimental setup is shown in Figure 2. The rectangular or sinusoidal thermal pulse of duration t_g (much shorter than the final time of measurement t_f) was generated by the electric thin-layer Kapton heater using a stabilized DC power supply PPS 2017 automatically controlled by a own computer program written in labVIEW environment. Temperatures Th1-Th5 were measured by using K-type thermocouples of diameter 80μm made by OMEGA applying 9-Ch scanner card Keithley 2001 TCSCAN (rectangular pulse) or NI 9211 (sinusoidal pulse). The time of pulse duration was 3s (rectangle) or 4s (sinus) and the voltage amplitude was 40V or 50V, respectively.

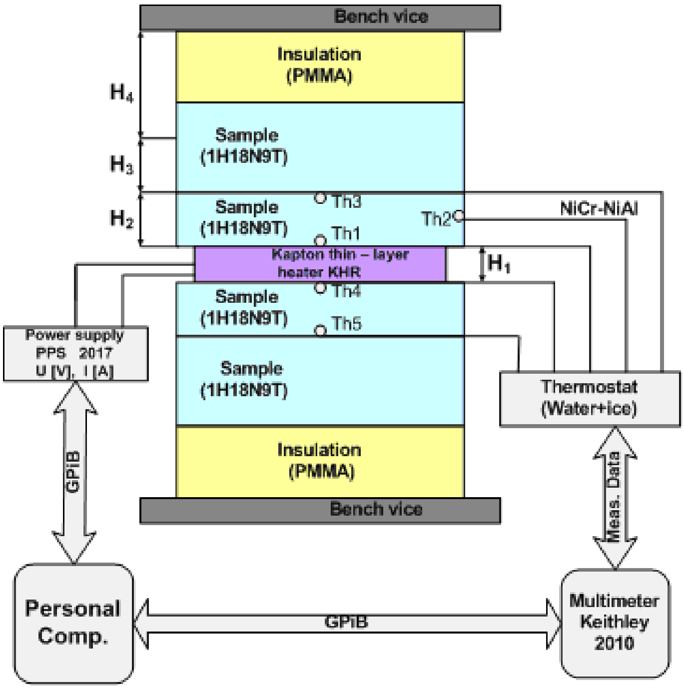

Figure 2: Sketch of measurement setup (scale not preserved)

Comparison of the measured and the calculated (from the direct problem) temperature at the back face of the sample (Th3) placed in the oven at +50 ^{0}C subjected to the both kind of pulses is shown in Fig. 3 and the temperature residuum corresponding to the rectangular pulse is shown in Fig. 4. One can observe in Fig. 3 that the measured data are more scattered in case of Keithley 2001 TCSCAN scanner card than in case of NI 9211 card, nevertheless it was easier to program the sinusoidal pulse with this Ni9211 scanner card. The temperature residuum visible in Fig. 4 do not exceed 7% with respect to the amplitude of temperature excess equals 0.19 ^{0}C when the rectangular pulse was used (see Fig. 3).

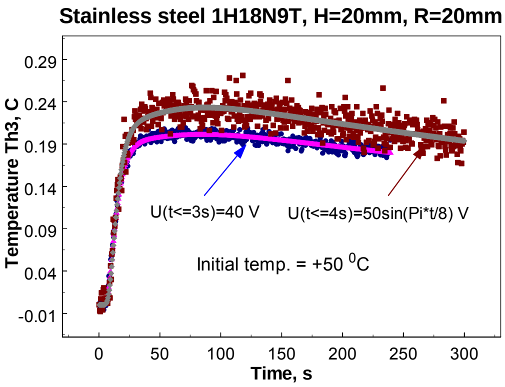

Figure 3: Measured and calculated temperature histories Th3

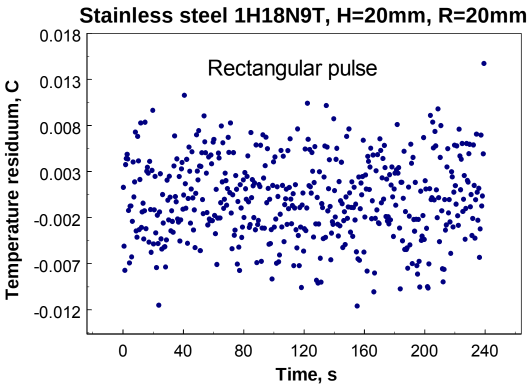

Figure 4: Temperature residuum corresponding to rectangular pulse at the back sample face

3.1 Numerical treatment

It was accepted a numerical mesh (NR × NZ × Nt) = 31 × 55 × 600 with the following elements:

Δr_i = /3*0.2, 0.4, 13*1.0, 0.4, 3*0.1, 0.3, 4*1.0, 5*0.2/ [mm], I = 1,2,…,NR

Δz_j = /3*0.03, 0.01, 0.05, 0.15, 0.2, 0.5, 8*1.0, 4*0.5, 8*1.0, 4*0.5, 8*1.0, 3*0.5,&
1.0, 1.5, 7*2.0, 3*1.0/ [mm], J = 1,2,…,NZ

Time step Δt = 0.5s was equal to the recording time step of the measured signals.

Sensitivity coefficients $X = \partial T/\partial u_i$ were calculated using a central differential scheme as follows

$$X_{i,j}^{n} \cong \frac{T[P^i,t_n;u_j(1+\varepsilon)]-T[P^i,t_n;u_j(1-\varepsilon)]}{2u_j\varepsilon}\Big|u_k = idem,\ k \neq j \tag{10}$$

where $\varepsilon = 10^{-4} \div 10^{-3}$

Components of the vector **u** (Eq. 5) were calculated iteratively using the Levenberg Marquardt optimization method in the following way [2]

$$\boldsymbol{u}^{(s+1)} = \boldsymbol{u}^{(s)} + [\boldsymbol{X}^{\mathrm{T}}(\boldsymbol{u}^{(s)})\cdot \boldsymbol{X}(\boldsymbol{u}^{(s)}) + \mu_s \cdot \boldsymbol{I}]^{-1}\ \boldsymbol{X}^{\mathrm{T}}(\boldsymbol{u}^{(s)})\cdot\left[\boldsymbol{Y} - \boldsymbol{T}(\boldsymbol{u}^{(s)})\right] \tag{11}$$

where *s* stands for the iteration number.

While solving the direct problem the Kapton heater and PMMA specimen were treated as media with known thermophysical parameters of constant values. Their thermal conductivity λ, specific heat c_p and density ρ were accepted as equal to: λ_g=1.666 W/m/K, $c_{p,g}$=1029 J/kg/K, ρ_g=1326 kg/m^3; λ_{PMMA}=0.190 W/m/K, $c_{p,PMMA}$=1460 J/kg/K, ρ_{PMMA}=1182 kg/m^3.

To solve the inverse problem initial values of the vector **u** were accepted as follows:

$$(\boldsymbol{u}^{\mathrm{T}})^{(0)} = [\lambda_r^0, \lambda_z^0, h_r^0, c_p^0] = [10.0, 10.0, 10.0, 450]$$

3.2 The results of parameter estimation

The results of parameter estimation are shown in figures 5-7 and in table 1. In Fig. 5 the reduced sensitivity coefficients $X' = u_i\,(\partial T/\partial u_i)$ are presented. These coefficcients refer to the case of sinusoidal pulse of duration t_g = 4s and the sample set being in thermal equilibrium with the oven of temperature T = +50 ^{0}C. One can observe in Fig. 5 that the amplitude of reduced sensitivity coefficients with respect to λ_z and c_p is almost twice as much as λ_r and h_r. Hence in the identification procedure only the thermal conductivity λ_z and the specific heat c_p were taken into account and the thermal conductivity λ_r and the heat transfer coefficient h_r played the role of additional degree of freedom.

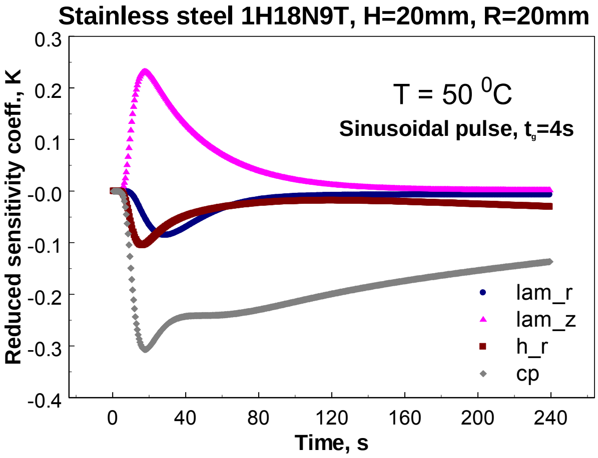

Figure 5: Reduced sensitivity coeffcients at the back face of sample (Th3)

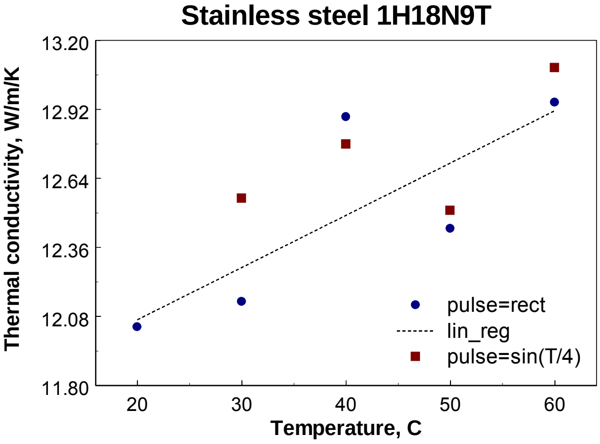

Figure 6: Estimated temperature dependent thermal conductivity with respect to pulse shapes

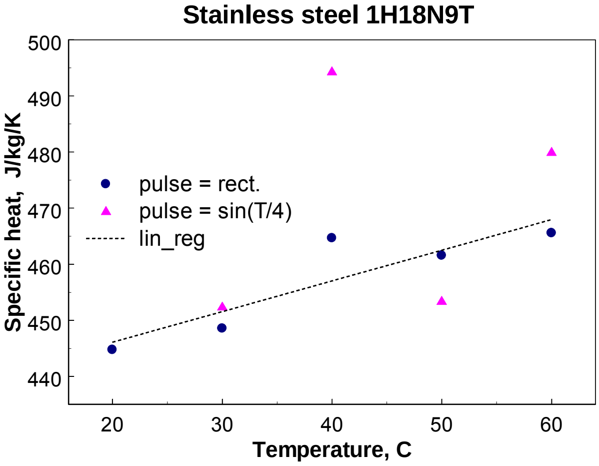

Figure 7: Estimated temperature-dependent specif heat with respect to pulse shapes

In Fig. 7 the estimated specific heat at 40 ⁰C corresponding to the sinusoidal pulse is unreliable. This is due to worse signal to noise ratio for the NI 9211 than the Keithley 2001 TC SCAN card.

Table 1:Results of parameter estimation for 1H18N9T stainless steel (± confidence intervals at $1-\alpha=0.99$)

<table>
<tr><th colspan="6">Rectangular pulse, t_g = 3s, Nt = 479, Δt=0.5s</th></tr>
<tr><td>Temp., ^{0}C</td><td>λ_z, W/m/K</td><td>c_p, J/kg/K</td><td>λ_r, W/m/K</td><td>h_r, W/m^2/K</td><td>J, K^2</td></tr>
<tr><td>20</td><td>12.0373±0.6711</td><td>444.79±4.72</td><td>6.5127±0.4556</td><td>19.05±2.45</td><td>0.0139</td></tr>
<tr><td>30</td><td>12.1446±1.0537</td><td>448.59±4.82</td><td>6.1047±0.4740</td><td>13.52±2.62</td><td>0.0139</td></tr>
<tr><td>40</td><td>12.8900±0.8326</td><td>464.68±5.42</td><td>7.1843±0.4951</td><td>28.99±3.15</td><td>0.0160</td></tr>
<tr><td>50</td><td>12.4369±0.4595</td><td>461.60±4.42</td><td>6.4108±0.3509</td><td>25.31±2.22</td><td>0.0094</td></tr>
<tr><td>60</td><td>12.9487±0.6111</td><td>465.60±4.77</td><td>5.9580±0.3826</td><td>11.49±2.56</td><td>0.0145</td></tr>
<tr><th colspan="6">Sinusoidal pulse, t_g = 4s, Nt = 600, Δt=0.5s</th></tr>
<tr><td>30</td><td>12.5594±0.8102</td><td>452.43±10.08</td><td>5.9581±0.7550</td><td>11.18±4.12</td><td>0.1045</td></tr>
<tr><td>40</td><td>12.7782±0.7586</td><td>494.35±11.41</td><td>5.6237±0.5915</td><td>30.30±4.28</td><td>0.0931</td></tr>
<tr><td>50</td><td>12.5096±0.6778</td><td>453.46±8.30</td><td>7.0227±0.9299</td><td>28.28±3.11</td><td>0.0920</td></tr>
<tr><td>60</td><td>13.0882±0.3774</td><td>480.67±9.31</td><td>7.7218±0.4740</td><td>4.57±3.62</td><td>0.0894</td></tr>
</table>

Analysing the results of parameter estimation given in table 1 one can observe that the confidence intervals corresponding to the thermal conductivity $\Delta\lambda_z$ and the specific heat Δc_p are greater in case of sinusoidal pulse than in case of rectangular pulse. This is caused by using different measuring cards (see Fig. 3) and uneven number of measurement data. However, realization of rectangular pulse by an electric heater is less accurate than sinusoidal pulse due to its thermal inertia. Hence there is a need to study how different forms of heat pulses affect the results of parameter estimation.

4. Conclusion

The austenic stainless steel 1H18N9T is widely used material in industry but there is difficult to find in literature its temperature characteristics of thermophysical properties. The cited equivalent A321 has density of about 9000 kg/m^3 at room temperature while 1H18N9T density equals about 7900 kg/m^3 at the same temperature. For this reason the temperature characteristics of thermal conductivity and specific heat given in commerical database MPDB v7.08 cannot be acceptable in this case.

The results of parameter estimation of the thermal conductivity and the specific heat obtained in this work for stainless steel 1H18N9T allow to draw the following conclusions:

- Both types of the thermal pulses (rectangular or sinusoidal) produce similar resuls but better correlation of the results was obtained using the rectangular pulse resulting from applying Keithley 2001 TC SCAN scanner card instead of NI 9211 one as it was in case of the sinusoidal pulse;
- An effect of the time duration of the heat pulse (t_g = 2s, 3s, 4s) on the estimated parameters under condition on preserving the same amount of energy supplied to the sample is

negligible. Some discrepancies of the results has been found when the time of pulse duration was shorter than 2s;

- The results of identification of stainless steel 1H18N9T thermophysical properties presented in this work should be verified using other methods of investigation and measurement stands to be more reliable

References

[1] ZMYWACZYK J.; WIELGOSZ M.; KONIORCZYK P.; GAPSKI M. Identification of some thermophysical and boundry parameters of black foamglas by an inverse method, Proc. Thermophysics 2009, 29-30 Oct. 2009 Valtice, Chech Republic, pp. 235-251

[2] OZISIK M.N.; ORLANDE H.R.B., *Inverse heat transfer. Fundamentals and applications*, Taylor&Francis, New York 2000

Photoacoustic spectroscopic investigation of temperature dependence of optical absorption in Cu_2GeSe_3

B. K. Sarkar[1], **A. S. Verma**[2]

[1]Department of Physics, VIT University, Vellore 632014, India, email: bksarkar@vit.ac.in

[2]Department of Physics, Panjab University, Chandigarh 160014, India

Abstract: *The ternary semiconducting compound Cu2GeSe3 has been investigated for optical properties with photoacoustic spectroscopy. Optical-absorption spectra of Cu2GeSe3 has been obtained in the range of 0.76 –0.81 eV photon-energy at temperatures between 80 and 300 K. The thermal variation of band-gap energy has been estimated from the optical-absorption spectra at different temperatures. The temperature variation of bandgap has been explained on the basis of electron-phonon interaction. Varshni's empirical relation in conjunction with Vina and Passler model has been taken in consideration for data fitting. The Debye temperature was calculated approximately as 240K. The acoustic phonons with a characteristic temperature as 160 K corresponding to effective mean frequency have been attributed to the thermal variation of the energy gap.*

Keywords: *Ternary semiconductor, Cu2GeSe3, Optical absorption, electron-phonon interaction.*

1. Introduction

The low melting point and small band gap Cu_2GeSe_3 has been investigated for acousto-optic (AO) applications in the IR region. [1,2]. It is of the type $A_2^{I}B^{IV}C_3^{VI}$ ternary compounds possessing considerable interest [2–6] as small band-gap semiconductors for electro-optic device application. Potential AO materials are selected based on proper choice of low band gaps, low melting points, high atomic weights and high refractive indices. Cu_2GeSe_3 has a low melting point (~770 ^{0}C) [7] and high refractive index (~3.2) [8] which enable this material to be used as potential candidate for AO applications in the IR region.

Several researchers have reported different crystal structure for Cu_2GeSe_3. Earlier Palatnik et al. [9] described its structure as cubic with lattice parameter a = 5.55 Å. Rivet [10] and Hanh [11] specified Cu_2GeSe_3 as tetragonal chalcopyrite structure with unit cell parameters a = 5.595, c =5.482 Å and a = 5.590, c = 10.197 Å, respectively. Later, on the basis of single crystal analysis, Cu_2GeSe_3 structure has been reported as orthorhombic with a = 11.860, b = 3.960, and c = 5.455Å. [12]. Further in an X-ray powder diffraction study the same structure was confirmed with the values of a, b and c as 11.878, 3.941, and 5.485 Å [13]. Thermal and elastic properties of Cu_2GeSe_3 were also investigated [14]. Debye temperature, Young's modulus, specific heat etc. were obtained from the measurement of thermal expansion, microhardness and velocity of ultrasonic waves. Regarding much concern about the applicability of $A_2^{I}B^{IV}C_3^{VI}$ ternary compound as AO material it is more important to give much emphasis on the investigation of optical properties. From optical absorption measurements [13].the temperature variation of the band gap E_g of Cu_2GeSe_3 showed band-to-band transition to be direct with Eg around 0.78 eV at room temperature.

In this paper for the first time we present the photoacoustic spectroscopic investigation of optical-absorption for Cu_2GeSe_3 obtained at temperatures T between 70 and 300 K. The temperature dependence of band gap Eg for Cu_2GeSe_3 will be determined from the photoacoustic signal spectra taken at different temperature. The theoretical background behind temperature induced band gap shrinkage (BGS) is still controversial. The change of band gap as a function of the temperature results from two contributions. (i) Thermal expansion will cause a change in the band gap energy [15]. (ii) The renormalization of the electronic energies due to electron- phonon interaction leads to the dominant contribution [16]. The first contribution is smaller than second one [15,16]. In our work the band gap shrinkage will be explained based on electron- phonon interaction [17]. The temperature dependence of Eg has been generally described by the empirical equation proposed by Varshni [18]. In this work the analytical approaches based on electron-phonon interaction proposed by Viña [19] and Pässler [20] to explain the band-gap shrinkage will be taken into consideration to analyze Eg vs T data for Cu_2GeSe_3.

2. Experiment

The Cu_2GeSe_3. crystals used were grown by the conventional Bridgman method. The quartz ampoule graphitized by acetone was filled with a charge of Cu:Ge:Se = 2:1:3 mixture in atomic ratio and then sealed off under 10^{-6} Torr. Cu, Ge, and Se were 99.9999% pure.

The ampoule was slowly heated from room temperature to 300 °C at the rate of 25 ^{0}C/h. The mixture was kept at this temperature for one day and then heated at 8 ^{0}C/h up to 950 ^{0}C. After keeping the mixture at this temperature for one day .again it was heated to 1100 °C at the rate of 25 °C/h., melted, and then equilibrated for at least 2 days. Crystals were grown by cooling at 50 ^{0}C/h down to 850 ^{0}C with a stay of 24 h followed by a cooling from 850 ^{0}C to 600 ^{0}C at 10 ^{0}C/h with a stay of 24 h. The ampoule was then cooled to 500 ^{0}C at 25 ^{0}C/h and the ingot was annealed at this temperature for about one week. The furnace was then cooled to room temperature at 35 ^{0}C/h. The energy dispersive X-ray spectroscopy (EDX) performed on samples taken from the central part of the ingots revealed the composition ratio close to the ideal value 2:1:3.

The single beam photoacoustic spectroscopy (PAS) was used for optical absorption measurement. PAS consists of a PA cell containing a sensitive microphone, a 1000W Xe lamp with power supply (Muller, type SVX 1000, Germany), monochromator (Oriel 77250), and a mechanical chopper (SR540) discussed elsewhere [21,22]. The PA signal produced is detected by a sensitive microphone (Bruel and Kjaer 4147) and processed by using a preamplifier and lock-in amplifier (SR530) with a chopping frequency of 110 Hz. The optical absorption spectra were estimated (as explained in Ref. 22) from the variation of the normalized PA signal intensity with the wavelength of the incident light. The PA spectrum obtained from highly absorbing carbon black powder was used to normalize the spectrum of the samples.

3. Theoretical models

During last decades several models [24-29] have been developed to describe the temperature dependence of energy band-gap or more specifically temperature induced band gap shrinkage. Varshni [18] proposed the empirical model described by the following equation:

$$E_g(T) = E_g(0) - \frac{\alpha T^2}{\beta + T} \tag{1}$$

where $E_g(0)$ is the band gap at 0 K, α is the slope, $dE_g(T)/dT$ at limiting case of $T\to\propto$ and β is a material specific parameter. This model represents a combination of a linear high temperature dependence with a quadratic low temperature asymptote for $E_g(T)$.

Viña [19] et al. proposed a semiempirical model based on Bose–Einstein occupation factor for photons as

$$E_g(T)=E_g(0)-\frac{A}{\exp(\Theta_B/T)-1} \tag{2}$$

where A represents the strength of the electron–phonon interaction, $\Theta_B\cong\hbar\omega/k_B$ is the characteristic temperature which represents the effective phonon energy on the temperature scale [19,30,31]. Another analytical model is proposed by Pässler [20] based on electron-phonon interaction. According to this model $E_g(T)$ can be analytically derived from the expression

$$E_g(T)=E_g(0)-\int f(\varepsilon)z(\varepsilon,T)d\varepsilon \tag{3}$$

where $f(\varepsilon)$ electron-phonon spectral function and $Z(\varepsilon,T)$ is the average phonon occupation number. Spectral function was assumed to be power-law type as $f(\varepsilon)\propto\varepsilon^r$ in the energy range from 0 to a cut-off value $\varepsilon_0=\frac{r+1}{r}k_B\Theta$. Here Θ_B is approximately average phonon temperature [32] and r is an empirical parameter which can be determined from experimental $E_g(T)$ data fitting. For concavity in the spectral function r will lie in the range from $1.2<r<1.8$. In such condition Eq. (3) can be approximated as

$$E_g(T)=E_g(0)-\frac{S\Theta}{2}\left[\left\{1+\left(\frac{2T}{\Theta}\right)^p\right\}^{1/p}-1\right] \tag{4}$$

where $p = r+1$ and $S=-\left(dE_g/dT\right)_{T\to\infty}$ is high-temperature limit value for the forbidden gap entropy.

4. Results and Discussion

The normalized PA spectra of Cu_2GeSe_3 as a function of incident wavelength at different temperatures are shown in Fig. 1.

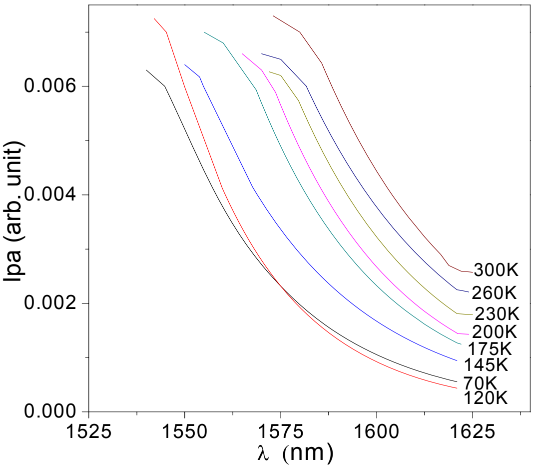

Figure 1: Normalized photoacoustic (PA) spectra of Cu_2GeSe_3 as a function of incident wavelength at different temperatures

The optical absorption coefficient α for thermally thick samples is calculated from the relation [22]

$$\alpha = \frac{q^2 + q\left(2 - q^2\right)^{1/2}}{\mu_s\left(1 - q^2\right)} \tag{5}$$

where q is the normalized PA amplitude and μ_s is the thermal diffusion length (□6.89×10−3 cm), defined as $\mu_s = (2\sigma/\omega)^{1/2}$, σ and ω being the thermal diffusivity and chopping frequency respectively [33]. The value of σ for Cu_2GeSe_3 is taken as 0.0127 cm^2s^{-1} from literature [34]. The variation of the absorption coefficient of Cu_2GeSe_3 with the incident photon energy at different temperatures is shown in Fig. 2.

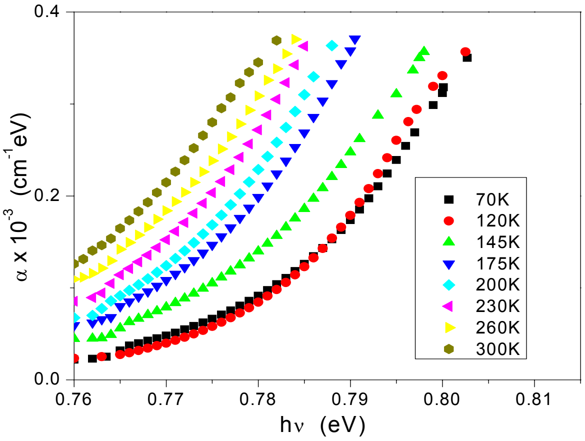

Figure 2: Variation of absorption coefficient (α) of Cu_2GeSe_3 as a function of incident photon energy. Absorption coefficient is determined using Fig. 1 and Eq. 5.

The absorption spectra show that the transition is allowed and direct in nature. In the high absorption region, the absorption coefficient α for the direct transition is governed by

$$\alpha h\nu = A\left(h\nu - E_g\right)^{0.5} \tag{6}$$

The direct transition is confirmed from the plot of $(\alpha h\nu)^2$ vs hν for Cu_2GeSe_3 at different temperatures as shown in Fig. 3.

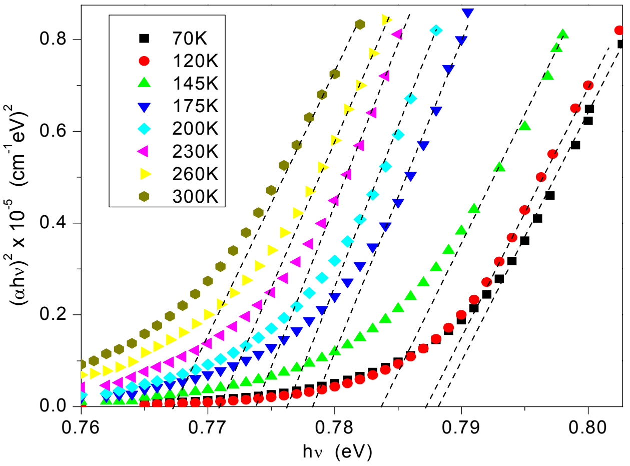

Figure 3: Plot of $(\alpha h\nu)^2$ versus $h\nu$ for Cu_2GeSe_3

The values of the corresponding optical bandgap (E_g) are estimated (where the extrapolated dotted lines meet the abscissa) at different temperature. Thus the estimated bandgap as a function of temperature is shown in Fig. 4.

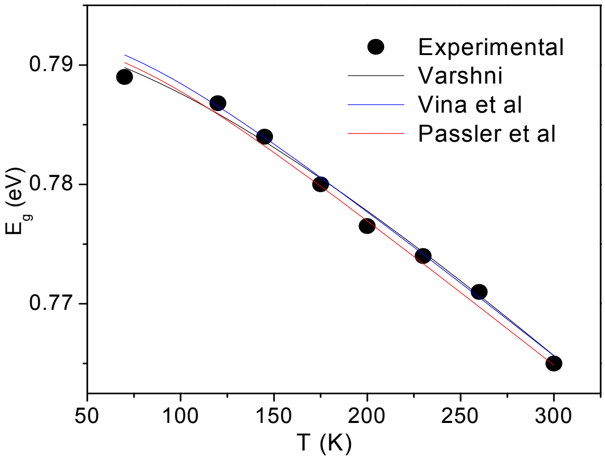

Figure 4: Temperature variation of band gap (Eg) of Cu_2GeSe_3. Data has been fitted according to Eq. (1), (2), and (4) respectively. The fitting parameters are given in Table I.

Temperature dependence of the bandgap of Cu_2GeSe_3 in the range from 70 to 300 K is fitted with Varshni, Viña, and Pässler model according to Eq. (1), (2), and (4) respectively. The fitting parameters are given in Table I.

Table I. Parameters for fitting the EG(T) data of Cu2GeSe3 according to Eqs. (1), (2), and (4).

Equation	$E_G(0)$ (eV)	α (meV/K)	β (K)	A (meV)	S (meV/K)	p	Θ_B (K)
(1)	0.79231	0.16	240	---	---	---	---
(2)	0.7923	---	---	26.3	---	---	206
(4)	0.7922	---	---	---	0.125	2.7	170

Theoretical curves from these equations are shown in Fig. 4. In the procedure of curve fitting, according to three models, the values of $E_g(0)$ are more or less the same, $E_g(0) \sim 0.792$ eV for all models. In the empirical relation due to Varshni, band-gap shrinkage falls linearly at the rate of 0.16 meV/K (= α) at higher temperature. The value of β is 240 K which is comparable with Debye temperature θ_D [34]. The effective phonon temperature Θ is related to θ_D as $\Theta \square \frac{2}{3}\theta_D$ [20]. Taking $\theta_D \sim 240$ K the value of Θ will come as 160 K which is more close to the value listed in Table I according to Pässler model which is more adequate for the extrapolation at high temperatures. The effective phonon energy $\varepsilon_{\text{effective}} = k_B\ \Theta$ and the cut-off phonon energy $\varepsilon_0 = \frac{p}{p-1} k_B \Theta$ are estimated from Pässler model as 14.7 meV and, 23.3 meV respectively. The cut-off phonon energy is comparable with the minimum optical phonon energy in ternary compounds and hence it is quite reasonable to assume that the temperature variation of band gap is much modulated through acoustic phonons.

5. Conclusion

The temperature induced BGS has been studied in Cu_2GeSe_3 in the temperature range from 70 to 300 K by photoacoutic spectroscopic method. The electron-phonon interaction has been taken into consideration to explain the band gap shrinkage. Data fitting was obtained by the empirical and semi-empirical models of Varshni, Viña, and Päassler. The Debye temperature and the effective phonon temperature of Cu_2GeSe_3 were estimated approximately as 240 K and 220 K respectively. Mostly the acoustic phonons contributed to the band gap shrinkage with effective phonon energy of 23.3 meV with cut-off phonon energy of 14.7 meV.

Acknowledgement

The first author (B. K. S.) is thankful to VIT University, Vellore, for its support and the second author (A. S. V.) acknowledges the assistance given by University Grant Commission, New Delhi, India, under the scheme of Dr. D. S. Kothari Post Doctoral Fellowship.

References

[1] Kulakova, L. A., Matveev, B. A., Melekh, B. T. In *J. Non Cryst. Sol.* 2000. 266-269. 969 – 972, ISSN: 0022-3093

[2] Samanta, L. K. In *Phys. Status Solidi A* 1987. 100. K93 – K97. ISSN: 1862-6300

[3] Lee, J. J., Yang, C. S., Park, Y. S., Kim, K. H., Kim, W. T. In *J. Appl. Phys.* 1999. 86. 2914 – 2916. ISSN: 0021-8979

[4] Onoda, M., Chen, X. A., Sato, A., Wada, H. In *Mater. Res. Bull.* 2000. 35. 1563 – 1570. ISSN: 0025-5408

[5] Piskach, L. V., Parasyuk, O. V., Romanyuk, Y. E. In *J. Alloys Compd.* 2000. 299. 227 – 231. ISSN 0925-8388

[6] Marcano, G., Rincón, C., de Chalbaud, L. M., Bracho, D. B., Sánchez Pérez, G. In *J. Appl. Phys.* 2001. 90. 1847 -1853. ISSN 0021-8979

[7] L. I. Berger, In *Ternary Diamond-like Semiconductors (Consultants Bureau, New York, 1969)*, pp. 55–63. ASIN: B0006BZ756

[8] Marvin Weber, In *Handbook of Optical Materials*, CRC Press 2003, ISBN: 978-0-8493-3512-9.

[9] Palatnik, L. S., Koshkin, V. M., Galchinetskii, L. P., Kolesnikov, V. I., Komnik, Y. F., In *Fiz. Tverd. Tela.* 1962. 4. 1430. ISSN 0367-3294

[10] Rivet, J. In *Ann. Chim.* 1965. 10. 243-270. ISSN: 0003-4592

[11] Hahn, H. In *Naturwissenschaften.* 1966. 53. 18. ISSN: 0028-1042

[12] Parthe, E., Garin, J. In *Monatsch. Chem.* 1971. 102, 1197-1208. ISSN: 1434 - 4475

[13] Marcano, G., Nieves, L. In *J. Appl. Phys.* 2000. 87. 1284.-1286. ISSN: 0021-8979

[14] Berger, L. I., Bulenkov, N. A. In *Izv. Akad. Nauk SSSR, Ser. Fiz.* 1964. 28. 1100. ISSN: 0367-6765

[15] J. Malloy, K. J., Van Vechten, J. A. In *J. Vac. Sci. Technol. B.* 1991. 9. 2212-2218. ISSN: 1071-1023

[16] Camassel, J., Auvergne, D. In *Phys. Rev. B.* 1975. 12. 3258-3267. ISSN: 0163-1829

[17] Zoliner, S., Gopalan, S., Cardona, M. In *Solid State Commun*. 1991. 77. 485-488. ISSN: 0038-1098

[18] Varshni, Y. P. In *Physica*. 1967. 34. 149-154. ISSN: 0031-8914

[19] Viña, L., Logothetidis, S., Cardona, M., In *Phys. Rev. B.* 1984. 30. 1979-1991. ISSN: 0163-1829

[20] Pässler R. In *Phys. Status Solidi B.* 1997. 200. 155-172. ISSN: 0370-1972

[21] Sarkar, B. K., Chatterjee, S., Mukherjee, R. K., Chaudhuri, B. K. In *J, Mater. Sci. Lett*. 1997. 16. 1499-1502. ISSN: 0261-8028

[22] Sarkar, B. K., Verma, A. S., Gupta, R. C., Singh, K. In *Int. J. Thermophysics,* 2010. 31. 620-629. ISSN: 1572-9567

[23] Sarkar, B. K., Chaudhuri, B. K. In *Int. J. Thermophysics.* 2005. 26. 295-303. ISSN: 1572-9567

[24] A. Manoogian and A. Leclerc, In *Phys. Status Solidi B*. 1979. 92. K23-K27. ISSN: 0370-1972

[25] Lárez, C., Rincón, C. In *J. Phys. Chem. Solids.* 1997. 58. 1111 -1114. ISSN: 0022-3697

[26] Alex, V., Finkbeiner, S., Weber, J. In *J. Appl. Phys.* 79, 6943-6946. ISSN: 0021-8979

[27] Hang, Z., Yan, D., Pollak, F. H. In *Phys. Rev. B*, 1991. 44. 10546-10550. ISSN: 0163-1829

[28] Sa´nchez-Almazan, F. G., Navarro-Contreras, H., Ram′rez-Flores, G., Vidal, M. A. In *J. Appl. Phys.* 1996. 79. 7713-7717. ISSN: 0021-8979

[29] Malikova, L., Huang, Y. S., Pollak, F. H., Feng, Z. C., Schuman, M., Stall, R. A. In *Solid State Commun.* 1997. 103. 273-278. ISSN: 0038-1098

[30] Logothetidis, S., Cardona, M., Garriga, M. In *Phys. Rev. B* 1991. 43. 11950. ISSN: 0163-1829

[31] Newmann, H., Ho¨ring, W., Bouamama, K. H., Riede, V., Ko¨ding, H. In *Phys. Status Solidi B.* 1992. 171. K79-K84. ISSN: 0370-1972

[32] Pässler, R. In *Phys. Status Solidi B.* 1999. 216. 975. ISSN: 0370-1972

[33] Ghosh, A. K., Sarkar, B. K., Chaudhuri, B. K. In *Solid State Commun.* 2000. 113. 41-45. ISSN: 0038-1098

[34] Berger, L. I. In *Semiconductor materials.* CRC Press, Inc., 1997. ISBN: 0-8493-8912-7

Thermal Stability of Glass Evaluated by the Induction Period of Crystallization

Peter Šimon

Institute of Physical Chemistry and Chemical Physics, Faculty of Chemical and Food Technology, Slovak University of Technology, Radlinského 9, SK-812 37 Bratislava, Slovak Republic; e-mail: peter.simon@stuba.sk

Abstract: *To evaluate the thermal stability of oxide glasses against crystallization, a new criterion based on the length of induction period of crystallization is suggested. It is discussed that the end of the induction period of crystallization corresponds to the moment where the crystallization nuclei have already been formed and the intense growth of crystals starts. Three silicate glasses were prepared and the validity of the criterion was tested. The results indicate that the new criterion enables to discriminate among the thermal stabilities of the silicate glass samples. It can be expected that it can be employed generally for the assessment of the thermal stability of any glass against crystallization, including metal and organic glasses.*

Keywords: *glass, thermal stability, induction period, crystallization*

1. **Introduction**

Features of the nucleation and crystallization processes are of basic importance in the control of glass formability in technological applications where the formation of nuclei and the subsequent crystal growth must be avoided [1-3]. On the other hand, the formation of nuclei and crystal growth by controlled crystallization can give rise to polycrystalline solids containing residual glass phase called the glass ceramics [4]. Therefore, it is very important to evaluate the thermal stability of glasses against crystallization [5,6]. Many authors based the evaluation of glass stability employing the characteristic temperatures of DTA or DSC curves [7-10], crystallization activation energy [11-13] or crystallization rate constants [14,15]. Unfortunately, these stability criteria are not fixed physical parameters, since they mostly depend on the heating rate and temperature [16].

In our previous paper, several criteria of glass stability have been reviewed and tested [17]. The results indicate that, in some cases, the criteria do not correspond fully to the order of thermal stability of glass systems under study. In this paper, a new criterion for evaluating the thermal stability of glasses based on the induction period of crystallization is suggested and its validity is verified by applying it to $Li_2O.2SiO_2.nTiO_2$ systems.

2. Theoretical Analysis

Mechanisms of the processes in condensed phase are very often unknown or too complicated to be characterised by a simple kinetic model. Rate of these processes is generally a function of temperature and conversion. The single-step approximation employs the assumption that the rate of a complex multi-step condensed-state process can be expressed as a product of two separable functions independent of each other, the first one, $k(T)$, depending solely on the temperature T and the other one, $f(\alpha)$, depending solely on the conversion of the process, α [18]:

$$\frac{\mathrm{d}\alpha}{\mathrm{d}t} = k(T)\,\mathrm{f}(\alpha) \tag{1}$$

The temperature function in Eq. (6) is mostly considered to be the rate constant ; hence, it is universally expressed by the Arrhenius equation

$$k(T) = A_k \exp\left[-\frac{E_\mathrm{a}}{RT}\right] \tag{2}$$

where A_k is the preexponential factor, E_a is the activation energy, T is absolute temperature and R stands for the gas constant.

Since Eq. (1) is general, we assume that it describes also the kinetics of the processes occurring during the induction period. Existence of these processes is not detected by the experimental technique used; however, they have to take place as a preparatory stage preceding the main crystallization process. Combination of Eqs.(1) and (2), after the separation of variables, gives the result:

$$\int_0^{\alpha_\mathrm{i}} \frac{\mathrm{d}\alpha}{\mathrm{f}(\alpha)} = \int_0^{t_\mathrm{i}} A_k \exp\left[-\frac{E_\mathrm{a}}{RT}\right] \mathrm{d}t \tag{3}$$

The conversion α_i in Eq.(3) is related to the processes occurring during the induction period and corresponding to the end of the induction period, i.e., to the start of the main process detected by the apparatus, and t_i is the length of the induction period. Further it is assumed that the conversion α_i is the same for any temperature. Then, after integration of the left side of Eq.(3) one can get:

$$\mathrm{F}(\alpha_\mathrm{i}) - \mathrm{F}(0) = \int_0^{t_\mathrm{i}} A_k \exp\left[-\frac{E_\mathrm{a}}{RT}\right] \mathrm{d}t \tag{4}$$

Since the conversion α_i corresponding to the end of the induction period is assumed to be independent of temperature, also the value of the integrated function $\mathrm{F}(\alpha)$ at the point α_i, $\mathrm{F}(\alpha_\mathrm{i})$, is constant. Therefore, Eq. (4) can be rewritten as:

$$1 = \int_0^{t_\mathrm{i}} \frac{\mathrm{d}t}{A\exp[B/T]} \tag{4}$$

where the constants A and B are given as:

$$A = \frac{A}{\mathrm{F}(\alpha_\mathrm{i}) - \mathrm{F}(0)},\quad B = E/R \tag{6}$$

The physical meaning of the denominator in Eq. (5) can be simply demonstrated for a special case of isothermal processes where the denominator is a constant equal to the induction period at the given temperature. Thus, the temperature dependence of the induction period can be expressed as

$$t_i = A\exp[B/T] \tag{7}$$

For the linear increase of temperature in DSC measurements, the sample temperature can be expressed as

$$T = T_0 + \beta t \tag{8}$$

where T0 is the starting temperature of the measurement and β stands for the heating rate. If one assumes that the temperature of the sample equals that of the furnace, combination of Eqs.(5) and (8) gives the result [19]

$$\beta = \int_0^{T_X} \frac{\mathrm{d}T}{A\exp[B/T]} \tag{9}$$

where T_X is the temperature of the end of induction period, i.e. the onset temperature of the crystallization peak. The starting temperature in Eq.(9) is set as $T = 0\,\mathrm{K}$ since the rate of the process at the starting temperature is negligible. When deriving Eqs.(3) and (4), the assumption is implied that the conversion function f(α) holds during the induction period which means that no change of the mechanism occurs.

3. Results and discussion

The criterion was applied for three silicite glasses of the composition $Li_2O.2SiO_2$ (a), $Li_2O.2SiO_2.0.03TiO_2$ (b) and $Li_2O.2SiO_2.0.1TiO_2$ (c). Preparation of the glasses is described in [20]. The onset temperatures, T_X, were directly determined from DTA curves. The parameters A and B in Eq. (9) have been obtained by minimizing the sum of squares between experimental and theoretical values of the onset temperature T_X for various heating rates by the simplex method [21]. The theoretical values of onset temperature are given by Eq. (9). The agreement between experimental and calculated values of the onset temperatures for various heating rates is shown in Fig. 1.

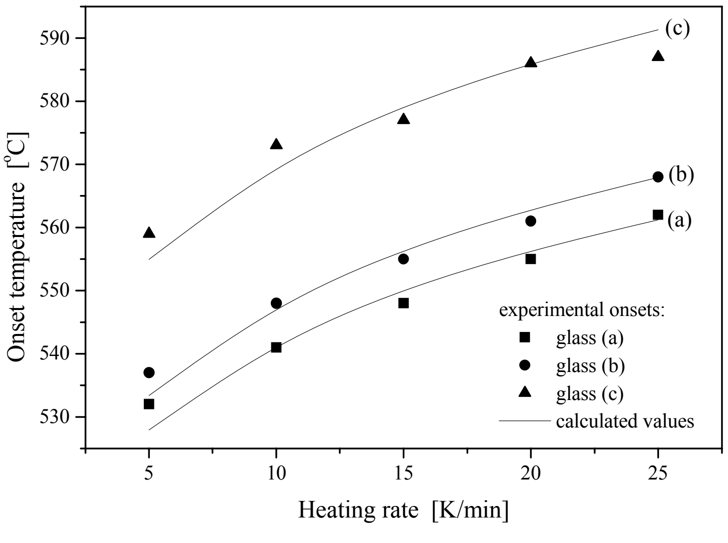

Figure 1: Experimental and calculated values of onset temperatures of glass crystallization for various heating rates.

Since the onset temperature is determined as a point of the steep increase of the DTA record due to crystallization, the end of the induction period of crystallization corresponds to the moment where the crystallization nuclei have already been formed and the intense growth of crystals starts. Using the new criterion, the stability of glasses is evaluated as the length of isothermal induction period for a given temperature. The length of induction period is calculated by Eq. (7). The range of temperatures for the calculation of the lengths of induction period of crystallization was chosen from the interval where the onset temperatures of crystallization have been observed. Hence, it can be expected that the values of calculated induction periods are quite realistic since no extrapolation outside the temperature region of the measurement has been carried out. The temperature dependence of the lengths of isothermal induction period for individual glasses is shown in Fig. 2. It can be seen that the stability of the glass samples against crystallization in the temperature region 750-850 K is in the order a<b<<c, i.e., the glasses containing TiO_2 are more stable against crystallization than the one without TiO_2. Eq. (5) enables to calculate the length of induction period for any time/temperature regime and, thus, to evaluate the order of thermal stabilities for that regime.

The program ARRHEN for the calculation of the parameters *A* and *B* in Eq. (9) is available on request.

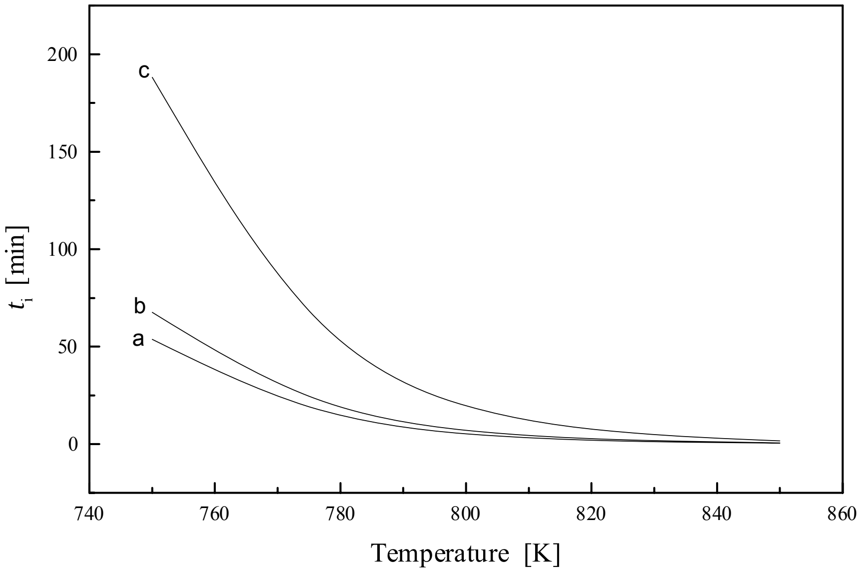

Figure 2: Induction periods of crystallization for individual glass samples calculated by Eq. (7).

Acknowledgement

The financial support from the Slovak Scientific Grant Agency, grant No. VEGA 1/0660/09, is gratefully acknowledged.

References

[1] ZANOTTO E.D., in *Nucleation and crystallization in glasses and liquids*. American Ceramic Society, Westerville, 1993, p. 65.

[2] VARSHNEYA A.K.: *Fundamentals of inorganic glasses*. Academic Press, New York 1994, p.13.

[3] DE OLIVEIRA A.P.N.; ALARCON O.E.; MANFREDINI T.; C.PELLACANI G.; SILIGARDI C.: Crystallisation kinetics of a $2.3Li_2O \bullet 1.1ZrO_2 \bullet 6.6SiO_2$ glass. In: *Physics and Chemistry of Glasses*. 2000. 41. p. 100-103.

[4] IORDANOVA R.; LEFTEROVA E.; UZUNOV I.; DIMITRIEV Y.; KLISSURSKI D.: Non-isothermal crystallization kinetics of V2O5-MoO3-Bi2O3 glasses. In: *Journal of Thermal Analysis and Calorimetry*. 2002. 70. p.393-404.

[5] PĂCURARIU C.; TITA D.; LAZĂU R.I.; KOVACS G.; LAZĂU I.: Kinetic study of the crystallization processes of some glass ceramics based on basalt, via thermal analysis. In: *Journal of Thermal Analysis and Calorimetry*. 2003. 72. p. 811-821.

[6] LEWIS M.H.: *Glasses and glass ceramics*. Chapman and Hall, London 1989, p. 226.

[7] DIETZEL A.: *Glasstruktur und Glaseigenschaften. In: Glastechnische Berichte*. 1968. 22. p. 41.

[8] UHLMAN D.R.: Glass formation. In: *Journal of Non-Crystalline Solids*. 1977. 25. p. 42-85.

[9] HRUBÝ A.: Evaluation of glass-forming tendency by means of DTA. In: *Czechoslovak Journal of Physics*. 1972. 22. p. 1187-1193.

[10] SAAD M; POULAIN M.: Glass forming ability criterion. In: *Materials Science Forum*. 1987. 19-20. p. 11-18.

[11] MAROTTA A.; BURI A.; BRANDA F.J.; PERNICE P.; ARONNE A.: Structure and devitrification behaviour of sodium, lithium and barium borophosphate glasses. In: *Journal of Non-Crystalline Solids*. 1987. 95-96. p. 593-599.

[12] ZHAO X.; SAKKA S.J.: Glass formation and crystallization in alkali-containing fluoride glasses. *Journal of Non-Crystalline Solids*. 1987. 95-96. p. 487-494.

[13] BRANDA F.; MAROTTA A.; BURI A.: Evaluation of glass stability from non-isothermal kinetic data. *Journal of Non-Crystalline Solids*. 1991. 134. p. 123-128.

[14] HU L.L.; JIANG Z.H.: A new criterion for crystallization of glass. In: *Journal of Chinese Ceramic Society*. 1990. 18. p. 315-321.

[15] SURINACH S.; BARO M.D.; CLAVAGUERA–MORA M.T; CLAVAGUERA N.: Glass formation and crystallization in the GeSe2-Sb2Te3 system. In: *Journal of Materials Science*. 1984. 19. p. 3005-3012.

[16] CHENG K.: A Criterion for Evaluating the Thermal Stability of Glasses. In: *Journal of Physical Chemistry B*. 1999. 103. p. 8272-8276.

[17] JÓNA E.; NEMČEKOVÁ K.; PLŠKO A.; ONDRUŠOVÁ D.; ŠIMON P.: Thermal properties of oxide glasses. Part I: Verification of various criteria of thermal stability vs. crystallization. *Journal of Thermal Analysis and Calorimetry*. 2004. 76. p. 85-90.

[18] ŠIMON P.: Considerations on the single-step kinetics approximation. In: *Journal of Thermal Analysis and Calorimetry.* 2005. 82. p. 651-657.

[19] ŠIMON P.: Induction periods – theory and applications. In: *Journal of Thermal Analysis and Calorimetry.* 2006. 84. p.263-270.

[20] ŠIMON P.; NEMČEKOVÁ K.; JÓNA E.; PLŠKO A.; ONDRUŠOVÁ D.: Thermal stability of glass evaluated by the induction period of crystallization. In: *Thermochimica Acta.* 2005. 428. p. 11-14.

[21] NELDER J.A.; MEAD R.A.: A simplex method for fiction minimization. In: *The Computer Journal*. 1965. 7. p. 308-313.

Thermodilatometry of the Brick Clay

Peter Šín, Rudolf Podoba, Igor Štubňa

Department of Physics, A. Hlinku 1, 949 74 Nitra, Slovak Republic, email: peter.sin@ukf.sk

Abstract: *Thermodilatometric analysis (TDA) and differential thermal analysis are performed on brick clay. Various processes (escaping physically bounded water, dehydroxylation of phyllosilicates and their collapse) affect the shape of the curves. Thermodilatometric analysis (TDA) was carried out using the heating/cooling rate 10 °C/min and soaking time at the maximum temperature 0, 10, 20, 40, 60 and 90 min. The maximum temperature was 1000 °C. A polynomial dependence between final relative contraction versus soaking time for the green samples during firing was found: The correlation coefficient R2 = 1 and the dependence is dl/lo = 5.10-8 t4 – 1.10-5 t3 + 1.10-3 t2 – 0,0422 t – 0,7181, where dl/lo is the relative contraction in % and t is the soaking time in minutes. Relative expansion of fired samples increases with increasing of the soaking time. Higher value of soaking time leads to the higher value of thermal contraction. That means that sample is shrinking also during constant temperature.*

Keywords: *TDA, DTA, dehydroxylation, relative expansion,*

1. Introduction

Since the kaolinitic clays have a basic importance for traditional ceramic industry, they are intensively studied. Different methods are used for investigation of the clay's properties, the most spread are thermal analyses, e.g. TDA, DTA, TGA and XRD analysis [1, 2, 3].

Thermodilatometric analysis (TDA) plays important role in ceramic research. It allows forecast of the changes in the sample made from input minerals. When ceramic powder containing kaolinitic clay and impurities such as quartz, iron and titanium oxides, carbonates and organic substances is heated, the dehydratation and sintering can be observed and studied through TDA. Because dilatometric patterns of most raw ceramic constituents are known, the dilatometric curve can be useful for estimation the composition of the green sample [4, 5, 6].

2. Experimental

The samples for the present investigation were prepared from the pit raw clay for a brick manufacture in Nitra region. The clay was ground, mixed with the water and cast into a gypsum mold. After drying, the samples had a prismatic form with dimensions 8×8×45 mm. A content of the physically bounded water was ~3.5 wt. %. Thermodilatometric analysis (TDA) was carried out with the push-rod horizontal dilatometer [7] using the heating/cooling rate 10 °C/min and soaking time at the maximum temperature 0, 10, 20, 40, 60 and 90 min. The maximum temperature was 1000 °C which is typical for brick manufacturing.

DTA was carried out with the bulk sample with dimensions 8×8×12 mm and a reference sample of the same dimensions was made from pressed alumina powder. A DTA/TG analyzer Derivatograph 1100 (Hungary) was used.

3. Results and discussion

Dilatomteric curves of all 6 green samples are identical in the heating interval. Here is seen a significant influence of the physically bounded water. This process is reflected by a less steep course of the TDA curve, i.e. by the expansion of the sample, and then by its small contraction (see Fig. 1) in the temperature range of 20 – 200 °C. A causal factor is the superposition of dual competing mechanisms [8]. One of them is thermal expansion of the all constituents, both minerals and water, of the green sample. The other factor is the contraction accompanying the escaping of physically bounded water. The escape of physically bounded water from the pores and crystal sides makes the distances between crystals lesser.

A DTA analysis was made in advance to obtain some auxiliary results for explaining the dilatometric curves. As follows from Fig. 2, the green sample contains a significant amount of the physically bounded water which releases from the room temperature up to 300 °C. Dehydroxylation of phyllosilicates occurs in the interval 450 – 700 °C and their collapse is evident through a small exothermic maximum at 950 °C.

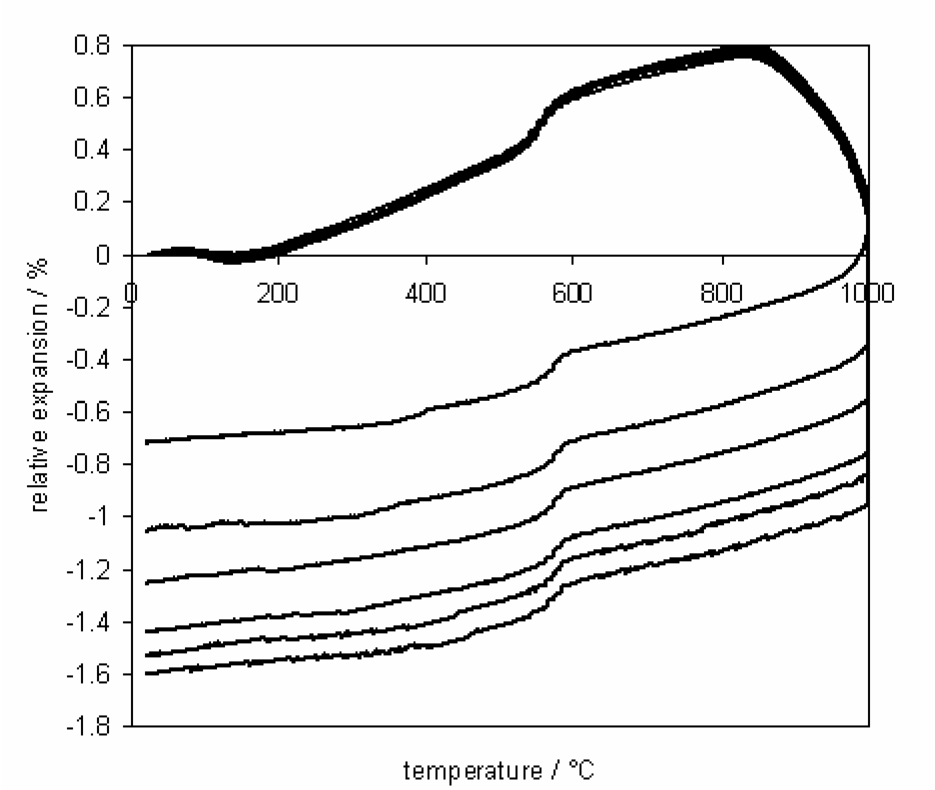

Figure 1: Dilatometric curves for soaking times (from the top) 0, 10, 20, 40, 60, 90 min

After escaping the physically bounded water, the length of the sample increases. A steep step above 500 °C is caused by $\alpha \rightarrow \beta$ transition of quartz which amount in the sample is significant. The next part of the dilatometric curve represents decreasing of the sample length above 800 °C. This is result of decomposition of calcite and rebuilding of the crystal lattice of clay minerals. And, also creating of the glassy phase takes place. Consequently, the course of the dilatometric curve is influenced with three high-temperature processes.

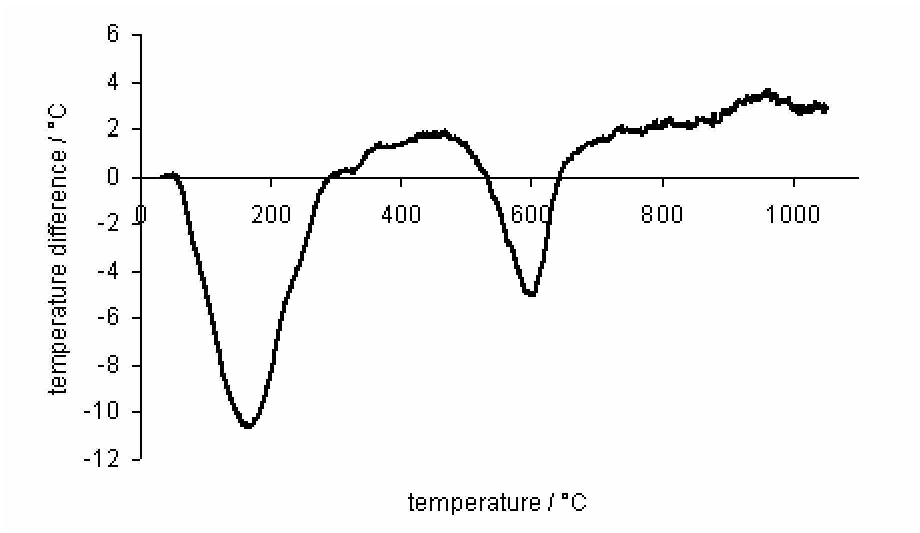

Figure 2: DTA curve of the green sample. Heating rate 10 °C/min

After reaching the highest temperature 1000 °C, the sample was exposed to soaking at this temperature. The longer the soaking time, the bigger the contraction of the sample. An intensive sintering is present and leads to the increase of the volume density, i.e. to the shrinkage of the sample [9].

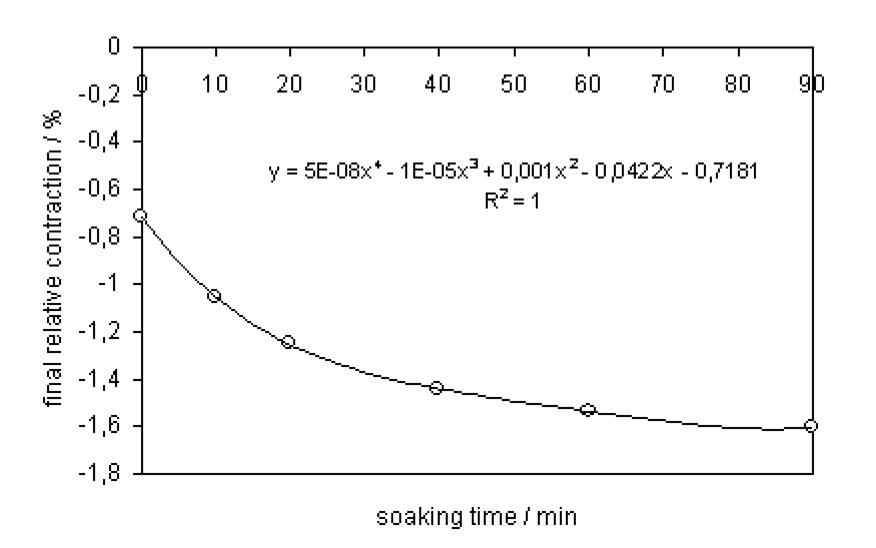

Figure 3: Relative contraction after firing

The final shrinkage measured at the room temperature is depicted in Fig. 3. As we can see, the dependence of the final relative shrinkage on the soaking time can be expressed by a polynomial function with high accuracy.

The samples which were used for obtaining of the Fig. 2 and Fig 3 were used again for TDA. The results are showed in Fig. 4. The lowest curve belongs to the soaking time 0 min. The other curves are mixed and no order is visible relating to the soaking time.

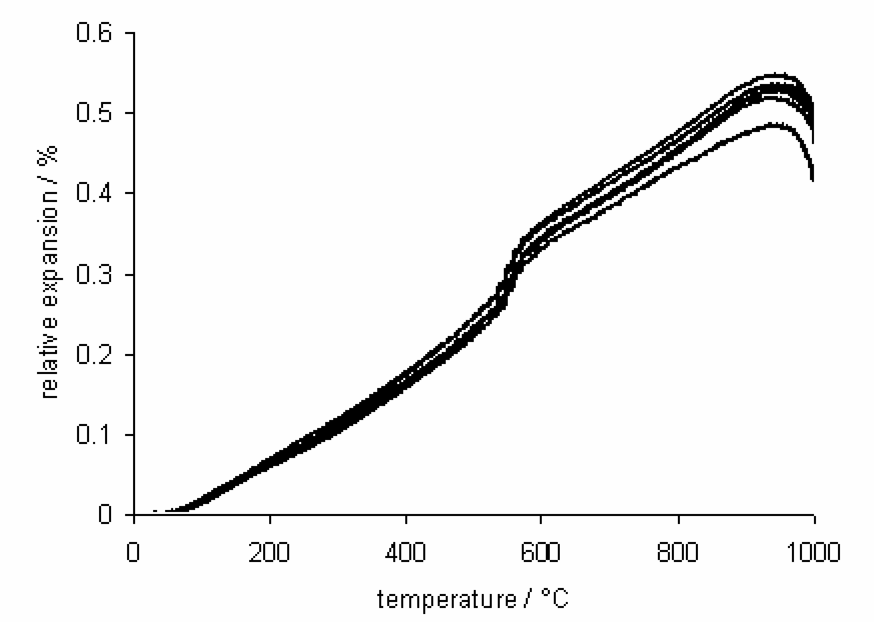

Figure 4: Dilatometric curves of the samples fired at soaking times 0 – 90 min at 1000 °C

4. Conclusion

Samples from kaolinitic clay were fired from the room temperature to 1000 °C with the heating rate 10 °C/min, soaked at 1000 °C for 0, 10, 20, 40, 60 minutes and cooled from 1000 °C to the room temperature with cooling rate 10 °C/min. Those samples were measured again from the room temperature up to 1000 °C.

Higher value of soaking time leads to the higher value of thermal contraction. That means that sample is shrinking also during constant temperature.

Final relative expansion measured at the room temperature after different soaking time vs. soaking time was also measured.

Relative expansion of fired samples increases with increasing of the soaking time.

Acknowledgement

This work was supported by the grant VEGA 1/0216/09 and VEGA 1/0302/09 and FCVV initiative of the Constantine the Philosopher University under grant I-06-399-01.

References

[1] MITRA, N.K. – ROY, D. – SAHA, S. – DAS, S. – MAITRA, S. Studies on the dehydration-rehydration behavior of some Indian kaolinitic clays under equilibrium conditions. In *Interceram*. 2007. 56. p. 246-248.

[2] DJANGANG, C.N. – ELIMBI, A. – MELO, U.C. Characteristics and ceramic properties of clays from Mayoum deposit (West Cameroon). In *Industrial Ceramics*. 2007. 27. p. 79-88.

[3] DESPOTOVIC, S. – BABIC, D. – FILIPOVIC-PETROVIC, L. Mineralogical changes in Zorka yellow clay as a function of firing temperature. In *Interceram*. 2006. 55. p. 277-280.

[4] CURTIS, W.F. Firing studies of Al_2O_3 porcelains by irreversible thermal dilatometry. 1978. MS Thesis. School of Ceramic Engineering of Alfred University. Alfred, NY.

[5] ŠAŠEK, L. et al. *Laboratory methods for silicate materials*. Ed. SNTL-Alfa, Praha – Bratislava, 1981.

[6] ŠŮCHA, L.; VRBSKÝ, J. *Analytická příručka*, I. Ed. SNTL, Praha, 1979, p. 271-325.

[7] ŠTUBŇA, I. – VOZÁR, L. High-temperature alumina push-rod dilatometer. In: *Proc. THERMOPHYSICS 2000*. 2000. p. 77-81. UKF Nitra, Nitra, Slovakia.

[8] ŠTUBŇA, I., – TRNÍK, A., – VOZÁR, L. Thermomechanical and thermodilatometric analysis of green alumina porcelain. In *Ceramics International*. 2009. 35. p. 1181-1185.

[9] MENČÍK, J. *Pevnost a lom skla a keramiky*. Ed. SNTL, Praha, 1990.

Properties of PCM-modified building materials

Stanislav Šťastník, Jiří Vala, Jaroslav Nováček, Daniel Kopkáně

Brno University of Technology, Faculty of Civil Engineering, Veveri 95, CZ-60200 Brno

***Abstract**: The analysis of Phase-Change-Materials (PCM) in the ninth decade of previous century at the Pensylvania State University (U.S.A.) initiated the massive technological usage of materials, whose physical properties, as volume, density, viscosity, electrical conductivity, etc., can be modified significantly during their phase changes. In the civil engineering such properties of PCM are applied to improve the thermal stability of buildings. The experimental works at FCE BUT pay special attention to materials for inner plaster layers.*

***Keywords**: Phase Change Material (PCM), gypsum plaster, thermal properties, calorimetric measurement*

1. Introduction

Some materials are able to change their phase at the temperature between 23 and 28 °C and consequently to obtain rather large latent heat. This property can be used to stabilize the inner temperature of building structures to some proposed value, which brings new user quality in comparison with the standard passive accumulation. During their transformation from the solid to the liquid phase, such materials, known as PCM (Phase Change Materials), get approximately 200-times more heat than the same amount of concrete thanks to the temperature increase of 1 K; in the solidification process the same heat is released.

The most widely used constructions, as massive masonry, concrete walls or ceiling plates can accumulate the thermal energy thanks to the thermal accumulation capacity of the corresponding material, depending on the mass of particular constructions and their parts.

However, the designers of advanced low-energy buildings with light-weighted claddings cannot avoid the application of additional thermal insulations. The usage of PCM offers a way how to reduce the volume of such artificial constructions significantly

2. Thermal accumulation

The following partial forms of thermal accumulation occur in PCM by [1]:

- the accumulation of sensible heat,
- the heat accumulation forced by the phase change,
- the thermo-chemical accumulation.

These forms are distinguished by the amount of accumulated heat, related to a mass or volume material unit, by the melting temperature and by the evolutional degree of accumulation technology.

2.1 The accumulation of sensible heat

In this case the accumulation of thermal energy is caused only by the temperature change of the accumulation medium. The amount of accumulated energy depends on the thermal capacity and amount of medium and on the temperature change. Various materials are applied, both solid and liquid ones. The physical process can be described mathematically as

$$Q_1 = \int_{\theta_1}^{\theta_2} m.c.d\theta = m.c.(\theta_2 - \theta_1)$$

where: Q_1 is the amount of accumulated heat,

m is the mass of the thermal-accumulation medium,
θ_1 is the initial temperature,
θ_2 is the final temperature.
c is the mean value of thermal capacity of such medium in the temperature range $\langle \theta_1, \theta_2 \rangle$,

The medium with the highest thermal capacity in nature is water. In technical applications, water must be located in the closed space (vessel). Water is also frequently used as a heat carrying medium. Stone, concrete constructions or masonry is used for accumulation reservoirs. Nevertheless, this method of accumulation brings is the least effective one.

2.2 The heat accumulation of heat forced by the phase change

The accumulation of this type exploits the reversible phase change of accumulation medium, most often between solid and liquid phases. The heat needed for the phase change is dominant, but the sensible heat must be involved into the consideration, too. Thus we have

$$Q_2 = \int_{\theta_1}^{\theta_m} m.c_p.d\theta + m.l_m.\Delta h_m + \int_{\theta_m}^{\theta_2} m.c_u.d\theta = m.\left[l_m.\Delta h_m + c_p.(\theta_m - \theta_1) + c_u.(\theta_2 - \theta_m)\right]$$

where: Q_2 is the amount of accumulated heat,
m is the mass of the thermal-accumulation medium,
θ_1 is the initial temperature,
θ_2 is the final temperature.
θ_m is the meeting temperature,
c_p is the mean value of thermal capacity of such medium in the temperature range $\langle \theta_1, \theta_m \rangle$,
c_u is the mean value of thermal capacity of such medium in the temperature range $\langle \theta_m, \theta_2 \rangle$,
l_m is the mass ratio of the phase changing medium,
Δh_m is the phase change heat of melting related to a mass unit.

The high thermal capacity of phase change accumulators offers a chance to reduce both the volume and the mass of accumulators.

2.3 Thermochemical accumulation

The thermochemical systems exploit the energy absorbed or released in consequence of the disintegration or the synthesis of molecular connections during the reversible chemical reactions. The accumulated heat can be evaluated from the formula

$$Q_3 = a_r.m.\Delta h_r,$$

where: Q_3 is the amount of accumulated heat,
m is the mass of the thermal-accumulation medium,
a_r is the mass ratio of the medium taking part in the thermochemical reaction,
Δh_r is the reaction heat related to a mass unit.

The thermal accumulators guarantee the long-time accumulation the higher efficiency without any insulation requirements. The applied medium is not allowed to react with other materials used in the construction or be dangerous for the environment. Thus, the design of such technology seems to be the most complicated.

3. The application of PCM

The materials applied as PCM are:

- inorganic materials,
- organic materials, paraffin and non-paraffin ones.

3.1 Inorganic materials

The phase change of such materials is between 0°C and 150°C – see Fig. 1. All salt hydrates exhibit the vapor tension caused by the involved water crystals, thus they must be closed in hermetically tight vessels.

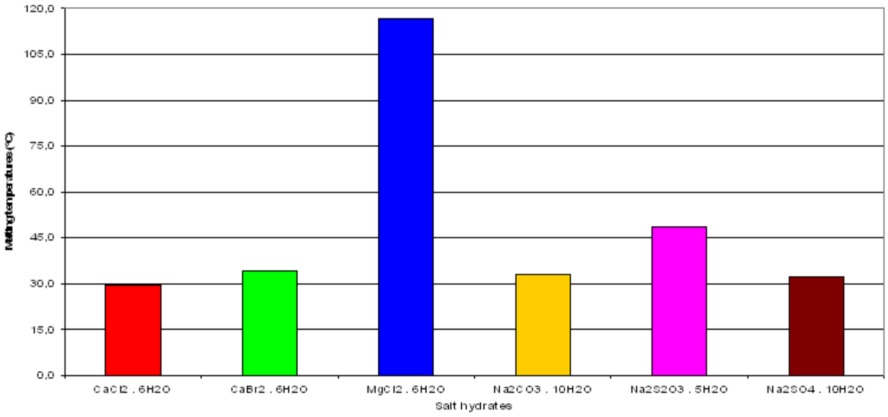

Figure 1: The meeting temperature for some selected salt hydrates by [2]

3.2 Organic materials

Organic PCM have usually lower density and are combustible. Namely the paraffines are products from mineral oils, belonging to a group of saturated hydrocarbons. Their good properties for application as PCM are: practical availability, low corrosion vulnerability, no toxicity, high melting heat, chemical stability, low density, low volume changes during the melting process.

4. Practical experiments

The aim of the study of PSC at the Brno University of Technology was the analysis of properties of the gypsum plaster with the additive Micronal PCM, produced by BASF – for all details see [3]. There is also mentioned, that the latent heat is approximately 105 kJ/kg PCM.

PCM substance is manufactured by using of nanotechnology. The final products are capsules in size from 5 microns to 20 microns created by health unobjectionable functional polymer with wax based natural polymer filling mass. Melting point of wax filling mass is 21, 23 or 26°C. These properties enable to keeping constant temperature value of surrounding building material around melting point of wax filter. Composite building material has due to admixture

Micronal PCM unique thermal properties, which are unattainable without PCM admixture. Building material containing PCM admixture becomes heat accumulator. Figure 2 shows temperature continuances during calorimetrical experiment with specimens of gypsum plaster without PCM admixture (red line) and gypsum plaster with addition of PCM admixture in amount of 300g/kg in relation to dry blend weight (green line). Hardened specimens were heated in closed calorimeter by electric wire spiral. Electrical resistance heating was source of Joule heat in the first period of experiment. The second period of experiment was unaffected cooling. Internal temperature of specimens has been logged during experiment as well as ambient temperature.

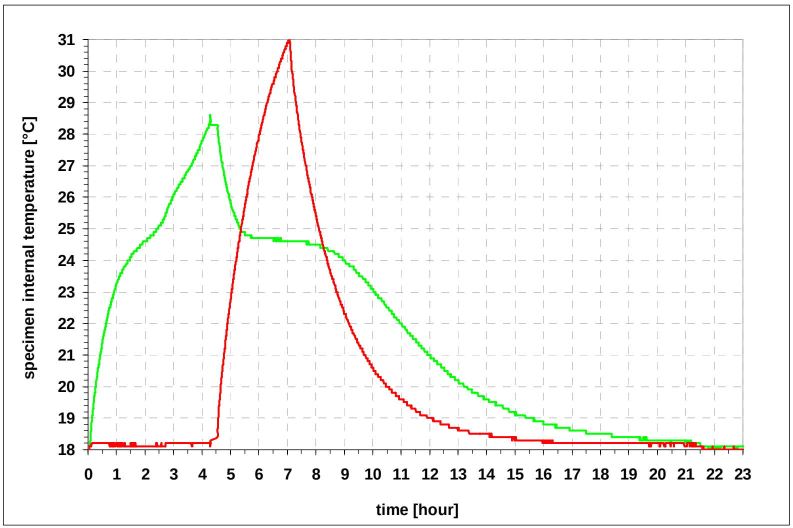

Figure 2: Temperature run in specimens of calcium-sulfate plasters with addition of PCM Micronal and with out PCM admixture. Green line – Specimen with PCM; Red line – Specimen of pure gypsum plaster

Curves of intensity of phase change latent heat were inferred by use of reversal numerical modeling. Figure 3 shows mentioned intensity curves describing phase change of PCM Micronal admixture. That curves are in form of exponential function related to normal distribution, which offer the lowest values of residual summation.

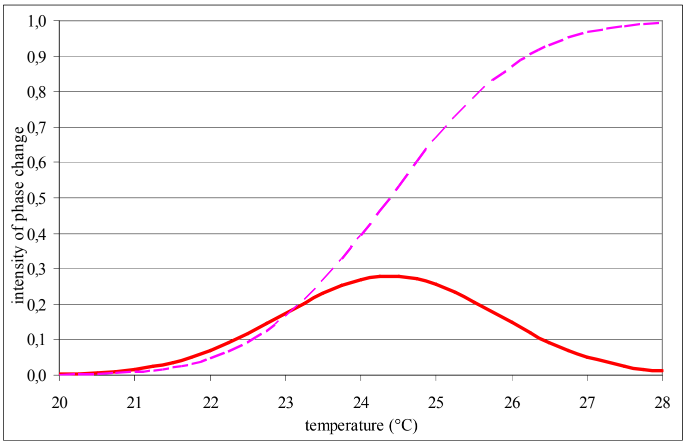

Figure 3: Progress of distributive function of latent heat intensity and summing curve in dependence on temperature of gypsum plaster specimen with addition of PCM Micronal. Red line – distributive curve; Pink line – progress of summation curve

5. Conclusions

Composite building materials with addition of PCM material shows positive properties in meaning of enhanced heat accumulation around melting point temperature of used PCM material. Temperature delays during heating period as well as cooling period were proved by executed calorimetric experiment with gypsum plaster with PCM. Temperature amplitude during heating of plaster specimen with PCM material was markedly lower than temperature amplitude during heating pure plaster blend. Details of experimental temperature progress shows figure 2.

Manifestation of unaccompanied PCM Micronal was calculated by reversal numerical modeling of non-stationary heating and subsequent cooling of calorimetric system with hardened specimens. Figure 3 describes distribution curve of intensity of phase change. Summating curve determines rate of PCM material capacity usage versus temperature.

Mentioned intensity dependences of phase change become basement for non-stationary modeling of heat transfer in buildings. The goal of the modeling is determination internal microclimatic properties in buildings, especially determination of the optimal layer thickness of material containing PCM for the defined geometrical dimensions of room, wall composition and overall form of thermal system.

Acknowledgement

This paper was created with financial support of internal project č. 904 FAST VUT Brno and project CEZ MŠMT č. 0021630511.

References

[1] LANE, G., Solar Heat Storage: Latent Heat Materials, Volume I: Background and Scientific Principles. CRP Press, Inc. Boca Raton, Florida 1983.

[2] OSTRÝ, M., Effect of the Thermal Storage properties of the phase Change Materials on the Indoor Environment, Ph.D. Thesis, Brno 2005, ISBN-80-214-2741-8

[3] Micronal® PCM Intelligent Temperature Management for Buildingsreference, http://www.micronal.de/, 2010

Determination of red brick heat conductivity coefficient depending on moisture

Zbigniew Suchorab[1]**, Henryk Sobczuk**[2]**, Mariusz Skwarczyński**[3]

[1]Faculty of Environmental Engineering, Lublin University of Technology, Nadbystrzycka 40B,
20-618 Lublin, Poland, email: Z.Suchorab@wis.pol.lublin.pl

[2]Faculty of Environmental Engineering, Lublin University of Technology, Nadbystrzycka 40B,
20-618 Lublin, Poland, email: H.Sobczuk@wis.pol.lublin.pl

[3]Faculty of Environmental Engineering, Lublin University of Technology, Nadbystrzycka 40B,
20-618 Lublin, Poland, email: M.Skwarczynski@wis.pol.lublin.pl

Abstract: *Buildings which suffer the external barriers moisture problem are prone to extended heat loses during winter season. Water, which is a good heat carrier, when occurs inside the porous structure of the building material influences its heat resistance parameters and thus runs to improper temperature distribution through the barrier, corrosion, material decay and degradation due to multiple processes of freezing and thawing, but also leads to development of allergic microorganisms or mould. The article presents the experiment determining moisture influence on heat conductivity coefficient of red brick which is an old but still popular building material. To determine the heat parameters a system of two climatic chambers was used which simulated artificial climatic conditions on both sides. Red, ceramic brick sample was provided with necessary sensors – temperature sensors (Dallas type) and heat flux sensors which were served by the Peltier modules used in electronics as electronic devices coolers. To determine heat conductivity parameter depending on moisture a climatic chambers system was used which generated cold and hot temperatures on both sides. Between them the red brick sample was placed which was temporally moistened with water and the measurement was repeated. After several steps the results were recalculated and a linear dependence was found between water content and heat conductivity parameter λ which may be useful in estimation of heat parameters of building objects but also in heat and moisture transport modelling across the building barriers.*

Keywords: *heat conductivity coefficient, moisture, red brick*

1. Introduction

Many buildings built of red brick suffer from moisture presence. Many of them are the old buildings or even historical ones, where moisture problems are caused by improper building process (lack of horizontal waterproof insulation, improper materials distribution, destroyed sanitary installations or rainwater disposal). The problem is more visible and important during winter season when moist building barriers do not keep needed insulation parameters which runs to improper temperature distribution through the barrier, corrosion, material decay and degradation due to multiple processes of water freezing and thawing. Apart of these problems the moisture phenomenon also leads to the development of allergic microorganisms or mould.

The most important parameter describing heat properties of building material is heat conductivity coefficient λ [W/mK] [1] which is normative for any building material. Value of this parameter depends on many factors, among them porosity, density, temperature and, which is the most important from the point of view of this article – moisture.

It is generally known, that heat conductivity grows with material apparent density, that's why the lowest λ values are typical for light insulation materials like polyurethane foam (below 0.035W/mK), mineral wool (below 0.043W/mK) or polystyrene (0.040 – 0.045W/mK). Some modern building materials like aerated concrete have also very attractive insulation parameters, lighter version of this material (about 400 kg/m^3) reach the value about 0.1 W/mK [2, 3]. Red ceramic brick is a very old, but still popular material with λ parameter value about 1 W/mK which means that it is not a good material from the point of view of thermal insulation and in order to be applied in building the barrier must be equipped with necessary insulation [4].

Building barriers suffer from moisture presence which is mainly caused by the fact that water filling the pores of building materials has heat conductivity value higher 20 times than the air [5]. Determination of moisture influence on building material heat parameters is a complicated task requiring material examinations. It is caused by the fact that heat transfer process in wet porous material involves various physical processes [6,7,8,9].

All above mentioned information and problems of moisture influence on heat parameters of rooms and buildings built of red brick indicate the necessity to determine them in laboratory conditions. In this paper we present the experimental of determination of heat conductivity coefficient in relation to water content.

2. Experimental Procedures

For the examinations the following equipment and materials were used: climatic chambers system for simulation of environmental conditions at the opposite sides of the sample (Fig. 1, Fig. 2) [10], digital temperature sensors, multimeter for temperature readouts from the temperature sensors, Peltier plates – used as heat flux probes, multimeter for voltage readouts from the Peltier plates, red brick sample (from Kraśnik manufacture, Poland) with the apparent density 1500 kg/m3 (Fig 2, Fig. 3, Fig. 4).

The sample of red ceramic brick, which was the full brick (Fig 2, Fig. 3) was prepared to install the Peltier modules and temperature sensors (necessary holes were drilled). Sensors (T) were put on two sides of the sample to determine the temperature between two sides of the material and three Peltier modules (P1, P2 and P3) where put in the middle of the sample (Fig. 3, Fig. 4). Then it was dried in the temperature of 105°C to dry (without sensors). Mass of dry sample was 3018.6 g. After cooling in dissicator the necessary sensors were installed and the sample was put between the climatic chambers and insulated from the external conditions with polystyrene and polyurethane foam. Boundary conditions were set as 0°C on cold side (chamber C1) and 25°C on hot side (chamber C2) and the measuring system was started. When the thermal conditions were balanced, heat fluxes values were determined (Table 1). After this part of the experiment the whole system was dismounted and the red brick sample was put into the water for saturation. Saturated sample mass was equal 3554.5 g which was 23% volumetric water content. Then the sensors were mounted and the climatic chambers systems was started to determine heat flux values in wet sample. After that the system was dismounted and the brick was dried to smaller moisture and the same step was repeated in some sequences.

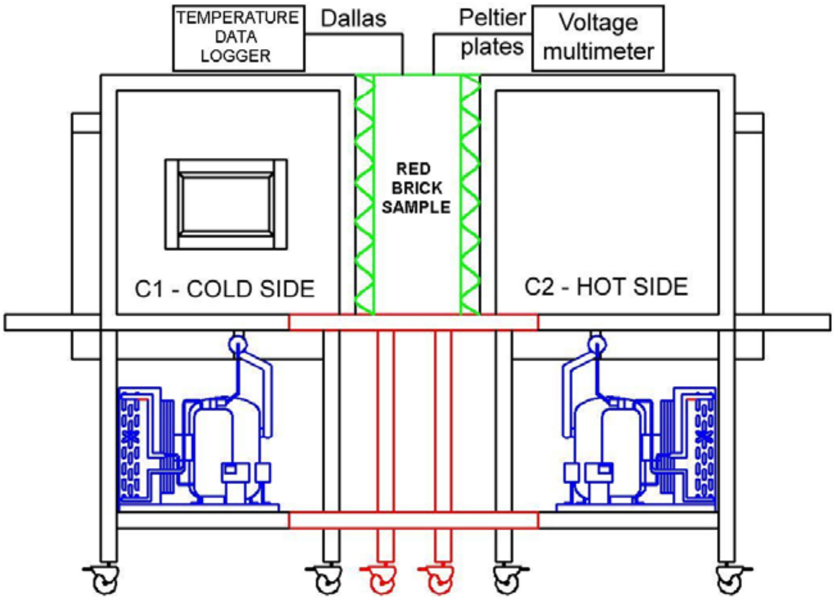

Figure 1: Climatic chambers system applied for the experiment together with measuring devices [10]

Figure 2: Red brick sample prepared for the experiment and during the experiment

The aim of the experiment was determination of the heat conductivity λ parameter in red brick depending on moisture content which is important from the point of view of the heat and water properties of exploited buildings.

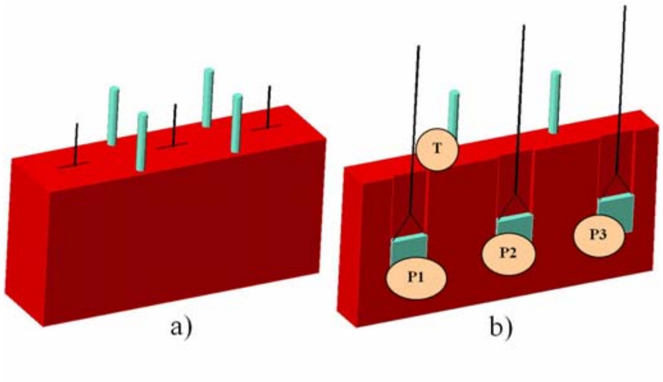

Figure 3: Red ceramic brick samples equipped with sensors. a) general view, b) cross-section. T – temperature sensor (Dallas), P1, P2, P3 – Peltier modules

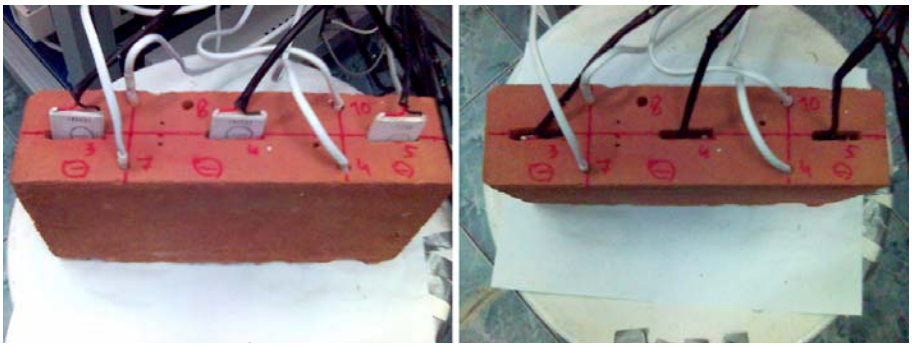

Figure 4: Red ceramic brick samples prepared for experiment

3. Results

With the described experiment heat conductivity coefficient was determined for red brick sample. Calculations were made using Fourier formula [1]:

$$q = -\lambda \, \mathrm{grad} T \tag{1}$$

q = heat flux determined using Peltier sensor [W/m²]; λ = heat conductivity coefficient (determined parameter) [W/mK]; gradT = temperature gradient between measuring points [K/m].

The experiment enabled the determination of heat conductivity value (λ) in relation to water content. First readouts presented in table 1 and diagram on fig. 5 are for dry samples read on three Peltier modules. Next readouts are presented for red brick saturated with different water contents.

Table 1: Heat conductivity in the relation of water content in the examined red trick sample

Water content	**λ 1**	**λ 2**	**λ 3**	$\bar{\lambda}$
[cm³/cm³]	[W/mK]			
0,00	0,996	0,805	0,846	0,882
0,00	0,985	0,808	0,854	0,883
0,00	0,941	0,793	0,829	0,854
0,00	0,941	0,789	0,832	0,854
0,00	0,930	0,780	0,830	0,846
0,23	1,394	1,476	1,329	1,400
0,21	1,343	1,414	1,217	1,324
0,18	1,320	1,337	1,212	1,290
0,16	1,269	1,287	1,170	1,242
0,13	1,278	1,294	1,178	1,250
Corelation coeff (r)	0,988	0,994	0,989	0,992

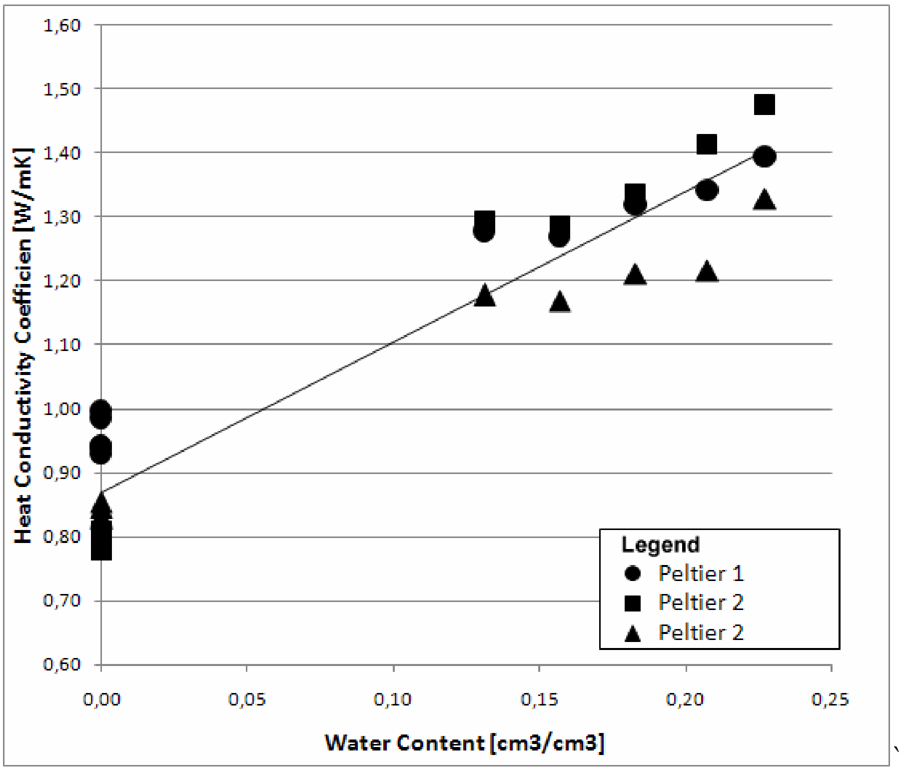

Figure 5. Heat conductivity in the relation of water content in the examined red brick sample

4. Discussion of Results

With the obtained results a characteristic of red brick heat conductivity depending on water content was described. All important data are presented in Table 2.

The characteristics assume the linear dependence between heat conductivity and moisture which is often used in models [11,12,13] of water and heat flow across building barriers according to the following formula:

$$\lambda(\theta) = \lambda_{dry} + \lambda_{mst} \cdot \theta \quad (2)$$

λ_{dry} = heat conductivity of dry material [W/mK]; λ_{mst} = increase of heat conductivity value due to moisture increase [W/mK]; θ = volumetric water content of aerated concrete [cm^3/cm^3].

Table 2: properties of examined red brick sample

Examined material	λ_{dry}	λ_{mst}
	[W/mK]	[W/mK]·[cm^3/cm^3]
Ceramic red brick 1600	0,869	2,356

Determined heat conductivity coefficient of examined red brick sample in dry state (λ_{dry}) was below 1 W/mK (average value for all heat flux sensors 0.88). The results obtained are convergent to the Polish normative [4], where red brick wall are characterized by λ coefficient equal 0.77 W/mK.

The increase of λ coefficient per $\%_{vol}$ (λ_{mst}) due to experimental measurements 2.356 W/mK which underlines the influence of water content on heat properties of building barriers. According to data contained in Delphin [3] heat moisture transport simulation program heat characteristics of red brick (apparent density 1720 kg/m^3) are λ_{dry} = 0,85W/mK and λ_{mst} = 1,5W/mK. Heat conductivity coefficient determined in the experiment in dry state is close to the data contained in Delfin program documentation. The increase of λ per $\%_{vol}$ differs which may be caused by different apparent density, differences of porous or chemical structure and finally production technology.

5. Conclusions

Applied measuring setup was suitable for determination of heat properties changes in red brick due to moisture changes. Peltier modules which are used in electronics can be successfully applied as heat flux meters after suitable calibration procedures.

The experiment proved the increase in heat coefficient value to moisture increase in porous building materials.

It should be underlined that red brick is a material which is often affected by water influence especially in old buildings without suitable horizontal water insulation. Houses affected by the phenomenon of moisture suffer from negative water influences and one of them is the decrease of heat insulation parameters.

Acknowledgement

This work is supported by the Ministry of Science and Higher Education of Poland, Nr: 4952/B/T02/2008/34.

References

[1] LIENHARD IV J.H.; LIENHARD V J.H. A heat transfer textbook; Third Edition, Phlogiston Press, Cambridge, Massachusetts, 2003, ISBN: 978-0971383524

[2] KLEMM P. Budownictwo ogólne (In Polish). Tom 2 (Fizyka budowli), Arkady, Warsaw, 2005, ISBN: 83-213-4408-9

[3] GRUNEWALD J.; PLAGGE R.; HAUPL P. A Two-leveled Hydrothermal Material Database for the Numerical Simulation Program DELPHIN4, Building Physics 2002 – 6th Nordic Symposium, 39-46, 2002, ISBN: 82-91412-02-2

[4] PN-EN ISO 6946:2008 Building Components And Elements – Heat Resistance And Overall Heat-Transfer Coefficient (Polish Normative, In Polish)

[5] DORF R.C. CRC Handbook of Engineering Tables, 2004, CRC Press LLC

[6] DE VRIES, D.A. Simultaneous transfer of heat and moisture in porous media. Trans. Amer. Geophys. Union 39(5), pp. 909-916, 1958

[7] LUIKOV AV. Heat mass transfer in capillary-porous bodies. Oxford: Pergamon Press, 1966.

[8] NASSAR I. N.; HORTON R. Heat, water and solute transfer in unsaturated porous media: I – theory development and transport coefficient evaluation, Transport in Porous Media 27, pp.17-38, 1997, ISSN: 0169-3913

[9] CHEN Z.Q.; SHI M.H. Study of heat and moisture migration properties in porous building materials, Applied Thermal Engineering 25, pp.61-71, 2005, ISSN: 1359-4311

[10] SOBCZUK H.; SUCHORAB Z.; KOWAL A.; WOROSZYŃSKA A. Scientific Project KBN 4 T09 052 22 (PL) report „Opracowanie modelu i zestawu pomiarowego do oceny charakterystyk cieplnych i wodnych materiałów budowlanych narażonych na oddziaływanie czynników klimatycznych w aspekcie ochrony środowiska (In Polish)", 2005

[11] GAWIN D.; KOSNY J.; DESJARLAIS A. Effect of Moisture on Thermal Performance and Energy Efficiency of Buildings with Lightweight Concrete Walls, Proc. Summer Study on Energy Efficiency in Buildings Efficiency & Sustainability, Pacific Grove, California (USA), 2000, pp. 149-160

[12] GRUNEWALD J. Documentation of the Numerical Simulation Program DIM3.1, Volume 2, User's Guide, 2000.

[13] WILLIAMS R., 2002. Overview of the project to determine the thermal resistance of masonry walls in dry and moist states and a conversion procedure to determine the appropriate design value, Building Physics 2002, 6-th Nordic Symposium, pp. 539-546, 2002, ISBN: 82-91412-02-2

High temperature stability of board composites

Jan Toman[1], Tomas Korecky[1], M. Frank[2], Robert Cerny[1]

[1]Czech Technical University in Prague, Faculty of Civil Engineering, Department of Materials Engineering and Chemistry, Thákurova 7, CZ-166 29 Prague 6, CZECH REPUBLIC

[2] VÚSTAH Brno, Hněvkovského 11, Brno, CZECH REPUBLIC

Abstract*: Boards made of composite materials are these days used as the lining of parts of building structure to improve the object's end-use properties. For the improvement of fire protection properties the temperature stability of both thermal technical and mechanical properties of used composite material, is important. This paper describes the elasticity coefficient and heat conductivity as executed on several materials. Measured samples had been heated on specific temperature and after cooling down were gauged. After comparing the results it is possible to verify the temperature stability of mechanical and thermal technical properties of particular materials.*

Keywords*: mechanical properties, thermal properties, composites, high temperature*

1. Introduction

Nowadays board materials are very often used as lining of building structures.

This solution brings two fundamental effects:

1. Structure protection against harmful external effects which could be, for example mechanical, chemical and physical. As standard procedure in the building industry veneer board is often used for increasing fire protection.
2. Aesthetic arrangement of the building is interior surfaces.

Composite materials are often used to improve mechanical properties. In order to consider the quality of fire protection it was decided to observe their mechanical and thermal material parameters **[1].**

2. Materials samples description

Observed board samples were delivered from VÚSTAH Brno. The samples were from two types of material:

- PROMATECT – white material, board thickness 3 cm
- FIREBOARD – grey material, board thickness 2.5 cm

These materials are made for commercial purposes and their composition has been kept secret by the firm. For this reason we don´t know the exact composition of the materials.

For measuring we prepared samples from the delivered boards. To find out thermal technical properties of the materials boards were cut into squares of size 7 x 7 cm from both materials. To determine the mechanical qualities 16 beams were cur into size 3 x 18 (or 15) cm x board thickness.

3. Methodology of measurement

Thermal properties of heat stability were measured on boards from given materials by apparatus **IZOMET 2114**, which determined the heat conductivity and volumetric heat capacity (product of specific heat capacity and specific density). **[2]**

The measurement of heat stability of mechanical qualities was executed by a non-destructive method on prepared samples by ultrasound apparatus **DIO 526**, with which it is possible to measure **speed of wave spreading** or **resonant method base frequency** and then is possible to calculate **dynamic modulus of elasticity** from dimensions **[3]**.

The parameters were observed in different temperature shocks because it is possible to presume that they depend on temperature **[1], [4]**.

Individual limits of temperature stress were set in reference (consideration) to theoretical temperatures of stability of concrete, i.e. decomposition of calciumhydroxid circa 470 °C and decomposition of hydrates circa 680 °C **[5]**. Measurement was realized on samples stressed with the following temperatures:

1. normal temperature 25 °C
2. drying 110 °C
3. medium heating 250 °C
4. higher heating - below the first critical temperature 450 °C
5. higher heating - between the first and the second critical tem. 650 °C
6. high heating – over the second critical temperature 750 °C
7. maximal temperature stress 1000 °C

4. Description of the process of the measurement

We created a bunch of samples in order to be able to examine the influence on gradual temperature increases. It means the comparison of repeated temperature stress and direct heating on high temperature (thermal shock). Each sample was stressed in a different way, which is documented in the enclosed table, where there colour-indicated temperature stress at particular samples.

The difference was also in the default conditions created before temperature stress. Samples 1 to 8 had been dried before at 110 °C for 7 days to ensure a constant weight. Samples 9 to 16 hadn´t been dried and thus maintained a stable level of moisture; these samples were stressed by temperature.

For each temperature stress the defined bunch of samples was always placed to an electrical kiln. The kiln was heated by constant rising to a particular temperature. Then the rising of temperature was stopped and the kiln was kept at the set temperature for 3 hours. After that heating was switch off and the tested samples cooled down to normal temperature.

Thermal qualities were measured in normal temperature around 25 °C.

5. Results of measurement

All results were analysed and represented in EXCEL editor.

Table 1: White material PROMATECT

Description of the sample		weight	relative loss in weight	lambda	c.ϱ x10E-6	a x10E6	E
		[g]	[%]	[W.m^{-1}.K]	[J.K^{-1}.m^{-3}]	[m^{2}.s^{-1}]	[MPa]
1	non-dried	89.1	100				
	dried at 110°C	85.70	96.18	0.111	0.557	0.199	944
	dried 3 hours at 250°C	86.20	96.75	0.108	0.583	0.185	1059
	dried 3 hours at 450°C	83.20	93.38	0.101	0.572	0.177	932
	dried 3 hours at 550°C	81.80	91.81	0.098	0.489	0.200	802
	dried 3 hours at 750°C	69.50	78.00	0.102	0.476	0.214	530
	dried 3 hours at 1000°C	63.20	70.93	0.079	0.380	0.207	362
2	non-dried	88.00	100.00				
	dried at 110°C	84.60	96.14	0.099	0.591	0.168	917
	dried 3 hours at 250°C	85.20	96.82	0.102	0.538	0.189	906
3	non-dried	87.00	100.00				
	dried at 110°C	84.20	96.78	0.102	0.599	0.170	855
	dried 3 hours at 450°C	81.50	93.68	0.099	0.570	0.173	809
4	non-dried	90.20	100.00				
	dried at 110°C	87.20	96.67	0.110	0.558	0.197	816
	dried 3 hours at 550°C	83.30	92.35	0.105	0.503	0.208	662
5	non-dried	89.00	100.00				
	dried at 110°C	85.90	96.52	0.102	0.586	0.175	805
	dried 3 hours at 750°C	75.70	85.06	0.098	0.532	0.185	597
6	non-dried	89.00	100.00				
	dried at 110°C	86.00	96.63	0.106	0.547	0.194	856
	dried 3 hours at 1000°C	63.60	71.46	0.080	0.392	0.205	455
7	non-dried	86.90	100.00				
	dry at 110°C	83.60	96.20	0.104	0.619	0.168	821
	dried 3 hours at 250°C	84.30	97.01	0.102	0.604	0.169	967
	dried 3 hours at 550°C	80.20	92.29	0.107	0.560	0.191	806
8	non-dried	89.60	100.00				
	dry at 110°C	86.60	96.65	0.101	0.607	0.167	899
	dried 3 hours at 450°C	84.10	93.86	0.101	0.561	0.181	975
	dried 3 hours at 750°C	75.80	84.60	0.083	0.378	0.219	580
	dried 3 hours at 1000°C	63.70	71.09	0.074	0.339	0.219	491

Different shading in the table indicates the intensity of stressing the samples. The more shading, the higher the temperature stress.

Measurement of the second type of material FIREBOARD – gray was made in the same way.

6. Processing of making results and discussion

All changes in measured values – i.e. relative decrement of weight, heat conductivity and volumetric heat capacity, measured on particular samples were plotted into figures depended on burn temperature. On these samples are good visible permanent changes in each value caused by temperature stress on both materials. To illustrate a graphic analysis of the dependence of heat conductivity λ on burn temperature for both examined materials is provided below.

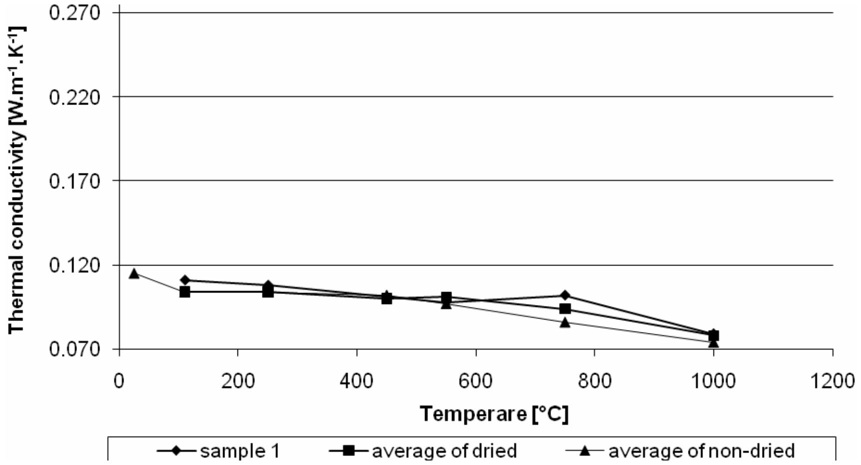

Figure 1: Lambda dependence on temperature - PROMATECT

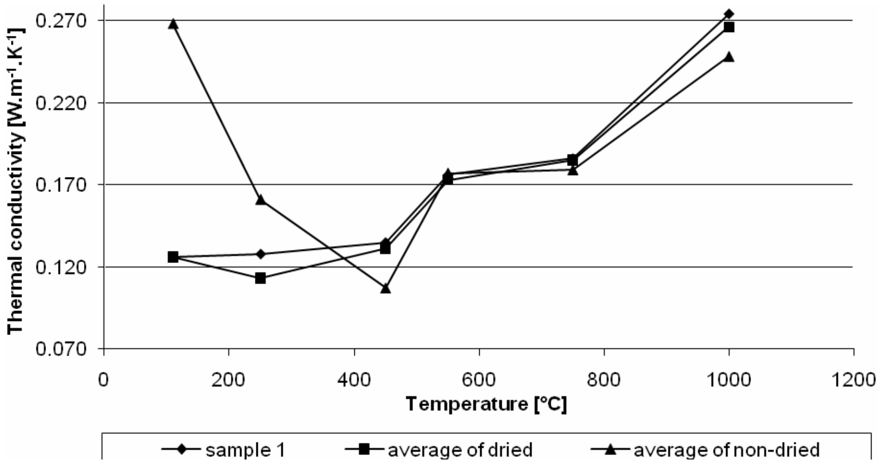

Figure 2: Lambda dependence on temperature - FIREBOARD

On the other graphs relative loss of weight during burn, volumetric specific heat capacity and thermal diffusivity are shown.

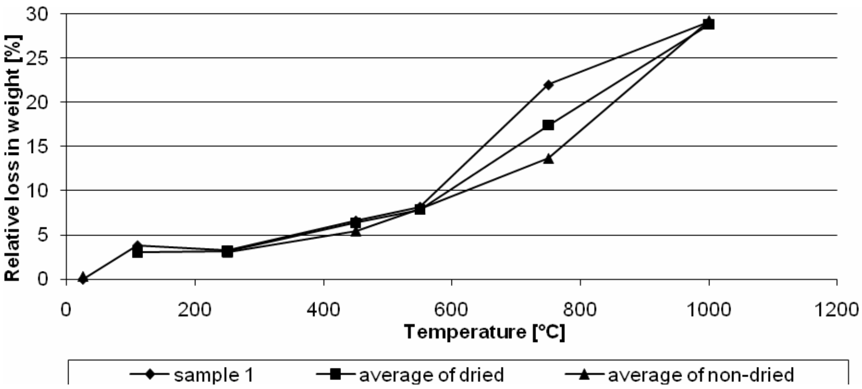

Figure 3: Relative loss in weight dependence on temperature - PROMATECT

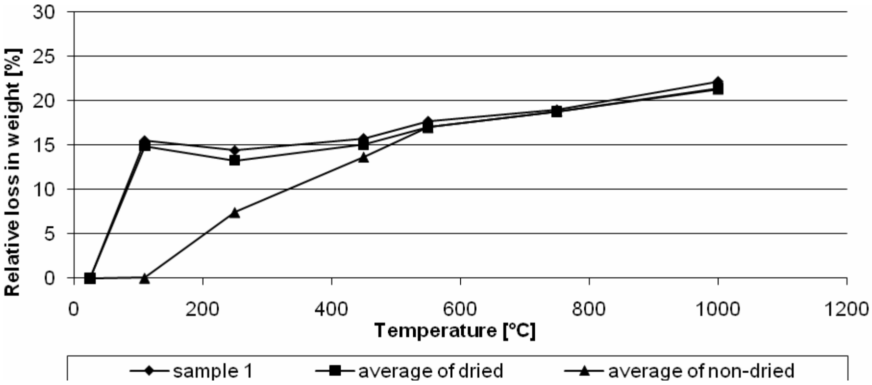

Figure 4: Relative loss in weight dependence on temperature - FIREBOARD

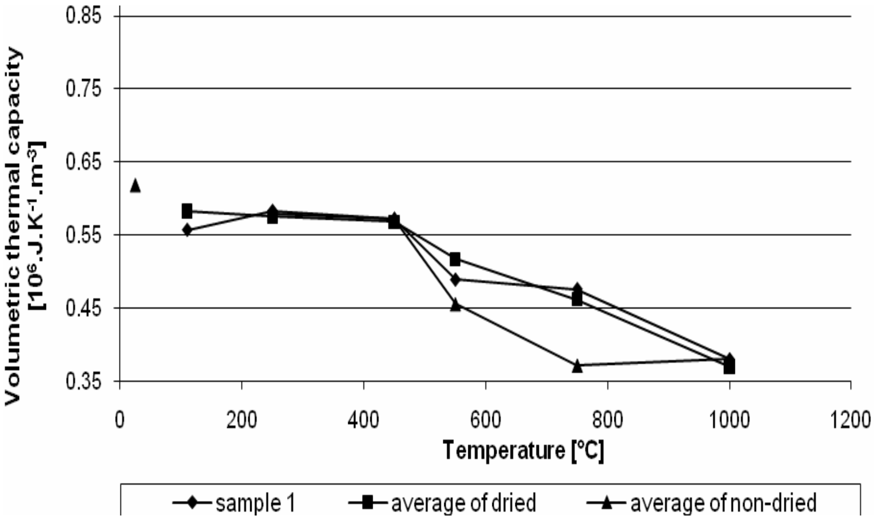

Figure 5: Volumetric thermal capacity dependence on temperature - PROMATECT

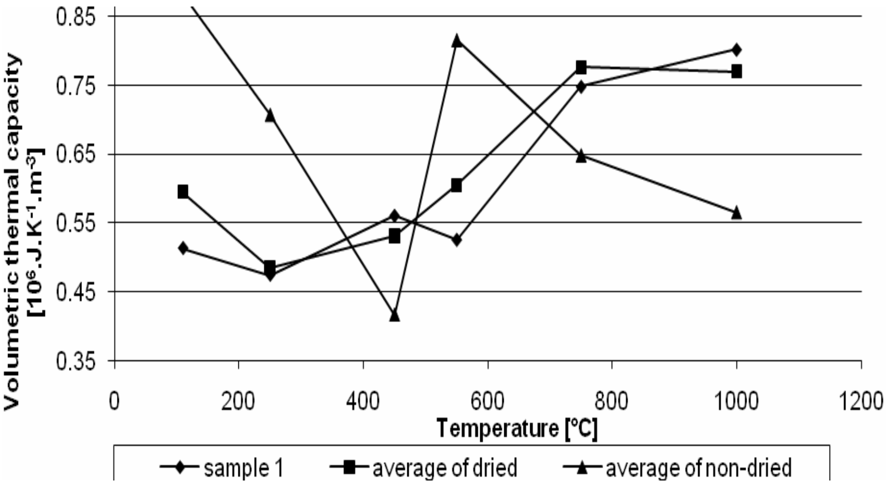

Figure 6: Volumetric thermal capacity dependence on temperature - FIREBOARD

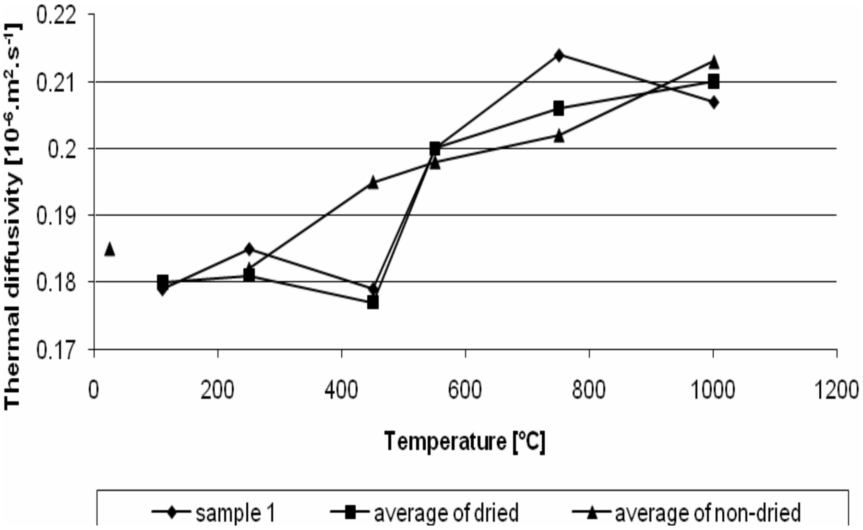

Figure 7: Thermal diffusivity dependence on temperature - PROMATECT

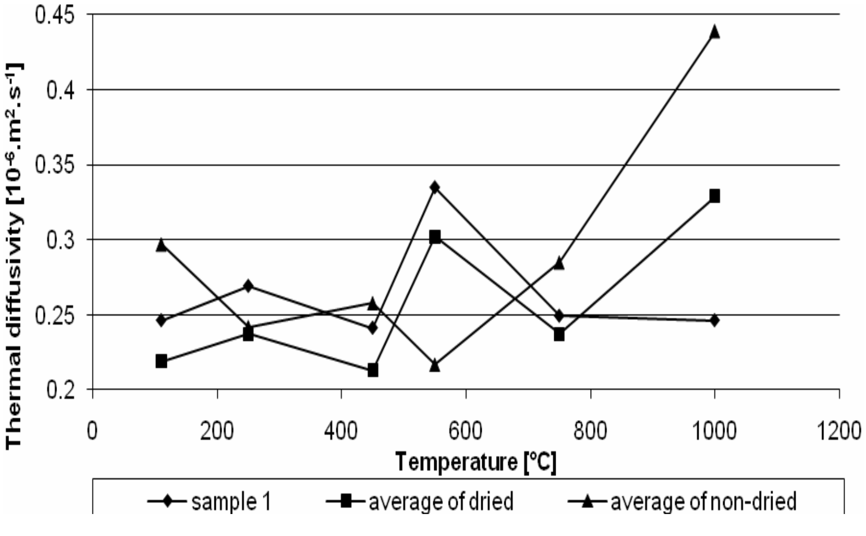

Figure 8: Thermal diffusivity dependence on temperature - FIREBOARD

7. Conclusions

By comparing the obtained figures it is possible to claim that the heat conductivity of PROMATECT material is relatively stable with a slightly decreasing trend. Differences in values in dependence on primary conditions in which material was observed aren´t important.

On the contrary, the FIREBOARD material has a stronger tendency to an increase in the heat conductivity dependent upon burn temperature. There is also the apparent bigger influence of previous drying, it meaning the influence of moisture on non-dried samples on thermal conductivity.

Using figures comparing the relative decrement of weight of the PROMATECT material it is possible to claim that for lower temperatures (up to 500°C) the values are not changed much (maximal change 7%). But higher temperatures caused bigger changes of values (circa 30%). In contrast, the FIREBOARD material is affected by more significant changes already of lower temperatures (below 500 °C) and with higher temperatures values get more fixed.

From figures of thermal diffusivity and volume caloric capacity (volume heat capacity, volume thermal capacity) of both materials it is evident that the important break point happens again at around 500 °C. The material PROMATECT has a decreasing trend of volumetric thermal capacity while on the material FIREBOARD it is possible to observe a gentle increase.

It was explicitly documented that on all samples which had been dried before, the dispersion of observed values is smaller than the dispersion of non-dried.

In conclusion it is possible to claim that all thermal technical parameter are comparable on both materials. Perhaps only the fact that the thermal conductivity on the material PROMATECT measured slightly lower and also the total structural stability was observed as better on this material (also visual aesthetic impression). It so follows that boards made of this material are more suitable as anti-fire lining.

From the point of view of mechanical qualities depending on temperature it is possible to claim that the modulus of elasticity calculated from the speed of waving dispersion corresponds to the curve determined by resonant method in total. Unfortunately it wasn´t possible to vibrate the samples of the material FIREBOARD which were burnt at higher temperatures because after hammering the samples was destroyed.

The advantage of the material PROMATECT is that it has smaller volume weight, and therefore better thermal isolation properties, than the material FIREBOARD.

Acknowledgement

This work has been financially supported by the Ministry of Education, Youth and Sports of Czech Republic, under project No MSM: 6840770031 and by the Ministry of Industry and Trade of Czech republic, under project No MPO FR – TI 1/216.

References

[1] Toman J.: Temperature and moisture influence on physicals parameters of buildings materials (in Czech), dissertation thesis DrSc. CVUT in Prague 1992.

[2] Carslaw, Jaeger: Conduction of heat in solids.Oxford.1959.

[3] Toman J., Semerák P.: Physic 10 – Practical lessons (in Czech), CVUT Prague 2001.

[4] Krempaský J.: Measuring of thermo-physical values (in Slovak), SAV Bratislava 1969.

[5] Concrete – source book of technologist, advertisement studio ARTIS, 2005.

Identification problems of heat transfer in building materials

Jiří Vala[1], Stanislav Šťastník[1]

[1]Faculty of Civil Engineering, Brno University of Technology, Veveří 95, CZ-602 00 Brno, Czech Republic, email: vala.j@fce.vutbr.cz, stastnik.s@fce.vutbr.cz

Abstract: *Reliable computational analysis of heat transfer in building materials needs realistic input data. New building constructions contain advanced composite materials whose macroscopic thermal technical (both insulation and accumulation) properties should be identified properly, following all available qualitative results from their microstructural analysis. However, the corresponding inverse problems are much more complicated than the original direct ones. The paper demonstrates the mathematical support of identification of basic thermal technical characteristics using inexpensive non-stationary measurement devices, generating certain thermal fluxes and recording the temperature in the whole system. The detailed knowledge of solutions of corresponding direct problems in multilayer systems enables us to construct a robust and effective optimization algorithm searching for the needed thermal technical characteristics, including the uncertainty analysis of measurements.*

Keywords: *Building materials, heat transfer, inverse problems, identification of material characteristics, computational modelling, partial differential equations of evolution.*

1. Introduction

The pore space of building materials can act both as an accumulation space and as a free space for liquid of gas flow. The modification of material structure, namely in the case of advanced composite materials, whose properties cannot be estimated by experience, force the change of their thermal conductivity λ and heat capacity c. Both these material characteristics are substantial for the analysis of behaviour of the whole structure, based on the cooperation of their building parts. Consequently, the analysis of thermal behaviour of a structure cannot avoid the experimental identification of thermal technical characteristics of all applied materials, even in such situations as in the prediction of behaviour of maturing mixtures for the floor layers, whose visible volume changes are prohibited.

The stationary measurements of λ and c (Czech technical standard ČSN 72 7012) do not give, according to the required measurement time, reliable results. The non-stationary measurement equipments (rather expensive) use typically some sets of calibration materials (ČSN 72 1105). Both these approaches require the strict size and shape of the specimen and the laboratory measurement conditions, thus their applicability to non-classical materials is limited. The endeavour to develop some alternative non-stationary identification methods of λ and c (both in technical physics and in engineering branches (the frequency-domain method, the step-heating method, the hot-strip / hot-wire method, the infra-red photography approach, etc.) is documented in [6]. The primary and inexpensive measurement device, created at the Faculty of Civil Engineering of tho Brno University of Technology, comes from the hot-wire method (compatible with ČSN EN 993 14 and 15), supported by the non-trivial mathematical analysis and MATLAB-based computational support.

2. Measurement device

The basic configuration of the measurement device, described originally in [4], consists of the following layers:

1. thick insulation layer (e.g. polystyrene),
2. active heating plate (e.g. aluminium),
3. material specimen (with unknown material characteristics),
4. passive additional plate (e.g. aluminium),
5. thick insulation layer (e.g. polystyrene).

The interfaces 1./2. and 4./5. contain two sets of temperature sensors. The interface 1./2. hides also a carefully controlled built-in generator of time-variable heat flux. (The example of an one-dimensional system of this type can be seen on Figure 1.) However, such configuration is not acceptable e.g. for measurements of maturing silicate mixtures in massive structures in situ: the remedy is to remove 4. and 5., considering the real massive structure (nearly the half-space) instead of 3.

For simplicity, let us assume that all layers can be taken as homogeneous and isotropic macroscopically, i.e. some effective characteristics λ and c really exist, and that only the heat conduction can be taken into account, neglecting heat convection, radiation, etc., i.e. we have the conduction dominated system in sense of Chap. 3 from [1]. Since the identification of material density ρ can be done is easily, we can work with two material characteristics $a = \lambda / c\rho$ and $b = 1/\lambda$. As a model problem we can take the analysis of the time development of an unknown temperature field $T(x,t)$ where t means the positive time (dot symbols are reserved for time derivatives) and x the vector of Cartesian coordinates in some domain Ω from the Euclidean space of dimension 3 (in general), 2 or 1 (for simplified configurations) following the equation

$$\dot{T} - a\nabla^2 T = 0 \quad \text{on } \Omega \tag{1}$$

where, alternatively, T is prescribed in the initial time (constant in our following considerations) and on the boundary $\partial\Omega$ of Ω (Dirichlet boundary condition), or the time-variable boundary heat flux q is supplied for

$$bq + \nabla T \cdot \nu = 0 \text{ on } \partial\Omega \tag{2}$$

(Neumann boundary condition); both boundary conditions can be applied on some parts of $\partial\Omega$. For the direct problem with given a and b and just one such boundary condition prescribed at every point of $\partial\Omega$ the solvability of (1), including the convergence of usual numerical methods, as the finite element method and the method of discretization in time (based on Rothe sequences) follows from the Lax-Milgram theorem and from the standard variational calculus. However, if a and b (or at least one of them) are unknown, some additional information is needed, e.g. both q and T simultaneously prescribed on the same part of $\partial\Omega$. Unfortunately, such formulations result typically in ill-conditioned mathematical problems and unstable numerical algorithms, as discussed in [2], p. 21.

The crucial step in the design of the announced inexpensive measurement device is the reliable mathematical and computational support of measurements, avoiding the unpleasant above sketched properties of inverse problems as much as possible. Let us consider the constant temperature at the beginning of every experiment at $t = 0$, preserved still in the external environment (as the boundary condition). The development of temperature in every layer can be then analyzed separately, using the heat fluxes at the interfaces, a priori unknown, but continuous except the interface 1./2. with certain q-jump. For the simplified one-dimensional problem the unknown heat fluxes can be pre-eliminated semi-analytically, as shown in [3], using the Fourier method with certain non-periodic basis and applying the least squares technique to the remaining unknowns, equivalent to our a and b. The drawback of this approach is the rather complicated pre-eliminating algorithm, whose simple and transparent generalization to more-dimensional problems is not available. The alternative approach, suggested in this paper, construct the effective least squares computational algorithm using numerical solutions of particular Dirichlet (with higher priority) and Neumann (if necessary) problems, interpretable as the algorithm of Newton type. The relative simplicity of the algorithm is conditioned by the appropriate arrangement of the experiment.

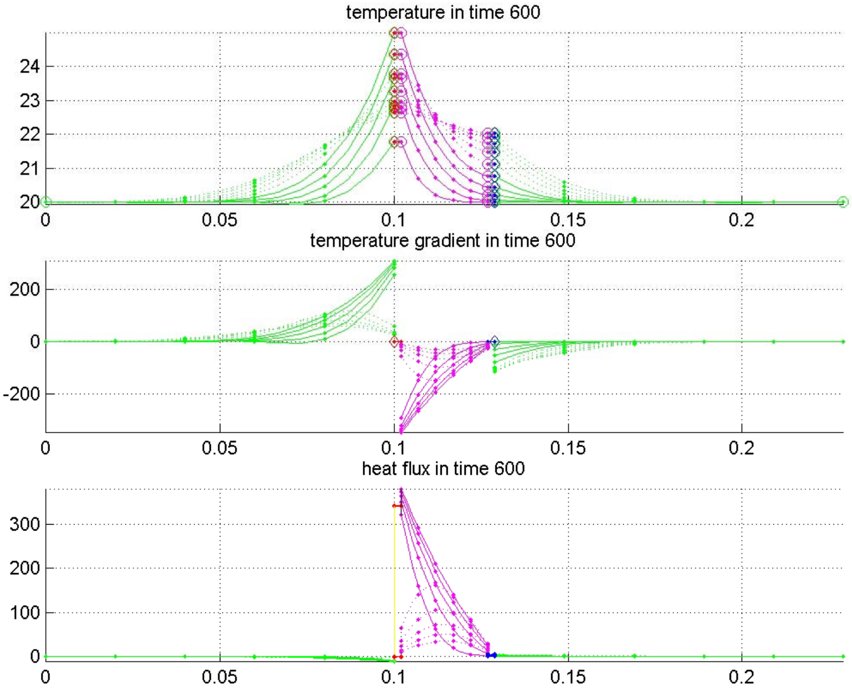

Figure 1: Example of the time development of some physical quantities in the one-dimensional system

3. Mathematical analysis

Considering an arbitrary test function Φ from the Sobolev space $W^{1,2}(\Omega)$ (or its appropriate subspace), we can seek for T in the space of abstract functions $L^2(I, W^{1,2}(\Omega))$ mapping the time interval $I = [0, H]$, H being the final time, to the above introduced space; $(.,.)$ will denote the scalar product in the Lebesgue space $L^2(\Omega)$ and $\langle .,. \rangle$ the similar one in $L^2(\partial\Omega)$. Using the Green-Ostrogradskii theorem, we are able to write alternatively (at least in sense of distributions, in stronger sense thanks to the regularity results – see [2], p. 256)

$$\frac{1}{a}(\Phi,\dot{T})-(\Phi,\nabla^2 T)=0\ ,$$

$$\frac{1}{a}(\Phi,\dot{T})+(\nabla\Phi,\nabla T)-\langle\Phi,\nabla T\cdot\nu\rangle=0\ , \tag{2}$$

$$\frac{1}{a}(\Phi,\dot{T})-(\nabla^2\Phi,T)-\langle\Phi,\nabla T\cdot\nu\rangle+\langle\nabla\Phi\cdot\nu,T\rangle=0$$

and implement the prescribed boundary conditions of both types into the integrals $\langle.,.\rangle$. Let us notice that the first equation of (2) corresponds to the classical formulation of the heat equation (cf. (1)), the second one to its variational formulation and the third one to the classical formulation for the adjoint problem; this enables (together with the detailed sensitivity analysis) the construction of T even in the case of ill-posed problems, applying the generalized conjugate gradient algorithm, suggested in [7], p. 21. The more detailed existence, uniqueness and convergence analysis should be published in [5].

If the boundary temperature is prescribed everywhere on $\partial\Omega$, then the last equation (2), being discretized both in x and in t, using the finite element technique and the Crank-Nicholson scheme, receives the form

$$\frac{1}{a}M(\psi_j-\psi_{j-1})-\frac{1}{2}K(\psi_j+\psi_{j-1})=\frac{1}{2}(g_j+g_{j-1}) \tag{3}$$

where M and K are real symmetrical square matrices of certain order n (a number of base functions), indices $j\in\{1,2,...,m\}$ (m is a number of equidistant time steps) refer to values at $t=jH/m$ (an index 0 to $t=0$), $\psi=(T,\nabla T)$ and g (at discrete times) are real column vectors of length n, all independent of a and b. Using the formal notation

$$S(a)=\frac{1}{a}M-\frac{1}{2}K,\quad Q(a)=\frac{1}{a}M+\frac{1}{2}K,\quad \gamma_j=\frac{1}{2}(g_j+g_{j-1})\ ,$$

we are able to rewrite (3) and then calculate, step by step, the first and second derivatives with respect to a with the result

$$S(a)\psi_j=Q(a)\psi_{j-1}+\gamma_j\ ,$$

$$S(a)\psi_{j,a}=Q(a)\psi_{j-1,a}+\frac{1}{a^2}M(\psi_j-\psi_{j-1})\ ,$$

$$S(a)\psi_{j,aa}=Q(a)\psi_{j-1,aa}-\frac{2}{a^2}M(\psi_{j,a}-\psi_{j-1,a})+\frac{2}{a^3}M(\psi_{j,aa}-\psi_{j-1,aa})\ ,$$

needed in the following calculations.

Since $bq+\nabla T$ should be a zero vector should be approximately a zero vector, our aim is to relax this requirement, using the least squares approach, minimizing a function

$$F(a,b)=\frac{1}{2}\langle bq+\nabla T(a),bq+\nabla T(a)\rangle_\times \tag{4}$$

where $\langle.,.\rangle_\times$ denotes the Bochner integral of $\langle.,.\rangle$ on I, i.e.

$$F_{,a}(a,b) = \left\langle \nabla T_{,a}(a), bq + \nabla T(a) \right\rangle_{\times} = 0, \quad F_{,b}(a,b) = \left\langle \nabla T_{,a}(a), bq + \nabla T(a) \right\rangle_{\times} = 0.$$

The iterative procedure of Newton type

$$\begin{bmatrix} F_{,aa}(a,b) & F_{,ab}(a,b) \\ F_{,ab}(a,b) & F_{,bb}(a,b) \end{bmatrix} \cdot \begin{bmatrix} a^{\prime} - a \\ b^{\prime} - b \end{bmatrix} = - \begin{bmatrix} F_{,a}(a,b) \\ F_{,b}(a,b) \end{bmatrix}$$

with $a^{\prime}$ and $b^{\prime}$ improving the previous estimate a and b is available because it is easy to evaluate

$$F_{,aa}(a,b) = \left\langle \nabla T_{,a}(a), \nabla T_{,a}(a) \right\rangle_{\times} + bq + \left\langle \nabla T(a), \nabla T_{,aa}(a) \right\rangle_{\times},$$

$$F_{,ab}(a) = \left\langle \nabla T_{,a}, q \right\rangle_{\times}, \qquad F_{,bb} = \left\langle q, q \right\rangle_{\times}.$$

If the boundary temperature is known only on a part of $\partial\Omega$ (which seems to be true for most realistic measurement configurations), all boundary heat fluxes on the rest of $\partial\Omega$ can be pre-eliminated from the thermal analysis of layers with a priori known material characteristics as linear functions of b, thus the form of derivatives of $F(a,b)$ from (4) with $\nabla T(a,b)$ instead of $\nabla T(a)$ is much more complicated. Nevertheless, the construction of an iterative procedure of Newton type is possible even in this case. Moreover, the above sketched algorithm can be even adopted transparently to provide a posteriori uncertainty analysis of both identified thermal technical characteristics: it is possible to substitute all integrals $\langle .,. \rangle_{\times}$ by the similar ones in the appropriate probabilistic spaces, as explained in [7], p. 8.

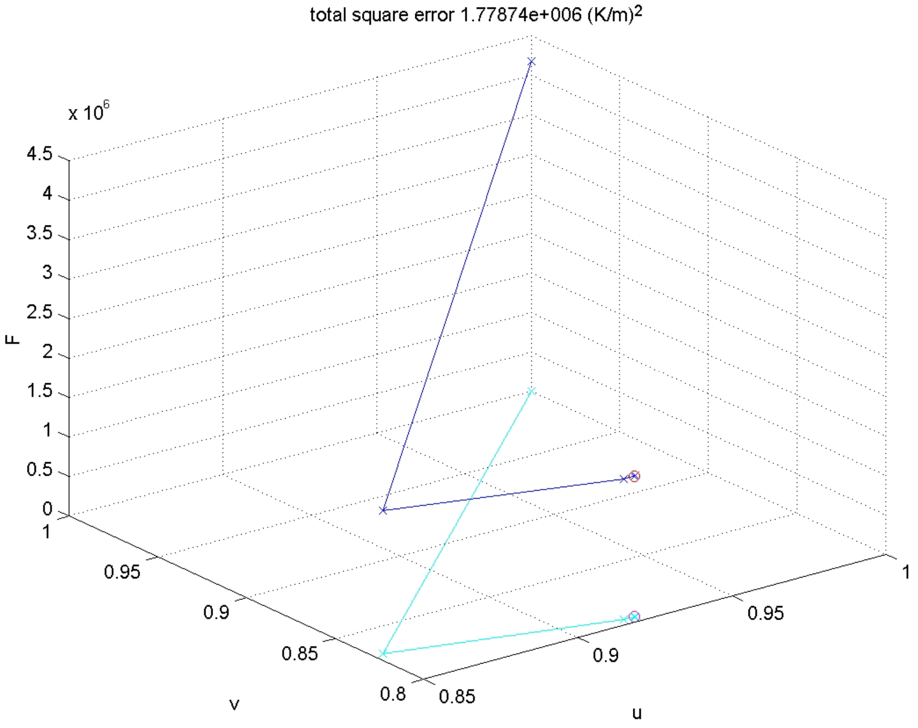

Figure 2: Example of practical use of the iterative minimization procedure

4. Computational support

The iterative minimization of a function $F(a,b)$ from (4) needs the knowledge of values of T on the interfaces 1./2. and 4./5. and of q on the interfaces 1./2.; the reasonable choice of m forces the coincidence of all measurement times with $t = jH/m$ fore some $j \in \{1,2,...,m\}$. The finite element approach based on the Hermite cubic spline interpolation includes then the corresponding values of $\psi = (T, \nabla T)$ as real parameters in (3) directly.

The above sketched computational algorithm has been implemented in the MATLAB environment; the original software code needs no additional packages. Two illustrative figures present the one-dimensional approach to the identification of a and b for a silicate composite specimen where $H = 600$ s. The heating is very special: constant for $t \leq H$, zero otherwise; the measurements are rather rough.

Figure 1 shows the resulting distribution of T, of its derivative with respect to x and of the corresponding heat flux (by the Fourier law) in selected time steps: full lines for $t \leq H$, dotted lines otherwise. The green lines correspond to the polystyrene insulation, the red ones to the active aluminium plate, the blue ones to the passive aluminium plate and the magenta ones to the specimen. The nodes of finite element discretization are highlighted. The non-zero system error of the interface discontinuity of heat fluxes can be observed.

Figure 2 documents the efficiency of the iterative algorithm of Newton type even in such case when the total square error by (4) is still much greater than zero; here $u = a/\tilde{a}$ and $v = b/\tilde{b}$, applying the initial estimates $\tilde{a}$ of a and $\tilde{b}$ of b by experience with similar materials. The blue line connects the values of F for particular iterations, the cyan line is only its projection to the plane of such normalized coordinates u and v. All results presented on Figure 1 come from the last iteration, highlighted on Figure 2.

5. Conclusions

We have demonstrated the development of the inexpensive and robust measurement device, based on the non-trivial mathematical analysis of the direct and inverse theory of heat transfer problems.n Clearly, most presented results need further generalization in several directions: analysis of anisotropic materials, effect of heat convection, radiation, etc., coupling with other physical processes, proper uncertainty analysis, etc. However, even the identification procedure documented on the figures, applying strong simplifications, seems to produce reasonable results.

Acknowledgment

Both the design of the measurement device and the software codes are still in progress. This research is supported by the by the project of specific research of the Brno University of Technology (Czech Republic), Reg. No. FAST-S-10-17, and by the project Education for Competitiveness, Reg. No. CZ.1.07/2.2.00/07.0410.

References

[1] DAVIES, M. G. *Building Heat Transfer*. John Wiley & Sons, Hoboken, 2004. ISBN 0-470-84731-2.

[2] ISAKOV, V. *Inverse Problems for Partial Differential Equations*. Springer, New York, 2006. ISBN 0-387-25364-5.

[3] ŠŤASTNÍK, S.; VALA, J.; KMÍNOVÁ, H. Identification of basic thermal technical characteristics of building materials. In *Kybernetika* 43 (2007), p. 561-576. ISSN 0023-5954.

[4] ŠŤASTNÍK, S.; VALA, J.; KMÍNOVÁ, H. Identification of thermal technical characteristics from the measurement of non-stationary heat propagation in porous materials. In *Forum Statisticum Slovacum* 2 (2006), p. 203-210. ISSN 1336-7420.

[5] VALA, J. Inverse problems of heat transfer. In *Proc. Programs and Algorithms of Numerical Mathematics 15 in Dolní Maxov* (2010). Mathematical Institute AS CR, Prague, to appear.

[6] VALA, J.; ŠŤASTNÍK, S. Výpočtová podpora identifikace tepelně technických vlastností stavebních materiálů. In *Proc. Maltoviny* in Brno (2009). FCE BUT, Brno, 2009. ISBN 80-214-3995-5.

[7] ZABARAS, N. Inverse problems in heat transfer. In *Handbook on Numerical Heat Transfer* (MINKOWYCZ, W. J.; SPARROW, E. M.; MURTHY, J. Y.; eds.), Chap.17. John Wiley & Sons, Hoboken, 2004. ISBN 0-471-34878-8.

Convection and radiation effects in thermophysical measurements at high temperatures

Eva Vejmelková, Robert Černý

Department of Materials Engineering and Chemistry, Faculty of Civil Engineering, Czech Technical University in Prague, Thákurova 7, 166 29 Prague 6, Czech Republic

Abstract: *Heat transport in compact solid materials is mostly described by conduction only. In porous materials the transport phenomena are more complex which affects also the measurements of thermophysical parameters. Temperature gradients always appear in the tested specimen, no matter which method is used. Thus, convection and radiation heat transfer occurs. While in the normal temperature range the effects of convection and radiation can often be neglected, in high temperature measurements this simplification is not so obvious. In this paper, a concept of apparent thermal conductivity is used which is sufficiently simple and makes it possible to deal with more complicated modes of heat transfer. In a practical application of the concept, hybrid PVA-fiber reinforced cement composite exposed to high temperatures up to 1000°C is investigated. The apparent thermal conductivity is calculated using an inverse analysis of measured temperature fields, and the effects of convection and radiation are discussed.*

Keywords: *apparent thermal conductivity, high temperatures, convection, radiation, fiber-reinforced cement composite*

1. Introduction

Cementitious composites reinforced by short, randomly distributed fibers began to gain in importance in the concrete industry since the 1960s. The benefits of fiber reinforcement in improving the fracture toughness, impact resistance, fatigue endurance, and energy absorption capacity of concrete were quite clear arguments for their increasing use. In the 1980s the fiber reinforcement gradually moved up towards multifunctionality, and hybrid-fiber reinforcement appeared in cement-based composites. The attractive advantages of hybrid fiber systems were seen in the convenient combination of their mechanical performance. Three basic hybrid fiber arrangements were devised [1]. In the first, the stronger and stiffer fiber improved the first crack stress and ultimate strength, and the flexible and ductile fiber improved the toughness and strain capacity in the post-cracking zone. The second hybrid fiber system consisted in using combination of smaller fibers, which bridged microcracks and controlled their growth, thus increasing the tensile strength of the composite, and larger fibers which could arrest the propagating macrocracks, thus substantially improving the toughness of the composite. In the third hybrid fiber arrangement, the durability of fiber types was different. The presence of the durable fiber increased the strength and/or toughness retention after age while another type was to guarantee the short-term performance during transportation and installation of the composite elements. The basic arguments for using hybrid-fiber reinforced cement composites formulated in [1] remained topical hitherto, but research activities on this composite type were not very extensive since their first appearance. The rare occurrence of references to this topic found in the scientific literature (only several tens in Web of Science (WoS) during the last 20 years) underlines well this statement. The experimental studies performed by Qian and

Stroeven [2] for the combination of steel and polypropylene fibers in cement matrix, Sun et al. [3] for steel, PVA, and polypropylene fibers, Ahmed et al. [4] for steel and polyethylene fibers, Sahmaran and Yaman [5] for two types of steel fibers, and Sivakumar and Santhanam [6] for steel and various non-metallic fibers (polypropylene, polyester and glass) belong to the few exceptions in this respect. Therefore, investigations of the proper preparation procedures and properties of hybrid-fiber reinforced cement composites still present an actual research problem. During the last two decades, fire safety considerations appeared as the additional sound argument for using hybrid fibers. With the increasing use of high-performance concrete having very low porosity, thus very limited capability of water and water vapor transport, in the building industry, the risk of explosive spalling in concrete elements at high temperatures became apparent. Incorporation of fibers with high melting points, which were responsible for the strength and/or toughness retention, and fibers with low melting points, which evaporated after high-temperature exposure and provided passages for water vapor to escape, presented a promising solution to enhance concrete resistance to spalling. For instance, a combination of steel and polypropylene fibers was found to be an effective solution in this respect by several researchers [7–9].

In this paper, the high-temperature thermal properties of a cementitious composite with two different types of PVA fibers are investigated and the effects of convection and radiation on heat transport are discussed.

2. Technology of specimens' preparation

The composition of the analyzed hybrid PVA-fiber reinforced cement composite is shown in Table 1. Water in the amount corresponding to the w/c ratio of 0.32 was added to the mixture.

Table 1. Composition of PVA-fiber reinforced cement composite

Component	Quantity
Cement CEM I 52.5	54.0
Siliceous aggregates	27.0
Microdorsillite 405	13.0
Microsilica 940 US	3.0
Kuralon RECS 100/12 mm	1.5
Kuralon RECS 7/6 mm	0.5
Glenium ACE 40	1.0

Samples for measurements were prepared in the laboratories of VUSTAH Brno using OMNI MIXER 10 EV vacuum mixing device. At first, cement, siliceous aggregates, microsilica and microdorsillite were homogenized in the mixing device, then water, plasticizer and shorter PVA fibers were added and the wet mixture mixed again. Finally, the longer PVA fibers were stirred into the mixture. The liquid mixture was cast into the forms and de-aerated during 1 hour. After the time period of 28 days after mixing, the samples were prepared for testing.

In the experimental measurements, four various sample pre-treatment conditions were tested:

- reference specimens not exposed to any load (denoted as K-ref in what follows)
- specimens exposed to a gradual temperature increase up to 600, 800 and 1000°C during two hours, then left for next 2 hours at the final temperature and slowly cooled (denoted as K-600, K-800 and K-1000 according to the loading temperature).

For every pre-treatment, 3 specimens were used for testing. Before the measurements of all parameters, specimens were dried in an oven at 110°C.

3. The apparent thermal conductivity approach

In the classical theory of linear irreversible thermodynamics [10] the conduction of heat in absence of cross effects can be expressed by the Fourier's Law

$$q = -\lambda \cdot \operatorname{grad} T \tag{1}$$

where q is the heat flux, λ the thermal conductivity and T the temperature, and consequently by the heat-conduction equation

$$\rho c \frac{\partial T}{\partial t} = \operatorname{div}(\lambda \cdot \operatorname{grad} T) \tag{2}$$

where ρ is the density, c the specific heat capacity and t the time.
In the case of materials containing moisture, the heat conduction is combined with moisture transfer. An analysis using the methods of linear irreversible thermodynamics leads to the replacement of the classical thermal conductivity λ for "pure" heat conduction by the generalized thermal conductivity λ^+

$$\lambda^+ = \lambda + \rho\delta\left[\Theta \frac{\partial \mu}{\partial u}\frac{\rho}{\rho_d} - T\left(\frac{\partial \mu}{\partial T} + \frac{\partial \mu}{\partial u}\frac{\partial u}{\partial T}\right)\right] \tag{3}$$

where u is the moisture content by mass, $u = \frac{m_m - m_d}{m_d}$, m_m is the mass of the moist sample, m_d the mass of the dried sample, ρ_d the partial density of the porous matrix, μ the chemical potential, δ the Soret's thermodiffusion coefficient, Θ the thermodiffusion ratio, $\Theta = \delta T / D$, D is the diffusion coefficient.
In addition, it is necessary to include one generalized thermodynamic force more, the moisture gradient in the relation for the heat flux,

$$q = -\lambda^+ \cdot \operatorname{grad} T - \beta \cdot \operatorname{grad}\ u, \tag{4}$$

where β is the Dufour's coefficient.
The heat balance equation can be then written only in a combination with the moisture balance equation,

$$\rho c \frac{\partial T}{\partial t} = \operatorname{div}(\lambda^+ \cdot \operatorname{grad} T) + \operatorname{div}(\beta \cdot \operatorname{grad} u) \tag{5}$$

$$\frac{\partial u}{\partial t} = \operatorname{div}(D \cdot \operatorname{grad} u) + \operatorname{div}(\delta \cdot \operatorname{grad} T). \tag{6}$$

In the case that also phase change processes, convection and/or radiation and chemical reactions occur in the material, new thermodynamic forces and fluxes arise and new balance equations are necessary to be taken into account. The heat balance equation is then modified by the addition of terms describing the heat sources or sinks due to these phenomena and can be schematically expressed as

$$\rho c \frac{\partial T}{\partial t} = \operatorname{div}\left(\lambda^{+} \cdot \operatorname{grad} T\right) + \operatorname{div}\left(\beta \cdot \operatorname{grad} u\right) + S_p + S_m + S_r \tag{7}$$

where S_p is the volume source or sink term expressing the influence of phase changes, S_m the term expressing the effect of other modes of heat transfer (convection and radiation), S_r the corresponding term for chemical reactions. The terms S_p, S_m, S_r can be replaced using "intensity" terms (similarly as in the theory of electromagnetic field) I_p, I_m,, I_r, $S_p = \operatorname{div} I_p$, $S_m = \operatorname{div} I_m$, $S_r = \operatorname{div} I_r$, where I_p, I_m,, I_r have the meaning of heat fluxes due to phase changes, convection and radiation and chemical reactions, respectively.

Thus, I_p, I_m,, I_r can be formally included into the value of the apparent thermal conductivity λ^* which leads to the heat balance equation formally identical with the Fourier's heat conduction equation. In the case of one-dimensional heat transfer we obtain

$$\rho c \frac{\partial T}{\partial t} = \frac{\partial}{\partial x}\left(\lambda^* \frac{\partial T}{\partial x}\right) \tag{8}$$

with

$$\lambda^* = \lambda + \rho\delta\left[\Theta \frac{\partial \mu}{\partial u}\frac{\rho}{\rho_d} - T\left(\frac{\partial \mu}{\partial T} + \frac{\partial \mu}{\partial u}\frac{\partial u}{\partial T}\right)\right] + \beta\frac{\partial u}{\partial T} + \frac{I_p}{\frac{\partial T}{\partial x}} + \frac{I_m}{\frac{\partial T}{\partial x}} + \frac{I_r}{\frac{\partial T}{\partial x}}\,. \tag{9}$$

The definition equation (9) for the apparent thermal conductivity λ^* is rather complex. Also, it contains terms which are either very difficult to determine (the gradients of chemical potential) or which are specific for a given experiment (the terms with temperature gradients). This greatly limits the chances of a direct calculation of λ^*. Therefore, the most convenient way to determine the apparent thermal conductivity is an experiment.

Taking the advantage of formal agreement of the heat conduction equation (8) with its common form (2), one can employ some of the dynamic methods based on the analysis of temperature field. The basic principle of these methods consists in measuring temperature fields in a material sample at one-sided heating and the subsequent solution of the inverse heat conduction problem (see, e.g., [11]-[13] for details). As it has been shown in a numerical analysis in [13], the most stable and reliable method among those employing the direct solution of the inverse problem of heat conduction was found the integration method proposed in [12]. Therefore, this method was used for determination of temperature dependent apparent thermal conductivity in this paper.

In the measuring procedure for determination of thermal conductivity by the integration method, one-side heating of a specimen with thermally insulated lateral faces is realized using a furnace where a constant temperature is maintained. Along the longitudinal axis of the sample, a set of temperature sensors is positioned, which makes it possible to record the temperature field through a measuring unit by a PC. From the measured $T(x,t_i)$ curves, a set of 8-10 curves is chosen, and these curves are used in the computational treatment. First, the measured $T(x,t_i)$ curves are subject of a regression analysis. Then, we choose a temperature value τ, determine the integration area for this value and calculate the corresponding value of thermal conductivity $\lambda(\tau)$ (see [12] for details). This procedure is repeated for a sufficient number of τ values so that we finally obtain a point-wise given function $[\tau_i, \lambda(\tau_i)]$.

The application of integration method for determination of thermal conductivity requires knowledge of the temperature dependence of density and specific heat capacity. The density can be measured directly by a simple thermogravimetry from the mass and volume of a sample, the specific heat capacity at high temperatures can be determined by the nonadiabatic method described in [14].

4. Results and discussion

As fundamental physical material characteristics, bulk density, open porosity and matrix density were analyzed. They were obtained using the gravimetric method and the water vacuum saturation method [15]. The measurement was done on the samples with the dimensions of 50 x 50 x 20 mm.

Table 2 shows that the most important change in porosity occurred between the unloaded state and the loading temperature of 600°C where the increase of porosity was as high as 54%. Later porosity changes were lower than 10%. This is in accordance with the behavior of most Portland cement based composite materials where the most important chemical reaction in the high temperature range is decomposition of calcium hydroxide at about 460-480°C [16, 17].

Table 2. Basic physical properties of PVA-fiber reinforced cement composite

	ρ [kg m^{-3}]	ρ_{mat} [kgm^{-3}]	Ψ [m^{3}m^{-3}]
K-ref	2030	2590	21.6
K-600	1940	2910	33.2
K-800	1880	2900	35.1
K-1000	1840	2910	36.7

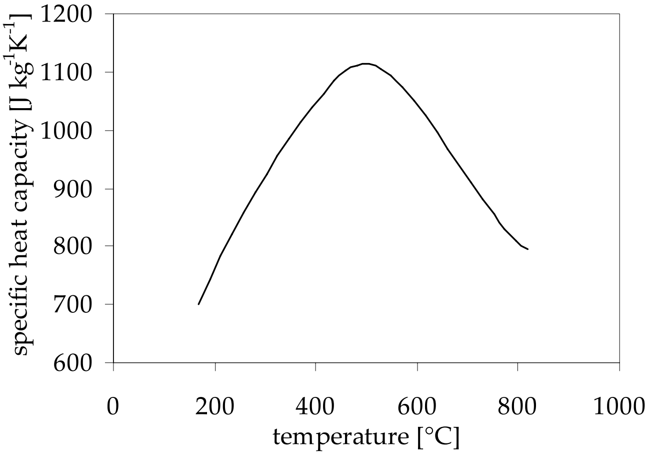

Figure 1: Specific heat capacity as a function of temperature

Figure 1 shows the measured dependence of specific heat capacity on temperature. In the lower-temperature range up to approximately 500°C, an increase of specific heat capacity was observed. The rapid decrease of specific heat capacity for temperatures higher than 500°C can be attributed to the partial loss of mass due to the decomposition of portlandite.

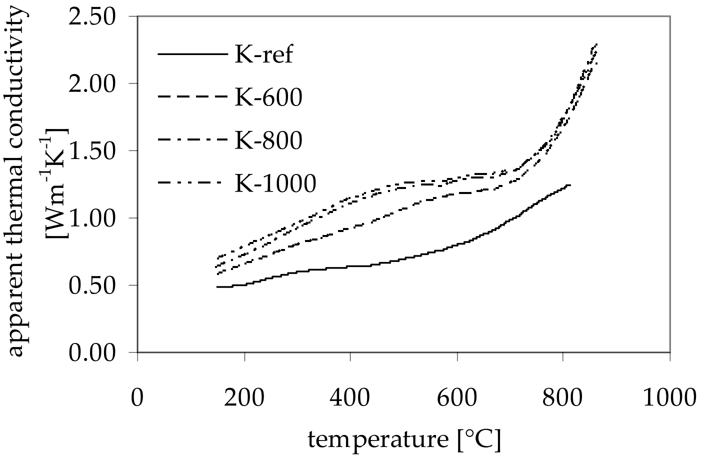

Figure 2: Apparent thermal conductivity as a function of temperature

Figure 2 presents the results of apparent thermal conductivity λ^* measurements as function of temperature. The values of λ^* increased with both the increasing actual temperature and the increasing pre-heating temperature, particularly in the range of higher temperatures. There was a clear difference between the reference specimen K-ref and the pre-heated specimens. On the other hand, the λ^* (T) functions of the pre-heated specimens K-600, K-800 and K-1000 differed only slightly each other which was in accordance with the changes of basic parameters in Table 2.

The explanation of the shape of the $\lambda^*(T)$ function of the reference material K involves two principal factors. The first of them was that the measurements were dynamic. The temperature fields were measured typically for only about 30 minutes because one of the limiting conditions of the applied inverse analysis method was that the heat flux at the end of the sample not being in contact with the hot environment of the furnace should be equal to zero. As a consequence, all chemical decomposition reactions and phase change processes taking place at elevated temperatures affected the temperature measurements, thus the values of apparent thermal conductivity, in a significant way. For the fiber-cement composite material studied in this paper the most thermally induced processes were endothermic (see, e.g., the DTA analysis of Portland-cement mortar in [18]). Therefore, they effectively decreased the apparent thermal conductivity. In the range of lower temperatures, evaporation of capillary condensed water (cementitious materials are mostly hygroscopic) presented another significant endothermic effect.

The second important factor influencing the calculated $\lambda^*(T)$ functions was convection and radiation effects in the high temperature range. In the experimental setup applied for temperature measurements in this paper where the temperature gradients existed in the whole volume of the sample these effects could not be avoided. Therefore, the apparent thermal conductivity included in certain extent also other modes of heat transfer which effectively increased its value.

The existence of two contradictory factors affecting the values of apparent thermal conductivity, namely the endothermic chemical reactions and convective and radiative modes of heat transfer, does not enable any generalization, as for the total effect of high temperatures on the heat flux. The importance of both factors depends on a particular material. It can be roughly assessed using the knowledge of either the values of thermal conductivity in room-temperature conditions after pre-heating to a specific temperature measured by a standard method or the results of high-temperature thermal conductivity measurements in thermally homogenized conditions. Both approaches have their positives and negatives. The room-temperature measurement is easy from the point of view of experimental setup, thus it has a higher overall accuracy, but on the other hand it neglects for instance the changes in thermal conductivity due to the volumetric changes or changes in phonon velocity at high temperatures. The direct high-temperature measurement in isothermal conditions includes more high-temperature induced effects and is therefore more realistic but the experimental setup is more difficult, which results in a lower accuracy, in general. In this paper, we have chosen for the assessment of factors affecting the apparent thermal conductivity the first approach.

Table 3 presents the room-temperature values of thermal conductivity λ after pre-heating to 600, 800 and 1000°C which were determined by an impulse technique (Isomet 2104, commercial device produced by Applied Precision, Ltd.). The thermal conductivity significantly decreased after high-temperature exposure. This was in a qualitative agreement with the increase in porosity (Table 2) due to thermal decomposition reactions in high-temperature range leading to an increase of significance of the low thermal conductivity of the air in the cement matrix-air system.

A comparison of thermal conductivities in Table 3 with the apparent thermal conductivity λ^* of the reference specimen K-ref in Figure 2 shows that in the range of lower temperatures up to approximately 400°C λ^* was approximately two times lower than λ. Here the endothermic chemical decomposition reactions and evaporation of capillary condensed water were the dominant factors affecting the apparent thermal conductivity. For the temperatures higher than 600°C λ^* was higher than λ, and the convective and radiative modes of heat transfer were more important, due to the higher porosity and crack formation in the material.

Table 3. Thermal conductivity measured at room temperature in dry state

Material	Thermal conductivity [$Wm^{-1}K^{-1}$]
K-ref	1.05
K-600	0.76
K-800	0.66
K-1000	0.58

The $\lambda^*(T)$ functions of the pre-heated specimens K-600, K-800 and K-1000 (Figure 2) showed that in this case the convective and radiative modes of heat transfer were clearly more important than in the reference specimen K-ref but still some endothermic processes decreasing the λ^*

values could take place in the materials. This was partially due to the evaporation of capillary condensed water but possibly also a consequence of the decomposition of products of secondary hydration induced by air moisture in the pre-heated materials after cooling in natural laboratory conditions.

5. Conclusions

Experimental results presented in this paper showed that convection and radiation can be considered important effects in heat transport in cementitious composites at high temperatures if high temperature gradients occur in a material. However, the chemical reactions taking place in cementitious composites at high temperatures are also important. As these two factors affecting the values of apparent thermal conductivity are contradictory, it is difficult to make any generalization, as for the total effect of high temperatures on the heat flux. Therefore, their importance should be assessed for any particular case using the knowledge of either the values of thermal conductivity in room-temperature conditions after pre-heating to a specific temperature measured by a standard method or the results of high-temperature thermal conductivity measurements in thermally homogenized conditions. In this paper, we have chosen for the assessment of factors affecting the apparent thermal conductivity the first approach. The second will be used in the near future and both approaches will be compared.

Acknowledgement

This research has been supported by the Ministry of Education, Youth and Sports of the Czech Republic, under project No MEB 0810004.

References

[1] BENTUR, A.; MINDESS, A. S. *Fibre Reinforced Cementitious Composites,* Elsevier, London-New York, 1990.

[2] QIAN, C. X.; STROEVEN, P. Development of hybrid polypropylene-steel fibre-reinforced concrete, In: *Cement and Concrete Research*, Vol. 30, 2000, p. 63-69.

[3] SUN, W.; CHEN, H.; LUO, X.; QIAN, H. The effect of hybrid fibers and expansive agent on the shrinkage and permeability of high-performance concrete, In: *Cement and Concrete Research,* Vol. 31, 2001, p. 595-601.

[4] AHMED, S.F.U.; MAALEJ, M.; PARAMASIVAM, P. Flexural responses of hybrid steel-polyethylene fiber reinforced cement composites containing high volume fly ash. In: *Construction and Building Materials*, Vol. 21, 2007, p. 1088-1097.

[5] SAHMARAN, M.; YAMAN, I. O. Hybrid fiber reinforced self-compacting concrete with a high-volume coarse fly ash, In: *Construction and Building Materials*, Vol. 21, 2007, p. 150-156.

[6] SIVAKUMAR, A.; SANTHANAM, M. Mechanical properties of high strength concrete reinforced with metallic and non-metallic fibres, In: *Cement and Concrete Composites*, Vol. 29, 2007, p. 603-608.

[7] CHEN, B.; LIU, J. Properties of lightweight expanded polystyrene concrete reinforced with steel fiber, In: *Cement and Concrete Research*, Vol. 34, 2004, p. 1259-1263.

[8] PENG, G. F.; YANG, W. W.; ZHAO, H.; LIU, Y. F.; BIAN, S. H.; ZHAO, L. H. Explosive spalling and residual mechanical properties of fiber-toughened high-performance concrete subjected to high temperatures, In: *Cement and Concrete Research*, Vol. 36, 2006, p. 723-727.

[9] SUHAENDI, S. L.; HORIGUCHI, T. Effect of short fibers on residual permeability and mechanical properties of hybrid fibre reinforced high strength concrete after heat exposition, In: *Cement and Concrete Research,* Vol. 36, 2006, p. 1672-1678.

[10] DE GROOT, S. R.; MAZUR, P. *Non-equilibrium Thermodynamics*. North-Holland, Amsterdam, 1962.

[11] ČERNÝ, R.; TOMAN, J. Determination of Temperature- and Moisture-Dependent Thermal Conductivity by Solving the Inverse Problem of Heat Conduction. In: *Proceedings of International Symposium on Moisture Problems in Building Walls, V.P. de Freitas, V. Abrantes (eds.).* University of Porto, Porto 1995, p. 299-308.

[12] ČERNÝ, R.; TOMAN, J. A Difference Method for Determining the Thermal Conductivity of Porous Materials in a Wide Temperature Range. *High Temp.-High Press*. 29, 1997,p. 51-57.

[13] ČERNÝ, R.; TOMAN, J. Solution of Inverse Problems of Heat Conduction in Building Materials. In: *Proceedings of Numerical Methods in Thermal Problems*, Vol. 10, R.W. Lewis and J.T. Cross (eds.). Pineridge Press, Swansea, 1997, p. 811-820.

[14] ČERNÝ, R.; TOMAN, J. Calorimetry of Building Materials. In: *Journal of Thermal Analysis*, Vol. 43, 1995, p. 489-496.

[15] ROELS, S.; CARMELIET, J.; HENS, H.; ADAN, O.; BROCKEN, H.; ČERNÝ, R.; PAVLÍK, Z.; HALL, C.; KUMARAN, K.; PEL, L.; PLAGGE, R. *Journal of Thermal Envelope and Building Science* 27:307, 2004.

[16] BAŽANT, Z. P.; KAPLAN, M. F. Concrete at High Temperatures, In: *Material Properties and Mathematical Models.* Longman, Harlow 1996.

[17] ČERNÝ, R.; ROVNANÍKOVÁ, P. *Transport Processes in Concrete*. Spon Press, London 2002.

[18] ČERNÝ, R.; MADĚRA, J.; PODĚBRADSKÁ, J.; TOMAN, J.; DRCHALOVÁ, J.; KLEČKA, T.; JUREK, K.; ROVNANÍKOVÁ, P. The effect of compressive stress on thermal and hygric properties of Portland cement mortar in wide temperature and moisture ranges. *Cement and Concrete Research*, Vol. 30, 2000, p. 1267-1276.

Mechanical, thermal and hygric properties of lime-pozzolana plasters for historical buildings

Eva Vejmelková[1], Martin Keppert[1], Radoslav Sovják[2], Robert Černý[1]

[1]Department of Materials Engineering and Chemistry, Faculty of Civil Engineering, Czech Technical University in Prague, Thákurova 7, 166 29 Prague 6, Czech Republic

[2]Experimental Center, Faculty of Civil Engineering, Czech Technical University in Prague, Thákurova 7, 166 29 Prague 6, Czech Republic

***Abstract**: For an assessment of the hygrothermal performance of renewed plasters in reconstructed historical buildings, it is necessary to determine besides the mechanical properties also the basic thermal and hygric transport and storage properties. In this paper, thermal conductivity, specific heat capacity, moisture diffusivity, water vapor diffusion permeability, compressive strength and bending strength of several types of lime-pozzolana plasters intended for renovation of historical buildings are determined. On the basis of the measurements performed, the suitability of the newly developed plasters for an application in reconstruction of historical buildings is assessed.*

***Keywords**: plasters, lime, pozzolana, mechanical properties, hygric properties, thermal properties*

1. Introduction

In the time of Ancient Rome, mixtures composed of quicklime and pozzolana fillers such as volcanic ash, tuff or spongilite were used for mortar production. In other parts of the world crushed or ground burnt clays were used. The reaction of these materials with lime resulted in the formation of hydrated calcium silicates and calcium aluminates. In the 16th century hydraulic lime was manufactured purposively, which substituted the mixtures of quicklime with hydraulically or pozzolanically reacting admixtures. Due to the higher resistance of these materials to the environment, some original plasters or plaster fragments were conserved up to now. The original pure lime plasters based on quicklime as exterior plasters were preserved no more. Portland cement substituted later the hydraulic materials. It was used as a binder in many countries since the end of the 19th century; as a component of plasters it was used since the 1920s.

From the point of view of a historian, it is not acceptable to use lime-cement plasters in Romanesque, Gothic, Renaissance and Baroque buildings. The requirements of conservators who take care of historical monuments are that the materials for repair or innovation of plasters must have the most similar composition as the historical materials and they have to be applicable by the original methods [1]. This concerns especially the number and the structure of coated layers, the way of plaster surface treatment by striking, indentation or smoothing. So, the demand for the substitution materials in the restoration of historical buildings appeared due to the necessity to imitate the appearance and the quality of the original materials. The methods for the application of these materials followed at first from empirical experience, which had the tradition of thousands of years. However, often an unsuitable material and an incorrect application was proposed, as a result of the fact, that some processes taking place during the formation of solid structure were not known exactly.

Pozzolanic admixtures were used in historical mortars frequently, although sometimes not on purpose but only as a consequence of low purity of the applied lime. However, in most cases their use led to substantial increase of durability. Therefore, they can be considered as prospective materials in producing renovation mortars. The most often used pozzolana in lime mortars was metakaolin, until now [2-8]. In this paper, several lime-metashale plasters are designed and their basic mechanical, thermal and hygric properties are measured.

2. Materials

The composition of lime-pozzolana plasters is shown in Table 1 (w/d is the water to dry substances ratio). The same lime (Kotouč Štramberk, CZ) was used in all mixtures. Their composition differed in the type of pozzolana admixture. Several types of metashale produced by České lupkové závody Inc., Nové Strašecí (CZ), were used, namely Mefisto L10 (in P9), Mefisto L05 – (in P10) and Mefisto L03 (in P11). The reference lime plaster without metashale was denoted as P8. One renovation plasters commercially produced in Czech Republic denoted as P12 was analyzed as well. The exact composition of this plaster was not known.

Table 1. Composition of used materials

Material	Lime [kg]	Natural quartz and basalt sand 0 to 4 mm [kg]	Metashale [kg]	w/d [-]
P8	2.5	7.5	-	0.26
P9	2.08	7.5	0.42	0.25
P10	2.08	7.5	0.42	0.18
P11	2.08	7.5	0.42	0.23
P12	3,33 kg of dry binder mix and 6.66 kg of 0-4 mm aggregates			0.375

3. Experimental methods

As basic physical properties, bulk density ρ_b [kg m^{-3}], open porosity ψ [Vol.-%] and matrix density ρ_m [kg m^{-3}] were determined. They were obtained using the gravimetric method and the water vacuum saturation method [9]. The particle size distribution of pozzolanic admixtures was measured by laser particle size analyzer Mastersizer 2000 (MALVERN). The pore size distribution of particular plasters was measured by Mercury Intrusion Porosimetry by help of porosimeters Pascal 140 and 440 (Thermo). The contact angle between mercury and surface of the plasters and surface tension of mercury were assumed to be 130° and 480 mN/m. The measurement of compressive and bending strength was done using the electromechanical testing device MTS Alliance RT 30. The wet cup method and dry cup method were employed in the measurements of water vapor transport parameters [9]. The water vapor diffusion coefficient D [m^2 s^{-1}] and water vapor diffusion resistance factor μ [-] were measured. The water sorptivity A [kg m^{-2} s$^{-1/2}$] and apparent moisture diffusivity κ [m^2 s^{-1}] were measured using a water suction experiment [10]. Thermal conductivity λ [W m^{-1} K^{-1}], and specific heat capacity c [J kg^{-1} K^{-1}], were determined using the commercial device ISOMET 2104 (Applied Precision, Ltd.).

4. Experimental results and discussion

Table 2 shows that lime plasters with metashale and reference plaster achieved similar values of all measured basic physical properties. The pure lime plaster without pozzolana admixture (P8) had slightly higher value of bulk density than materials with metashale which is probably a consequence of the different microstructure (in lime plaster it is formed by calcium carbonate only, in lime-pozzolana plasters partially also by hydrated calcium silicates). The commercial plaster P12 had about 20% higher open porosity than the other plasters but its matrix density was similar to lime-pozzolana plasters.

Table 2. Basic physical properties

	ρ [kg m^{-3}]	ρ_{mat} [kgm^{-3}]	Ψ [m^{3}m^{-3}]
P8	1730	2650	34.6
P9	1660	2570	35.5
P10	1690	2530	33.3
P11	1690	2540	33.6
P12	1780	2540	41.8

The particle size distribution of the tested pozzolanic admixtures (three grades of metashale) is presented in Figure 1. All three distribution curves were rather broad; the smallest particles present in all kinds of metashale were of the same size 0.5 μm; the largest particles were present in metashale L10. The average particle size (median of cumulative passing curve) of metashale L03 was 4 μm, for L05 it was 9 μm and for L10 10 μm.

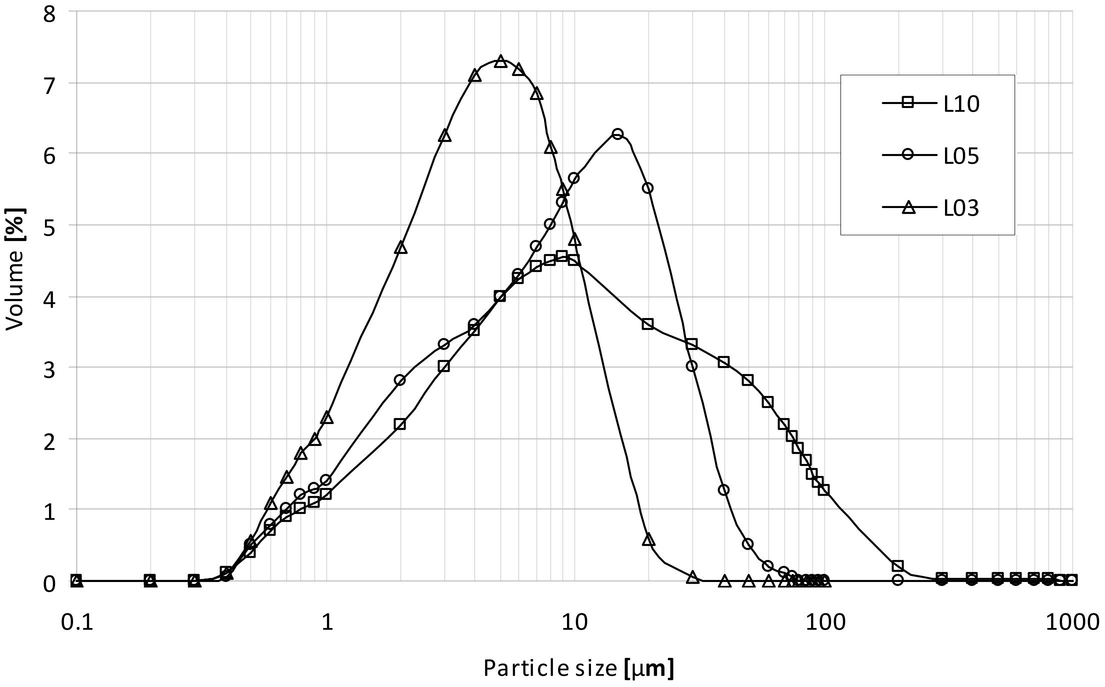

Figure 1: Particle size distribution of metashales L03, L05 and L10

The pore size distribution curves of plasters P8 – P12 are presented in Figure 2. The pore systems of plasters P8 to P11 were almost identical. The average pore size was in all materials about 0.8 μm. Only the plaster P12 featured higher porosity; it was caused by the presence of higher amount of small pores below 1 μm in diameter as compared to the other plasters. It was in agreement with measurement of total porosity presented in Table 2.

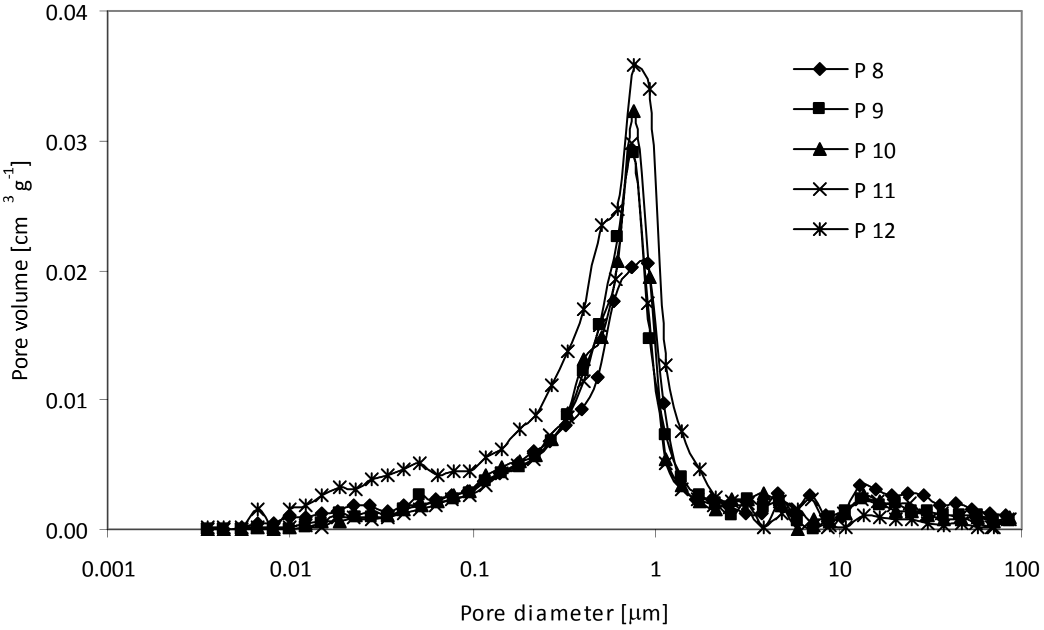

Figure 2: Pore size distribution of plasters P 8 to P 12

Table 3 shows that the addition of metashale to lime at the production of renovation plasters remarkably improved the compressive strength which increased up to 10 times. The best result was obtained for P11. The commercial plaster P12 achieved similar values of compressive strength as P11 despite its higher porosity. The improvement of bending strength of lime-metashale plasters as compared to the lime plaster P8 was less distinct but the measured approximately two to four times higher values than for P8 were quite satisfactory. The commercial plaster P12 had only slightly lower value of compressive and bending strength then P11.

Table 3. Mechanical properties

	Compressive strength [MPa]	Bending strength [MPa]
P8	0.56	0.4
P9	4.2	1.0
P10	3.1	0.9
P11	5.9	1.5
P12	5.3	1.4

Table 4 shows that the water vapor diffusion coefficient D of lime-metashale plasters P9-P11 was approximately 40 - 50% lower than for the lime plaster P8. The commercial plaster P12 exhibited similar values of water vapor diffusion parameters as the lime-metashale plaster P11 despite its higher porosity. This was probably due to the different topology of the pore space as already indicated in the pore distribution curves in Figure 2.

Table 4. Water vapor transport properties

	5/25 %			97/25 %		
	δ [s]	D [m^2s^{-1}]	μ [-]	δ [s]	D [m^2s^{-1}]	μ [-]
P8	1.19E-11	1.64E-06	14.05	3.10E-11	4.52E-06	5.24
P9	8.46E-12	1.16E-06	19.83	2.20E-11	3.02E-06	7.69
P10	8.10E-12	1.11E-06	20.83	2.36E-11	3.24E-06	7.15
P11	7.40E-12	1.02E-06	22.71	1.93E-11	2.66E-06	8.70
P12	7.23E-12	9.93E-07	23.32	2.55E-11	3.50E-06	6.67

The water absorption coefficient of pure lime plaster P8 was approximately 30% higher than for the lime plasters P10 and P11 and about 10% higher than lime plaster P9. The commercial plaster S12 exhibited similar values of water absorption coefficient as lime plasters S10 and S11 despite its very high porosity. This was probably caused by the application of hydrophobization admixtures .

Table 5. Water transport properties

	A [kg $m^{-2}s^{-1/2}$]	κ [m^2s^{-1}]
P8	0.215	5.17E-07
P9	0.197	3.13E-7
P10	0.140	1.78E-7
P11	0.145	1.86E-7
P12	0.145	1.18E-7

Tables 6 and 7 show a remarkable increase of thermal conductivity of all studied materials with increasing moisture content. Its values in wet state were about two to three times higher than values in dry state. The highest thermal conductivity achieved the pure lime plaster P8. Differences in values of thermal conductivity for the pure lime plaster and plasters with pozzolana were about 12 %. The commercial plaster P12 had the lowest thermal conductivity in dry state about two times lower than pure lime plaster P8 and 40% lower than plasters with pozzolana. This corresponds with its higher open porosity (Table 2). The values of volumetric heat capacity significantly increased with increasing moisture, as a consequence of the added water with high specific heat capacity. The thermal diffusivity values reflected the differences in thermal conductivity and volumetric heat capacity of the studied materials.

Table 6. Thermal properties in dry state

	u [kgkg^{-1}]	λ [Wm^{-1}K^{-1}]	cρ [10^{6}Jm^{-3}K^{-1}]	a [10^{-6}m^{2}s^{-1}]
P8	0.000	0.836	1.497	0.556
P9	0.000	0.747	1.597	0.467
P10	0.000	0.751	1.527	0.493
P11	0.000	0.749	1.583	0.473
P12	0.000	0.464	1.470	0.315

Table 7. Thermal properties in water saturated state

	u [kgkg^{-1}]	λ [Wm^{-1}K^{-1}]	cρ [10^{6} Jm^{-3}K^{-1}]	a [10^{-6} m^{2}s^{-1}]
P8	0.188	2.393	2.130	1.160
P9	0.210	2.023	2.165	0.940
P10	0.198	2.247	2.185	1.035
P11	0.203	2.040	1.820	1.085
P12	0.300	1.547	2.100	0.751

5. Conclusions

Mechanical, thermal and hygric properties of three lime-pozzolana plasters intended for application to renovation of historical buildings were studied in the paper and compared with the corresponding parameters of common lime plaster and a commercial renovation plaster. Experimental results showed that among the three lime-pozzolana plasters P9-P12 which differed in the particle size of applied pozzolana, the material P11 with the finest pozzolana particles was the most successful solution. The apparent reason was the faster hydration of metashale particles leading to a more effective formation of the complex system of lime-pozzolana hydration products. P11 exhibited 30-50% higher strength values than P9 and P10, while its water and water vapour transport properties, as well as thermal properties, were similar to the other two lime-pozzolana plasters. All three lime-pozzolana plasters had significantly better mechanical properties than the common lime plaster; up to four times higher strength values were measured. They also exhibited up to 50% lower water transport parameters. On the other hand, the water vapour diffusion in lime-pozzolana plasters was only slightly slower than in common lime plaster. The commercial renovation plaster P12 had similar mechanical, water and water vapour transport properties as the lime-pozzolana plaster P11 although its open porosity was about 20% higher. As the exact composition of P12 was not known, we can only speculate about the possible reasons. A logical explanation could be the use of small amount of cement in P12, together with a moderate amount of hydrophobization admixture.

Acknowledgement

This research has been supported by the Czech Science Foundation, under grant No. 103/09/0780 and grant SGS10/232/OHK1/3T/11.

References

[1] Šefců, O. 1998. Importance of plaster composition in in the care of historical monuments (in Czech). *Vápenné omítky* Křivoklát'98, STOP Praha.

[2] J. Cabrera and M. F. Rojas, 2001, Mechanism of hydration of the metakaolin-lime water system. Cem. Conc. Res., Vol. 31, pp. 177-182.

[3] M. F. Rojas and J. Cabrera, 2002, The effect of temperature on the hydration rate and stability of the hydration phases of metakaolin-lime-water systems. Cem. Conc. Res., Vol. 32, pp. 133-138.

[4] M. F. Rojas and M. I. Sánchez de Rojas, 2003, The effect of high curing temperature on the reaction kinetics in MK-lime and MK-blended cement matrices at 60 °C. Cem. Conc. Res., Vol. 33, pp. 643-649.

[5] A. Shvarzman et al., 2003, The effect of dehydroxylation/amorphization degree on pozzolanic activity of kaolinite. Cem. Conc. Res., Vol. 33, pp. 405-416.

[6] R. Černý, A. Kunca, V. Tydlitát, J. Drchalová, P. Rovnaníková, Effect of Pozzolanic Admixtures on Mechanical, Thermal and Hygric Properties of Lime Plasters. Construction and Building Materials 20(2006), 849-857.

[7] R. Pernicová, M. Pavlíková, R. Černý, Effect of metakaolin on chloride binding in lime-based composites. Proceedings of Computational Methods and Experimental Measurements XIII, C.A. Brebbia and G.M. Carlomagno (eds.). WIT Press, Southampton 2007, 357-365.

[8] Z. Pavlík, E. Vejmelková, L. Fiala, R. Černý, Effect of Moisture on Thermal Conductivity of Lime-Based Composites. International Journal of Thermophysics 30(2009), 1999-2014.

[9] Roels, S., Carmeliet, J., Hens, H., Adan, O., Brocken, H., Černý, R., Pavlík, Z., Hall, C., Kumaran, K., Pel, L,, Plagge, R., Interlaboratory Comparison of Hygric Properties of Porous Building Materials. Journal of Thermal Envelope and Building Science 27 (2004) 307-325.

[10] Kumaran, M.K., Moisture Diffusivity of Building Materials from Water Absorption Measurements.IEA Annex 24 Report T3-CA-94/01, Ottawa 1994.

Numerical analysis of temperature field in heterogeneous materials

Viliam Vretenár and Ľudovít Kubičár

Institute of Physics, Slovak Academy of Sciences, Dúbravská cesta 9, 845 11 Bratislava, Slovakia,
email: vretenar@savba.sk

Abstract: *Heterogeneous materials as typical samples used for thermophysical properties testing are inspected in order to understand the role of their heterogeneities. Simple two-phase model consisted of circular particles embedded into matrix is proposed and used for temperature field calculations as a numerical experiment. Temperature responses as results from numerical simulations are analysed and compared with theoretical ones coming form analytical solution of corresponding homogeneous system and measuring regime. Deviations of temperature responses correlated to heterogeneity size as well as homogeneity criterion are discussed.*

Keywords: *heterogeneity, thermophysical properties, pulse transient method*

1. Introduction

Heterogeneous material is a solid object consisted of different constituent materials called phases and its properties can vary either discontinuously or continuously across the interfaces of these phases. In addition, discontinuous variations are often accompanied by a process of creation of new thin inter-layers, which have completely different properties. Real heterogeneous materials possess usually complex structures, where many different ways for heat transport exist. In such situation, a question regarding reliability or limits of methods used for thermophysical properties measurements arises.

Along with the expansion of transient methods, many measurements of heterogeneous materials showed serious differences between thermophysical parameters measured by transient on the one hand and steady-state and equilibrium methods on the another hand, i.e. discrepancies in the consistency relation were observed [1, 2]. One possible source of these discrepancies may be that the measuring methods use working equations which were derived from a heat equation related to homogenous solids [3]. The goal of this study is to investigate the influence of heterogeneities on temperate field spreading through sample and consequently to analyse its effect on thermophysical parameters evaluation when using the pulse transient method [4]. Instead of stochastic or analytical method, the numerical approach is chosen. The "experiment" realized by numerical simulation of the heterogeneous model is compared with temperature function calculated from exact analytical solution of the homogenous one.

2. Model of heterogeneous structure

In order to be able to analyse heterogeneous structure, following simple 2D model (Fig. 1, solid bounded by two parallel planes) is taken into consideration. Two-phase heterogeneous structure consists of matrix of phase 1 and heterogeneities of phase 2, which are periodically distributed through the matrix in the form of circles. A unit cell is marked by square (dot line) with dimension *l* having inner circle (heterogeneity) of radius *r*. According to the pulse transient method, the sample is temperate stabilized at one side (*L*), while the pulse of heat is introduced at another one. Due to the periodical structure and unlimited size of model in one dimension, region chosen for numerical solution was confined as depicted by hatched area.

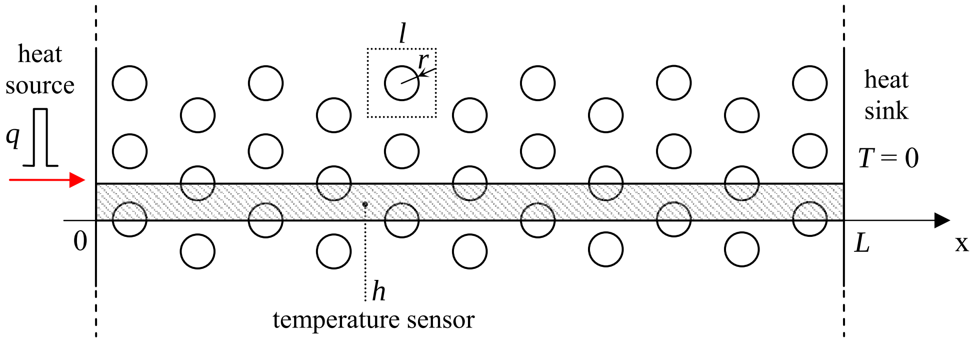

Figure 1: Schematic diagram of heterogeneous model

Equation of heat conduction of the model has the form

$$\frac{1}{a}\frac{\partial T(x,y,t)}{\partial t}=\frac{\partial^2 T(x,y,t)}{\partial x^2}+\frac{\partial^2 T(x,y,t)}{\partial y^2} \tag{1}$$

where *T* is the temperature and *a* stands for the isotropic thermal diffusivity. Then the initial and boundary conditions are as follows

$$T(x,y,t\to 0)=0 \tag{2}$$

$$-\lambda\frac{\partial T(x=0,y,t)}{\partial x}=q\Big|_{t<t_0} \tag{3}$$

$$T(x=L,y,t)=0 \tag{4}$$

where q is the heat flow per unit area generated during the time t_0, λ is the isotropic thermal conductivity and *L* represents the size of sample. The grade of heterogeneity might be expressed as ratio of heterogeneities area to total one. According to unit cell the heterogeneity ratio *P* is defined by function

$$P=\frac{S_{het}}{S_{tot}}=\frac{\pi r^2}{l^2} \tag{5}$$

where *r* is radius of heterogeneities and *l* is the dimension of corresponding unit cell (Fig. 1).

3. Analytical solution

A numerical solution of the model described in previous section is compared with analytical one, which is based on the same model excepting heterogeneities themselves. Such model is reduced to pure 1D problem and its analytical solution is easily found [5] as function

$$T(x,t)=T_s(x,t) \text{ for } t\le t_0 \tag{6}$$

$$T(x,t)=T_s(x,t)-T_s(x,t-t_0) \text{ for } t>t_0 \tag{7}$$

$$T_s(x,t)=\frac{q(L-x)}{\lambda}-\frac{8qL}{\lambda\pi^2}\sum_{n=0}^{\infty}\frac{(-1)^n}{(2n+1)^2}e^{\frac{-a(2n+1)^2\pi^2 t}{4L^2}}\sin\left(\frac{(2n+1)(L-x)\pi}{2L}\right) \tag{8}$$

where a is the thermal diffusivity, λ is the thermal conductivity, q is the heat flow per unit area generated during the time t_0, and L stands for the thickness of sample.

4. Samples and numerical apparatus

A set of three samples having different grade of heterogeneities as well as different thermophysical properties of individual phases have been selected (Table 1). For described heterogeneous model, two different possibilities of thermophysical properties of matrix/heterogeneity system can be taken into consideration, namely, conductor/insulator and insulator/conductor system. Intuitively, the matrix composed of good thermal conductor having heterogeneity of poor thermal properties affects the temperature field of the system and its time evolution in more remarkable way than the perfect thermal conductor heterogeneities in insulator, which was also confirmed by numerical analysis.

Table 1: The thermophysical properties of inspected samples and their individual phases

	Parameter	Thermal diffusivity a [m^2 s^{-1}]	Thermal conductivity λ [W m^{-1} K^{-1}]	Specific heat c [J kg^{-1} K^{-1}]	Density ρ [kg m^{-3}]	Heterog. radius r [mm]	Heterog. ratio P [%]
Sample 1	Phase 1	6.584×10^{-5}	160	900	2700	0.5 0.05	19.63
	Phase 2	1.124×10^{-7}	0.19	1420	1190		
	Effective	4.665×10^{-5}	106.6	950.5	2403.6		
Sample 2	Phase 1	6.584×10^{-5}	160	900	2700	0.9 0.09	63.62
	Phase 2	1.124×10^{-7}	0.19	1420	1190		
	Effective	1.511×10^{-5}	29.6	1126.3	1739.3		
Sample 3	Phase 1	2.208×10^{-4}	490	690	3216	0.75 0.075	44.18
	Phase 2	1.124×10^{-7}	0.19	1420	1190		
	Effective	9.089×10^{-5}	180.4	855.4	2320.9		

The thermophysical values of individual phases are related to real material properties (Table 1). The phase 2 (heterogeneity) for all three samples represents the PMMA material as thermal insulator, whereas phase 1 (matrix) as good thermal conductor is related to aluminum for sample 1 and 2 and to ceramic SiC(6H) for sample 3, respectively. The general thermophysical parameters of such heterogeneous structures are then treated as effective ones, highlighted in Table 1 by gray color, where the thermal conductivity is estimated by numerical solution of the model in steady-state regime with equations 1 to 4 being simplified for space domain only. The density of heterogeneous structure is calculated by simple mixing rule

$$\rho_{eff}=\rho_1(1-P)+\rho_2 P \tag{9}$$

and the effective specific heat using Kopp-Neumann rule [6] in the form

$$c_{eff} = \frac{c_1 \rho_1 (1-P) + c_2 \rho_2 P}{\rho_{eff}} \tag{10}$$

where P is heterogeneity ratio (eq. 5). The effective thermal diffusivity as the last parameter is then estimated by equation

$$a_{eff} = \frac{\lambda_{eff}}{c_{eff} \rho_{eff}} \tag{11}$$

For all samples, their length L and position of temperature sensor h (place from where the temperature response was used for analysis) are 50 mm and 20 mm, respectively. In order to investigate the influence of heterogeneity size, the model is calculated for two values of the unit cell length l, 2 mm and 0.2 mm, respectively, with corresponding radiuses of heterogeneities (two values of radius for each sample in Table 1). Since the ratio of heterogeneity area to unit cell remains equal, the calculated effective parameters remained also the same for both lengths of the unit cell.

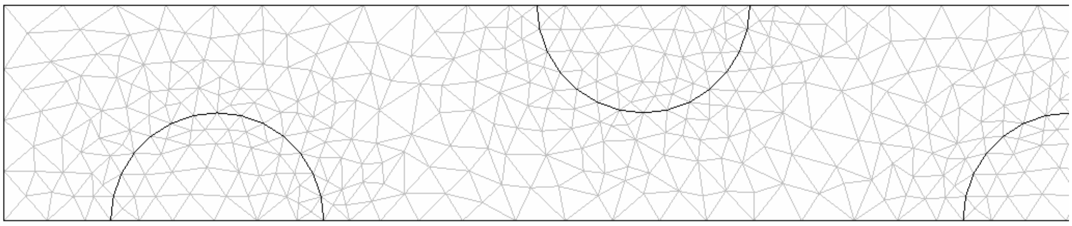

Figure 2: Section of mesh structure used for numerical analysis of heterogeneous model

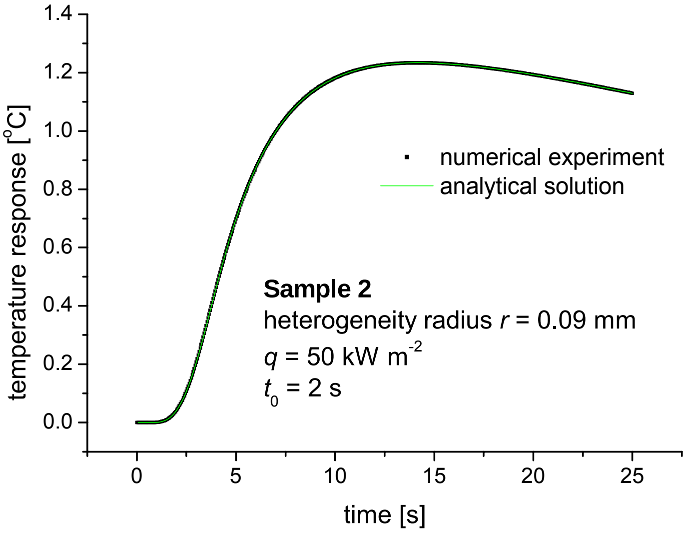

Figure 3: Model verification (homogeneous solution) of sample 2 with small heterogeneities

Comsol Multiphysics, ver. 3.2, is employed as a numerical instrument for both transient and steady-state experiment simulation, using the finite element method. The model structure contains about 25 and 250 circular heterogeneities for 2 mm and 0.2 mm of unit cell length, respectively. To design enough dense mesh for precise simulation of such complex structures, the number of around 300 elements per unit cell is chosen. For illustration the section of such triangular mesh structure is shown in Fig. 2. Prior the calculation of the individual heterogeneous samples, their numerical models (containing different heterogeneity ratio as well as unit cell length) were verified by means of their simulation with unified phases into one phase defined by effective thermophysical parameters but preserving heterogeneous mesh structure. Comparison of such simulation with analytical solution (eq. 6) is shown in Fig. 3, where excellent agreement is clearly visible.

5. Numerical "experiments"

A typical temperature distribution through sample area, as a result of numerical experiment, is drawn in Fig. 4. Even for longer time, the different temperatures in certain circular heterogeneities (detail in enclosed inset) in comparison with bounded matrix area could be observed. The distribution was calculated for sample 1 with radius $r = 0.5$ mm and time $t = 8$ s.

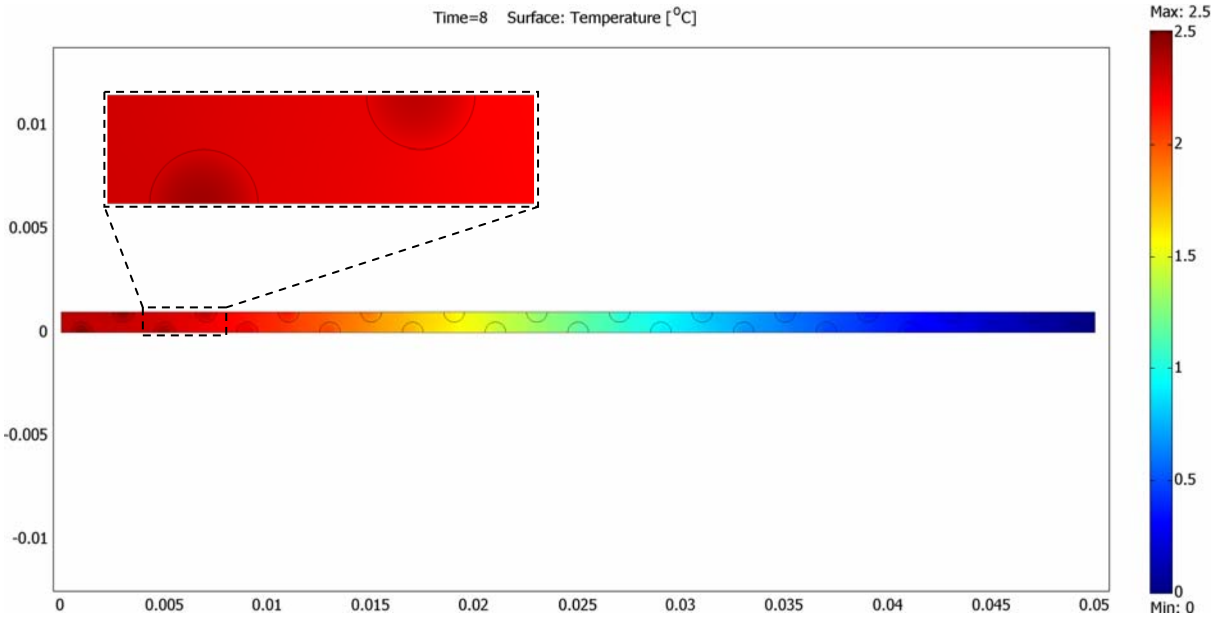

Figure 4: *Temperature distribution in sample 1 with heterogeneity radius of 0.5 mm*

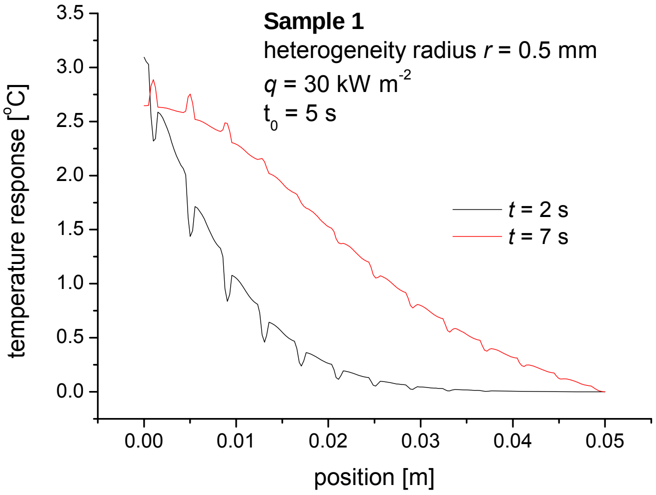

Figure 5: *Cross-section plot of temperature distribution in sample 1*

In order to analyse in more details the influence of heterogeneities on temperature field the cross section along the x-axis is depicted in Fig. 5 for different time evolutions. Visible defects on the temperature distribution are caused by presence of the heterogeneities. It's evident that at the beginning of heat spreading, they can not catch the temperature rise meanwhile for the longer times (finally penetrated by heat) start to act as heat sources.

5.1 Influence of heterogeneities size

The effect presented in Fig. 4, 5 strongly depends on the size of heterogeneities with respect to the thickness *h*, where the temperature response is measured. The set of three samples is inspected for two different length of unit cell *l*, scaled by factor of 10. As seen in Fig. 6-8, calculated curves of all samples exhibit strong discrepancy between numerical experiment and analytical solution of homogenous model when relatively big sizes of heterogeneities are chosen. This implies that measuring regime sees the heterogeneities in material and that such sample can not be treated as homogenous one. Decreasing these sizes only by 10, the satisfactory agreement between curves pops up and the sample might be considered for particular measuring regime as thermally homogenous. Biggest discrepancy was found for sample 3 even if the heterogeneity size was not the bigger one. The reason is in extreme high thermal conductivity of matrix being chosen for this sample, which also manifested in shorter time of temperature response.

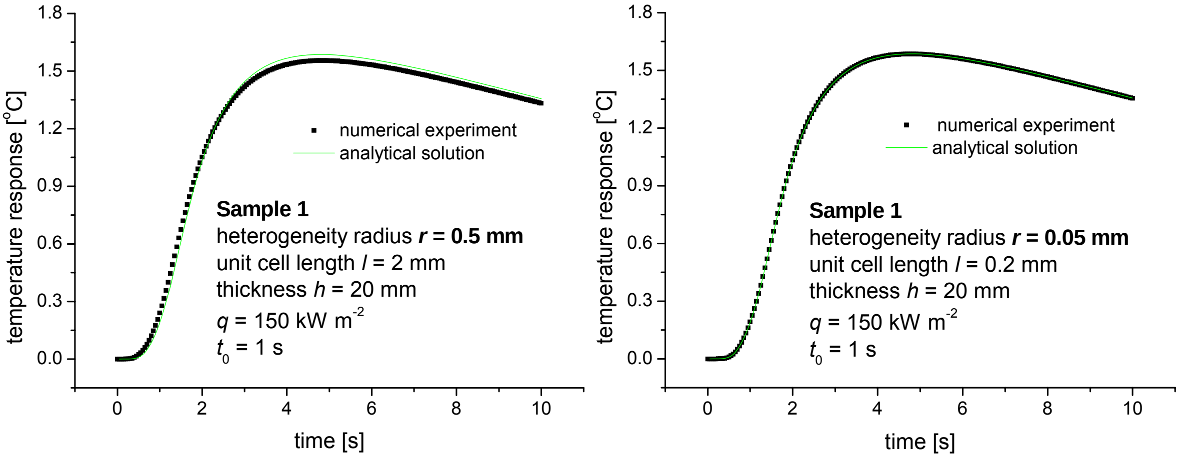

Figure 6: Comparison of numerical and analytical solution of sample 1 for two heterogeneity sizes.

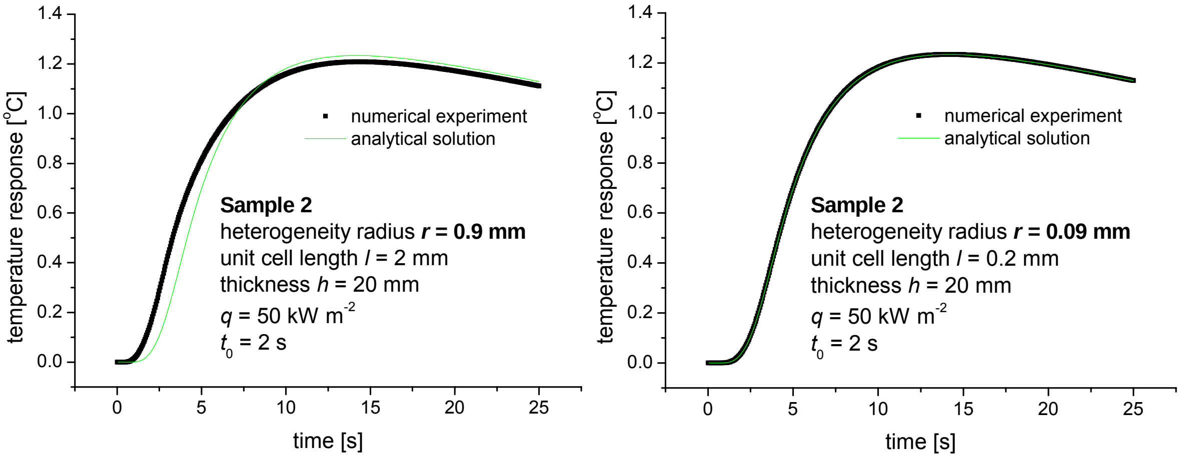

Figure 7: Comparison of numerical and analytical solution of sample 2 for two heterogeneity sizes.

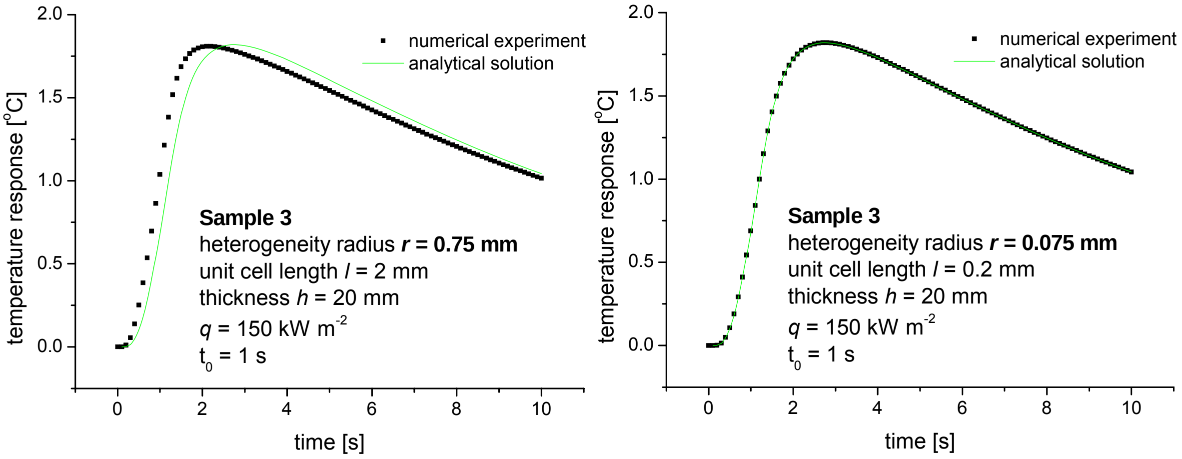

Figure 8: Comparison of numerical and analytical solution of sample 3 for two heterogeneity sizes.

5.2 Homogeneity criterion

The pure mathematical approach of such problem can be found in works [7, 8], where the flash method was taken into consideration. The concept of thermal wavelength is introduced and criterion that limits the scale of heterogeneity of the material is expressed as the minimum thermal wavelength associated with the problem (measuring regime). Since heterogeneity of real materials is very complex, oftentimes varying between different microscopic levels, there is no sense to try to find an exact solution of homogeneity criterion. Contrariwise, the phenomenological approach should be chosen. Then the thermal effect of individual heterogeneity can be expressed as its ability to cope with temperature change of its nearby surroundings. In order words, deviation of temperature response at certain position of the sample depends on how big volume or area is, wherein the temperature of heterogeneities is not equal with their surroundings. For the pulse transient method, the rate of temperature change in sample might be related with time of the temperature maximum, having form [4]

$$t_m = \frac{h^2}{2a_{eff}} \tag{12}$$

During this time the heat penetrates the heterogeneity and eq.(12) is also written as

$$t_m = \frac{r^2}{2a_2} \tag{13}$$

Then t_m substitution of eq.(12) into eq.(13) yields the radius of heterogeneity as

$$r = h\sqrt{\frac{a_2}{a_{eff}}} \tag{14}$$

Finally, considering the ratio of heat capacities the homogeneity criterion has form

$$r << h\sqrt{\frac{a_2}{a_{eff}}\frac{c_2\rho_2 P}{c_1\rho_1(1-P)}} \tag{15}$$

The derived homogeneous criterion roughly quantifies the limit of heterogeneity size. Practically, the size of heterogeneities should be two or three orders lower than calculated radius by eq.(15).

6. Conclusions

Both numerical and analytical approach to the heterogeneous materials have been proposed and presented. Three different samples having various thermophysical properties as well as heterogeneities sizes were investigated. As a result the following fact might be summarized that the thermal diffusivity can only by calculated from the thermal conductivity and heat capacity when the measured heterogeneous material might be considered as homogeneous.

Acknowledgement

The paper was supported by the project APVV–0497–07, the project MVTS - MAFINCO and by the VEGA projects 2/0161/08 and 1/0499/08.

References

[1] Kubičár, Ľ., Boháč, V., Vretenár, V., Barta, Š., Neuer, G., Brandt, R.: *Thermophysical properties of heterogeneous structures measured by pulse transient method*, Int. J. Thermophys., Vol.24, No. 6, 2005, p. 1949-1962

[2] Vretenár, V.: *Thermophysical properties of heterogeneous solids. Measurements by the Pulse transient methos*, Ph.D. Thesis, Slovak Academy of Sciences, Bratislava, 2006, pp.136

[3] Barta, Š.: *Effective thermal conductivity and diffusivity in heterogeneous materials*, Thermophysics, 2003, p. 31-38

[4] Kubičár, Ľ.: *Thermal Analysis: Pulse Method of Measuring Basic Thermophysical Parameters*, in Comprehensive Analytical Chemistry, Vol XII, Part E, G. Svehla, ed. Amsterdam, Oxford, New York, Tokyo ELSEVIER, 1990, p. 350

[5] Carslaw, H., S., Jaeger, J., C.: *Conduction of Heat in Solids*, 2nd ed., Oxford University press, New York, 1959, p. 113

[6] Grimvall, G.: *Thermophysical properties of materials*, Enlarged and revised edition, Elsevier, 1999, pp. 424

[7] Kerrisk, J., F.: *Thermal Diffusivity of Heterogeneous Materials*, J. Appl. Phys., Vol. 42, No. 1, 1971, p. 267-271

[8] Kerrisk, J., F.: Thermal *Diffusivity of Heterogeneous Materials.II. Limits of the Steady-State Approximation*, J. Appl. Phys., Vol. 43:1, 1972, p. 112-117

Analysis of thermophysical parameters measurements of chosen foams, polymers and metals by transient plane source method

Monika Wielgosz, Piotr Koniorczyk

Institute of Aviation Technology, Department of Mechatronics, Military University of Technology, Kaliskiego 2, 00-908 Warsaw, Poland, email: piotr.koniorczyk@wat.edu.pl

***Abstract**: In this paper the authors' approach to transient plane source method for measurements of thermophysical properties of chosen materials: foams – extruded polystyrene foam (XPS), polyurethane foam (Syspur SH 4055/1), polymers – plexiglas (PMMA), polyamide 6 (Pa6), metals – alloy steel 1H18N9T, duralumin 6 (PA6) is studied. This method is presented for simultaneous determination of three thermophysical parameters – thermal conductivity, thermal diffusivity and specific heat in one single measurement. In this technique, a 0.2 mm thick copper heater KHR 2/10 (Omega, USA) is sandwiched between two identical pieces of sample material. The sample material must completely cover the heater. A step-wise heating power is applied to this heater, resulting in a transient temperature response that is recorded by the two thermocouples mounted on the samples on the both sides of the heater. From temperature response in this sandwich-sample setup configuration the thermal conductivity is obtained by plotting the temperature increase* $\Delta T\left(\sqrt{t}\right)$ *and extracting the thermal conductivity from the slope of the best line-fit. The thermal diffusivity is obtained by an iterative procedure producing the best model fit to the experimental data points.*

***Keywords**: transient plane source method, thermal conductivity, thermal diffusivity and specific heat*

1. Introduction

Transient plane source method is based on the generation of the dynamic temperature field inside the specimen [1, 2]. The measuring process can be describes as follows: The temperature of the specimen is stabilized and uniform. Then a small disturbance in the form of a step-wise function is applied to the specimen. A thermometer placed apart from the heat source measures the temperature change (temperature response). From the temperature response to this small disturbance, the thermophysical parameters are calculated according to the model used. Technically, the dynamic temperature field is generated by the passage of the electrical current through a plane electrical resistance KHR 2/10 (460÷470 Ω). The model was tested on data measured on chosen foams: XPS and Syspur SH 4055/1, polymers: PMMA and Pa6, metals: 1H18N9T and PA6.

2. Theory

It was assumed that as a result of appearance of surface heat source of continuous activity in time t_o in isotropic and homogeneous semi-infinite medium the heat transfer occurs only by heat conduction – Figure 1. Non-stationary temperature field is a result of resolving of heat transfer equation [3]:

$$\frac{\partial^2 T(r,x,t)}{\partial r^2}+\frac{1}{r}\frac{\partial T(r,x,t)}{\partial r}+\frac{\partial^2 T(r,x,t)}{\partial x^2}=\frac{1}{a}\frac{\partial T}{\partial t} \tag{1}$$

with homogeneous initial condition:

$$T(r,x,0)=T_o=const \tag{2}$$

and boundary conditions of the first and second kind:

$$-k\frac{\partial T(r,0,t)}{\partial x}=\dot{q}_o,\ 0\le r\le r_o \tag{3}$$

$$-k\frac{\partial T(r,0,t)}{\partial x}=0,\ r>r_o \tag{4}$$

$$\frac{\partial T(0,x,t)}{\partial r}=0 \tag{5}$$

$$\frac{\partial T(r,\infty,t)}{\partial x}=0 \tag{6}$$

$$T(r,\infty,t)=T,\ T(\infty,x,t)=T_o \tag{7}$$

$$\frac{\partial T(\infty,x,t)}{\partial r}=0, \tag{8}$$

where: $\dot{q}_o=const$ is the heat flux density formulated in W/m^2.

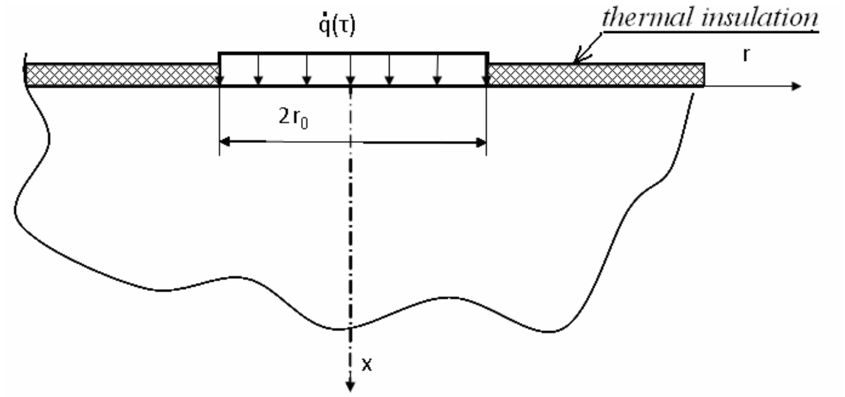

Figure 1: Model of semi-infinite medium heated by surface heat source in the shape of disc of $2r_o$ *diameter. Heat flux density of heater amounts to* $\dot{q}(t)$*. Because we have two samples and heat flux density of electric heater is constant, therefore* $\dot{q}(t)=\dot{q}_o=\frac{U\cdot I}{2\pi r_o^2}$ *(U – voltage drop on the heater, I – current of the heater).*

We receive solution of initial-boundary problem (1)-(8) for $\Delta T(0,x,t)=T(0,x,t)-T_o$ in the form [3]:

$$\Delta T(0,x,t)=\frac{2\dot{q}_o\sqrt{t}}{b}\left[ierfc\left(\frac{x}{2\sqrt{at}}\right)-ierfc\left(\frac{\sqrt{r_o^2+x^2}}{2\sqrt{at}}\right)\right], \tag{9}$$

where: b is thermal effusivity, i.e. $b=\sqrt{k\rho c_p}$, whereas *ierfc(z)* is integral of complementary error function [4].

For $x=0$ we have $ierfc0=1/\sqrt{\pi}$. Then, from expression (9) we have:

$$\Delta T(0,0,t)=\frac{2\dot{q}_o\sqrt{t}}{b}\left[\frac{1}{\sqrt{\pi}}-ierfc\left(\frac{r_o}{2\sqrt{at}}\right)\right]. \tag{10}$$

Expression (9) is the basis of experimental method of simultaneous evaluation of three thermophysical parameters: thermal conductivity k, thermal diffusivity a and heat capacity c_p during one measurement. For argument $\frac{r_o}{2\sqrt{at}}>2.2$ function $ierfc\left(\frac{r_o}{2\sqrt{at}}\right)<0.003$ and expression (10) reduces to the form:

$$\Delta T(0,0,t)=\frac{2\dot{q}_o\sqrt{t}}{b}\cdot\frac{1}{\sqrt{\pi}}. \tag{11}$$

then, we can evaluate value of thermal effusivity b from the expression:

$$b=\frac{2\dot{q}_o\sqrt{t}}{\Delta T(0,0,t)}\cdot\frac{1}{\sqrt{\pi}}. \tag{12}$$

If the expression (12) is presented in figure for the dependence $\Delta T\left(\sqrt{t}\right)$ (Figure 2), the initial part of this chart is used to determine the value of thermal effusivity b.

The second part of dependence $\Delta T\left(\sqrt{t}\right)$ (Figure 2) is used to determine the value of thermal diffusivity a. Procedure for determining a results from transformation of the expression (10) to the form:

$$\frac{1}{\sqrt{\pi}}-\frac{b\Delta T(0,0,t)}{2\dot{q}_o\sqrt{t}}=ierfc\left(\frac{r_o}{2\sqrt{at}}\right). \tag{13}$$

Hence through iterative solution of the nonlinear equation (13) the value of thermal diffusivity in each point of the curve $\Delta T\left(\sqrt{t}\right)$ is evaluated - Figure 3. Final thermal diffusivity is evaluated as an average value of the results a in the chosen range of values $\sqrt{t}$ above the point A.

Then, from the thermal effusivity b we calculate respectively: thermal conductivity $k=b\sqrt{a}$ and heat capacity $c_p=k/(a\rho)$.

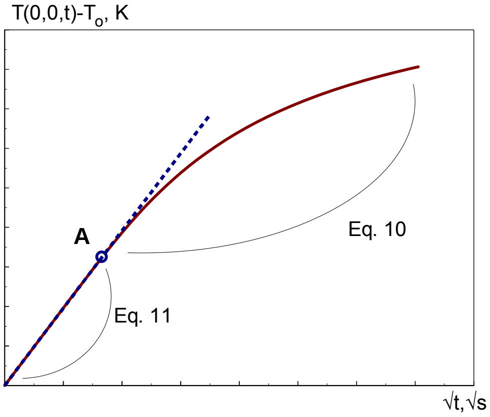

Figure 2: Dependence $\Delta T\left(\sqrt{t}\right)$. Illustration of the method of determination of thermal effusivity b. Point A – the end of linear portion of dependency described by Eq. 10.

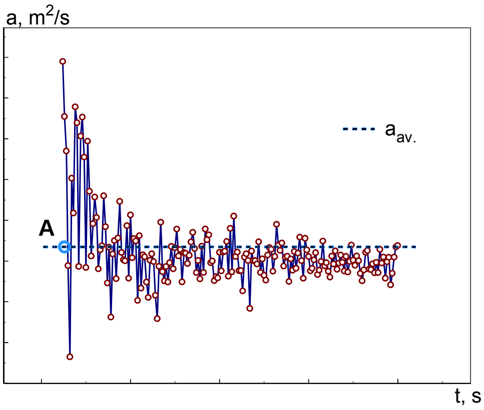

Figure 3: Technique of calculations thermal diffusivity $\bar{a} = a_{av.}$ on the basis of averaging solutions of Equation 10.

3. Experimental arrangements

In our Transient Plane Source technique, a 0.2 mm thick heater KHR 2/10, *cf.* Figure 4 is sandwiched between two identical pieces of sample material, *cf.* Figure 5. The same material must completely cover the sensor probe. Temperature measurement is carried out using thermoelements type *J* (Fe-CuNi) in points *Th3* and *Th4* (Figures 6 and 7) of the stock-pile. Wires of thermoelements are routed in the groves on the sample's surfaces along the diameter of the each sample. Thermoelements welds are located in the centre of the sample's surfaces along the axis of symmetry of the stock-pile. Heater KHR is supplied with direct current of a given voltage *U* and specified time duration t_o using a computer control power supply PPS 2017 (Meeter International Corp. - USA). Time t_o is also recording time of the thermal response system, i.e. signals from thermoelements *Th3* and *Th4*. Thermoelectric voltages are measured automatically by computer control multimeter Keithley 2000 by the card GPiB. A circle of radius $r_o = 22.5\ \text{mm}$ was adopted as an effective surface area of electric heater [5]. A step-wise heating power is applied to this heater, resulting in a transient temperature response that is recorded by the thermoelements *Th3* and *Th4.* To determine thermophysical properties of selected materials it is sufficient to measure the temperature as a function of time of only one termoelement. However, if this is possible it is beast to take the average of both signals, i.e. from thermoelements *Th3* i *Th4* (figs. 6 and 7). Assuming the thermally heated region, which grows into the surrounding sample with a time-dependent thermal penetration depth (depth of probing), never reaching the lateral or outer surfaces of the sample material. From presented model (Eqs. 9÷13), the thermal conductivity is obtained by plotting the temperature increase $\Delta T\left(\sqrt{t}\right)$ and extracting the conductivity from the slope of the best line-fit (Eq. 11). The thermal diffusivity *a* is obtained by an iterative procedure producing the best model fit of Equation 10 to the experimental data points.

Figure 4: Heater KHR 2/10: diameter - 50 mm.

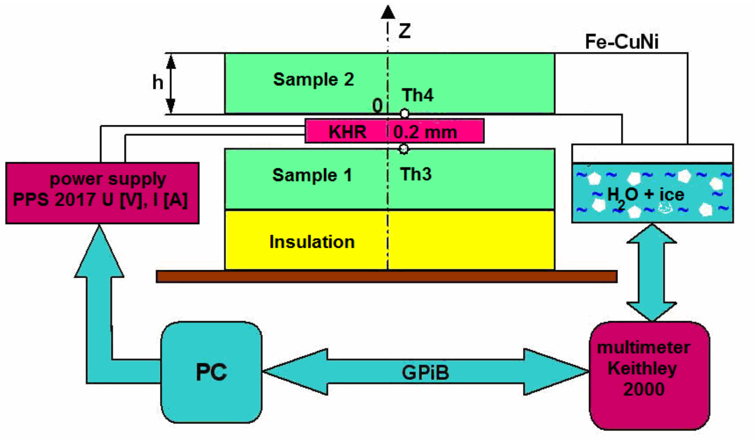

Figure 6: Diagram of measurement system: h - thickness of the samples 1 and 2, Th3 and Th4 - thermoelements.

Each of measurement samples 1 and 2 had a radius $r_o + \Delta p$ larger than the radius of the heater r_o. Criterion of selection Δp was connected with the dept of penetration of heat into the interior of the sample. Coordinate of a point $x = \delta = \Delta p$ at which the temperature change is 1% difference in temperature $T(0,0,t_o) - T_o$ was adopted as the depth of penetration heat into the interior of the sample. We obtain the desired value $x = \delta = \Delta p$ by iterative solution of equation:

$$\left[ierfc\left(\frac{\delta}{2\sqrt{at_o}}\right) - ierfc\left(\frac{\sqrt{r_o^2+\delta^2}}{2\sqrt{at_o}}\right)\right] = 0.01 \cdot \left[\frac{1}{\pi} - ierfc\left(\frac{r_o}{2\sqrt{at_o}}\right)\right]. \qquad (14)$$

As in the other dynamic methods, for example in the heat pulse method, so in the transient plane source method it is enough that the temperature excess over the ambient temperature $\Delta T(0,0,t) = T(0,0,t) - T_o$ (Fig. 7) does not exceed 2K and in fact should be between 0.4K and 1÷2K [6, 7].

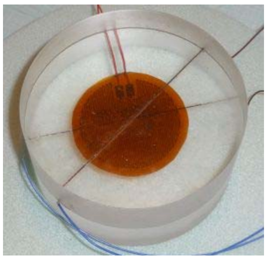

Figure 5: Stock-pile: heater KHR 2/10 and two samples PMMA

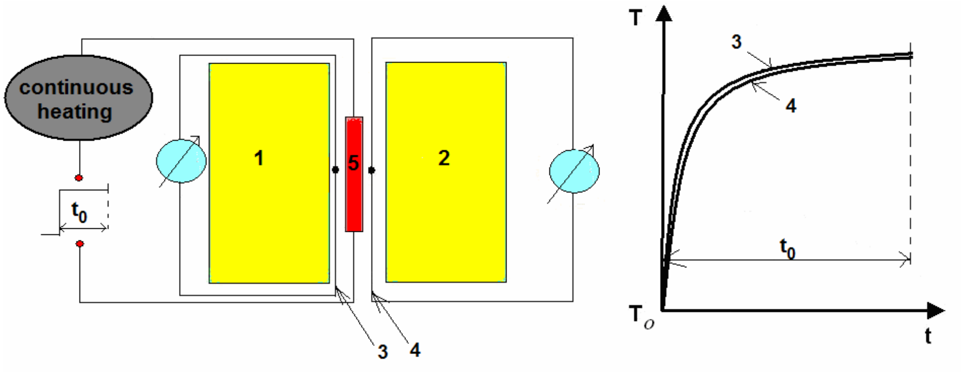

Figure 7: Scheme of transient plane source method: 1, 2 - samples, 5 - surface

4. Experimental results

For selected materials: foams – extruded polystyrene foam (XPS), polyurethane foam (Syspur SH 4055/1), polymers – plexiglas (PMMA), polyamide 6 (Pa6), metals – alloy steel 1H18N9T, duralumin (PA6), thermophysical coefficients: thermal conductivity *k*, thermal diffusivity *a* and specific heat c_p were determined by transient plane source method at room temperature. Dimensions of the disc-shaped samples of selected materials are shown in Table 1. Thermoelements types *J* (Heraus, Germany) of 0.1 mm in diameter, in Teflon coatings were used in our investigations. In metal samples the thermoelement welds were mounted in grove with pieces of about 1÷2 mm of soft solder wire, in the case of polymers and foams - the epoxy resin was used. In the case of duralumin due to the short sampling time 0.1 s a signal of only one thermolement was considered. In other cases it was the average signal from two thermelements. For example, for selected metals – alloy steel 1H18N9T (sampling time 1 s, *A*=11 s) and duralumin (PA6) (sampling time 0.1 s, *A*=0.7 s) in Figures 8 and 9 the calculation technique of transient plane source method was presented, i.e. the location of point A, evaluations of thermal effusivity *b*, evaluations of thermal diffusivity *a* and comparison evaluations with experiment. A comparison based on the correlation factor R^2, which determines the accuracy of an experiment, is carried out. For example, if at least R^2=0.995 or better, i.e. 0.999 - the experiment was performed correctly. Obtained results were as follows: for alloy steel 1H18N9T - R^2=0.9995, for duralumin PA6 - R^2=0.9975, for polyurethane foam Syspur SH 4055/1 - R^2=0.99795. For polyurethane foam (Syspur SH 4055/1) (sampling time 10 s) in Figures 10 and 11 results obtained by the transient plane source method were compared with measurements made with instrument Isomet 2104, which in this case were treated as reference data.

Table 1: Dimensions of the disc-shaped samples of different materials

metal	**1H18N9T**	**PA6**
sample diameter, mm	130.0	130.0
thickness sample *h*, mm	50.0	52.0
polymer	**Pa6**	**PMMA**
sample diameter, mm	94.5	100.0
thickness sample *h*, mm	33.1	30.4
foam	**Syspur SH 4055/1**	**XPS**
sample diameter, mm	130.0	130.0
thickness sample *h*, mm	40.0	40.0

According to the authors in the case of the apparatus Isomet 2104 we can not control the accuracy of an experiment, because the correlation factor R^2 is not given.

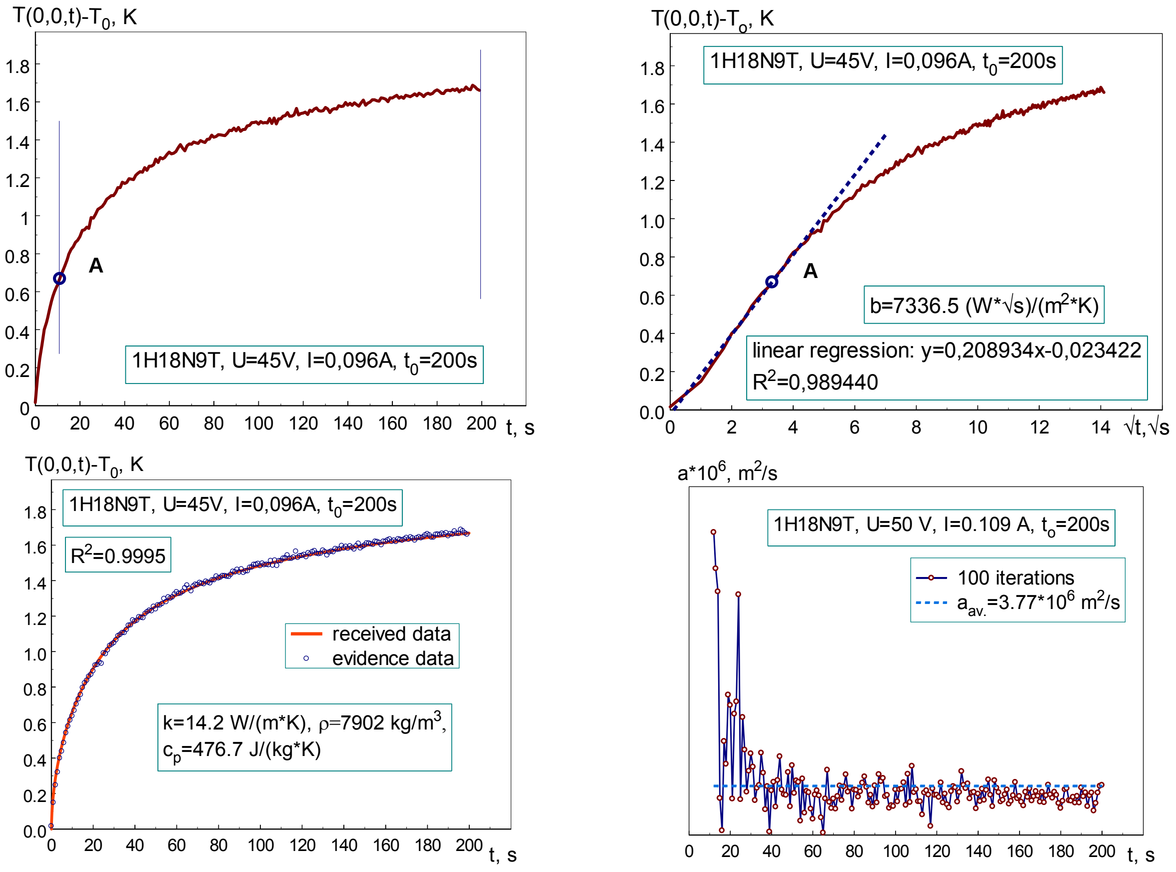

Figure 8 (4 upper figures - 1H18N9T)

Figure 9 (4 lower figures - PA6).

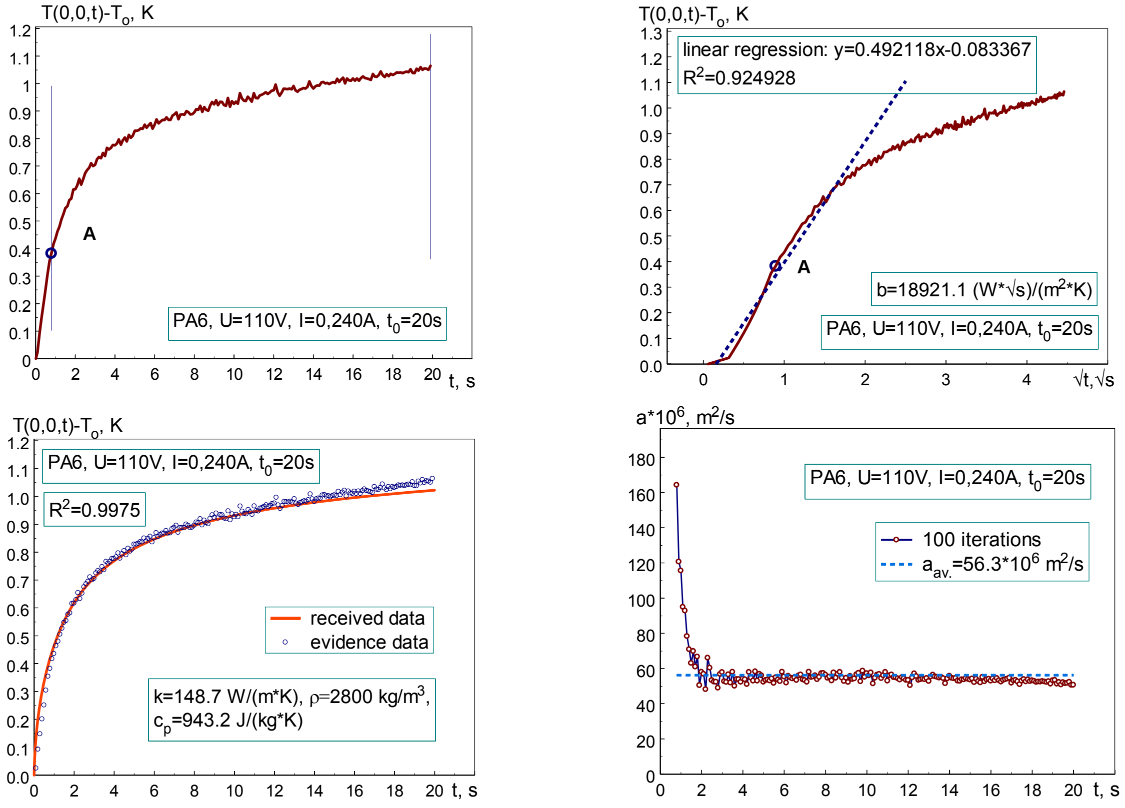

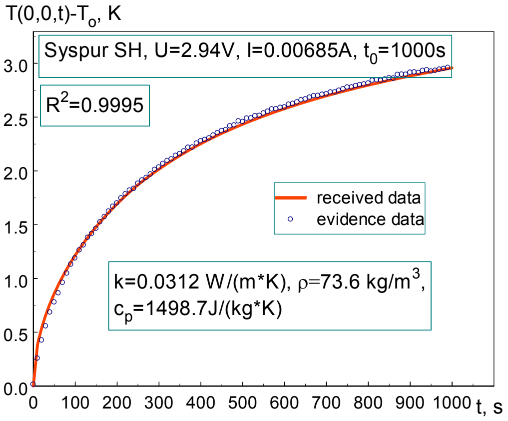

Figure 10. Comparison of dependence $T(0,0,t)-T_o$ obtained from experiment with dependence calculated from data obtained from this signal.

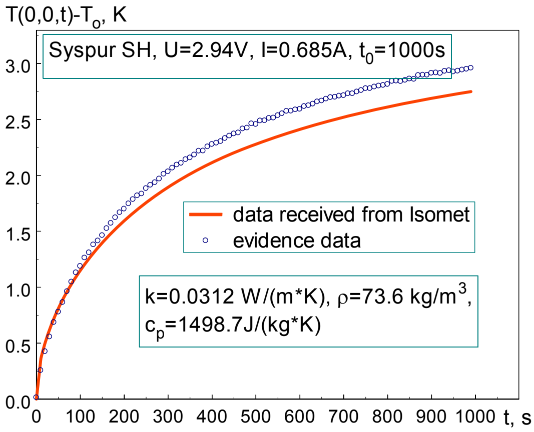

Figure 11. Comparison of dependence $T(0,0,t)-T_o$ obtained from experiment with dependence calculated from data obtained from Isomet 2104.

Results of measurement of thermophysical properties: *k, a* and c_p of selected materials are shown in Table 2.

Table 2: Reference data and results of measurements: k, a and c_p for selected materials together with measurement error (- Isomet 2104 – data received from Isomet 2104).*

material	**1H18N9T**	**PA6**	**PMMA**	**Pa6**	**XPS 3032 CS**	**Syspur SH 4055/1**
density ρ, kg/m^3	7902	2800	1181.0	1147.8	33 (BASF)	73.6
k, W/(m*K)	14.2	148.7	0.172	0.295	0.0402	0.0312
$k_{reference}$, W/(m*K)	12.8 [8]	134.0 [9]	0.192 [11]	0.311 [10]	0.0373 [*]	0.0339 [*]
$\lvert \Delta k/k_{reference} \rvert$, %	10.9	10.9	10.4	5.1	7.8	7.9
$a*10^6$, m^2/s	3.77	56.3	0.160	0.217	0.872	0.283
$a_{reference}*10^6$, m^2/s	3.44 [8]	54.8 [9]	0.120 [11]	0.221 [10]	0.956 [*]	0.297 [*]
$\lvert \Delta a/a_{reference} \rvert$, %	9.5	2.7	33.7	1.8	8.8	4.7
c_p, $J/(kg*K)$	476.7	943.2	900.0	1183.5	1397.0	1498.7
$(c_p)_{reference}$, $J/(kg*K)$	471.0 [8]	873.0 [9]	1319.0 [11]	1228.5 [10]	1181.82 [*]	1541.98 [*]
$\lvert \Delta c_p/c_{p\ reference} \rvert$, %	1.2	8.0	31.8	3.7	18.2	2.8

5. Conclusions

In the paper results of thermal properties of chosen materials including metals by transient plane source method were presented. Especially for metals flatness and smoothness of surfaces, perfect contact of sample's surfaces with surface of thin-layer heater and big pressure on stock-pile are required. Method gives promising results also for metals of big thermal conductivity, for example for copper. The authors already have the first results. In the case of copper thin thermoelements, big pressure and faster acquisition system of thermoelements reading are used.

Requirements described above are not valid in practice if we calibrate the measurement system and thereby obtain the calibration coefficients by conducting measurements on reference materials. Due to the limited volume of this paper, the authors will present the calibration technique for thermal effusivity b measurement by transient plane source method at the conference. Reference samples used in the calibration process do not have to meet the high requirements for surface smoothness. The big pressure for stock-pile is also not required.

At the end it should be stressed that for some materials the results should be treated as preliminary due to lack of reference data. In these cases the results were related to the measurements obtain using the apparatus Isomet 2104.

References

[1] GUSTAFSSON S.E. Transient plane source technique for thermal conductivity and thermal diffusivity measurements of solid materials, *Rev. Sci. Instrum.* 62:797-804, 1991

[2] GUSTAFSSON S.E., KARAWACKI E. and KHAN M.N., *J. Phys. D: Appl. Phys.* 12, 1411, 1979

[3] KOZLOW W.P. Two-dimensions axial non-stationary heat transfer problems, *Science and Technology*, Minsk 1986, in Russian

[4] ABRAMOWITZ M., STEGUN I.A. Handbook of Mathematical Functions with Formulas, Graphs and Mathematical Tables, *Dover Publications*, Inc, New York, 1965

[5] ZMYWACZYK J. Estimation of thermophysical parameters of solids by using of selected methods of optimization, DSc Thesis, Warszawa WAT 2006, in Polish

[6] KUBIČÁR Ľ. *Pulse Method of Measuring Basic Thermophysical Parameters, in Comprehensive Analytical Chemistry Vol. XII Thermal Analysis Part E*, Ed. Svehla G., Amsterdam, Oxford, New York, Tokyo: Elsevier 1990

[7] BOHÁČ V., DIEŠKA P., KUBIČÁR Ľ. The progress in development of New models for pulse transient method, Proc. THERMOPHYSICS 2007, 24-33, October 11 – 12, 2007, Kočovce chateau, Slovakia

[8] CORSAN J., BUDD N. and HEMMINGER W. High Temp. – High Press., 23, 119-128, 1991

[9] http://www.aluminum.w7m.pl

[10] KONIORCZYK P. Identification of heat transfer model in materials appearing in determination of thermal conductivity of selected plastics, *Doctors Thesis*, Military University of Technology, Warsaw, 1990

[11] RUDTSCH S., HAMMERSCHMIDT U., *International Journal of Thermophysics*, Vol. 25, No. 5, September 2004, pp. 1475-1482

Determination of Thermal and Moisture Parameters from the Transient Responses

Oldřich Zmeškal[1], Jaroslav Polcer[2], Lenka Hřebenová[1], Pavla Štefková[1]

[1]Brno University of Technology, Faculty of Chemistry, Purkyňova 118, CZ-612 00 Brno, CZECH REPUBLIC

[2]Romill s.r.o., Tkalcovská 799/14, CZ-658 92 Brno, CZECH REPUBLIC

Abstract: *The contribution is focused on the use of semi-differential method for transient (step wise) measurement evaluation to the determination of thermal and moisture parameters of different materials. A vacuum bottle with a planar thermal heat source (for the measurement of liquid and powdery materials) and a moisture chamber (for the measurement building material) were used.*

Analysis is based on a real thermal model that includes heat source thermal losses and losses to sample surrounding. A step-wise or pulse heating mode was used. The result s of analysis are presented as thermal parameters of studied (homogeneous, composites, liquids and powdery) materials – specific heat, thermal diffusivity, thermal conductivity.

A moisture chamber was used for the moisture properties study. The mass increment of absorbed water was measured after dipping a porous material into water. The sorption parameters were calculated from transient responses of increment mass (moisture diffusivity, moisture mobility, moisture volume).

Both very simple methods can be used for a quick determination of thermal and moisture parameters in different sectors (industry, agriculture, and building industry).

Keywords: *thermal parameters, moisture parameters, fractal parameters, step wise transient method*

1. Introduction

Many models have been earlier derived for heat transfer though the material and for determining of thermal parameters [1], [2]. Now it is evident that these models do not describe the experimental dependences accurately enough. The non-homogeneity of heat source, limited sample thickness, heat losses into surrounding and many other influences affect the measured results. So, new models which include some of these influences have been developed [3], [4]. Better agreements between the model and experimental data have been obtained with their application.

The article is based on the new data evaluation method, which was described in our previous paper [8]. The method results from generalized relations that were designed for the study of physical properties of fractal structures [6]. As is shown, these relations are in a good agreement with the equations used for the description of temperature time responses for a pulse input of supplied heat [1], [2]. Comparable outcomes of the thermal parameters (specific heat, thermal diffusivity, and thermal conductivity) with a classical method were obtained.

The new model originates from the non-homogeneity of heat source, limited sample thickness, and heat losses into surrounding and from other influences [10]. Better agreements between model and experimental data have been obtained with its application.

The vacuum bottle with resistive heat source of the diameter 72 mm (for water) was used. The temperature was measured by a thermocouple or platinum RTD.

A moisture chamber was used for the moisture properties study. The mass increment of absorbed water was measured after dipping a porous material into water. The lower parts of the sample may be sealed to prevent absorption into the surface pores (50×50) mm. The sorption parameters were calculated from transient responses of increment mass.

The method was applied for the studying of thermal (thermal diffusivity a, specific heat c, and thermal conductivity ◎) and moisture properties (moisture diffusivity ◎, sorptivity S, water absorption coefficient A) of various kinds of materials (water, concrete, aramid fibber, mineral wool).

2. Theory

The fractal theory of the thermo-physical properties description is derived, in general, from the field theory. It can describe the dependence of a change in physical quantities (e.g., in our case the temperature) on the energy (e.g., heat) transport process through a material. The trend of change can be expressed by the parameter *D* (so called fractal dimension) and the parameter *K* (so called fractal measure). The fractal dimension can describe the average change of properties of a physical quantity (e.g., temperature) in the whole material (it has a global character). The results for the special cases (point, linear and planar heat source – Dirac pulse) and a homogeneous infinite material were derived from a system of differential equations [9], [10]. The fractal dimension expresses the character (dimension) of the heat source (D = 1, 2, 3), see Fig. 1.

The fractal dimension gives the information about the properties of a real heat source (immediately after heating) and about the heat drain from the material to the surroundings in this case. The fractal dimension will be upper for a planar heat source and cylindrical sample ($D > 2$) or less ($D < 2$) then for an ideal heat source.

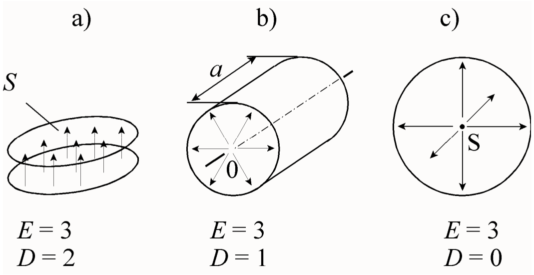

Figure 1: Heat flow geometry for (a) plane-parallel, (b) cylindrical, and (c) spherical coordinate Euclidean space

General fractal model of heat transport

The model will be derived from the fractal theory of physical field published by authors in [6]. The dependence of temperature on radius for the thermal field [8] can be written for this model as

$$\Delta T(r) = -\frac{\hbar c}{k_{\mathrm{B}}} \, \frac{K\, r^{D-E+2}}{D(D-E+2)}, \tag{1}$$

where k_{B} is Boltzmann constant, $\hbar$ is modified Planck constant, c is speed of heat propagation and K, D are fractal measure and fractal dimension, respectively. After some mathematical derivation we can rewrite Eq. (1) to the form

$$\Delta T(t) = \frac{P}{2\lambda} \frac{(4at)^{1-s}}{\pi^{s}} \exp\left[-\left(\frac{h^2}{4at} + \frac{4at}{R^2} \right) \right], \tag{2}$$

where the power of heat source (for three dimensional space: $E = 3$) can be written as $P = \lambda K \hbar c \pi^{s} \big/ \left[k_{\mathrm{B}} (2s-3)(1-s)^{s} \right]$, where $\lambda = c_{\mathrm{p}} \rho a$ is a thermal conductivity of real material, ρ is its mass density and c_{P} specific heat.

The dependence of cumulative mass of water (in kg/m^2) on radius for the moisture field [8] can be written for this model analogically as for temperature dependences

$$\Delta M(t) = \Delta M_0 \left(\frac{4\kappa t}{h^2} \right)^{1-s} \exp\left[-\left(\frac{h^2}{4\kappa t} + \frac{4\kappa t}{R^2} \right) \right], \tag{3}$$

where the moisture diffusivity κ, the parameter of sorption surface s and the parameter of moisture drain from the material during the sorption process R can be determined by the similar way as for temperature dependences [11] and the mass $\Delta M_0 = A (4\kappa / h^2)^{1-s}$ proportional to water absorption coefficient $A = S \rho_{\mathrm{w}}$, where S is a sorptivity of material and ρ_{W} is a density of water can be determined from the calculated the moisture diffusivity κ, parameter of contact quality s, the losses parameter R (the value $R \to \infty$ is for negligible losses).

Semi-differential method for evaluation of transient measurement

The described method can be used for the determination of the real fractal model parameters (2) using differential (difference) analysis. From the derivation

$$\frac{\mathrm{d} \ln \Delta T}{\mathrm{d}(1/t)} = -\frac{t^2}{\Delta T} \frac{\mathrm{d}\Delta T}{\mathrm{d}t} = \left[\frac{4at^2}{R^2} + (s-1)t - \frac{h^2}{4a} \right] = At^2 + Bt - C \tag{4}$$

of this fractal model, the parabolic shape is evident. The parameters of this parabola A, B, C determines the parameters: thermal diffusivity $a = h^2 / 4C$, quality of the thermal contact $s = B + 1$, its fractal dimension $D = E - 2s$ respectively, and the parameter proportional to measured sample diameter $R = h / \sqrt{AC}$.

Analogically to Eq. (4), the derivation of the logarithmic dependence of mass increment on the reciprocal time can be written

$$\frac{\mathrm{d} \ln \Delta M}{\mathrm{d}(1/t)} = -\frac{t^2}{\Delta M} \frac{\mathrm{d}\Delta M}{\mathrm{d}t} = \left[\frac{4\kappa t^2}{R^2} + (s-1)t - \frac{h^2}{4\kappa} \right] = At^2 + Bt - C\,. \tag{5}$$

The parameters of this parabola A, B, C determines the parameters: moisture diffusivity $\kappa = h^2 / 4C$, quality of the water contact $s = B + 1$, its fractal dimension $D = E - 2s$ respectively, and the parameter proportional to measured sample diameter $R = h / \sqrt{AC}$.

3. Experimental

3.1 Thermal measurement of water

The thermal properties of water were measured from temperature 0 °C (ice in the water) to temperature 100 °C (steam under water). The diameter of heat planar source was $2R = 0.072$ m and the distance of Pt resistor temperature detector (RTD) that was used for measuring the temperature was $h = 30$ mm. The heating power was in interval (1 – 20) W. The measurement was taken at a thermally insulated vacuum bottle.

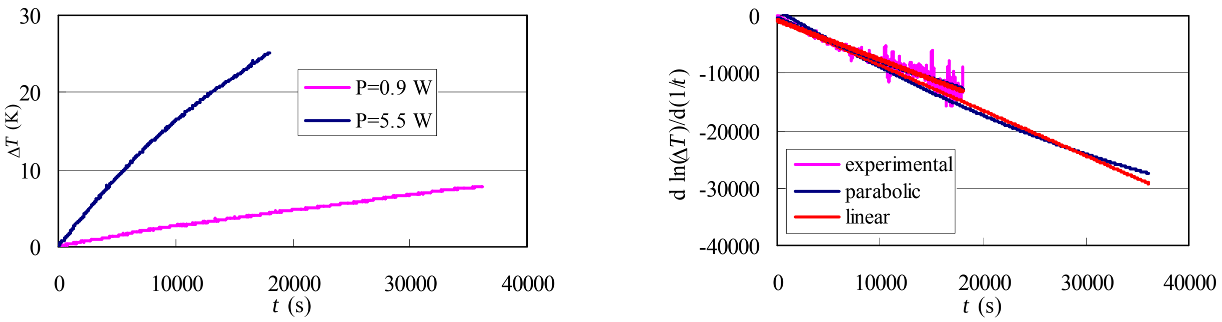

Figure 2: Transient response of temperature after a step-wise heating $\Delta T = f(t)$ *(left graph) and derivation* $\mathrm{d}\ln(\Delta T)/\mathrm{d}(1/t) = f(t)$ *for the determination of heat system parameters after the heating (right graph), see text.*

The responses of temperature of water after applying of two types of heat pulses are sets at the *Figure 2, left*. From the derivation of these dependences $\mathrm{d}\ln(\Delta T)/\mathrm{d}(1/t) = f(t)$ and their linear (or parabolic) approximation (*Figure 2, right*) we can calculate the thermal parameters, see Eq. (4). The results for non-losses cases (linear approximation) are at the *Table 1* together with tabulated parameters (at Wikipedia).

Table 1: Water thermal parameter (tabulated and calculated from step wise method, h = 30 mm, ρ *= 1000 kg.m*^{3}*)*

	material	**ΔT (K)**	**a (m^2/s)**	**D (–)**	**$2R$ (m)**	**λ (W/m/K)**	**c_p (J/kg/K)**
tabulated values	water (4 °C)		*1.4×10−7	2.000	0.072	*0.6	*2080
measured values	water (25 °C, $P = 5.5$ W)	25.2	2.80×10^{-7}	2.368	→ ∞	1.242	4436
	water (25 °C, $P = 0.9$ W)	7.8	3.14×10^{-7}	2.588	→ ∞	0.934	2979

* http://en.wikipedia.org/wiki/Thermal_diffusivity
* http://en.wikipedia.org/wiki/Thermal_conductivity
* http://en.wikipedia.org/wiki/Heat_capacity

3.2 Moisture measurement of concrete

The moisture properties (sorptivity) of water into concrete were measured in a moisture chamber. The material sample was in the form of a prism of a uniform cross-section. A typical size is (50×50×50) mm. The lower parts of the sample may be sealed to prevent absorption into the surface pores.

First the sample is dried at 105 °C to a constant mass in a hot-air oven and its dry mass is noted. After cooling to a room temperature, the sample is immersed in a tray of water. It should rest on rods or pins to allow a free access of water to the inflow surface. The water level should not be more than 5 mm above the base of the specimen. The quantity of water absorbed is measured at intervals (for instance 1, 4, 9, 16, and 25 min) by weighing the specimen. The water on the surface of the specimen should be wiped off with a dampened tissue. Each weighing operation should be completed as quickly as possible (typically within 30 s). Time measuring should not be interrupted during weighing.

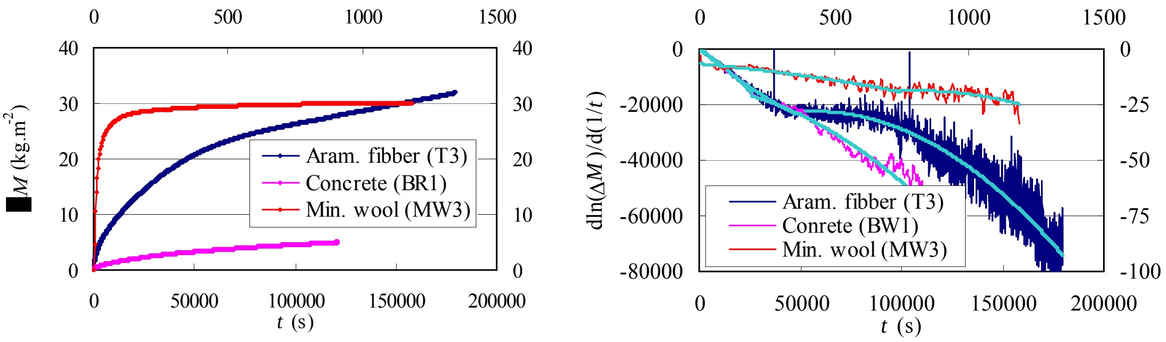

Figure 3: Transient responses of cumulative increment of moisture into concrete (material BR1), aramid fibber (T3) and mineral wool (MW3) $\Delta M = f(t)$ *and the dependences for the determination of sorption system parameters during the water sorption into materials* $\mathrm{d}\ln(\Delta M)/\mathrm{d}(1/t) = f(t)$*, see text. The dependences for concrete and aramid fibber are on the left and lower axes; the dependence for mineral wool is on the right and upper axes.*

Table 2: Moisture parameters calculated from step wise method responses (h = 50 mm)

material		κ **(m²/s)**	***D*** **(–)**	***R*** **(m)**	$\Delta M/\Delta M_0$	ΔM_0 **(kg m⁻²)**	**A (kg m²/s¹ᐟ²)**
Conrete	BM3	8.37×10^{-6}	2.207	3.08	12.4	0.058	0.00195
	BS2	1.42×10^{-4}	2.466	21.5	168.8	0.004	0.00003
	BP4	1.06×10^{-5}	2.372	2.42	28.3	0.048	0.00196
	BR1	7.73×10^{-6}	1.964	2.69	7.1	0.128	0.00266
Aramid fibber	T1	3.44×10^{-5}	2.023	376.81	35.2	0.543	0.00967
	T2	4.46×10^{-6}	2.374	3.39	22.6	0.896	0.12756
	T3	3.93×10^{-6}	2.271	5.55	18.2	1.115	0.12702
	T4	3.82×10^{-6}	2.353	2.97	22.8	1.026	0.15232
Mineral wool	MW1	1.73×10^{-4}	0.990	23.69	0.94	30.479	0.07535
	MW2	2.69×10^{-4}	1.015	35.81	1.04	27.737	0.07026
	MW3	2.41×10^{-4}	1.021	113.62	1.05	28.459	0.07258
	MW4	2.09×10^{-4}	0.918	5.20	0.88	30.141	0.06932

The results for three types of materials are presented in the *Figure* 3 and at the *Table* 2. From the figure is evident that different kinds of building materials have different properties. From the left *Figure 3* is evident that the sorption by concrete is least and on the other hand the sorption by mineral wool is largest. From the parameter analysis (*Figure 3, right*) we can see that the losses are negligible if the dependence $\mathrm{d}\ln(\Delta M)/\mathrm{d}(1/t) = f(t)$ is linear (for concrete it is to the time about 50 000 s). If the dependence is parabolic the losses have influence to the measurements.

From the *Table 2* we can see the basic parameters calculate from dependences at the Figure 4, right at the beginning part of dependences (small times). The interesting results give the parameter *D* (fractal dimension) what characterize the quality of sorption to material. The concrete and aramid fibber have better contact with water source as the mineral wool.

4. Conclusion

In this article, the method of transient responses analysis of different kind of dependences is described. This method was applied to thermal and moisture responses after step-wise initiations (supply of heat or moisture). The functionality of proposed method was confirmed by the agreement of tabulated and measured results. In addition, the method can be used for getting other parameters such as losses, the phase change reason parameters or moisture transport parameters).

Acknowledgment

This work was supported by grant KAN401770651 from the Academy of Sciences of the CR and by grant FR-TI1/144 from the Ministry of Industry and Trade of the CR

References

[1] CARSLAW H. S., JAEGER J. C. *Conduction of Heat in Solids*. Clarendon Press London. 1959

[2] KUBIČÁR Ľ. *Pulse method of measuring basic thermophysical parameters*. Elsevier, Amsterdam, Tokyo, Oxford, New York, 1990

[3] BOHÁČ V., DIEŠKA P., KUBIČÁR Ľ.: The Heat Loss Effect at the Measurements by Transient Pulse Method. In *Measurement Science Review*. 7: 24-27 (2007)

[4] BOHÁČ, V., KUBIČÁR, Ľ., DIEŠKA, P., NÉMETHY L.: Investigation of moisture influence on thermophysical parameters of PORFIX aerated concrete, in *Thermophysics 2009*, Valtice Chateau, Czech Republic, p.13 - 19 (2009), ISBN 978-80-214-3986-3

[5] VEJMELKOVÁ, E., PAVLÍKOVÁ, M., JERMAN, M., ČERNÝ, R.: Free Water Intake as Means of Material Characterization, *Journal of Building Physics*. 2009: 33(1). p. 29 - 44. ISSN: 1744-2591

[6] KUMARAN, M. K., Report on Measurements to Determine Moisture Diffusivity of Eastern White Pine, IEA Annex XXIV Report T3-CA-92/04 (1994)

[7] ZMEŠKAL, O.; BUCHNÍČEK, M.; VALA, M.: Thermal properties of bodies in fractal and Cantorian physics. *Chaos, Solitons & Fractals*. 2005. 25(5). p. 941 - 954. ISSN 0960-0779.

[8] ZMEŠKAL, O.; VALA, M.; WEITER, M.; ŠTEFKOVÁ, P.: Fractal-Cantorian geometry of space-time. *Chaos, Solitons & Fractals*. 2009. 42(3). p. 1878 - 1892. ISSN 0960-0779.

[9] ZMEŠKAL, O., HŘEBENOVÁ L., ŠTEFKOVÁ P.: Use of step wise and pulse transient methods for the photovoltaic cells laminating films thermal properties study, in *Thermophysics 2009*, Valtice Chateau, Czech Republic, p. 200 - 207 (2009), ISBN 978-80-214-3986-3

[10] ZMEŠKAL, O., ŠTEFKOVÁ, P., HŘEBENOVÁ, L., BAŘINKA R.: Pulse Transient Method as a Tool for the Study of Thermal Properties of Solar Cell Laminating Films. International *Journal of Thermophysics*. 2009. DOI 10.1007/s10765-009-0687-y

[11] ZMEŠKAL O., HŘEBENOVÁ, L., ŠTEFKOVÁ, P.: A New Differential Method for the Evaluation of Step Wise and Pulse Transient Measurements, 9th Asian Thermophysical Properties Conference. Beijing, China, China National Convention Center. October, 19 - 22, 2010.

List of participants

Prof. RNDr. Ing. Stanislav Šťastník CSc.
Brno University of Technology
Faculty of Civil Engineering
Žižkova 17
60200 Brno
CZECH REPUBLIC

Prof. Peter Šimon DrSc.
Slovak University of Technology
Faculty of Chemical and Food Technology
Radlinského 9
812 37 Bratislava
SLOVAKIA

M.Phil. Muhammad Abid
Physikalisch Teschnische Bundesanstalt
Arbeitsgruppe 1.74
Bundesallee 100
38116 Braunschweig
GERMANY

Beatrix Armero Lavie
Slovak Academy of Sciences
Dúbravská cesta 9
85411 Bratislava
SLOVAKIA

Prof. RNDr. Ivan Baník Ph.D.
Slovak University of Technology
Faculty of Civil Engineering
Radlinského 11
813 68 Bratislava
SLOVAKIA

Prof. Rachel Becker Ph.D.
Technion - Israel Institute of Technology
Haifa
Faculty of Civil and Environmental
Engineering Technion
Haifa 32000
32000 Haifa
ISRAEL

Dipl.-Ing. Andrea Binder
Fraunhofer Institute for Building Physics
Fraunhoferstr. 10
83626 Valley
GERMANY

Dipl.-Ing. Christian Bludau
Fraunhofer Institut of Building Physics
Fraunhoferstr. 10
83626 Valley
GERMANY

Ing. Vlastimil Boháč CSc.
Slovak Academy of Sciences
Institute of Physics, SAS
Dúbravská cesta 9
845 11 Bratislava 45
SLOVAKIA

Doc. RNDr. František Čulík, Ph.D.
Slovak University of Technology
Faculty of Civil Engineering
Radlinského 11
813 68 Bratislava
SLOVAKIA

Prof. Ing. Robert Černý DrSc.
Czech Technical University
Faculty of Civil Engineering
Thákurova 7
16629 Prague
CZECH REPUBLIC

Ing. Lukáš Fiala
Czech Technical University
Faculty of Civil Engineering
Thákurova 7
16629 Prague
CZECH REPUBLIC

Ing. Danica Fidríková
Slovak Academy of Sciences
Institute of Physics
Dúbravská cesta 9
84511 Bratislava
SLOVAKIA

MSc. Marcin Gapski, PhD student
Wojskowa Akademia Techniczna
Faculty of Mechatronics
Kaliskiego 2
00-908 Warsaw
POLAND

D.Sc. Darius Gawin Ph.D., M.E.
Technical University of Lodz
Department of Building Physics &
Building Materials
Al. Politechniki 6
90-590 Lodz
POLAND

Ing S. Olof Hägerstedt M.Sc.
Lund University
Building Physics
Box 118
221 00 Lund
SWEDEN

Mgr. Matúš Holúbek
Slovak University of Technology
Faculty of Civil Engineering
Radlinského 11
813 68 Bratislava
SLOVAKIA

Bc. Kamil Ďurana
Czech Technical University
Faculty of Civil Engineering
Thákurova 7
16629 Prague 6
CZECH REPUBLIC

Dipl.-Ing. Matthias Kersken
Fraunhofer Institut für Bauphysik
Fraunhoferstrasse 10
83626 Valley
GERMANY

Ing. Jan Kočí
Czech Technical University
Faculty of Civil Engineering
Thákurova 7
166 29 Prague 6
CZECH REPUBLIC

Ing. Václav Kočí
Czech Technical University
Faculty of Civil Engineering
Thákurova 7
16629 Prague 6
CZECH REPUBLIC

Assoc. Prof. Piotr Koniorczyk Ph.D., DSc., Eng.
Military University of Technology
Institute of Aviation Technology
Kaliskiego 2
00-908 Warsaw
POLAND

Daniel Kopkáně
Brno University of Technology
Faculty of Civil Engineering
Veveøí 95
60200 Brno
CZECH REPUBLIC

Ing. Tomáš Korecký
Czech Technical University
Faculty of Civil Engineering
Thákurova 7
166 29 Prague 6
CZECH REPUBLIC

prom. fyz. Ol'ga Koronthályová CSc.
Slovak Academy of Sciences
Institute of Construction and Architecture
Dubravska cesta 9
845 03 Bratislava
SLOVAKIA

Jozef Kováč
Constantine the Philosopher University
Tr.A.Hlinku 1
949 74 Nitra
SLOVAKIA

Ing. Ludovít Kubičár, DrSc.
Slovak Academy of Sciences
Institute of Physics SAS
Dubravska cesta 9
845 11 Bratislava
SLOVAKIA

doc. RNDr. Jozefa Lukovičová, Ph.D.
Slovak University of Technology
Faculty of Civil Engineering
Radlinskeho, 11
81368 Bratislava
SLOVAKIA

doc. Ing. Svetozár Malinarič, CSc.
Constantine the Philosopher University
Faculty of Natural Scientes
Trieda Andreja Hlinku 1
94974 Nitra
SLOVAKIA

Ing. Peter Matiašovský, CSc.
Slovak Academy of Sciences
Institute of Construction and Architecture
Dúbravská cesta 9
845 03 Bratislava 45
SLOVAKIA

doc. RNDr. Igor Medveď, Ph.D.
Constantine the Philosopher University
Faculty of Natural Sciences
Tr. A. Hlinku 1
94974 Nitra
SLOVAKIA

Ing. Peter Mihálka, PhD.
Slovak Academy of Sciences
Institute of Construction and Architecture
Dubravska cesta 9
845 03 Bratislava
SLOVAKIA

Jaroslav Nováček
Brno University of Technology
Faculty of Civil Engineering
Veveøí 95
60200 Brno
CZECH REPUBLIC

Mgr. Ján Ondruška
Constantine the Philosopher University
Faculty of Natural Sciences
Tr. A. Hlinku 1
94974 Nitra
SLOVAKIA

Prof. Andrzej Panas, Ph.D., DSc. Eng.
Military University of Technology
Faculty of Mechatronics
gen. S. Kaliskiego 2
00-908 Warsaw
POLAND

Ing. Gabriela Pavlendová Ph.D.
Slovak University of Technology
Faculty of Civil Engineering
Radlinského 11
813 68 Bratislava
SLOVAKIA

doc. Ing. Zbyšek Pavlík, Ph.D.
Czech Technical University
Faculty of Civil Engineering
Thákurova 7
166 29 Prague 6
CZECH REPUBLIC

Prof. B K Sarkar, Ph.D.
VIT University
Department of Physics
Vellore 632014
632014 Tamil Nadu
INDIA

Peter Šín
Constantine the Philosopher University
Faculty of Natural Sciences
Tr. A. Hlinku 1
949 74 Nitra
SLOVAKIA

Ing. Petr Slanina, Ph.D.
Benvelop
Jugoslávských Partyzánù 1580/3
16000 Prague
CZECH REPUBLIC

Prof. Henryk Sobczuk, Ph.D.
Lublin University of Technology
Faculty of Environmental Enginering
ul. Nadbystrzycka 40B
20-618 Lublin
POLAND

Ing. Zbigniew Suchorab, Ph.D.
Lublin University of Technology
Faculty of Environmental Enginnering
ul. Nadbystrzycka 40B
20-618 Lublin
POLAND

Prof. Mgr. Jan Toman, DrSc.
Czech Technical University
Faculty of Civil Engineering
Thákurova 7
166 29 Prague 6
CZECH REPUBLIC

RNDr. Anton Trník, Ph.D.
Constantine the Philosopher University
Faculty of Natural Sciences
Tr. A Hlinku 1
94974 Nitra
SLOVAKIA

Prof. Ing. Jiří Vala CSc.
Brno University of Technology
Faculty of Civil Engineering
®i¾kova 17
60200 Brno
CZECH REPUBLIC

Ing. Eva Vejmelková, Ph.D.
Czech Technical University
Faculty of Civil Engineering
Thákurova 7
166 29 Prague 6
CZECH REPUBLIC

Ing. Viliam Vretenár, PhD.
Slovak Academy of Sciences
Institute of Physics
Dúbravská cesta 9
84511 Bratislava
SLOVAKIA

Prof. Ing. Oldřich Zmeškal, CSc.
Brno University of Technology
Faculty of Chemistry
Purkyòova 118
612 00 Brno
CZECH REPUBLIC

Assoc. Prof Janusz Zmywaczyk, Ph.D
Military University of Technology
Faculty of Mechatronics
Kaliskiego 2
00-908 Warsaw
POLAND

Title	Thermophysics 2010 - Proceedings
Editor	Oldřich Zmeškal
Publisher	Brno University of Technology, Faculty of Chemistry, Purkyňova 464/118, CZ-612 00 Brno
Print	Brno University of Technology, Faculty of Chemistry, Purkyňova 464/118, CZ-612 00 Brno
Edition	first
Year of first edition	2010
Number of pages	350
Number of copies	80

ISBN 978-80-214-4166-8